UNIVERSITY OF SOUTHAMPTON

Faculty of Engineering and Physical Sciences
School of Physics and Astronomy

The Selection, Analysis and Implications of Rare AGN in Large Surveys

by

C. L. Greenwell

ORCiD: 0000-0002-7719-5809

A thesis for the degree of
Doctor of Philosophy

April 2023

University of Southampton

Abstract

Faculty of Engineering and Physical Sciences
School of Physics and Astronomy

Doctor of Philosophy

The Selection, Analysis and Implications of Rare AGN in Large Surveys

by C. L. Greenwell

There is a known connection between supermassive black hole growth and galaxy evolution (e.g., Kormendy and Ho, 2013). Grasping the nature of this connection requires understanding of both the growth of black holes via accretion, and how these processes can affect their host galaxies. In order to understand the feedback between them it is necessary to work towards a full census of the highly diverse population of AGN types. This thesis aims to address the work needed to complete this census by assessing the 'missing' AGN, applying different selection techniques to fill the gaps, and analysing the AGN found in this way.

Lack of a complete census of AGN means that knowledge of vital population statistics such as accretion rates or obscuration depths is incomplete. This thesis takes a first step to solving this problem through all-sky searches in the immediate, local universe via the Local AGN Survey (LASr; Asmus et al., 2020). In Chapter 2 we construct an unbiased sample of local AGN, including both known AGN and candidate AGN. We select these candidates using mid-infrared techniques, to identify AGN that have been missed in photometric surveys at other wavelengths. The aim of this is to work towards a complete sample of local AGN, and thus we must follow up the AGN candidates to confirm them as true AGN or discard them from the census. We construct the most complete all-sky galaxy sample within 100 Mpc (90% completeness for $\log(M_\star/M_\odot)\sim9.4$), four times deeper than the current reference (the Two Micron All-Sky Survey Redshift Survey; 2MRS), which misses $\sim$20% of known luminous AGN. Using MIR selection with *WISE*, we find 221 galaxies with $L_{nuc}(12\,\mu m)\gtrsim10^{42.3}$ erg s^{-1}. Among these are 61 new AGN candidates. We begin a follow-up campaign with these objects, aiming to use optical and near-infrared spectroscopy to perform AGN diagnostics and assess the results of our AGN candidate selection. Here we present results from the first three targets where we find two probable AGN, and analysis of an object believed to be a Compact Obscured Nucleus.

A major difficulty in selecting AGN - and hence an area where known AGN in LASr are scarce - is recognising heavily obscured AGN. Almost every selection technique is significantly biased against these objects and thus they are often missed from surveys, despite possibly representing periods of intense growth in AGN life cycles. The most promising method of selection is with hard X-rays (>10 keV). Selected from the 80-month *NuSTAR* Serendipitous survey (Klindt et al., 2022, submitted), and expanding on previous work on the 40-month catalogue (Lansbury et al., 2017a,b), in Chapter 3 we find sources with an excess of emission in the hard band (8-24 keV) compared to the soft band (3-8 keV), implying thick obscuration. We combine the *NuSTAR* data with available soft X-ray data (*XMM-Newton*, *Chandra*, or *Swift*-XRT depending on availability and exposure) to study the properties of these rare AGN. From 14 hard X-ray selected candidate Compton thick (CT) AGN we analyse the 9 with net sources >100, finding 4 CT (log $N_{\rm H}$>24 cm^{-2}) and the remainder heavily obscured (log $N_{\rm H}\gtrsim$23 cm^{-2}), implying a Compton thick fraction for *NuSTAR* selected AGN within $z < 0.07$ of 15^{+10}_{-6}% (combined with previous results from Lansbury et al., 2017a). Of the CT AGN, 29^{+21}_{-12}% appear to be in actively interacting systems.

In Chapter 4, at higher redshift we focus on one specific niche – Optically Quiescent Quasars (OQQs) – which are optically bright, IR-coloured AGN (*WISE* $W1-W2$ >0.8, and monochromatic luminosity above $\lambda L_\lambda(12\,\mu{\rm m}) \approx 3\times10^{44}\,{\rm erg\,s^{-1}}$) that lack major optical signatures. Initially we examine SDSS J075139.06+402810.9, a prototypical candidate at z=0.587, with an [O III] λ5007Å limiting flux about two dex below Type 2 quasars at similar IR power. The source is significantly detected over 0.5–16 keV with *XMM-Newton* and *NuSTAR*, unambiguously confirming the presence of current accretion activity. Spectral modelling yields an intrinsic luminosity $L_{2-10\,{\rm keV}} \approx 4.4\times10^{43}$ erg s^{-1}, well within the AGN regime, but underluminous relative to its infrared power. Expanding to the wider population in Chapter 5, we select 64 objects that show no significant [O III]λ5007 emission as our OQQ sample. This would typically be a strong optical emission line in AGN, and thus objects without it would normally be discarded. As a comparison sample, we examine SDSS-selected Type 2 quasars (QSO2s), which show a significant [O III]λ5007 line, but have otherwise similar properties to OQQs. We find a 1:16 ratio of OQQs compared to QSO2s, suggesting that the OQQ duty cycle is likely much shorter than the duty cycle of QSO2s (though selection biases are not fully quantified). These may represent the fully enshrouded or 'cocooned' phase of AGN growth, and comprehensive searches of such populations are thus vital to constrain AGN properties at important junctions in their evolution. Well-tested techniques based on searching for isotropically emitted AGN signatures would be ineffective to find such 'cocooned' phases, so this research aims to combine multi-wavelength selection techniques to uncover these hidden black holes. Alternatively, the observed lack of optical signatures may represent a *true* intrinsic lack of emission lines; for example, from a 'young' AGN only recently 'switched on'. Either of these possibilities make OQQs an interesting and under-studied avenue of AGN evolution.

With these three sections, I demonstrate the incomplete nature of our knowledge of the *true* AGN population. I show how different selection techniques can begin to fill in the gaps - firstly with ideal selection instruments operating over small areas to discover objects that are hard to find but not intrinsically rare, and secondly with more general vast surveys across large areas of the sky, finding rarer objects that may represent under-examined areas of AGN evolution. With *NuSTAR* I reveal three previously unknown Compton thick AGN and confirm another. Using a combination of MIR selection and optical *non*-AGN appearance I select a group of AGN and classify them as 'Optically Quiescent Quasars'. I make a detailed study of their properties, including an in depth analysis of a prototype OQQ. Finally, in Chapter 6 I conclude by placing these chapters into context with each other and with the wider AGN zoo.

Contents

List of Figures

List of Tables

Declaration of Authorship

I declare that this thesis and the work presented in it is my own and has been generated by me as the result of my own original research.

I confirm that:

1. This work was done wholly or mainly while in candidature for a research degree at this University;
2. Where any part of this thesis has previously been submitted for a degree or any other qualification at this University or any other institution, this has been clearly stated;
3. Where I have consulted the published work of others, this is always clearly attributed;
4. Where I have quoted from the work of others, the source is always given. With the exception of such quotations, this thesis is entirely my own work;
5. I have acknowledged all main sources of help;
6. Where the thesis is based on work done by myself jointly with others, I have made clear exactly what was done by others and what I have contributed myself;
7. Parts of this work have been published as:
   Asmus, D., Greenwell, C.L., Gandhi, P. et al. Local AGN survey (LASr): I. Galaxy sample, infrared colour selection, and predictions for AGN within 100 Mpc. *MNRAS*, 494(2):1784–1816, May 2020.
   Greenwell, C., Gandhi, P., Stern, D. et al. A candidate optically quiescent quasar lacking narrow emission lines. *MNRAS*, 503(1):L80–L84, May 2021.
   Greenwell, C., Gandhi, P., Lansbury, G. et al. XMM and NuSTAR Observations of an Optically Quiescent Quasar. *ApJ*, 934(2):L34, Aug. 2022.

Signed:..... Date:.....

Acknowledgements

I am not good at putting my feelings into words, but if I have spoken to you at all in the last four years then you have been a part of making this happen, and thank you.

I would like to thank my main supervisor, Poshak Gandhi, for giving me a chance, supporting me throughout, and giving me the opportunity to do so many things during my PhD I never would have thought I could. Thanks also to my ESO supervisor Vincenzo Mainieri for the support and guidance in a new country (and an unusually difficult time). Thanks to Daniel Asmus for all the help near the start. I also couldn't have done this without the help of Peter Boorman, who kept answering my questions even though he hasn't worked at Southampton for ages. And finally George Lansbury, for the invaluable help at ESO. I enjoyed working with all of you.

The whole Astronomy group at Southampton has been a wonderful place to work, they are the friendliest and most supportive group you could ask for. Thanks to Dale for being consistently supportive and cheerful, even from across the sea. Bella for great advice, and all your work as student rep. And particularly office 4057: Jakub, Miika, Alex, Mayukh, everybody who came in for coffee and a chat, and most of all my best desk buddy Arianna.

Thanks to my friends, especially Lydia for all the distractions.

I would also like to thank my family for their support and for so many things, but especially Mum for the big box of food I couldn't buy in Germany, Dad for managing to read this, Natalie for all the fun and games when I'm back home, and my grandparents for all the many cups of tea.

Finally: Izzy, I doubt this was how you thought it would go when someone suggested me for a housemate, but I don't think it could have gone better. I really couldn't have done this without you (and not just because of all the food).

This work has been supported by a Mayflower Scholarship provided by the University of Southampton, and an ESO studentship.

To my family.

Chapter 1

Introduction

This section will introduce background concepts, physics, and other information relevant to the thesis. It will also introduce the main questions this thesis aims to address, their background, and relevance to the wider field. It will outline the importance of finding and identifying unknown Active Galactic Nuclei (AGN), how a more complete AGN census will contribute to and enhance the interlinked topics of AGN and galaxy evolution, and how previously unidentified AGN could fill some gaps in current understanding.

1.1 General AGN Background

The evolution of galaxies over the lifetime of the universe is a major field of study in astronomy. One of the primary factors in this process is the presence of a supermassive black hole (SMBH; $\sim$ 10^6-10^9 $M_\odot$) in almost all but the smallest galaxies. Mass (and therefore growth) of SMBH and galactic bulge have been established as related in the local universe ($M_{\rm BH}\sim 0.006 M_{bulge}$; see e.g., Magorrian et al., 1998). In the further universe (see e.g., Yang et al., 2019, $z \sim 0.5-3$; Mullaney et al., 2012, $z \sim 1-2$) it has been shown that SMBH growth rate and star formation rate (SFR) are closely related for bulge dominated galaxies, but not for non-bulge dominated galaxies, indicating that it is the central bulge rather than the entire galaxy that evolves most closely with the SMBH. Evolution of SFR and SMBH growth rate have also been shown to be related on long timescales, peaking at similar redshifts (Aird et al., 2010; although there is no strong relation over shorter periods, possibility due to high AGN variability that gets averaged out over Gyrs).

Not all SMBHs accrete matter for all of their lives - most go through shorter phases of active growth between longer periods of inactivity. Accretion feeds the powerful source of electromagnetic radiation that we call Active Galactic Nuclei (AGN). The precise

fraction that are accreting (such as bright quasars) versus dormant (e.g., Sagittarius A* in the Milky Way) is unknown, partly due to the difficulty in estimating the numbers of highly obscured AGN.

1.1.1 AGN power

The extreme energy output from AGN originates from accretion (see e.g., Alexander and Hickox, 2012) - gas that comes close enough to the BH ($\ll$ parsec distances) to be affected by its gravity is drawn inwards. In the process large amounts of gravitational potential energy are lost from this material, and this energy is radiated outwards. The luminosity produced by a mass accretion rate of $\dot{M}$ onto a BH of mass M is given by:

$$L = \frac{GM\dot{M}}{R} \tag{1.1}$$

Conservation of angular momentum of the bulk of accreting material leads to the formation of an accretion disc. In an optically thick, geometrically thin disc (e.g., Shakura and Sunyaev, 1973) viscosity causes angular momentum from the infalling gas to be transferred outwards as the gas falls towards the BH. At low mass accretion rates the disc can instead be optically thin, and energy is lost via different processes; e.g. outflows. The temperature of the disc increases towards the BH, resulting in a spectrum that is a combination of different temperature black-body profiles.

Thus AGN can be seen to accrete with widely varying processes - to compare AGN behaviour across different scales, we can use measures of accretion such as the Eddington ratio and the radiative efficiency. The radiative efficiency is measure of how much of the gravitational potential energy in converted into radiation, and for a BH (mass M) accreting at a rate of $\dot{M}$ and with luminosity L it is given by:

$$\epsilon = \frac{L}{\dot{M}c^2} \tag{1.2}$$

Raimundo and Fabian (2009) find that high values of $\epsilon > 0.1$ and rapidly spinning BHs are required to reproduce the observed local mass function. High accretion rates ($L_{\rm Edd}/\epsilon c^2 \sim 0.01$-1) ensure that a geometrically thin disc is a good approximation of behaviour. At lower accretion rates, the disc 'puffs up' and becomes geometrically thick, with cooling becoming inefficient in optically thin discs. The effect of magnetic fields becomes more dominant. With weak magnetic fields in an accretion disc with decreasing angular velocity towards the outside, the rotation becomes unstable - magnetorotational instability (MRI; see e.g., Balbus, 2003). Simulations show this contributes to accretion processes in geometrically thin (e.g., Balbus and Hawley, 1991) or thick (e.g., Chan and Krolik, 2017) discs.

The Eddington luminosity is the maximum achievable luminosity before radiation pressure outstrips gravitational attraction (assuming spherical accretion and gas composed only of hydrogen), and is given by:

$$L_{\mathrm{Edd}} = \frac{4\pi G M_{\mathrm{BH}} m_{\mathrm{p}} c}{\sigma_{\mathrm{T}}} \tag{1.3}$$

where m_{p} is the mass of a proton and σ_{T} is the electron cross-section. In reality accretion is rarely spherical due to angular momentum, but L_{Edd} nevertheless provides a useful reference point. The Eddington ratio (λ_{Edd}) is the AGN bolometric luminosity (L_{bol}) as a fraction of Eddington luminosity (L_{Edd}).

$$\lambda_{\mathrm{Edd}} = \frac{L_{\mathrm{Edd}}}{L_{\mathrm{bol}}} \tag{1.4}$$

AGN show a wide variation in L_{Edd} and λ_{Edd}, with values depending on AGN class and redshift (Lusso et al., 2012). L_{bol} is not easily directly measurable, but can be estimated from various measurements: for example MIR luminosity as a reasonable probe of intrinsic disc luminosity (e.g., Vasudevan et al., 2010); alternatively assuming an SED can allow calculation of luminosities across a limited wavelength range, which can then be used to estimate bolometric luminosity. For example, Sagittarius A* has $\lambda_{\mathrm{Edd}} \sim 10^{-8} - 10^{-9}$; an extremely low end of the scale. Typical AGN have values in the range $10^{-4} - 1$, depending on mass.

1.1.2 Classification of AGN

There have been many efforts to classify observed AGN by their various properties. A comprehensive review of many of the classifications based on different properties across the electromagnetic spectrum can be found in Padovani et al. (2017).

Optical classification is generally based on strengths, ratios, and widths of typical AGN emission lines, for example [O III], H β, H α (noting that these may be present in e.g., star-forming galaxies - parameters of these in combination inform us about the source of emission). Other parts of the spectrum can also be used to classify AGN; some of these are observational classifications only, some suggest intrinsic physical properties of the AGN, and some result from interaction with the larger scale environment. A summary list follows, with details in further cited sections.

- **Optical classification (see Section 1.2.1.3):**
  - Quasi-Stellar Object (QSO) - first noted by Schmidt (1963), these are bright point sources found at larger redshifts and therefore higher luminosities than is possible for stars.

  - Seyfert Type 1 - galaxies showing bright, broad emission lines from the central region (FWHM $\geq$1000 km s^{-1}).
  - Seyfert Type 2 - galaxies showing bright, narrow emission lines from the central region (FWHM $\leq$1000 km s^{-1}).
  - Low Ionisation Nuclear Emission-line Regions (LINERs) - galaxies with low ionisation, narrow emission lines produced by gas irradiated by a non-stellar source. Although many of these are AGN, it is likely that a significant number are not (e.g., Márquez et al., 2017), and are instead ionised by alternative sources, e.g., shocks.
  - Blazars - AGN with jets that are directly - or near to - pointed towards the observer (i.e., viewed at $\sim$0° or 180° in Figure 1.1). Jet speed is relativistic and thus emission is beamed, making these sources extremely bright and variable. They generally also show strong radio emission (as the jet is a major source of this; Section 1.2.1.1) and in shallow imaging appear point-like as the nucleus far outshines the host galaxy.

- **Radio classification (see Section 1.2.1.1):**
  - Radio-loud/radio-quiet - these can be similar over most of the spectrum but with an observed flux difference of several orders of magnitude in the radio.
  - FRI/FRII (Fanaroff and Riley, 1974) - based on the spatial distribution of observed radio emission from the jets, possibly due partly to interaction with the inter-galactic medium.

- **IR classification (see Section 1.2.1.2):**
  - Ultra-Luminous Infra-Red Galaxies (ULIRGs) - extremely bright in the MIR, these tend to be disturbed galaxies. ULIRGs do not necessarily contain AGN, and thus this classification does not describe a type of AGN, instead a set of properties of galaxies that commonly host AGN.
  - Extremely Red Quasars (ERQs) - these show a relative excess of IR emission compared to optical.
  - IR Power-law AGN - objects selected to have an IR spectral shape heavily associated with AGN output; this is commonly the basis of MIR colour selection (Section 1.2.1.2, or e.g., Donley et al., 2012).

- **X-ray classification (see Section 1.2.1.5):**
  - Unobscured - with very low line-of-sight column density ($\log N_{\rm H}<22$ cm^{-2}) these sources have an apparent X-ray spectrum not significantly changed from its intrinsic shape, analogous to Seyfert Type 1 optical AGN.
  - Obscured - thicker line-of-sight column densities ($22<\log N_{\rm H}<24$ cm^{-2}) result in parts of the spectrum being attenuated, along with reflection and fluorescence effects appearing.

– Compton thick - column density increases beyond the Thomson scattering cross-section ($\log N_{\rm H}$>24 cm^{-2}), resulting in extreme absorption of the spectrum except at very high energies.

This list provides only an overview of major classifications. Many more detailed and well-defined sub-classes have been identified, such as XBONGs (X-ray Bright Optically Normal Galaxies; e.g., Caccianiga et al., 2007).

The generally accepted theory is that standard SMBH accretion takes the form of a disc of matter orbiting and falling towards the central mass. The Broad Line Region (BLR) outside of this consists of heated ionised gas, moving with very high velocity, and producing the broadening of emission lines characteristic of Type 1s. The Narrow Line Region (NLR) lies further out, consisting of cooler gas at lower velocities, and producing the narrower emission lines we associate with Type 2s. Surrounding this is a dusty 'torus', stretching from the sublimation radius (the point at which dust can no longer exist at the high temperatures closer to the black hole) out to scales much larger than this (see Figure 1.1). The exact arrangement of these components, the sizes, the spatial geometry, the radiative properties, and the range of these properties that occur are difficult to determine. While many individual AGN, and small samples, have been studied in detail, deducing anything about the wider population of related objects can be difficult.

1.1.3 Unification theory

The unification scheme of AGN (discussed in many papers, e.g., Ueda et al., 2014) attempts to unify these disparate classes into a single group, with the differences being mainly due to orientation angle, intrinsic luminosity (e.g., some suggestion of dependence of covering factor on intrinsic luminosity; Stalevski et al., 2016) and, to a lesser extent, other intrinsic variations (e.g., the presence or absence of jets). Line of sight to the AGN can be directly onto the accretion disc, resulting in an unobscured AGN (e.g. $\sim$0 degrees in Figure 1.1), through the 'torus' so that the accretion disc and BLR are not visible, but NLR is ($\sim$90 degrees in Figure 1.1), or at angles in between. This model suggests that all AGN are fundamentally similar. However, this unification does not explain every observed property of AGN (e.g., 'Changing Look' AGN, or those with intrinsically weak emission lines), but goes a long way towards explaining a large number of objects. AGN that are not completely explained by any existing scheme can be among the most interesting objects, but also frequently have very little data available.

Seyfert galaxies have been further classified into subgroups between 1 and 2 (e.g., 1.5, 1.8) derived from the relative strength of the broad and narrow components of emission lines. The unification of Seyferts is based on the dusty 'torus' obscuring the broad line region from some angles, leaving the narrow region only visible. From higher viewing

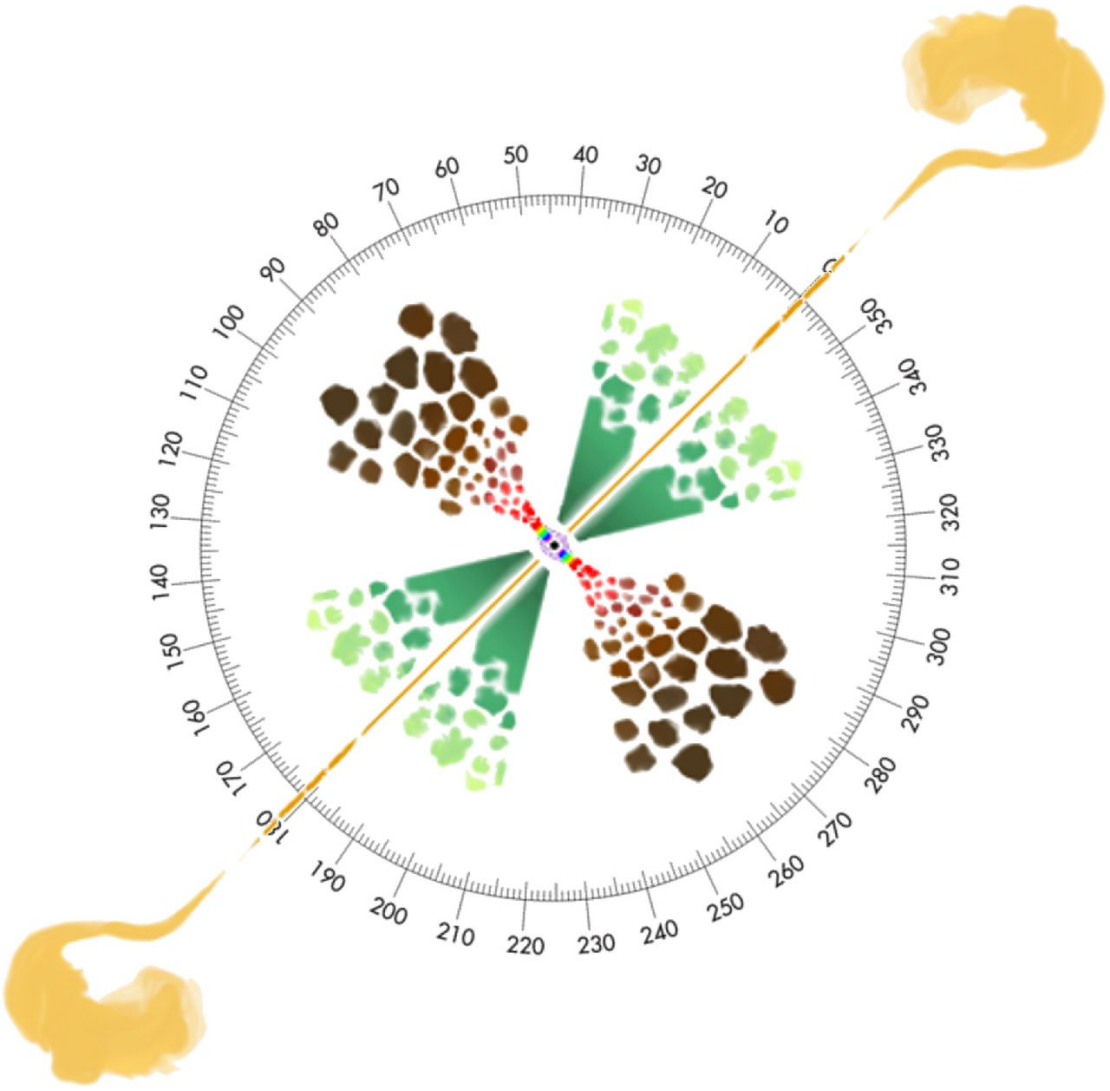

FIGURE 1.1: Graphic and caption from Marin (2016). Unscaled sketch of AGN unification theory. Colour code: the central SMBH is in black, the surrounding X-ray corona is in violet, the multitemperature accretion disc is shown with the colour pattern of a rainbow, the BLR is in red and light brown, the circumnuclear dust is in dark brown, the polar ionised winds are in dark green and the final extension of the NLR is in yellow-green. A double-sided, kilo-parsec jet is added to account for radio-loud AGNs.

angles, both regions are visible. Intermediate Seyfert types derive from viewing angles looking through the edge of the dust, where it is less obscuring. The average covering factor (the fraction of a full sphere that is obscured by dust) can be estimated by looking at the ratio of numbers of different Seyfert types, but the values found from these are not always in agreement, and may vary with other properties of the AGN (i.e., intrinsic luminosity). The exact geometry of the dust distribution is also under debate - it is often referred to as a 'torus', but this is thought to be an oversimplification of the structure. Many models try and account for observed data with a more accurate intrinsic geometry. For example, Figure 1.1 is an unscaled schematic of AGN structure (Marin, 2016) that shows the result of differing angular views: a type 1 AGN is seen at

approximate inclinations 0°–60° (i.e., when an observer would have line-of-sight to the NLR) while a type 2 AGN is seen at 60°–90° (when the line-of-sight is blocked by the torus).

1.1.4 AGN evolution

Knowledge of the demographics of the AGN population is essential to our understanding of how they evolve and influence their host galaxies. The majority of AGN are affected by obscuration, which hides signatures from the centre (e.g., Ananna et al., 2020).

The orientation-based unification paradigm has helped enormously in providing structure to this quest (e.g., Antonucci, 1993, Netzer, 2015, Ramos Almeida and Ricci, 2017). However, it has long been clear that this cannot be the whole story. In particular, AGN have been shown to grow together with their host galaxies, on average, and the effect of changing external influences (such as interaction with other galaxies) on their environment remains poorly understood. Finding AGN at various evolutionary phases requires not only probing to higher redshifts, but also adapting and combining common AGN selection strategies in new directions.

AGN do not remain in a single state of luminosity or obscuration for their lifetimes. They have been shown to vary over short timescales (e.g., Aranzana et al., 2018). Long term variation may be due to varying amounts of mass available for accretion. For example, Hopkins et al. (2008) describe the possible evolution of AGN activity due to a gas rich merger (see Figure 1.2). The initial gas influx of the merger causes a sharp increase in star formation rate, then as the gas reaches the central SMBH, causes the AGN to become dominant, although still obscured. The remaining gas and dust is pushed away by the increased power of the AGN, and it becomes unobscured. Once the accreting material is used up, the AGN fades. This is only one possible narrative for the changing views of AGN. Dramatic changes in AGN output unrelated to mergers have also been observed. On shorter timescales (∼years compared to Myrs) 'Changing Look' AGN display the signs of different classes over time - this can be optically (i.e., from Seyfert 1 to Seyfert 2) or X-ray (e.g., obscuring clouds moving through the line of sight). These differences can be due either to changes in accretion or variable obscuration; see Section 1.1.6. The source of these changes is not always well understood, and the advent of high repeat timing surveys like *LSST* (see Section 1.3.9) will start to shed light on these processes.

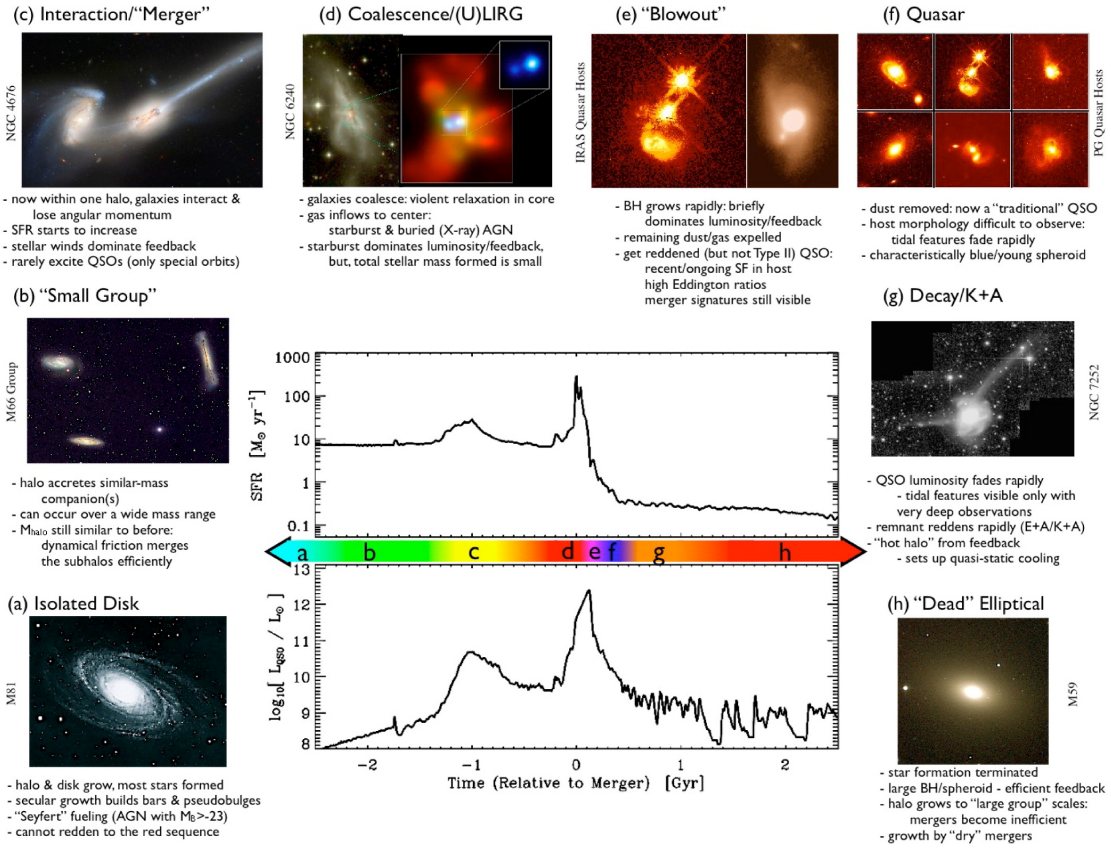

FIGURE 1.2: Schematic outline of the phases of growth in a "typical" galaxy undergoing a gas-rich major merger. Graphic from Hopkins et al. (2008). Image credit: (a) NOAO/AURA/NSF; (b) REU program/NOAO/AURA/NSF; (c) NASA/STScI/ACS Science Team; (d) optical (left): NASA/STScI/R. P. van der Marel & J. Gerssen; X-ray (right): NASA/CXC/MPE/S. Komossa et al.; (e) left: J. Bahcall/M. Disney/NASA; right: Gemini Observatory/NSF/University of Hawaii Institute for Astronomy; (f) J. Bahcall/M. Disney/NASA; (g) F. Schweizer (CIW/DTM); (h) NOAO/AURA/NSF.

1.1.5 Obscuration Models

Large scale accretion onto AGN is unlikely to be perfectly isotropic, or perfectly disc-like, for the entirety of their accreting lifespans. Studies of the Cosmic X-ray Background (CXB, see Section 1.4.1) conclude that there must be many highly obscured AGN contributing to the observed X-rays. The observed shape of the X-ray luminosity function (XLF) cannot be reproduced with observed proportions of AGN at different N_H levels. Works on population synthesis models find that high fractions of Compton thick AGN are required to produce the observed XLF due to their distinctive humped spectrum, contributing only at a restricted range of energies (see e.g. Fig. 11 of Ananna et al., 2019). The geometric form of the obscuring dust depends strongly on luminosity, implying a response by the dust to the intrinsic AGN radiation. As AGN are known to be intrinsically variable, and this response cannot be instantaneous, there must exist some objects where the AGN is extremely bright, but the dust has not yet been reshaped and its covering factor reduced. AGN variability may not always result in

changes in obscuration - for example, if the variation is on shorter timescales or over smaller ranges of luminosity, the obscuring material may not respond. Many models deduce that a large proportion of SMBH growth occurs in highly obscured phases like these. These high covering factors could indicate strong but temporary growth rates (in the absence of specific quantitative information like Eddington ratios, large amounts of material around the BH could imply that accretion is greater than in a less busy system). They could be the result of merger-driven turbulence (with the large influx of material producing a transient, unstable, phase of higher covering factor than would be sustainable long-term). The high luminosity could indicate a 'switch on' in AGN power due to this increase in available accretion matter. An alternative explanation could be that these are not a transient state for the AGN, but a semi-stable longer term form, for example if the accretion rate is slow or the dust cocoon is being consistently fed.

Sources with extreme covering factors approaching unity could probe a unique phase in AGN evolution, indicating either strong growth rates with plenty of available circumnuclear matter for accretion, or perhaps sky covering as a result of merger-driven turbulence. Several studies have linked galaxy mergers with higher rates of obscured AGN in MIR selected samples (e.g., Glikman et al., 2012, Weston et al., 2017, Satyapal et al., 2017). Although Seyfert galaxies with high covering factors approaching unity have been inferred in detailed individual studies (Ramos Almeida et al., 2009), the covering factor of AGN is seen to decrease in higher luminosity objects (see Section 1.2.1.2; Lawrence, 1991). Theoretically, accretion from large scales is not expected to be isotropic and is likely to be mediated via discs, warps and other instabilities (e.g., Hönig, 2019). In certain models of AGN evolution, for instance, significant growth occurs while the central engine is completely enshrouded by obscuring material with $\sim 4\pi$ sky covering factors (e.g., Fabian, 1999). Well-tested techniques based on searching for isotropically emitted AGN signatures would be ineffective in finding such 'cocooned' phases.

As discussed above, there are two natural conclusions: high covering factors are associated with high growth (and consequently high intrinsic luminosity); and covering factors are observed to decrease with high observed luminosity. These are not incompatible. Firstly, if we consider AGN growing along the 'typical' path shown in Figure 1.2 then highly obscured AGN will occur in phase (d), with large influxes of material causing both extensive covering and fast growth. In phase (e) the increased AGN luminosity blows out material and covering factor is reduced for more luminous sources. In this case, we might expect luminous, fully covered AGN to be rare, but interesting sources that may expose this brief phase in AGN evolution. Secondly, not all AGN will follow the same evolutionary path - the reduction of covering factor with luminosity is not universally found. Considering also that the unification model does not explain all observed properties (e.g., Klindt et al., 2019), and that AGN do not complete their

growth in a single active phase (e.g., Schawinski et al., 2015) then investigating these unusual sources could provide insight into the complex puzzle of AGN growth.

One limitation of most works on covering fraction to date is the requirement for the presence of AGN emission lines (typically forbidden lines from the narrow line region) in the optical or near-infrared, which are used to confirm the presence of an AGN and/or redshift identification. If AGN emission lines are observed, this implies that some optical power must be escaping the AGN environment and the source cannot be fully covered. The presence of dust in AGN NLRs has been known for some time (e.g., Netzer and Laor, 1993, Haas et al., 2005, Netzer et al., 2006) and can attenuate forbidden line fluxes, but selecting *fully* covered AGN is difficult, given the obvious observational biases against identifying such a population. Searches for such AGN could be promising at wavelengths less susceptible to dust (e.g. NIR emission lines; Gandhi et al., 2002, Imanishi et al., 2010 or hard X-rays; Ueda et al., 2007), but the prevalence of such populations still remains unclear, especially at the luminous end. However, recent large surveys now enable studies such as these, searching for elusive AGN subtypes, to be carried out.

The obscuration is also not likely to be generally either static or uniform. Hönig (2019) shows that IR and sub-mm observations of the AGN system at very high resolution can be best explained by a disc of accreting matter that puffs up towards the centre combined with a dusty outflow. Thus the picture presented above in Section 1.1.3 is a much simplified ideal, and considering the ways that real AGN deviate from this is vital to understanding the overall population. The material that makes up the 'torus' is now thought to be clumpy rather than smooth (e.g., Nenkova et al., 2008a,b), which is reflected in detailed X-ray models such as XCLUMPY (Tanimoto et al., 2019). For lower resolution observations, this structure is harder to distinguish and hence considering the obscuration as a uniform 'torus' can be a useful simplification – but it is still a simplification.

Obscuration is not limited to AGN-local material. Galaxy-scale obscuration has been shown to play a role in AGN obscuration, although it is unlikely to approach Compton thick column densities. For example, Buchner et al. (2017) analyse gamma ray bursts and find a relationship between stellar mass and galaxy $N_{\rm H}$ with this column density varying from $10^{20-23}\,{\rm cm}^{-2}$. In Buchner and Bauer (2017) they use this relationship to distinguish between galaxy and AGN obscuration, and show that galaxy-scale obscuration may be responsible for a reasonable fraction of Compton thin AGN.

1.1.6 Changing Look AGN

The column density and geometry of obscuring matter are expected to naturally evolve as AGN and their host galaxies grow, and many models posit that the bulk of supermassive black hole growth occurs in highly obscured phases (e.g., Fabian, 1999, Di Matteo et al., 2005, Hopkins et al., 2006). AGN are also known to appear to change classification over time, from Type 1 to 2 and vice versa (Yang et al., 2018). These objects, referred to as 'Changing Look' AGN, show changes in emission line and continuum flux over timescales up to a few years. The physical mechanisms behind these changes are not well understood: the two main theories are variation in line-of-sight obscuration (e.g., a clumpy torus; Elitzur, 2012), or change in accretion rate (e.g., Sheng et al., 2017, Stern et al., 2018). The timescales over which many CLAGN are observed to vary makes this second scenario – variable emission – more likely than changes in obscuration, which happen on larger scales and thus over longer times (e.g., LaMassa et al., 2015, MacLeod et al., 2019). Any unusual AGN appearance must be considered in this context - lack of emission lines could be a transitional state of changing obscuration, or a change in intrinsic line production. Obscuration can take many forms, both stable (resulting in diverse AGN classes, e.g., Seyfert 1, Seyfert 2; Padovani et al., 2017), and transient (some 'Changing Look' AGN e.g., Risaliti et al., 2005, Ricci et al., 2016).

Similarly, AGN undergoing transitions may fail to be recognised as such. A sudden onset of accretion activity on to a SMBH would require time to manifest itself on kpc scales, due to the light-travel time to the NLR. During this phase, AGN may appear to be 'optically elusive', and finding such objects can constrain AGN duty cycles (e.g., Schawinski et al., 2007). Comprehensive searches of such populations of objects are thus vital to constrain AGN at important junctions in their evolution. Objects in the process of 'switching on' are a rare, brief chapter in the growth of AGN; an important but not well understood period.

1.2 How do we search for AGN?

Understanding Active Galactic Nuclei (AGN) growth and evolution remains an active research theme. Much of the uncertainty and contention arises from the fact that AGN selection is a non-trivial problem. Broadband multiwavelength emission originates over a vast range of (logarithmic) physical scales of accreting and outflowing matter around the central engine, and is further sculpted by obscuration and scattering due to dust and gas (e.g., Brandt and Alexander, 2015, Hickox and Alexander, 2018) – AGN that are obvious in one selection regime can be well hidden in others. If we are to find and understand the complete AGN population, broadband strategies are therefore necessary.

AGN selection in each regime of the electromagnetic spectrum has both advantages and drawbacks (Brandt and Alexander, 2015, Padovani et al., 2017). Optical selection, using typical AGN emission lines, can miss heavily obscured or intrinsically faint objects (Hickox and Alexander, 2018). Infrared (IR) selection offers the chance to investigate AGN without optical signatures – the majority of IR emission from AGN is reprocessed in the dusty regions, and therefore relatively unbiased (Gandhi et al., 2009, Asmus et al., 2015). Multi-wavelength studies using combinations of large surveys can be used to select AGN with interesting properties; furthermore extreme, unusual objects can be found in these vast datasets.

1.2.1 What signals do we see from them?

The direct emission from the accretion disc in AGN (see Section 1.1.1) is highest in the UV (see Section 1.2.1.4), but AGN are generally strong sources of radiation across the whole electromagnetic spectrum. This intrinsic emission is modified by various processes, resulting in the observed spectrum. These processes (and their signatures) are different for various wavelength regimes. Figure 1.3 shows a typical AGN Spectral Energy Distribution (SED) across the spectrum, and in this section I will outline the AGN signals found in each region, their physical origins, and considerations on selecting AGN based on emission in each band.

1.2.1.1 Radio

Radio emission is not observed in all AGN - 'radio loud' and 'radio quiet' galaxies show a large difference in observed flux (see the yellow lines in Figure 1.3), which is parameterised in various ways (e.g., Baloković et al., 2012). These may be intrinsically different types of AGN (e.g., Padovani, 2016). The bulk of radio emission is seen in large scale jets which can extend over kiloparsecs (see Figure 1.1), and the shape of these leads to another divide in radio galaxy class: type I and II (Fanaroff and Riley, 1974, ; distinct from Seyfert types). FRI galaxies show radio emission close to the nucleus, and FRII show a large separation between the brightest regions.

The physical process by which radio emission in AGN is produced is synchrotron emission - relativistic charged particles accelerated in magnetic fields. The spectral shape produced by this is a powerlaw $\propto \nu^{-\alpha}$, and is often described as non-thermal emission. Star-forming galaxies also produce synchrotron radiation, although this is usually intrinsically weaker and does not appear in kpc-scale jets.

In this thesis radio emission is not considered in depth - indeed, as blazars (see Section 1.1.2) are generally very strong radio sources and confidently known to be AGN, in

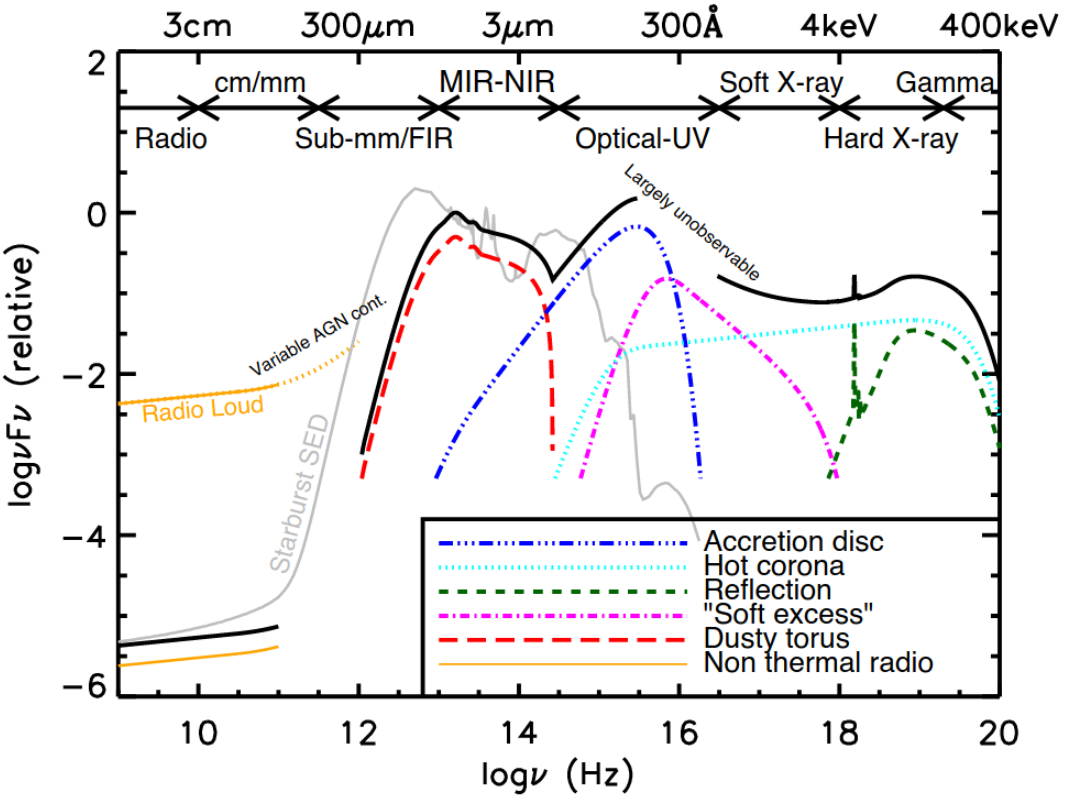

FIGURE 1.3: Multi-wavelength unobscured AGN SED (black curve), with the main physical components in coloured curves, In grey the SED of a star-forming galaxy is shown for comparison. Figure from Harrison (2014)[a].
[a] http://etheses.dur.ac.uk/10744/

Chapter 5 we consider strong radio emission to be a sign that the apparently flat spectrum of our 'hidden' AGN is not flat for the reasons we are searching for. However, there is evidence that heavy obscuration and more luminous radio emission can be associated: Andonie et al. (2022) find that heavily obscured AGN show an excess of radio emission compared to unobscured systems, possibly from either compact jets or AGN outflow shocks. These systems also show increased star-formation and the differences are unlikely to be due to a difference in orientation alone.

Radio can be used to select AGN that are low apparent luminosity due to dust extinction or obscured optically: Glikman et al. (2012) select dust-reddened quasars based on 2MASS colour and detections at 1.4 GHz in FIRST. They consider the distinction between *reddened* Type 1 AGN and *obscured* Type 2 AGN, and find that red quasars are intrinsically luminous and thus likely to be in highly accreting phases, postulating that this reddened phase is part of the evolution of AGN from enshrouded growth to unobscured. In Glikman et al. (2022) they investigate radio-independent selection of red quasars and their radio detection fraction, finding that red quasars are both brighter and have steeper spectral slopes.

1.2.1.2 Near and Mid-Infrared

The infrared regime is particularly effective for studies of AGN dust covering factors, and for studies of AGN with absorbed optical signatures. This is because dust serves as a bolometer, absorbing and reprocessing the AGN power to the mid-infrared (MIR) and providing a probe of the obscuring material in *emission* – as opposed to the *absorption* pathway provided in optical and X-ray studies. This material is predominantly located in the 'torus' (see Figure 1.1), but can also be found in dusty outflows and on larger scales. IR is less affected by extinction than e.g., optical emission, and hence can better penetrate dusty obscuration. High angular resolution multiwavelength studies suggest that the MIR emission is effectively isotropic (Gandhi et al., 2009, Levenson et al., 2009, Asmus et al., 2015, Stalevski et al., 2016). Covering fractions derived from MIR AGN number counts and modelling of individual spectral energy distributions may also be inversely related to luminosity (Maiolino et al., 2007, Alonso-Herrero et al., 2011, Assef et al., 2013, Toba et al., 2013, 2014), though this remains controversial (Roseboom et al., 2013, Lawrence and Elvis, 2010, Assef et al., 2015).

For example, Maiolino et al. (2007) use the ratio of MIR and optical luminosity in spectroscopic observations as a proxy for covering factor. Figures 4 and 7 of this paper show an anti-correlation of covering factor with both optical luminosity (5100 Å and [O III] luminosity. Alonso-Herrero et al. (2011) use SED fitting and MIR spectroscopy in combination, constraining torus model parameters, including an angular size representing the scale of the torus in the CLUMPY models. They find the geometrical covering factor to be high at low bolometric luminosities (0.9-1 at $L_{\rm bol} = 10^{43-44}$ erg s^{-1}) and low at high luminosities (0.1-0.3 at $L_{\rm bol} \gtrsim 10^{45}$ erg s^{-1}) - a similarly inverse relationship found with different methodology.

At lower luminosity spectral dilution of AGN emission by the host galaxy cannot be neglected in many cases (e.g., Moran et al., 2002, Comastri et al., 2002, Cocchia et al., 2007, Civano et al., 2007, Caccianiga et al., 2007). At high luminosities, it becomes increasingly difficult for the host galaxy to dilute the AGN, so quasar studies can offer a clean probe of nuclear activity. The IR region is also useful for reddened and high-redshift AGN.

IR flux is dominated by emission from dust and gas surrounding the central engine at larger distances than the accretion disc; commonly referred to as the torus (see Section 1.1.5). Emission due to star formation can be difficult to distinguish from AGN based emission, but generally peaks at a cooler temperature, meaning some parts of the spectrum are more contaminated than others. This difference in spectral shape due to different dominant sources leads to selection by IR colour as a tool in identifying AGN. A range of criteria have been suggested by different authors, based on *WISE* and other IR instruments (e.g., *Spitzer*), and resulting in selected sets of AGN with different reliability and completeness levels. The IR provides a balance between more reliable

selection - i.e., easier to distinguish from host galaxy contamination than optical measurements - and more large scale datasets than X-rays. It also represents the selection method least biased towards orientation and obscuration.

de Grijp et al. (1985) used IRAS (Section 1.3.8) to compare the IR continuum across 25 µm, 60 µm, and 100 µm, finding that a flat spectrum in this region indicated a high likelihood of a Seyfert galaxy. In de Grijp et al. (1987) they select AGN candidates via their IRAS colours; a first example of MIR colour selection of AGN.

$$-1.5 < \alpha < 0.0 \tag{1.5}$$

where α is the spectral index from the shape of the flux density spectrum between 25 µm and 60 µm $F_\nu \propto \nu^\alpha$. They find a 'success rate' for AGN selection of 0.75 - i.e., analogous to the 'reliability' criterion referred to in later selection papers, this is the fraction of sources that pass according to Eq. 1.5. Thus they estimate the number of AGN in the IRAS Point Source Catalogue to be ∼900, biased towards bright, nearby AGN.

Since IRAS, MIR telescopes have advanced significantly in resolution and sensitivity. The next key MIR tool was *Spitzer* (Section 1.3.8). Where de Grijp et al. (1987) could examine results from the whole sky, the field-of-view of Spitzer is much lower, but its measurements of higher quality. Many different selection criteria have been suggested and iteratively improved on (e.g., Lacy et al., 2004, Stern et al., 2005, and for better exclusion of star-forming galaxies, Donley et al., 2012). Inclusion of *WISE* and 2MASS across the sky today give us a plethora of MIR colour AGN selection methods, each of which has strengths and drawbacks. Two major comparable parameters are 'completeness' (the fraction of AGN that are selected) and 'reliability' (the fraction of selected objects that are truly AGN). Figure 1.4 shows the trade off that exists between these parameters for different suggested selection criteria - high reliability comes at the cost of lower completeness, and vice versa - because of the overlap in appearance between AGN and dusty star-formation, a clean, full selection is impossible.

Stern et al. (2012) present a selection criterion based on *WISE* magnitude data of W1 - W2 $\geq$ 0.8. This was modified by Assef et al. (2013, 2018) to add a magnitude cut of W1 $<$ 15.05, giving a selection strategy with 95% reliability and 78% completeness.

1.2.1.3 Optical

A major advantage of optical detection of AGN is the large amount of detailed imaging and spectroscopic data and telescopes available; on the other hand there are many more potential sources of contamination in any selected group - i.e., stars and AGN can often be mistaken for one another. Many bright sources are non-AGN, unlike for example X-rays, where the majority of bright sources are likely to be AGN.

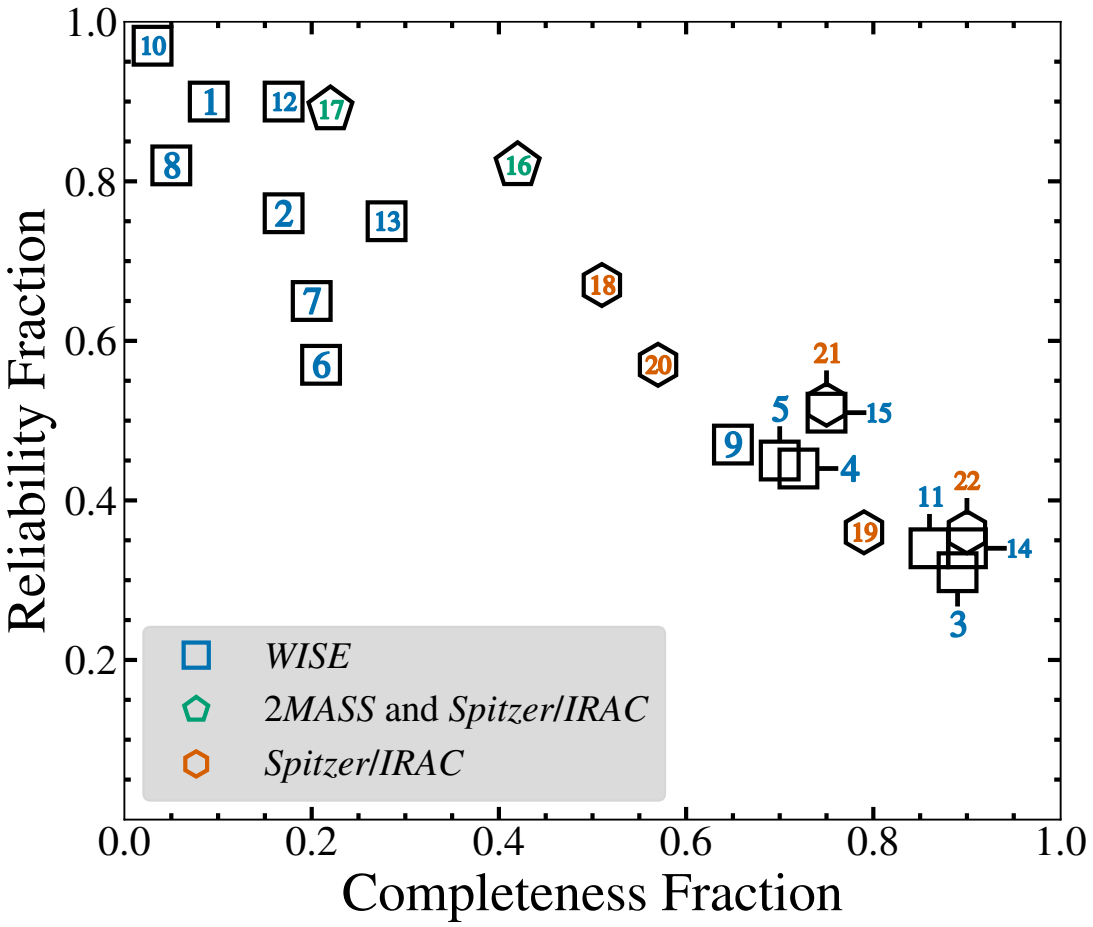

FIGURE 1.4: Completeness-reliability diagram for various MIR selection criteria, adapted from Padovani et al. (2017), with data from Table 1 of Assef et al. (2013) (using magnitude limits of $W1 < 18.50$ and $W2 < 17.11$, and an AGN control sample selected where best-fit UV–mid-IR SEDs have a strong AGN component). Additional selection criteria from Assef et al. (2018). Numbers in plot refer to: (1),(2),(3),(4) Assef et al. (2013) (R90, R75, C90, C75); (5) Stern et al. (2012); (6) Jarrett et al. (2011); (7),(8) Mateos et al. (2012) (3band, 4band); (9),(10) Assef et al. (2010) (2band, 4band); (11) Wu et al. (2012b); (12),(13),(14),(15) Assef et al. (2018) (R90, R75, C90, C75); (16),(17) Messias et al. (2012) (3band, 4band); (18) Stern et al. (2005); (19) Lacy et al. (2004); (20) Lacy et al. (2007); (21) Donley et al. (2012); (22) Lacy et al. (2013).

Except in high-redshift AGN, many useful emission lines are often visible (e.g., [O III]λ5007, [N II]λ6584, Hα, etc.). These forbidden lines arise from photoexcitation in the Narrow Line Region (NLR) on kiloparsec scales. They arise above the classical unified torus, and are thought to be only modestly impacted by host galaxy reddening (e.g., Baldwin et al., 1981, Risaliti et al., 1999, Zakamska et al., 2003). Emission lines can be used to classify a galaxy on the BPT diagram (Kewley et al., 2006), although this does not provide a complete or 100% reliable selection (Agostino and Salim, 2019).

AGN signatures in the optical do not come from a single part of the AGN system (see Section 1.1.2). In unobscured AGN emission lines can also be seen from the BLR (broad lines; originating close to the SMBH in high velocity gas) as well as the NLR (narrow

lines; ionised in gas further from the centre), and the optical continuum shows a blue contribution from the Rayleigh-Jeans tail of the accretion disc emission. The width of the emission lines can be used to estimate the BH mass (Vestergaard and Peterson, 2006) based on broadening of the lines due to matter orbiting around the BH.

Any search in the optical regime is likely to be biased against obscured AGN, where the broad lines and accretion disc emission are largely absorbed by the surrounding dust. The principal visible signatures will be from the NLR; these are produced at great enough distances that (in the standard AGN picture) they are not blocked from view by the 'torus'. Narrow lines can still indicate AGN presence, but many are also produced to some extent by star formation and identification is thus less conclusive. In extreme obscured cases the NLR can also be attenuated, making optical spectroscopic selection biased specifically against these rare types of AGN.

With the large amount of optical data available, it is also a promising regime for variability selection of AGN (e.g., Villforth et al., 2010); particularly for low luminosity AGN which are commonly missed by other selection methods. Intrinsic variability of the central region occurs on observable timescales, and the scale of the variability depends on source wavelength and thus (if observing with a particular filter passband) the observed strength of variability changes with redshift. Not all sources have sufficient multi-epoch data to make this a complete large scale selection technique, but for dedicated fields with repeated measurements robust catalogues can be produced.

Colour selection can also be applied to the optical continuum (e.g., Richards et al., 2001); however, the host galaxy can dominate the optical colours to a greater extent and at lower SFRs than in the MIR and thus selection can be highly contaminated, depending on the galaxy type and amount of star formation. It is also heavily affected by strong optical emission lines coinciding with filters as the redshift of an AGN changes. Rather than selection, it is potentially more useful to use optical AGN colours as an indication of their properties (e.g., Rovilos and Georgantopoulos, 2007).

1.2.1.4 UV

Between optical and X-ray emission is the region of ultra-violet radiation. Due to atmospheric and Galactic absorption, detection here is near-impossible for ground based telescopes and difficult for space based telescopes (see blue and dot-dash purple in Figure 1.3). This region contains a part of the 'big blue bump' also seen in soft X-ray spectra, which is thought to arise from thermal emission from the accretion disc. Its appearance is a combination of black-body emission spectra at different temperatures from different parts of the accretion disc. This continuum can also be highly variable, meaning that multi-wavelength measurements in different epochs may lead to incorrect conclusions. Collisionally excited emission lines and multiplets such as

[O III]$\lambda\lambda$1661,1666 and recombination lines such as He IIλ1640 can be used to identify AGN in the same way as the BPT can in the optical (Feltre et al., 2017).

This problem lies with UV as observed - at redshifts ($z \sim 2-3$) where the rest-frame UV is shifted into the more easily observed optical range (e.g., Hainline et al., 2011) the UV emission from galaxies can be studied and used for AGN selection. This approach is not without downsides: loss of flux and spatial resolution with distance make extracting AGN-specific emission more difficult, especially if the intrinsic UV emission is obscured by local galaxy-scale material or the stellar emission is high. IR instruments (e.g., *JWST*) can examine rest-frame UV emission lines out to even higher redshifts.

For this project, which does not extend in redshift beyond $z \sim 1.5$, investigation of the UV continuum and emission lines would be informative given targeted observations with e.g., *HST* or *Swift*-UVOT. However, given that the nature of this work is mainly based on selecting from large sources of archival data, UV investigations are outside the current scope.

1.2.1.5 X-rays

The section of the spectrum included in X-ray studies is broad: soft X-ray emission starts at far-UV, and hard X-rays end with γ-rays - covering orders of magnitude in photon energy. X-rays are particularly well suited for AGN studies. Emission appears to be present (intrinsically) in the vast majority of AGN, with the caveat that this is not always *observationally* so clear - heavy obscuration absorbs large fractions of the X-ray power, particularly soft X-rays. Intrinsically X-ray weak AGN make up a small part of the population (e.g., Risaliti et al., 2001), but still generally brighter than X-rays from host galaxy stellar emission. To measure the relative strength of X-ray emission compared to optical, a commonly used parameter is defined as:

$$\alpha_{OX} = -\frac{\log \frac{L(2500\ \text{Å})}{L(2\ \text{keV})}}{\log \frac{\nu(2500\ \text{Å})}{\nu(2\ \text{keV})}} \tag{1.6}$$

where ν and L are the rest-frame frequency and monochromatic luminosity. Higher values indicate X-ray weak AGN – noting that this is *observed* rather than *intrinsic* weakness – and as such may be due to obscuration. Values of α_{OX} tend to be higher for AGN than stars - a higher proportion of their bolometric luminosity is emitted in X-rays (e.g., Brandt and Alexander, 2015). Variation of α_{OX} among AGN is also observed, correlated with $L_{2500\mathring{A}}$ and Eddington ratio, taking values around 1.2-1.6 (Lusso et al., 2010).

The source of X-ray emission in high accretion rate AGN is inverse Compton scattering of photons from the accretion disc that reach the 'corona' - a poorly understood region

above the accretion disc (e.g., Haardt and Maraschi, 1991). It is thought to be composed of a hot electron plasma (kT$\sim$65$\pm$10 keV; Akylas and Georgantopoulos, 2021), but the exact geometry is a matter of debate; a common description is the 'lamppost' model where the corona is considered a point source above the BH. Simulations (e.g., Gonzalez et al., 2017) and reverberation mapping (e.g., Uttley et al., 2014) can be used to study the corona and its interaction with the accretion disc. The scattered photons from the corona appear in X-rays as a powerlaw $\propto E^{-\Gamma}$ (with Γ taking values of $\sim$1.6-2.2; Ricci et al., 2017a) with a high energy cut-off ($\sim$80-300 keV), and is modified via interaction with components of the X-ray system (e.g., Ricci, 2011). The main elements of this are as follows:

- **'Torus' reprocessing:** radiation is absorbed and reprocessed, and observed primarily as thermal IR emission (see Section 1.2.1.2).
- **Reflection features:** reprocessing via torus and BLR gas interaction produces fluorescent emission lines (most notably Fe Kα at 6.4 keV, with a typical equivalent width of 100-200 eV, and often containing both broad and narrow components; relativistically broadened components indicate high BH spin, e.g., Baronchelli et al., 2020) and the Compton hump (if the obscuring material is Compton thick; $N_{\rm H}\gtrsim1.5\times10^{24}$ cm^{-2}, peaking at $\sim$30 keV).
- **Soft excess:** emission above the powerlaw at $\lesssim$2 keV. In unobscured AGN the origin of this emission is unknown - possible explanations include a cool corona, or blurred reflection or absorption. It may also be the extension of the UV-optical 'big blue bump' into X-rays.
- **Photoelectric absorption:** at $\lesssim$10 keV and low column densities the observed emission is reduced due to photoelectric absorption.
- **Compton thick absorption:** where the obscuring column density becomes larger than the inverse of the Thomson cross-section ($N_{\rm H}\gtrsim1.5\times10^{24}$ cm^{-2}) higher energy emission is reduced (see Figure 1.5), drastically changing the overall shape of the spectrum as photons are down-scattered (e.g., Comastri, 2004, Gandhi, 2005). A Compton hump is observed.

X-ray emission appears strongly in the spectrum of every AGN, and as hard X-rays can penetrate through the dust and obscuring matter of the 'torus' in all but the most highly obscured objects (i.e., Compton thick AGN) this region can provide a more complete selection algorithm. The downside, however, is that sufficiently deep and high resolution data for a complete census is not available for every part of the sky, often only areas that have been specifically targeted for AGN studies.

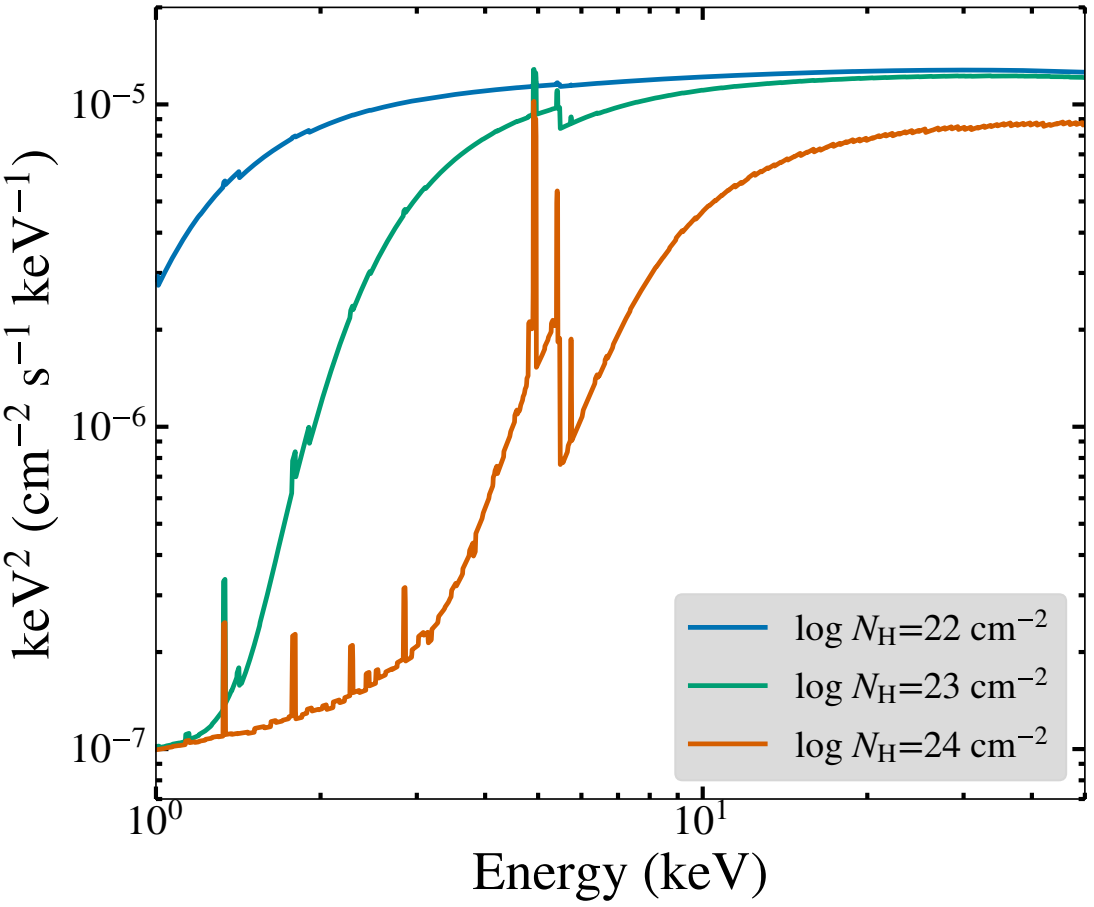

FIGURE 1.5: AGN X-ray spectrum with `borus02` (Baloković et al., 2018) - all parameters kept constant, with N_H varying. Lower obscuration results in a flatter spectrum, i.e., that the flux in the hard band (8–24 keV) and soft band (3–8 keV) are similar; higher obscuration increases the relative strength of the hard band).

Other sources in the host galaxy of an AGN can also produce a measurable amount of X-rays. Emission from X-ray binaries and hot gas is generally lower than AGN emission (in X-ray AGN), and can be modelled with some assumptions about galaxy properties. Commonly these contributions are assumed to be low for bright AGN; this is often reasonable with low count or high energy data. However, SED fitting (e.g, X-CIGALE; Yang et al., 2020) or (for low-z AGN) high resolution X-ray data from *Chandra* can distinguish the contributions and allow fitting of both components. A more problematic aspect is that X-ray in non-AGN from galactic sources may be confused for an X-ray weak AGN, resulting in incorrect identifications. Avoiding these contaminants can be done by fitting the data with AGN and non-AGN models and comparing fit statistics. Strong hard X-ray detections (>10 keV) would increase the likelihood of an AGN, as does higher luminosity. Cuts based on X-ray luminosity can remove much of the contamination from SF galaxies, but interesting X-ray weak sources may be lost.

1.2.1.6 γ-rays

At higher energies than hard X-rays we find γ-rays, generally considered to be in the 100 MeV to 10 TeV range. Detection in this range is difficult, requiring technology very different to telescopes used for much of the rest of AGN emission, for example *Fermi*-LAT (Atwood et al., 2009). The majority of sources detected in γ-rays are blazars (see Section 1.1.2), with intense non-thermal radiation Doppler-boosted towards an observer in the jet (see Section 1.2.1.1) - thus achieving the extremely high energies of γ-rays. As blazars are not the focus of this work we will not delve further into γ-rays here.

1.2.1.7 Broadband summary

Each of these parts of the detectable AGN spectrum suggests a different way of selecting for AGN presence, and will allow us to infer information about different components of AGN structure and activity. In summary:

- Optical and NIR spectroscopy: allows us to probe ionised gas both near to and far from the central SMBH via emission lines. Broad lines are Doppler broadened due to originating closer to the BH, and thus virial BH mass can be inferred from their width. Apparent presence or absence of broad lines is often ascribed to the apparent orientation of the AGN system (see Section 1.1.2), but this simple explanation does not fully cover all observed phenomena. Heavy or large-scale obscuration can mask these signals, and emission lines from significant star formation can dominate over AGN emission lines in heavily star-forming galaxies. Thus optical and NIR spectroscopic selection (Figure 1.6, left panel) is less effective in the low AGN dominance and high obscuration regimes.

  → Sources with weak AGN or dominant galaxy contributions are most likely to be missed, along with obscured sources (a bias that decreases towards the NIR). Star-forming galaxies producing with high ionisation levels may produce emission lines comparable to AGN levels and thus form the primary contaminants in this selection, although it is generally reliable; particularly if broad lines are visible.

- Optical and NIR photometry: Similarly to colour selection in the MIR, the shape of the continuum in the visible part of the electromagnetic spectrum can be used to select AGN. However, due to higher interference from non-AGN host galaxy and greater effects from reddening, it is less reliable as a selection process, especially in obscured and host-dominated AGN. Optically selected AGN nevertheless represent a large part of many AGN catalogues, including SDSS.

→ Vulnerable to failing to select AGN with low dominance over their hosts at lower galaxy contributions to the overall emission, particularly for obscured AGN where the continuum emission is predominantly from the host. Star-forming galaxies will again form a significant number of incorrectly selected sources.

- Infra-red: IR emission from the AGN comes from reprocessing in obscuring material - hence is relatively unaffected by obscuration structure and orientation. Colour selection is reliable up to high levels of obscuration (Figure 1.6, middle-left panel), but selection can be contaminated by star-forming galaxies and miss lower luminosity AGN. Spectroscopy in the MIR can detect signals from AGN through both heavy obscuration and above host galaxy emission, and can thus be sensitive and unbiased for AGN analysis; conversely, of course, the number of objects where this data is available is relatively few.

  → Low-luminosity AGN, especially those in bright SF or dusty galaxies, are most likely to be missed by photometric selection. Star-forming galaxies contaminate this sample, and the source of MIR emission can be difficult to distinguish. MIR spectroscopy is a highly reliable technique, even for low luminosity and obscured AGN overlooked by other methods.

- X-rays: Both hard and soft X-rays can be very effective in AGN selection (Figure 1.6, middle left panel). Star-formation can produce significant emission, especially in the soft band - most AGN will outshine this, but very low luminosity AGN are still biased against. As obscuration depth increases, lower energy X-rays are absorbed more and thus selection of heavily obscured AGN is more effective in hard X-rays ($>$10 keV). At extreme column depths, even very high energy emission is attenuated.

  → Particularly with soft X-ray measurements, heavily obscured AGN are most likely to be missed, as their emission is primarily at higher energies. X-ray weak AGN may be assumed to be star-forming galaxies, and conversely with soft X-ray selection at low luminosities, star-forming galaxies will contaminate a sample.

1.3 Practical Considerations: What instruments are suitable?

For selecting AGN, we can take two approaches for a parent sample. Large surveys, such as SDSS, *WISE*, and eROSITA provide (or will provide) a large number of targets, and thus are promising sources for selecting objects that we believe to have very low overall number counts. However, we must also consider that if we are searching for obscured AGN it is likely that the flux from these will be low; hence larger surveys may

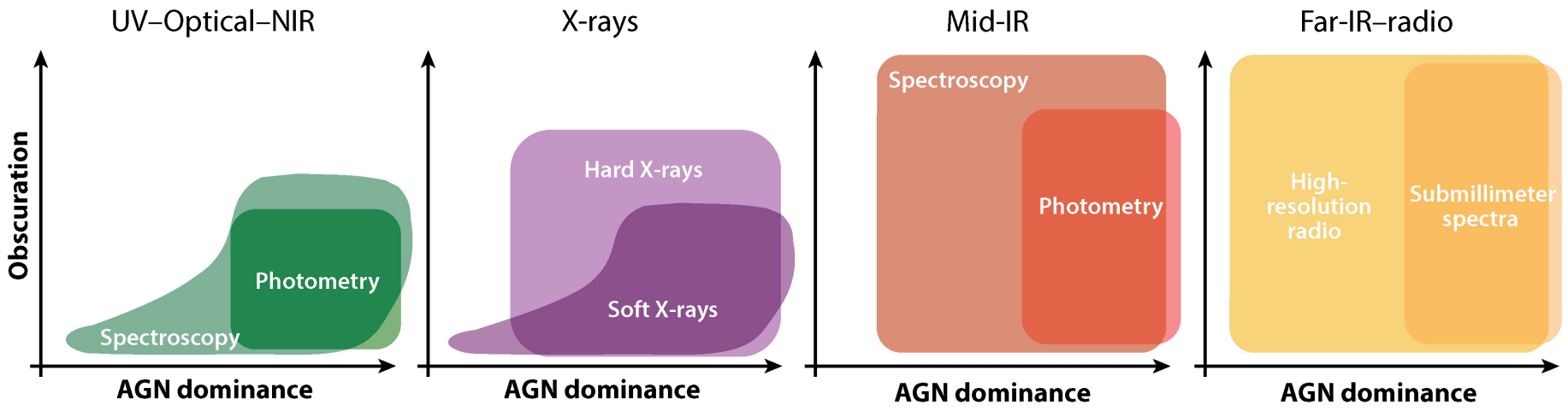

Hickox RC, Alexander DM. 2018.
Annu. Rev. Astron. Astrophys. 56:625–71

FIGURE 1.6: Schematic diagram illustrating the effectiveness of different AGN selection techniques with regards to (a) obscuration depth, and (b) AGN dominance over the host galaxy (figure from Hickox and Alexander, 2018).

miss significant numbers of these. This brings us to the second approach: serendipitous sources from within targeted observations. When telescopes such as *XMM-Newton* and *NuSTAR* observe their targets unrelated extra sources can often be detected within the field of view. Thus armed with these serendipitous catalogues, we can use deeper measurements to investigate objects that may be missed in wider surveys. In this section I will summarise the major surveys and targeted instruments that are relevant for this work.

1.3.1 SDSS

The Sloan Digital Sky Survey (hereafter SDSS) encompasses imaging, optical spectroscopy, infrared spectroscopy, and integral field unit (IFU) spectroscopy. More than 20 years of measurements combine to make SDSS an invaluable resource for objects across the northern hemisphere sky, and as of SDSS-IV the southern sky. Many derived parameters are also available, such as redshifts and fluxes. In the most recent data release (DR17; Abdurro'uf et al., 2022) there are a total of 5,801,200 optical spectra and 1,231,051,050 photometric measurements available; although not all of these are unique objects, repeat measurements are useful for many areas of research. These datasets come from a number of different surveys with different scientific aims. Originally imaging half the northern sky and mapping many galaxies and quasars (York et al., 2000), and later including wide-ranging aims such as the Baryon Oscillation Spectroscopic Survey (BOSS; Dawson et al., 2013, which made a large scale map of galaxies), and the Apache Point Observatory Galactic Evolution Experiment (APOGEE; Majewski et al., 2017, which looks at Milky Way structure and evolution with IR spectroscopy). This diversity of objectives makes the biases for any SDSS-derived selection strategy hard to quantify.

The main instruments used in SDSS and relevant to this work are as follows:

- Original SDSS instrument (York et al., 2000): comprises two spectrographs, with wavelength ranges of 3800–6100 Å and 5900–9100 Å. These measure spectra from 640 points simultaneously via multiple fibre input at spectral resolution between 1850 and 2200.
- BOSS instrument: rebuilt from the original spectrographs, it has improved response and can measure with more fibre inputs than the original instrument. The wavelength range is extended to 3600–10400 Å, and spectral resolution 1560-2270 (red) and 1850-2650 (blue). It is currently the active spectrograph as of SDSS-V (Kollmeier et al., 2017).

  → Optical spectra selected from SDSS for a population of objects (see Chapter 5) will be a combination of results from these two instruments. Many targets

have been measured multiple times, and each has a spectrum flagged in the database as '`sciencePrimary`' - the best available (see Section 5.3.3).

- Original SDSS photometric camera (Gunn et al., 1998): takes images with 2048×1361 pixels (13.51×8.98 arcminutes) across a full field of 2.5° with five filter bands (u: 3551Å, g: 4686 Å, r: 6165 Å, i: 7481 Å, z: 8931 Å - the exact responses have changed over time; Doi et al., 2010). PSF varies with band and sky brightness, but median values are from 1.26″–1.53″.

The optical extra-galactic observing programs that contribute to the spectroscopic datasets we will use are the following:

- Legacy Survey (SDSS-I/II) which includes both Legacy Galaxies (a magnitude limited but otherwise complete set, and a colour and magnitude selected sample of Luminous Red Galaxies; Strauss et al., 2002, Eisenstein et al., 2001) and Legacy Quasars (identified as outliers from expected stellar appearance; Richards et al., 2002). This quasar selection automatically finds quasars out to z∼5.8, and additionally extended sources at low redshift were targeted. As an optical colour selection, this is likely to select primarily disk dominated AGN.

  → Selections from this parent dataset may therefore be biased in favour of LRGs over other galaxies.

- BOSS (SDSS-III) also includes targeting of a Galaxy sample (selected to achieve the science requirement of measuring the cosmic distance scale, and thus extends the legacy sample to fainter objects in two redshift ranges: 0.15<z<0.45 and 0.4<z<0.7; LOWZ, CMASS) and a Quasar sample (targeted towards quasars at z>2.1 to trace large scale structure; Ross et al., 2012, - this sample still contains a number of low-z sources).

- SEQUELS was an ancillary program targeting LRGs (at redshifts greater than the Legacy and BOSS samples using joint selection with *WISE*; Prakash et al., 2016), Quasars (directly probing the large scale structure at 0.8<z<2.2; Myers et al., 2015), and Emission Line Galaxies (Section 2.5.2 of Comparat et al., 2015).

- eBOSS (SDSS-IV) also targets LRGs, ELGs, and QSOs (Dawson et al., 2016), aiming to cover redshift gaps from BOSS

  → Bias from the BOSS, SEQUELS, and eBOSS selection criteria is thus against low redshift objects.

- Spectroscopic IDentification of ERosita Sources (SPIDERS) targets soft X-ray selected objects - clusters (Clerc et al., 2016) and AGN (Dwelly et al., 2017).

→ With targets selected from soft X-rays (*XMM-Newton* and *ROSAT*, later to be eROSITA) these will primarily be bright, unobscured or lightly obscured AGN.

Many secondary products derived from photometric and spectroscopic measurements are produced by SDSS and available for use, including products from SDSS, BOSS, and eBOSS spectra.

- Classification - each spectroscopic object is assigned a class based on the best match to available templates (`GALAXY`, `QSO`, or `STAR`), with further subclasses for galaxies (`STARFORMING` - emission lines consistent with star formation, `STARBURST` - starforming with wide Hα, or `AGN` - emission lines consistent with Seyfert or LINER appearance) and stars. Galaxies and quasars can also be assigned the subclass `BROADLINE`.
- Redshift - the best fit template will also include a determination of the redshift and error. Various flags can be applied, based on how trustworthy the redshift is determined to be.
- Photometric properties - calibrated outputs from the pipeline, such as various magnitude and flux model fits. Depending on the target type and the science aims of the data usage, different fluxes may be appropriate: for example `PSFFLUX` (point spread function flux only), `CMODELFLUX` (a combination of De Vaucouleurs and exponential model fits), `PETROFLUX` (flux within the Petrosian radius of the source).

1.3.2 *WISE*

From 2009-2011 the Wide-field Infrared Survey Explorer (Wright et al., 2010) scanned the entire sky in four bands: $W1$ (3.4 µm), $W2$ (4.6 µm), $W3$ (12 µm), and $W4$ (22 µm). It took data in three phases, with reduction in the longer wavelength capability due to lack of coolant in later years: 4-band cryo, 3-band cryo ($W1$, $W2$, and $W3$), and post-cryo ($W1$ and $W2$). The post-cryo phase (NEOWISE; Mainzer et al., 2011) is primarily aimed at detected moving objects within the solar system but nevertheless is useful for a wide variety of studies.

There are a number of catalogues of *WISE* data available, updated at different stages of the mission lifetime. The main relevant catalogues are:

- WISE All-Sky Data Release (Cutri and et al., 2012)[1] - all data from the main mission phase (i.e., measurements with all four bands) for >563 million objects.

[1] `https://wise2.ipac.caltech.edu/docs/release/allsky/`

- AllWISE Data Release (Cutri et al., 2021, 2013)[2] - updated from the All-Sky DR by combining *WISE* and NEOWISE data and improving the photometry, it has fluxes in four bands for more than 747 million objects; additionally flux measurements over time are available for each object. The AllWISE Images Atlas contains >18 thousand $1.56^\circ \times 1.56^\circ$ images. More than 4 million objects are also available in the Reject Table - low SNR, duplicate sources, and image artifacts. Mainly these are not real, but some fainter objects may be present. The Source Catalogue contains information such as profile fit photometry, magnitudes within different aperture radii, and quality flags informing the user of the confidence in the source measurement and its SNR.

- NEOWISE post-cryo Data Release (2013)[3] - images and source data from $W1$ and $W2$ in the post-cryo phase, covering ∼70% of the sky. This data release is mainly focused on moving objects rather than stationary sources such as AGN.

- CatWISE (Eisenhardt et al., 2020, Marocco et al., 2021) - the most up to date catalogue available for $W1$ and $W2$, this includes all NEOWISE data - more than 16 times as long as AllWISE; this is a particularly good resource for examining the variability of IR sources, and fainter sources that were undetected in AllWISE.

AGN emission around the *WISE* bands is thought to be relatively unbiased, coming from reprocessing in the obscuring dust (see Section 1.2.1.2). Thus *WISE* has become an extremely valuable resource for AGN selection: Stern et al. (2012), Assef et al. (2013), Blecha et al. (2018), and many more (see Figure 1.4).

1.3.3 2MASS

2MASS (Skrutskie et al., 2006) is a 3-band survey covering the J (1.25 µm), H (1.65 µm), and K_S (2.16 µm) bands. Unlike *WISE* it was performed from ground based telescopes; one in Arizona and one in Chile, thus covering essentially the entire sky. Prior to *WISE*, this was the best resource for all sky IR coverage and it remains valuable, covering a slightly bluer part of the spectrum.

- All-Sky Data Release (2003)[4] - combined data from the two facilities covers 99.998% of the sky with >4 million images and a pixel size of 2.044″.

- Point Source Catalogue (Cutri et al., 2003) contains >470 million point sources, and is >99% complete for J<15.8, H<15.1 and K_S<14.3 magnitudes.

[2] https://wise2.ipac.caltech.edu/docs/release/allwise/
[3] https://wise2.ipac.caltech.edu/docs/release/postcryo/
[4] https://www.ipac.caltech.edu/2mass/releases/allsky/

- Extended Source Catalogue (Jarrett et al., 2000) contains >1.6 million sources which are resolved when compared to the point spread function. 97% are likely to be galaxies, and the rest are Milky Way objects.

1.3.4 *NuSTAR*

The Nuclear Spectroscopic Telescope Array (*NuSTAR*; Harrison et al., 2013) is a focusing X-ray telescope operating in the range 3–79 keV. Its spatial resolution, spectral resolution, and sensitivity is a step up from other hard X-ray telescopes, and as such it is a powerful resource for investigating obscured AGN. As a targeted instrument rather than a wide area survey instrument such as *WISE* or *Swift*-BAT, *NuSTAR* does not have an all-sky source catalogue; however, its years of measurement include both dedicated surveys and serendipitous source detections:

- *NuSTAR* Extragalactic Surveys - a deep, small area survey in the *Chandra* deep field (Mullaney et al., 2015) and a larger survey in the COSMOS field (Civano et al., 2015).
- *NuSTAR* Master Catalogue - the list of all planned and observed targets. All observations taken are available after a certain proprietary period, and thus all observations together combine to cover a significant area of the sky. These can be used to measure fluxes - or upper limits - for specific sources, but they have also been combined to detect previously unknown sources in the serendipitous catalogues:
  - *NuSTAR* Serendipitous Survey: 40-month Catalogue (NSS40; Lansbury et al., 2017b) - ∼500 sources detected over 3–24 keV in the 40 months of operation, which cover ∼13 deg^2. These are mainly AGN, with a small number of Milky Way sources.
  - *NuSTAR* Serendipitous Survey: 80-month Catalogue (Klindt et al., submitted, 2022) - ∼1300 sources (822 new detections compared to NSS40), covering ∼36 deg^2.

1.3.5 *XMM-Newton*

ESA's X-ray Multi-Mirror Mission (*XMM-Newton*; Jansen et al., 2001) was launched in 1999 and remains an active X-ray telescope. *XMM-Newton* is an X-ray telescope operating in the energy range 0.2–15 keV with three CCD detectors (pn, 2×MOS; Strüder et al., 2001, Turner et al., 2001). It has a FOV of 30′ and angular resolution of 6″ (PSF FWHM). Similarly to *NuSTAR*, in addition to targeted objects serendipitous sources can be detected in the *XMM-Newton* observation fields.

- *XMM-Newton* Serendipitous Source Catalogue (most recent 4XMM-DR12; Webb et al., 2020) has >900,000 detections across ∼1280 deg^2, of which >300,000 have spectra.
- *XMM-Newton* Slew Survey - between observations, the EPIC-pn camera records as the telescope slews from one target to the next (XMMSL1, Saxton et al., 2008; XMMSL2, XMM-SSC, 2018). This complementary catalogue expands the coverage of *XMM-Newton* to a significant proportion of the sky (∼84%) and includes >70,000 detections. Many sources are observed multiple times as the slew paths overlap repeatedly, particularly at the ecliptic poles.
- *XMM-Newton* Upper Limits (Ruiz et al., 2022) - for sources without a detection but within the pointed or slew fields, upper limits can be obtained.

With the combination of these catalogues, *XMM-Newton* is a powerful resource for soft X-ray studies of AGN.

1.3.6 *Chandra*

The *Chandra* X-ray Observatory (Weisskopf et al., 2000, Wilkes et al., 2019) comprises four instruments: Advanced CCD Imaging Spectrometer (ACIS), High Resolution Camera (HRC), High Energy Transmission Grating (HETG), and Low Energy Transmission Grating (LETG). The two transmission gratings are designed for high resolution spectroscopy over 0.4–10 keV and 0.07–0.2 keV respectively. ACIS and HRC have larger imaging FOVs (16×16 arcminutes, 31×31 arcminutes). HRC has better spatial resolution (<0.5 arcseconds), but ACIS has better spectral resolution. Thus for the purposes of AGN selection and analysis ACIS can provide the best balance between spatial coverage and spectral resolution; with the low background of *Chandra* it is ideal for fainter sources and the excellent spatial resolution helps to distinguish the source of X-ray emission. However, a smaller field of view than *XMM-Newton* and a lack of slew data means fewer serendipitous sources are available.

- *Chandra* Source Catalog Release 2.0 (Evans et al., 2010, 2020a) contains >300,000 unique detected sources from ACIS and HRC.

1.3.7 *Swift*

The *Swift* telescope has three instruments:

- Burst Alert Telescope: *Swift*-BAT (Barthelmy et al., 2005) is designed to detect gamma ray bursts and trigger other observations. It is a coded mask instrument

with a large field of view, and operates from 15–150 keV. Results from the first 105 months of observations are available in Oh et al. (2018), which presents a hard X-ray survey that covers 90% of the sky. However, its spatial resolution is significantly worse than *NuSTAR* and the soft X-ray telescopes (with *Swift*-BAT at $17'$, compared to e.g., *NuSTAR* at $18''$ FWHM), and the flux limit is higher.

- X-ray Telescope: *Swift*-XRT (Burrows et al., 2005) is a grazing incidence focusing telescope operating over 0.2–10 keV. Its FOV is smaller than *Swift*-BAT, but its spatial resolution is better. It is designed for moderate resolution spectroscopy and accurate positioning for following up alerts from *Swift*-BAT. Its energy range and resolution make it a useful instrument for AGN studies in addition to its primary purpose; as with the other instruments a catalogue of detected sources is available (2SXPS; Evans et al., 2020b, - covering $\sim$3790 deg^2, with $>$200,000 detections), along with a continually updated transient detecting catalogue (Evans et al., 2022).

- Ultra-violet Optical Telescope: *Swift*-UVOT (Roming et al., 2005) provides simultaneous, aligned, optical and UV measurements with *Swift*-XRT. After an alert from *Swift*-BAT it goes through a standard cycle of filter measurements, and locates the source to even better precision.

1.3.8 Other past telescopes/instruments

Launched in 1983, the Infrared Astronomical Satellite (IRAS; Neugebauer et al., 1984)[5] was the first IR space telescope, and detected $\sim$350,000 sources in an all-sky survey at 12 µm, 25 µm, 60 µm, and 100 µm. The Spitzer Space Telescope (Werner et al., 2004), has three instruments. The Infrared Array Camera (IRAC; Fazio et al., 2004) takes 5.2×5.2 arcminute images in four bands: 3.6 µm, 4.5 µm, 5.8 µm, and 8 µm. It was launched in 2003 and operated in all bands until 2009, when coolant was depleted. The 3.6 µm and 4.5 µm channels continued operation until 2020. Thus it is similar to *WISE* but targeted rather than all-sky. The Multiband Imaging Photometer for Spitzer (MIPS) takes images and photometry at 24 µm, 70 µm, and 160 µm, along with low resolution spectroscopy at 55 µm-95 µm. These two IR instruments have been the basis of much of AGN IR studies, and their legacy datasets continue to provide valuable long wavelength photometry not readily available from other sources.

1.3.9 Other upcoming/early-stage telescopes/instruments

There are a number of upcoming or recently commenced surveys that will vastly improve the number and flux limit of detected extra-galactic sources, and thus also the

[5] https://irsa.ipac.caltech.edu/IRASdocs/iras.html

number of AGN. Launched in 2019, the 'extended ROentgen Survey with an Imaging Telescope Array' (eROSITA; Merloni et al., 2012) is an instrument on the Russian-German 'Spectrum-Roentgen-Gamma' (SRG) mission[6]. It will accomplish the first all-sky survey over the energies 0.5-10 keV, and hopes to detect around 3 million AGN, including both obscured and unobscured. The Early Data Release (June 2021) contains initial results from the 'Calibration and Performance Verification' phase, including a number of catalogues with detected source information.

The Vera C. Rubin Observatory (originally the Large Synoptic Survey Telescope, *LSST*; LSST Science Collaboration et al., 2009) is a 8.4 metre telescope based in Chile. The start of science operations is currently estimated to be late 2024, and after that it will observe 18,000 square degrees 825 times over 10 years with 6 filter bands (*ugrizy*; similar to SDSS, with an expansion to longer wavelengths in the *y*-band). Strategy planning for the survey is still ongoing, but it is likely to observe many millions of AGN, and will be particularly useful for studies of AGN variability.

The next generation of optical spectroscopic surveys will be done by 4MOST (4-metre Multi-Object Spectroscopic Telescope; de Jong et al., 2016). It will survey a large fraction of the southern sky from the VISTA telescope (Visible and Infrared Survey Telescope for Astronomy) in Chile, simultaneously observing ∼2400 sources with a minimum separation of ∼17″ (enabling observations of closely interacting pairs, essential for studies of merging and dual AGN). It will cover the optical and NIR range, from 370 nm-950 nm. Currently, the aim for starting operations is late 2023, so as with *LSST* targeting strategy is ongoing. The AGN survey (Merloni et al., 2019) aims to improve the completeness of the current AGN census by (a) following up detected eROSITA sources, and (b) targeting candidate heavily obscured AGN selected in the MIR. It aims to spectroscopically identify ∼1 million AGN up to z∼6, using these for: studying massive, luminous AGN on a larger scale than ever before; improving measurements of AGN fractions within specific galaxy types (e.g., mergers); examining the relationship between AGN and their larger-scale environments, and more.

1.4 What is the aim of AGN searches?

Selecting an unbiased sample of AGN across these properties is challenging (e.g., Hickox and Alexander, 2018, Asmus et al., 2020), but necessary in order to have a complete – or at least representative – census of AGN. Biases in selection depend on techniques used (see Section 1.2), but are most commonly biased against (a) low luminosity AGN, and (b) obscured AGN, particularly Compton thick sources.

[6]Science operations of eROSITA have been paused since February 2022 (to date October 2022) due to freezing of co-operation with Russia.

The necessity of this census is to enable us to answer significant questions about the evolution and growth of AGN, how they affect their host galaxies, and the mechanisms by which this occurs. We observe that the SMBH and galaxy bulge mass are correlated (Kormendy and Ho, 2013); thus we can infer that there is a connection between AGN and galaxy growth. However, *understanding* this connection requires accurate knowledge of the AGN population. For example, if the number of galaxies containing an active SMBH is unknown, then the length of active phases of SMBH are also unknown, and it is impossible to understand how the AGN activity in these phases affects the host galaxy and greater environment.

We should also note that the difference between active and inactive galaxies may be not completely distinct. Many sources that are considered inactive and are below most detection thresholds are accreting at low levels: for example, as mentioned above, Sagittarius A* does accrete material, but is not thought of as an AGN. Many typical components of the AGN system are unlikely to be present in such sources. Thus, even in the most thorough searches, some SMBH accretion will not be detected.

1.4.1 What can we learn from population statistics?

The intrinsic Compton thick fraction of AGN is highly uncertain, due to this population being one of the hardest to select for across the whole range of AGN emission (see Section 1.2). The Cosmic X-ray Background – a peak in X-ray radiation observable in across the sky, first discovered by Giacconi et al. (1962) – has been gradually shown to be composed of distinct X-ray sources as X-ray instruments improve and can resolve these sources (e.g., Cappelluti et al., 2017). A significant fraction remains unresolved, particularly at higher energies, and it is likely that this is composed of more obscured sources. An X-ray luminosity function (the number density of AGN as a function of luminosity and redshift) that reproduces the observed CXB implies that 50$\pm$9% (56$\pm$7%) of AGN within z$\sim$0.1 (z$\sim$1.0) are Compton thick (Ananna et al., 2019). Observed numbers of CT AGN are generally much lower than this - for example, Ricci et al. (2015) find only $7.6^{+1.1}_{-2.1}$% of their hard X-ray sample to be Compton thick (in the local universe, with an average z $\sim$0.055; lower than considered in Ananna et al., 2019) Even when corrected for selection bias, they calculate an intrinsic CT fraction of 27$\pm$4%; thus we can see that there is a large uncertainty in the numbers of AGN existing in highly obscured phases.

Given an MIR-selected population of AGN candidates, we might be interested to estimate how many of these would be detectable with, for example, eROSITA. The nuclear MIR luminosity and *intrinsic* X-ray luminosity are related (Asmus et al., 2015, Stern, 2015), but to predict the *observed* X-ray luminosity we must assume a distribution of $N_{\rm H}$ values. Large uncertainties in the assumed ratios, particularly for the CT fraction,

will have correspondingly large effects on the predicted observed fluxes (see Chapter 2, section 2.3.3).

As many models of AGN evolution suggest that much of AGN growth happens in obscured phases (e.g., Fabian, 1999, Di Matteo et al., 2005, Hopkins et al., 2006), accurate knowledge of AGN evolution is not possible without understanding the statistics of these obscured chapters in the life cycle.

SMBH do not accrete consistently over their lifetimes - instead they grow in active phases (periods of high accretion). The amount of time spent in these phases can be described in terms of 'duty cycles': the fraction of their lifetimes spent active. Non-accreting SMBHs can only affect their environments via gravitational interaction, as they are without strong electromagnetic emission. Thus if we are interested in how AGN interact with their hosts and larger scale environments, constraint of the duty cycle is important to understand the numbers of AGN compared to numbers of inactive SMBHs, the accretion rates of AGN, and therefore the intensity of feedback we might expect. Estimates of the duty cycle are $\sim 10^7$–10^9 years (Martini and Weinberg, 2001, Yu and Tremaine, 2002, Marconi et al., 2004: respectively, from modelling at $z > 2$; based on BH mass function at $0.01 \leq z \leq 0.3$ and for quasars with $L_{bol} \gtrsim 10^{46}$ erg s^{-1}; $z < 3$ with lifetime depending on BH mass); this is a small fraction of the history of the universe where SMBHs can be observed, implying that SMBHs are active in total for only a small portion of their lifetimes, although this is not generally a single growth period but several separate phases. Schawinski et al. (2015) (using *Swift*-BAT matched SDSS AGN at $0.0165 < z < 0.4$) find that growth phases can be somewhat shorter ($\sim 10^5$ years) and theorise that accretion does not happen in one single consistent phase, but instead grow in shorter bursts, 'flickering' on and off over shorter timescales ($\sim 10^4$ years); this is consistent with a total 'on time'of $\sim 10^7$–10^9 years if the 'flickers' happen repeatedly. AGN in these 'switching on' or 'switching off' phases will appear different to a 'mature' AGN, due to light travel time between the accretion disc and e.g., the 'torus' or narrow line region (see Section 1.1.6).

This discussion has so far made the underlying assumption that AGN properties are the same across cosmic time, and that any study of them can be applied generally. The focus of this thesis is mostly in the relatively local universe where this is an acceptable approximation, but considering the entire population of AGN this is not the case. Luminosity functions (the number density of AGN as a function of luminosity and redshift) can show how populations of AGN vary in number and properties across the lifetime of the universe. For example, Aird et al. (2015) use X-ray data (0.5–7 keV) to show that the shape of the luminosity function varies with redshift (up to z$\sim$5) and absorption (unabsorbed: 20<log $N_{\rm H}$<22 cm^{-2}, and absorbed: 22<log $N_{\rm H}$<24 cm^{-2}). Differences in luminosity and obscured fraction thus imply that AGN accretion rate and growth in obscured phases are not consistent across time. Delvecchio et al. (2020)

examine the change in AGN duty cycle up to z∼3 and find that AGN had a longer active phase in the early universe, based on the numbers of highly accreting AGN.

The activity of AGN is not only different across time, but also across space. AGN are not evenly distributed; each galaxy does not have an equal chance of hosting an AGN. Interactions of the host galaxy with nearby galaxies may power AGN (e.g., Lackner et al., 2014), but whether mergers are a dominant trigger of AGN is a matter of debate (e.g., Gao et al., 2020, Ellison et al., 2019, Mechtley et al., 2016, Villforth et al., 2017). The obscuration of AGN does seem to be associated with mergers (e.g., Kocevski et al., 2015, Glikman et al., 2015). On even larger scales, AGN activity is associated with membership of galaxy clusters (e.g., Gilli et al., 2009). Obscured AGN are found in denser environments than unobscured (Powell et al., 2018). The spatial distribution of AGN, and effects of large scale environment on AGN, is therefore not simple. As with other properties a complete view requires a thorough census.

1.5 What could AGN searches be missing?

From Section 1.2 we have seen that however we select for AGN, it is inevitable that the result is incomplete. Although all AGN are accreting (albeit with a wide variation in rates) and interacting with their environments, they are not all equally likely to be missed. Hence these are important elements of the full story of AGN evolution; the following list outlines some common categories of AGN that are elusive in some way.

- **Obscured AGN:** one of the major roadblocks to unbiased selection of AGN is obscuration, covering a wide range of effects. Seyfert 2 AGN are viewed on a line-of-sight that hides a direct view of the SMBH and accretion disc, and thus signals are less obvious; for example, only narrow optical emission lines are visible. Compton thick AGN have thick enough obscuration that even the normally reliable high energy emission in X-rays is depleted. Unfortunately, as AGN growth is linked to these obscured phases, it is particularly important to ensure a complete account of more heavily obscured sources.
- **Intrinsically Low Luminosity AGN:** AGN that are intrinsically weak accretors, or those that have relatively bright host galaxies are hard to select for due to the difficulty in disentangling host and AGN emission. SED modelling (see e.g., Section 4.2.2) with sufficient multi-wavelength data can estimate how much of the total emission is due to the AGN, but this quantity of data is not available for a large number of sources. In many ways, these suffer from similar selection issues to obscured AGN.
- **Reddened Quasars:** AGN embedded in dusty galaxies, these show an excess of MIR emission compared to optical. Unlike obscured quasars, the AGN signatures

are attenuated in a different way - these may be reddened and unobscured Type 1 AGN. The unusual combination of properties means that they are not as simply classified as more typical AGN.

- **Weak Line AGN:** selection by optical emission line - one of the easiest and most reliable large scale methods, due simply to the quality and amount of data available - will miss objects that do not present with typical AGN emission lines. For example, weak line quasars (e.g., Meusinger and Balafkan, 2014) show X-ray emission, but no [O III] - these may not have an ionised broad line region, and thus with only optical data may look like inactive galaxies.

- **Variable and Changing Look AGN:** through their lifetimes, AGN do change in appearance. This can be due to change in environment (e.g., 'cloudy' obscuration; Elitzur, 2012), or change in intrinsic accretion rate (e.g., Sheng et al., 2017) and can result in differing classifications. Thus AGN measured only once or infrequently may be misclassified - e.g., considered a Type 2, when this is only a temporary state. Alternatively AGN may be caught as they 'switch on or off' (e.g., Schawinski et al., 2015) leading to an interesting combination of properties that may be a transient state. These AGN may be more likely to be *misclassified* than not selected, but this is equally detrimental to the completeness of the AGN census.

- **Distant AGN:** though beyond the scope of this project, AGN in the high redshift universe provide particular challenges in selection (due to redshift of common features) and analysis (low fluxes and extreme attenuation).

1.5.1 How can these gaps be filled?

Many surveys attempt to identify and study AGN of these fringe appearances, along with the more commonly observed AGN types. Small area but deep surveys (e.g., COSMOS, Weaver et al., 2022; AGES, Kochanek et al., 2012; GOODS, Dickinson et al., 2003; CANDELS, Grogin et al., 2011; etc.) aim to produce highly complete catalogues over their target region. These result in detailed multi-wavelength catalogues and allow for tight constraints on general properties (e.g., Cappelluti et al., 2017) - on the other hand, being restricted to a small area results in low total number counts and thus low numbers of rare AGN. They are also vulnerable to large scale inconsistencies like voids or structures. Surveys aimed at wider areas can vastly increase the number of sources for statistical analysis, but acquiring this large amount of data means trade-offs in what can be measured. Selection effects therefore play a large role, for example in SDSS a large fraction of the sky is covered, but the number of different surveys with different aims that make up the full SDSS database (see Section 1.3.1) introduce individual biases that, when combined, make it hard to quantify completeness. AGN surveys (e.g., Lacy et al., 2015) rely on specific selection strategies - MIR selection is a common and

relatively unbiased choice, but with limited measurement time for multi-wavelength confirmation, many AGN will still go unseen.

To complete the census of AGN and understand the full population unbiased by selection effects, we must consider how to combat them, where possible, and understand them where impossible. In this thesis I will begin with the construction of a local census of the AGN population, by combining contributions from several disparate databases. Based on this I will estimate the number of known AGN in the local universe and with a combination of MIR selection, spectral follow-ups, and careful consideration of selection biases we will estimate how many local AGN remain unknown. Having thus quantified the size of the deficit in the AGN census, I will consider how unusually obscured AGN could be deliberately selected for, establish search procedures, and analyse the resulting populations.

Chapter 2

Starting Local: what can we learn from a census of Active Galactic Nuclei at low redshift?

The Local AGN Survey (LASr) is a project which aims to create a census of the AGN in a limited local volume, relatively unbiased against obscuration. This catalogue provides a starting point in order to find nearby AGN that have been so far overlooked. This chapter will describe the construction of the Galaxy Parent Sample (LASr-GPS), selection of AGN within it, and estimates of total and unknown space density of AGN; published as Asmus et al. (2020), hereafter A2020. It will then describe the next stage of this research, in which I followed up AGN candidates with good quality spectroscopy: confirming the presence of an AGN, investigating why these objects have been missed in the past, and assessing the number counts of similar objects that may exist. Sections 2.1 to 2.4 are based on A2020, work done in collaboration with Daniel Asmus. I made a significant contribution to this paper, particularly in visual checks and comparison with AGN catalogues, including analysis of biases. Sections 2.5 to 2.7 contain my additional analysis.

2.1 Aims of the LASr Project

Empirical relationships between SMBH and galaxy mass (e.g., Kormendy and Ho, 2013) show that a connection exists. The exact nature of this interaction is not known - feedback from AGN into the galaxy, affecting the star formation and growth is likely, but details of the mechanism still elude us. AGN demographics - for example, distribution of intrinsic accretion rates and obscuration (e.g., Ricci et al., 2015) - greatly influence analysis of this AGN-galaxy connection. More precise knowledge of these properties, and of the AGN duty cycle (i.e., the proportion of the lifetime of a SMBH where it is active) would help to constrain the interaction processes. Thus, an accurate local census of AGN that could constrain AGN population statistics would provide an important stepping stone towards solving this problem.

The local universe is known far better than the high-redshift universe: low luminosity objects are visible, high spatial resolution measurements are possible, and a detailed picture of local structure can be made. However, even in this ideal zone, databases are incomplete. The current most commonly used consistently collected dataset of local galaxies is the 2MASS Redshift Survey (2MRS; Huchra et al., 2012) and although this is a thorough sample, it is not complete even at very low redshifts (see Sections 2.2.1 and 2.4). All selection methods for AGN are known to be incomplete in some way (see Section 1.2.1.7), and without a complete census of local galaxies, even the most complete selections cannot find all AGN - particularly those that are heavily obscured, intrinsically low luminosity, or suffer from significant host galaxy dilution. For example, Ananna et al. (2019) estimate from the cosmic X-ray background that the fraction of AGN within $z < 0.1$ should be 50%$\pm$9%, but observations do not reproduce this number. Thus with our constructed local catalogue we will have the most complete collated sample of local galaxies to date, and with this will be able to uncover new local AGN candidates.

The eventual ultimate goal of LASr is to produce a complete local census of AGN. The local universe is ideal for (1) finding missing AGN that are representative of as much of the full range of luminosities as possible; (2) selecting AGN with the minimum possible bias; and (3) studying their nuclear environments in detail. The steps this project takes towards this goal are as follows:

1. A complete census of local galaxies - active *and* inactive. This will form the 'Galaxy Parent Sample'(LASr-GPS), from which known AGN and AGN candidates will be selected $\rightarrow$ **Sections 2.1.1-2.4**

2. Selection of AGN candidates from the galaxies in the LASr-GPS that are not known to be AGN $\rightarrow$ **Section 2.3**

3. Multi-wavelength investigations of the AGN candidates to assess the fraction of AGN that are thus unknown in the local universe → **Optical and NIR spectroscopy in Section 2.5.2; further work to come in other parts of the electromagnetic spectrum**

2.1.1 Other AGN catalogues

The ongoing all-sky scan with *Swift*-BAT (the Burst Alert Telescope on the *Swift* satellite; Barthelmy et al., 2005, Gehrels et al., 2004) provides hard X-ray (14-195 keV) coverage, and therefore local AGN catalogues that are relatively unbiased. In this work we use the 70-month catalogue (hereafter B70; Koss et al., 2017, Ricci et al., 2017a) as a reliable sample of AGN, including some Compton thick (CT) sources. However, due to low sensitivity in this hard X-ray regime, the flux limit for B70 is high, and many bright AGN - including many CT - are not detected.

The Véron-Cetty & Véron catalogue (13th edition; Véron-Cetty and Véron, 2010, , hereafter VCV) aims to present a complete catalogue of known AGN, including 169k objects with redshift and absolute magnitude, with other basic information where available. These are classed into quasars, BL Lacs, and AGN. Only a small fraction (1135) are within the LASr-GPS volume, but these comprise a significant fraction of the known AGN within the LASr-GPS catalogue. This catalogue is a compilation of other AGN catalogues, and should thus be expected to present a thorough list.

Zaw et al. (2019) (hereafter ZCF) analyse the 2MRS spectra, producing a catalogue of optical AGN based on the initial infra-red selected sample. They analyse emission line widths and fluxes, enabling AGN selection based on various optical methods. They remove host galaxy contribution then fit Gaussians to various emission lines, identifying broad line AGN with a FWHM threshold of 1000 km s^{-1} in broad H α and/or H β. In the absence of broad lines they identify AGN with the BPT diagram (Baldwin et al., 1981, Kewley et al., 2006). This catalogue contains 8.5k AGN, of which 3078 are within the LASr-GPS volume.

2.1.2 Lack of completeness and the reasons for it

All attempts at complete AGN catalogues are inevitably biased. The key to this is understanding the causes of these biases, and combining different methods in order to mitigate their effects. The B70 AGN are biased towards X-ray bright, local AGN - an all-sky survey struggles to make deep measurements, and sacrifices this for wide coverage. ZCF relies on emission line analysis of optical spectra, which is more likely to miss obscured AGN, weakly accreting AGN, or AGN that are dominated by their host galaxies. VCV aims to be a complete compilation, but relies on the completeness of

ifts contributing surveys. These catalogues of known AGN may be reliable - we can trust that most objects in them are indeed AGN - but even in combination will not be complete.

2.2 Construction of Galaxy Parent Sample

2.2.1 Base databases

Extended galaxies from 2MASS (the Two Micron All Sky Survey; Skrutskie et al., 2006) were gathered with a combination of known redshifts and dedicated follow-ups into the 2MASS Redshift Survey (2MRS), containing 43.5k galaxies at K magnitude $\leq$11.75, with low foreground extinction and out of the galactic plane. 15k of these are within the range of the LASr-GPS, and form the initial core of the project. However, as only 13% of the B70 AGN host galaxies are included in this sample (this low number is due in part to the K-band threshold), it is imperative that it must be extended, as there are evidently many galaxies - potentially many AGN hosts absent. → **Fig. 2.1, Step 1**

NED[1] is a large database of extra-galactic objects, compiled over many years from a wide range of sources, and including data from across the electromagnetic spectrum. It includes redshift measurements - often multiple - and information on object classification, making it an invaluable source when compiling information on a catalogue such as LASr is aiming for. It contributes 157k objects to the LASr-GPS. → **Fig. 2.1, Step 1**

SIMBAD (Wenger et al., 2000)[2] is a reference database for all astronomical objects, both extra-galactic and galactic. Similarly to NED, it includes basic data on each object, including classifications. It contributes 60k objects to the LASr-GPS. → **Fig. 2.1, Step 1**

SDSS - the Sloan Digital Sky Survey - is a long running project that includes images, optical spectra, infrared spectra, IFU spectra, stellar library spectra, and catalogue data for a large number of objects in the Northern sky. For this work we use Data Release 15 (Aguado et al., 2019), the most recent available at the time of the project. The optical photometry and spectra are used to produce classifications and redshifts, which we use here to contribute to the LASr-GPS - 22k objects. → **Fig. 2.1, Step 1**

The Wide-field Infrared Survey Explorer (*WISE*; Wright et al., 2010) is an all-sky infrared survey telescope with four filter bands, at 3.4, 4.6, 12, and 22 microns. It provides magnitudes with a number of different fitting models; for the purposes of AGN selection, the most relevant are the profile fitting magnitudes, as they should most closely trace the nuclear emission, rather than that of the whole galaxy. → **Fig. 2.1, Step 7**

[1] https://ned.ipac.caltech.edu/; the NASA/IPAC Extragalactic Database (NED) is funded by the National Aeronautics and Space Administration and operated by the California Institute of Technology.

[2] https://simbad.u-strasbg.fr/simbad/sim-fid

2.2.2 Combining these and other selection steps

Armed with each of the contributing databases, these were combined into a final sample. No objects with photometric redshifts are kept, as these are statistical measurements that can be quite uncertain. Any objects at very low redshift (z <0.001) and classified as stars are very likely to be correctly identified as such; these are excluded. Some objects have contradictory classifications, for example if an outdated SDSS class has been included in NED, and these are assessed based on the number of classifications as Galactic objects and a redshift threshold designed for a high probability of removing Galactic sources. → **Fig. 2.1, Steps 5, 6**

The remaining galaxies are cross-matched with *WISE* sources, and visually checked. In most cases, the *WISE* source closest to the database coordinates is most likely to be the correct one. For the rest, some have inaccurate coordinates for the galaxy nucleus, or have no clear nucleus. The former can be corrected, and the latter is flagged in the database. In a very small number of sources, the *WISE* catalogue does not contain an entry for the coordinates, despite emission there - most of these were present in the original *WISE* data release (Cutri and et al., 2012) and can be added (with corresponding flag). With these steps, 99.94% of the LASr-GPS has *WISE* data. 1.4% are dominated by a nearby bright source, and the *WISE* photometry for these are taken as upper limits. Any sources associated with the same *WISE* source were removed. → **Fig. 2.1, Step 7**

Any duplicate objects were blended - no repeats are wanted in the final list, but information from one database may be missing from another, and any useful data should not be lost. → **Fig. 2.1, Step 8**

A final check of redshifts was then done - it is important that it is known accurately, as for most sources it is the best measure of distance available, and therefore important for accurate luminosity measurements. Sources are flagged if they have (a) an unverified but not suspicious redshift value (low confidence in SDSS, or only a single measurement), or (b) highly different measurements with an unclear solution. NED contains a number of redshift-independent distances. We find that at >50 Mpc, the redshift-derived luminosity distance and redshift-independent distance converge. Therefore, where available, we adopt the redshift-independent distances for the galaxies at < 50 Mpc. → **Fig. 2.1, Step 9**

A summary of the steps taken can be found in Figure 2.1.

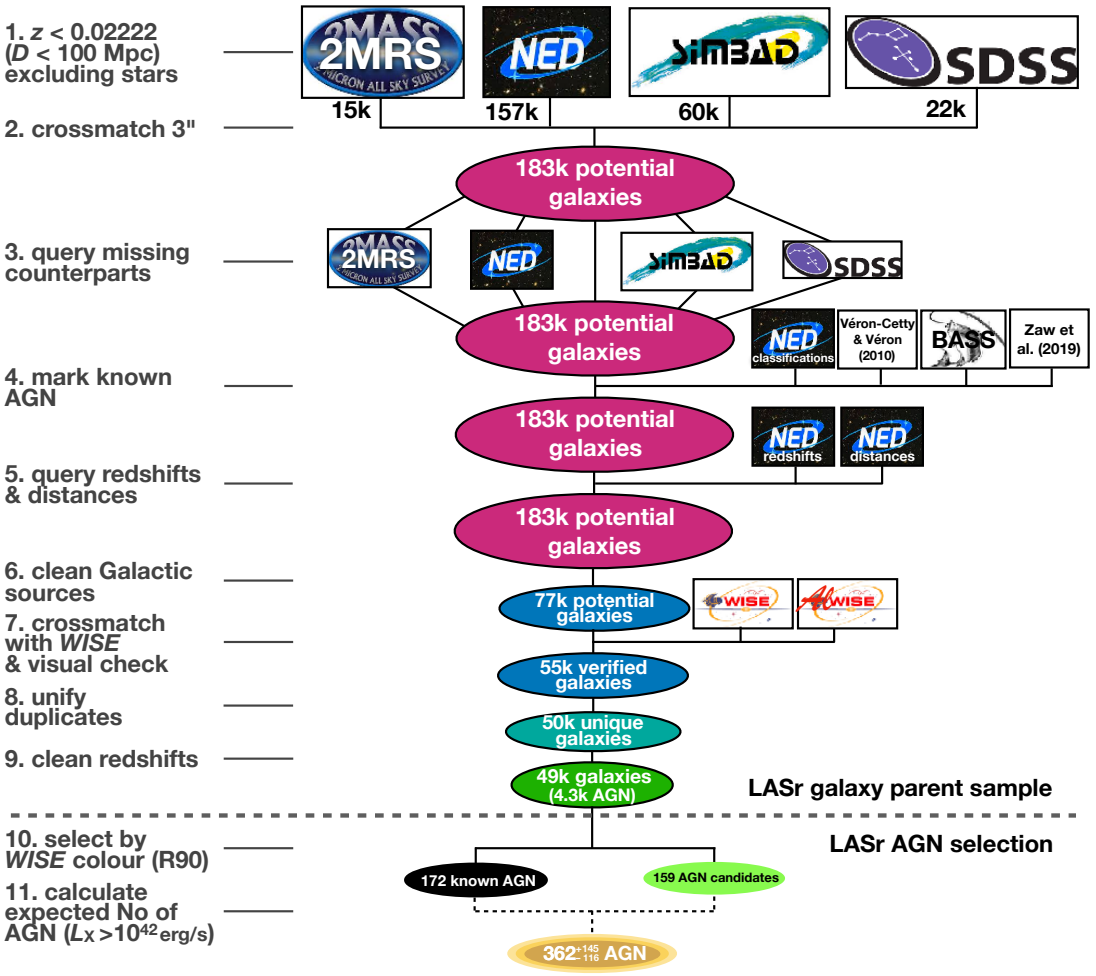

FIGURE 2.1: Selection steps involved in combining existing databases into the LASr-GPS (figure from A2020).

2.3 AGN Selection

2.3.1 Prior Information

After compilation of the LASr-GPS, there are many sources that are already known to be AGN in one or more of the contributing databases (see Section 2.2.1). This population will form a core part of our understanding of how much is already known of AGN in the local volume, and allow us to statistically assess how many AGN may lie hidden in other galaxies.

NED and SIMBAD have together collected classifications from many different references, for a large number of sources. SDSS identifies AGN based on template fitting to optical spectra. In addition to these, we have known AGN from the dedicated catalogues VCV (Véron-Cetty and Véron, 2010) and ZCF (Zaw et al., 2019), and X-ray selected AGN from *Swift*-BAT (B70) - see Section 2.1.1.

Finally, there are 4309 known AGN within the LASr-GPS. Most of these are selected with optical emission line analysis, with the main exception being the B70 AGN. → **Fig. 2.1, Step 4**

A key parameter for tracing the AGN power is the 12 micron luminosity, which follows the warm AGN heated dust. At very low redshifts, such as is the case for LASr, we can use the *WISE* $W3$ luminosities directly, with no k-correction needed. Emission from star formation can also contribute in this range, and full decoupling of these sources needs detailed SED modelling (e.g., AGNFITTER; Calistro Rivera et al., 2016, ; see Section 4.2.2), which is out of the scope of this section. A comparison of *WISE* and higher angular resolution measurements can be done to derive a rough correction factor (Asmus et al., 2014), but only a weak relationship between $L(W3)$ and the correction ratio is found for the sources in the LASr-GPS. This relationship shows some change with optical classification (e.g., Seyferts, starburst) and thus we can apply corrections to the known AGN population, based on their optical type. This correction must be heavily caveated: the scatter on the relationship is large, and is therefore only acceptable for statistical analyses, and not for individual sources.

When focusing on AGN, one major source of contamination in the MIR is starburst galaxies (Hainline et al., 2016). As stated above these also produce emission in the same MIR range, so it is important to understand how selection of candidate AGN might be affected. Similarly to AGN, we can find starburst classifications in our base databases, and although the list of starbursts will also be incomplete it will still indicate where we might find them when considering AGN selection. PAH emission in low-z star-forming galaxies can also cause red colours, and Galactic contaminants such as brown dwarfs may also be present.

2.3.2 Applying MIR AGN selection

Many MIR selection criteria focus on the $W1 - W2$ colour (e.g., Stern et al., 2012, Assef et al., 2013), as a good indicator that the shape of the SED in that region is more likely to be caused by AGN heated dust than by any other sources. In Figure 2.2 we show the distribution of this attribute for the entire parent sample (light blue), and for various subsets. The sub-sample showing the clearest difference in distribution is the B70 AGN, emphasised by the median values shown. Figure 2.3a shows these values as compared to $W2 - W3$, and indicates where objects lie on this plane. Most galaxies lie on the star forming main sequence across $W2 - W3$, caused by increasing warm dust emission from star formation leading to redder colours (as found by Jarrett et al., 2019).

Selection of desired sources can be done to prioritise reliability (i.e., most of the selected sources are correct), or completeness (most of the correct sources are selected), and a balance between the two is hard to find. In this case our aim is to select new AGN

$$\begin{array}{ll} W1 - W2 > 0.65 & \text{if } W2 < 13.86\,\text{mag} \\ W1 - W2 > 0.65\exp(0.153(W2 - 13.86)^2) & \text{otherwise} \end{array}$$

candidates, and use these to assess how many AGN are missing from the current catalogues. For this purpose, it is better that we get a *reliable* sample of AGN candidates, so that we can compare their numbers to the known AGN in same region, and extrapolate further.

With this in mind, we use the criterion from Assef et al. (2018), which is designed to have 90% reliability (hereafter R90):

This is shown (for $W2 < 13.86$ mag) in Figure 2.3a as a horizontal grey dashed line, and Step 10 in Figure 2.1. Out of the known AGN, 172 ($\sim$4%) are above this threshold. The majority of these are classified as Seyferts, and have a type 2 to type 1 ratio of classifications of 0.52, similar to the whole population - indicating that there is no significant bias towards either obscured or unobscured.

In Figure 2.3b we can see that there is a bias towards selecting more luminous AGN, as expected. This is discussed further in Section 2.4.3. Figure 2.3 shows that a significant number of known AGN are not included in colour selection. Further analysis in this work is limited to brighter objects where completeness increases significantly (see Figure 2.10).

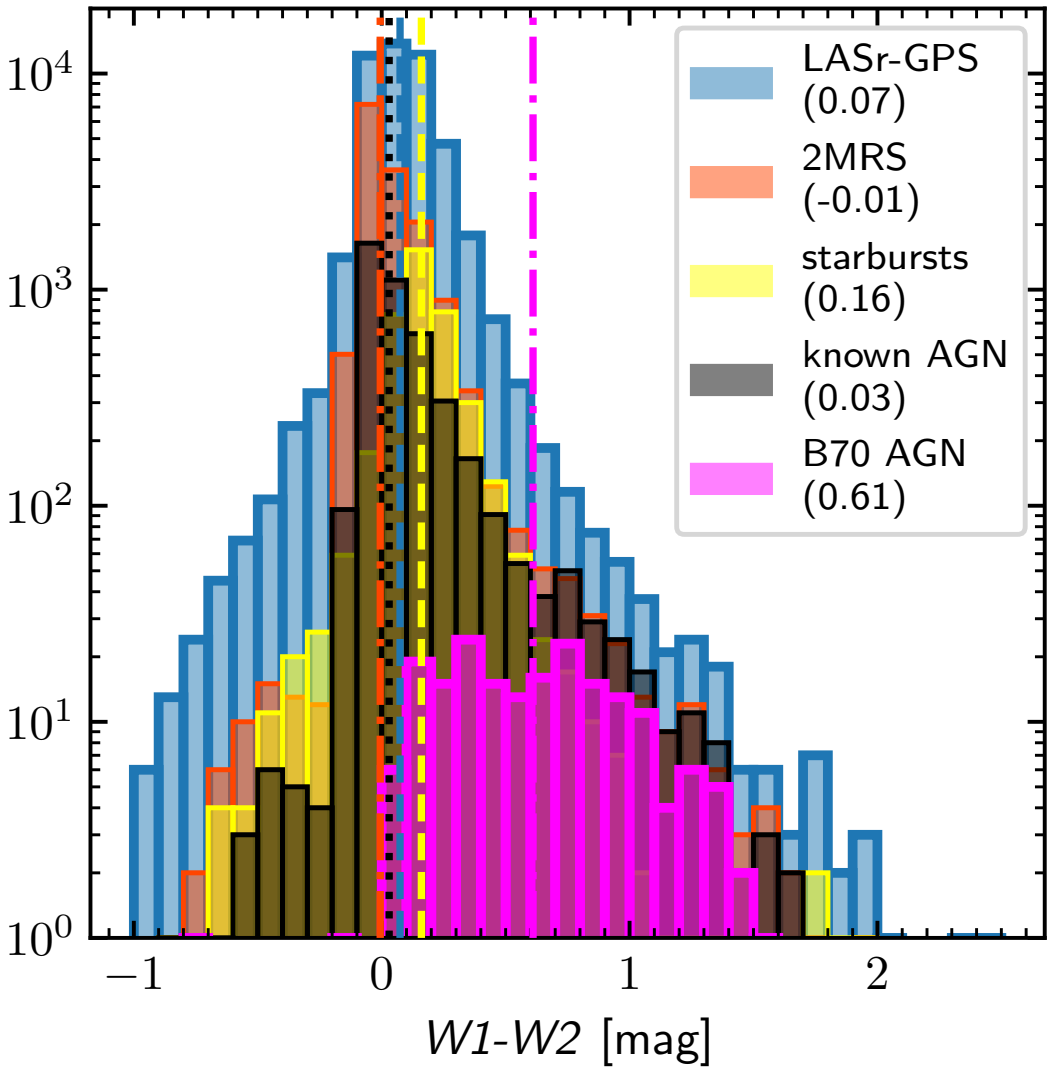

FIGURE 2.2: Distribution of *WISE* $W1 - W2$ colours for all galaxies in the 2MRS (orange), combined GPS (blue), and B70 AGN (magenta). Galaxies classified as known starbursts (yellow) and known AGN (black) are also shown. Vertical lines show the median value for each category (figure from A2020).

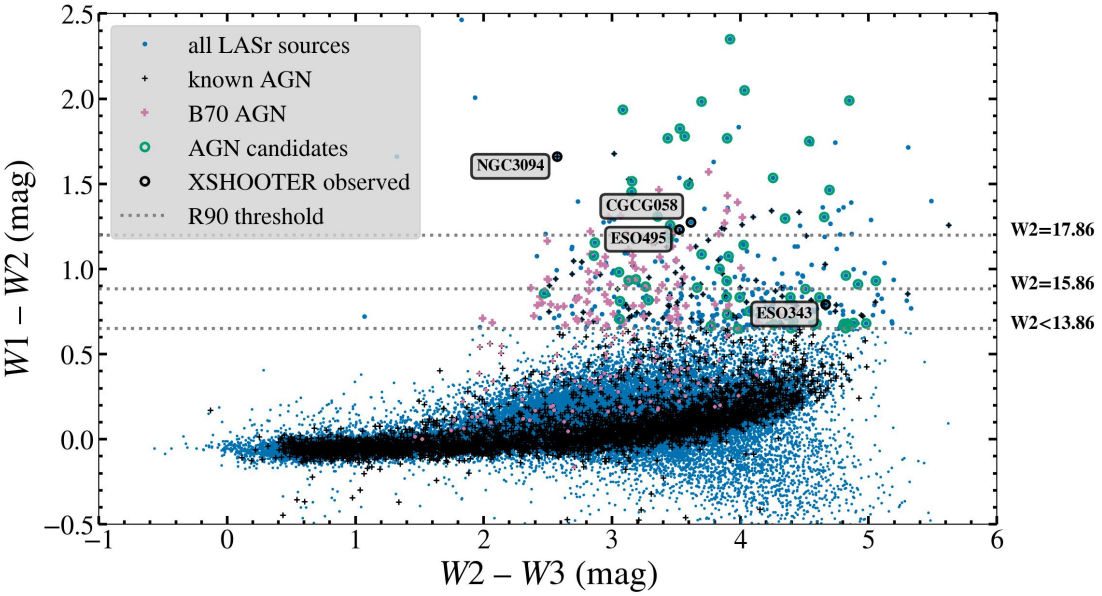

(A) $W1 - W2$ versus $W2 - W3$ colour-colour diagram, with all detected galaxies in the combined GPS (blue). Classified galaxies are shown: known AGN (black crosses), and B70 AGN (magenta crosses). R90 selection threshold is shown as a set of dashed grey lines, and galaxies that pass this are shown with enlarged symbols. Green circles highlight R90 AGN candidates with $L(W3) > 10^{42.3}$ erg s^{-1}.

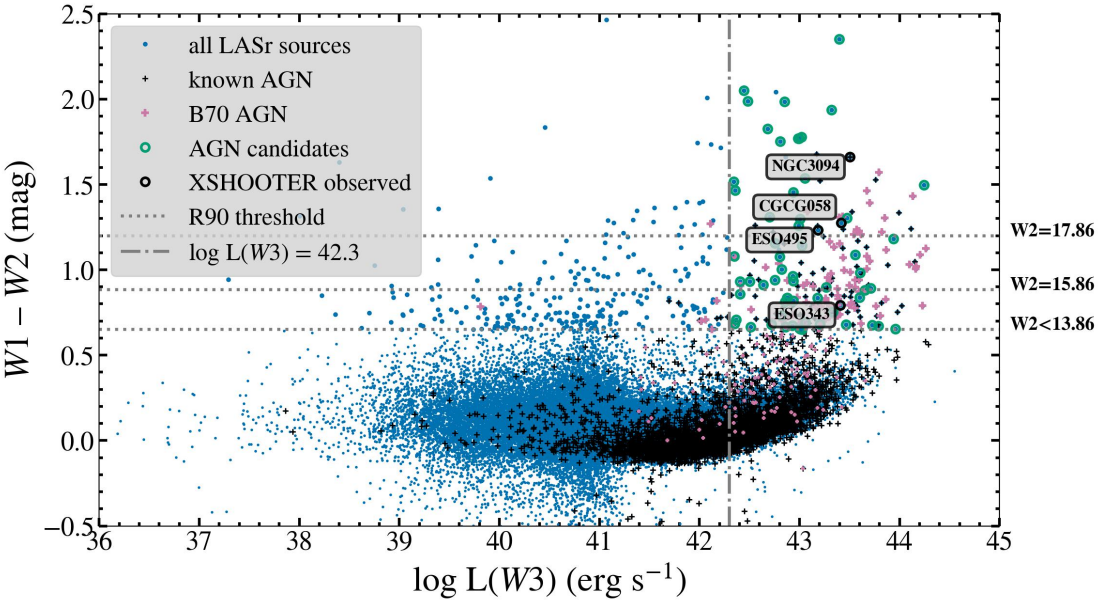

(B) As in (a), but with $W3$ luminosity on the x-axis. Vertical dot-dash line marks the threshold $L(W3) > 10^{42.3}$ erg s^{-1}.

FIGURE 2.3: The LASr-GPS and MIR selection: new candidates are highlighted, in colour (a), and luminosity (b).

2.3.3 Future Application of X-ray AGN selection

Selection of AGN in X-rays is one of the most reliable. Most AGN are intrinsically luminous in X-rays due to Compton up-scattering of UV photons from the accretion disc. The resulting high intensity means that AGN stand out from other non-transient X-ray sources in the sky. Star formation can also produce X-rays, but at generally lower luminosities. X-ray emission is also less affected by obscuration, particular at higher energies, making selection in this regime less bias against heavily obscured sources.

The BAT 70 month catalogue (see Section 2.1.1) provides a reliable local list of AGN, relatively unbiased compared to other catalogues. However, it is constrained by high flux limits, and while this will be deepened as the satellite continues its work, it will not improve greatly.

In 2019 the *SRG* mission launched, comprising two instruments: eROSITA (the extended ROentgen Survey with an Imaging Telescope Array; Predehl et al., 2010, Merloni et al., 2012, , at 0.2–10 keV) and ART-XC (the Astronomical Roentgen Telescope - X-ray Concentrator; Pavlinsky et al., 2011, 2018, , at 4–30 keV). Early results from these telescopes look promising[3], and they are expected to be approximately ten times deeper than the current *Swift*-BAT survey, and should therefore be an excellent opportunity to enhance numbers of known local X-ray AGN, particularly less luminous and Compton thick AGN. Expected numbers of detections can be estimated as follows:

1. **R90 AGN candidates**: we have selected a number of reliable candidates for thus far unknown AGN, based on their MIR colour and luminosity. In Figure 2.3b, these are found in the top right corner (i.e., $W1 - W2 > 0.65$ and $L(W3) > 10^{42.3}$ erg s^{-1}).
2. ***L*(*W*3)**: MIR luminosity is a good predictor for intrinsic X-ray luminosity, so we start with the best available MIR for all candidates.
3. **Simulation of expected flux**: the following steps are then based on predicted relationships, or assumed underlying distributions, and as such include an inherent uncertainty. We therefore perform a Monte Carlo re-sampling of these steps; with 10^4 iterations, the results become stable.
   (a) $L^{\mathrm{nuc}}_{12\,\mu\mathrm{m}}$ **prediction**: as described in Section 2.3.1, we can decontaminate the $W3$ luminosity to predict the nuclear only luminosity - an improved estimate of AGN-only emission. The probability distribution for the uncertainty on this relationship is assumed to be Gaussian.
   (b) $L_X^{intrinsic}$ **prediction**: based on the MIR–X-ray luminosity relationship from Asmus et al. (2015), we can use the predicted nuclear $L_{12\,\mu\mathrm{m}}$ to determine the

[3]Operations are currently on pause.

expected *intrinsic* X-ray flux. The probability distribution for the uncertainty on this relationship is assumed to be Gaussian.

(c) **N_{H} assignment**: this intrinsic X-ray flux can become a predicted *observed* flux with the application of obscuring column depth. The true values for these are unknown, so each candidate is randomly assigned an N_{H} based on the B70 AGN bias-corrected distribution (Figure 2.4a).

(d) **Absorption prediction**: finally, the intrinsic predicted X-ray flux and assigned column depth (N_{H}) are combined with the absorption curve (Figure 2.4b) to produce an expected observed source flux for each candidate.

Starting from 61 R90 AGN candidates, we find that eROSITA should detect 43$\pm$6 of these in the all-sky survey. The remainder would be expected to be highly obscured. Based on the predicted flux distribution, we would expect 20$\pm$10 of the 61 R90 to be already detected in the *Swift*-BAT 70 month survey; however, we know that none were.

This leads us to two possible explanations:

- There are more CT AGN in the R90 than assumed in the N_{H} distribution; a conclusion that seems reasonable given that we know CT AGN are harder to select. If the R90 selection is unbiased to N_{H} then according to the intrinsic N_{H} distribution used above (Ricci et al., 2015) we should expect 54 CT objects from the full R90 passing list of sources. From the known AGN, only 18 are CT. Thus, there may be many more CT AGN present in the R90 candidates as assumed, and the expected detection numbers for *Swift*-BAT correspondingly lower. This will be discussed further in Section 2.4.4.

- A significant fraction of the 61 R90 candidates are contaminant objects. By design the selection should contain 10% non-AGN galaxies - given that the rest are confirmed AGN, we would expect that all of these are likely to be in the unconfirmed candidate group.

Whether a higher than expected number of CT AGN or non-AGN contaminants is present in the R90 AGN candidate list, we should still expect that a significant number appear as X-ray AGN in the all-sky eROSITA survey.

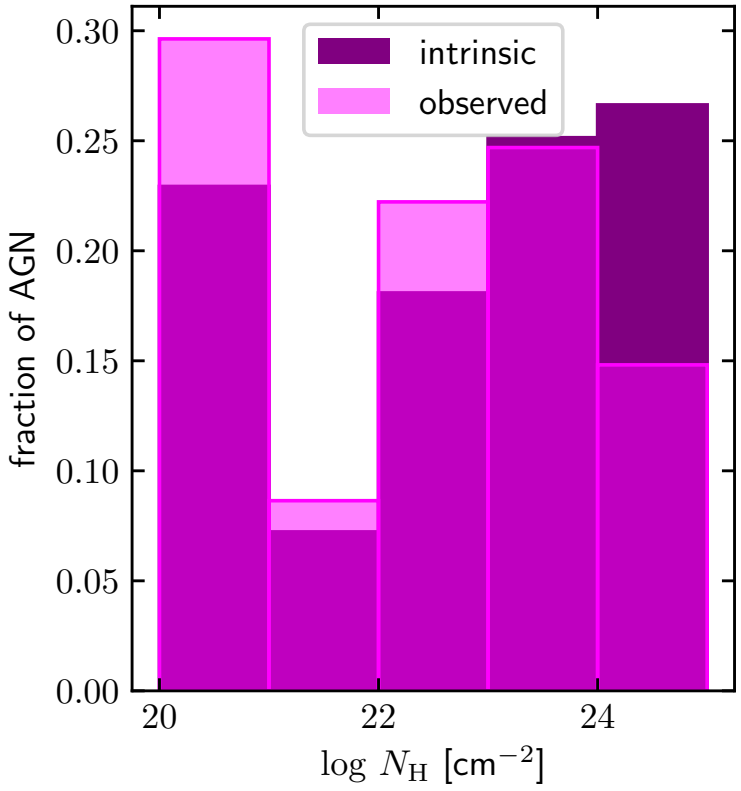

(A) Observed distribution of $N_{\rm H}$ for B70 AGN (light magenta) and inferred intrinsic distribution from Ricci et al. (2015) (dark purple). In Section 2.3.3 this distribution is assumed in order to predict the number of AGN we may expect to detect in X-rays.

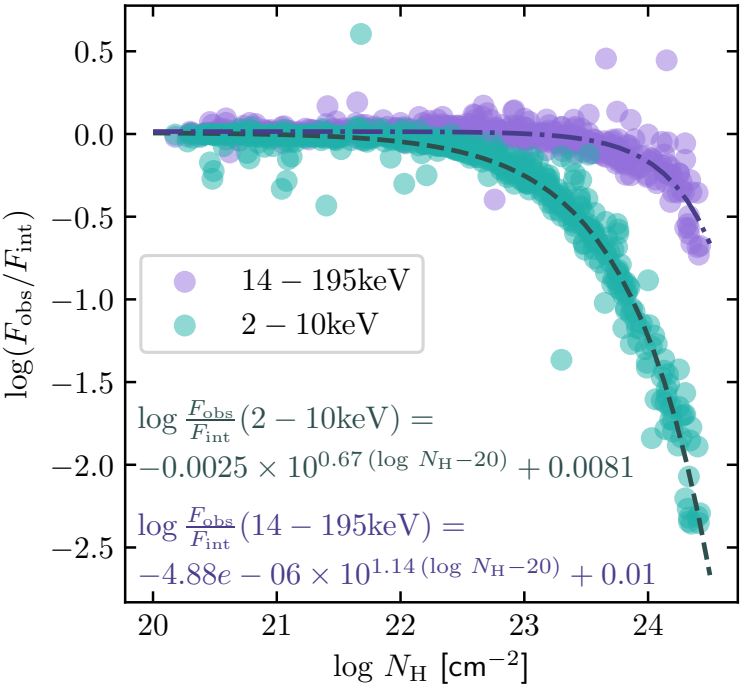

(B) X-ray absorption of 2–10 keV and 14-195 keV fluxes for BAT70 AGN, with $N_{\rm H}$ values from Ricci et al. (2017a).

FIGURE 2.4: Difference in intrinsic and observed $N_{\rm H}$ and the effect of $N_{\rm H}$ on flux drop-out at soft energies (figures from A2020).

2.4 Completeness and Reliability

The method used to construct the LASr-GPS aims to have a higher completeness of potential AGN host galaxies than previous catalogues, including the 2MRS catalogue. To assess this in simple physical terms – without making assumptions about the nature of the host galaxies – we can examine the depth in terms of the central $W1$ luminosity. At 100 Mpc (the limiting distance of the LASr-GPS), the maximum depth is $\sim 10^{41}$ erg s^{-1}. Completeness above this luminosity is affected by other factors, which will be discussed in the rest of this section.

We can make empirical assessments of the contributing databases by cross-checking the results. Here we look at the numbers of galaxies with known redshifts compared to those without.

- **NED:** Kulkarni et al. (2018) compared the rates of detected supernova in NED galaxies with and without redshifts, and concluded that the z-completeness of NED is $\sim$78% (at $z < 0.03$; higher than the LASr-GPS redshift limit). As NED is only part of the parent sample, this places a lower limit on the completeness of the LASr-GPS.

- **SDSS:** examination of an SDSS 'core area' (an area with maximum coverage by the surveys). Assuming that the LASr-GPS is 100% complete in this area, we find that the SDSS z-completeness is 88%, close to the average redshift completeness of SDSS. SDSS is less complete in brighter galaxies, and the 2MRS galaxies fill in this region (see Figure 2.5). Assuming this number of galaxies is the correct expected number for an area of sky this size allows us to assess how many galaxies are missing across the whole sky. Completeness assessed in this way reveals a strong dependence on luminosity.

- **GAMA:** the Galaxy and Mass Assembly Survey (GAMA; Liske et al., 2015) is a survey across a smaller area than SDSS, and here we use two deep fields (G12 and G15; DR3, Baldry et al., 2018), with a completeness of 98.5%, and 811 in the LASr-GPS volume. Importantly, GAMA DR3 is not included in the versions of NED or SIMBAD used for this selection, so it provides an independent test of completeness. From the GAMA galaxies, we find 68 with a *WISE* counterpart and $L(W1) > 10^{42}$ erg s^{-1}; 94% are in the LASr-GPS, consistent with our high completeness aim.

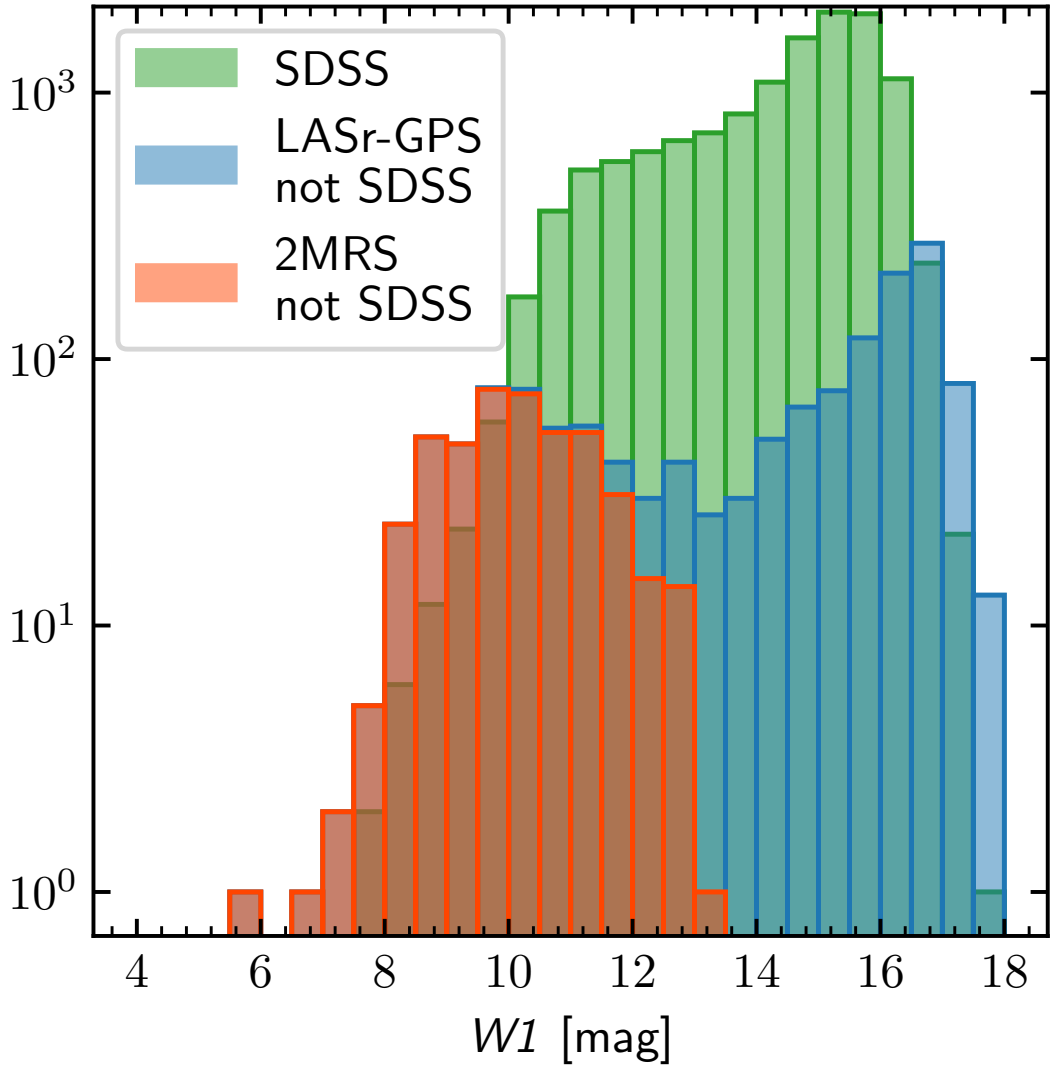

FIGURE 2.5: Distribution of all galaxies in SDSS (green), and in the 2MRS (orange) and combined GPS (blue) excluding SDSS: *WISE W*1 magnitudes (figure from A2020).

2.4.1 Sky covering

It is also worthwhile examining the effect of sky position on completeness. One major source of incompleteness is the Milky Way plane - between high extinction and numerous galactic sources, it is difficult to extract background galaxies that have coordinates in this region. The projection map of sources in Figure 2.6 makes the under-density of sources at low latitudes clear, with an obvious gap in both 2MRS and the full LASr-GPS. In Figure 2.7 the distribution of sources with Galactic latitude is shown, with dashed lines representing a cosine curve – the theoretical shape of the distribution, given fully random underlying sources. At low latitudes, the observed distributions fall sharply away from the theoretical value, resulting in a deficiency of 6.4$\pm$0.8%. There is no simple way to include galaxies hidden by the Milky Way in this study, so this region will

be excluded from calculations of the AGN population.

A second feature worth noting in Figure 2.7 is an under-density between $\sim 35^{\circ}$ and $\sim 45^{\circ}$. This is caused by voids in the local volume - at this level of completeness and local z, the cosmic structure is visible, and the distribution is not, as assumed, completely random. Figure 2.6 clearly shows the galaxies following this filamentary structure. This is, therefore, not a source of incompleteness in our galaxy sample, but conversely demonstrates that our completeness is high enough that these structures are readily visible.

Finally, we must note that although much of the LASr-GPS comes from the 2MRS, an all-sky survey, a large number of sources come from SDSS - a ground based Northern hemisphere survey. As such, there is some bias towards better completeness in the SDSS region than outside it, which is visible in Figures 2.6 and 2.8 as a higher density of points in the North. However, when comparing SDSS core region numbers (described at the start of Section 2.4) it is not found to have a significant effect.

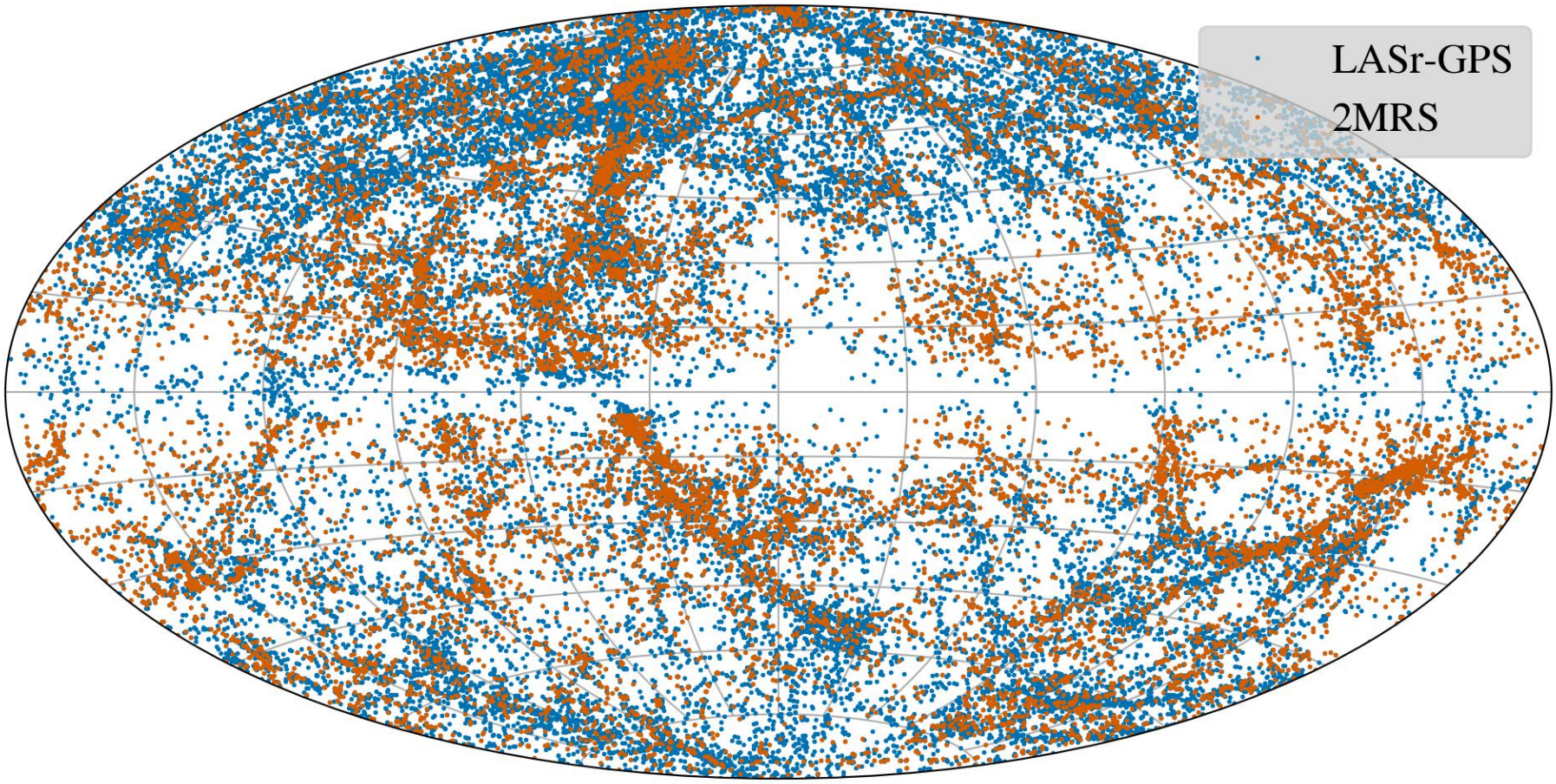

FIGURE 2.6: Distribution of all galaxies in the 2MRS (orange) and combined GPS (blue): Aitoff projection of Galactic coordinates (figure from A2020).

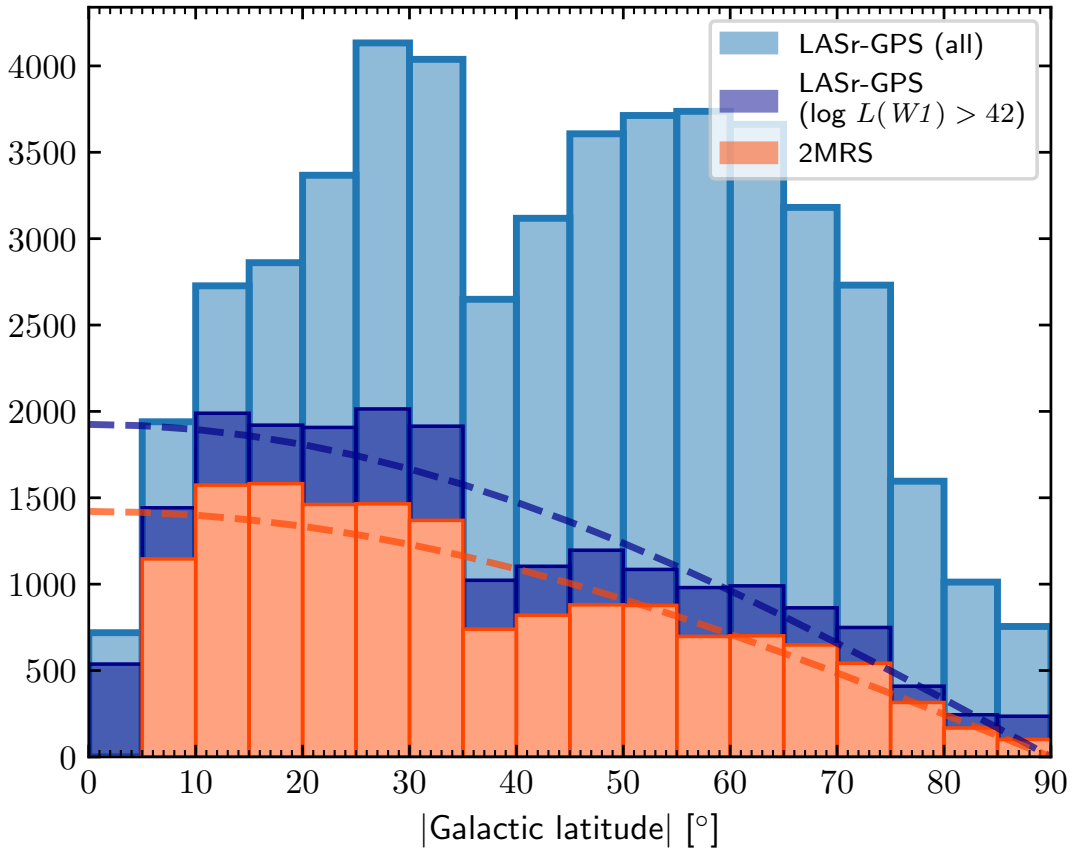

FIGURE 2.7: Distribution of all galaxies in the 2MRS (orange), combined GPS (light blue), and GPS with $L(W1) > 10^{42}$ erg s^{-1} (dark blue): Galactic latitude histogram, with cosine fits to the data shown as dashed lines (figure from A2020).

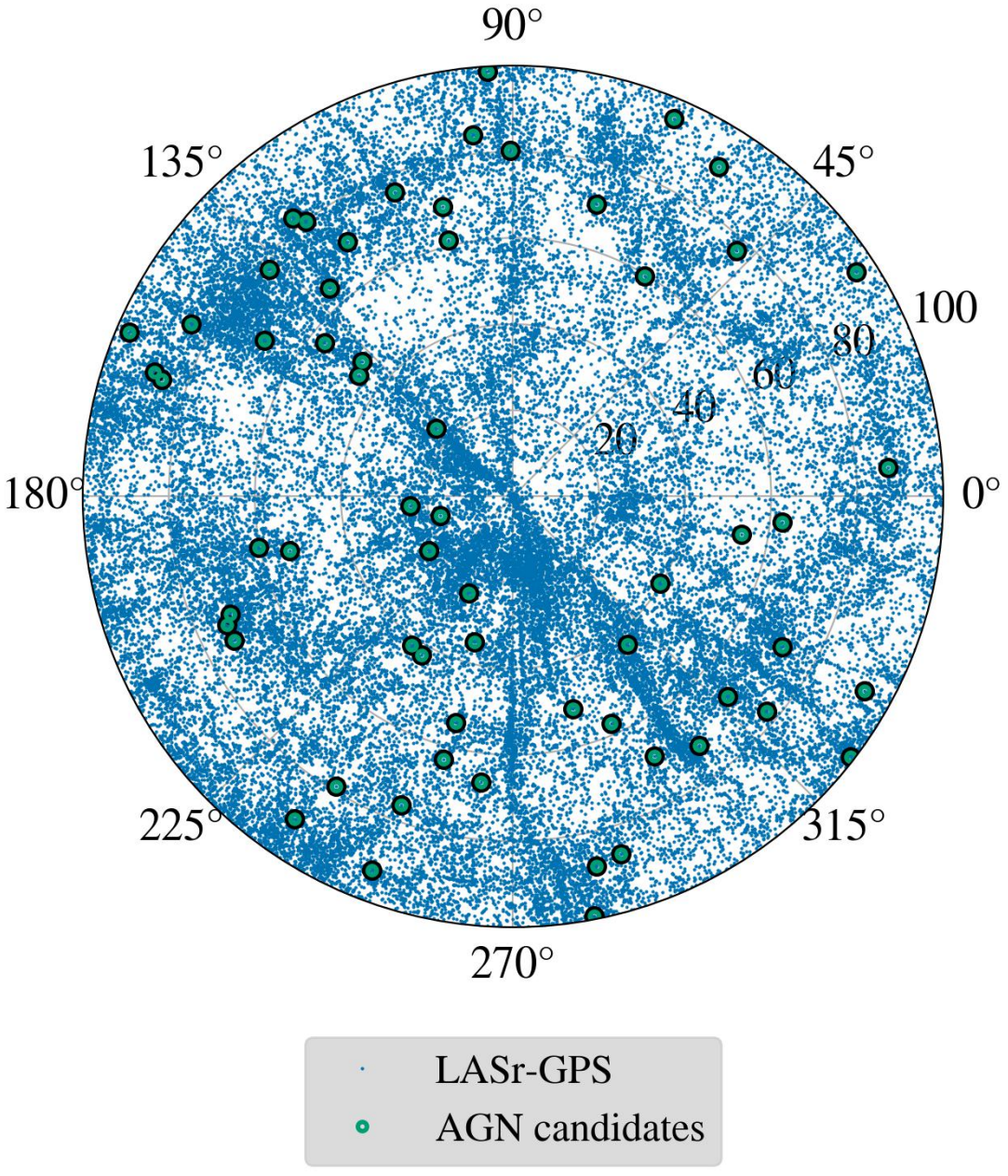

FIGURE 2.8: Distribution of all galaxies in the combined LASr-GPS (blue), and AGN candidates (green circles): Galactic longitude projection into Galactic plane, with distance in Mpc.

2.4.2 Redshift

Redshift completeness - i.e., the proportion of galaxies in the volume that have measured redshifts and can therefore be included - is difficult to assess, given the nature of the contributing databases. As outlined above, the completeness in NED can be estimated at ∼78%, and this will not be unbiased - redshifts are only available for objects that have been selected for targeting, and (if selected) with a measurable redshift. Figure 2.9 shows the distribution of galaxies with redshift across the total LASr-GPS, rising with increasing volume as expected for approximately uniform number densities. As in the latitude distribution, the anisotropy of the local universe is visible in a small dip at $z \sim 0.01$. The redshift distribution of the 2MRS galaxies decreases after $z \sim 0.017$, indicating that the brightness cut causes it to miss galaxies at greater distances, even in this small volume.

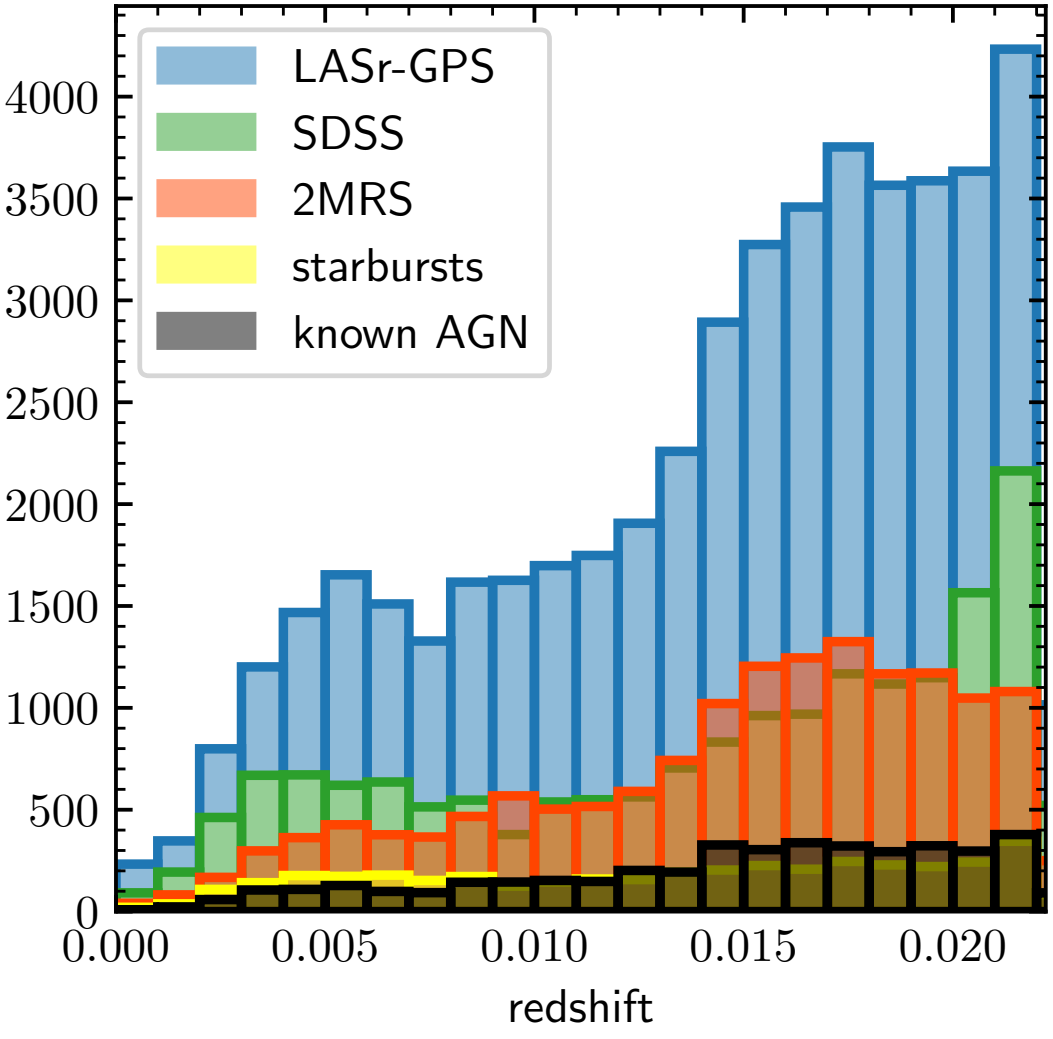

FIGURE 2.9: Distribution of all galaxies in the 2MRS (orange), combined GPS (blue), known AGN (black), and known starbursts (yellow): redshifts of all objects (figure from A2020).

2.4.3 Magnitude and Luminosity

While there have been no specific luminosity or magnitude cuts made to the LASr-GPS, it is nevertheless clear that there must be completeness effects and biases due to the various flux limits of the contributing catalogues. For example, Figure 2.5 shows that different catalogues are better for different magnitude ranges.

The 2MRS catalogue is a large part of the LASr-GPS construction, and Figure 2.10 shows the ratio of 2MRS galaxies to total LASr-GPS galaxies as a function of a lower limit cut on $L(W1)$. It shows that the 2MRS is missing many galaxies and low luminosity - this is expected, given the K-band magnitude cut in its selection process - but remains incomplete even at luminosities where it would be expected to be safely detecting a very high fraction of galaxies. In fact, the 2MRS completeness peaks at $L(W1) > 10^{42.9}$ erg s^{-1}, easily into the range of AGN luminosities. The 2MRS is therefore likely to be missing a significant number of AGN host galaxies, and is not alone a sufficient base catalogue.

Returning to our comparison with the SDSS core area, taking this as an approximately 100% complete sample to $W1 \leq 17$ mag, we can again examine how the completeness varies with $L(W1)$ for the complete LASr-GPS. For $L(W1) \leq 10^{41}$ erg s^{-1} completeness is 50-60% and reaches 90, then 100% at $L(W1) \leq 10^{42}$ erg s^{-1} and $L(W1) \leq 10^{42.3}$ erg s^{-1}, respectively[4].

High completeness at expected AGN luminosities implies that we can be confident in the inclusion of the majority of AGN hosts, with the caveat that this is true for hard X-ray selected AGN, and less so for the majority optically selected subset. We know that this subset is biased against obscured AGN and would thus be expected to be less complete. In Assef et al. (2018), the source of the R90 selection criteria, they use photometry and spectroscopy from UV to MIR to select AGN and find a completeness of 17% for this threshold (with a magnitude limit of $W2 = 17.11$; see point 12 in Figure 1.4). In fact, apparent low completeness in MIR selection of known AGN demonstrates that the selection of known AGN in this volume is lacking, except for hard X-ray selected sources (B70 AGN). Incompleteness at the lower luminosity end may consequently cause the exclusion of some weak or heavily obscured AGN, especially those in e.g., dwarf galaxy hosts. Selection of new AGN candidates at this end of the scale is unreliable in the MIR. Figure 2.11 shows the effect on completeness of introducing a luminosity cut to Figure 2.3a on MIR selection completeness.

[4]The Milky Way plane, i.e., $|b| > 8°$, has been excluded.

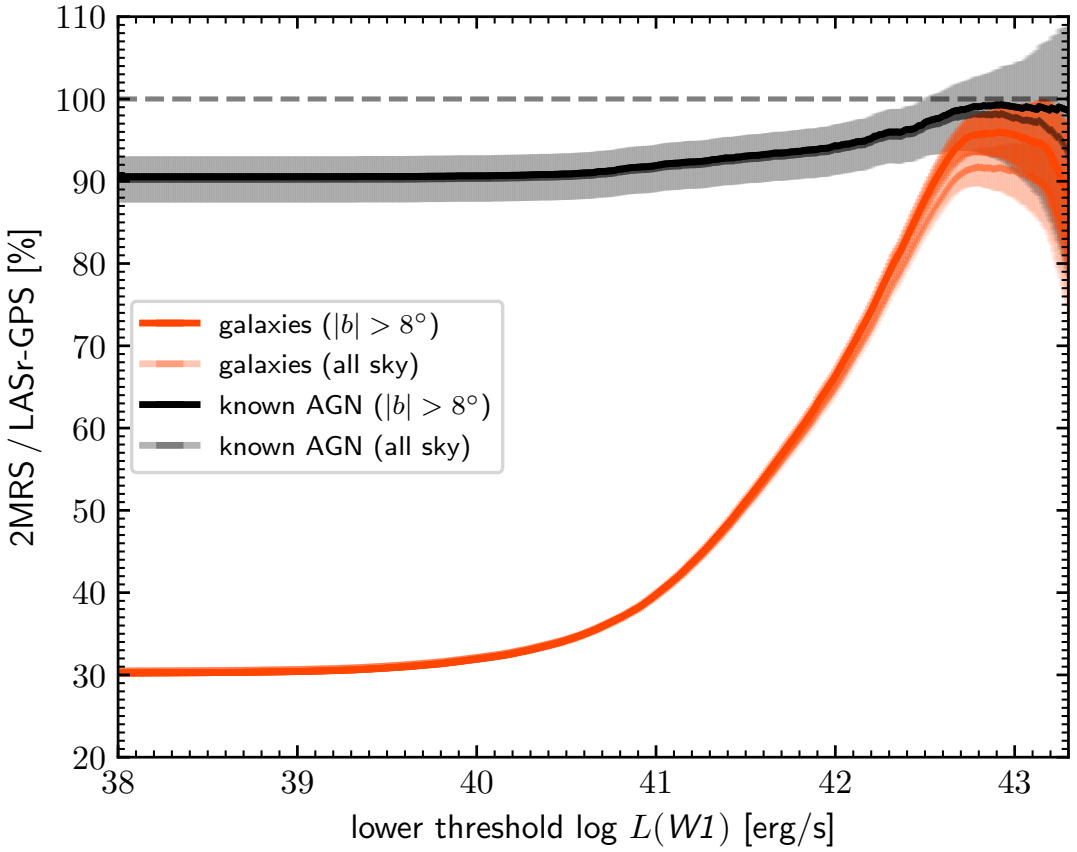

FIGURE 2.10: Ratio of galaxy count in 2MRS to the full GPS of all galaxies (orange), and known AGN (black), as a function of a lower *WISE* W1 magnitude threshold (figure from A2020).

2.4.4 Obscuration

While the LASr-GPS as a parent sample of potential host galaxies may be unbiased to AGN obscuration - it does not include any cuts that may exclude these objects - the lists of known AGN are likely to be biased against Compton thick AGN (hereafter CT AGN). The extent of this bias depends on the selection and identification method of each contributing catalogue. Hard X-rays are the most reliable method of selecting CT AGN, but even the B70 AGN list is likely to be missing many (see Section 2.1.1). Figure 2.4b shows how the soft (2–10 keV) and hard (14–195 keV) observed fluxes change with column density (log $N_{\rm H}$ (cm^{-2})). At CT obscuration ($> 10^{24}$ cm^{-2}) the observed flux is decreased by orders of magnitude, even in hard X-rays.

In Section 2.3.3 we discussed the construction of a predicted *observed* X-ray flux distribution. We found that this distribution is heavily biased by the assumed underlying distribution of $N_{\rm H}$; the fraction of CT AGN is highly uncertain (e.g., Gandhi and Fabian, 2003, Ricci et al., 2015, Ananna et al., 2019), making it difficult to estimate the expected number of new AGN detections by eROSITA. Even if our assumed intrinsic $N_{\rm H}$ distribution (Figure 2.4a) is correct, comparing the number of known CT AGN to

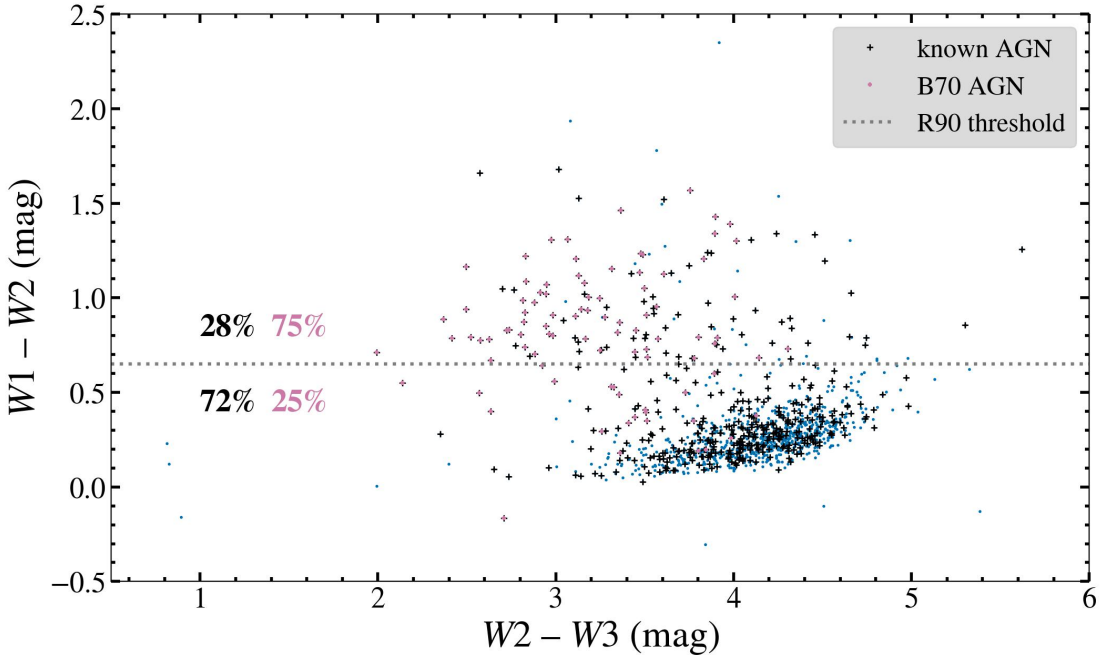

FIGURE 2.11: Subset of LASr-GPS sources with $L(12) \geq 10^{43}$ erg s^{-1} on the *WISE* colour-colour plane. Blue points are all sources, black crosses are known AGN, and pink cross are B70 AGN. Text shows the percentage of known AGN (black, left), and B70 AGN (pink, right) that pass the R90 selection.

the fraction of all known AGN that would be expected to be CT reveals a deficit. There are not enough known CT AGN to line up with the theoretical distribution.

One of the aims of this project is to assess what gaps there are in our knowledge of AGN demographics, and it is clear that the CT AGN fraction is a major area of uncertainty. Starting with the known AGN from the LASr-GPS, we can determine what the demographics of this sample imply about the CT AGN; this will be a *lower* limit, if we posit that the AGN candidate sample contains a higher proportion of CT AGN. Considering the numbers of AGN in the hard X-ray selected sample of B70 and those selected by R90, Table 2.1 summarises the CT AGN fraction found in this way, with a final value for R90 known AGN of 11%.

TABLE 2.1: Assessment of CT fraction based on numbers of known sources.

Group	$L^{int}_{2-10\mathrm{keV}}$ threshold erg s^{-1}	No. AGN	No. CT AGN	CT fraction %
(1)	(2)	(3)	(4)	(5)
B70 AGN	10^{42}	153	20	13%
R90 and B70 AGN	$10^{42.3}$	84	10	12%
R90 *not* B70 AGN	$10^{42.3}$	76	8	11%
Overall R90 known AGN	$10^{42.3}$	160	18	11%

However, the true CT fraction is likely to much higher than 11%. Ricci et al. (2015) gives us a CT fraction of 27%, and with this we can investigate further.

- **All R90 passes, $L^{int}_{2-10keV} > 10^{42}$ erg s^{-1}**: 221 objects.
- **Assuming a CT fraction of 27%**: 60 CT AGN expected out of these 221 objects.
- **B70 CT AGN**: 10 known CT AGN in the R90 subset of B70 leaves 50 more expected CT AGN out of 137 R90 non-B70 objects.
- **Expected detections:** repeating the simulations from Section 2.3.3, we would expect 60$\pm$25 of the 137 R90 non-B70 objects to have been detected by *Swift*-BAT.
- **90% reliability**: assuming 10% contamination, i.e., 22 non-AGN objects; 38$\pm$25 expected *Swift*-BAT detections remain, of which none are found.

Given that this implies more detections by *Swift*-BAT than have been seen, the CT fraction is likely to be higher than assumed here; 40% would be consistent with no *Swift*-BAT detections and thus places a lower limit on the CT fraction. From the 137 R90 non-B70 objects, 14 are known to be type 1 AGN and thus unlikely to be CT. If the remaining 123 objects are CT, this places an upper limit of $\sim$55% on the CT fraction in this selection.

Much of the uncertainties here come from the unknown nature of the R90 candidates. Are they truly AGN? How many are actually star forming contaminant galaxies? For those that are AGN, are they CT? Alternatively, are they an intrinsically X-ray weak population and thus *Swift*-BAT- undetected for this reason? If we can begin to define and classify these 'missing' AGN, we can narrow down the CT fraction in the local universe further.

2.4.5 Estimated AGN Number Density

For the LASr-GPS we have excellent completeness for objects with $L(W3) > 10^{42.3}$ erg s^{-1}, and can be confident in the 90% reliability for the R90 selection criteria above this threshold. This luminosity limit corresponds to an approximate stellar mass of $\log(M_*/M_\odot)$ $\sim$9.7 (using the relation from Wen et al., 2013), with the caveat that this value is highly dependent on galaxy properties, and that we may be missing a significant fraction of stellar light. Thus, we can use our parent sample along with estimates of AGN counts and incompleteness from various sources to calculate an AGN number density for the local volume, summarised in Table 2.2.

- **R90 galaxies**: from 221 R90 galaxies, we expect 90% to be AGN hosts, i.e., 199 objects, consistent with 160 of these being known AGN.

TABLE 2.2: Summary of correction factors applied to R90 selected galaxies to obtain estimated number counts of AGN in galaxies with $L^{\rm nuc}_{12\,\mu{\rm m}} > 10^{42.3}$ erg s^{-1}. Columns: (1) Step in the process; (2); Correction factor applied due to over/under-counts of total AGN due to effects from this factor; (3) number counts of AGN.

Step (1)	Correction factor (2)	Number (3)
R90 galaxies		221
90% reliability	0.9	
Colour selection	$1.95^{+0.48}_{-0.32}$	
*W*3 host contamination	0.85±0.1	
LASr-GPS	1.11±0.04	
Final count		362^{+145}_{-116}

- **Incompleteness from colour selection**: our selection criterion (Assef et al., 2018) was chosen for high *reliability*, and sacrifices completeness to achieve this. For this luminosity threshold, 51±10% are selected by R90. This completeness fraction is calculated based on the fraction of B70 AGN selected by R90 at the chosen luminosity threshold (see Fig. 18 of Asmus et al. 2020), as this sub-sample is assumed to be the least biased due to its hard X-ray selection.. Therefore, we apply a correction factor of $1.95^{+0.48}_{-0.32}$.

- **Host contamination of *W*3**: intrinsic AGN luminosity may be overestimated due to contributions from the host galaxy. The correction to *nuclear* 12 µm luminosity (see Section 2.3.1) is not accurate for individual sources, but can be used for the sample population. Applying the correction to the 221 R90 leaves 187±22 (85±10%) with nuclear luminosities above this threshold. The correction factor for this effect is 0.85±0.1.

- **LASr-GPS**: incompleteness of the parent sample is can be estimated for *W*3 similarly to *W*1 in Section 2.4.3. Outside of the Milky Way, the LASr-GPS completeness at $L(W3) > 10^{42.3}$ erg s^{-1} is 96.1±4.2%. Correcting for the MW shadow adds another 6.4±0.8% (see Section 2.4.1), putting the final correction at 1.11±0.04.

- **Others not accounted for**: there are smaller factors that have not been included in this calculation, e.g., lack of redshift-independent distances. The effects from these are estimated to be $\ll$1%, and are ignored here.

Finally, applying these factors gives an expected number of AGN of 362^{+145}_{-116}, equivalent to a density of $8.6^{+3.5}_{-2.8} \times 10^{-5}$ Mpc^{-3}, for AGN with $L^{\rm nuc}_{12\,\mu{\rm m}} > 10^{42.3}$ erg s^{-1}. Repeating the calculation for X-ray luminosity thresholds instead gives us a number count of 101^{+55}_{-25} (4^{+2}_{-1}) for $L^{\rm int}_{2-10{\rm keV}} > 10^{43}$ (10^{44}) erg s^{-1}. There are 53 (2) known AGN above this threshold.

2.5 Are the 'Candidate AGN' Truly AGN?

Having selected a number of candidate AGN from the LASr-GPS - galaxies that can be expected to host AGN based on their IR colour and luminosity - the next step is to assess which of these are AGN, and what their properties might be. Many of the candidate AGN may be expected to be Compton thick, and some may be contaminated by host galaxy IR light. Either of these scenarios may mean low soft X-ray flux, and therefore difficult to confirm AGN presence with upcoming eROSITA data. An independent assessment of AGN power is to examine emission lines from the NLR, which should be further from the BH than any Compton thick obscuring matter. High quality optical and NIR spectra is a useful tool for detailed emission line diagnostics, and a multi-year follow-up campaign is underway with X-SHOOTER (Vernet et al., 2011). Optical emission line diagnostics (e.g., Kewley et al., 2006) should identify the majority of objects, but in extremely obscured sources (or even rarer objects, e.g., weak line quasars; Meusinger and Balafkan, 2014, or Optically Quiescent Quasars; Chapters 4 and 5) optical lines may not indicate AGN presence. In this case we can use NIR emission lines, which are less likely to be extincted by thick obscuration.

2.5.1 X-SHOOTER follow-up campaign aims

To reach these goals, we proposed X-SHOOTER bad weather spectroscopy of all 43 AGN candidates found in A2020 that are expected to have $L_X > 10^{42}$ erg s^{-1} and are visible from Paranal (DEC$<$30). The wide spectral coverage at relatively high spectral resolution of X-SHOOTER allows us to:

- Perform optical AGN BPT diagnostics based on the ratios of, e.g., Hα, Hβ, [O I], [O III] and [N II] (diagrams based on the first three observed candidates shows the inconclusive results from this method alone);
- Perform infrared AGN diagnostics based on the ratios of Fe II 1.26 µm, Paβ, H_2 2.12 µm, Brγ and the presence of coronal lines, e.g., [Si VI] 1.96 µm.

These new AGN candidates may be extreme in their obscuration properties - they have not been found in previous surveys, despite being local. Therefore, it is important to combine multi-wavelength AGN diagnostics to verify and characterise these systems. Any single diagnostic might fail; however, the combination will uncover any AGN with high confidence.

2.5.2 Initial Follow-up Sources

To date, four targets have been measured and processed, and the results from these follow. The first three sources shown here are not currently known to be AGN - these are followed up for confirmation (or rejection) of the presence of an AGN. The final source is known – or thought – to be an AGN, and conjected to be an object called a Compact Obscured Nucleus (CON; e.g., Falstad et al., 2021). These are optically normal galaxies containing dense, IR bright cores (see Figure 2.21). This core may contain an enshrouded AGN or a compact starburst, and it is difficult to identify the source of power. A deep silicate absorption feature can indicate visual obscuration.

A summary of the four follow-up objects, their properties, and basic results is found in Table 2.3a. Figure 2.12 shows the optical emission line diagnostic results (Kewley et al., 2006) for each, and Figure 2.13 shows the NIR emission line diagnostic diagram from Riffel et al. (2013).

Table 2.3b contains a summary of the X-SHOOTER observations. The follow-up spectra were taken in ESO P106 (1 October 2020 – 31 March 2021) and P109 (1 April 2022 – 30 September 2022). In order to achieve the scientific aims of this work, we requested the following sky conditions: seeing 2″, sky transparency 'thin cirrus' (transparency variations above 10%), airmass 2, fraction of lunar illumination 1 (i.e., fully illuminated is acceptable), moon distance 30°, and precipitable water vapour 30 mm. These are generally fairly relaxed, given the nature of these AGN candidates as bright, local galaxies. With the exception of seeing all constraints were met for all observations. Spectra were processed with the standard pipeline, as described in ESO phase 3 documentation[5], with sky subtracted and calibration applied.

[5] https://ftp.eso.org/pub/dfs/pipelines/instruments/xshooter/xshoo-pipeline-manual-3.6.1.pdf

(A) Basic information about the four AGN candidate follow-up sources. Column details: (1) object name; (2),(3) sky position; (4) redshift; (5) Distance; (6) 12 µm nuclear luminosity; (7) in the 2MRS catalogue; (8) known AGN; (9) AGN according to optical emission lines (Fig. 2.12); (8) AGN according to NIR emission lines (Fig. 2.13).

Name (1)	RA (J2000) (2)	DEC (J2000) (3)	z (4)	Distance (Mpc) (5)	L_{12} (log erg s^{-1}) (6)	2MRS (7)	known AGN (8)	new AGN (optical) (8)	new AGN (NIR) (9)
CGCG 058-009	113.931	11.709	0.0163	72.83	42.68±0.23	✓		✓	
ESO 495- G 005	124.811	-25.188	0.0056	24.77	42.83±0.57	✓			✓
NGC 3094	150.358	15.770	0.0080	38.50	43.66±0.04	✓	✓		?
ESO 343-IG 013 NED02	324.046	-38.542	0.0195	87.37	42.67±0.23				

(B) Information about the observations used for each source. Column details: (1) object name; (2) ESO observing period; (3) observation grade (based on requested parameters); (4) observation date; (5) exposure time.

Name (1)	Observing Period (2)	Grade (3)	Date (4)	Exposure Time (minutes) (5)
CGCG 058-009	P106	C (poor seeing)	27/28-Nov-2020	19:34
ESO 495- G 005	P106	A	14/15-Jan-2021	17:15
NGC 3094	P106	A	4/5-Mar-2021	15:28
ESO 343-IG 013 NED02	P109	C (poor seeing)	12/13-Jul-2022	20:03

(C) Line flux fitting results. Fluxes are corrected as in Kewley et al. (2006) using the Balmer decrement and reddening curve from Cardelli et al. (1989). Column details: (1) object name; (2) A_V; (3)-(11) line fluxes in erg s^{-1} cm^{-2}.

Name (1)	A_V (2)	H β 4863 Å (3)	[O III] 5008 Å (4)	[O I] 6302 Å (5)	H α 6565 Å (6)	[S II] 6725 Å (7)	Fe II 12570 Å (8)	Paβ 12822 Å (9)	H_2 21213 Å (10)	Brγ 21661 Å (11)
CGCG 058-009	3.77	1.15e-13	3.72e-14	1.55e-14	3.56e-13	1.15e-13	6.69e-15	1.58e-14	5.11e-15	3.85e-15
ESO 495- G 005	1.73	1.97e-13	2.26e-12	5.12e-14	6.12e-13	1.45e-13	9.58e-16	1.97e-14	1.11e-15	3.25e-15
NGC 3094	3.43	6.87e-14	3.63e-14	1.98e-14	2.13e-13	9.58e-14	4.73e-15	2.82e-15	5.69e-15	–
ESO 343-IG 013 NED02	3.14	9.82e-14	3.75e-14	1.12e-14	3.04e-13	8.81e-14	4.32e-15	1.65e-14	2.04e-15	5.39e-15

TABLE 2.3: Summary details for LASr AGN candidate follow-up spectroscopy with X-SHOOTER.

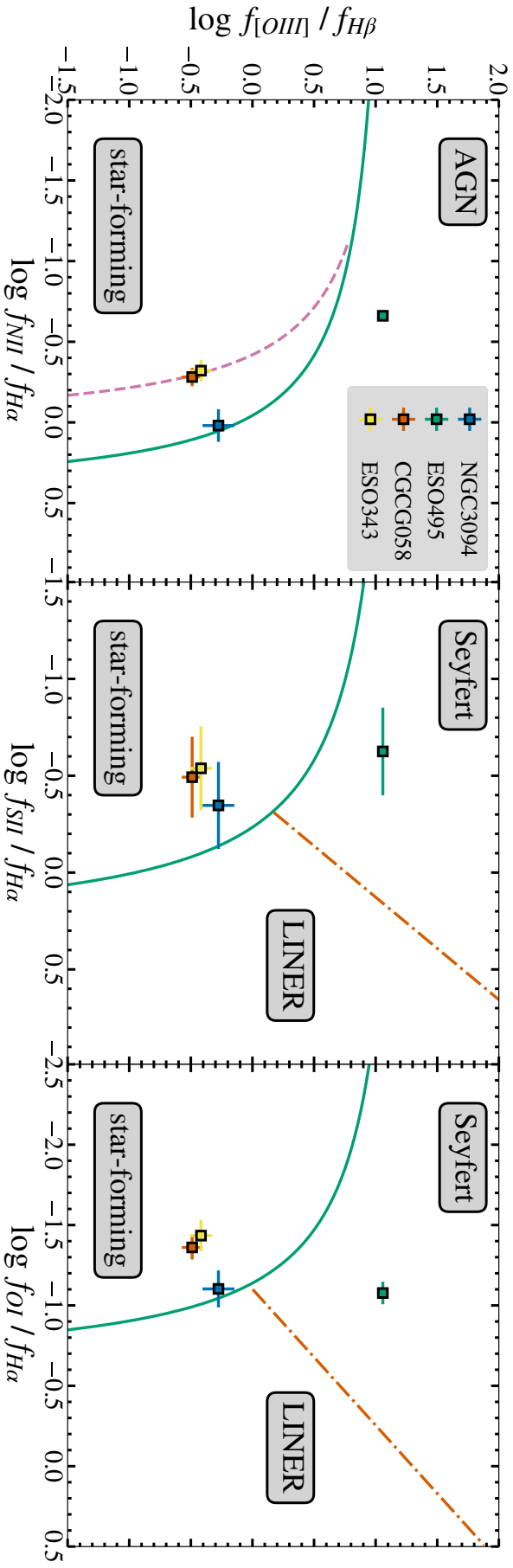

FIGURE 2.12: X-SHOOTER follow-up sources on the BPT diagram (Kewley et al., 2006), showing their optical classification based on emission lines. Only ESO495 appears decisively to be an AGN by this method.

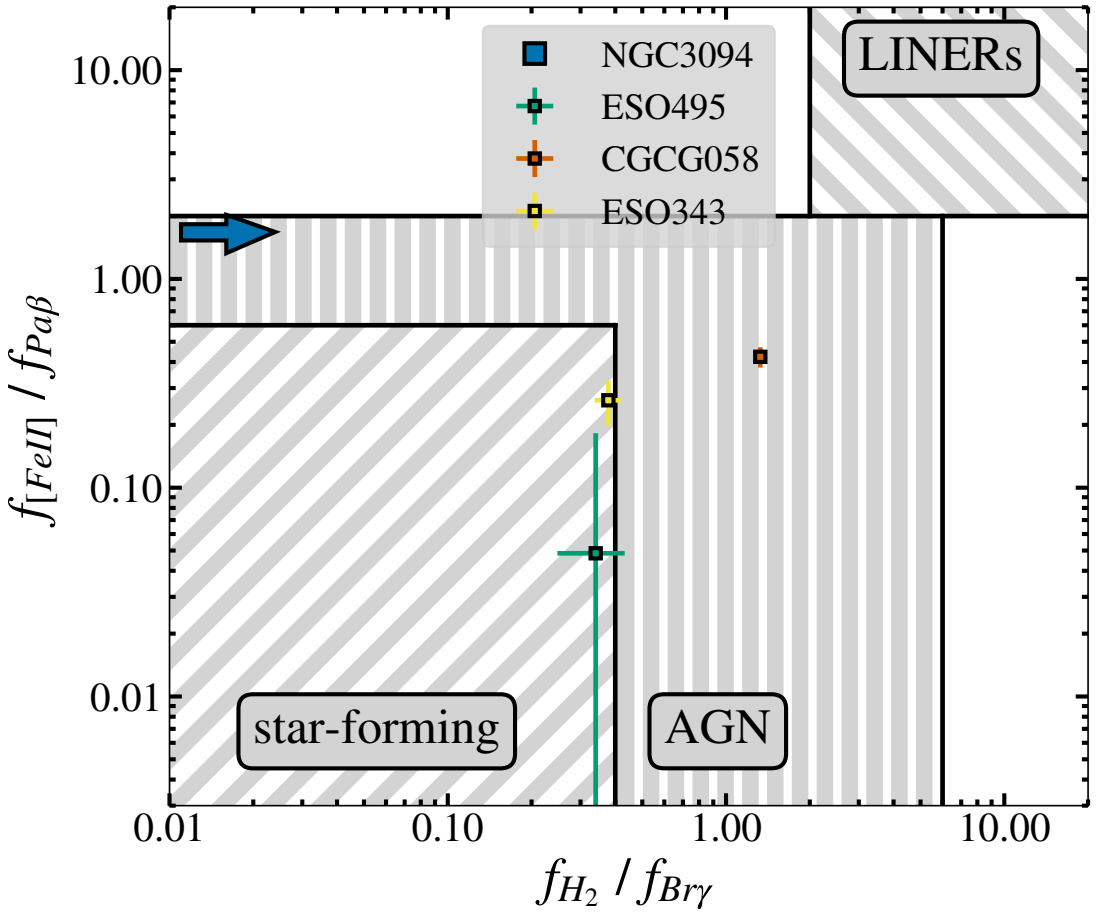

FIGURE 2.13: X-SHOOTER follow-up sources on the NIR diagnostic diagram (Riffel et al., 2013), showing their NIR classification based on emission lines. Only CGCG058 appears decisively to be an AGN by this method..

2.5.2.1 CGCG 058-009

Not classified as an AGN in any of the LASr-GPS base catalogues, CGCG 058-009 (hereafter CGCG058) is included in some recent studies of heavily obscured AGN, but is not previously confirmed either optically or in X-rays. For example Tsuchikawa et al. (2021)[6] present a study of silicate absorption features at 10-20 µm, selected from *Spitzer* (Houck et al., 2004, Werner et al., 2004) spectra as AGN-dominated galaxies according to their small polycyclic aromatic hydrocarbon (PAH) 6.2 µm feature. The presence of deep silicate absorption in this system implies the presence of heavy obscuration, but does not by itself confirm AGN presence. Optical imaging (Figure 2.15) appears to show a disturbed morphology, perhaps the remnant of past galaxy interaction; this may be associated with higher likelihood of AGN presence, but the evidence is not conclusive (see Section 3.4.2). The ratios of emission line fluxes from new X-SHOOTER measurements (Figures 2.14, 2.12) place it outside the AGN region, in either star-forming or transitional galaxy regions. However, NIR emission line ratios (Figure 2.13) positively identify it as an AGN. This evidence, along with the silicate feature, implies that this may be a good candidate for a heavily obscured AGN, possibly even a Compact Obscured Nucleus (CON; e.g., Falstad et al., 2021, and Section 5.13.1). Some emission lines are not particularly bright compared to the noise (see e.g., [O III] and [O I] in Figure 2.16), and we must also bear in mind that this spectrum was not taken with ideal seeing, and thus may include more galaxy contamination than others.

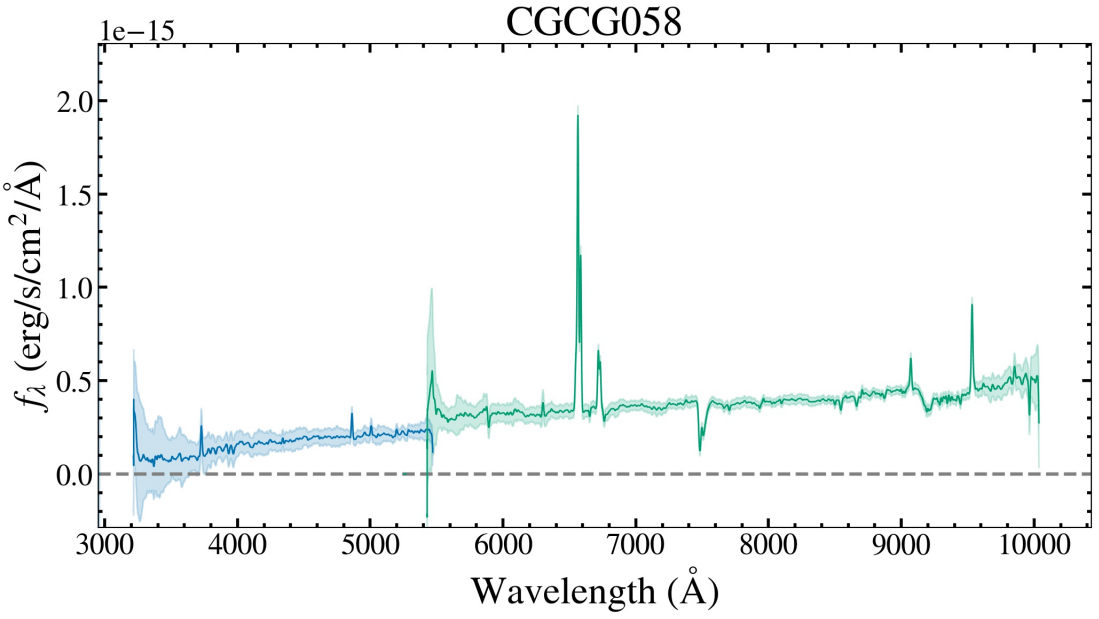

FIGURE 2.14: Optical and NIR spectra of CGCG058. Smoothed with a Gaussian kernel, width 25 pixels. Shaded area shows flux uncertainty.

[6] Included as MCG +02-20-003.

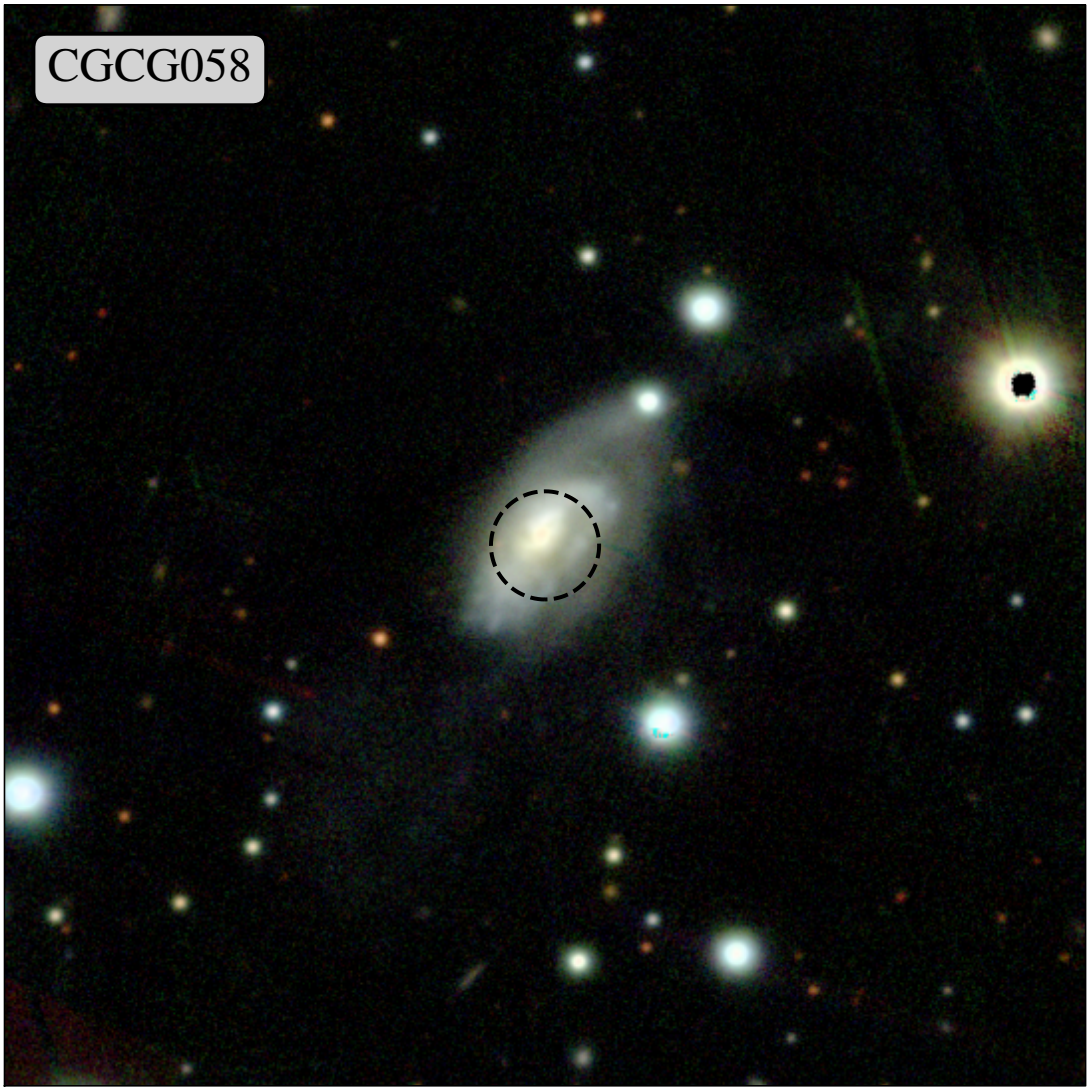

FIGURE 2.15: PanSTARRS *irg* bands converted to RGB image of CGCG058. Circle has 9 arcsec radius and is centred on the catalogue source coordinates.

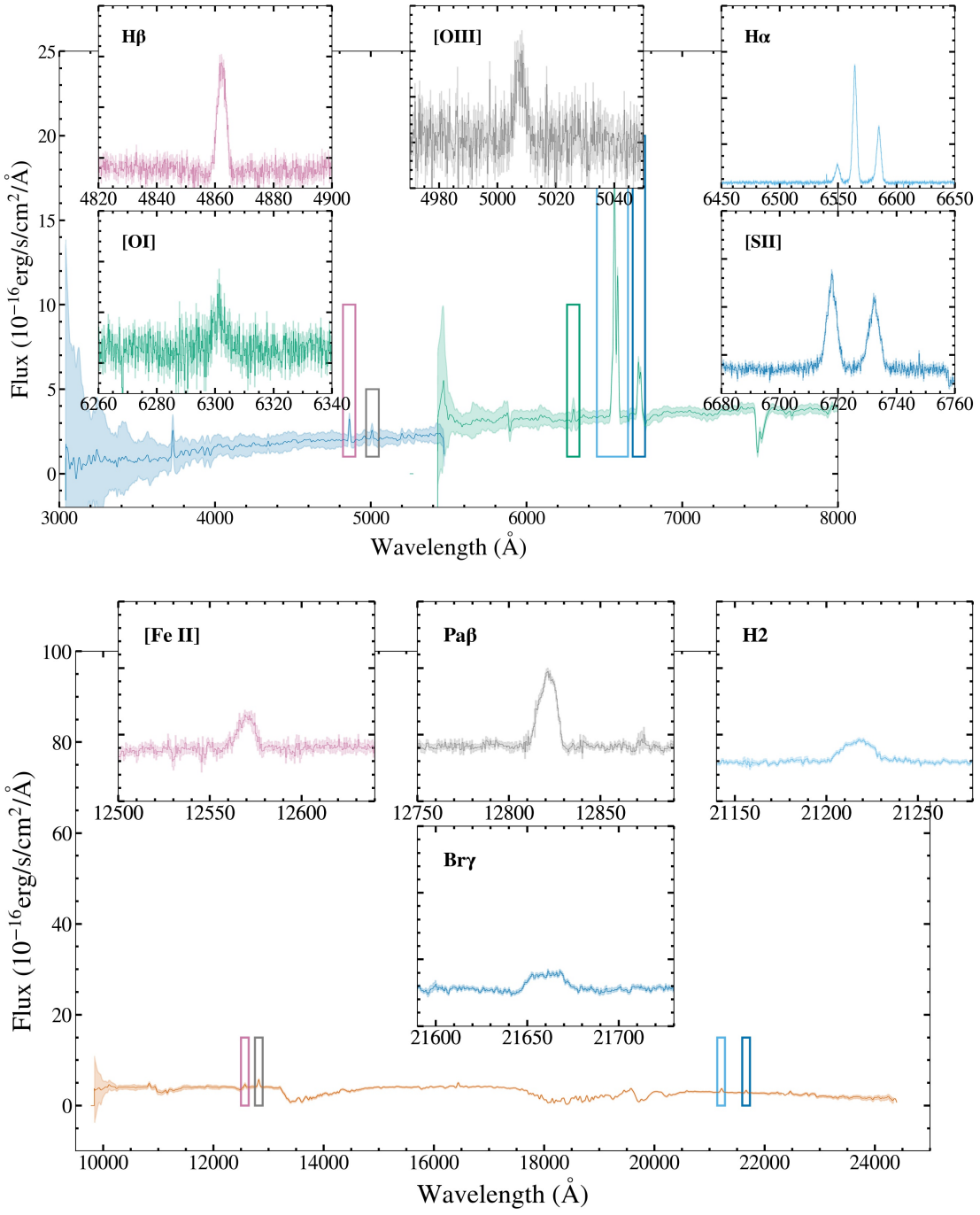

FIGURE 2.16: Optical and NIR spectra of CGCG058, with emission lines highlighted.

2.5.2.2 ESO 495-G 005

ESO 495-G 005 (hereafter ESO495) is a face-on galaxy, with a bright nucleus (see Figure 2.18). A second bright optical region is visible within the galaxy, but it is clear from the location of the *WISE* sources that these are separate, and that the central source is the location of the candidate AGN. Its optical spectrum shows a clear 4000Å break (see Figure 2.17, indicating an older, metal-rich stellar population. An X-ray source associated with it is present in a now-outdated version of the BAT catalogue (54 month; Cusumano et al., 2010), with 15–150 keV flux $6.8 \pm 3.8 \times 10^{-12}$ erg s^{-1} cm^{-2}. This source is not found in newer versions of the catalogue (i.e., the 70 month version used here), which may indicate that it was either better associated with a different source, a statistical error, or a faint source at the edge of the limits of *Swift*-BAT. It also may be a ROSAT source (Voges et al., 1999), but due to positional uncertain and low source counts, it cannot be confirmed as an AGN from that alone. It was selected as a promising CT AGN candidate from its unusually high MIR-to-hard-X-ray flux ratio; i.e., it is undetected by *Swift*-BAT (in the latest version of the catalogue), but has *WISE* $W3$ magnitude much greater than that corresponding to the B70 flux limit, and is also not known to host a starburst. However, although it is not present in the *Swift*-XRT source catalogue (2SXPS; Evans et al., 2020b) a detection can be found with the online tool (Evans et al., 2009). Without X-ray data at $>$10 keV it is difficult to constrain the parameters with much confidence, but with the soft data alone it appears to be very lightly obscured ($\log N_{\rm H} \approx 20.8$ cm^{-2}) and under-luminous (observed $L_{2-10\ \rm keV} \approx 5.3 \times 10^{40}$ erg s^{-1} cm^{-2}) - see Appendix A.1. Deeper hard X-ray data would help distinguish between a truly under-luminous AGN, and an extremely obscured one. With the new X-SHOOTER data (Figures 2.17, 2.19, and Appendix A) optical emission line flux ratios indicate that the presence of an AGN is likely (Figure 2.12). On the other hand, IR emission lines are less conclusive (Figure 2.13), possibly due to higher flux uncertainties on these lines, or contamination from star formation. It does not show broad lines in the optical, and thus can be tentatively classed as a type 2 AGN, and remains a CT candidate.

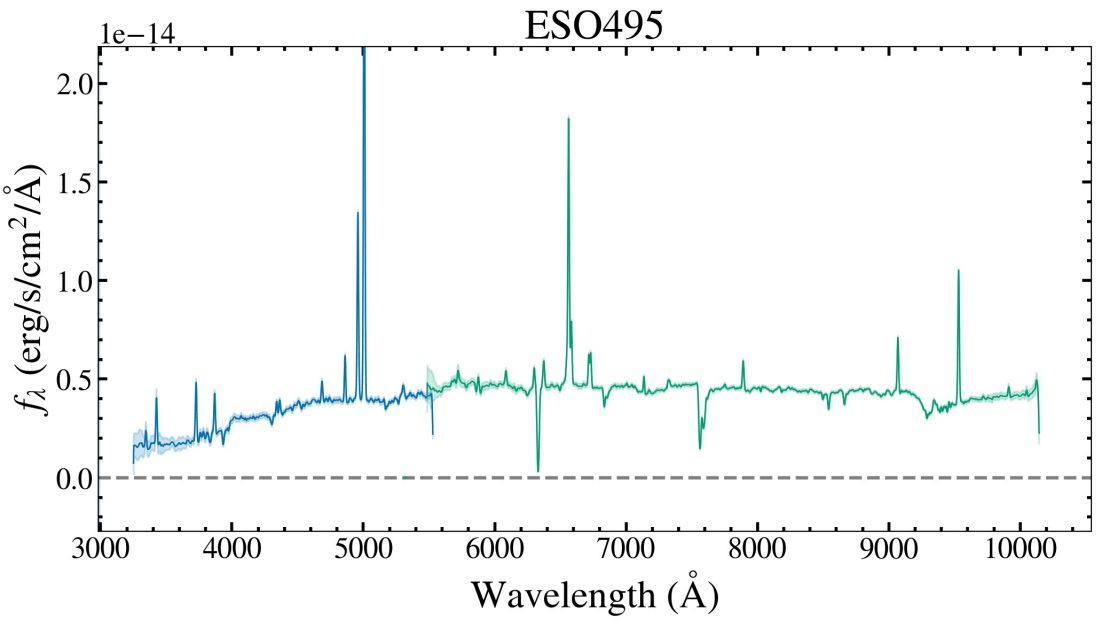

FIGURE 2.17: Optical and NIR spectra of ESO495. Smoothed with a Gaussian kernel, width 25 pixels. Shaded area shows flux uncertainty.

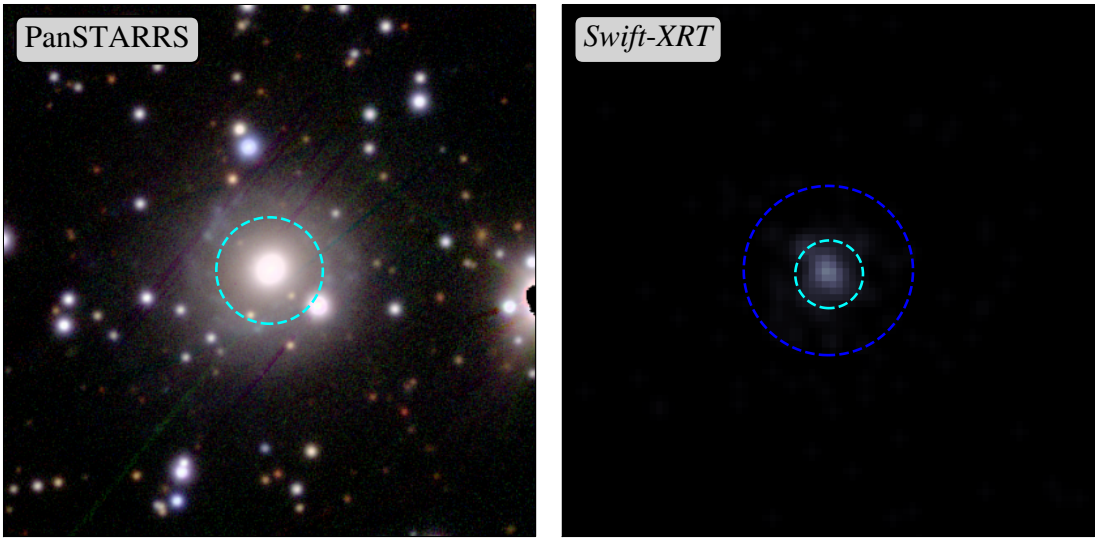

FIGURE 2.18: (left) PanSTARRS *irg* bands converted to RGB image and (right) *Swift*-XRT full band image of ESO495. Circle (cyan, smaller) has 9 arcsec radius and is centred on the catalogue source coordinates.

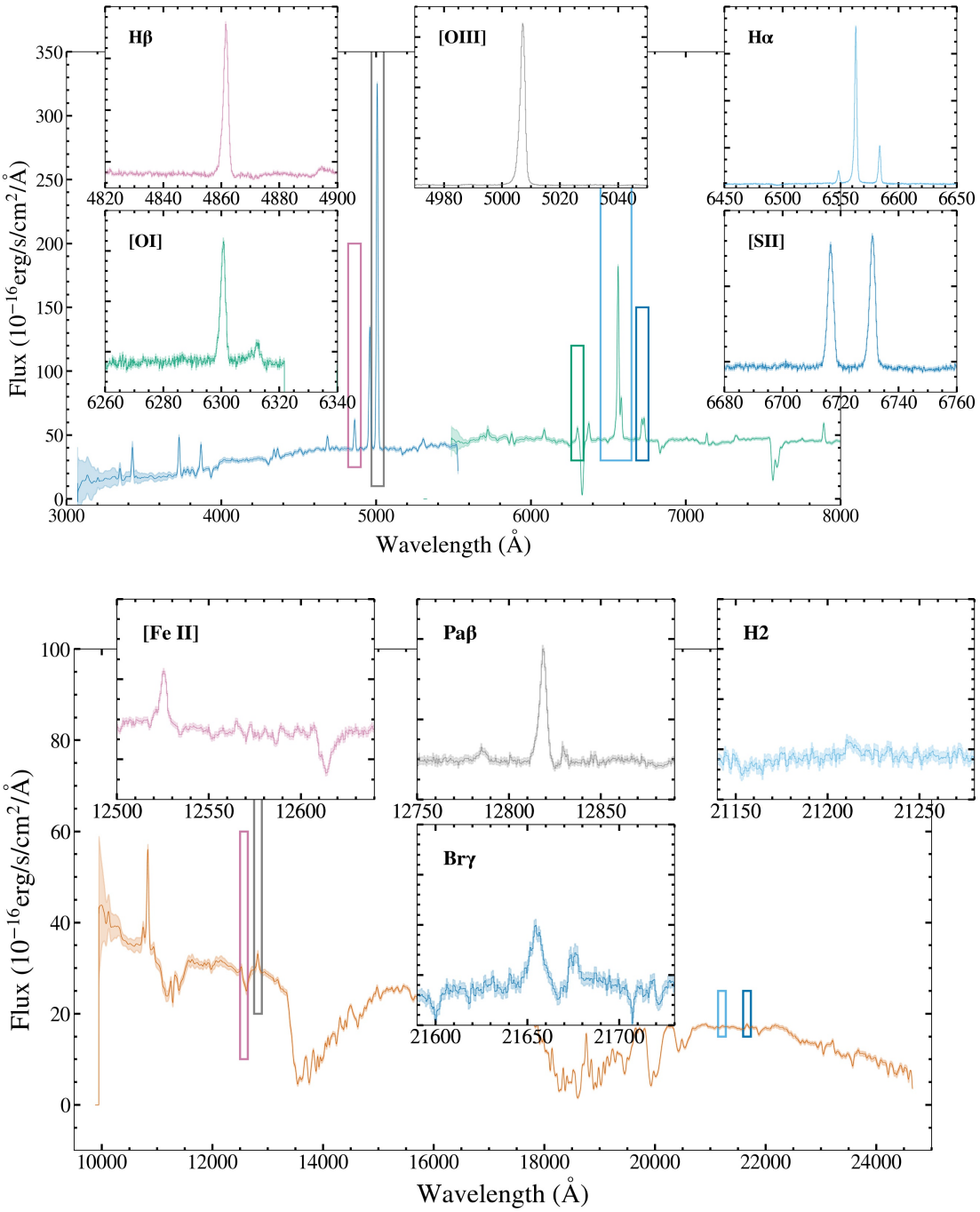

FIGURE 2.19: Optical and NIR spectra of ESO495, with emission lines highlighted.

2.5.2.3 NGC 3094

Unlike the other follow-up targets discussed here, NGC 3094 is classed as an AGN in the LASr-GPS (classification from NED, based on optical spectra and absorption features: Armus et al., 1989, Imanishi, 2000, respectively). However, it is a candidate Compact Obscured Nucleus (e.g., Falstad et al., 2021) - despite having many features of an AGN (e.g., strong nuclear IR emission), the power source for this could instead come from dense, obscured star formation localised around the nucleus. Whether CONs contain AGN or SF may different across different objects. They are also, by definition, heavily obscured and thus difficult to discover and understand; simultaneously, these extremely obscured AGN may be an important insight into AGN growth and evolution, which occurs in a large part under very obscured conditions. It is included as an X-SHOOTER target in order to gain some insight into the activity within the nucleus – NIR spectroscopy has the best chance of observing emission lines through the obscuration. Optically it appears like a spiral galaxy with a bright nucleus (Figure 2.21) - the nearby bright source is a foreground star and is not associated.

As expected, optical emission line diagnostics do not reveal AGN activity within NGC3094, although it is not conclusively in any one region of Figure 2.12. NIR diagnostics are hampered by an undetected Brγ line (see Figure 2.22), and optically by low intensity lines (Figure 2.20). In Figure 2.13 the position on the Fe II/Paβ axis is indicated with an arrow - placement on the H_2/Brγ axis is undefined. However, the Fe II/Paβ value implies that it is more likely to lie in the AGN region, being too high for star-forming. It may be near to the LINER region, but as dense star formation is the primary alternative explanation for the AGN-like nuclear activity, this is the class we wish to distinguish.

Optical and NIR spectroscopy alone cannot probe the CON of NGC3094. A multi-wavelength campaign can provide different angles into the activity present; for example, hard X-rays (e.g., *NuSTAR*) could detect intrinsic nuclear activity even through thick enshrouding material.

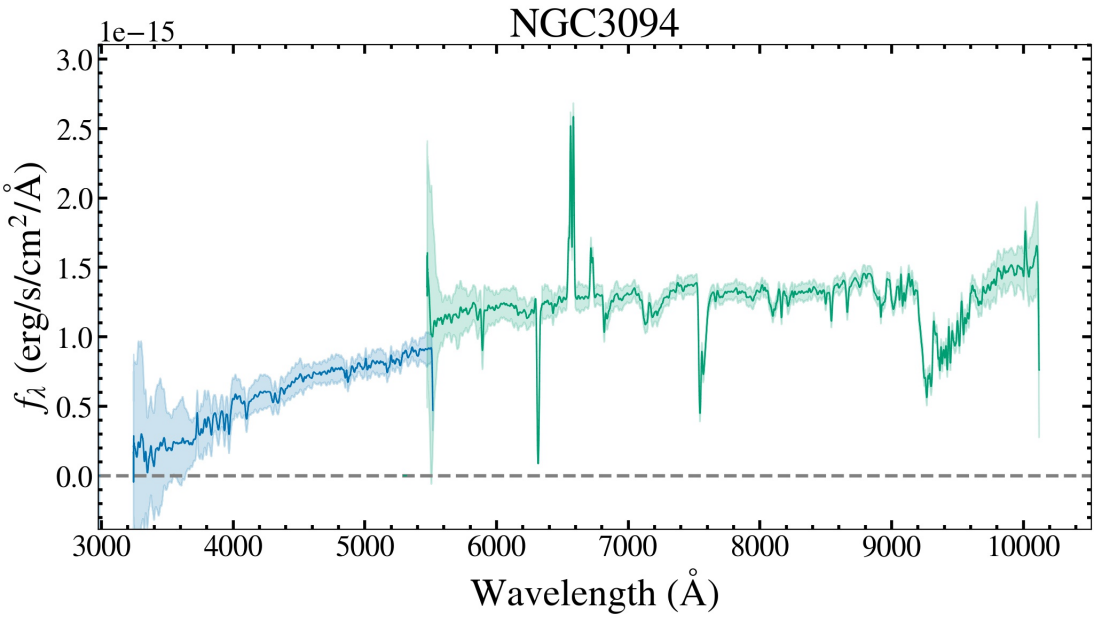

FIGURE 2.20: Optical and NIR spectra of NGC3094. Smoothed with a Gaussian kernel, width 25 pixels. Shaded area shows flux uncertainty.

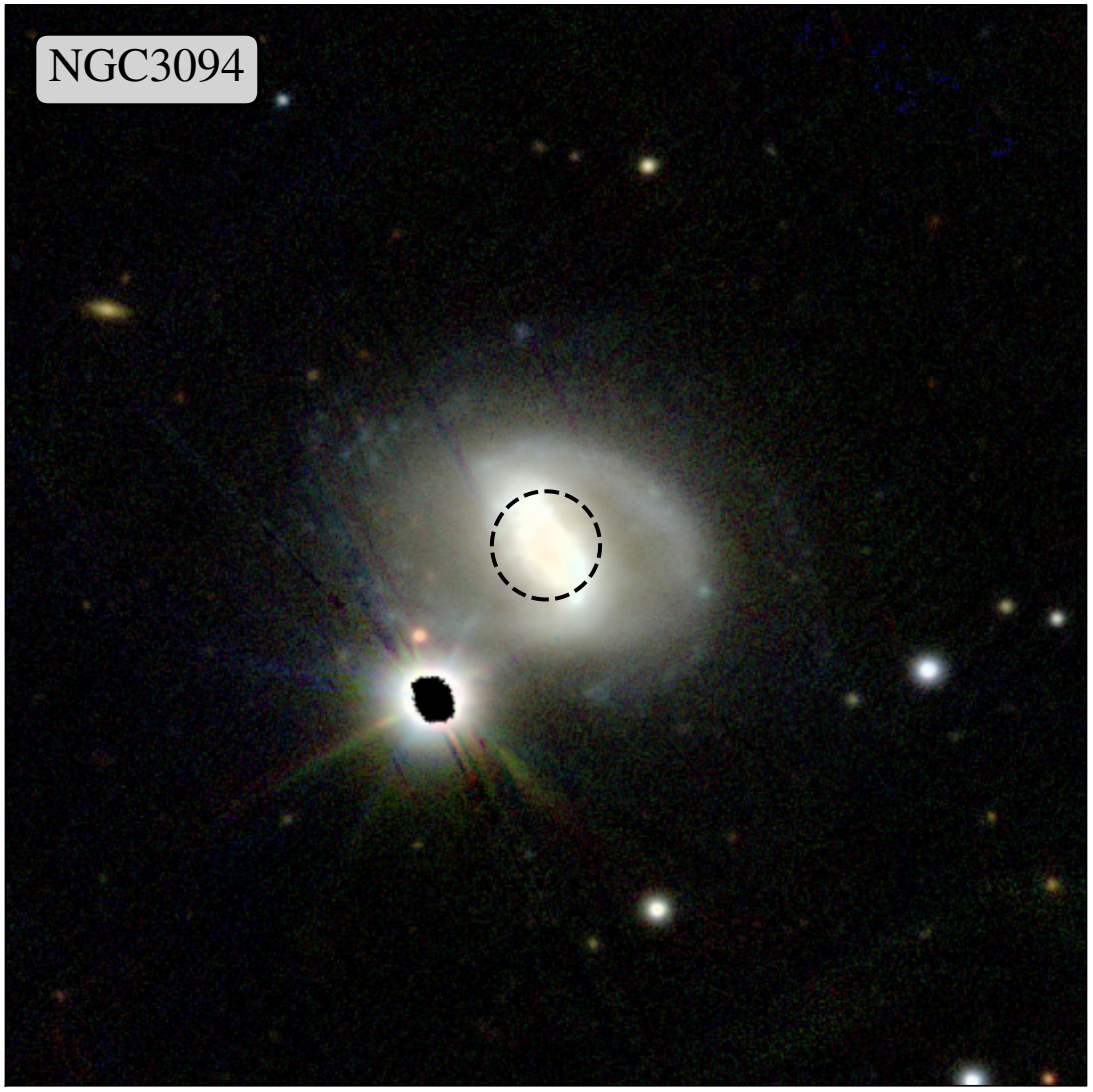

FIGURE 2.21: PanSTARRS *irg* bands converted to RGB image of NGC3094. Circle has 9 arcsec radius and is centred on the catalogue source coordinates.

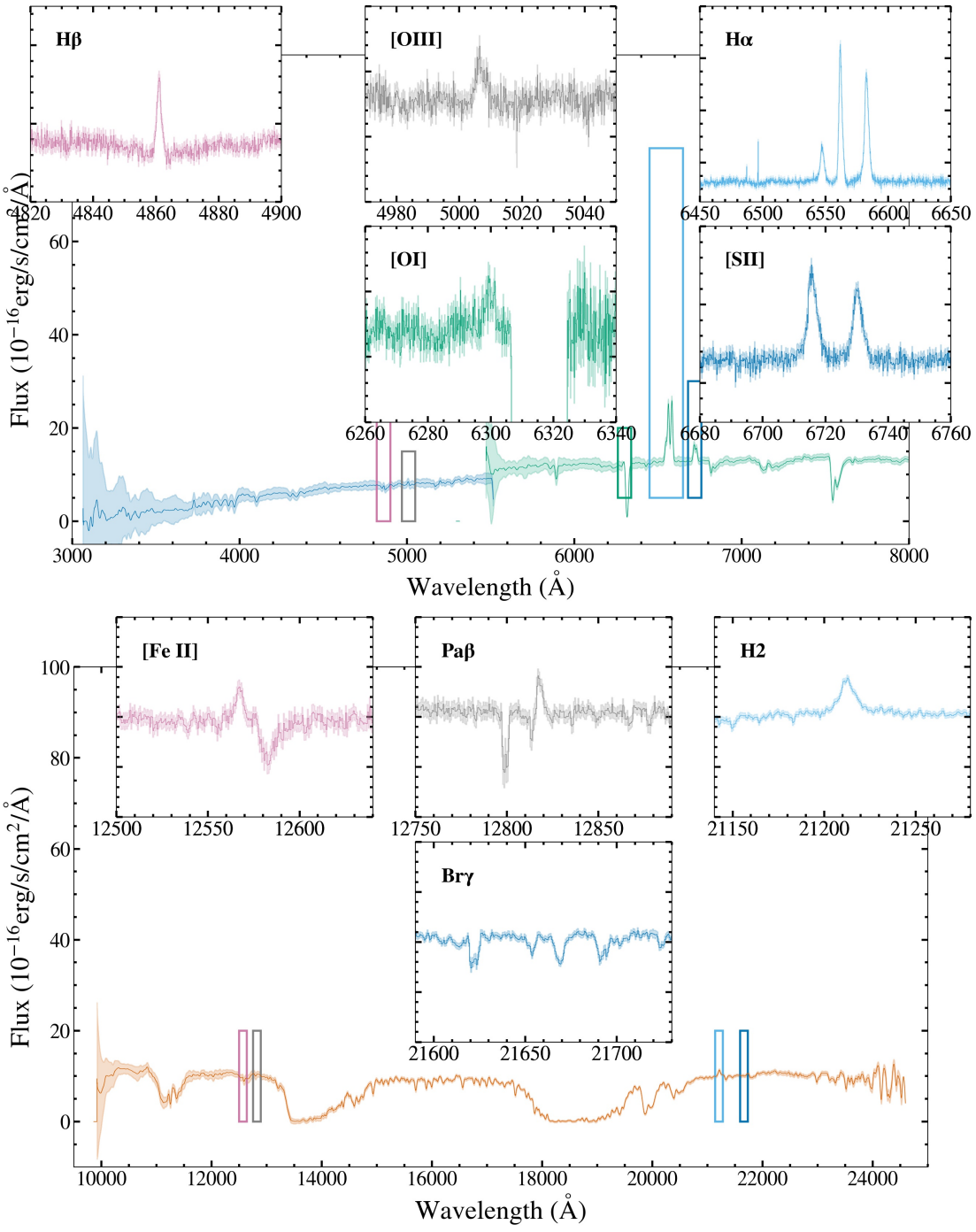

FIGURE 2.22: Optical and NIR spectra of NGC3094, with emission lines highlighted.

2.5.2.4 ESO 343-IG 013 NED02

ESO 343-IG 013 NED02 (hereafter ESO343) is part of a closely interacting galaxy pair (see Figure 2.23). Its partner, ESO 343-IG 013 NED01, is also in the LASr-GPS - it is not known to be an AGN, and is excluded from the follow-up program based on its *WISE* $W1 - W2$ colour of 0.37 being below the selection threshold, despite high luminosity. However, as discussed above, this selection threshold is aiming for high reliability, not completeness, and therefore we cannot rule out this system as a potential dual AGN at this point. Supporting this theory is the presence of *Chandra* point sources in each nucleus (Wang et al., 2016). ESO343 is detected to a high significance (18.2); its partner less so (2.8). Its position in the star-forming region of both optical and NIR emission line diagnostic graphs (Figures 2.12 and 2.13) implies that this fairly weak, soft X-ray emission could be from star formation. Conversely, its position in all diagnostics is close to borderline regions; it could be, for example, a weak line or obscured AGN. Optical emission lines show no apparent broad component (Figure 2.25).

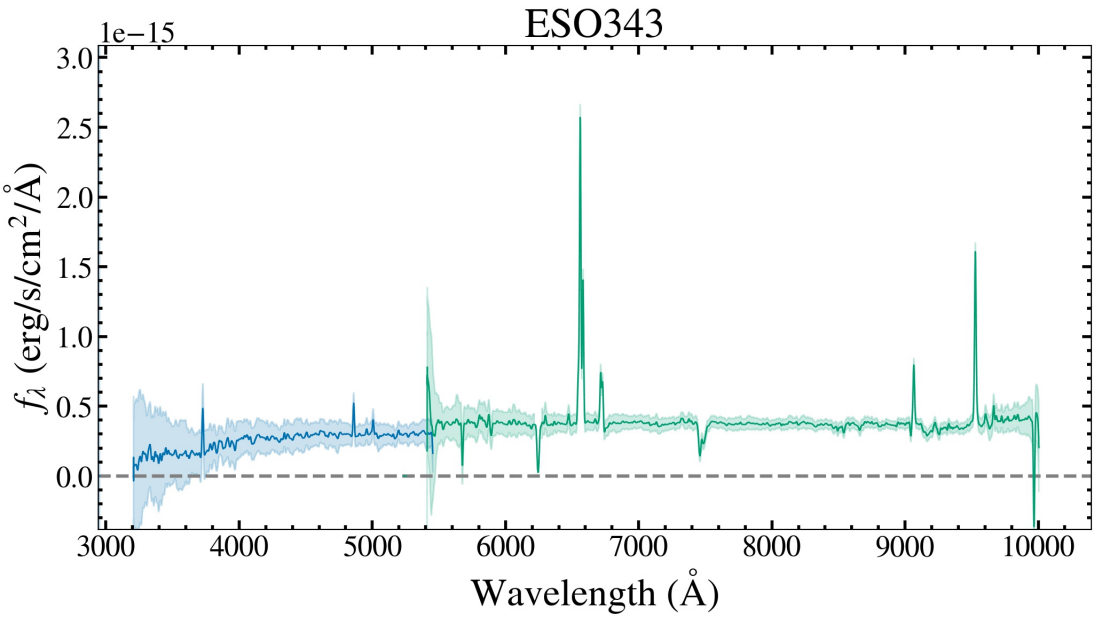

FIGURE 2.23: Optical and NIR spectra of ESO343. Smoothed with a Gaussian kernel, width 25 pixels. Shaded area shows flux uncertainty.

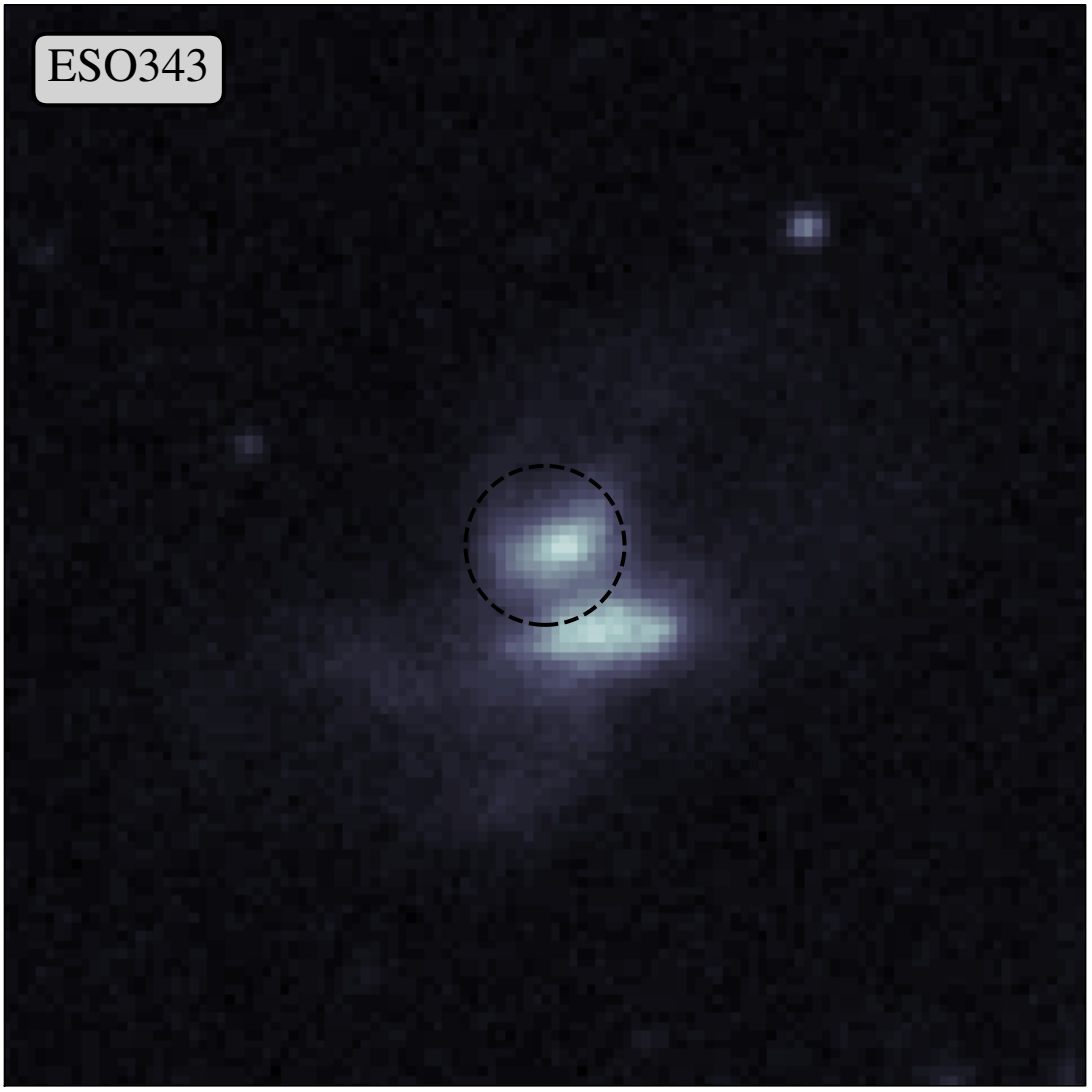

FIGURE 2.24: DSS2 red band image of ESO343. Circle has 9 arcsec radius and is centred on the catalogue source coordinates.

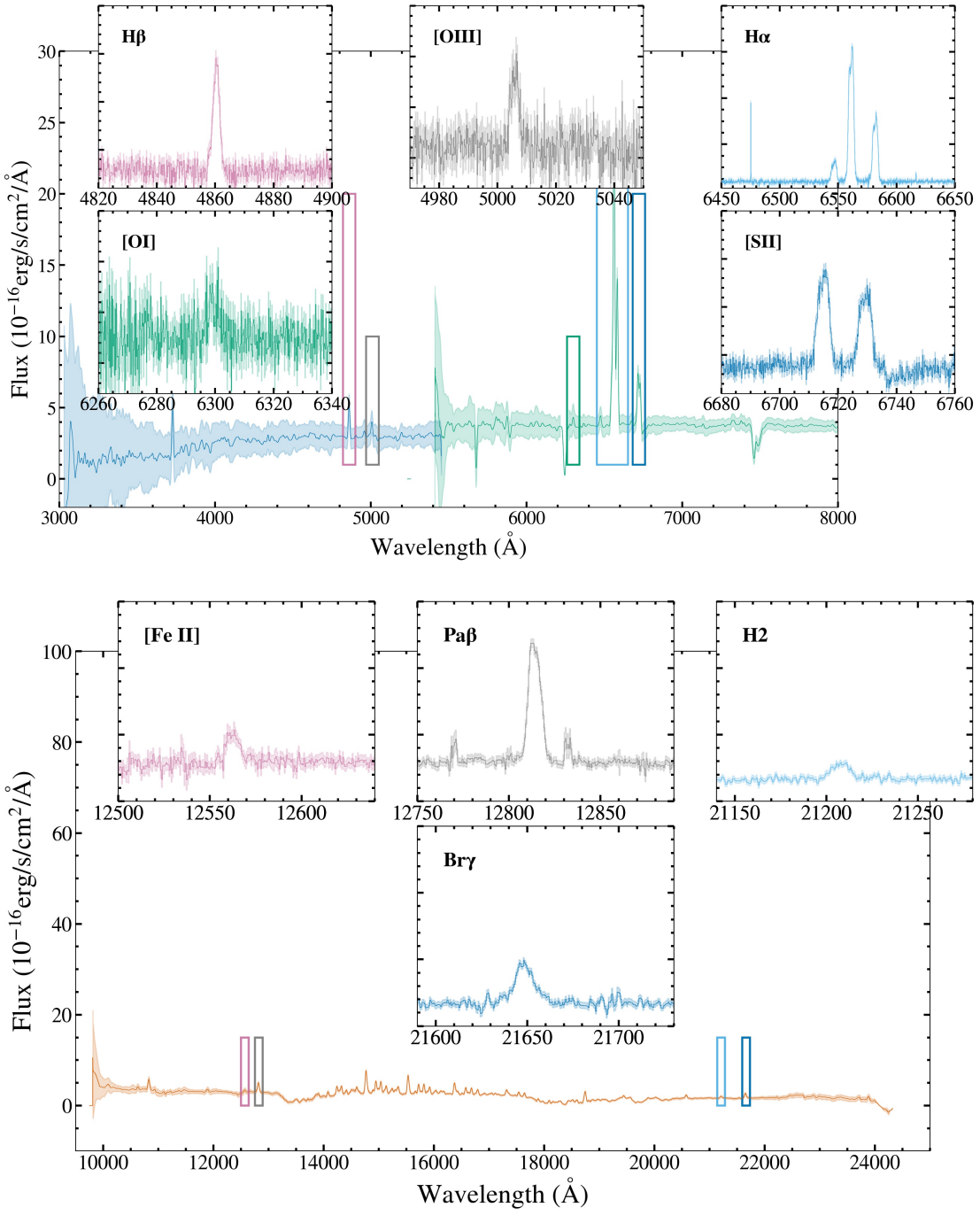

FIGURE 2.25: Optical and NIR spectra of ESO343, with emission lines highlighted.

2.6 Discussion

With this campaign, I have so far examined four candidate AGN out of 43 proposed for observations. Work on this is ongoing; more will be observed and analysed.

- **CGCG 058-009:** is in the star-forming region of the optical BPT diagram, but the AGN region of the NIR diagram. This result, along with previous measurements of a deep silicate absorption, implies that this is likely to be a heavily obscured AGN.
- **ESO 495-G 005:** an AGN according to optical diagnostics, and borderline in the NIR. It has strong emission lines, and a clear 4000 Å break in the continuum. It is a potential X-ray source, present in older catalogues but not newer ones. Comparing the upper limits on this X-ray data to its relatively high MIR luminosity imply possible CT obscuration.
- **NGC 3094:** unlike the other sources, NGC3094 was previously defined as an AGN in the literature. Optically it lies on the border between star-forming galaxy and AGN/LINER. In the NIR it is harder to define as we can place it on only one dimension of the diagram. However, this position places it above the star-formation region - whatever value the Brγ flux takes, it is likely to indicate AGN presence. Thus in Table 2.3c we indicate the uncertainty of this result. Multi-wavelength investigations into this source as a potential CON are ongoing.
- **ESO 343-IG 013 NED02:** ESO343 is very close to CGCG058 on the BPT diagram, but with NIR diagnostics is much less conclusive, lying on the borderline between star-forming and AGN. It is in a closely interacting pair, and is detected in soft X-rays ($<$10 keV). Results from this source are inconclusive: soft X-rays could be the result of star-formation, and neither diagnostic diagram indicates strongly the major source of power.

In summary, we have found one conclusive optical AGN (ESO495), one NIR AGN (CGCG058), and one more inconclusive. NGC3049, previously known to be an AGN, is not clearly an AGN according to either diagnostic - demonstrating how even this combination of methods can miss obscured AGN. However, none are significantly shown to be inactive galaxies, and (if active) are likely to be obscured AGN, based on narrow emission line width (all measured line widths lie in the approximate range 120–200 km s^{-1}, which is lower than typically seen in the NLR, and may be a counter-indication of AGN presence).

We can consider the new 'known AGN' in context with the previous objects. We assume that both ESO495 and CGCG058 are AGN, and ESO343 is not[7]. Thus the reliability of

[7] As a previously known AGN, we discard NGC3094 from this discussion.

selection from these candidates is $\sim 67^{+20}_{-28}$%, compared to an expected 90%. They are *not* B70 AGN; without X-ray data we cannot conclusively say whether these candidate AGN are Compton thick. However, as AGN that are not detected by *Swift*-BAT, they are either low X-ray luminosity (L_X) or Compton thick. *Swift*-XRT data from ESO495 shows a low observed $L_{2-10\mathrm{keV}}$, and based on this data alone does not indicate a heavily obscured model. However, given that these were selected for follow-up based on *luminous* MIR data and MIR luminosity is correlated with X-ray luminosity (e.g., Stern, 2015) we can speculate that they are unlikely to be intrinsically low L_X[8] and are thus more likely to be CT sources. In Section 2.4.4 we calculate that 38 R90 passes *should* have been detected by *Swift*-BAT and were not, implying that many of these may be CT AGN. Deeper hard X-ray data from *NuSTAR* would help to unravel the true nature of these sources.

[8] Although this is possible (see Chapter 4) these sources are significantly closer, and thus the limit on L_X based on *Swift*-BAT non-detections would be extremely constricting.

2.7 Summary

This chapter has set up the idea, practice, and difficulties of creating and confirming AGN catalogues. It has demonstrated that there are significant gaps in our census of AGN; we are missing many interesting and important objects, particularly heavily or unusually obscured objects. In Figure 2.26 the region of redshift and $N_{\rm H}$ covered by the *known* AGN in the LASr-GPS is shown, including the subset of B70 AGN. Regions show where 68% of sources in each category lie. For comparison, we show the space covered by SPIDERS (Comparat et al., 2020), optical follow-up spectra of soft X-ray selected targets in the SDSS footprint. $N_{\rm H}$ values for this group are not known but given the selection from *ROSAT* and *XMM-Newton* sources are likely to be less than Compton thick[9]. We can see, therefore, what regions are lacking and where we can start to focus our efforts in completing the AGN census.

The two AGN census deficits the next chapters of this thesis will address are:

- **heavily obscured/CT AGN**: investigation of number counts of CT AGN within the known AGN in the LASr-GPS and calculations of expected numbers have shown that there are likely to be significant numbers yet to be found.
- **non-optical AGN**: the known AGN within the LASr-GPS are largely optically selected and thus are biased towards lightly obscured and/or low covering factor AGN.

In Section 2.4.5 we calculated the expected number densities of AGN in the volume explored by the LASr-GPS. If we wish to explore how we can add rarer and more elusive AGN to the census of known AGN, we cannot be restricted to the same volume with currently available data.

The most reliable way of selecting CT AGN is via hard X-ray data. Currently, the best all-sky survey in this regime is *Swift*-BAT; as discussed in this chapter there is a severe flux limit on the results, and thus a deficit of CT sources. Thus if we wish to plan an exploration of CT AGN found in deeper available hard X-ray data, we must be restricted to much smaller areas of sky. To compensate for this in terms of number counts - i.e., if we aim to find reasonable numbers of CT AGN candidates, we must be willing to be far less restricted in volume. This brings us to Chapter 3, where I explore the potential of *NuSTAR* to select CT AGN, analyse the results, and place them into context with the LASr-GPS.

[9]For illustration purposes, values for $N_{\rm H}$ have been randomly selected for each source from a distribution centred around log $N_{\rm H}$=22 cm^2.

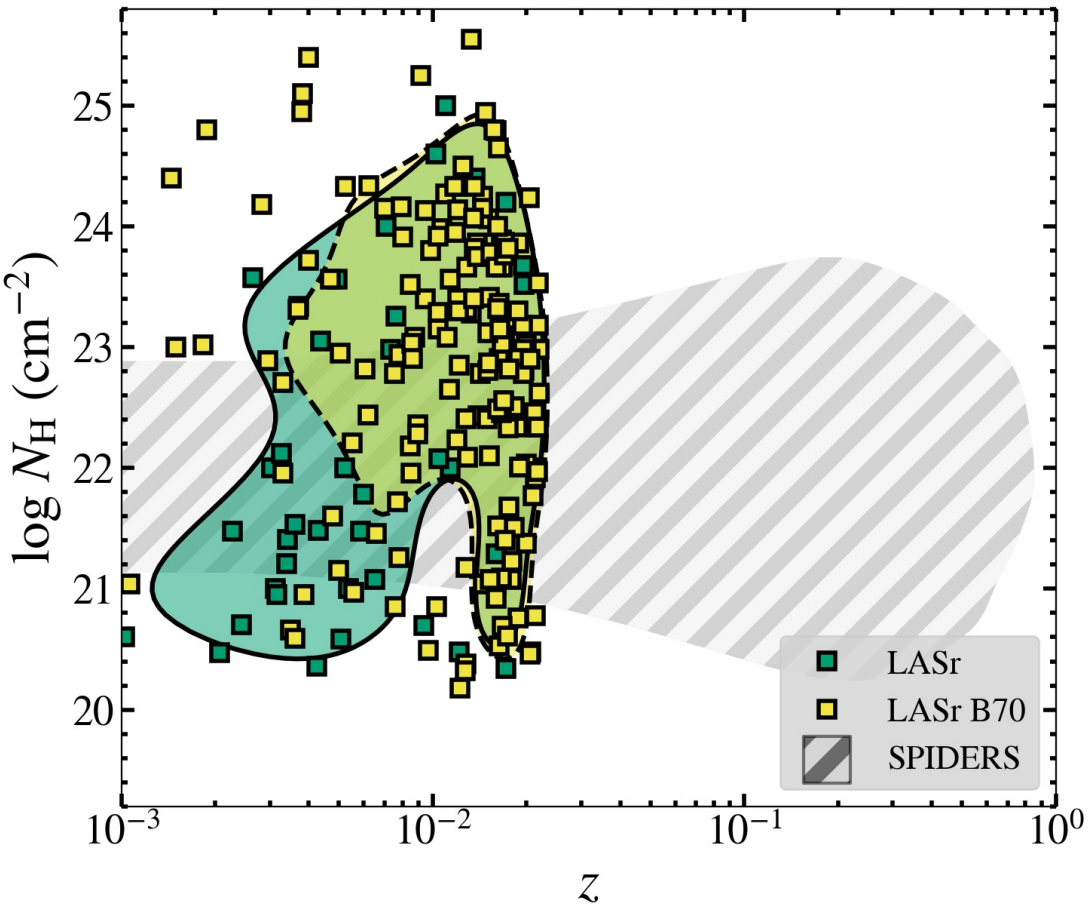

FIGURE 2.26: Parameter space covered by the known AGN in the LASr-GPS (green shaded region), by the B70 AGN (yellow shaded region), and by SPIDERS targets (grey dashed region).

Chapter 3

Piercing the Clouds: Using serendipitous hard X-ray detections to select new Compton thick AGN

The LASr project has demonstrated that in the very local universe and using strict diagnostic criteria we are missing a significant number of AGN. This project relied on comprehensive catalogues and thus is most reliable at low redshift – however, as we move further out, the number of overlooked AGN is likely to rise due to the limited depth of large-scale surveys. We have also demonstrated that a large number of unconfirmed AGN candidates are likely to be heavily obscured. This leads us to consider: how might we select extremely obscured AGN? Can deeper X-ray data provide robust new candidates? Especially, how might we find the AGN that are *most likely* to be overlooked?

Obscured AGN (column depth of obscuration $N_{\rm H}\gtrsim10^{22}$ cm^{-2}), and in particular Compton thick (CT) AGN ($N_{\rm H}\gtrsim10^{24}$ cm^{-2}) can be difficult to select for, with reduced or even absent signatures across the electromagnetic spectrum. These AGN can represent the largest growth period in AGN evolution (e.g., Fabian, 1999, Hopkins et al., 2006), and it is therefore of great importance to a rigorous AGN census to include heavily obscured AGN.

In Figure 3.1, I reproduce Figure 2.26 with the addition of the region we target in this chapter: heavily obscured AGN, with redshift unrestricted to the LASr-GPS volume[1]. LASr constructed a sample of local galaxies, and from those we selected candidate AGN; the previously known AGN from LASr are shown in the green and yellow regions on this figure. Over the smaller sky region observed by *NuSTAR* (Figure 3.2

[1]For illustration purposes, values for $N_{\rm H}$ and z have been selected to be representative across a distribution centred around log $N_{\rm H}$=24 cm^2 and up to the redshift where the shape of the spectrum in the *NuSTAR* range changes.

shows a not-to-scale diagram of the *NuSTAR* observation areas compared to LASr) we would expect correspondingly fewer obscured AGN, hence we expand to further redshifts to select a statistically significant number of sources.

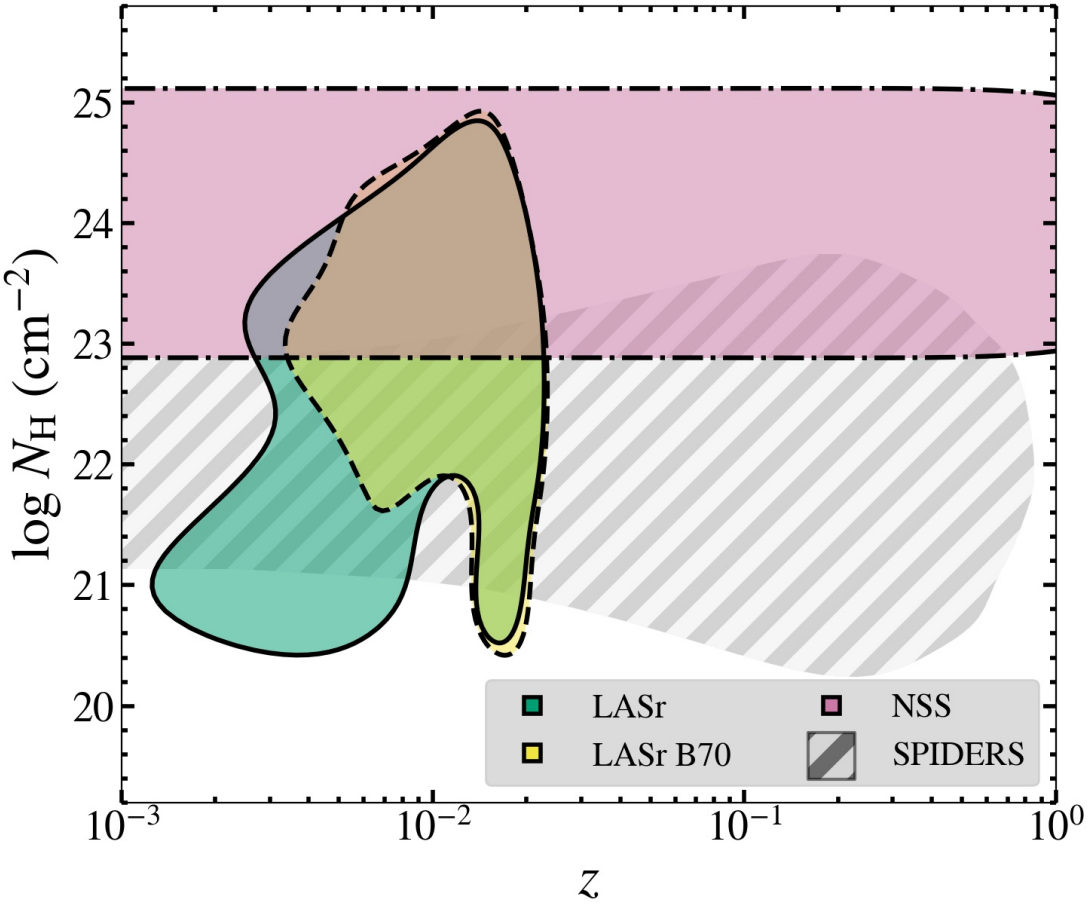

FIGURE 3.1: Parameter space covered by the known AGN in the LASr-GPS (green shaded region, solid edge), by the B70 AGN (yellow shaded region, dashed edge), and the region targeted by this chapter, the *NuSTAR* serendipitous survey extreme sources (pink shaded area, dot-dash edge).

In this section I present the selection of CT AGN candidates using *serendipitous* hard X-ray observations. As discussed in Section 1.3.4, *NuSTAR* is a hard X-ray telescope that has been active for 10 years, contributing invaluably to the study of obscured AGN. It is sensitive from 3-78 keV – thus detecting emission from the AGN corona that can pass through even CT obscuration. Luminous sources in this regime are unlikely to be anything other than AGN, as these extreme high energies require an extreme environment to produce for an extended period of time. Hence, hard X-rays comprise a reliable selection regime.

The drawback of this reliable selection technique is the lack of available data. No all-sky survey exists with (a) high resolution, and (b) sufficiently deep flux limits to count anything beyond bright or very local obscured AGN. *Swift*-BAT (see Section 2.1.1) contributes many X-ray selected AGN (as seen in Chapter 2), but is limited in flux depth.

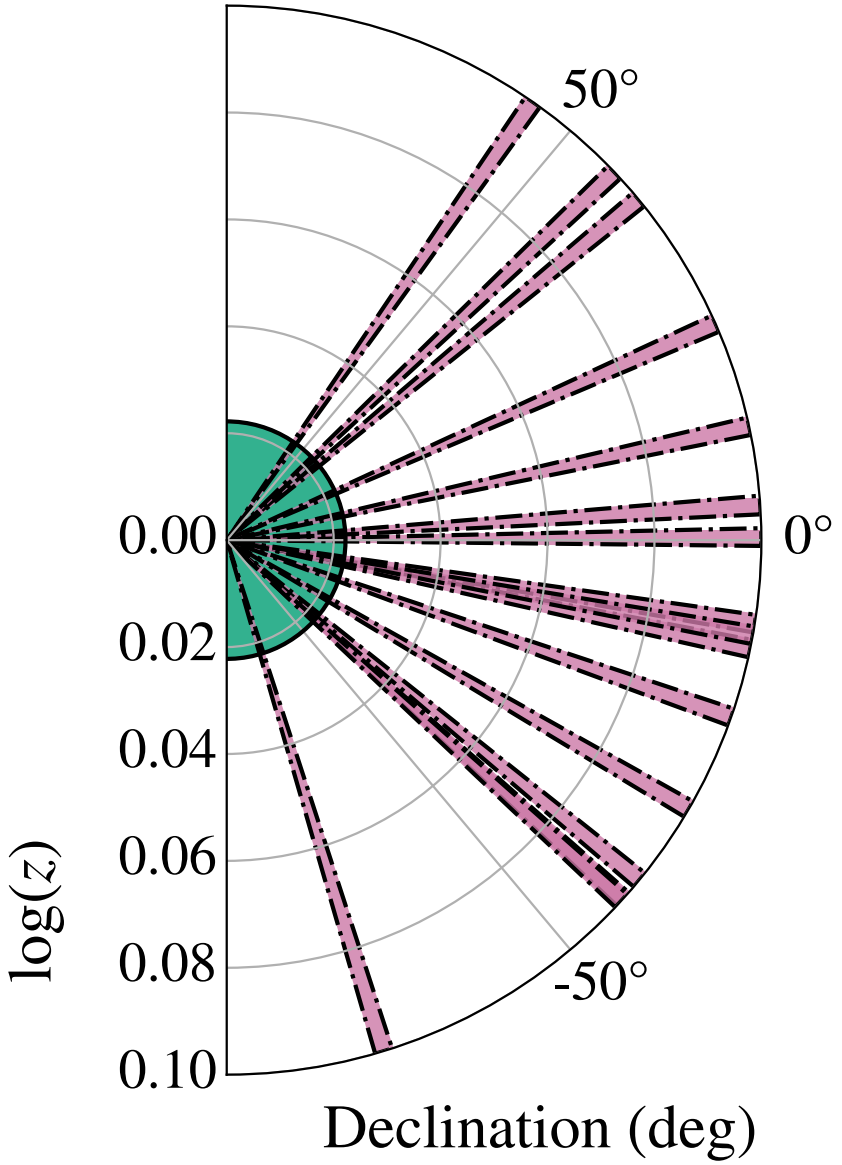

FIGURE 3.2: Parameter space covered by the LASr-GPS (green shaded region, solid edge), and the regions targeted by this chapter (pink shaded area, dot-dash edge). Widths of NSS regions not to scale.

We can take limited area but deeper observations and carefully select from those regions – many searches of this kind involve deliberate targeted observations over small areas, e.g., COSMOS (Civano et al., 2015). Without systematic all-sky coverage we have another option: to take the available data from many years of targeted observations and, by discarding the targets of those, take the objects observed by chance. In this part of my work I take serendipitously discovered sources from *NuSTAR* select promising candidates for heavily obscured AGN, and analyse the results in the context of previously known populations of CT AGN.

3.1 The *NuSTAR* Serendipitous Survey 80 month catalogue and updates from the 40 month

For this selection process I take as a base catalogue the 80-month *NuSTAR* Serendipitous Source Catalogue (hereafter NSS80; Klindt et al., 2022, submitted), which builds on the 40-month catalogue (hereafter NSS40; Lansbury et al., 2017b). *NuSTAR* (see Section 1.3.4) is a focusing hard X-ray telescope, sensitive over 3–79 keV, which provides a large increase in sensitivity over previous instruments. This high energy, high resolution instrument can select AGN with excellent efficiency, even at high absorption column densities. NSS80 stacks all *NuSTAR* observations (excluding observations from dedicated surveys e.g., COSMOS, Civano et al. 2015; the *NuSTAR* Extra-Galactic Survey, Alexander et al. 2013) from the full 80 months of *NuSTAR*'s operation to search for previously unidentified background X-ray sources, totalling $\sim$62 Ms (increased $\sim$20 Ms in NSS40) of exposure time over $\sim$36 deg^2 ($\sim$13 deg^2 in NSS40). It finds 1274 sources (822 of which are new since NSS40; also excluding 214 sources in extended optical galaxies and clusters). A significant campaign of spectroscopic followups added to archival data to provide redshifts for 550 sources, the large majority of which are AGN. The catalogue includes the likely optical, IR, and soft X-ray counterparts (selected via NWAY; Salvato et al., 2018) for a number of the sources.

Using this catalogue as a parent sample, we can use the information it contains to select candidates with a high likelihood of heavy obscuration: the target of this chapter's exploration.

3.2 The Hunt for Extreme Sources

The spectral shape in the hard X-ray region can be considered a proxy for obscuration (see Figure 3.3, or Koss et al., 2016), and in order to estimate this I use the Band Ratio (BR) – the ratio of what we define in this work as the 'hard band' (8–24 keV) and 'soft band' (3–8 keV) flux. The higher this value, the steeper the shape of the spectrum in that region, and the more likely an AGN is to be heavily obscured. This selection method is reliable but not necessarily complete - an in depth analysis selecting for the more thorough spectral curvature (Koss et al., 2016) could discover more CT AGN candidates. We also checked for any sources already known as AGN; see Appendix B.1.

The observed spectrum can be approximately described by a power law function of the energy: $E^{-\Gamma}$. To select the most probable sources, only those with an upper limit or exact BR value $>$1.7 are included. This value corresponds to an observed Γ of $\lesssim$0.6, and is based on values seen in CT AGN modelling, as described in Lansbury et al. (2017a). This is different to the *intrinsic* power law spectrum of the AGN, which takes a shape with Γ likely to be closer to $\sim$1.9 (see e.g., Ricci et al., 2017a); the **apparent** Γ

values may be more widely varied. Figure 3.3 shows a typical AGN X-ray spectrum at different $N_{\rm H}$ levels. If the AGN is obscured, the flatter spectrum from the hot corona becomes less dominant, and the overall X-ray spectrum is harder - i.e., more luminous at higher energies, thus increasing the Band Ratio.

Lansbury et al. (2017a) (hereafter L2017) selected eight sources with BR>1.7 from the 40-month *NuSTAR* Serendipitous Source Catalogue. Of these, they found four to be confirmed CT AGN, and the rest possibly CT or at least somewhat obscured. Of the confirmed CT AGN, 50% $\pm$ 33% are found in major galaxy mergers, higher than the fraction in the remainder of the serendipitous source catalogue. In this chapter I will build on this work, analysing new sources and calculating how these new sources impact the statistics of CT AGN properties.

The updated 80-month catalogue contains more than twice as many sources as the 40-month catalogue. Figure 3.4 shows the distribution of BR across the two catalogues - the shape is broadly consistent and we may expect, therefore, to find slightly more new CT AGN in this iteration of the search. To begin with, we do not discard any sources that are found in both catalogues. Most of the NSS40 sources appear in NSS80, but some have additional observations and may have updated values for selection criteria: for example, updated BR or redshift. Figure 3.5 includes any sources with >10% change in BR from NSS40 to NSS80. More have become softer (i.e., BR from NSS80 is lower than BR from NSS40, moving further from our region of interest). The main sources of note are those outside the bottom left corner: the top left quadrant shows sources that were *not* selected in NSS40, but are now above the threshold; the top right sources that were selected in NSS40, but have changed significantly[2].

In Figure 3.6 we make our selection of candidate CT AGN. Every NSS80 object with a measured redshift is shown; green circles are those with BR<1.7, and orange squares have BR>1.7. Blue squares highlight sources that are above the threshold, and were in NSS40. If they were analysed in L2017 they are shown with a star - these sources are not included in this analysis, with the exception of NuSTARJ150646+0346.2, which was deliberately targeted with joint *XMM-Newton-NuSTAR* observations as a follow-up to L2017. It therefore now has new, high quality, simultaneous soft and hard X-ray observations not previously analysed. Also of note is NuSTARJ231840-4223.0, which in NSS40 was below the selection threshold, and is now above.

To summarise, sources are selected as follows:

1. NSS80 sources with known redshifts.
2. Band Ratio >1.7.

[2]The bottom right quadrant would contain sources that *were* selected in NSS40, but are now below the threshold. However, the only source here is an *upper limit*; i.e., it would have been rejected as the hard band data is an upper limit only.

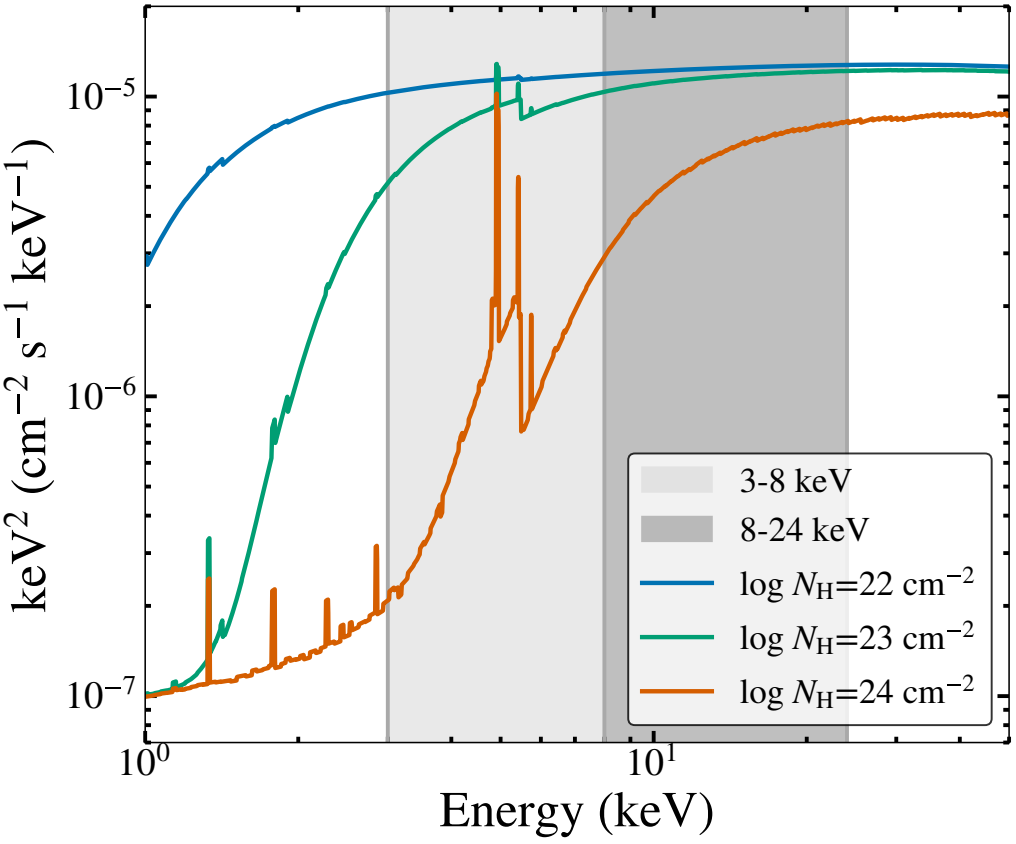

FIGURE 3.3: AGN X-ray spectrum with torus reprocessing X-ray model BORUS02 (Baloković et al., 2018, see Section 3.3.1) - all parameters kept constant, with N_H varying. Vertical grey bands show energy ranges used to calculate the band ratio. Lower obscuration results in a flatter spectrum across both bands; as the obscuration increases the soft band intensity decreases more than the hard band, changing the ratio.

3. Exclude any that are upper limits - a detection in the hard band is required (lower limits - i.e., no soft band detection - are accepted).

4. Exclude sources from L2017 (except J1506, as discussed above).

After these steps, there are 16 sources with *new NuSTAR* observations. Although all entries in NSS80 are, by design, detected *NuSTAR* sources, some are fainter than others. As a primary step before proceeding with analysis of the sources, we perform false probability testing on each source. The aim of this is to calculate the Poisson false probability and obtain an estimate of the net counts of each source. The analysis can then be focussed on those sources which are most significantly detected, with sufficient counts to make detailed model fitting possible.

The steps for this process are as follows:

1. Stack *NuSTAR* FPMA and FPMB detector images and exposure maps for energy ranges:

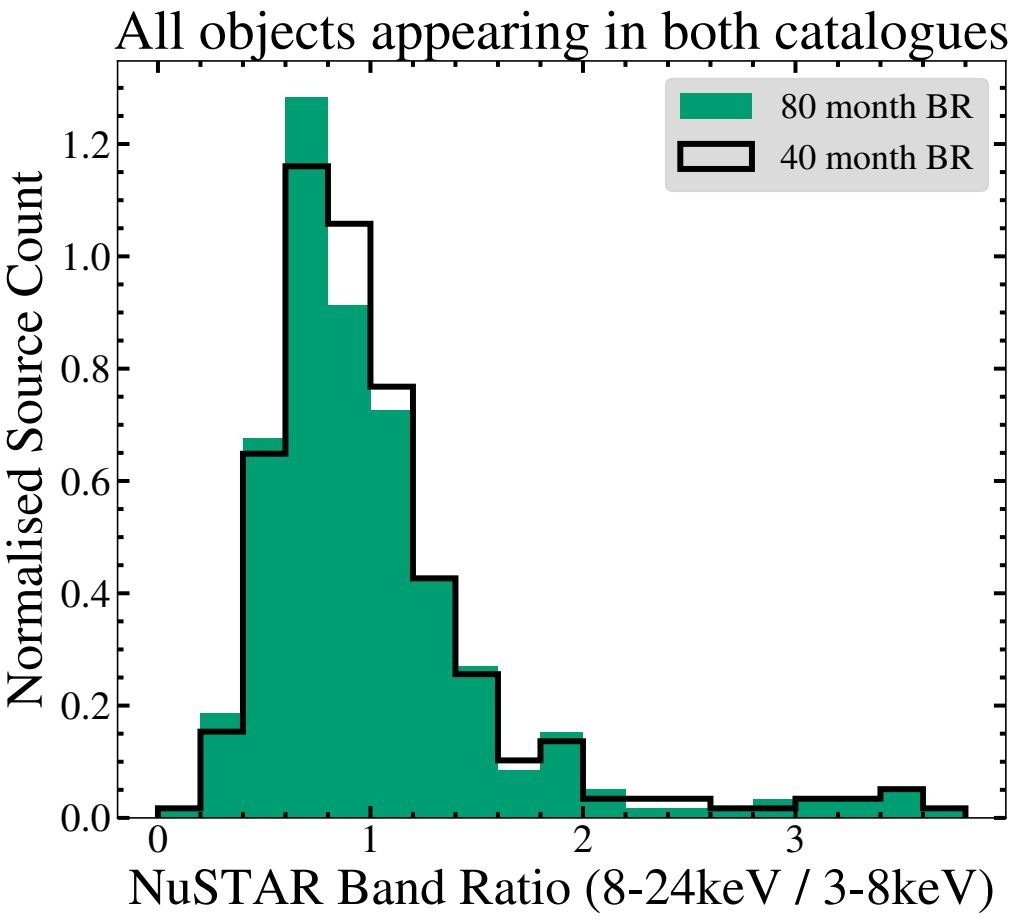

FIGURE 3.4: Distribution of band ratio measurements - NSS40 to NSS80.

- 3–8 keV (soft band)
- 8–24 keV (hard band)
- 3–24 keV (full band)
- 24–50 keV (ultra hard band)

2. Create regions in imaging viewing software SAOImageDS9[3] (Joye and Mandel, 2003) to use for background - the basic assumption is that these regions are an annulus centred on the source coordinates, with inner radius 100 arcseconds and outer radius 180 arcseconds. However, as these sources are *serendipitous* observations in many cases they lie near the edge of a sensor chip or potential contamination from a nearby bright source. The background regions are adjusted on a case by case basis to avoid these problems.

3. Create source regions - similarly, the basic assumption is that a circle centred on the source coordinates with radius 45 arcseconds; where this is not possible, 30 arcseconds is used.

[3] https://sites.google.com/cfa.harvard.edu/saoimageds9

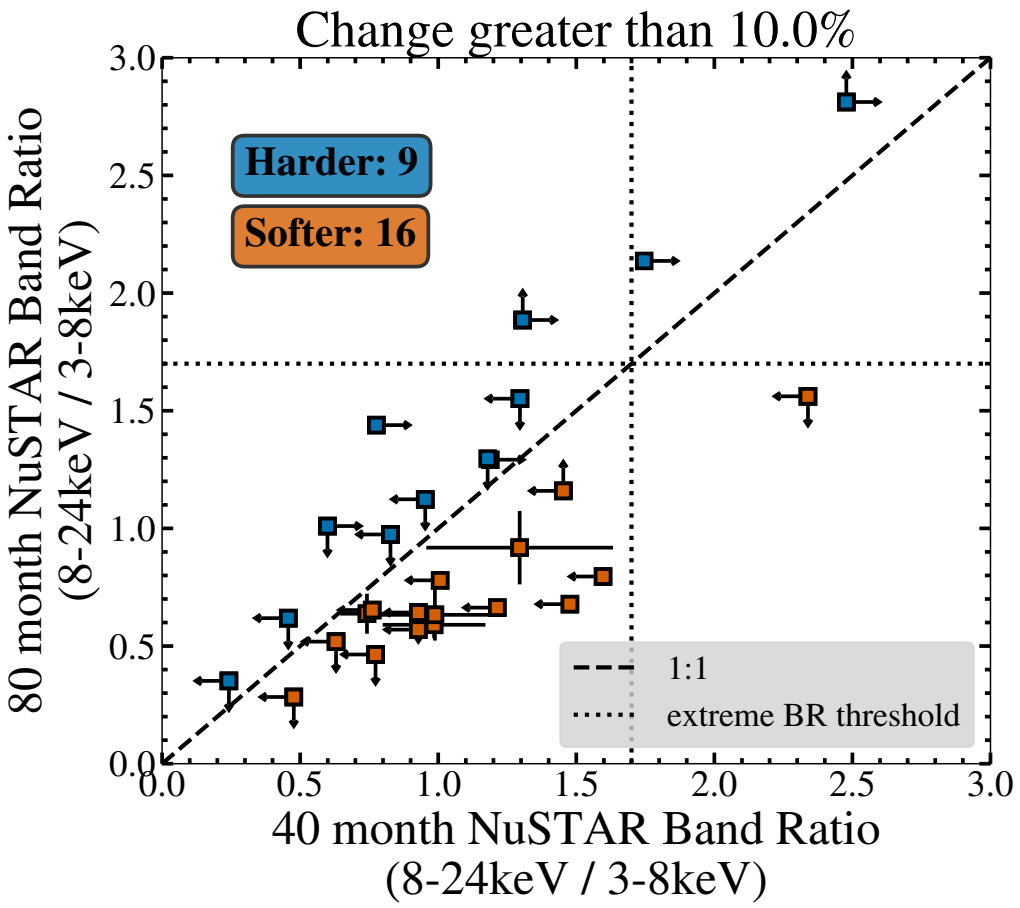

FIGURE 3.5: Significantly changed band ratio measurements (>10% including uncertainties). Arrows represent upper or lower limit values.

4. Correct the background source counts by ratio of exposure times contained in each region.

5. Use the two values (source counts, and exposure time corrected background counts) to produce a binomial probability that the source is false.

6. If this probability is <0.01, consider the source significantly detected in that energy range.

With the different statistical detection method used here, some objects are found to be not significantly above the local background level. This does not mean that they are not real sources, however they are excluded from this analysis. Two sources are removed for this reason.

A further five sources are statistically likely to be present, but have low net counts (<100 in 3-24 keV, or 8-24 if only detected in that range)[4]. While these sources are

[4]These are net source counts from the specific source by source processing done in this work. The NSS80 catalogue contains an automatic estimate of that value, which is not identical but provides a rough guide. Thus from 1274 total sources, there are ∼460 with sufficient counts, of which ∼200 also have redshifts.

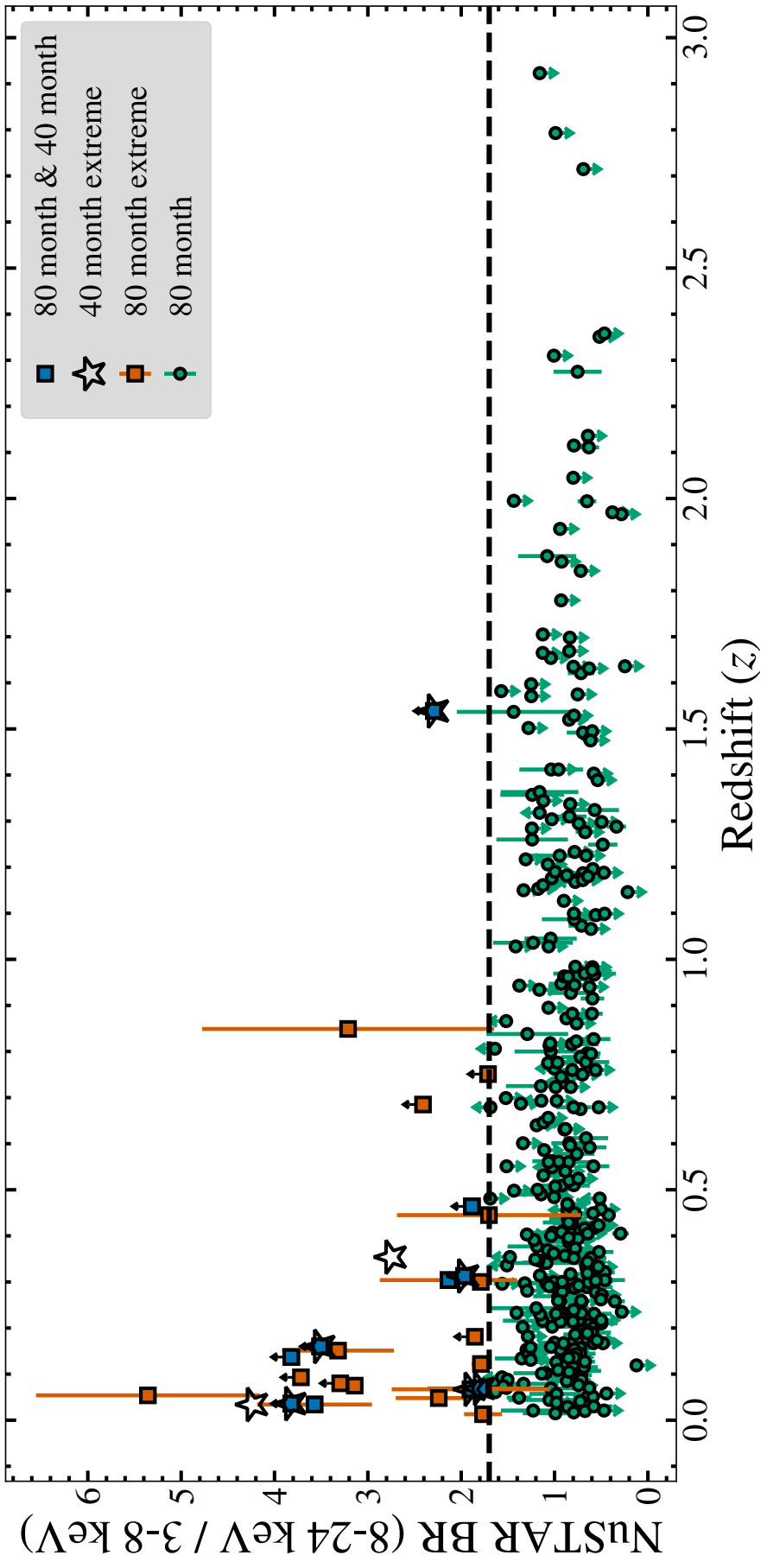

FIGURE 3.6: Selection of sources with extreme BR from NSS80. Orange squares are 80 month sources. Blue squares are both 40 month and 80 month sources. Black stars are 40 month extreme sources. Notes: J0505 appears twice in NSS80, with different redshifts; J1653 is no longer a significant detection; J1506 has an updated BR in NSS80, but still extreme; J2318 has an updated BR in NSS80, moving from below to above the threshold; J2242 was considered in L2017 but rejected due to contamination.

potential real examples of extreme obscured AGN, the weak flux means that they are less suited for detailed modelling and have therefore been excluded from further X-ray analysis at this stage.

The *NuSTAR* data from these sources is shown in Figure 3.7 - the first five are the detected but sidelined sources[5], and the final two are not detected[6].

[5]NuSTARJ022951-0856.4, NuSTARJ035951-3009.9, NuSTARJ163126+2357.0, NuSTARJ194234-1011.9, NuSTARJ231840-4223.0

[6]NuSTARJ160817+1221.4, NuSTARJ190813-3925.7

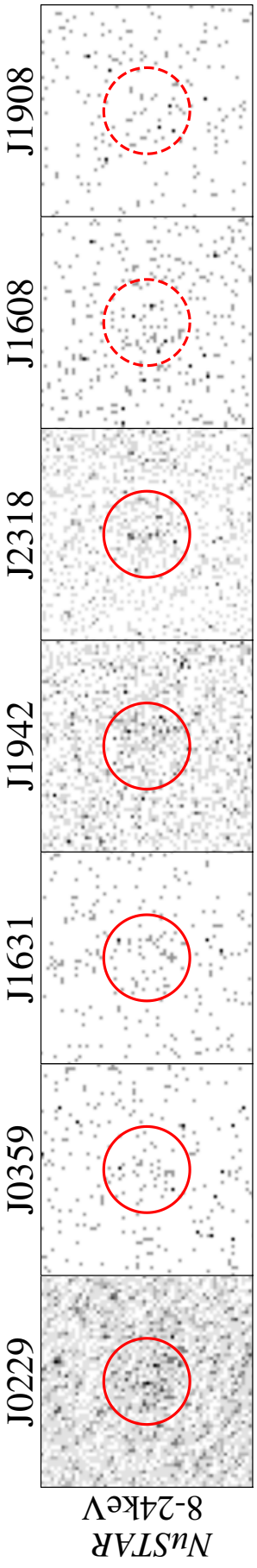

FIGURE 3.7: *NuSTAR* and soft X-ray data for each source not being followed up at this time.

3.3 Final Candidates

At this point there are nine candidate obscured AGN remaining. In this section I will present a description of and results from each source. Each of these are detected in *NuSTAR*, by design, but in order to make a detailed spectral fit of each source we require additional soft X-ray data, if possible. I searched the HEASARC archive for data from three major X-ray telescopes: *XMM-Newton*, *Chandra*, and *Swift*-XRT. *XMM-Newton* provides good spectral and angular resolution; *Chandra* covers a smaller spectral range, but has better angular resolution; and *Swift*-XRT covers a large portion of the sky, and is likely to be a good source of data where *XMM-Newton* and *Chandra* are not available.

Not every object in the *NuSTAR* 80-month catalogue has a known soft X-ray counterpart, but most do - and in the case of these nine candidates each has counterpart coordinates available. In Figure 3.8 the *NuSTAR* coordinates are indicated with a red circle (radius 30 arcseconds) and soft coordinates a blue circle (radius 10 arcseconds). Hard-band (8-24 keV) images from *NuSTAR* in the first row, then (where available) *XMM-Newton*, *Chandra*, and *Swift*-XRT full-band images in the remaining rows. In each soft image, there is a clear source at the soft X-ray coordinates indicated in the 80-month catalogue.

These images are the stacked total of all available measurements for each source, for each instrument. However, it is not necessary to use every observation for spectral fitting. For example, some sources have several short observations or observations from drastically different epochs. Including low quality spectra where high quality is available will not help the fitting. If measurements from different epochs are used, assumptions must be made about e.g., the consistent shape of the spectrum, even if the cross-calibration constants are allowed to vary. This is unavoidable in cases where the *NuSTAR* and soft data was taken at different times - it is better to include some soft data than none - but in order to minimise any adverse effects, not every spectrum available is included in each fit. The observations used are listed in Table 3.1.

3.3.1 Method

To analyse the combined soft and hard X-ray data of the candidates, the data were reduced using standard recommended selection criteria, including removal of appropriate background, using the *XMM-Newton* Science Analysis Software[7] and HEASoft[8]. The data were fit within `xspec` (Arnaud, 1996), v.12.12.0, with initial cross calibration

[7] `http://xmm.esa.int/sas/`
[8] `https://heasarc.gsfc.nasa.gov/docs/nustar/analysis/`

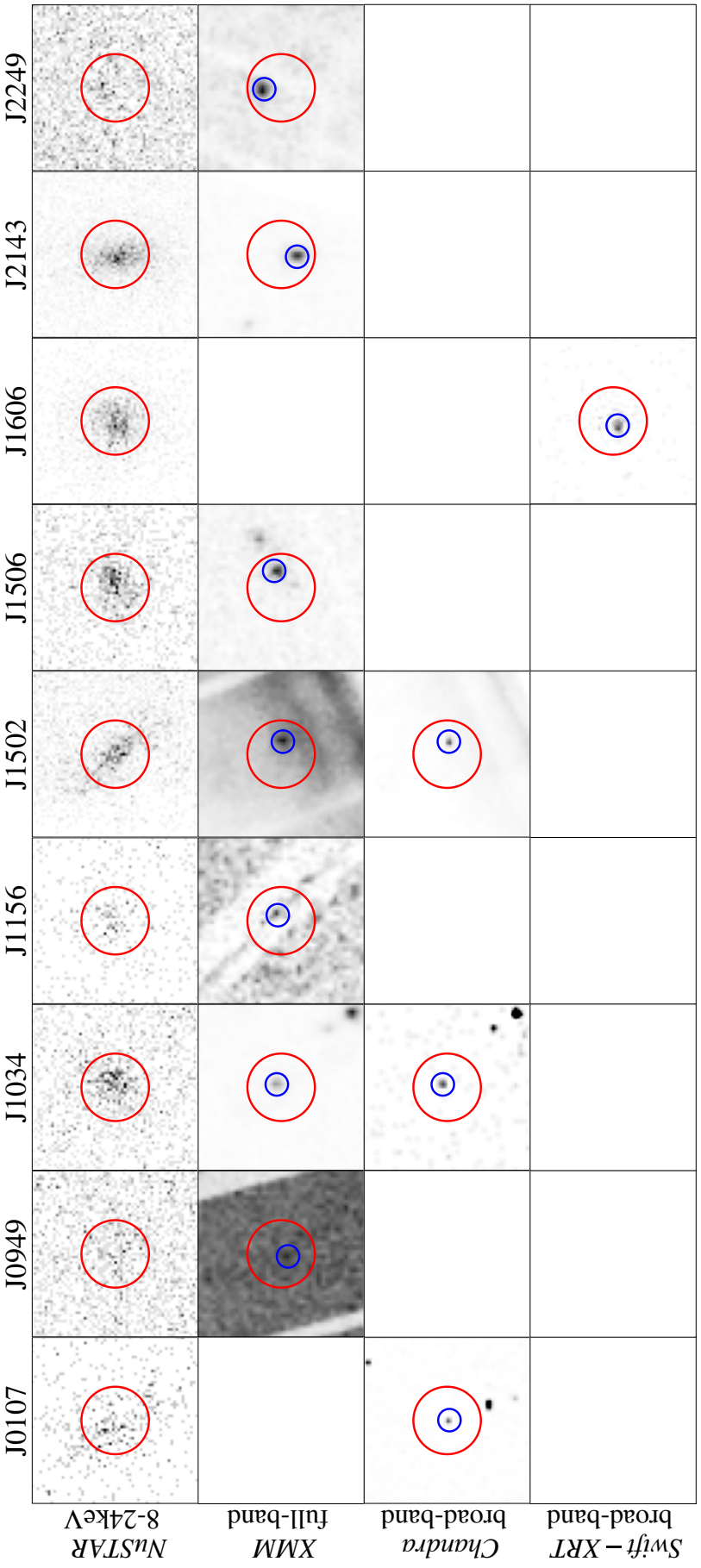

FIGURE 3.8: *NuSTAR* and soft X-ray data for each selected source.

TABLE 3.1: Data used for modelling in Section 3.3.1. Column details: (1) Source name; (2) Date of measurement, if different; (3) Galactic $N_{\rm H}$; (4) redshift; (5) *NuSTAR* observation IDs; (6) *XMM-Newton* observation IDs; (7) *Swift*-XRT observation IDs.

Name	Epoch	Gal. $N_{\rm H}$ 10^{20} cm^{-2}	RA J2000	Dec J2000	z	*NuSTAR*	*XMM-Newton*	*Swift*-XRT
(1)	(2)	(3)	(4)	(5)	(6)	(7)	(8)	(9)
J0107		2.470	16.915	-11.653	0.048	60260004002		
J0949		4.710	147.294	0.382	0.093	60201052002	0673730101	
J1034		1.280	158.736	39.660	0.151	60401004002	0824030101,0506440101	
J1156		1.010	179.244	55.138	0.080	60375001002	0204651201	
J1502		7.240	225.607	-42.140	0.054	40110002002	0653860101	
J1506		3.540	226.695	3.771	0.034	60301023002,60061261002	0795670101	
J1606		7.540	241.524	-72.877	0.122	60161629002		7 observations[a]
J2143	2016	26.000	325.834	43.580	0.013	80202036002	0791000201	
	2018	26.000	325.834	43.580	0.013		0820230101	
	Jan 2021	26.000	325.834	43.580	0.013	90701304002		
	Feb 2021	26.000	325.834	43.580	0.013	90702309002		
	Mar 2021	26.000	325.834	43.580	0.013	90702309004		
J2249		1.880	342.355	-19.293	0.445	60502004004,60101027002	0840230201,0840230501	

[a]00031454001,00031454002,00038074001,00038074002,00038074003,00038074004,00090181001

constants of 0.93:1.02:0.98:1.00:1.10:1.04 (Madsen et al., 2015) for *XMM-Newton*(pn):*XMM-Newton*(MOS1):*XMM-Newton*(MOS2):*NuSTAR*:*Chandra*:*Swift*-XRT; fixed if the observations were quasi-simultaneous, or if variation was not needed. Spectra were binned to 3/1 counts per bin for *NuSTAR*/soft data, and fit with `wstat` (Wachter et al., 1979) – the version of `cstat` (Cash, 1979) used by `xspec` when a background is included[9].

The initial model used was a simple absorbed powerlaw: in `xspec` terms PHABS×CABS×ZWABS×POWERLAW. Intrinsic AGN emission is described by a powerlaw ($E^{-\Gamma}$), then absorbed by redshifted photoelectric absorption (ZWABS) and Compton scattered (CABS), and finally attenuated by galactic photoelectric absorption (PHABS)[10]. This model assumes that the AGN continuum is only viewed through this obscuration, not directly, and is thus a fully obscured (but simple) model. This model proves a reasonable fit for some sources, but for others struggles to reproduce the soft emission, indicating that these objects require some other contribution.

The second, more complicated, model applied is BORUS02 (Baloković et al., 2018), which assumes an intrinsic cutoff powerlaw (i.e., similar to POWERLAW, but with a high energy cut off, as seen in sources observed in ultra-hard X-rays). This intrinsic emission is then reprocessed through a simplified obscuring torus, modelled as a sphere with polar cutouts. The opening angle and viewing angle are free in the model - for each source here we have set the opening angle to a non-extreme value of 0.5, and the viewing angle to either 0.05 (viewed through the torus) or 0.9 (viewed from above), depending on the appearance of the source optical spectrum. For simplicity, we adopt the linked $N_{\rm H}$ version of the model.

3.3.2 Individual Sources

In the following sections I will discuss the results from each individual source found to be Compton thick ($N_{\rm H}$ >1.5×10^{24} cm^{-2}); the remainder may be found in Appendix C. Table 3.2 summarises the specific results arising from each model fit from all nine sources.

[9] https://heasarc.gsfc.nasa.gov/xanadu/xspec/manual/node318.html#AppendixStatistics

[10] Values of galactic $N_{\rm H}$ are taken from HEASARC (HI4PI Collaboration et al., 2016), and can be found in Table 3.1

TABLE 3.2: Spectral modelling results. Column details: (1) Source name; (2) Data epoch; (3) XSPEC model; (4) photon index Γ; (5) column density N_H; (6) observed 10-40 keV luminosity; (7) fit statistic (cstat/d.o.f.); (8) selected fit; (9) source appears Compton thick; (10) notes on included data.

Name	Epoch	Model	Γ	log N_H cm^{-2}	log $L_{10-40\,keV}$ erg s^{-1}	C/n	Accept?	CT?	Note
(1)	(2)	(3)	(4)	(5)	(6)	(7)	(8)	(9)	(10)
J0107		CABS×ZWABS×POW	$1.18^{+0.41}_{-0.35}$	$23.62^{+0.15}_{-0.18}$	$43.23^{+0.05}_{-0.58}$	179/176	✓		
J0949		CABS×ZWABS×POW	[1.9]	$24.23^{+0.27}_{-0.23}$	$42.47^{+0.11}_{-0.74}$	590/533		✓	
J0949		BORUS02	[1.9]	$24.35^{+0.38}_{-0.24}$	$42.55^{+0.11}_{-0.44}$	459/490	✓	✓	
J1034		CABS×ZWABS×POW	[1.9]	$24.10^{+0.06}_{-0.07}$	$43.59^{+0.03}_{-0.07}$	465/445			*NuSTAR* only
J1034		BORUS02	$2.55^{+0.06}_{-0.06}$	$24.21^{+0.01}_{-0.01}$	$43.52^{+0.07}_{-0.11}$	2003/2033	✓	✓	
J1034		BORUS02+APEC	[1.9]	$24.12^{+0.02}_{-0.02}$	$43.59^{+0.05}_{-0.05}$	2023/2033			
J1156		CABS×ZWABS×POW	[1.9]	$24.24^{+0.11}_{-0.11}$	$43.11^{+0.06}_{-0.20}$	240/346		✓	
J1156		BORUS02	[1.9]	$24.23^{+0.10}_{-0.10}$	$43.16^{+0.09}_{-0.16}$	186/150	✓	✓	
J1502[a]		CABS×ZWABS×POW	$1.40^{+0.26}_{-0.24}$	$23.76^{+0.09}_{-0.11}$	$43.07^{+0.02}_{-0.24}$	1821/1801			
J1502		BORUS02	$1.45^{+0.17}_{-0.17}$	$23.73^{+0.20}_{-0.20}$	$43.04^{+0.06}_{-0.38}$	1736/1800	✓		
J1506		CABS×ZWABS×POW	[1.9]	$24.21^{+0.07}_{-0.07}$	$42.43^{+0.04}_{-0.06}$	513/459		✓	*NuSTAR* only
J1506		BORUS02	$1.89^{+0.15}_{-0.16}$	$24.20^{+0.04}_{-0.04}$	$42.49^{+0.03}_{-0.11}$	789/781	✓	✓	
J1606		CABS×ZWABS×POW	$1.52^{+0.12}_{-0.11}$	$23.58^{+0.06}_{-0.06}$	$44.53^{+0.02}_{-0.05}$	763/794	✓		
J2143[b]	2016	CABS×ZWABS×POW	$1.68^{+0.43}_{-0.35}$	$23.56^{+0.19}_{-0.22}$	$41.94^{+0.03}_{-0.83}$	346/350			*NuSTAR* only
J2143	2016	BORUS02	$1.58^{+0.22}_{-0.17}$	$23.60^{+0.11}_{-0.08}$	$41.96^{+0.03}_{-0.27}$	646/741			
J2143	Jan 2021	BORUS02	$1.45^{+0.12}_{-0.12}$	$23.59^{+0.05}_{-0.05}$	$42.14^{+0.03}_{-0.27}$	736/797			
J2143	Feb 2021	BORUS02	$1.57^{+0.10}_{-0.10}$	$23.58^{+0.05}_{-0.05}$	$42.27^{+0.04}_{-0.08}$	910/1058			
J2143	Mar 2021	BORUS02	$1.45^{+0.08}_{-0.08}$	$23.57^{+0.04}_{-0.04}$	$42.53^{+0.01}_{-0.18}$	1340/1250			
J2249		CABS×ZWABS×POW	[1.9]	$23.44^{+0.36}_{-2.07}$	$43.66^{+0.09}_{-0.37}$	354/341	✓		*NuSTAR* only

[a] Complicated background - see Section C.2.
[b] Variable source - see Section C.4.

3.3.2.1 NuSTARJ094910+0022.9

NuSTARJ094910+0022.9 (hereafter J0949) is a slightly complicated system. It has two overlapping galaxies (see Figure 3.9) - a larger edge on galaxy, and a smaller elliptical galaxy. The latter of these is the source of the optical spectrum (which shows narrow lines only; measured at Keck), and the position of the soft X-ray and optical PanSTARRS coordinates. According to SDSS, the redshift of the larger galaxy is 0.110, similar to the redshift of J0949 at 0.093 (see Section 3.4.2) but far enough away that it is unlikely to be closely associated. The *WISE* source assigned by the catalogue appears to be a blend of emission from these two objects, and thus cannot be used to draw any conclusions about the MIR emission of J0949 itself. It is also not certain that the X-ray emission is coming from the optical source - the radii of both *NuSTAR* and *XMM-Newton* are much larger than the separation between these two objects (see Figure 3.10), and thus the results from this fitting must be understood with this in mind. There is also a separate *WISE* source within the *NuSTAR* radius, but the brightness of this source drops off in $W3-4$ (see Figure B.7), and is therefore less likely to host an AGN.

In X-rays, it is detected from 3–24 keV with *NuSTAR*, and with a single *XMM-Newton*-pn observation (see Figure 3.10). Fitting with a simple absorbed powerlaw failed to produce a good fit to the soft data in particular, so J0949 was fit with the more complex BORUS02. The results of this can be seen in Figure 3.11. To improve the fit, the intrinsic photon index of the powerlaw was fixed at a typical AGN value of 1.9 (see e.g., Ricci et al., 2017a). Even with BORUS02 the model does not fit very well to the soft data - however, due to the low counts no more detailed fitting was deemed possible.

The obscuration depth was found to be $\log N_{\rm H}=24.35^{+0.38}_{-0.24}$ cm^{-2} – a Compton thick source. The observed luminosities were $L_{2-10\ \rm keV}=2.28\times10^{41}$ erg^{-1} s^{-1} and $L_{10-40\ \rm keV}=3.54\times10^{42}$ erg^{-1} s^{-1}. Both these values have high uncertainties, and are lower than usual AGN luminosities - even if corrected for absorption. It is possible that this is an intrinsically X-ray weak AGN, or that the true AGN is the other optical source.

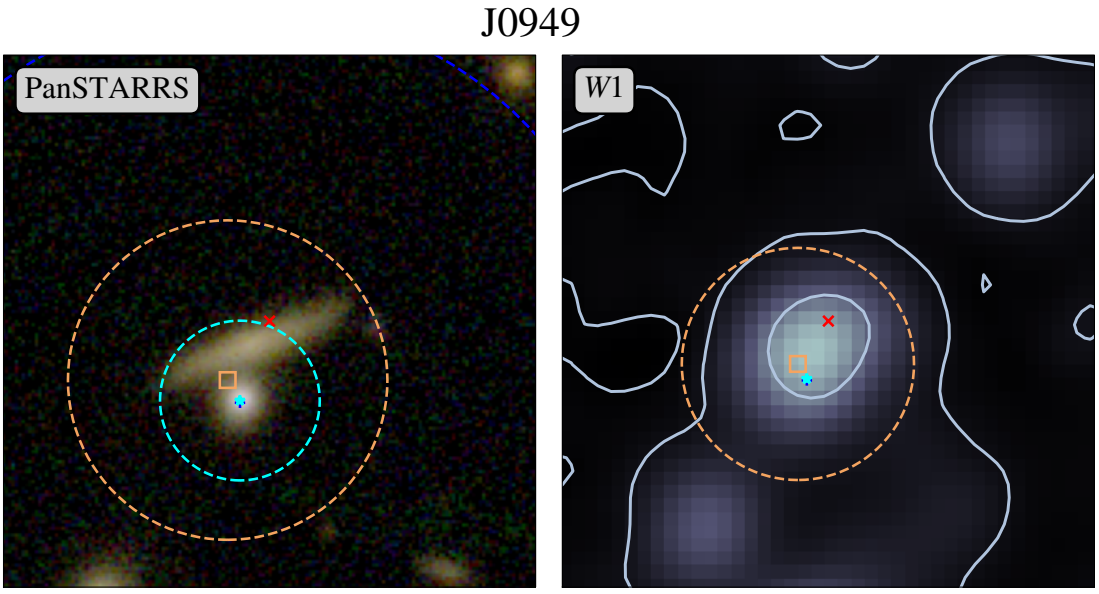

FIGURE 3.9: J0949: (left) PanSTARRS *irg* image, (right) *WISE W*1 image. Coordinates as in Figure 3.10.

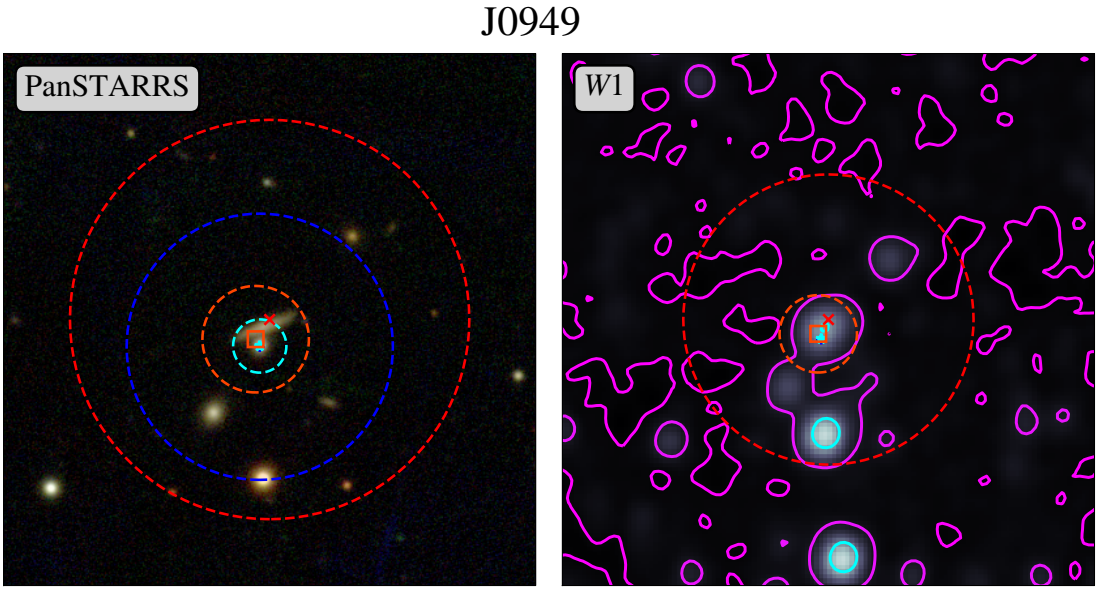

(A) J0949: (left) PanSTARRS *irg* image, (right) *WISE W*1 image.

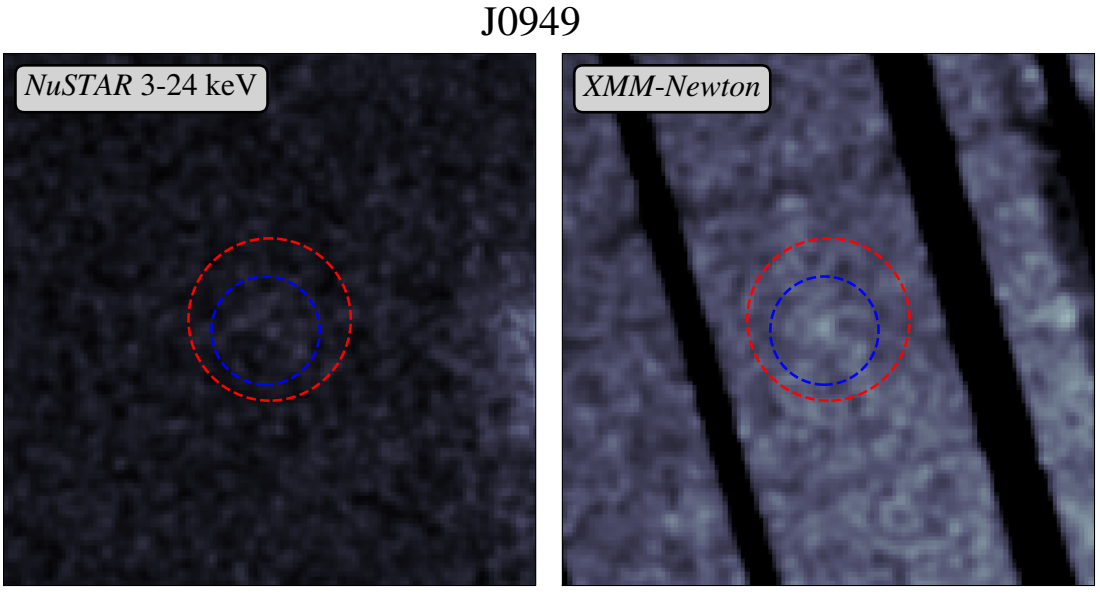

(B) (left) *NuSTAR* 3–24 keV image, (right) *XMM-Newton* 0.5–10 keV image.

FIGURE 3.10: Images of J0949, with multi-wavelength coordinates shown as follows: *NuSTAR* (red, 45 arcseconds), *XMM-Newton* (blue, 30 arcseconds), *WISE* (yellow, 12 arcseconds), PanSTARRS (cyan, 6 arcseconds).

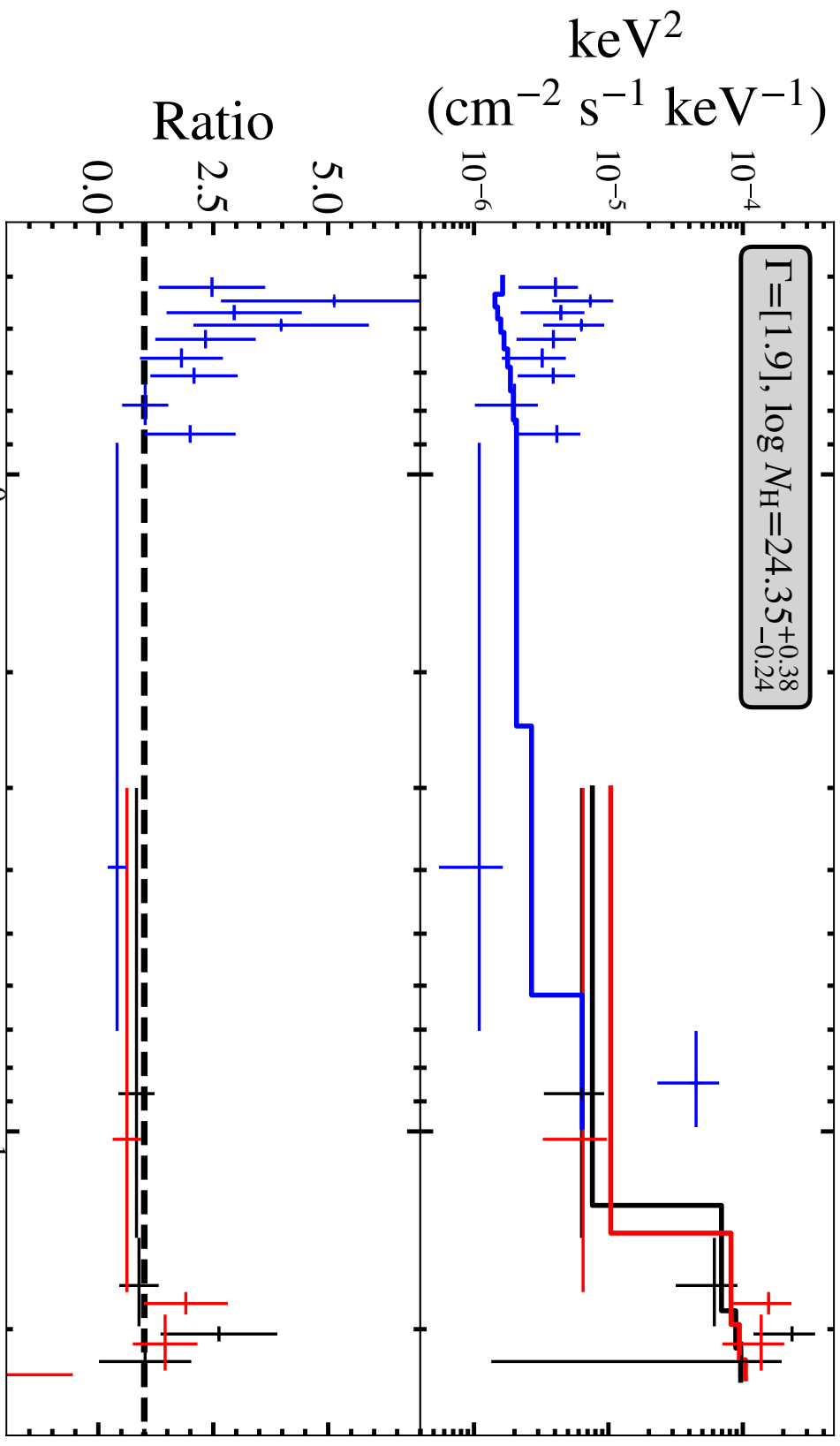

FIGURE 3.11: J0949: (top) Spectrum of best fit BORUS02 model; (bottom) ratio between data and model. Shown is each observation separately, as listed in Table 3.1, binned to a minimum of 2 counts per bin.

3.3.2.2 NuSTARJ103456+3939.6

The PanSTARRS image of NuSTARJ103456+3939.6 (hereafter J1034) shows an elliptical galaxy with a bright nucleus (see Figure 3.12a, left) . An optical spectrum is available from SDSS shows that it is a Type 2 AGN and therefore we assume that the AGN system is viewed edge on. Automatic processing from SDSS classes it as a 'QSO', sub class 'AGN BROADLINE (see Section 1.3.1), but in the VCV catalogue (13th edition; Véron-Cetty and Véron, 2010) it is classed as a Seyfert 2 - all based on the same SDSS spectrum. The multi-wavelength coordinates are well aligned, and there are no nearby optical companions visible. Kong and Ho (2018) find a BH mass ($M_{\odot}$)=8.38±0.35, and Eddington ratio -1.11±0.37.

Similarly, the *WISE* data (see Figure 3.12a, right) shows only a single bright source. Its $W1 - W2$ colour is 0.854, placing it into the range of the AGN selection process from LASr (see Section 2.3.2).

In X-rays, it is detected from 3–50 keV with *NuSTAR*, and with the full range of both *XMM-Newton* and *Chandra* (see Figure 3.12). For the spectral fitting, only the *XMM-Newton* spectra are used, as they are of higher quality. The X-ray images show additional sources, but none are bright enough or close enough to contaminate the spectrum as long as the background region is carefully chosen.

J1034 has a complex spectrum, particularly in the soft X-rays. The absorbed powerlaw could only fit the data well if only *NuSTAR* was fit, and thus this was discarded. With all data included, two models were tried: BORUS02, as described above (Figure 3.13); and BORUS02 with additional emission from collisionally-ionised diffuse gas with APEC (Figure 3.14). For the latter, Γ was fixed to 1.9. Other than this, there is not a large difference in either the fit quality or the results, so for the sake of simplicity the BORUS02 only model is used for the results. Results from both these models are included in Table 3.2.

The intrinsic photon index of the powerlaw was found to be $2.55^{+0.06}_{-0.06}$. The obscuration depth was found to be $\log N_{\rm H}$=$24.21^{+0.01}_{-0.01}$ cm^{-2}, indicating that this is a Compton thick source. The observed luminosities were $L_{2-10\ \rm keV}$=2.62×10^{42} erg^{-1} s^{-1} and $L_{10-40\ \rm keV}$=3.29×10^{43} erg^{-1} s^{-1}. Koulouridis et al. (2016) find J1034 to be a candidate Compton thick AGN using the *XMM-Newton* data only, but place only a lower limit on $N_{\rm H}$. LaMassa et al. (2014) fit a spherical obscuration model (again, to *XMM-Newton* only) and find $\log N_{\rm H}$=23.72. However, with the new *NuSTAR* data included - and noting how the model needed multiple components to constrain - we can be confident that it is more likely to be a CT AGN than not.

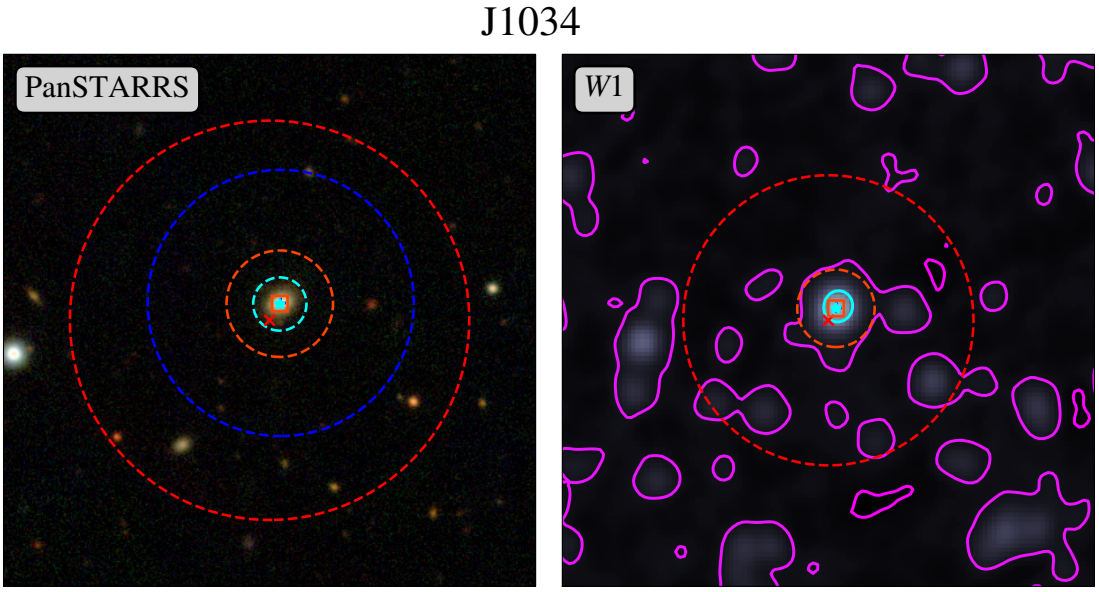

(A) J1034: (left) PanSTARRS *irg* image, (right) *WISE* W1 image.

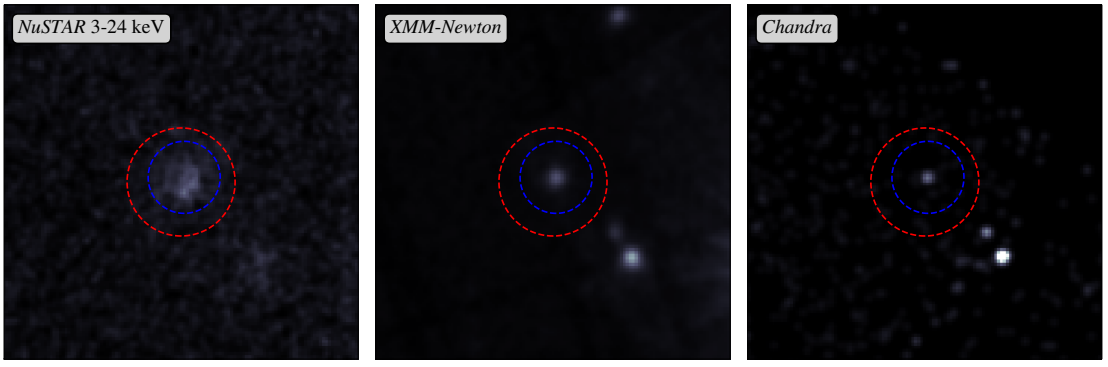

(B) (left) *NuSTAR* 3–24 keV image, (middle) *XMM-Newton* 0.5–10 keV image, (right) *Chandra* full band image.

FIGURE 3.12: Images of J1034, with multi-wavelength coordinates shown as follows: *NuSTAR* (red, 45 arcseconds), *XMM-Newton* (blue, 30 arcseconds), *WISE* (yellow, 12 arcseconds), PanSTARRS (cyan, 6 arcseconds).

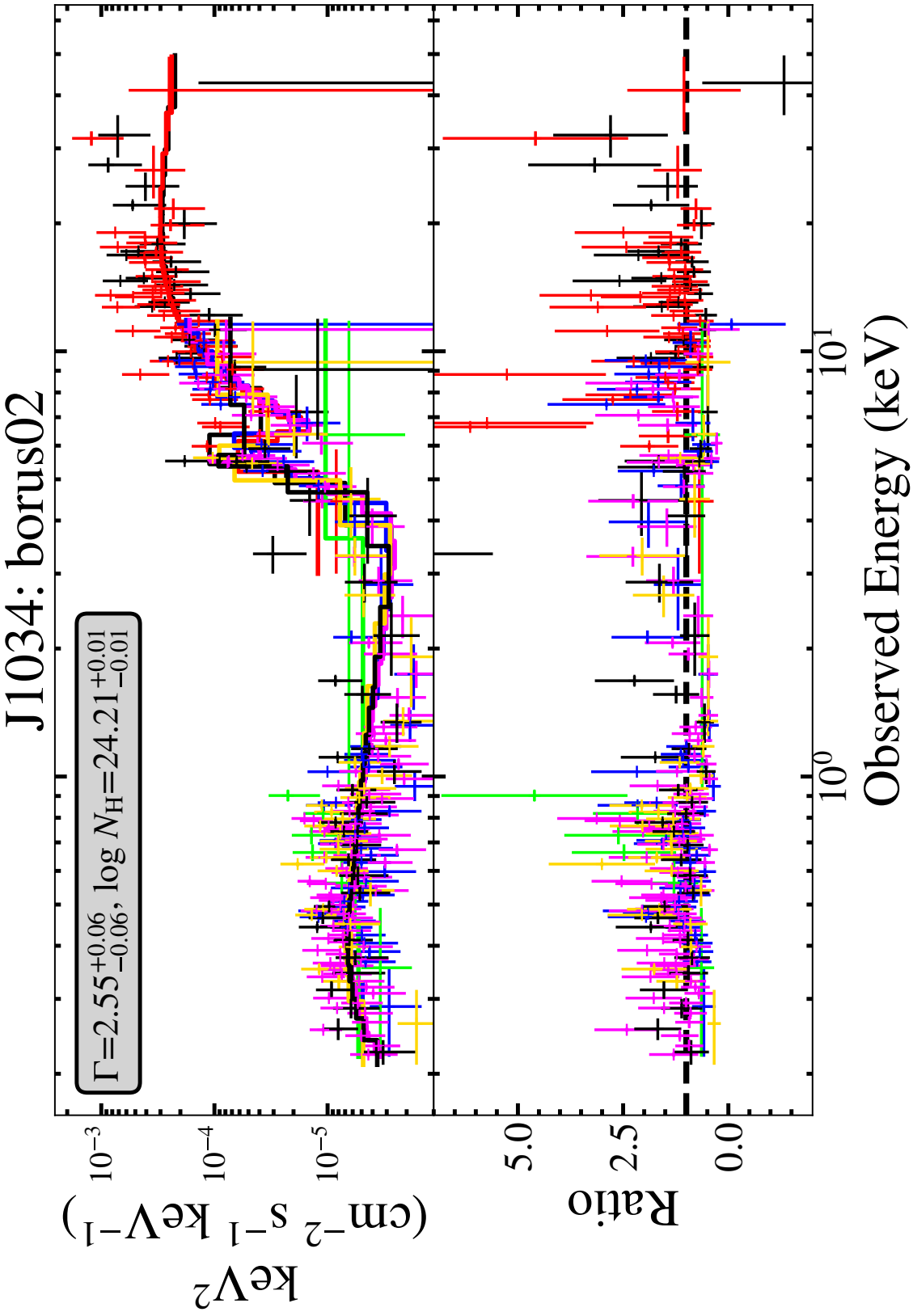

FIGURE 3.13: J1034: (top) Spectrum of best fit BORUS02 model; (bottom) ratio between data and model. Shown is each observation separately, as listed in Table 3.1, binned to a minimum of 2 counts per bin.

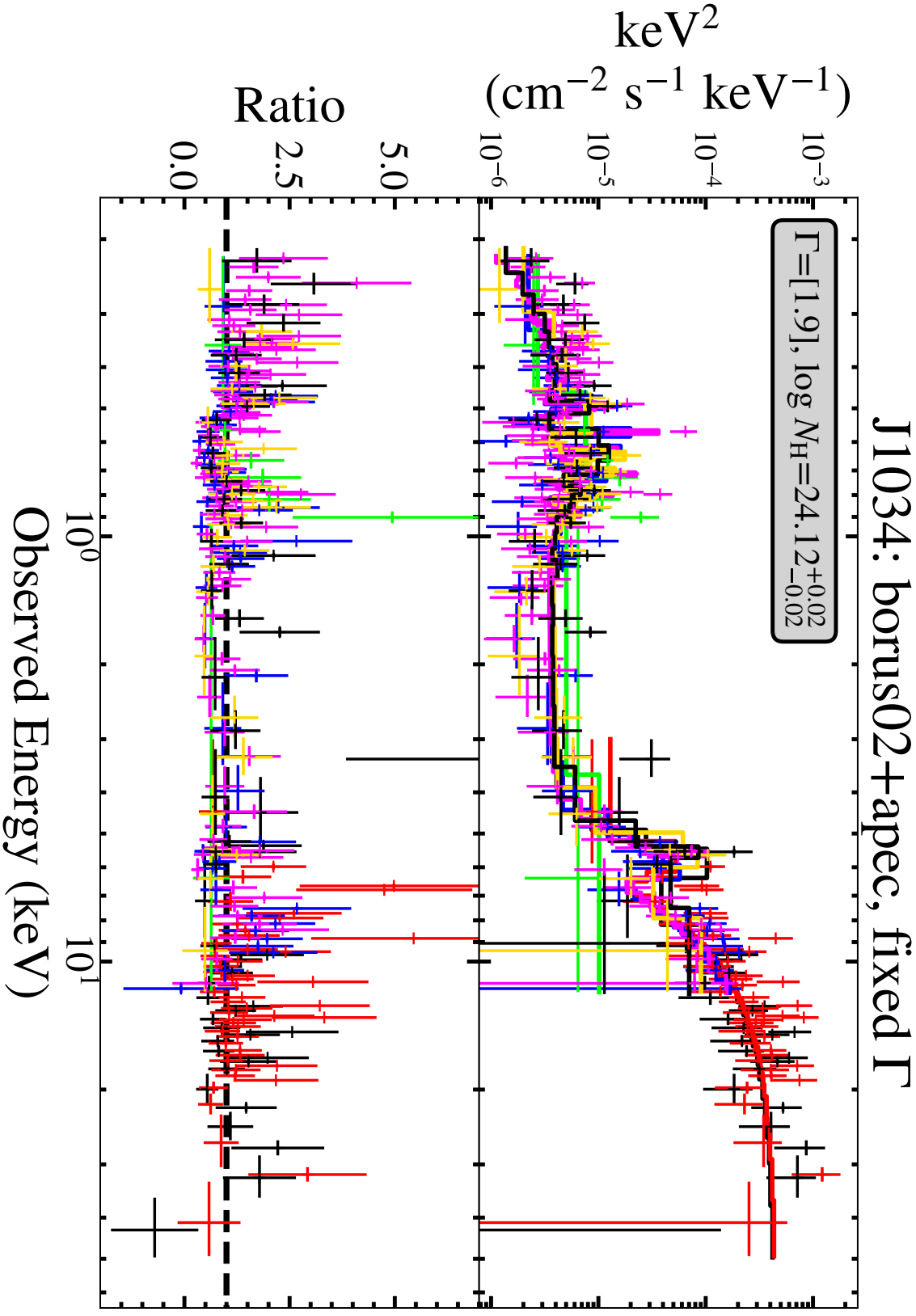

FIGURE 3.14: J1034: (top) Spectrum of best fit BORUS02+APEC model; (bottom) ratio between data and model. Shown is each observation separately, as listed in Table 3.1, binned to a minimum of 2 counts per bin.

3.3.2.3 NuSTARJ115658+5508.2

In optical imaging (PanSTARRS) NuSTARJ115658+5508.2 (hereafter J1156) appears to be a face-on or elliptical galaxy (see Figure 3.15a, left). The *NuSTAR*, soft X-ray, IR and optical coordinates are closely aligned. In its optical spectrum (from SDSS) it shows only narrow lines and is automatically classed as an AGN; thus for spectral fitting we assume that the system is being viewed at a low angle. A second galaxy at similar redshift is present ∼100 arcseconds away (∼1 Mpc).

It is bright in *WISE* (see Figure 3.15a (right), and Figure B.9), although dropping out somewhat in *W*4. Its *W*1-*W*2 colour is 0.235 - below the Stern et al. (2012) and Assef et al. (2013) threshold for selection of AGN. As these thresholds are chosen for *completeness* rather than *reliability* (see Chapter 2 for more detail), this does not indicate that J1156 is not an AGN - just that it may represent the subset of AGN missed by MIR selection.

In X-rays, it is detected from 3–24 keV with *NuSTAR*, and in a single *XMM-Newton*-pn observation (see Figure 3.15). The *XMM-Newton* source lies on a chip boundary, and therefore background and source extraction regions had to be selected carefully and conservatively. The *XMM-Newton* spectrum is therefore of moderately low quality.

J1156 was not fit well with the absorbed powerlaw, and was fit instead with BORUS02, the results of which are shown in Figure 3.16. The intrinsic photon index of the powerlaw was fixed at 1.9. The obscuration depth was found to be $\log N_{\rm H}$=$24.23^{+0.10}_{-0.10}$ cm^{-2} – a Compton thick source. The observed luminosities were $L_{2-10\ \rm keV}$=5.39×10^{41} erg^{-1} s^{-1} and $L_{10-40\ \rm keV}$=1.43×10^{43} erg^{-1} s^{-1}. Based on MIR indicators and X-ray/[O III] flux ratio, Goulding et al. (2011) find J1156 to be a candidate Compton thick AGN, consistent with our result.

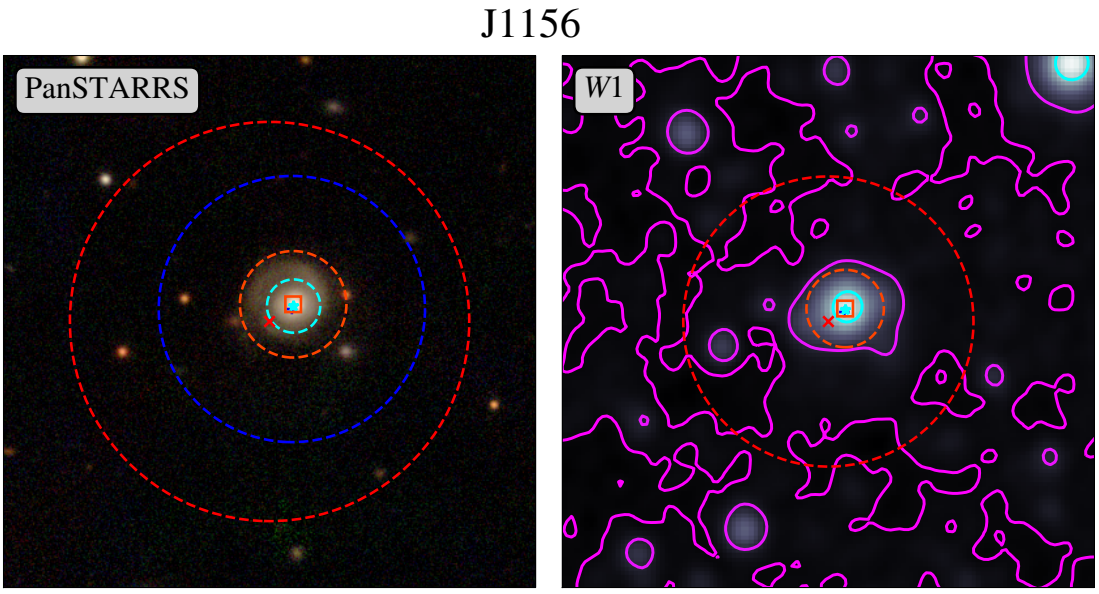

(A) J1156: (left) PanSTARRS *irg* image, (right) *WISE* W1 image.

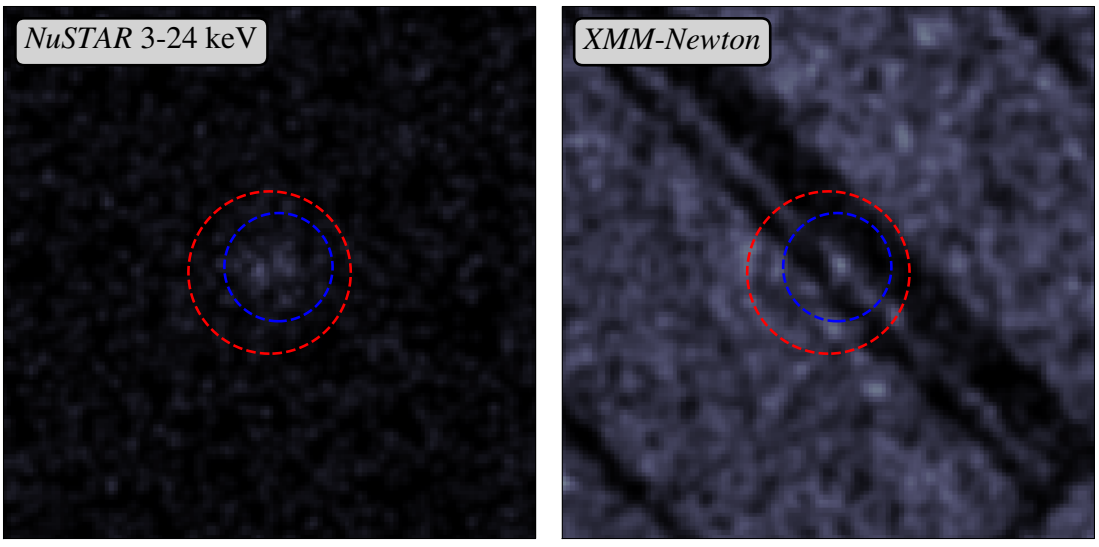

(B) (left) *NuSTAR* 3–24 keV image, (right) *XMM-Newton* 0.5–10 keV image.

FIGURE 3.15: Images of J1156, with multi-wavelength coordinates shown as follows: *NuSTAR* (red, 45 arcseconds), *XMM-Newton* (blue, 30 arcseconds), *WISE* (yellow, 12 arcseconds), PanSTARRS (cyan, 6 arcseconds).

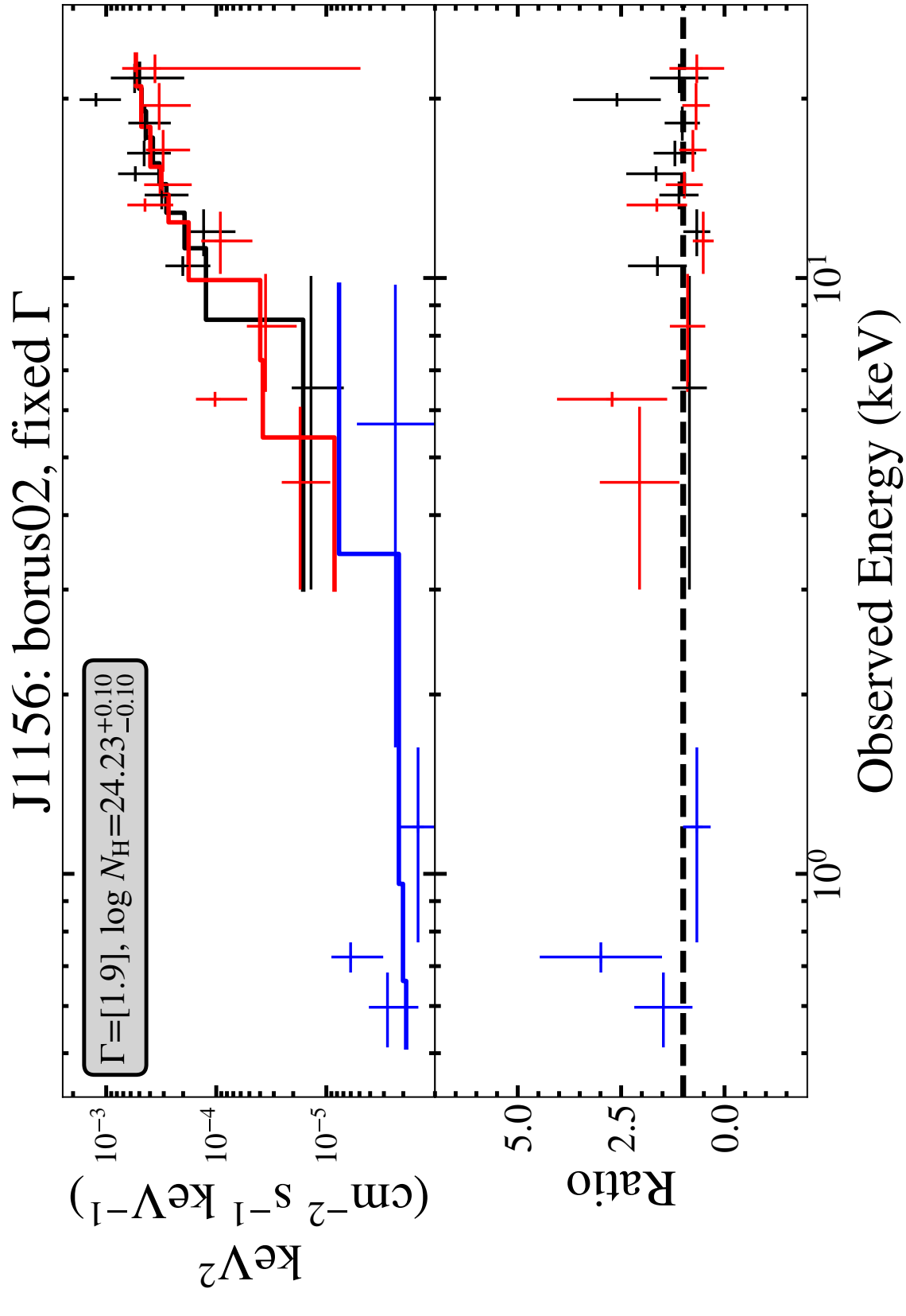

FIGURE 3.16: J1156: (top) Spectrum of best fit BORUS02 model; (bottom) ratio between data and model. Shown is each observation separately, as listed in Table 3.1, binned to a minimum of 2 counts per bin.

3.3.2.4 NuSTARJ150646+0346.2

NuSTARJ150646+0346.2 (hereafter J1506) is also known as UGC 09710. It has one large close companion at similar redshift (IC 1087). In the PanSTARRS optical imaging (Figure 3.17a, left) a spur to the side is visible, which may be a small third galaxy, or a consequence of the interaction. J1506 was found in the NSS40 extreme source sample, and was selected for follow-up as it lacked a soft X-ray counterpart - no *XMM-Newton* or *Chandra* coverage, and undetected in *Swift*-XRT. It is a known optical AGN, and appears in Zaw et al. (2019) where it is identified as a Type 2 AGN based on its SDSS spectrum.

Both J1506 and its companion are bright in *WISE* (see Figure 3.17a (right), and Figure B.11), with the companion reduced in brightness at longer wavelengths. Its $W1$-$W2$ colour is 0.401 - below MIR selection thresholds, as with several other sources.

In X-rays, it is detected from 3–50 keV with *NuSTAR* and in the simultaneous *XMM-Newton* observation (see Figure 3.17). The companion is detected in *XMM-Newton* but not *NuSTAR* - it may also be an AGN, but is not a likely Compton thick candidate.

Only the targeted simultaneous observations were used for the model fitting. The absorbed powerlaw did not fit the soft data well, but BORUS02 provides a more reasonable fit. The results are shown in Figure 3.18 - the fit to the soft data is still not perfect, with some excess visible in the ratio around 1 keV, but it is statistically acceptable. The intrinsic photon index of the powerlaw was found to be $\Gamma=1.89^{+0.15}_{-0.16}$ cm^{-2}. The obscuration depth was found to be $\log N_{\rm H}=24.20^{+0.04}_{-0.04}$ cm^{-2} – a Compton thick source. The observed luminosities were $L_{2-10\ \rm keV}=1.45\times10^{41}$ erg^{-1} s^{-1} and $L_{10-40\ \rm keV}=3.08\times10^{42}$ erg^{-1} s^{-1}.

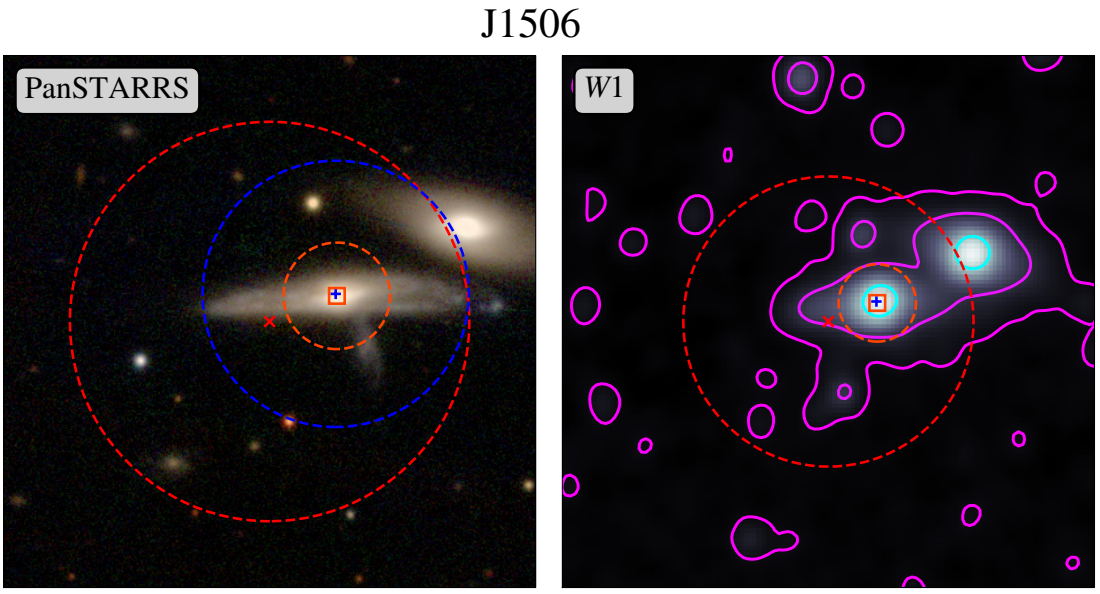

(A) J1506: (left) PanSTARRS *irg* image, (right) *WISE W*1 image.

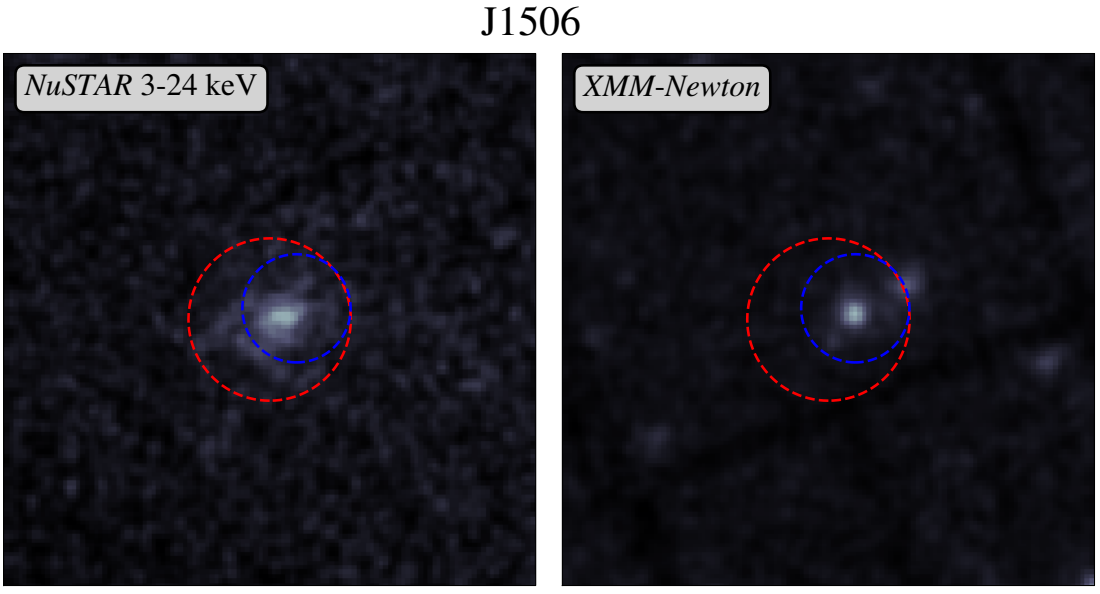

(B) (left) *NuSTAR* 3–24 keV image, (right) *XMM-Newton* 0.5–10 keV image.

FIGURE 3.17: Images of J1506, with multi-wavelength coordinates shown as follows: *NuSTAR* (red, 45 arcseconds), *XMM-Newton* (blue, 30 arcseconds), *WISE* (yellow, 12 arcseconds).

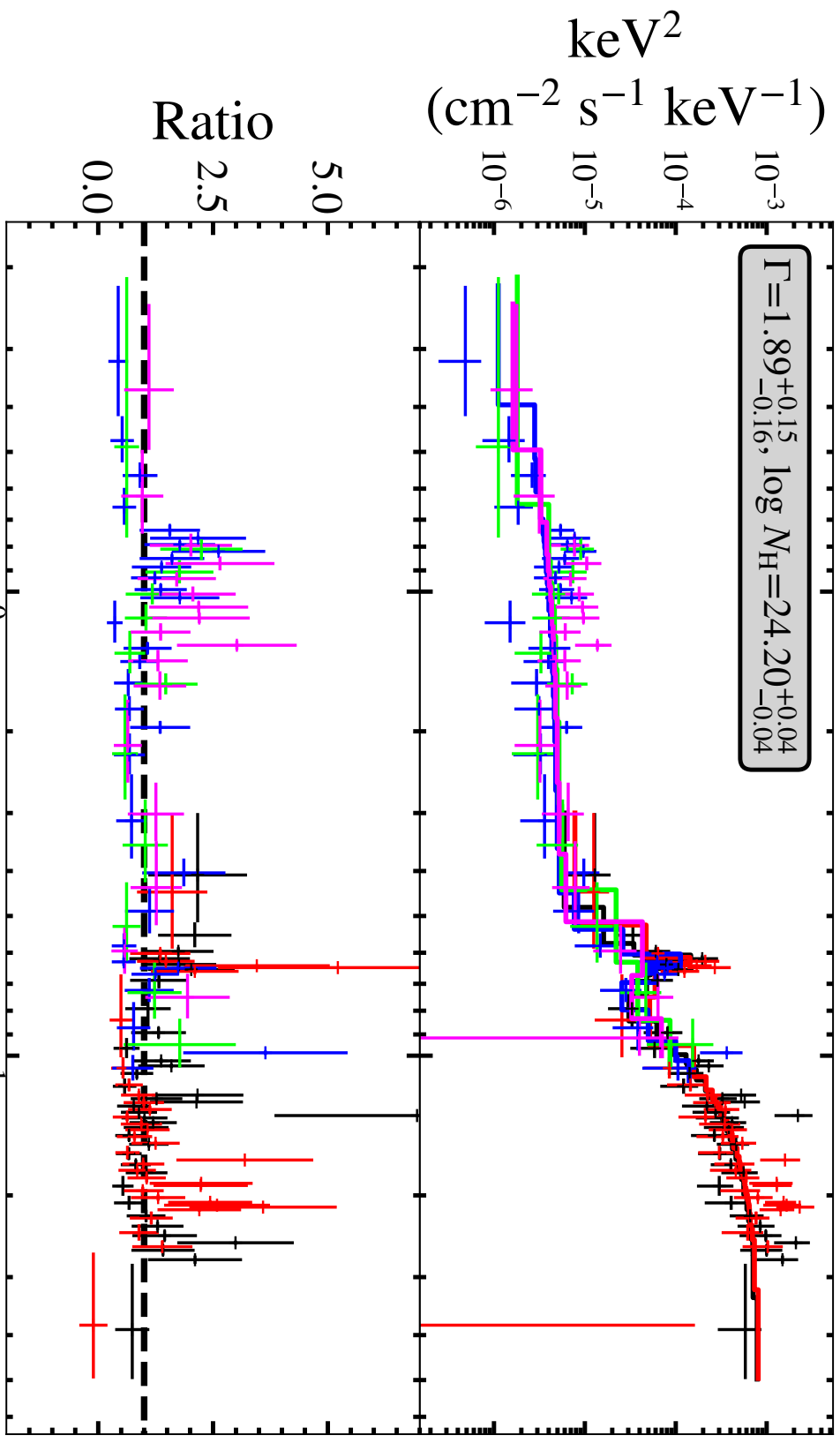

FIGURE 3.18: J1506: (top) Spectrum of best fit BORUS02 model; (bottom) ratio between data and model. Shown is each observation separately, as listed in Table 3.1, binned to a minimum of 2 counts per bin.

3.4 How do these Extreme AGN Contribute?

In the final section of this chapter, I will put the heavily obscured and CT AGN discovered in this work into context: how do they influence our knowledge of the AGN population?

3.4.1 Compton thick fraction

Compton thick AGN are difficult to find and difficult to characterise. This chapter has aimed to select and analyse sources with the highest probability of being CT AGN in order to expand our knowledge of these elusive objects.

The cosmic X-ray background (CXB) - the unresolved X-ray emission present across the sky - is thought to be the sum of emission from many AGN, too far away or too weak to be resolved by current instruments. Studies show that to reproduce the shape of this emission we require large numbers of CT AGN, their distinctive absorbed spectral shape essential to the shape of the observed CXB. Ananna et al. (2019) find a CT fraction of 50%±9% for AGN within z=0.1 (of this sample only J1034 and J1606 are at >0.1, but <0.2). Other past estimates have found a wide range of intrinsic CT AGN fractions (e.g., Ueda et al., 2014).

Values for observed CT AGN fraction are generally lower. With *Swift*-BAT and *Swift*-XRT data (combined 0.3–195 keV), Akylas et al. (2016) use Bayesian methods to examine the CT probability of 604 sources from the *Swift*-BAT 70-month survey. They first exclude sources likely to be Compton thin based on a simple powerlaw fit, and fit the remaining 70 sources with a more detailed model[11]. Their aim is not to make a definitive answer about the CT nature of each source, but instead to assign a probability based on the $N_{\rm H}$ and Fe K_α best-fit values. Based on this they calculate an estimate of the number of CT sources in the sample and find a CT fraction of ∼7% of their AGN sample. Without *NuSTAR* it is harder to make solid conclusions about individual objects. This is demonstrated by Torres-Albà et al. (2021) who examine *Swift*-BAT-selected CT AGN candidates with *NuSTAR*. They find that *NuSTAR* is vital for characterising CT AGN accurately. Within the *Swift*-BAT sample they find a CT fraction of ∼8% at z <0.05 (rising to ∼20% at z <0.01). Ricci et al. (2015) find $7.6^{+1.1}_{-2.1}$% of their hard X-ray sample to be Compton thick; correcting for selection bias, they calculate an intrinsic CT fraction of 27±4%.

To assess the fraction of CT AGN found by this analysis we must begin with assessing the completeness of the parent sample and of each selection step, as with the LASr work. This is summarised in Figure 3.19. NSS80 contains 1274 sources, of which 507

[11]The TORUS model from Brightman and Nandra (2011) - note that is now outdated and contains a minor inaccuracy.

have reliable redshifts. From these, we select 16 objects with high band ratios (indicating likely CT candidates) and *new NuSTAR* data, with 7 already known from L2017. The parent catalogue for this work includes most sources from NSS40, and all confident CT sources. The major difference of note between these works is that here we restrict detailed analysis to sources with high net source counts, whereas L2017 include all sources. If we apply this cut to sources found in that work, two sources remain - one of which is Compton thick.

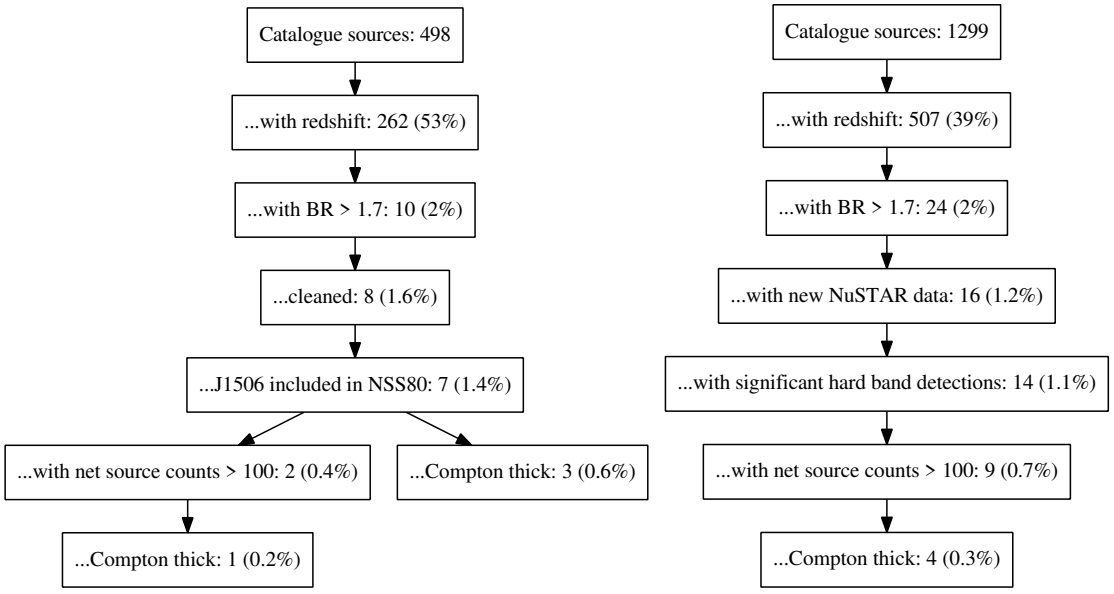

FIGURE 3.19: Selection process for NSS40 (left) and NSS80 (right). Note that difference in redshift completeness between the two iterations of the catalogue is due to a large number of new serendipitous *NuSTAR* sources present in NSS80. Approximately the same number of new spectroscopic follow-ups were performed for NSS80 as for NSS40, but the *fractional* completeness is lower.

For comparison with previous results, we consider different low-z cuts. At higher redshifts, the shape of the spectrum changes the BR threshold that predicts a CT AGN candidate (see Figure 3.20) and thus we will be missing higher numbers of CT AGN and number counts in the more local universe will be more accurate. We include J1506 in L2017 for number counts as its initial discovery there is more relevant. However, we use the results from this analysis for its properties, as this work contains the most up to date data.

$z < 1.5$: Initially we consider the redshift range over which we are most likely to find CT sources. At redshifts larger than $\sim$1.5 it becomes harder to distinguish these AGN with a simple band ratio cut, and thus here we count sources within that range.

- Initial source list: 189 *NuSTAR* serendipitous sources at $z < 1.5$ with a detection in the hard band (8–24 keV).
- NSS80: 13 detected sources, 2 non detections.

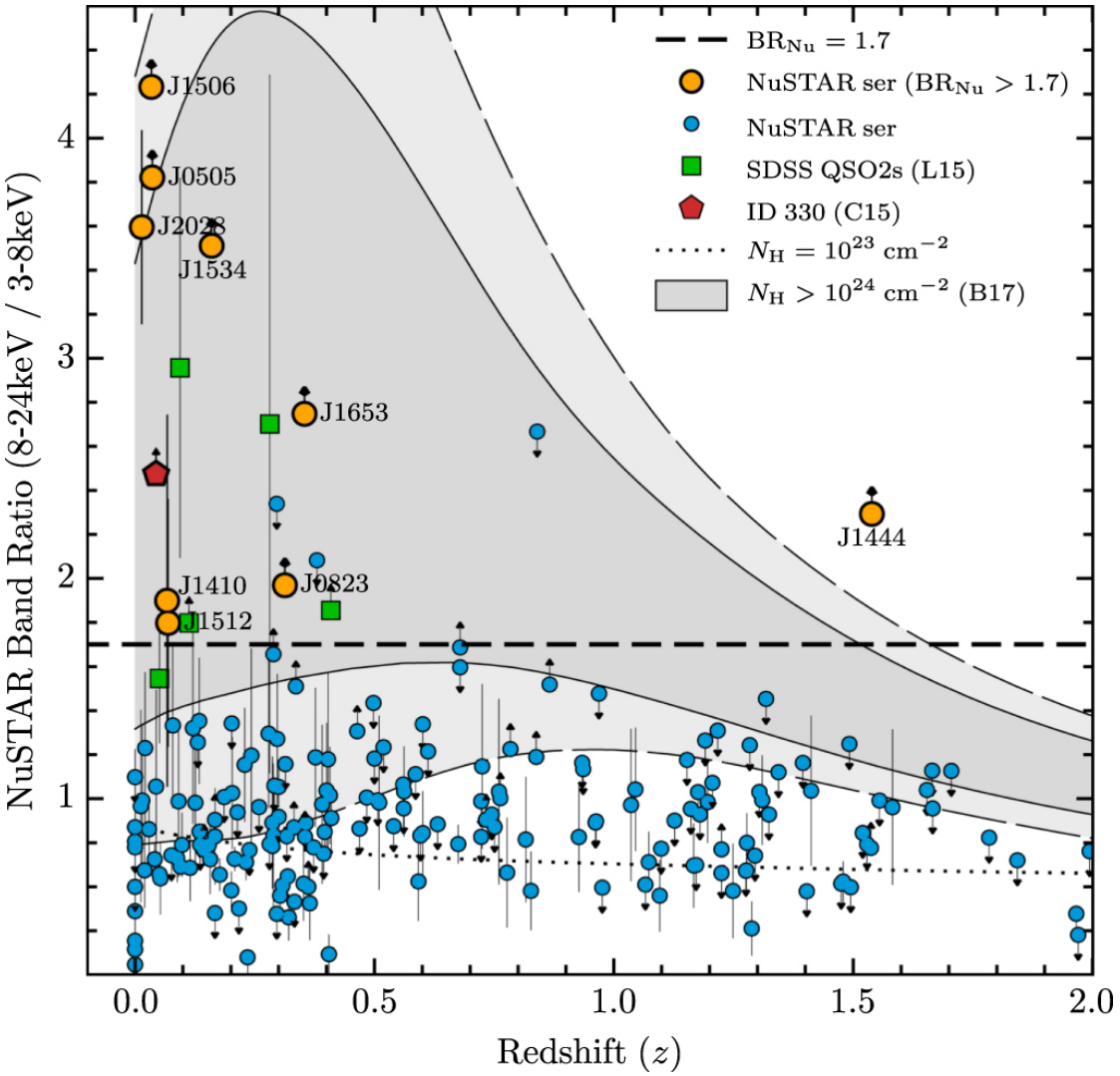

FIGURE 3.20: Band Ratio of NSS40 sources, with the region most likely to contain Compton thick sources based on spectral modelling of local CT AGN highlighted in grey (Fig. 1 of L2017)).

- NSS80: 8 high count sources, 3 CT AGN found.
- NSS40: 7 detected sources, 4 CT AGN found.
- NSS40: sources with less than 100 net counts (i.e., those that would have been removed from this work) include 5 detected sources with 2 CT AGN found - thus a CT ratio of 0.4.
- NSS80: 5 low count sources - an estimated 2 more CT AGN would be found if consistent with the ratio from NSS40.
- Total: 20 sources, 2 non detections, 9 CT AGN found (including estimates from low count sources).
- Correct the initial source list, assuming a consistent non-detection fraction (i.e., assuming ∼10% false inclusions): ∼170 sources in the parent sample.

- Nine CT AGN found gives a CT fraction of 5^{+2}_{-1}%.

This low value is not unexpected - we have fewer sources in the catalogue in total at larger redshifts, and a combination of the decrease in bolometric flux as well as moving spectral shape makes the bias against Compton thick AGN increase with redshift. Thus this fraction becomes our lower limit on the overall CT fraction. To make better estimates, we must consider much smaller volumes.

$z < 0.07$: In L2017 a redshift limit of 0.07 was used for the low redshift regime. To integrate this work, we consider sources in this range - no new CT AGN at <0.07 were found here, so an update to the parent source counts is sufficient to update the CT fraction.

- Initial source list: 22 *NuSTAR* serendipitous sources at $z < 0.07$ with a detection in the hard band (8–24 keV).
- NSS80: 3 detected sources, 0 non detections, 0 CT AGN found.
- NSS40: 4 detected sources, 3 CT AGN found.
- Total: 7 detected sources, 0 non detections, 3 CT AGN found.
- Correct the initial source list, assuming the same non-detection fraction as before (i.e., assuming ∼10% false inclusions): ∼20 sources in the parent sample.
- Five CT AGN found gives a CT fraction of 15^{+10}_{-6}%.

L2017 find a value of 30^{+16}_{-12}%. They note that their value is above that expected from models at the time of publication (Fig. 11, L2017) but this update brings the observed CT fraction into line with their predictions for intrinsic CT fraction. The large decrease in fraction between L2017 and this work is due to an increase in total sources found within the redshift limit with the improved coverage and depth of NSS80. However, we would expect new Compton thick sources in this work, especially with the large CT fraction found before.

$z < 0.1$: this low redshift cut is chosen to match Ananna et al. (2019). In this set no sources were removed due to low net counts, so we can make a consistent comparison of this work and L2017 without removing any.

- Initial source list: 35 *NuSTAR* serendipitous sources at $z < 0.1$ with a detection in the hard band (8–24 keV).
- NSS80: 5 detected sources, 1 non detection, 2 CT AGN found.
- NSS40: 4 detected sources, 3 CT AGN found.

- Total: 9 detected sources, 1 non detection, 5 CT AGN found.
- Correct the initial source list, assuming a consistent non-detection fraction (i.e., assuming ∼10% false inclusions): ∼32 sources in the parent sample.
- Five CT AGN found gives a CT fraction of 16^{+8}_{-5}%.

When comparing with the CT fraction from Ananna et al. (2019) (50%±9%), our fraction is lower - however, this is not unexpected. We can assume that the CT counts found here are a *lower limit* - there are likely to be CT AGN that were not selected with the band ratio method, particularly at higher redshifts. *NuSTAR* provides a large improvement on depth in the 8–24 keV band but will still miss fainter objects, which naturally includes CT AGN; despite being an improvement on soft X-ray selection techniques *NuSTAR*-based selection is still biased against CT AGN (see e.g., NuLANDS; Boorman et al., in prep.). For example, we can also consider the five sources not included in the spectral analysis. These sources were excluded because their source counts were lower than our chosen threshold. If we applied the same cut to L2017 sources, we find 5 low count sources, of which they find two to be CT. If we assume that the same fraction of the NSS80 excluded sources is CT that is an additional 2 CT AGN. This does not update the low redshift CT fraction, as they are all higher redshift sources. We may also be missing some sources that lie in the galactic plane[12] due to heavier line-of-sight obscuration or confusion with foreground sources. This is less of an issue than in LASr where we are examining optical and MIR sources (see Section 2.4.1), but it nevertheless may be a cause of some deficit. Additionally, we must keep in mind that this selection *requires* a spectroscopic redshift, and is thus limited to sources that are (a) associated with optical counterparts; (b) where those counterparts have sufficient emission lines detectable to fit a reliable redshift; and (c) where observations have been completed. Comparing spectroscopic completeness fractions in the catalogue across band ratios (i.e. an approximate comparison of completeness across obscuration depths) shows that at band ratios above the selection threshold ($>$1.7) but at $\lesssim$2.7 (where most of the candidates in this chapter lie) spectroscopic completeness is similar to that of the overall catalogue. At larger band ratios the completeness is lower, and thus our conclusions may retain a small bias against the most heavily obscured sources from this part of the selection process.

On the other hand, our observed CT fraction is higher than others (e.g., Akylas et al., 2016, Torres-Albà et al., 2021, , as above). If we would ideally expect to see observed CT AGN numbers match those expected from the CXB - or at least tend towards them - then this increased count is a step in the right direction.

[12] L2017 exclude sources with $|b| < 10^{\circ}$, but they are not removed from this work.

3.4.2 Merger fraction

It has been demonstrated that galaxy bulge mass and SMBH mass are connected (e.g., Kormendy and Ho, 2013), implying a connection between galaxy and AGN growth. In particular, the contribution of obscured phases of AGN to their overall growth is thought to be large (e.g., Di Matteo et al., 2005, Hopkins et al., 2006); thus any study of galaxy growth must have a clear view of the obscured AGN activity across time. Models (e.g., Springel et al., 2005) suggest that galaxy mergers are a major source of increased star formation and AGN activity - gas is funnelled to the centre of the galaxy and fuels the AGN, as well as the increased density powering new star formation. This predicts an obscured phase as the AGN grows in luminosity, until radiative pressure strips the obscuring material. The development of the merged galaxy and what features can be detected will also depend on the properties of the pre-merger galaxies, such as mass ratio.

However, the observation evidence for a connection between major galaxy mergers and AGN activity is mixed. It seems likely that mergers *can* power AGN (e.g., Lackner et al., 2014) - but is this the dominant way that AGN grow?

Studies of optical and MIR selected AGN find high merger fractions for AGN (e.g., Gao et al., 2020). Ellison et al. (2019) find that although many optically selected AGN show disturbances, the majority are *not* triggered by AGN mergers but conversely, the majority of MIR selected AGN are. Optical selection, unlike MIR selection, is biased against obscured AGN, and this study also finds that obscured AGN are also preferentially associated with merger triggering. Red and obscured quasars selected in FIRST and 2MASS (Glikman et al., 2015) at $1.7< z < 2.3$ show merger signatures in *HST* images of their host galaxies. The AGN luminosity fraction varies, but appears systematically higher in late-stage mergers (Dietrich et al., 2018), implying that a difference in AGN triggering may cause different AGN appearance. Highly obscured AGN ($N_{\rm H} >$ 3e23) have higher rates of interaction than less obscured AGN (Kocevski et al., 2015). Extending that to *Swift*-BAT selected likely CT AGN high close merger fractions are found (Koss et al., 2016).

On the other hand, not all studies find a clear connection. For AGN across the luminosity range Villforth et al. (2014, 2017) find that major mergers are unlikely to be the main trigger event behind most AGN, and that minor mergers and secular processes play a larger role. Mechtley et al. (2016) examine the fraction of high mass galaxies that show evidence of disturbed morphologies - an indicator of merger activity - and find that AGN hosts do not show a significantly higher proportion.

Simulations by Blecha et al. (2018) suggest that MIR selection of AGN in mergers may miss AGN, particularly low apparent luminosity and very late stage mergers. Observationally, high resolution IR images of *Swift*-BAT selected AGN show greater numbers

of obscured nuclear mergers (double nuclei too close to be resolved in most imaging) than matched inactive galaxies, particularly for obscured luminous AGN.

To summarise: links between mergers and AGN activity are clearest for obscured AGN, but controversial for the general AGN population. As discussed in Section 3.4.1 numbers of known CT AGN - the most heavily obscured AGN - are likely to be much less than the true numbers, and thus we can postulate that the merger fraction for CT is highly uncertain, and merger fractions across AGN types is affected by selection biases. Numbers of known CT AGN are small, therefore adding the contribution to that count from this work will improve statistics on AGN growth in this regime.

Table 3.3a presents the details of nearby galaxies from the non-CT AGN and 3.3b presents the CT sources, including those from L2017. In Figure 3.21 optical imaging from the four new CT AGN shows the position and redshift of each closest companion.

J0949 is a small elliptical galaxy at only $\sim$7 kpc projected offset from the centre of the closest galaxy (see Figure 3.21a). The difference in redshift is large ($\sim$18%) and both redshifts are from optical spectra and have a high degree of confidence (J0949 with a targeted Keck spectrum, and the nearby galaxy in SDSS). The difference in luminosity distance between the two sources - i.e., the separation along the line of sight, assuming all motion is due to Hubble flow - is $\sim$80 Mpc, much further than we would consider for interacting galaxies. There is also no sign of disturbance in either galaxy, so we consider J0949 as not interacting.

J1156 has a far-off companion galaxy, and shows no sign of morphological disturbance (see Figure 3.21c). The secondary galaxy near J1034 is at a large redshift difference - however, this is a photometric redshift from SDSS and has a large uncertainty (0.190 ± 0.0380) bringing it almost into agreement with the spectroscopic redshift of J1034 (see Figure 3.21b). At a much larger distance ($\sim$4 times as far) is another similar galaxy with reliable spectroscopic redshift 0.7% different from that of J1034[13] - these galaxies may be part of a larger cluster. Based on the large projected distances ($>$100 kpc) we consider neither to be interacting, but are associated.

Finally, J1506 has a very close companion ($\sim$23 kpc) and is showing clear signs of disturbance (see Figure 3.21d). As concluded in L2017 we will consider this galaxy to be undergoing a major merger.

Considering only the CT sources and including those from L2017 we have 7 CT AGN, 2 of which are in closely interacting pairs (separation $<$30 kpc; J1506 and J1534), giving a merger fraction of 29^{+21}_{-12}%, updated from 50 ± 33% in L2017.

[13] WISEA J103502.19+393721.6

For comparison, Kocevski et al. (2015) found that for highly obscured AGN (log $N_{\rm H}$ $>$ 23.5) the merger fraction is $21.5^{+4.2}_{-3.3}$ %[14], compared to unobscured AGN at $7.8^{+1.9}_{-1.3}$ %. Previous *NuSTAR* serendipitous 'normal' AGN (L2017) show merger fraction of 8^{+12}_{-5} %.

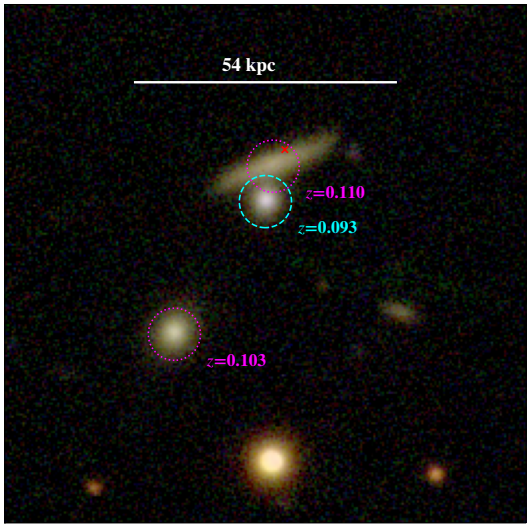

(A) J0949 PanSTARRS *irg* image, with J0949 and nearby galaxies shown with cyan/magenta circles respectively (radius 3 arcseconds).

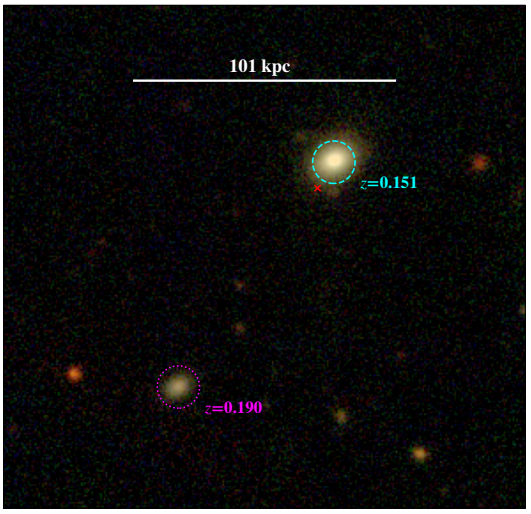

(B) J1034 PanSTARRS *irg* image, with J1034 and nearby galaxies shown with cyan/magenta circles respectively (radius 3 arcseconds).

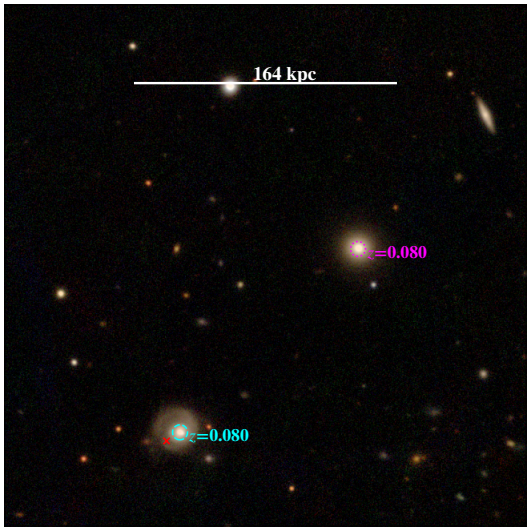

(C) J1156 PanSTARRS *irg* image, with J1156 and nearby galaxies shown with cyan/magenta circles respectively (radius 3 arcseconds).

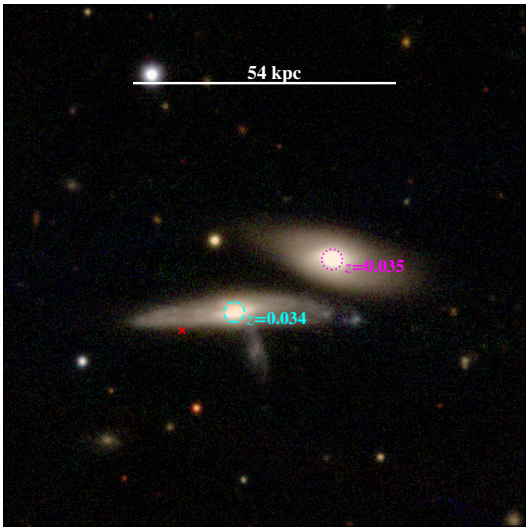

(D) J1506 PanSTARRS *irg* image, with J1506 and nearby galaxies shown with cyan/magenta circles (radius 3 arcseconds).

FIGURE 3.21: PanSTARRS *irg* images of sources from this work that have close nearby galaxies.

[14]For log $N_{\rm H}$ $>$ 23.5 in this work, statistics would include J1502 and J2143 as well - increasing the fraction from 2/7 to 3/9.

(A) Closest nearby objects to each non-Compton thick source in Appendix C.

Name	Source	z	Sep_{close} kpc	z_{close}	z_{diff}	N_{close}	Visually merging?	CT?
(1)	(2)	(3)	(4)	(5)	(6)	(7)	(8)	(9)
J0107	Sec. C.1	0.048	52.356	0.048	-1.0 %	1		
J1502	Sec. C.2	0.054	–	–	–	–		
J1606	Sec. C.3	0.122	–	–	–	–		
J2143	Sec. C.4	0.013	29.210	0.013	3.4 %	2	✓	
J2249	Sec. C.5	0.445	–	–	–	–		

(B) Compton thick sources only, from this work (Section 3.3.1) and L2017 (L17).

Name	Source	z	Sep_{close} kpc	z_{close}	z_{diff}	N_{close}	Visually merging?	CT?
(1)	(2)	(3)	(4)	(5)	(6)	(7)	(8)	(9)
J0949	Sec. 3.3.2.1	0.093	7.476	0.110	18.1 %	2		✓
J1034	Sec. 3.3.2.2	0.151	105.415	0.190	25.8 %	1		✓
J1156	Sec. 3.3.2.3	0.080	161.268	0.080	-0.6 %	1		✓
J1506	Sec. 3.3.2.4	0.034	22.922	0.035	3.0 %	1	✓	✓
J1506	L17	0.034	–	0.035	1.0%	1	✓	✓
J0505	L17	0.036	–	–	–	–		✓
J1512	L17	0.069	–	–	–	–		✓
J1534	L17	0.160	∼22	–	–	1	✓	✓

TABLE 3.3: Column details: (1) Source name; (2) Source name; (2) Source redshift; (3) Distance to closest nearby object; (4) Redshift of closest nearby object; (5) Percentage difference in redshift; (6) Number of close sources; (7) Visibly interacting galaxies; (8) Compton thick (as in Table 3.2). Note that although the redshift for the companion to J1534 is unknown, it is clear from the optical imaging that the objects are interacting.

3.5 Summary

With this chapter we see how searches over small sky areas - compared to LASr - but with instruments optimised for extreme AGN selection can significantly increase known objects, in this case Compton thick AGN. We find eight new CT AGN candidates, of which three are confirmed to be new CT AGN. Additionally we examine new data on a previously selected CT AGN from L2017 and verify that result. We find that the fraction of CT AGN among the *NuSTAR* serendipitous sources is $15.2^{+12.0}_{-6.0}$% at z <0.07; higher than many observed fractions but lower than predicted by the cosmic X-ray background (Ananna et al., 2019). The fraction of *NuSTAR* serendipitous CT AGN in observable major mergers is $28.5^{+21.4}_{-12.3}$%; uncertain due to low total number counts, it is in line with some other estimates for heavily obscured AGN (e.g., Kocevski et al., 2015). Figure 3.22 updates Figure 3.1 with the z and $N_{\rm H}$ values of the CT AGN analysed in this chapter. These results cover a large area of the region our approach was targeted at - high $N_{\rm H}$ objects at a range of redshifts - mainly beyond the range of LASr[15].

Having selected AGN in this chapter with hard X-rays - known to be a very reliable indicator of AGN presence - over relatively small areas of the sky, we next return to wide area surveys. Known AGN in LASr are largely optically or hard X-ray (*Swift*-BAT) selected. Thus we address the remaining gap: AGN that are not X-ray bright enough to appear in the *Swift*-BAT catalogues, do not show typical optical AGN signatures, but appear convincingly AGN-like in the MIR. This set of criteria directs the search towards *unusually* obscured or structured AGN - no optical signatures means either that the large narrow line emission region is obscured or not producing lines.

[15]J2143, the only source from the chapter within the redshift limit of LASr, does appear in the LASr-GPS but is not a known AGN and its *WISE* *W*1-*W*2 colour is too low to be selected as an AGN candidate; see Section C.4

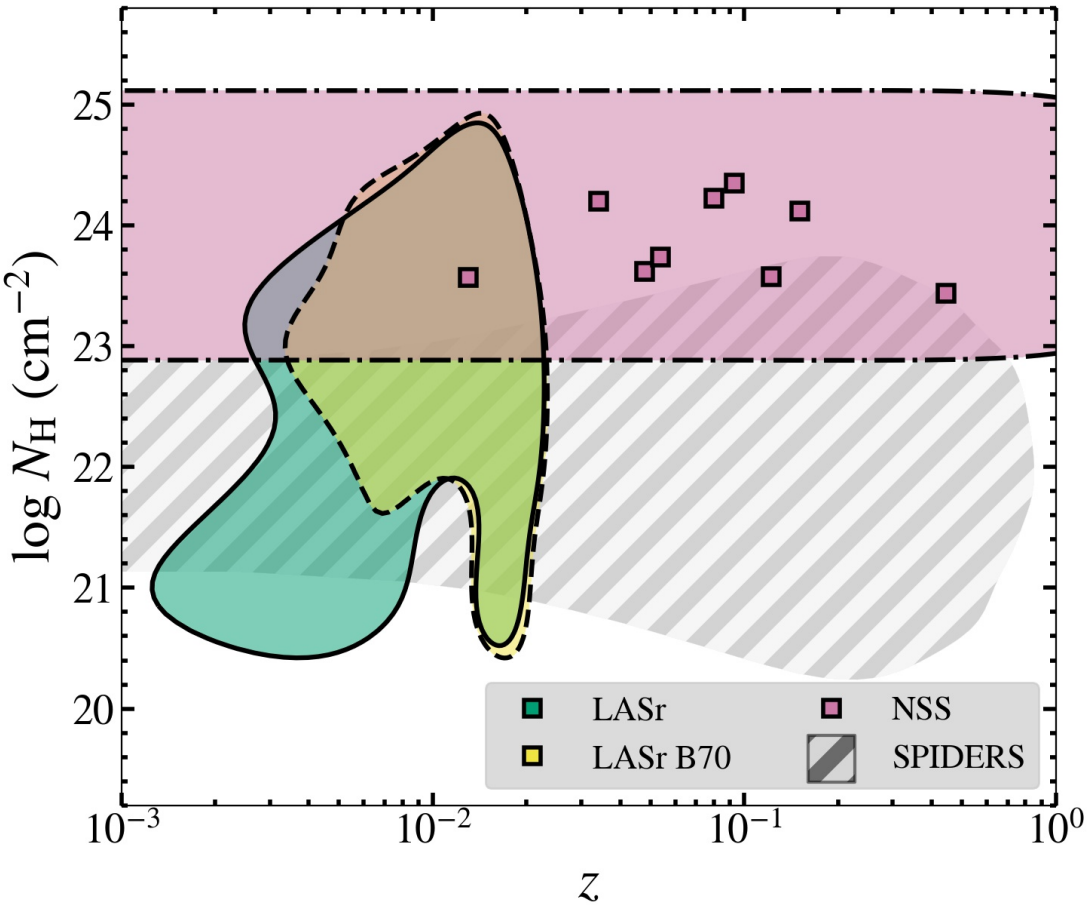

FIGURE 3.22: Parameter space covered by the known AGN in the LASr-GPS (green shaded region, solid edge), by the B70 AGN (yellow shaded region, dashed edge), the region targeted by this chapter (pink shaded area, dot-dash edge), and the sources discovered in NSS80 (pink squares).

Chapter 4

A Jewel in the Dust: Insights from a detailed study of a strong MIR AGN with an optically inactive spectrum

In Chapter 2 we constructed a near-complete sample of local galaxies (∼90% complete for galaxies with L($W1$)>10^{42} erg s^{-1}). From this we flagged the known AGN, and selected AGN candidates based on their MIR colour and luminosity. We then began the process of examining these candidates in detail with spectroscopic follow-ups. One of the primary theoretical causes for AGN to lie undiscovered in local galaxies is the high proportion of AGN that are likely to be obscured. Chapter 3 sees us investigate sources that may be *heavily* obscured, with high column densities into the Compton thick regime (log $N_{\rm H}$>24 cm^{-2}). In this chapter, we consider whether obscuration of a different form can similarly hide AGN from sight. Specifically, high covering factors - the fraction of solid angle around the central AGN that has enough material to obscure it from sight. Much of AGN growth is thought to occur in obscured phases, and a short-lived phase of high obscuration could be a critical part of some paths of AGN evolution.

Many of the R90 selected candidate AGN are likely to be obscured in some way - due to a combination of the MIR selection criteria and the fact that they are not previously known AGN. We know from the construction of the catalogue that many of the *known* AGN are optically selected, but what about AGN that are lacking optical signatures? These would be promising candidates for 'cocooned' AGN - the MIR signatures are expected to remain strong, with emission reprocessed in the dust, but optical signatures would be heavily reduced. We call these objects 'Optically Quiescent Quasars' and in the following chapters will discuss their selection, properties, and where such objects might fit with other AGN classes. Figure 4.1 shows where the region of interest for this chapter lies on the z-$N_{\rm H}$ diagram. OQQs are likely to be obscured, but the selection

process makes no assumptions about the depth of the obscuration - thus we extend the expected N_H across the typical range for obscured AGN. We expect low number counts for these AGN as they are by definition difficult to find, and the most likely intrinsic structures for them are likely to be a short transient phase in the life cycle of an AGN (see Chapter 5). In order to increase the chances of selecting promising OQQs and drawing conclusions about their nature, we must extend the redshift criteria for selection beyond that of LASr.

This chapter will describe the selection and analysis of a prototypical OQQ, based on my published papers Greenwell et al. (2021, 2022). I start with defining the ideal appearance for this object, then the selection process, and finally describe the properties of the chosen object (J0751) in detail, comparing it to its closest QSO2. We will discover what we can learn from focusing on a specific example of a previously unknown AGN.

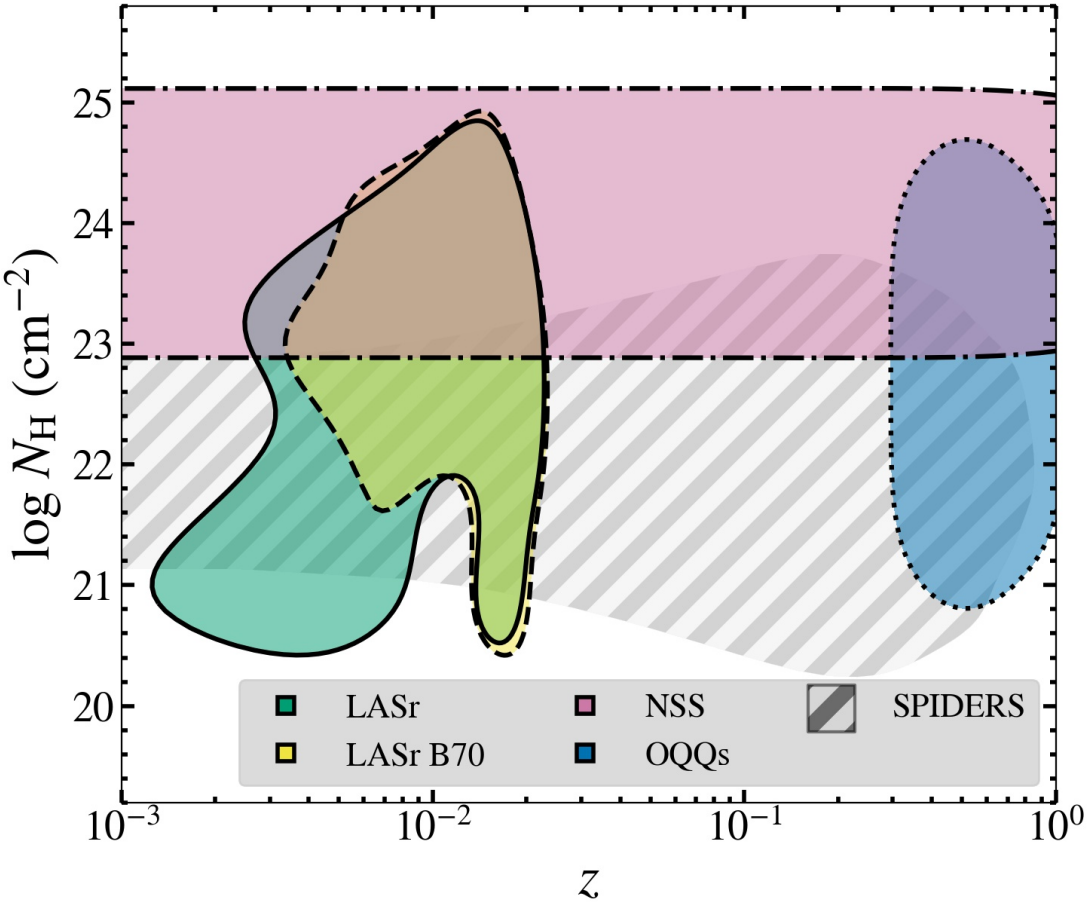

FIGURE 4.1: Parameter space covered by the known AGN in the LASr-GPS (green shaded region, solid edge), by the B70 AGN (yellow shaded region, dashed edge), the region targeted by *NuSTAR* serendipitous selection (pink shaded area, dot-dash edge), and the region targeted by this chapter (blue shaded area, dotted edge).

4.1 Selection of a Prototypical Object

4.1.1 What we are looking for in an ideal OQQ

With the ansatz of a cocooned AGN (an AGN enshrouded in obscuring matter; CAGN) in mind as a guide, we assume that typical optical and ultraviolet emission signatures will be reddened and scattered. Optical spectroscopy would therefore indicate these objects to be similar to 'normal' galaxies. In order to efficiently block all lines-of-sight with the least mass of obscuring material, the size of any such cocoon must be small, plausibly similar to the canonical pc-scale torus. Many studies have indicated that reprocessed emission from these tori appears to be effectively optically-thin in the mid-infrared (MIR). Several physical models have been proposed to explain this, but the salient detail of relevance here is that the MIR is largely isotropic, irrespective of obscuring geometry (e.g., Gandhi et al., 2009, and references therein). If the same holds for CAGN, then MIR selection of OQQ is a promising route to uncovering them. However, during this analysis we must also bear in mind that lack of narrow emission does not necessarily mean that they are present and extinguished, as in a CAGN. There are three main possibilities we will consider:

1. Cocooned AGN - obscuring matter on scales large enough to hide ionised emission in the narrow line region exists with enough optical depth to hide optical AGN signatures.
2. Young AGN - a recently active AGN, where radiation from the centre of the system has not yet reached and ionised the larger scale gas and no narrow emission lines are produced.
3. Intrinsically weak line AGN - high Eddington ratio sources can be connected with low narrow emission line luminosities (Eigenvector 1; Boroson and Green, 1992).

4.1.2 Selecting a target

I used infrared data from the *Wide-Field Infrared Survey Explorer* (*WISE*, Wright et al. 2010), which carried out an all-sky survey in four bands, centred on wavelengths of 3.4, 4.6, 12, and 22 μm. Redshifts and optical classifications were obtained from the fifteenth data release of the Sloan Digital Sky Survey (SDSS DR15, Aguado et al. 2019). Targets with good quality spectra, not classified by SDSS as stars or quasars, and within a redshift range that would put the [O III] emission line within the spectrum ($z < 1.08$; observed wavelengths $\sim$ 5007Å to 10400Å) were cross-matched with objects from the *AllWISE* catalogue (Wright et al., 2010). The resulting candidates included a large number of spectra that were optically classified as normal galaxies. MIR classification as

AGN was carried out by using well-tested colour thresholds. Specifically, I chose to use the colour threshold $W1 - W2 \geq 0.8$, shown by Stern et al. (2012) to be an efficient selector of luminous AGN. To ensure that the AGN dominates above stellar emission and star formation, I required a rest frame k-corrected monochromatic 12 µm luminosity of $L_{12} \geq 3 \times 10^{44}\,\mathrm{erg\,s^{-1}}$. This is typical of quasars with $L_{\mathrm{Bol}} \approx 10^{45}\,\mathrm{erg\,s^{-1}}$, and distinguishes our study from searches for so-called X-ray bright optically normal galaxies (XBONGs), which appear well explained by host galaxy dilution of less luminous AGN (e.g., Moran et al., 2002). Despite careful choices of colour and luminosity threshold, the possibility remains that non-AGN will be selected, which is further discussed in Section 5.2.1. A key aim of Section 4.3 is confirmation of AGN presence in the prototype source.

The final requirement was the lack of any significant [O III] emission in the SDSS spectra. I assessed the presence – or lack of – [O III] with MCMC simulations (described in detail in Section 5.3.1), and Figure 4.2 shows the upper limit on [O III] emission from J0751, compared to the measured emission from QSO2s (see Section 4.1.3). In this chapter, I present a first candidate, representative of our desired properties in terms of its high bolometric luminosity, reliability of redshift and optical spectral type, as well as a deep limit on the (expected) optical emission line flux.

4.1.3 Comparison Population

As a better understood 'control' group with similar (but complementary) selection in terms of key parameters we choose to use the population of Type 2 quasars (QSO2s), as selected by Reyes et al. (2008) and Yuan et al. (2016). These objects are bright obscured (classical) AGN, similar in redshift and broad-band luminosity range to our OQQ. The key exception is the presence, by design, of strong emission lines, particularly [O III], in QSO2s. This selection is described in more detail in Section 5.5.

4.2 The Model OQQ: J0751

The prototype OQQ candidate chosen is SDSS J075139.06+402810.9 (hereafter J0751). We also choose a QSO2 close in redshift and luminosity to use as a direct comparison – SDSS J125612.97+144121.0. Ideally we would also match the SFR of the two objects in order to minimise host galaxy dilution – however due to the uncertainty in assessing the SFR of J0751 (see Section 4.2.2), at this stage we focused only on matching the most important properties. Spectra of these two objects are presented in Figure 4.3, showing the stark difference in [O III] strength between the two object types. Note also the similarity in continuum shape, with the main difference being emission line strength in the QSO2. Table 4.1 presents basic information about the two objects.

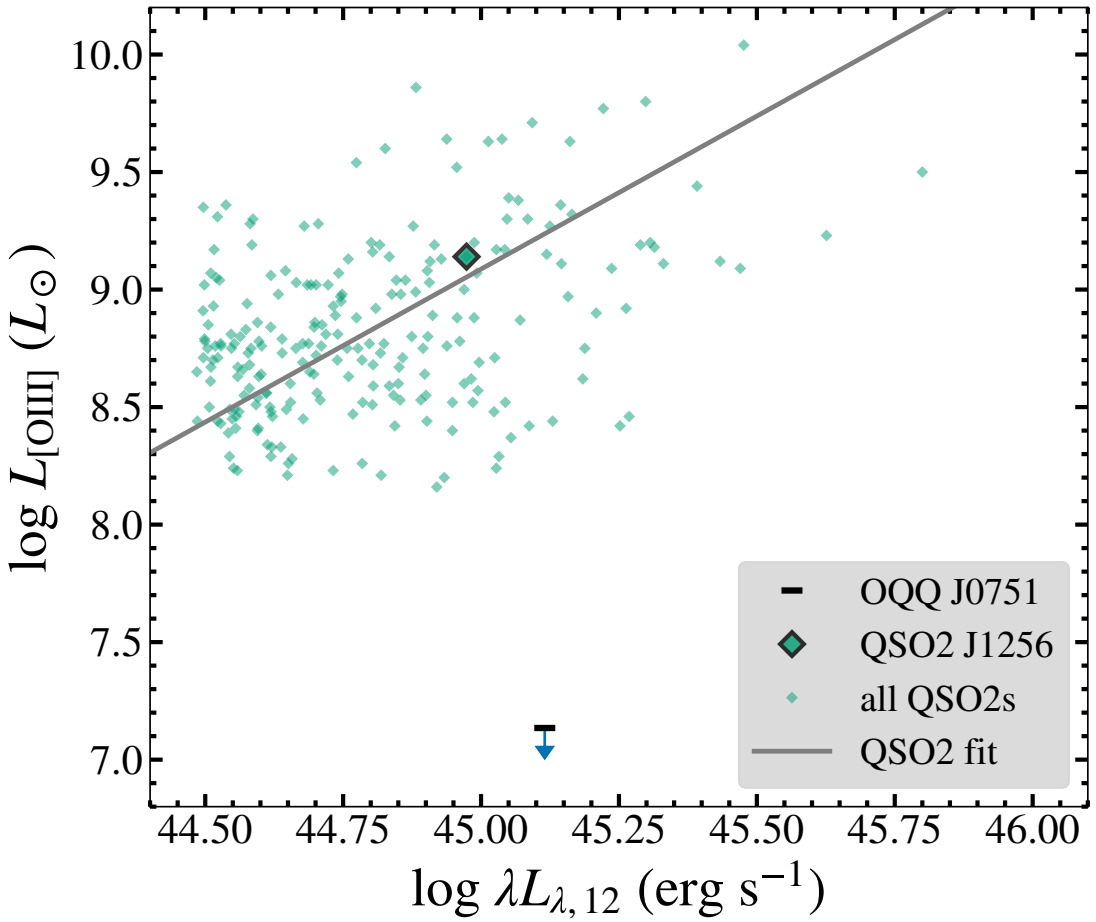

FIGURE 4.2: Upper limit of [O III] luminosity of OQQ (black dash, blue arrow) compared to the measured [O III] fluxes of QSO2s.

TABLE 4.1: Basic information about the primary OQQ candidate and the QSO2 closest in redshift and 12 µm luminosity. Column details: (1) object type, (2) object name as known in NED, (3) redshift, (4) rest frame 12 µm luminosity.

Type (1)	NED name (2)	z (3)	$\log L_{12}/\mathrm{erg\,s^{-1}}$ (4)
OQQ	SDSS J075139.06+402810.9	0.587	45.12 ± 0.05
QSO2	SDSS J125612.97+144121.0	0.580	45.04 ± 0.05

4.2.1 MIR Colour and Luminosity

The most convincing evidence for the presence of an AGN lies in the MIR. A k-corrected 12 µm luminosity of $\sim 10^{45}$ erg s^{-1} (estimated by linear interpolation between *WISE W3* and *W4* measurements) implies a very low chance that this object lacks an AGN. SED fitting (see Section 4.2.2 and Figure 4.5) shows that a significant contribution from AGN-heated dust is required to reproduce the observed MIR data. The MIR colour selection criterion has a predicted reliability of 95% (Stern et al., 2012), depending on the reliability of the source data for this. Figure 4.4 shows the position of J0751 on the *WISE* colour selection diagram; it is decisively AGN coloured, well above the Stern

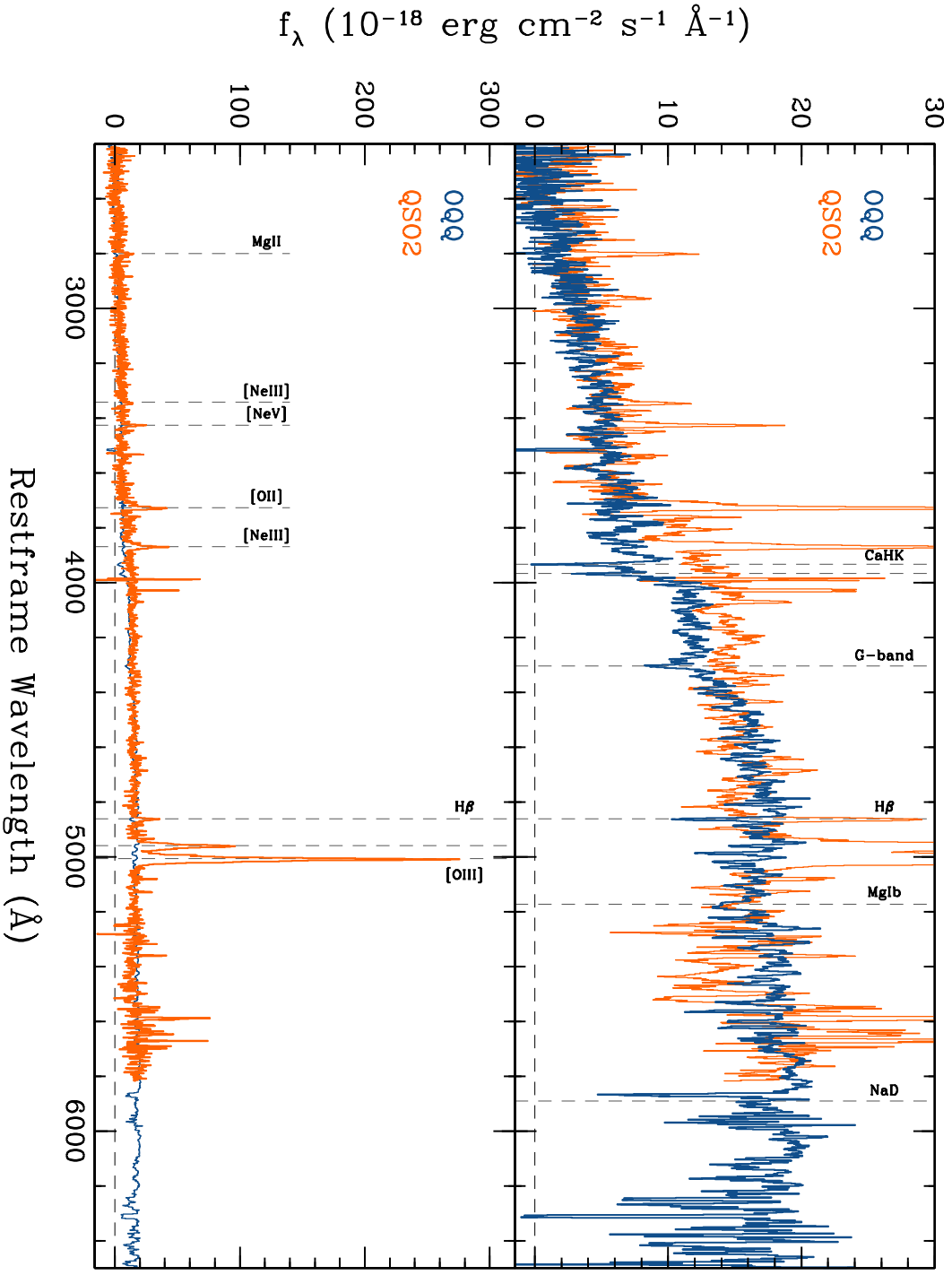

FIGURE 4.3: Spectra, obtained by SDSS, of the primary QQQ candidate, J0751, compared to the QSO2 J1256. The top panel is scaled to show the QQQ (blue), which is a typical early-type galaxy with stellar absorption features and a strong D4000 break. Note that the QSO2 (orange) shows a similar continuum shape, with stronger continuum redwards of [O II]. The bottom panel is scaled to show the QSO2, which has multiple strong, narrow emission lines. [Plot credit: D. Stern].

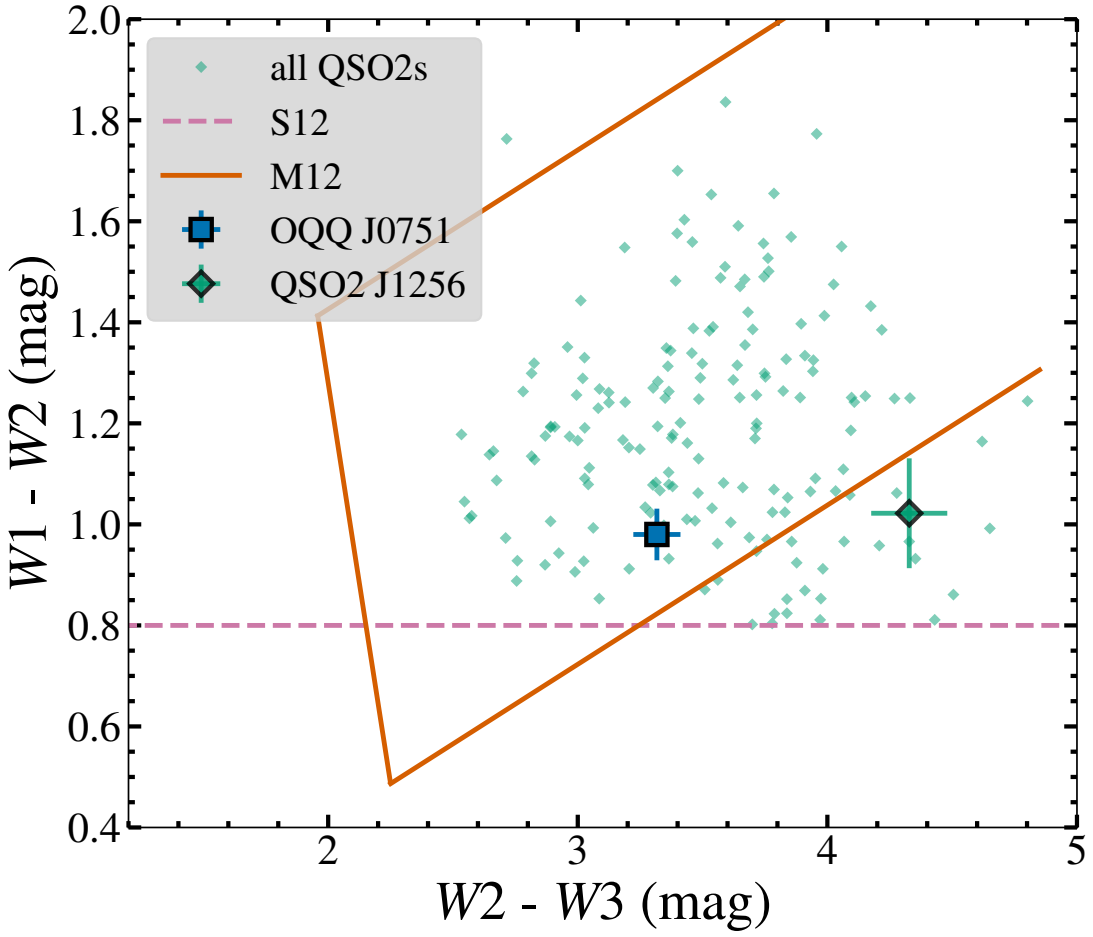

FIGURE 4.4: The *WISE* colours of the prototype OQQ plotted on the MIR colour-colour plane. The dotted line shows the Stern cut (Stern et al., 2012); which all candidates pass by selection. The solid orange lines show the AGN wedge proposed by Mateos et al. (2012). Shown for comparison are QSO2s.

et al. (2012) threshold (by selection) and additionally within the Mateos et al. (2012) wedge. There is a small chance that similar colour and luminosity may be caused by star formation. If this were the case we would expect to see bright emission lines typically associated with star formation, such as [O II], as the distribution of star formation throughout the galaxy (rather than localised at the nucleus) means that they are unlikely to be blocked by the same obscuring matter. Conversely, if the star formation is localised at the nucleus we may not expect to detect strong [O II] emission, but the SED fitting (see Section 4.2.2) should provide a better estimate of SFR. We also see very little radio emission (an upper limit on radio flux is available from FIRST (Becker et al., 1995): $<$0.695 mJy/beam).

4.2.2 Spectral Energy Distribution (SED)

We use `agnfitter` (Calistro Rivera et al., 2016) to fit the SED of J0751 and determine the relative galaxy and AGN system contributions to the observed emission. This method uses the multiwavelength data available to find the most likely weighted contributions to the overall SED, from sources near the AGN and in the host galaxy. Lack of IR data at wavelengths redward of *WISE* produces some uncertainty on these results, but we can use them to constrain further some properties of the target. The most important parameter for our analysis is the contribution to the SED from the AGN obscuring material in the MIR – a significant amount of emission is needed from this component in order to reproduce the total. After experimenting with different Markov Chain Monte Carlo (MCMC) chain lengths, we selected one sufficient to achieve an auto-correlation time indicating convergence for the OQQ AGN-heated dust component (see Foreman-Mackey et al. (2013) & Calistro Rivera et al. (2016) for details). More detail can be found in Section 5.10.1.

`agnfitter` makes two separate estimates of SFR – one in the optical, and one in the FIR. The FIR SFR would provide some estimate of potential obscured star formation, but due to the lack of FIR data available for our fits, we discard this version and focus only on the optical. This estimate (and that of stellar mass) is obtained from host galaxy template parameters (for more detail, see Calistro Rivera et al. 2016). As shown in Table 4.2 the SFR obtained for J0751 is low and very poorly constrained, essentially an upper limit only, and is significantly higher for J1256. The uncertainty on the optical SFR is higher than for other `agnfitter` derived properties (excluding the FIR SFR) – e.g., 6–8% for J1256. Further extended photometry, particularly at long IR wavelengths, would help constrain the SF in both sources and thus allow accurate assessment of the contribution of SF to the MIR luminosity. With current data, there are no significant signs of star formation in J0751: the best fit 12 µm luminosity is $\sim$10 times higher for the hot dust component than the SF component. However, it cannot be completely ruled out.

It is possible that the star formation may be located very close to the nucleus, and as such may have [O II] obscured. If this were the case, a large SFR would still be necessary to explain the *WISE* data without a significant AGN dust component.

4.3 Targeted Measurement: what can we learn?

4.3.1 Data

In order to (a) confirm the presence of an AGN, and (b) constrain its spectral properties, the optimal tracer is X-ray emission. Luminous, nuclear X-ray radiation is unlikely to

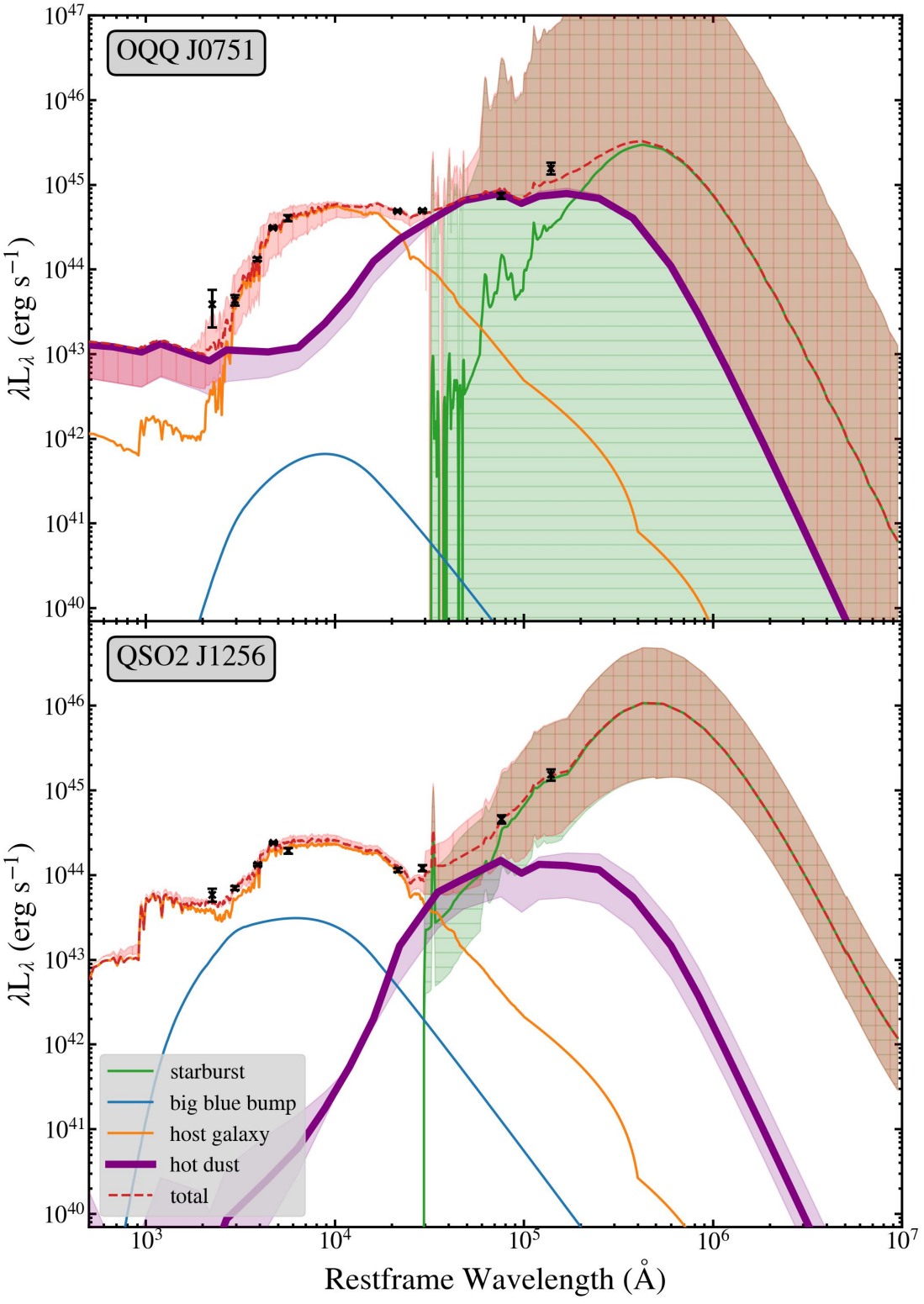

FIGURE 4.5: `agnfitter` results. Known data is shown as black crosses, and the lines show contributions from starburst (green), host galaxy (yellow), hot dust emission (purple), and big blue bump (blue; originates from the accretion disc). AGN-heated dust emission is highlighted in dark purple. The 1 sigma uncertainty range is also shown for the hot dust (plain purple shaded area), star-formation (green shaded area, horizontal hatching) and total (red shaded area, vertical hatching) only. Blue emission directly from the accretion disc is much more prominent for J1256 than for J0751, whereas the hot dust emission from J0751 is required to be higher.

TABLE 4.2: Stellar mass and star formation rates of J0751 and J1256. Column details: (2) SFR derived from [O II] luminosity (Kennicutt, 1998), (3), (4) SFR and stellar mass according to `agnfitter` (see Section 4.2.2).

Object (1)	[OII] based SFR $M_\odot$ per year (2)	`agnfitter` SFR $M_\odot$ per year (3)	stellar mass log $M_\odot$ (4)
J0751	$<0.40\pm0.11$	$0.001^{+0.216}_{-0.001}$	$11.15^{+0.11}_{-0.04}$
J1256	5.11 ± 1.46	$1.69^{+0.11}_{-0.14}$	$10.74^{+0.03}_{-0.04}$

originate from any source other than an AGN – intense star formation may produce (weaker) X-rays, but given the optically quiescent nature of OQQs (<0.4 $M_\odot$ per year, stellar mass $\sim 10^{11} M_\odot$; Greenwell et al., 2021), sufficient star formation processes are not likely. *XMM-Newton* provides good angular resolution and sensitivity, ideal to examine the soft X-rays. *NuSTAR* (Harrison et al., 2013) looks at the harder X-rays, allowing us to measure the intrinsic X-ray luminosity if SDSS J075139.06+402811.2 (hereafter OQQ J0751+4028) proves to be heavily obscured. Based on the IR–X-ray relationship (Asmus et al., 2015, Stern, 2015) we predict that OQQ J0751+4028 should be easily detected (under the assumption that it is indeed an AGN, and not heavily Compton-thick, at z=0.587, $L^{\rm predicted}_{2-10\,\rm keV} \sim 2.6 \times 10^{44}$ erg s^{-1}), and analysis of its properties should be possible.

This analysis here uses the following coordinated observations:

- *NuSTAR* OBSID 60701009002: 50.6 ks, 2021 September 25 (start time: 12:06:09)
- *XMM-Newton* OBSID 0884080101: 36.9 ks[1] of exposure, 2021 September 25 (start time: 13:28:37)

The data were reduced using standard recommended selection criteria, including removal of appropriate background, using the *XMM-Newton* Science Analysis Software[2] and HEASoft[3]. The target was detected significantly with *XMM-Newton* pn, MOS1 and MOS2[4], and with *NuSTAR* FPMA[5]. Source extraction regions were circles with radii 45 and 20 arcsec for *NuSTAR* and *XMM-Newton* respectively (see Figure 4.6). Background regions were annuli with inner radius 100 arcsec, outer radius 180 arcsec (partially cutout to avoid a chip edge) and circles of radius 90 arcsec for *NuSTAR* and *XMM-Newton* respectively. In optical data (PanSTARRS) it appears small and red, with no visible morphological disturbances (see Figure 4.7).

[1] After cleaning 16.4/28.3/29.3 ks on pn/MOS1/MOS2.
[2] http://xmm.esa.int/sas/
[3] https://heasarc.gsfc.nasa.gov/docs/nustar/analysis/
[4] 0.5-10 keV; net counts 87/36/65
[5] 3-16 keV; net counts 55. Not detected in FPMB alone, due to higher background flux.

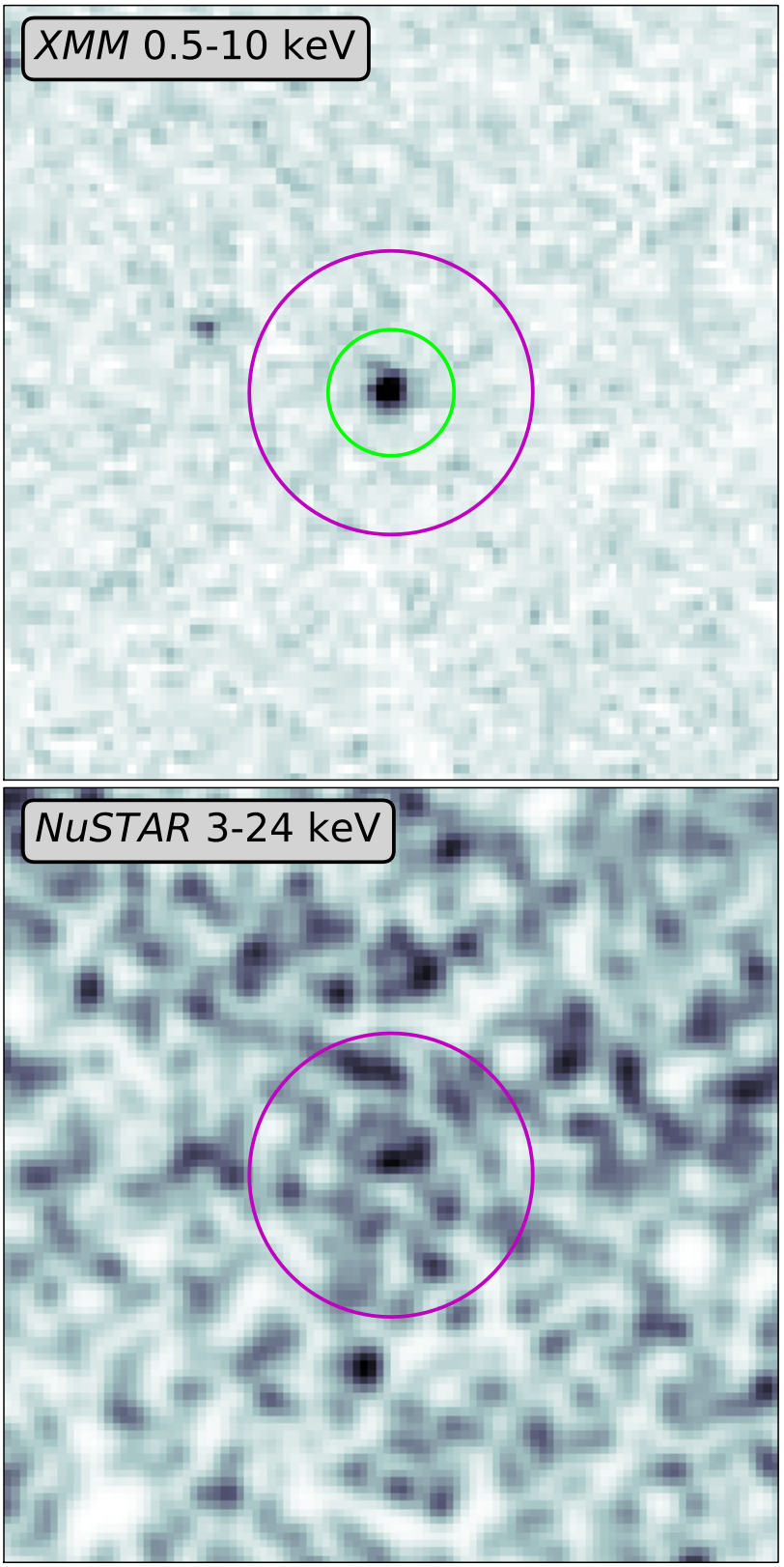

FIGURE 4.6: (top) *XMM-Newton* stacked image; (bottom) *NuSTAR* FPMA 3–24 keV image. Green circle has 20 arcsec radius, magenta circles have 45 arcsec radius; all are centred on the optical source coordinates.

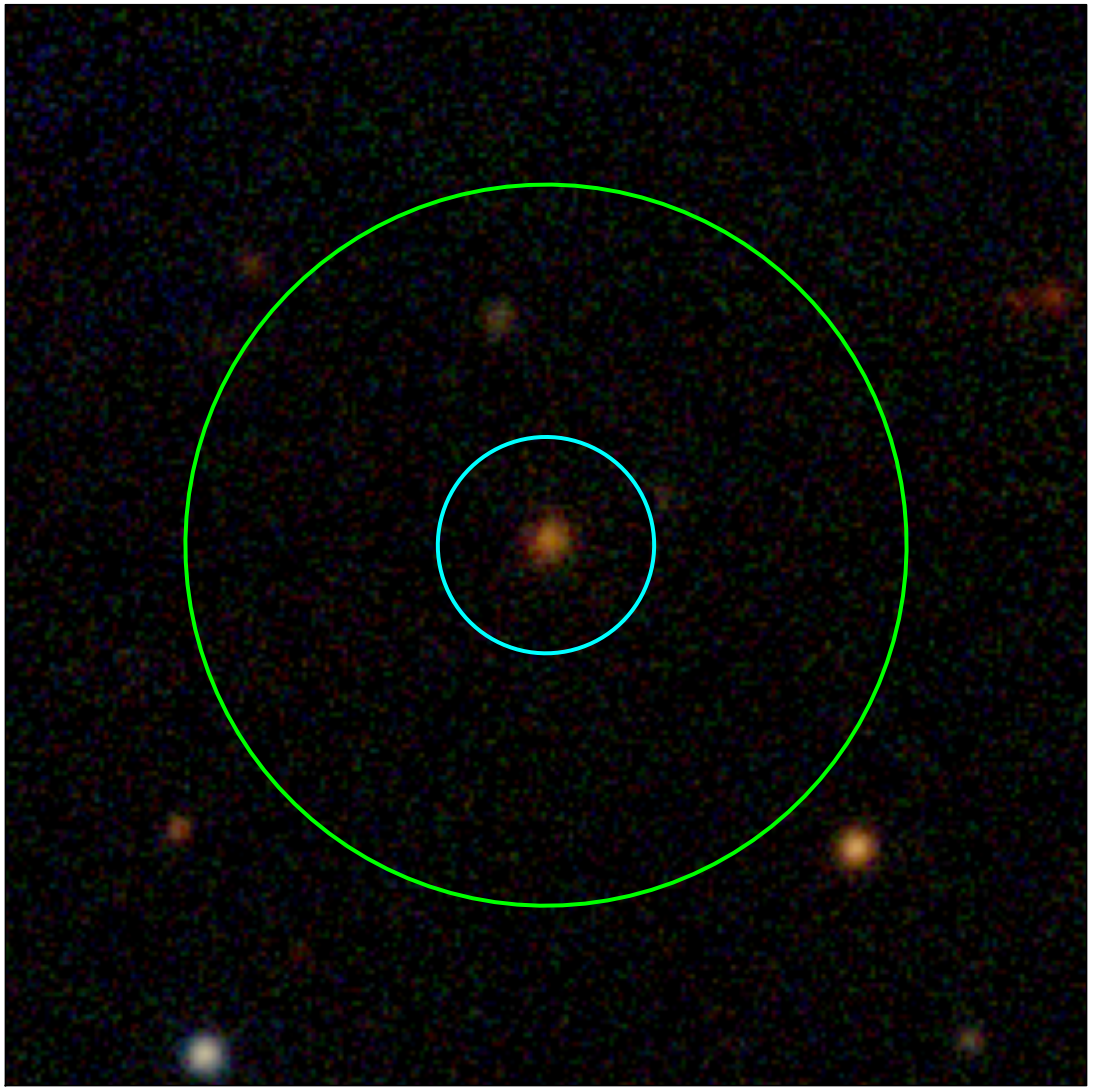

FIGURE 4.7: PanSTARRS *irg* bands converted to RGB image. Green circle has 20 arcsec radius, cyan circle has 6 arcsec radius; both are centred on the optical source coordinates.

4.3.2 Methods

The data were fit within `xspec` (Arnaud, 1996), v.12.12.0 with several models covering various types and structures of obscuration, with different levels of complexity. Relevant parameters were allowed to vary freely (although tied between datasets): normalisation, Γ and $N_{\rm H}$. All models include Galactic absorption (PHABS) of $N_{\rm H}$=5.6 $\times$ 10^{20} cm^{-2} (HI4PI Collaboration et al., 2016). A cross calibration constant of 0.93:1.02:0.98:1.00 (e.g., Madsen et al., 2015) was used for *XMM-Newton*(pn):*XMM-Newton*(MOS1):*XMM-Newton*(MOS2):*NuSTAR*; this was fixed because the observations were simultaneous. Spectra were binned to 3/1 counts per bin for *NuSTAR*/*XMM-Newton*, and fit with `wstat` (Wachter et al., 1979) – the version of `cstat` (Cash, 1979) used by `xspec` when a

background is included[6].

Under the assumption that OQQ J0751+4028 is an obscured AGN, the most basic combination of models we might expect to make a reasonable fit to the data is an absorbed powerlaw (photoelectric absorption at the source redshift and Compton scattering attenuating an intrinsic powerlaw; see top panel in Figure 4.8). This model can produce an acceptable fit to the data, with light absorption (see Table 4.3). However, the best fit Γ=1.08$\pm$0.16 is unusually hard for an AGN compared to typical intrinsic spectral indices of $\Gamma \sim$1.9 (Ricci et al., 2017a). There is some degeneracy between $N_{\rm H}$ and Γ values (see Figure 4.9), so in order to investigate the likelihood of a more typical intrinsic AGN power law, we fit the same model, but with a fixed Γ=1.9. This also produces an acceptable fit, with a slight increase in $\log(N_{\rm H}; {\rm cm}^{-2})$=21.56 to 22.30 (see Table 4.3).

Given the consistently hard Γ seen in the absorbed powerlaw model we next investigate two more physically realistic models, still relatively simple: torus reprocessing (MYTORUS in coupled mode with covering factor fixed at 0.5; Murphy and Yaqoob, 2009); and the spherical obscuration (TRANS model from BNTORUS; Brightman and Nandra, 2011, hereafter BNSPHERE).

BNSPHERE represents the physically expected obscuring structure around a 'Cocooned' AGN. MYTORUS does not specifically allow full covering, and is restricted to $\Gamma \geq$1.4, higher than previously found Γ values. BNSPHERE is also limited, but to $\Gamma \geq 1.0$. Other parameters are fixed to simplify the modelling. MYTORUS inclination was set to 90 deg (i.e., through the torus, to fit with our assumption of an obscured AGN). BNSPHERE iron and total elemental abundances were set to solar values.

The results for the models thus far consistently produce a hard photon index Γ ($\leq$ 1.5). This would be an unusual intrinsic value for an AGN, and could indicate that we are underestimating the optical depth of obscuration present in the system, a possibility also hinted at by the lower than expected luminosity. None of the models above can produce a $\log(N_{\rm H})$ greater than $\sim$22.3, thus we propose an alternative: a thick spherical obscurer (represented in XSPEC with BNSPHERE) in tandem with a scattered fraction (CONSTANT) of the intrinsic powerlaw (ZCUTOFFPL). The scattered fraction represents a 'leak' through Compton thin obscuration from an otherwise Compton thick sphere. With this we can investigate higher $N_{\rm H}$ values while still providing a satisfactory fit to the softer X-rays, i.e., dominated by the scattered powerlaw rather than a Compton hump. Here we show the results with scattering fraction fixed at 12%, which produces an intrinsic X-ray luminosity close to that predicted from the 12 µm luminosity.

Fixing the value of Γ makes a firm assumption about the nature of the intrinsic AGN emission, which we can make less stringent with Bayesian X-ray Analysis (BXA; Buchner et al., 2014). We can include knowledge about the likely physical characteristics

[6] https://heasarc.gsfc.nasa.gov/xanadu/xspec/manual/node318.html#AppendixStatistics

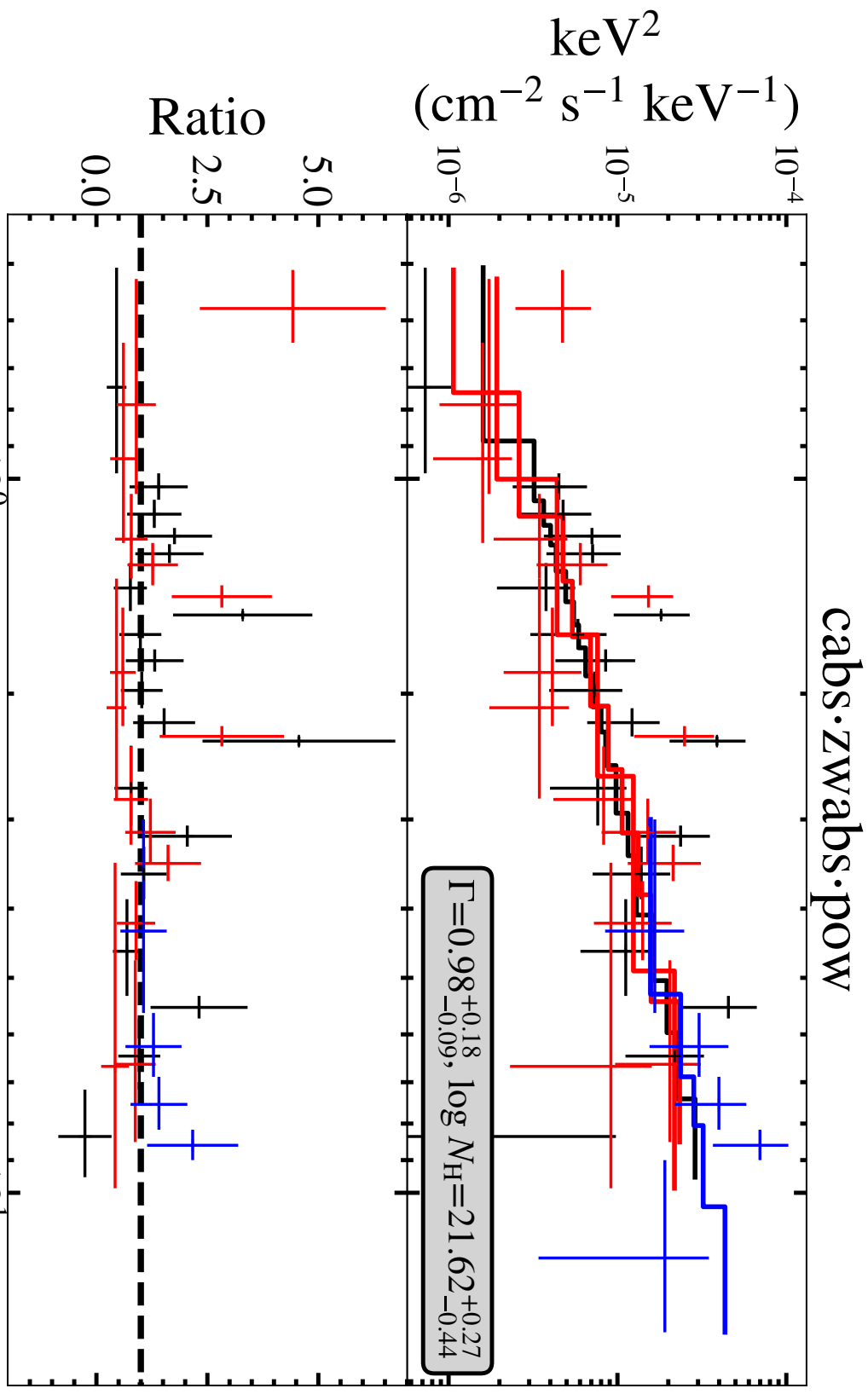

FIGURE 4.8: (top) Spectrum of best fit absorbed powerlaw model; (bottom) ratio between data and model. Shown is *XMM-Newton*-pn (black), *XMM-Newton*-MOS (red) and *NuSTAR* FPMA (blue), binned to a minimum of 2 counts per bin.

TABLE 4.3: Spectral modelling results. Column details: (1) XSPEC model; (2) Γ prior; (3) Γ; (4) $N_{\rm H}$; (5) 'sphere' $N_{\rm H}$; (6) unabsorbed 2-10 keV luminosity; (7) fit statistic; (8) Bayes factor compared to BNSPHERE.

Model	Γ prior	Γ	log N_H 10^{22} cm^{-2}	log $N_{\rm H,sphere}$ 10^{22} cm^{-2}	log $L_{2-10\,\rm keV}$ erg s^{-1}	cstat/d.o.f.	Bayes factor (normalised)
(1)	(2)	(3)	(4)	(5)	(6)	(7)	(8)
CABS*ZWABS*POW	Uniform	$0.98^{+0.18}_{-0.09}$	$21.62^{+0.27}_{-0.44}$		43.64±0.04	334.1/377	–
CABS*ZWABS*POW	Fixed 1.9	1.90	$22.30^{+0.08}_{-0.11}$		43.68±0.05	346.2/378	31.6
CABS*ZWABS*POW	1.9±0.1	$1.79^{+0.09}_{-0.10}$	$22.26^{+0.08}_{-0.13}$		43.67±0.05	337.7/377	12.6
CABS*ZWABS*POW	2.0±0.3	$1.26^{+0.25}_{-0.16}$	$22.03^{+0.15}_{-0.41}$		43.64±0.05	334.1/377	1.6
MYTORUS	2.0±0.3	$1.47^{+0.17}_{-0.08}$	$22.05^{+0.12}_{-0.00}$		43.65±0.04	336.6/377	2.0
BNSPHERE	2.0±0.3	$1.32^{+0.21}_{-0.19}$	$21.95^{+0.15}_{-0.36}$		43.64±0.05	334.1/377	best (≡1.0)
'leaky sphere', 12%	2.0±0.3	$2.19^{+0.18}_{-0.22}$	$22.26^{+0.10}_{-0.17}$	$24.08^{+0.14}_{-0.14}$	44.45±0.09	341.9/376	6.3

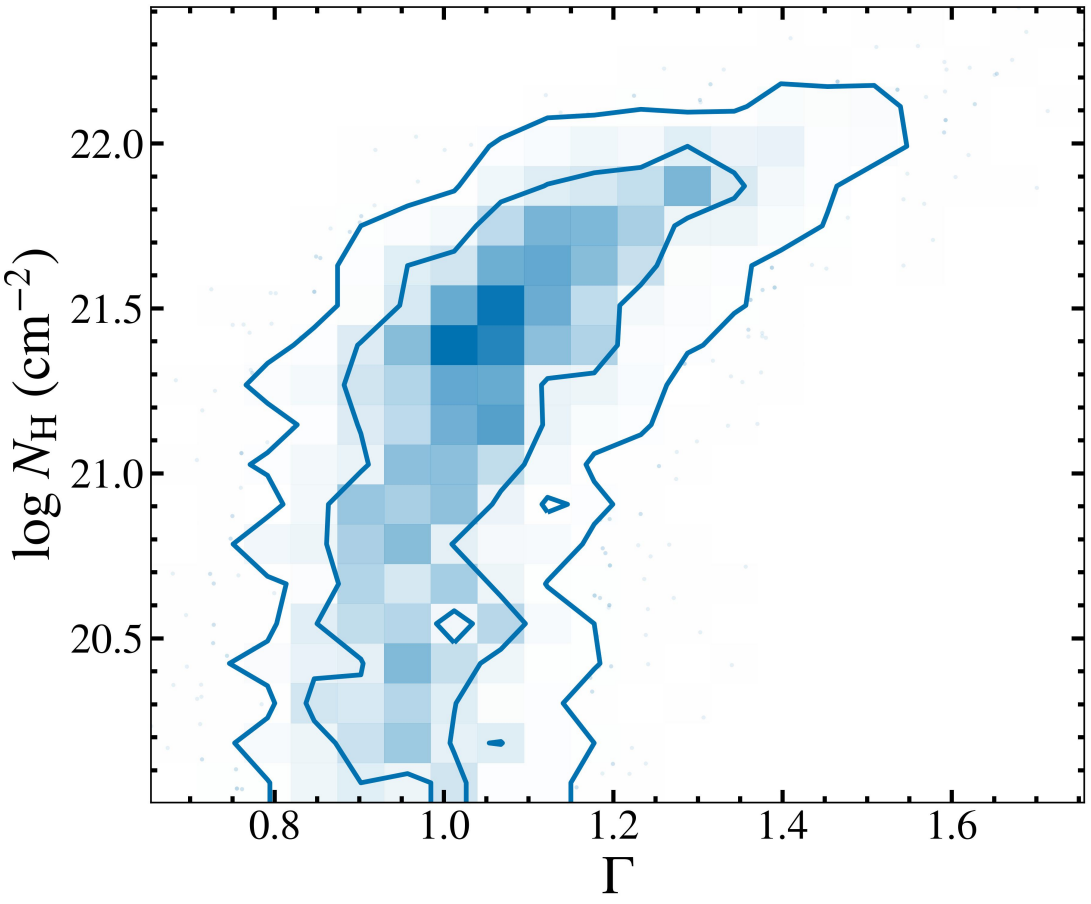

FIGURE 4.9: Relationship between Γ and N_H results for the absorbed powerlaw.

by selecting an appropriate prior: a Gaussian prior for Γ[7] is appropriate as it allows a physically motivated preference towards likely values, and excludes unphysical values. We try (a) a loose Gaussian prior: Γ=2.0±0.3; and (b) a stricter Gaussian prior Γ=1.9±0.1, along with the original uniform likelihood assumption, and fixed Γ=1.9 (see Figure 4.10). As shown in Table 4.3, both Gaussian priors produce an acceptable fit to the data but struggle to produce a Γ value not unusually hard for an AGN. We can use the Bayesian evidence to compare the models, and therefore determine which is most likely to have produced the observed data. Figure 4.11 demonstrates the change as different models are introduced. The top subplot shows the hard values resulting from the absorbed powerlaw - even when Γ is coerced with a restrictive prior, a lower median value is favoured. In the middle MYTORUS and BNSPHERE are added, and despite their restrictions still result in low median values. In the final subplot the 'leaky sphere' model is highlighted, showing that with an identical prior to the previous models, it attains a higher, more physically likely, value for Γ.

[7] N_H and normalisation have log uniform priors.

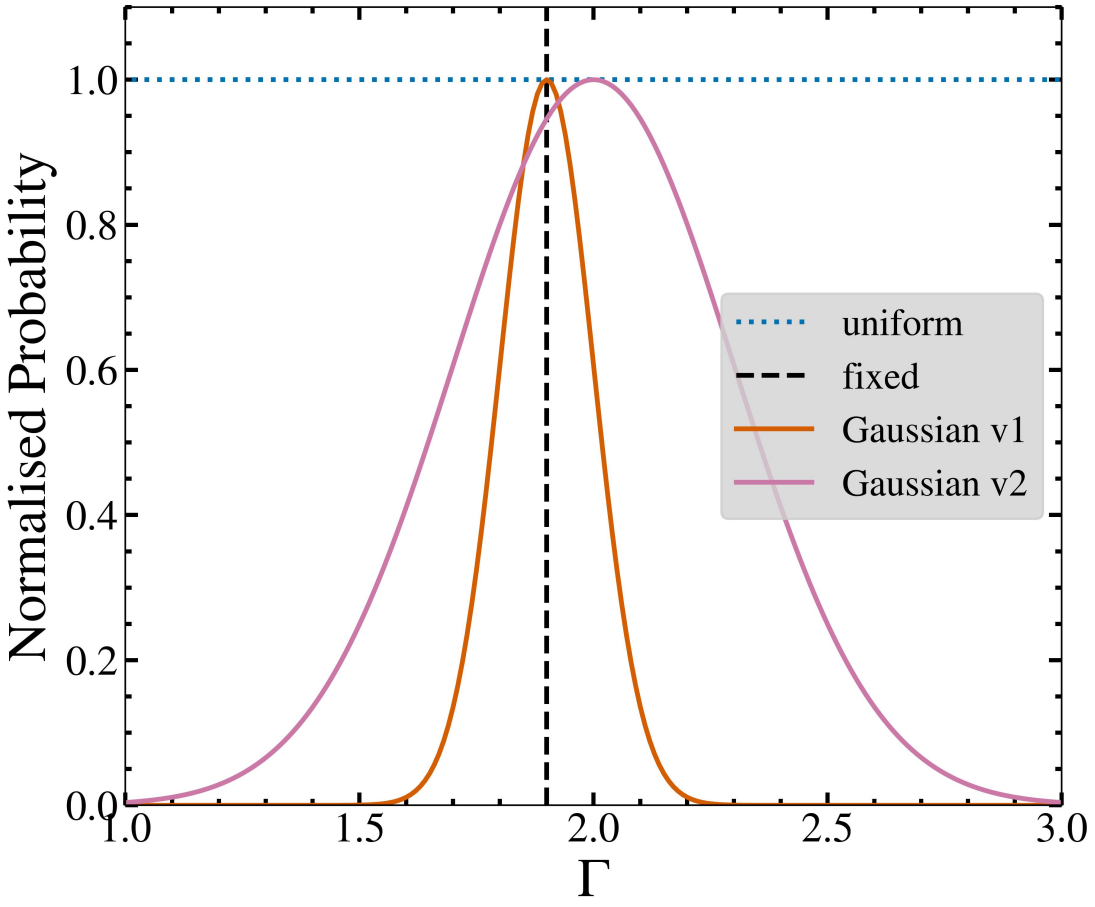

FIGURE 4.10: Priors on Γ used in BXA of various models.

The final set of models we compare is: (a) CABS*ZWABS*POW: with uniform, single value and Gaussian priors on Γ; (b) MYTORUS; (c) BNSPHERE[8]; and (d) 'leaky sphere'.

These models as defined in `xspec` are as follows:

- Absorbed powerlaw: CONSTANT*PHABS*CABS*ZWABS*POW
- MYTORUS: CONSTANT*PHABS(ZPOWERLW*ETABLE{MYTORUS_EZERO_V00.FITS} + CONSTANT*ATABLE{MYTORUS_SCATTEREDH500_V00.FITS})
- BNSPHERE: CONSTANT*PHABS*ATABLE{SPHERE0708.FITS}
- 'leaky sphere': CONSTANT*PHABS*(ATABLE{SPHERE0708.FITS} + CONSTANT*ZWABS*ZCUTOFFPL)
- Absorbed powerlaw with neutral iron line: CONSTANT*PHABS(CABS*ZWABS*POWERLAW+ZGAUSS)

[8] BNTORUS is known to have inaccuracies in the reflected component (e.g., Baloković et al., 2018); here we only consider the spherical component with no opening angle which should not be affected.

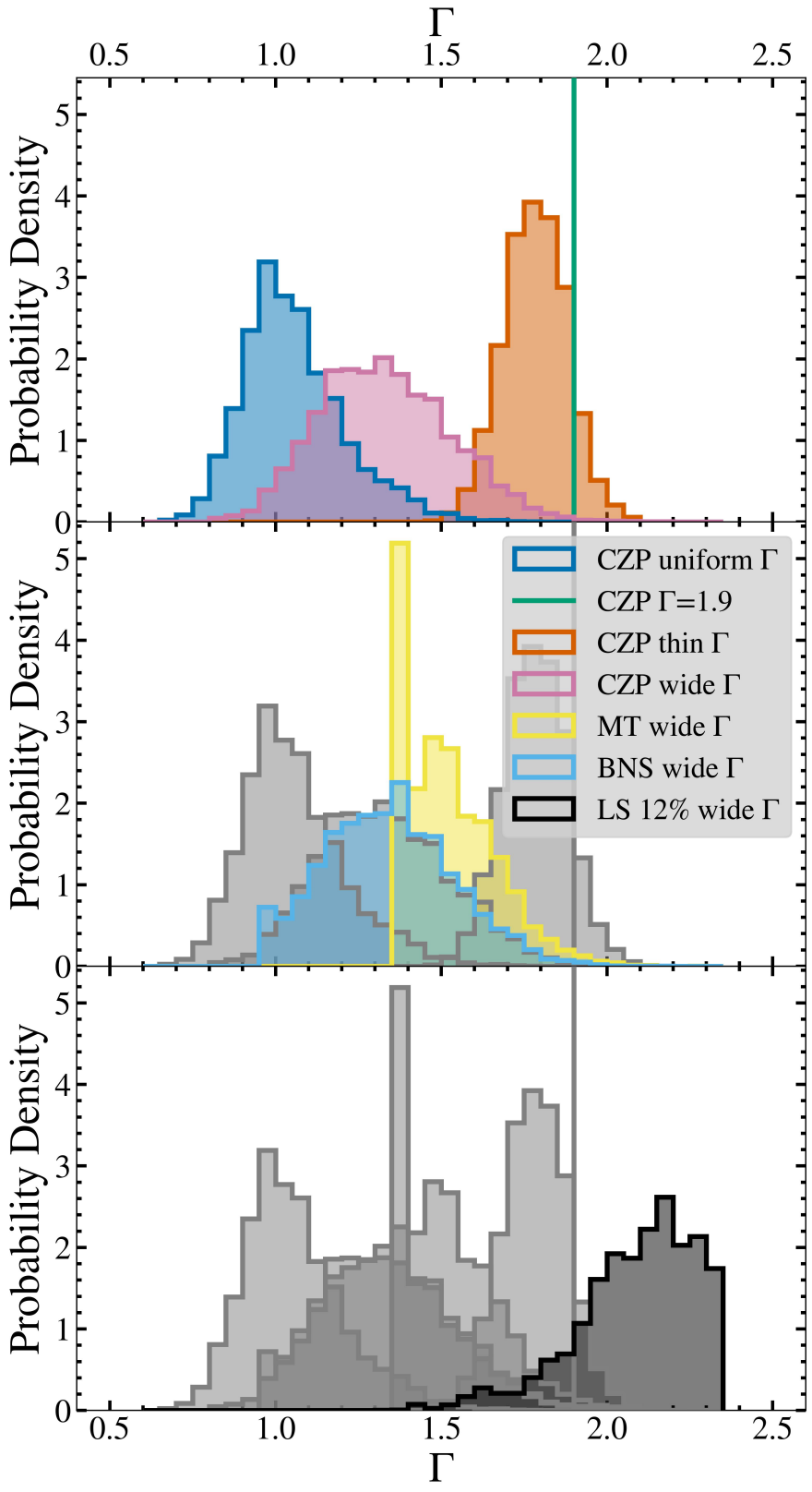

FIGURE 4.11: Γ posteriors for different models. (top) absorbed powerlaw only; (middle) with physical models added; (bottom) with the 'leaky sphere' model. Priors used are shown in Figure 4.10.

4.3.3 Results

Across all models, the results show that the data can be explained by an obscured AGN. The parameters vary, and in some cases may indicate unusual values, but all are consistent with the presence of an AGN. Full results for all models are shown in Table 4.3. None of the models show significant residuals, except possibly towards the hard end, and all are reasonable fits to the data (see Figures 4.8, 4.12, and 4.13).

The preferred solution according to the Bayes factors is BNSPHERE (Table 4.3, Figure 4.12)[9]. Comparison of (a) BNSPHERE and (b) 'leaky sphere' (scattering fraction 12%; Figure 4.13) shows that LS is not favoured. However, it is also not strongly counter-indicated (i.e., the relative Bayes factor is low; a value of 6.3 is 'substantial evidence' in favour of BNSPHERE, but not decisive, according to the Jeffreys scale (Buchner et al., 2014)).

BNSPHERE returns a preferred $\Gamma=1.32^{+0.21}_{-0.19}$ — unusually hard but not impossible for an AGN (e.g.; Ricci et al., 2017a) — and $\log(N_{\rm H} / {\rm cm}^{-2}) = 21.95$ (see Figure 4.14). Forcing Γ to a more typical AGN value of 1.9 increases the $\log(N_{\rm H} / {\rm cm}^{-2})$ slightly to 22.3, but does not significantly affect the intrinsic luminosity (see Figure 4.14). The 12% 'leaky sphere' model produces a softer Γ and, if closer to the truth, may imply a luminosity much closer to expected.

That BNSPHERE is a reasonable fit to the data implies that the 'cocooned AGN' scenario may be a feasible explanation for the observed properties. Obscuring material relatively close to the AGN may prevent ionising radiation from within reaching farther out, and thus no narrow [O III] emission. We can also consider a situation where the NLR exists within a cocoon on intermediate scales between the torus and the inner galaxy (perhaps $\sim$ tens of pc), just large enough to cocoon the inner NLR. Depending on the gas–to–dust ratio in the obscuring material, relatively thin columns may be sufficient to extinct any [O III]. Based on the [O III] deficit between the general OQQ population and QSO2s (Chapter 5), a median $A_{\rm V} = 4.7$ mag is sufficient to extinct the theoretical [O III] line. This is equivalent to an NLR obscuring neutral gas column density of $\log(N_{\rm H} / {\rm cm}^{-2}) \sim 22.8$ (assuming gas–to–dust ratios in AGN environments from Maiolino et al., 2001). This is higher than found in this analysis; however, the NLR–obscuring column is distinct from the line of sight X-ray–obscuring column, which may explain this difference.

The Fe Kα line (rest energy 6.4 keV) observed in many AGN spectra (e.g., Nandra, 2006) originates from reprocessing of AGN emission in optically thick obscuring matter. For lightly obscured AGN, Shu et al. (2010) find a relationship between detected narrow Fe Kα EW and unabsorbed 2-10 keV luminosity. Noting that this has large scatter, and

[9] CABS*ZWABS*POW with uniform prior fit is discarded from this point; the lack of constraint allows values of Γ that are not physically likely.

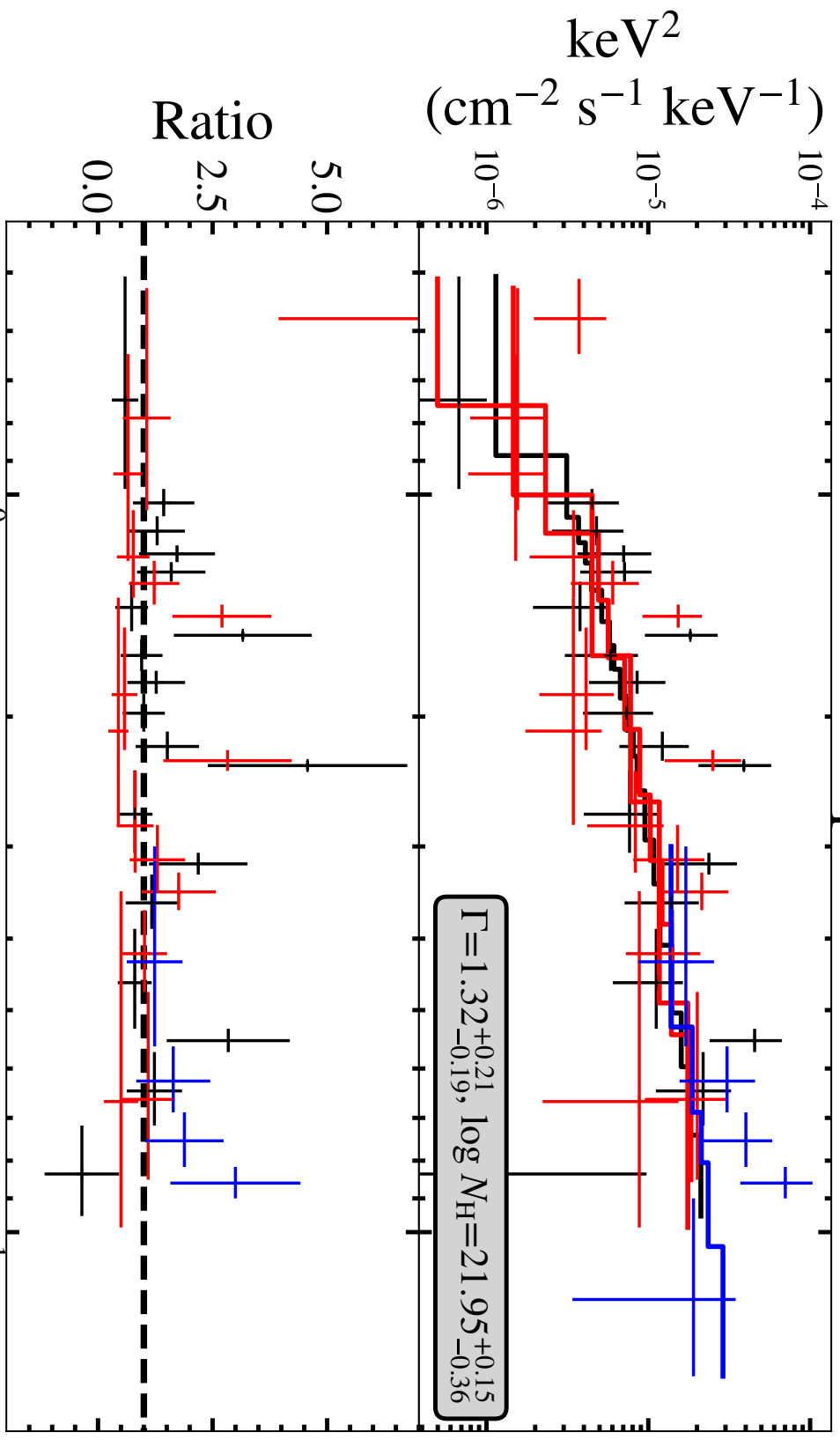

FIGURE 4.12: (top) Spectrum of best fit BNSPHERE model; (bottom) ratio between data and model. Shown is *XMM-Newton*-pn (black), *XMM-Newton*-MOS (red) and *NuSTAR* FPMA (blue), binned to a minimum of 2 counts per bin.

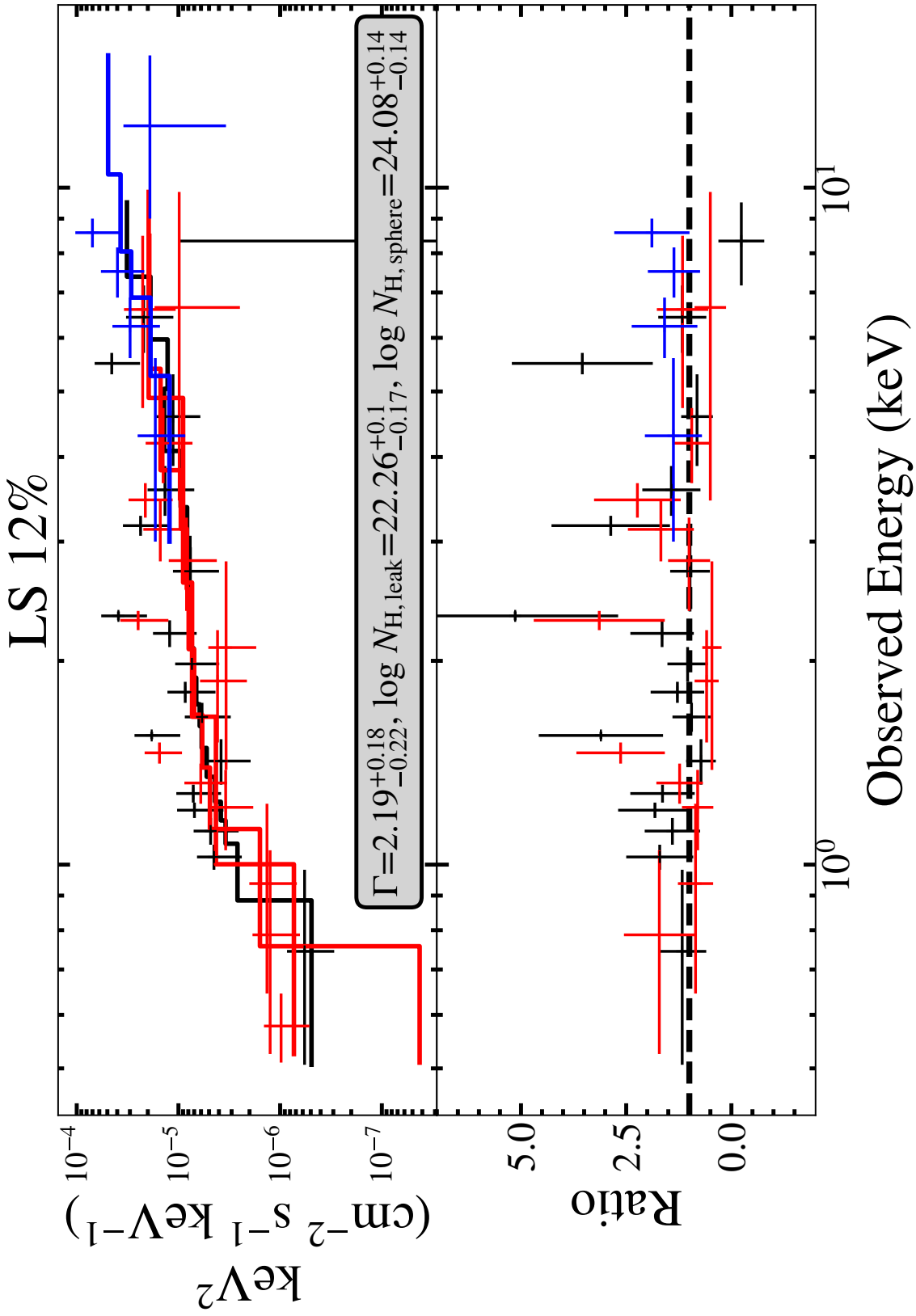

FIGURE 4.13: (top) Spectrum of best fit ' leaky sphere'model; (bottom) ratio between data and model. Shown is *XMM-Newton*-pn (black), *XMM-Newton*-MOS (red) and *NuSTAR* FPMA (blue), binned to a minimum of 2 counts per bin.

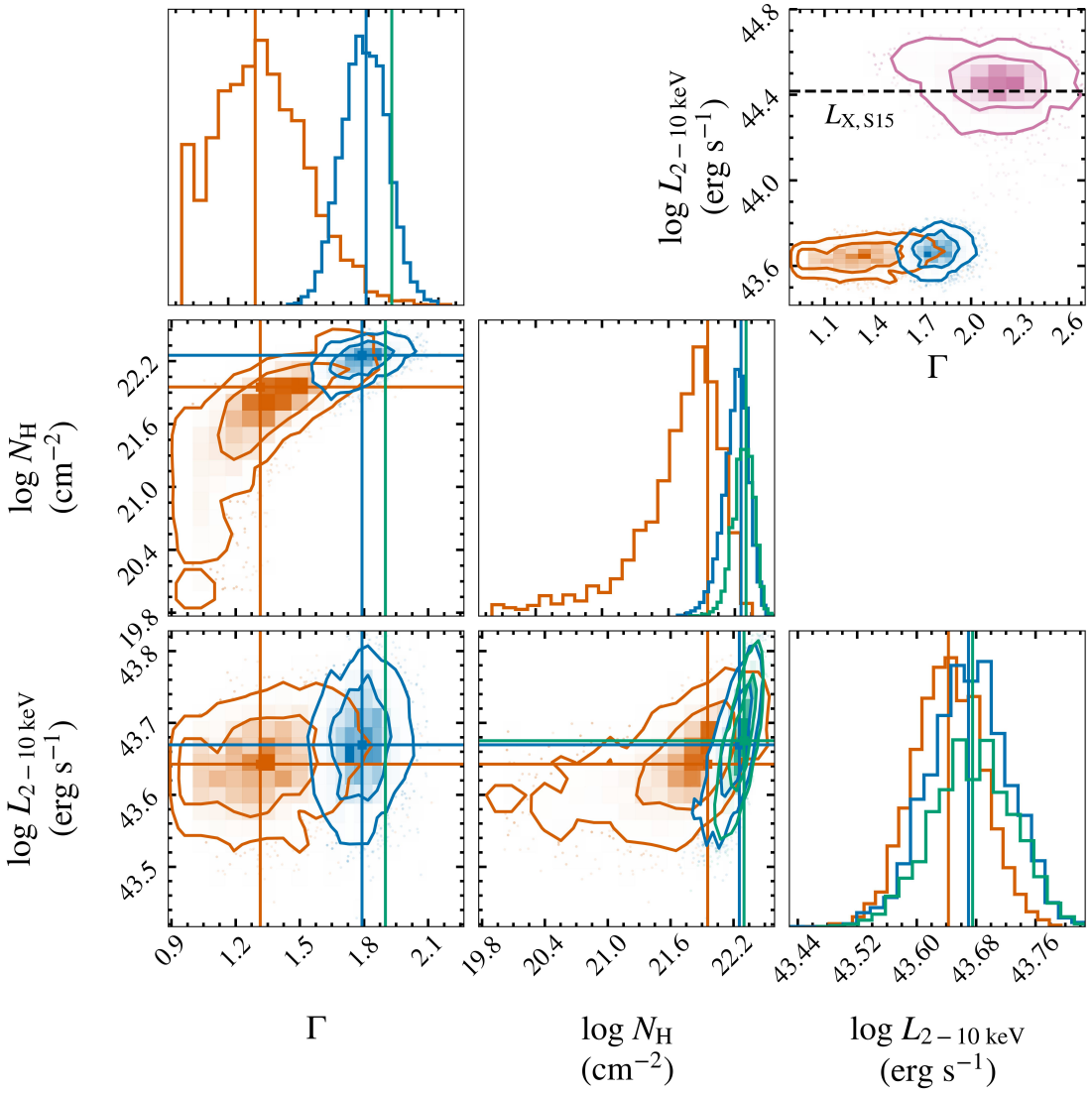

FIGURE 4.14: Corner plot of results with: (a) CABS*ZWABS*POW, restrictive prior on Γ (blue); (b) BNSPHERE, physically representative prior on Γ (orange), (c) CABS*ZWABS*POW, fixed Γ=1.9 (green). Best fit values for each parameter are shown with a solid line. (top right) L_{2-10} vs. Γ contour with the IR-predicted luminosity shown (Stern, 2015, dashed line) – the luminosity contours for the lightly obscured models are decisively below this level. Also shown are the results for the 12% scattered 'leaky sphere', which is closer to predicted (pink).

from higher resolution *Chandra* data, we can use to roughly estimate an expected Fe Kα EW of 45 eV. We place an upper limit on the equivalent width (EW) of a putative narrow line by adding an unresolved Gaussian component to our transmission spectrum, with a width of 0.1 keV, finding an EW$\lesssim$26 eV – a low value that implies no line is likely to be present, further reinforcing the conclusion that OQQ J0751+4028 is only lightly obscured. Figure 4.15 shows that adding this line has no effect on other parameters, and that only an upper limit can be obtained.

The intrinsic rest frame 2-10 keV luminosity (according to BNSPHERE) is 4.39 $\times$ 10^{43}

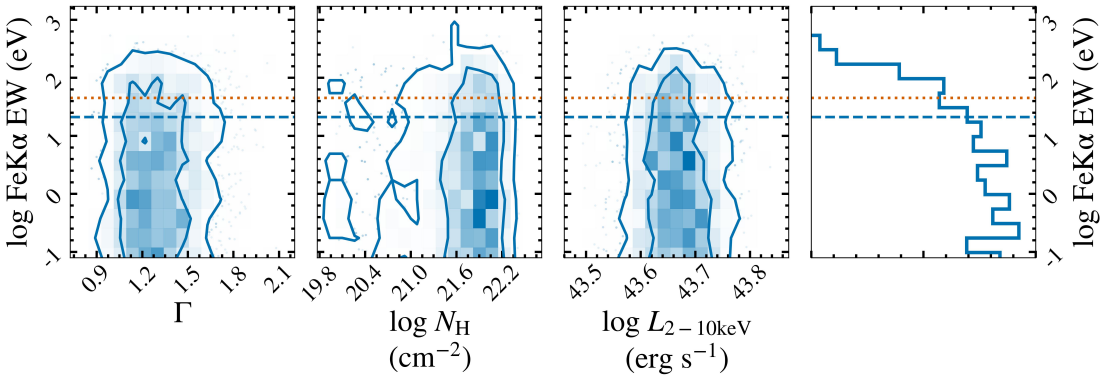

FIGURE 4.15: Contour plots showing the relationship between Fe Kα equivalent width (vertical axis) and other intrinsic parameters for an absorbed powerlaw with additional Gaussian emission line. Blue dashed line is the 1-sigma upper limit on the EW; orange dotted line is the predicted value from Shu et al. (2010).

erg s^{-1}. The IR luminosity (1.30×10^{45} erg s^{-1} at 12 µm) of OQQ J0751+4028 implies a 2-10 keV luminosity of 2.61×10^{44} erg s^{-1} (from the 6 µm/2-10 keV relation; Stern, 2015). Comparing these values, we find that the unabsorbed luminosity is ∼6 times lower than expected, but still easily above the threshold of 10^{42-43} erg s^{-1} generally accepted for an AGN. In Figures 4.16 and 4.17 we compare the properties of OQQ J0751+4028 against a sample of Type 2 QSOs selected from SDSS with significant [O III] emission (QSO2s; Reyes et al., 2008, Yuan et al., 2016). Figure 4.16 shows the measured X-ray luminosities of the QSO2s, along with the reported [O III]/X-ray relationship from Lamastra et al. (2009) – the majority of QSO2s lie close to the empirical prediction, but OQQ J0751+4028 is far from typical. Figure 4.17 shows that OQQ J0751+4028 lies below the IR-predicted values from Asmus et al. (2015) or Stern (2015), and also below the majority of QSO2s, which tend to fall closer to their predicted values. Conversely, if we consider the 'leaky sphere' model, the intrinsic X-ray luminosity may be closer to IR-predicted expectations (see Table 4.3); however, it would be further offset from the [O III]/X-ray relationship.

4.4 Discussion

4.4.1 X-ray discussion

One important aim of this work is to place OQQ J0751+4028 (and in the future, its fellow OQQs) into context with the wider ranks of AGN. We begin by considering what the results from this X-ray study allow us to infer about the intrinsic nature of this object. Crucially, the absorption-corrected luminosity shows that OQQ J0751+4028 is an AGN, regardless of the specific best-fit model that we adopt. This confirms the presence of ongoing accretion activity, and gives credence to our IR selection, despite the apparent optical quiescence.

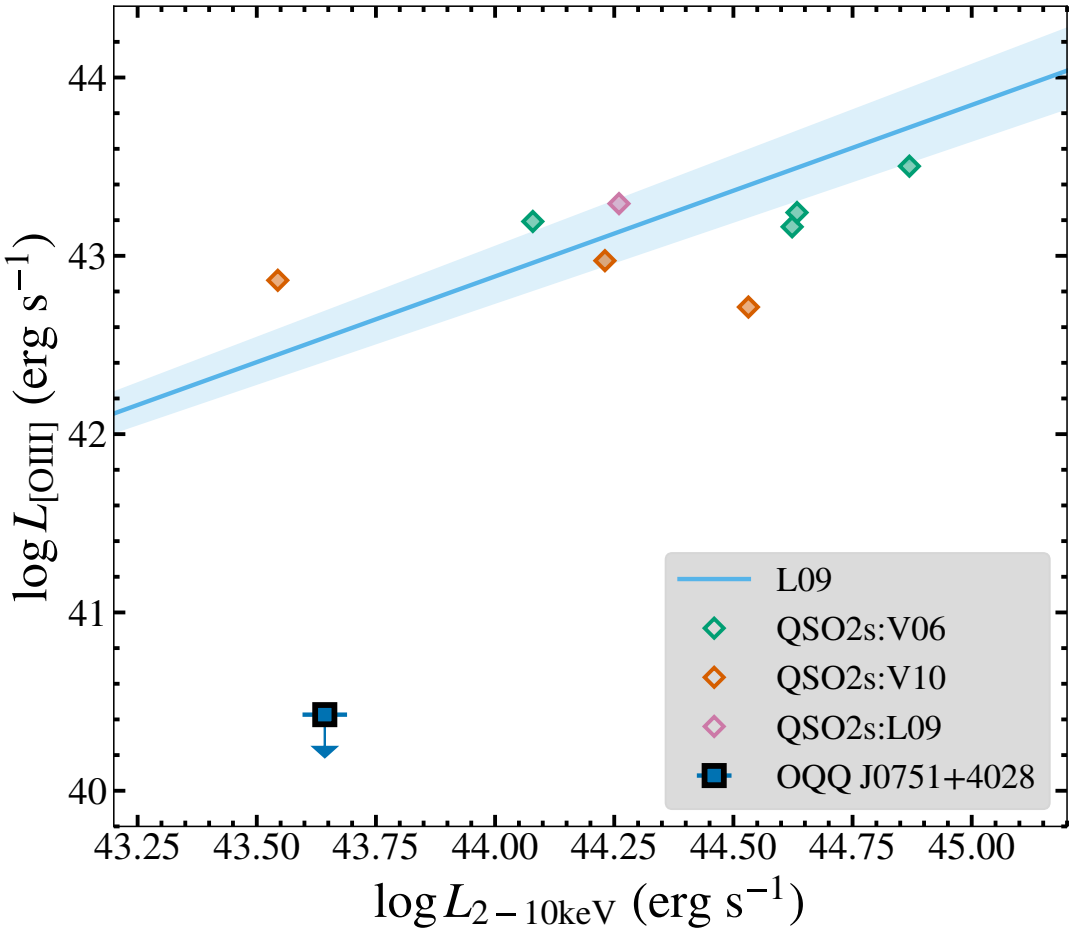

FIGURE 4.16: A comparison between OQQ J0751+4028 and QSO2s: unabsorbed 2-10 keV luminosity against [O III] luminosity. X-ray luminosities for QSO2s are from Vignali et al. (2006) (V06; green diamonds), Vignali et al. (2010) (V10; orange diamonds), and Lamastra et al. (2009) (L09; pink diamonds). Relationship from Lamastra et al. (2009, L09) shown as a grey line. OQQ J0751+4028 shows an upper limit on [O III], indicated by an arrow.

OQQ J0751+4028 must be obscured in X-rays, but is less likely to be Compton thick than thin. The Bayes factor for the highly obscured 'leaky sphere' compared to the lightly obscured BNSPHERE is ∼6: a less likely fit but not decisively so. Recalling from the introduction our suggested scenarios regarding the nature of an optically quiescent AGN ('cocooned' and 'young' AGN), we can only conclude at this stage that both remain possible. Nuclear optical extinction is also required in both scenarios in order to hide the broad line region, which we do not see.

The light obscuration we observe could be a more physically likely possibility for enshrouding material than optically thick material, supporting the idea of a 'cocooned' AGN, or similar to larger-scale host obscuration (e.g., Buchner and Bauer, 2017). This interpretation could be consistent with a low intrinsic X-ray luminosity AGN if the Eddington ratio is low, as higher intensity AGN are associated with lower covering factors (e.g., Ricci et al., 2017b).

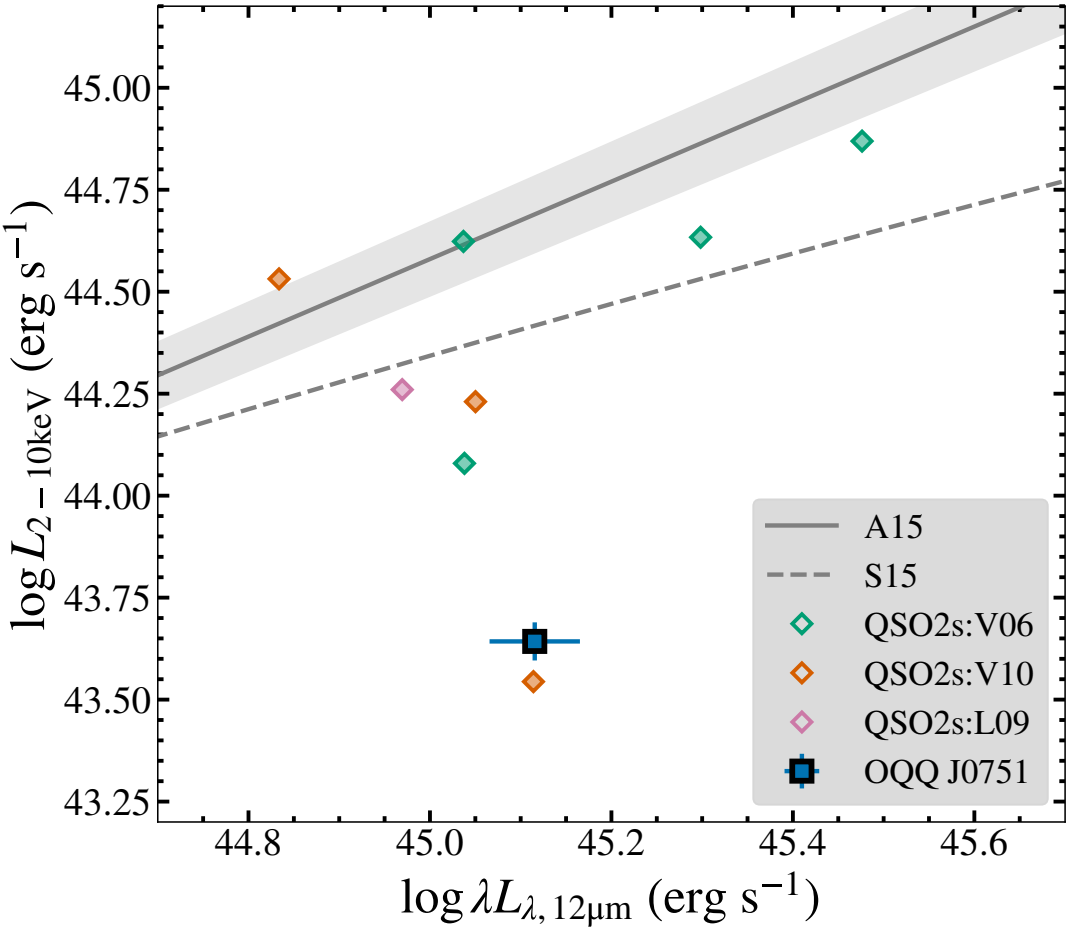

FIGURE 4.17: A comparison between OQQ J0751+4028 and QSO2s: unabsorbed 2-10 keV luminosity against 12 μm luminosity. X-ray luminosities for QSO2s are from Vignali et al. (2006) (V06; green diamonds), Vignali et al. (2010) (V10; orange diamonds), and Lamastra et al. (2009) (L09; pink diamonds). Relationships from Asmus et al. (2015, A15), and Stern (2015, S15; 12 μm luminosities were converted to 6μm luminosities using a relationship derived from the QSO template of Hao et al. (2007)), are shown as grey lines. .

An AGN in the process of switching on (a 'young' AGN) might also show weak X-ray emission as it transitions to full accretion power. Kollatschny et al. (2020) present the opposite case – a *switching off* AGN – in which they see a dramatic decrease in observed X-ray luminosity concurrent with a change in type from Seyfert 1 to 1.9 (i.e., a reduction in the broad emission lines, but still with clear narrow lines). They find no evidence that this change is caused by absorption, indicating that it is an intrinsic luminosity change. Reversing this, we might expect to see the X-ray increase before the appearance of narrow lines.

Finally, we must consider the possibility that OQQ J0751+4028 is a fully 'mature' AGN *intrinsically* lacking [O III]. Analysis of relationships between various emission-line properties of AGN has shown that many of these properties correlate (Eigenvector 1; Boroson and Green, 1992). Shen and Ho (2014) show that the observed anti-correlation

between [O III] and the relative strength of Fe II emission can be explained by changes in Eddington ratio; an AGN seen to lack [O III] could then be explained by a very high accretion rate. The higher Γ and intrinsic luminosities of the 'Leaky Sphere' model may suggest this to be the case, however a low 'leak fraction' would be required, and the fit statistics indicate this is unlikely. The stellar mass of OQQ J0751+4028, while uncertain, implies a high BH mass ($\sim 5 \times 10^8 M_\odot$; Kormendy and Ho, 2013), and consequently a very high luminosity to reach Eddington accretion levels – higher than seen in the *WISE* measurements.

OQQ-like objects are not new. For example, other groups of AGN that have notable similarities to OQQs include weak line quasars (WLQs) with weak X-ray emission and weak or absent emission lines (e.g., Wu et al., 2012a, Luo et al., 2015), and X-ray bright, optically normal galaxies (XBONGs) selected as AGN in X-rays, but showing no optical AGN signatures. In some cases, this is due to dilution by bright host galaxies of lower luminosity AGN (Moran et al., 2002) – in contrast to the OQQs, where AGN emission in the IR is bright, and dominates over their hosts.

Our OQQ selection is a first attempt to systematically search for this class of optically quiescent AGN and our work unambiguously establishes that some AGN can present bright ongoing nuclear accretion activity in X-rays, yet show no signs of this in the optical. Details of our full sample are presented in Chapter 5.

4.4.2 Cocooned AGN growth and the merger paradigm

AGN grow in proportion with the bulge of their host galaxies, on (Kormendy and Ho, 2013). One possible evolutionary track that could explain this is merger-driven evolution (Fabian, 1999, Hopkins et al., 2006), where galactic mergers funnel large amounts of material inwards, boosting both AGN growth and star formation (e.g., Springel et al., 2005).

The influx of material provides the fuel for AGN as well as star formation, and also obscures the nucleus. As the AGN brightens, radiation pressure clears away the obscuring material, revealing the nucleus in a bright unobscured phase. Eventually, when all the gaseous fuel is exhausted, the AGN returns to its dormant state. One plausible interpretation of the OQQ characteristics is a short phase in this cycle, when the infalling material has ignited the AGN, but it still remains obscured along all lines-of-sight. If this scenario were appropriate for J0751, we might expect to see (a) signs of recent merger activity, and (b) significant ongoing star formation, as seen in some local samples including starburst-AGN composites (Goulding and Alexander, 2009).

Optical images from SDSS and PanSTARRS show a compact, red galaxy, with no apparent ongoing merging activity. Higher resolution images may be able to shed more light on the recent history of this galaxy – PanSTARRS provides a median image quality of

just above 1 arcsecond (Magnier et al., 2020) (∼11 kpc). The red colour, presence of an early-type galaxy spectral continuum, and lack of optical emission lines in J0751 (Figure 4.3) imply that there is very little star formation. The prominent 4000 Å break also distinguishes J0751 from other featureless systems such as BL Lacs, where continuum emission is dominated by nuclear jet emission.

Based on the broadband photometry rather than emission line strengths, SED modelling by `agnfitter` gives slightly different values of 0.001 and 1.69 $M_{\odot}$ per year, respectively. In principle Hα could also provide useful constraints here, but is shifted redward of our current spectral coverage. High quality near-IR spectroscopy (to determine Hα) and longer wavelength photometric measurements (to constrain the `agnfitter` SED decomposition) would provide a more accurate value for the SFRs and further constrain the presence of an AGN.

The lack of star formation does not easily fit into the merger-driven AGN and host galaxy evolutionary paradigm. If this is the result of obscuration, it would require that any ongoing star-formation (SF) is also obscured, or that there be a delay between AGN ignition and subsequent SF triggering (or vice versa). Neither of these solutions is likely. There is no reason to expect SF triggering to await AGN triggering if there is plentiful gas supply in the environment.

4.4.3 Recently triggered AGN activity?

A second possible origin that can explain our observation is the young AGN theory – if the 'switch on' occurs through secular processes local to the AGN, and is recent enough that the NLR (the usual origin of the narrow [O III] emission) is not yet active. This would not require the presence of a cocoon, but instead line-of-sight obscuration of the accretion disc and the broad line region.

Typical AGN feeding timescales are thought to be of order $\sim 10^5$ years (Schawinski et al., 2015). If we happen to have detected the AGN within a few years of its trigger, radiation would have had time to be reprocessed in the pc-scale torus, but not yet excite the kpc-scale NLR, through neither radiative nor collisional processes. In many ways, this would be the opposite of the preferred scenario to explain Voorwerp systems where strong, offset NLR emission is seen with no strong nuclear activity evident (e.g., Sartori et al., 2018). The Voorwerp are believed to be AGN that have recently turned off, but the NLR is sufficiently distant to be responding to earlier AGN activity. There are also suggestions that some of these systems contain hidden AGN - Lansbury et al. (2018) show a Voorwerp system where the central AGN is luminous but hidden. Typical recombination times in nearby QSO2s are estimated to be between a few years to a few hundred years, depending upon gas density Trindade Falcão et al. (2021), so a steady source of excitation is important. A final possibility is that the NLR gas is no

longer confined and has dissipated or over-ionised over time. Though this cannot be excluded, it is unclear why this should be the case in these particular objects. The AGN would still need to be obscured along the line-of-sight in order to extinguish BLR and disc continuum signatures.

4.4.4 Conclusions

I have presented the first prototype in an effort to formalise the population of OQQs. Similar objects have cropped up in various other studies, but have not yet been systematically collated. For instance, Hviding et al. (2018) select AGN using WISE, but aim for a different part of the WISE colour-colour plane that restricts their targets to the most heavily obscured objects. There is no overlap, however some of this sample may be interesting cousins to OQQs. Most (70%) of their targets are actually identified as AGN through common optical emission line diagnostics - all but one of these have detectable [O III] lines. Glikman et al. (2012) use cross-matches between FIRST (Becker et al., 1995) and 2MASS (Skrutskie et al., 2006). Ueda et al. (2007) selected 'geometrically thick torus' AGN by looking for low-scattering X-ray fractions in the Swift/BAT survey; these could be lower luminosity cousins to OQQs. All such objects, although not identical to OQQs, could represent a similar population, or a close phase in a life-cycle containing both, so a population wide study is crucial and will be the subject of a follow-up work.

There remains a possibility that J0751 does not contain an AGN, but is a coincidence of emission from other sources that give the impression of one. However, to reproduce the emission I have without an AGN, the spectrum would need to be heavily dominated by starburst activity in the IR. The weakness of the non-[O III] emission lines present make this extremely unlikely.

Polarimetric observations, infrared spectroscopy and X-ray observations could help to reveal the true nature of these objects. X-ray observations would be particularly useful to prove the presence of an accreting nucleus; if the line-of-sight obscuring column is Compton-thick then hard X-ray data, such as from *NuSTAR*, would be necessary.

Irrespective of the true nature of these objects, they appear to represent an ill-studied phase of AGN (or AGN-like) activity. It should eventually be possible to constrain the duty cycle of this phase through demography of this population.

4.5 Summary

In this chapter I have shown that it is both possible and informative to select an interesting and unusual AGN from wide MIR and optical surveys. Starting from these large datasets allows discovery of rare AGN types, and with this detailed study of J0751 it is clear that some of these are still elusive and poorly understood. Figure 4.18 places J0751 into context with our other search regions, but this plot does not show everything that makes this object a discovery that adds to the populations of known AGN from LASr and NSS80. It has no optical AGN signatures, but is likely to derive most of its MIR power from AGN activity. It is lightly X-ray obscured, but the most likely geometry is spherical obscuration - a structure unlikely to be stable and hence representing a transient phase in the life of this galaxy.

Having gained what we can from this single prototype OQQ the natural progression is to consider what we might learn from a population of OQQs. Do they all have consistent properties? Are they likely to come from the same intrinsic populations, or are they similar in appearance only?

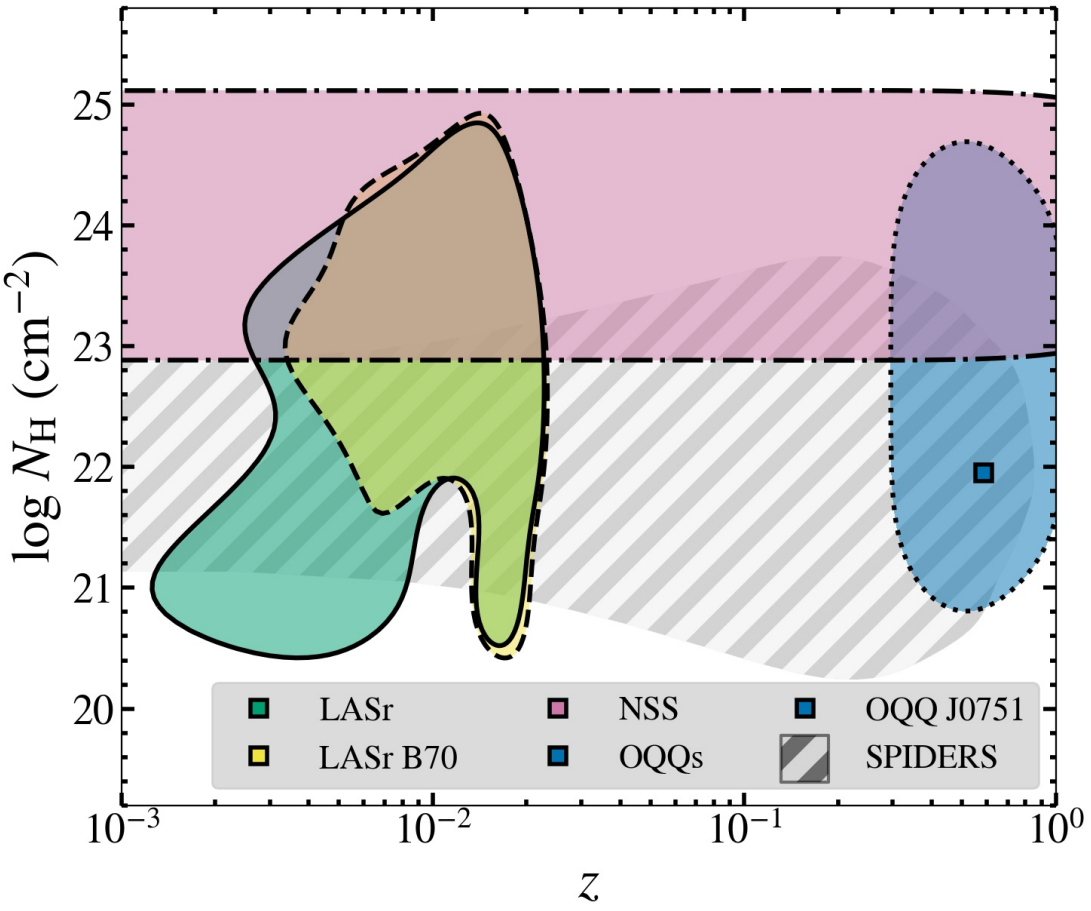

FIGURE 4.18: Parameter space covered by the known AGN in the LASr-GPS (green shaded region, solid edge), by the B70 AGN (yellow shaded region, dashed edge), the region targeted by *NuSTAR* serendipitous selection (pink shaded area, dot-dash edge), the region targeted by this chapter (blue shaded area, dotted edge), and the result from OQQ J0751+4028 (blue diamond).

Chapter 5

Buried Treasure: Uncovering the population of abnormally obscured AGN with multi-wavelength selection

Chapter 4 presented a prototype of an AGN with unusual properties that make it evasive in terms of common AGN identification. We discussed its properties in context with theories about its true nature, and explored how targeted X-ray measurements can give us insight into the genuine inherent structure. However, there is only so much we can infer from a single example. In this chapter I continue the Optically Quiescent Quasar work, expanding the detailed study on J0751 into an investigation of the population properties of OQQs, a comparison of their appearance with more familiar AGN classes, and consideration of their true intrinsic nature. At higher redshifts than those covered by LASr, I search for IR AGN that show no optical signatures - specifically a lack of [O III] emission. These may be cocooned AGN, i.e., AGN with a 4π covering of obscuring material, may have their NLR prevented from forming, may have yet to form an NLR, or may be intrinsically emission-line weak. Here I will describe the selection process for these objects: base datasets, assumptions made, testing for lack of [O III], and the final sample. An important part of assessing the nature of the OQQs is having a set of similar but well-studied AGN to compare them to; thus I describe a QSO2 comparison sample - objects similar in IR and optical photometric appearance, but chosen to have high [O III] emission, in sharp contrast to the OQQs.

5.1 SDSS and *WISE* as a Starting Point

5.1.1 Recap of the available data, and its strength and weaknesses

5.1.1.1 *WISE*

The Wide-field Infrared Survey Explorer (*WISE*) satellite (Wright et al., 2010) has carried out a highly-sensitive all-sky survey in four bands ($W1$, $W2$, $W3$ & $W4$ centred on wavelengths of ≈3.4, 4.6, 12 and 22 µm, respectively). The effective angular resolution corresponds to a Gaussian with full-width-at-half-maximum ≈6″ in $W1 - W3$, and 12″ in $W4$. The SDSS fifteenth Data Release (Aguado et al., 2019) includes pre-calculated astrometric cross matches with the earlier *WISE* data release (*WISE*-AllSky[1]). The AllWISE release[2] includes data from both the cryogenic and post-cryogenic phases of the mission, and therefore contains better quality data, with better photometric sensitivity, particularly in the W1 and W2 bands. The cross matching with SDSS and *WISE*-AllSky was used, and the *WISE* magnitudes updated with AllWISE values.

We choose to use the AllWISE data rather than the more recent CatWISE (Marocco et al., 2021) because the $W3$ and $W4$ measurements are vital to the selection process, and these two bands were only in operation in the earlier years of *WISE*. Although CatWISE may have provided more accurate photometry, (a) we are only looking at bright sources, which should be present in the earlier catalogues, and (b) in case of variation in source output it is best to use measurements from all four bands taken in the same time period.

5.1.1.2 SDSS

Data from the SDSS data release 15 (DR15; Aguado et al. 2019), including Baryon Oscillation Spectroscopic Survey (BOSS) spectra (Dawson et al., 2013), were used for cross-matching with the *WISE* catalogue.

The relevant tables are:

- `SpecObjAll`: the base SDSS table for spectroscopic observations, containing all measured spectra, including potentially bad or duplicate data. Contains 4,851,200 sources.
- `SpecObj`: the sub table of `SpecObjAll`, containing only the clean data, filtered for duplicates. Contains 4,311,571 sources.
- `PhotoObjAll`: the base SDSS table for all photometric observations. Contains 1,231,051,050 measurements.

[1] `http://wise2.ipac.caltech.edu/docs/release/allsky/`
[2] `http://wise2.ipac.caltech.edu/docs/release/allwise/`

- `PhotoObj`: the subset of `PhotoObjAll` containing only primary and secondary objects (i.e., not a family object, outside the chunk boundary, or within a hole [3]). Contains 794,328,715 measurements.
- `wise_allsky`: the *WISE* catalogue from the *WISE*-AllSky data release. Contains 563,921,584 sources.
- `wise_xmatch`: a join table that contains pointers to SDSS and *WISE*-AllSky measurements, from astrometric cross-matches between the two. Contains 495,003,196 cross-matches.

In this work we use only sources with available spectroscopy (i.e. members of `SpecObj`), and cross-match with photometric tables for further information.

5.1.1.3 Cross-matching

The SDSS to *WISE* crossmatch (table `wise_xmatch`) uses a 4 arcsecond distance threshold. The nominal *WISE* positional accuracy is actually significantly better than this.[4] This is also seen in the distribution of associated counterpart distances shown in Fig. 5.1, which peaks at $<0.2''$. A few selection tests showed that an increasing fraction of ambiguous counterpart identification (e.g., two potential SDSS sources for a single *WISE* source) for distances of more than 1 arcsecond. In fact, the vast majority ($\sim$ 90%) of associations lie at distances of less than $1''$, so this is the threshold used to build our catalogue. For our selection we use an initial set based on the SDSS `wise_xmatch` catalogue, with every spectral and photometric match joined (where one existed). The total number of objects in this table is 495,003,196 [5].

5.2 OQQ Selection Process

5.2.1 Overview of selection

From the cross-match results, we selected sources using the following criteria:

1. $\mathbf{W1 - W2 \geq 0.8}$: This colour threshold has been shown by Stern et al. (2012) to be an efficient AGN selection criterion, yielding AGN samples with very high ($\sim$95%) reliability and good ($\sim$80%) completeness at high X-ray luminosities. AGN are expected to heat dust to temperatures of several hundred degrees K,

[3] https://www.sdss.org/dr15/algorithms/masks/
[4] http://wise2.ipac.caltech.edu/docs/release/allwise/expsup/sec2_5.html
[5] 3252 of these have W1 magnitude=9999, i.e., are not usable.

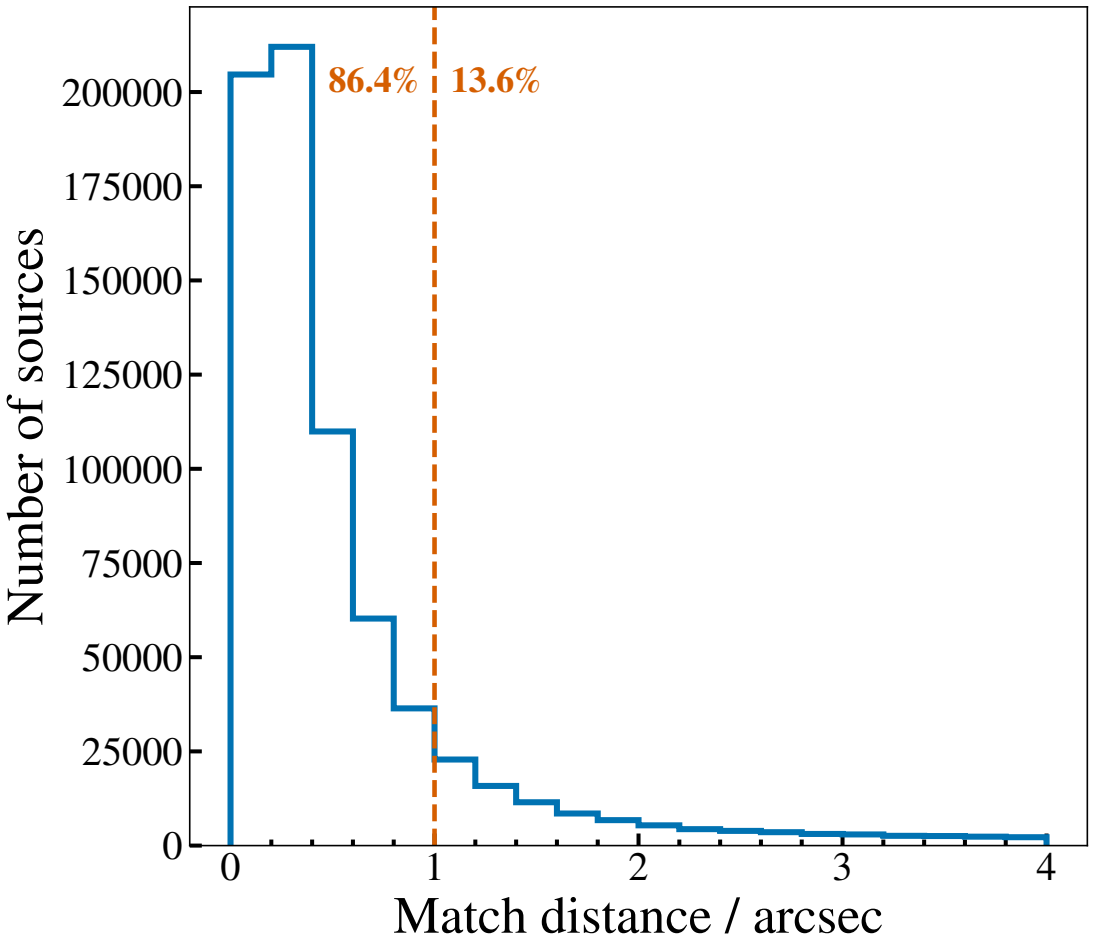

FIGURE 5.1: SDSS–*WISE* nearest counterpart cross-matching distance distribution. Numbers indicate the fraction of sources in the accepted (left) and rejected (right) sections.

approaching sublimation, resulting in an SED peaking at a few microns and with a red $W1 - W2$ colour. Whereas the colour cut alone can be contaminated by cool brown dwarfs, dust-reddened stars and star-forming galaxies (e.g., Stern et al., 2012, Yan et al., 2013, Assef et al., 2018), our additional luminosity selection of only the most powerful sources is expected to weed out most such contaminants, preferentially selecting AGN alone. As shown in Section 2.4.3, particularly Figure 2.11, reliability increases swiftly with luminosity. In order to further reduce contamination and confirm, detailed multi-wavelength data would be required; in this work I explore the potential of X-rays (Sections 4.3 and 5.9) and SED fitting (Sections 4.2.2 and 5.10.1), but with the caveat that the vast majority of data for these sources is serendipitous and thus not always deep or wide-ranging enough for conclusive results. However, they do show that each approach could provide promising avenues, and I discuss these and other options further in Section 6.3.3. As shown in previous chapters, the completeness (the fraction of all AGN

selected) of this method can vary depending on source properties (e.g. luminosity, obscuration column density) and we may expect to ignore a number of true OQQs that lie below this threshold. However, this chapter focuses on obtaining a *clean* sample over a complete one - further work to select OQQs that are missed by both optical and MIR selection is beyond the scope of this chapter.

2. ***WISE* - SDSS cross match distance** - cut to be $<1''$ as discussed above.

3. **Reliable redshift:**

   - `z_ERR/z` $\leq$ `0.01` - a fractional error of 1 % or less on the redshift, indicating an accurate value. This criterion was introduced because a good `zWarning` flag does not necessarily imply a robust redshift measurement. Note that the median fractional z uncertainty in our final sample is 0.00016, i.e., much smaller than the adopted threshold of 1 % which is designed to weed out the most obvious unreliable sources.
   - `zWarning` flag (SDSS) = 0, indicating high confidence in the redshift. Possible causes for a warning flag include poor or inconclusive fits, insufficient wavelength coverage, or problems with the instrumentation.

4. **Redshift limit:** $0 < z \leq 0.83$ (for SDSS spectrometry) or $0 < z \leq 1.065$ (for BOSS spectrometry) - this ensures that all spectra cover the redshifted [O III]λ5007 line. For SDSS spectrometry it is identical to the redshift cut adopted by Reyes et al. (2008) for selecting [O III]–luminous Type 2 quasars, thus allowing us to contrast this class of objects with our targets. We additionally include spectra from newer survey programmes, and as these use a wider wavelength range spectrometer, we can include some further objects.

5. **Reliable *WISE* data:**

   - *WISE* `cc_flags` = '0000'. The four zeroes refer to the four *WISE* bands and indicate that the *WISE* data are not affected by any known artifacts that can cause confusion or contamination in any of the bands.
   - *WISE* `W?ph_qual` $\neq$ 'U' AND `W?ph_qual` $\neq$ 'X' AND `W?ph_qual` $\neq$ 'Z'. This ensures a detection, reliable photometry, and measurable uncertainty in all four *WISE* bands (with a signal:noise above 2), allowing a robust measurement of the MIR source monochromatic fluxes (see next point) as well as MIR SEDs.

6. **IR luminosity:** $L_{12} \geq 3 \times 10^{44}\,\mathrm{erg\,s^{-1}}$ - Here L_{12} is the k-corrected monochromatic 12 µm luminosity (λL_λ), computed by simple linear interpolation between $\log(\lambda L_\lambda(W3))$ and $\log(\lambda L_\lambda(W4))$ to rest-frame. For the MIR vs. X-ray relation of Gandhi et al. (2009), this L_{12} corresponds to an intrinsic 2-10 keV X-ray luminosity of $\geq 10^{44}\,\mathrm{erg\,s^{-1}}$, widely adopted as the threshold for selection of sources with quasar X-ray luminosities (e.g., Gandhi et al. 2004, Mainieri et al. 2011, Brusa et al.

2009). Furthermore, the *WISE* extragalactic source population above this 12 µm luminosity threshold (corresponding to $\approx 10^{11}\,L_{\odot}$) comprises AGN almost exclusively (Donoso et al., 2012).

7. **SDSS classification:** `CLASS` = 'GALAXY' and `SUBCLASS` = '' - the `CLASS` selection removes sources with detected emission lines characteristic of QSOs (stars already having been culled by the redshift criteria). The `SUBCLASS` selection further removes sources with emission lines characteristic of Seyfert and LINERs, as well as star-forming and starburst systems[6].

8. **Best available spectrum:** `SciencePrimary`=1. This indicates that the spectra are considered by SDSS to be the best available for each object.

9. **No significant detection of [O III]λ5007**. The `emissionLinesPort` table contains detailed flux fitting of a large number of SDSS spectra, but has the disadvantage of not having been applied to many newer spectra. In order to include the maximum number of possible spectra, the significance of the [O III]λ5007 line flux was measured directly, similarly to the method used to fit [O III] lines when selecting for QSO2s (Reyes et al., 2008): Gaussian curves were fit to rest frame positions of [O III]λ5007 in the spectral data from SDSS. The outcome of this trial was that a subset of the objects had no apparent [O III] emission line, and therefore these will comprise the final sample. A more detailed explanation of this trial can be seen in Section 5.3.1.

10. **Continuum SNR limit:** Estimate of SNR in the direct region around where an [O III] line would be detected. This is to remove any objects where the noise in the region of interest is overwhelming the measurement, leading to artificially high upper limits for the line flux. A more detailed explanation of this trial can be seen in Section 5.3.2.

11. **Visual inspection of sources:** Automatic classification is not perfect, and a small number of sources with e.g., obviously wrong redshift or classification were rejected in this final step.

5.3 Final Steps

5.3.1 Lack of [O III] Emission

We start with the primary SDSS spectrum for each OQQ candidate, which was cut down to the region around the [O III] doublet (rest frame wavelength 4860 Å to 5100 Å - see Figure 5.2). We aim to find upper and lower bounds for a fit to the [O III] line,

[6] https://www.sdss.org/dr15/spectro/catalogs/#Objectinformation

based on a Gaussian on top of a straight line. In Reyes et al. (2008), they used a double Gaussian fit to find the presence of strong [O III]. However, we found that due to the low level of our target [O III] lines, the second peak caused the fit to be confused by the noise. We therefore fit only one Gaussian. Next we assess the uncertainty on the line flux, with the aim of checking whether the lower bound is less than zero, and hence whether only an upper bound can be placed on the emission. The continuum can be ignored in this simulation, as it cancels out from the equation. Finally, we select OQQs from the candidate objects that pass all other tests (as outlined in Section 5.2).

TABLE 5.1: Bounds imposed on fit parameters for [O III] emission line testing.

Parameter	Symbol	Bounds
Slope	m	none
Intercept	c	none
Line wavelength / Å	x_0	up to 1.0e+03 km/s from centre
Line FWHM / Å	σ	physical min up to 5.0e+02 km/s
Line height / flux units	h	max based on data

Method:

1. cut to local region around [O III] line wavelength (see Figure 5.2)
2. Set bounds for all parameters (see Table 5.1)
3. Remove regions where any spectral lines other than [O III] would be found, if present (see Figure 5.2)
4. Fit function to data ($y = mx + c + gaussian(x_0, \sigma, h)$)
5. Simulate an [O III] line for parameters randomly selected from their uncertainty bounds
6. Calculate line flux for each simulated line
7. Look at lower bound on line flux from simulations - if less than zero, we can conclude that the line only has an upper limit (Figure 5.3 shows spectra for a selection of [O III] detected and non-detected candidates)
8. Select subset to pass onto the next step (see Figure 5.4 - this shows the outcome of each tested object against this criterion - candidates on the left side of the graph are selected)

5.3.2 S/N Ratio Checks

To eliminate sources where the spectrum in the region of [O III] is significantly noisy – i.e., that there may be [O III] present at a low level – we estimate the noise as follows (summary of results in Table 5.2 as 'Poor S/N'):

1. Cut the spectrum to two regions on either side of the theoretical position of [O III] (vertical bands in Fig. 5.2, bottom right panel), avoiding any other potential emission or absorption lines.
2. Estimate the noise in these regions as the standard deviation on the flux data.
3. Estimate the signal as the mean on the flux data.
4. Discard any candidate OQQ with S/N ratio >2.

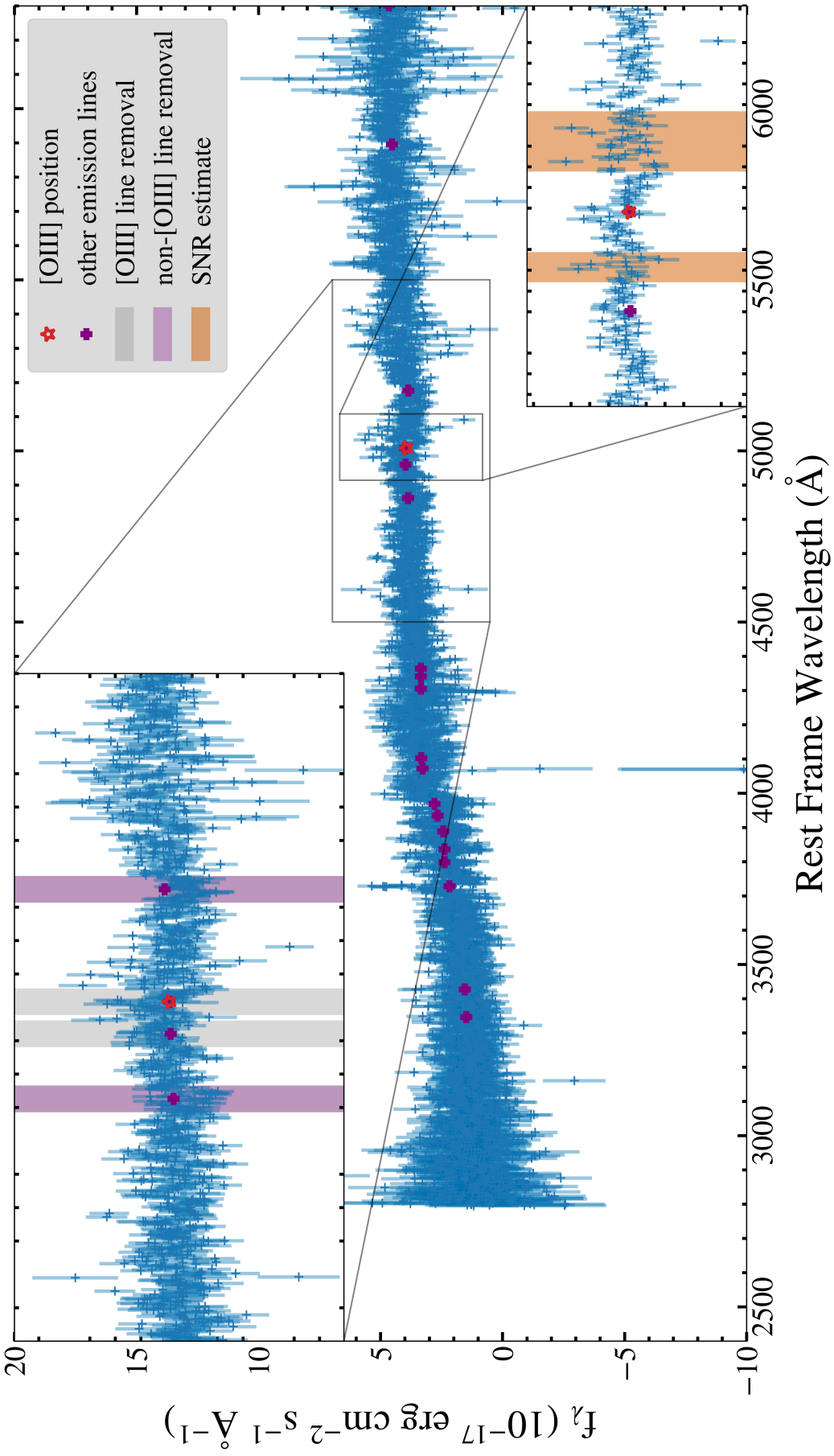

FIGURE 5.2: Full example SDSS spectrum, showing cut-outs with the region used in the fits. Purple + markers show the possible location of any spectral lines. Red star marker shows the location of [O III]. Vertical shaded regions show emission lines cut for the fit. Bottom right panel shows the region used for SNR calculations. Vertical shaded areas show the SNR estimate regions. Noise is estimated from these and compared to the continuum flux, as described in Section 5.3.2.

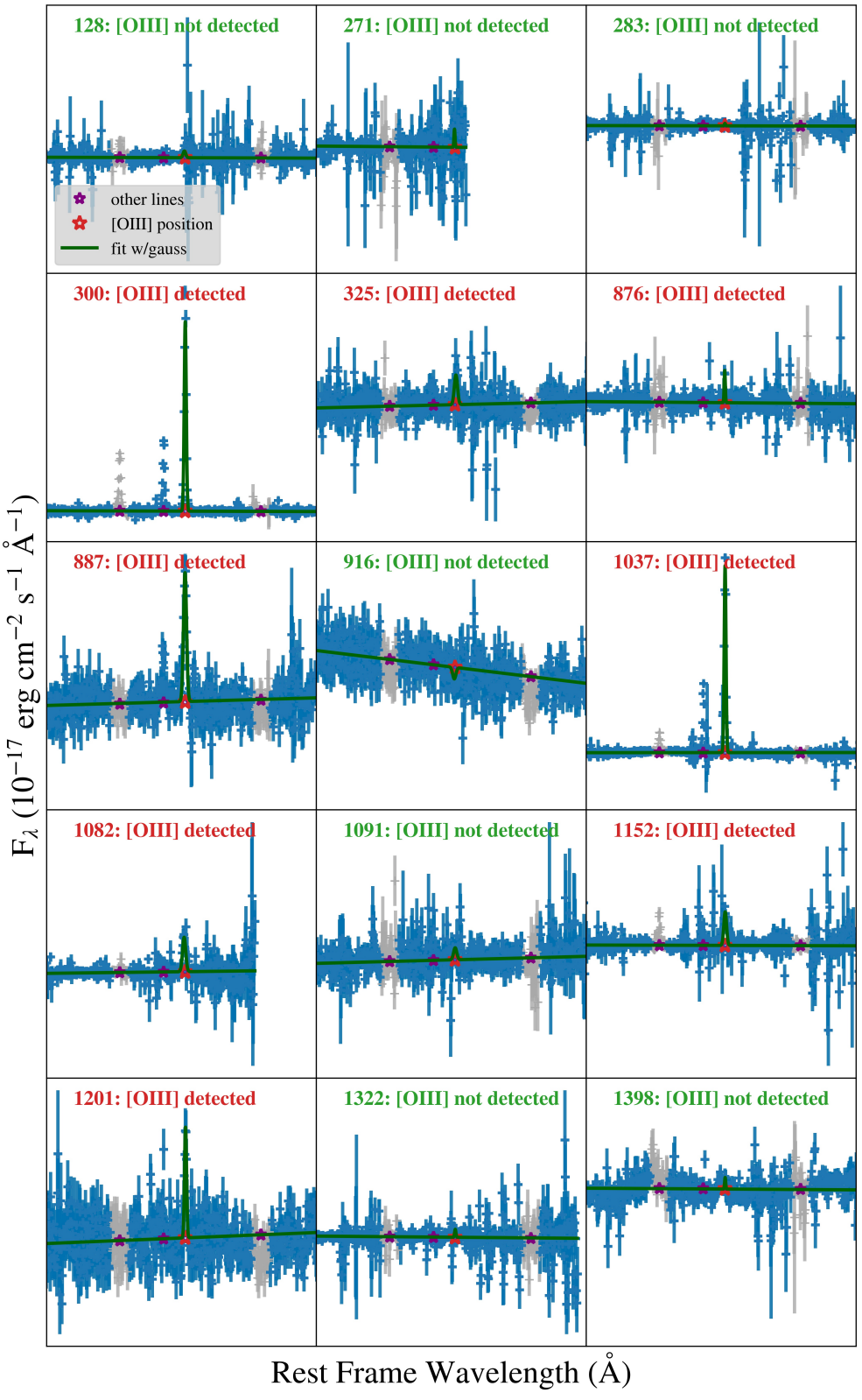

FIGURE 5.3: Randomly selected candidates, showing the difference between passing and failing.

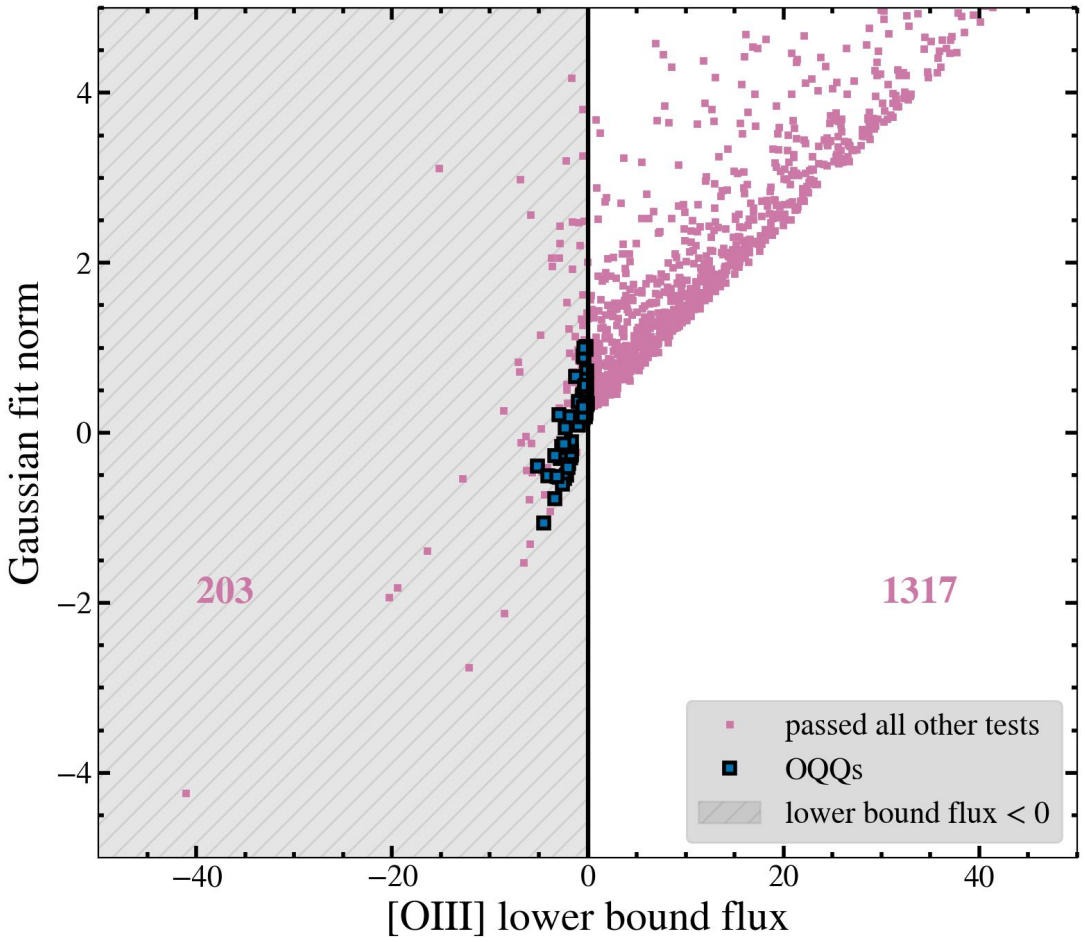

FIGURE 5.4: Results from simulating flux, comparing normalisation of Gaussian fit (y axis), with lower bound on [O III] line flux (x axis). Candidates that pass all other tests for inclusion in the paper are shown as purple points. The positions of the OQQs are shown as blue squares - these are distributed around fit normalisation of zero. The shaded area shows the passing candidates: row 2 in Table 5.2.

TABLE 5.2: Counts of objects showing no conclusive [O III] with each method.

	Original candidates	%
Total	1520	
Lower bound flux < 0	203	13.4
Keep (after basic vis check)	98	48.3
Remove (visible [O III])	48	23.6
Remove (noisy)	42	20.7
Remove (wrong class)	14	6.9
Keep (after detailed vis check)	64	64.3
Uncertain redshift	20	20.4
Poor S/N	12	12.2
Extremely blue continuum	3	3.1

5.3.3 Visual Confirmation Checks

All spectra that passed the automatic check were then inspected by eye, and discarded or flagged based on several criteria. These cuts were done with the aim of making a highly reliable rather than complete sample, so that we are as certain as possible about the relevant nature of each passing candidate. A summary of these results is shown in Table 5.2.

1. Visible [O III] - the automatic check sometimes fails to find a significant [O III] signal, despite there being a small but clearly apparent peak. We visually examine each spectrum, and based on the region around [O III] and the width and height of the visible peak, we discard or keep objects based on whether the [O III] seems truly absent .
2. Noisy data - we discard any candidates where the noise in the region of the [O III] line is visibly worse than the flux there, in order to remove any where the [O III] is likely to be lost in the noise. The S/N is calculated in detail in a later step (Section 5.3.2)
3. Incorrect class - candidates were selected based on SDSS spectroscopic classifications, but rarely an object is misclassified, and we discard any objects where the class appears unreasonable .
4. Uncertain redshift - candidates were already selected based on SDSS spectroscopic redshift showing no warning, but this automatic fit fails occasionally. We discard any objects where it is not clear how the redshift has been assigned.

For the fitting and selection process, and the properties in the main sections of the paper, we use only the spectra assigned by SDSS as `SciencePrimary` (a flag that indicates that this spectrum is considered the best available for this source). However, for a minority of sources there are multiple spectra available, so we compare these to see if there is any significant difference in flux, class, redshift, or emission line flux.

Most of these duplicate spectra are either well-matched, or are candidates that are dismissed for high levels of noise. We discuss the exceptions to this below.

5.3.3.1 J0002: 0.592036, -0.4320923

Two available spectra; generally consistent in appearance and flux, but one has been assigned the SDSS subclass `STARFORMING` (our selection process requires subclass `NULL`). This may be due to a change in emission line height. We choose to keep this candidate based on its otherwise promising appearance.

5.3.3.2 J0231: 37.99002, 0.648491

Fifteen available spectra; generally consistent in appearance and flux, but again one has been assigned the SDSS subclass `STARFORMING`. We also choose to keep this candidate based on its otherwise promising appearance; as the potentially star-forming galaxy is only one of the available spectra, and the rest are `NULL`, as required.

5.3.3.3 J0911: 137.96392, 29.824825

Three available spectra. All with consistent SDSS class and redshift, but clear changes in flux between spectra, particularly noting a change in shape in one. The primary spectra is the most recent, so we have retained this object in the sample, but note that it may be variable.

5.4 The Optically Quiescent Quasar Sample

5.4.1 Description of the final sample

The number of sources that cumulatively pass all sections is 64 (0.08% of 83,418 sources with reliable data, in redshift range; 4.2% of 1520 remaining prior to [O III] checks). In this work we will refer to this sample as 'Optically Quiescent Quasar' or OQQs. Information on the final list of objects can be found in Tables 5.3 and 5.4. A sample of their close-up spectra can be seen in Figures 5.5.

5.5 An Analogous Sample: QSO2s

5.5.1 Overview of selection of samples to include

As a comparative and complementary sample, we use a combination of:

- The SDSS-selected sample of Type 2 quasars from Reyes et al. (2008). These are sources that are high luminosity ($L_{\rm bol} > 10^{45}$ erg s^{-1}), show a significant [O III]λ5007 line, and are obscured (Reyes et al., 2008).
- A later, but similar, sample from Yuan et al. (2016) selecting QSO2s from both SDSS and BOSS spectroscopy.

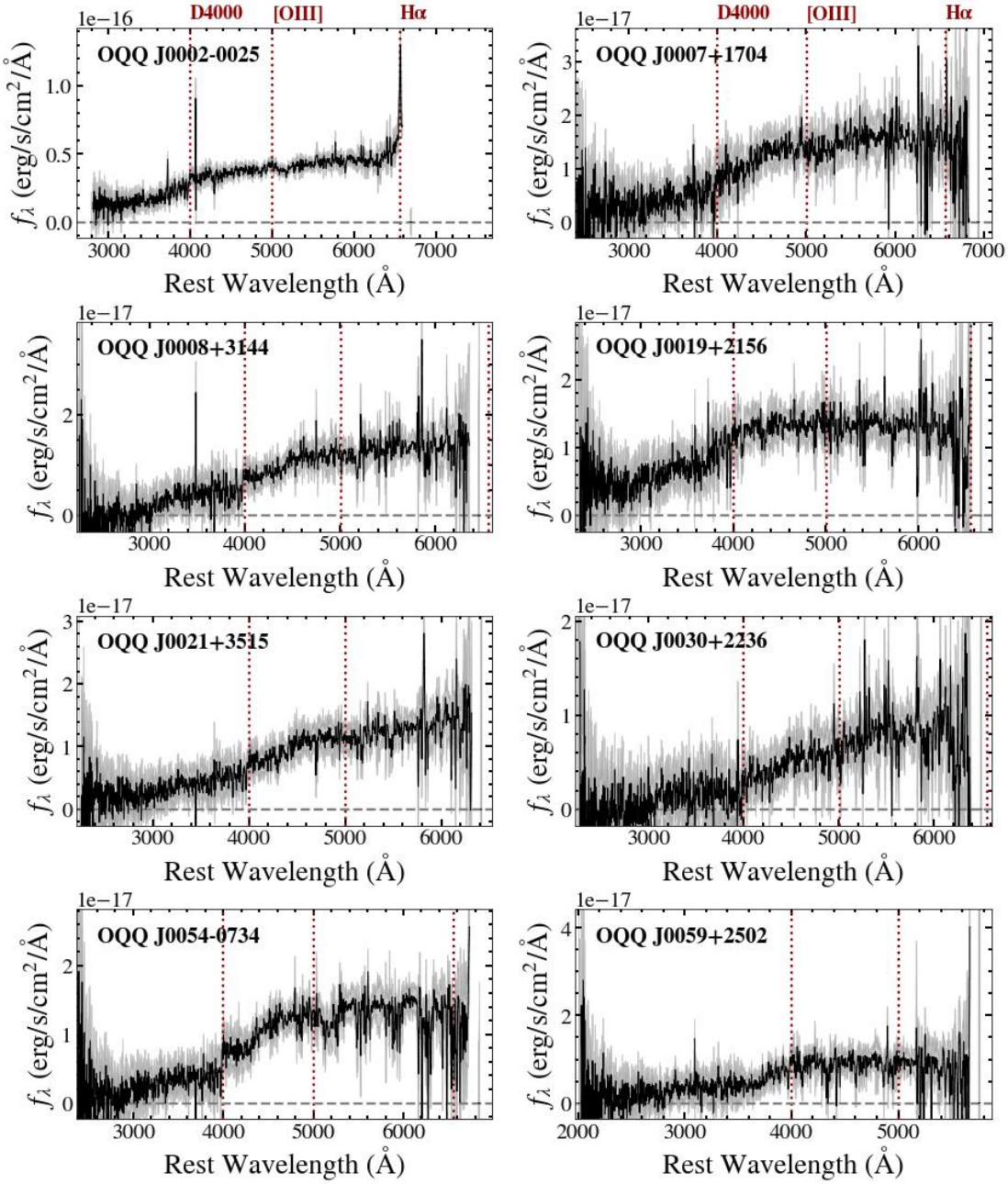

FIGURE 5.5: SDSS spectra of the first eight OQQs by RA. The remainder are available in Appendix D.

TABLE 5.3: Basic information about the first half of the OQQs from the 64 that passed the selection tests. Column details: (1) short object name; (2),(3) sky position; (4) redshift; (5) rest frame 12 µm luminosity interpolated from *W*3 and *W*4 luminosities; (6) rest frame 5100 Å luminosity; (7) 4000 Å break; (8), (9) [O III], H α luminosity upper limits; (10), (11) A_V derived from different emission line luminosities; (12), (13) N_H, derived from A_V.

Name (1)	RA (J2000) (2)	DEC (J2000) (3)	z (4)	L_{12} / log erg s^{-1} (5)	L_{5100} / log erg s^{-1} (6)	D4000 (7)	[O III]λ5007 (8)	H $\alpha\lambda$6562 (9)	A_V ([O III] derived) (10)	A_V (H α derived) (11)	N_H / log cm^{-2} ([O III] derived) (12)	N_H / log cm^{-2} (H α derived) (13)
OQQ J0002-0025	0.592	-0.432	0.371	44.81 ± 0.02	44.00 ± 0.04	1.32 ± 0.21	<57.28	58.74	5.87	–	22.91	–
OQQ J0007+1704	1.985	17.072	0.490	44.60	43.93 ± 0.15	1.52 ± 0.42	<57.17	57.41	5.58	–	22.89	–
OQQ J0008+3144	2.226	31.749	0.600	44.71 ± 0.10	44.03 ± 0.08	1.71 ± 0.41	–	–	–	–	–	–
OQQ J0019+2156	4.841	21.936	0.556	44.57	43.94 ± 0.15	1.15 ± 0.16	<57.50	<58.26	4.65	2.19	22.81	22.63
OQQ J0021+3515	5.362	35.264	0.618	45.27 ± 0.03	44.00 ± 0.08	1.51 ± 0.27	<56.84	–	8.15	–	23.05	–
OQQ J0030+2236	7.719	22.616	0.599	44.58	43.74 ± 0.14	2.38 ± 2.39	–	–	–	–	–	–
OQQ J0054-0734	13.635	-7.575	0.510	44.58	43.82 ± 0.07	2.04 ± 0.60	–	–	–	–	–	–
OQQ J0059+2502	14.757	25.049	0.802	45.02 ± 0.17	44.21 ± 0.11	1.22 ± 0.21	<56.59	–	8.14	–	23.05	–
OQQ J0101+0731	15.309	7.518	0.563	44.68 ± 0.14	44.40 ± 0.09	1.36 ± 0.14	<57.79	58.57	4.24	–	22.77	–
OQQ J0103-0349	15.792	-3.830	0.507	44.52 ± 0.11	43.69 ± 0.11	1.28 ± 0.28	<57.25	58.64	5.17	–	22.85	–
OQQ J0109+0103	17.379	1.063	0.784	45.24 ± 0.13	44.47 ± 0.05	1.36 ± 0.08	<56.84	–	8.06	–	23.05	–
OQQ J0114+2002	18.622	20.047	0.589	44.61 ± 0.14	44.13 ± 0.08	1.59 ± 0.25	<55.33	–	10.22	–	23.15	–
OQQ J0121+0034	20.278	0.582	0.722	44.91	43.72 ± 1.62	1.76 ± 0.36	<57.76	–	4.91	–	22.83	–
OQQ J0141+1050	25.294	10.835	0.580	44.65 ± 0.11	44.01 ± 0.09	1.52 ± 0.29	<57.36	–	5.21	–	22.86	–
OQQ J0143+0151	25.844	1.859	0.334	44.72 ± 0.02	43.54 ± 0.05	1.42 ± 0.13	<56.66	<57.20	7.16	5.32	22.99	23.01
OQQ J0149+3232	27.464	32.547	0.543	45.15 ± 0.02	44.10 ± 0.09	1.53 ± 0.97	<57.36	<58.38	6.53	3.63	22.95	22.84
OQQ J0151+2540	27.929	25.671	0.661	45.07 ± 0.07	44.13 ± 0.17	1.25 ± 0.13	<56.54	–	8.39	–	23.06	–
OQQ J0217+0224	34.310	2.403	0.482	44.48	43.79 ± 0.07	1.75 ± 0.34	<57.04	<57.58	5.58	3.65	22.89	22.85
OQQ J0231-0351	37.944	-3.859	0.450	44.51 ± 0.05	43.74 ± 0.09	1.41 ± 0.26	–	<57.76	–	3.28	–	22.80
OQQ J0231+0038	37.990	0.648	0.488	45.06 ± 0.03	44.14 ± 0.03	1.51 ± 0.11	<57.21	58.19	6.69	–	22.96	–
OQQ J0237+0448	39.323	4.812	0.647	44.94 ± 0.08	44.07 ± 0.26	1.49 ± 0.18	<57.39	–	5.90	–	22.91	–
OQQ J0745+4301	116.493	43.021	0.517	44.74 ± 0.08	43.83 ± 0.08	1.82 ± 0.52	<56.84	57.74	6.77	–	22.97	–
OQQ J0751+4028	117.913	40.470	0.587	45.12 ± 0.05	44.09 ± 0.06	1.71 ± 0.22	<57.43	–	6.28	–	22.94	–
OQQ J0805+3724	121.404	37.414	0.653	45.14	44.08 ± 0.13	1.65 ± 0.35	<57.45	–	6.28	–	22.94	–
OQQ J0835+4428	128.827	44.482	0.837	45.32	44.04 ± 0.33	1.38 ± 0.26	<57.88	–	5.66	–	22.89	–
OQQ J0853+4533	133.324	45.554	0.776	45.89 ± 0.03	44.30 ± 0.09	1.21 ± 0.16	<58.24	–	6.27	–	22.94	–
OQQ J0911+2949	137.964	29.825	0.446	44.58 ± 0.06	44.36 ± 0.06	1.12 ± nan	<57.65	58.30	4.32	–	22.78	–
OQQ J0926+6347	141.639	63.795	0.556	45.41 ± 0.02	44.32 ± 0.04	1.26 ± 0.09	<57.35	58.16	7.24	–	23.00	–
OQQ J0929+3253	142.306	32.896	0.781	45.05 ± 0.15	44.33 ± 0.06	1.58 ± 0.21	<58.05	–	4.55	–	22.80	–
OQQ J0948+0958	147.132	9.968	0.464	44.69	44.08 ± 0.05	1.35 ± 0.18	<56.63	58.43	7.17	–	22.99	–
OQQ J1015+2638	153.802	26.643	0.478	44.52 ± 0.10	43.88 ± 0.08	1.49 ± 0.25	<57.33	58.07	4.99	–	22.84	–
OQQ J1019+0658	154.881	6.977	0.632	44.92	44.24 ± 0.06	1.39 ± 0.21	<57.46	–	5.70	–	22.89	–

TABLE 5.4: Basic information about the second half of the OQQs from the 64 that passed the selection tests. Column details: (1) short object name; (2),(3) sky position; (4) redshift; (5) rest frame 12 µm luminosity interpolated from *W*3 and *W*4 luminosities; (6) rest frame 5100 Å luminosity; (7) 4000 Å break; (8), (9) [O III], H α luminosity upper limits; (10), (11) A_V derived from different emission line luminosities; (12), (13) N_H, derived from A_V.

Name (1)	RA (J2000) (2)	DEC (J2000) (3)	z (4)	L_{12} / log erg s^{-1} (5)	L_{5100} / log erg s^{-1} (6)	D4000 (7)	[O III]λ5007 (8)	H$\alpha\lambda$6562 (9)	A_V ([O III] derived) (10)	A_V (Hα derived) (11)	log N_H (cm^{-2}; [O III] derived) (12)	log N_H (cm^{-2}; Hα derived) (13)
OQQ J1024+0210	156.191	2.170	0.549	44.59 ± 0.13	43.85 ± 0.09	1.77 ± 0.45	<57.09	<57.90	4.75	2.17	22.82	22.62
OQQ J1051+1857	162.751	18.963	0.617	45.66 ± 0.02	44.06 ± 0.09	1.18 ± 0.23	<57.51	–	6.90	–	22.98	–
OQQ J1051+3241	162.794	32.699	0.932	45.94 ± 0.03	44.54 ± 0.17	1.11 ± 0.08	<57.88	–	6.12	–	22.93	–
OQQ J1116+4938	169.074	49.637	0.561	44.83 ± 0.06	44.12 ± 0.14	1.85 ± 0.42	<57.52	<58.17	5.28	3.19	22.86	22.79
OQQ J1130+1353	172.614	13.894	0.635	44.93 ± 0.07	44.41 ± 0.05	1.04 ± 0.06	<57.15	–	6.41	–	22.95	–
OQQ J1156+0901	179.014	9.031	0.635	45.00	44.20 ± 0.07	1.23 ± 0.15	<57.53	–	5.56	–	22.88	–
OQQ J1156+3913	179.031	39.232	0.501	44.54 ± 0.09	43.81 ± 0.10	1.56 ± 0.39	<56.69	<57.69	6.66	3.60	22.96	22.84
OQQ J1208+1159	182.155	11.994	0.369	44.77 ± 0.03	44.54 ± 0.03	1.08 ± 0.04	<58.38	<58.45	5.03	4.35	22.84	22.92
OQQ J1242+5124	190.621	51.400	0.524	44.59 ± 0.10	43.99 ± 0.07	1.39 ± 0.19	<57.52	57.92	4.86	–	22.83	–
OQQ J1306+4028	196.613	40.472	0.582	45.38 ± 0.02	44.07 ± 0.13	1.44 ± 0.27	<57.62	–	6.14	–	22.93	–
OQQ J1320+5816	200.131	58.278	0.714	44.99 ± 0.08	44.17 ± 0.09	1.46 ± 0.18	<57.59	–	5.79	–	22.90	–
OQQ J1321+0402	200.294	4.047	0.648	44.75	43.83 ± 0.47	1.25 ± 0.11	<57.56	–	4.73	–	22.81	–
OQQ J1346+4639	206.582	46.654	0.522	44.59 ± 0.06	43.78 ± 0.15	1.73 ± 0.60	<57.93	58.50	4.50	–	22.79	–
OQQ J1356+0801	209.026	8.017	0.736	44.75	44.31 ± 0.10	1.24 ± 0.12	–	–	–	–	–	–
OQQ J1412+1750	213.181	17.849	0.444	44.64 ± 0.04	43.88 ± 0.08	1.85 ± nan	<54.71	–	11.09	–	23.18	–
OQQ J1417+1247	214.286	12.794	0.608	44.88 ± 0.07	44.15 ± 0.11	1.30 ± 0.18	<57.48	–	5.24	–	22.86	–
OQQ J1435+5844	218.894	58.738	0.638	44.68	44.20 ± 0.47	1.18 ± 0.13	<57.93	–	3.98	–	22.74	–
OQQ J1443+3955	220.869	39.929	0.817	44.90 ± 0.16	44.30 ± 0.09	1.11 ± 0.11	<57.22	–	4.83	–	22.82	–
OQQ J1454+1440	223.732	14.673	0.577	45.63 ± 0.02	44.15 ± 0.05	1.31 ± 0.14	<57.25	–	7.42	–	23.01	–
OQQ J1507+5932	226.885	59.550	0.620	44.90 ± 0.06	43.99 ± 0.09	1.34 ± 0.52	<57.21	–	5.65	–	22.89	–
OQQ J1526+5603	231.723	56.066	0.495	44.52 ± 0.06	43.98 ± 0.09	1.42 ± 0.22	<55.88	–	9.30	–	23.11	–
OQQ J1538+2911	234.691	29.193	0.477	44.58 ± 0.05	43.84 ± 0.12	1.66 ± 0.37	–	<57.70	–	3.86	–	22.87
OQQ J1540+4640	235.193	46.667	0.573	44.98 ± 0.03	43.99 ± 0.09	1.33 ± 0.22	<57.58	<58.77	5.61	2.22	22.89	22.63
OQQ J1611+2247	242.864	22.787	0.809	44.98 ± 0.20	44.38 ± 0.11	1.18 ± 0.14	<57.68	–	4.71	–	22.81	–
OQQ J1611+2115	242.985	21.266	0.654	45.16 ± 0.05	44.07 ± 0.97	1.19 ± 0.10	<58.16	–	5.22	–	22.86	–
OQQ J1616+1802	244.070	18.045	0.528	44.62	43.85 ± 0.10	1.59 ± 0.28	<57.67	58.65	5.41	–	22.87	–
OQQ J1617+0854	244.340	8.901	0.555	44.71	44.17 ± 0.08	1.67 ± 0.28	<56.00	<58.15	8.22	2.35	23.05	22.65
OQQ J1626+5049	246.532	50.817	0.522	44.57 ± 0.05	43.48 ± 0.25	1.35 ± 0.37	<56.42	<57.52	7.55	4.24	23.02	22.91
OQQ J1629+4303	247.271	43.058	0.644	44.99 ± 0.07	44.31 ± 0.09	1.22 ± 0.08	–	–	–	–	–	–
OQQ J2209+3044	332.427	30.734	0.482	44.68 ± 0.06	43.87 ± 0.06	1.58 ± 0.26	<57.05	58.01	5.99	–	22.92	–
OQQ J2229+2351	337.440	23.853	0.427	44.64 ± 0.04	44.00 ± 0.10	1.57 ± nan	<57.19	58.42	5.93	–	22.91	–
OQQ J2244+0409	341.184	4.164	0.495	44.62	43.97 ± 0.08	1.68 ± 0.31	–	–	–	–	–	–

These objects provide a valuable counterpoint to our selection, which will also be based on high luminosity, but with no detectable [O III]λ5007 flux. We combine the two tables, removing any duplicates. A small minority of sources were selected by Yuan et al. (2016) as having the wrong redshift fit by SDSS, and their corrected redshift is used in the processing. These are flagged in the table.

The same luminosity cuts as outlined below are applied to the combined catalogue to produce the final comparison set. The sample includes only objects at $z<1.06$; the region where [O III] can be detected in BOSS.

5.6 How do these Populations Compare?

This part of this chapter will go into detail on the properties of the OQQ sample, describing their appearance - spectroscopically and photometrically, and across all available wavebands. I will also include SED fitting where the data allows a good fit to be produced.

5.6.1 Distribution Comparison

The sources span a range in redshift of $0.33 \leq z \leq 0.94$ (see Figure 5.6). No sources show significant [O III]λ5007 lines, by selection, but other low level emission lines are present in several cases.

Figure 5.6 (top left) shows the relationship between 12 µm luminosity and redshift for the OQQ sample and the QSO2 comparison set. There are no OQQs brighter than all the QSOs, but a higher proportion of OQQs appear to sit at higher luminosities.

Figure 5.6 (bottom) shows the redshift distribution of both the OQQ sample and the QSO2 comparison sample. The K-S statistic comparing the OQQ and QSO2 distributions is 0.073 for L12 and 0.209 for redshift, with p-values 0.874 for L12, and 0.007 for redshift. These results indicate that the samples are likely to come from populations with the same distribution in terms of luminosity, but with a different distribution in redshift. This does not invalidate their use as physical counterpart objects, but may have implications for any detailed analysis of evolution over time.

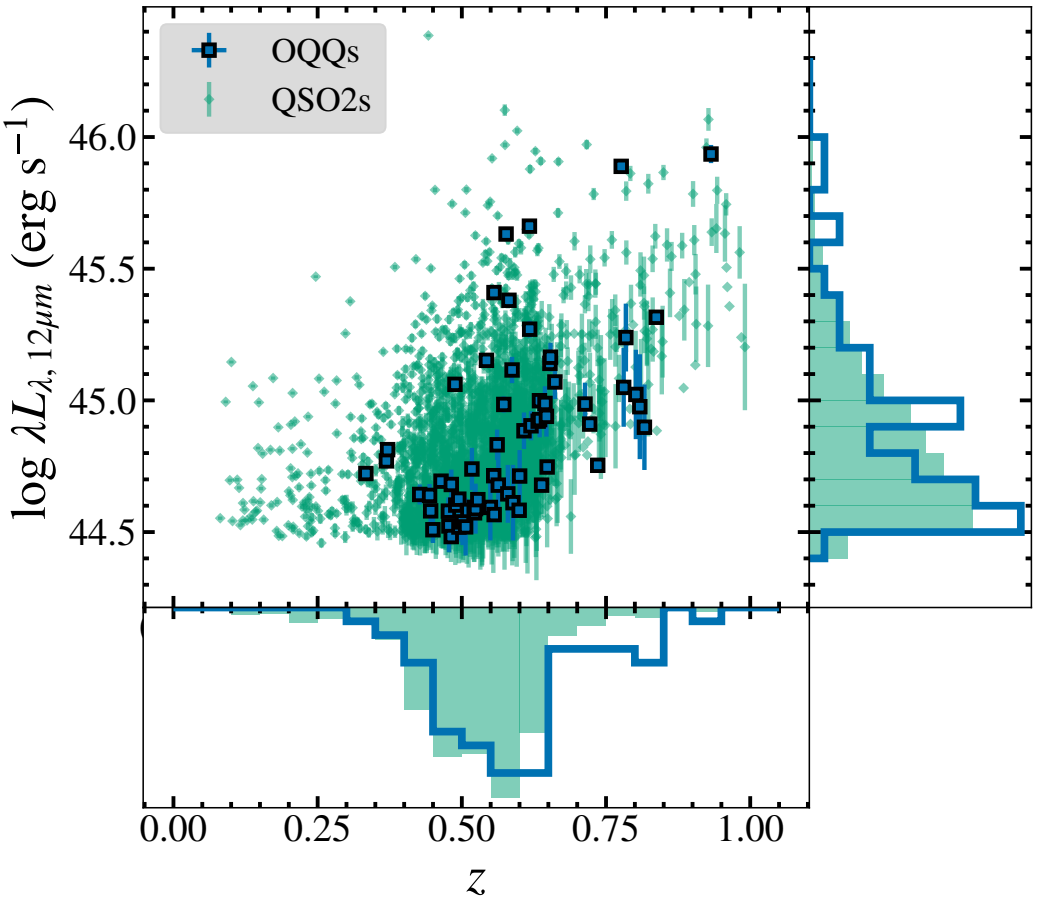

FIGURE 5.6: The 12 µm luminosity and redshift distribution of the OQQ sample and the QSO2s.

5.7 Spectroscopic Properties

5.7.1 Continuum Properties

Fig. 5.7 compares the *WISE* and SDSS luminosities of the sources. For each source, we plot the monochromatic 12 µm and 5100 Å observed (i.e., not intrinsic) rest-frame luminosities (in λL_λ). As we assume that OQQs are obscured and thus their accretion disc is not directly visible, the optical luminosity will be dominated by galaxy emission.

The same figure also includes QSO2s: as already mentioned, QSO2s are likely to be a complementary sample to OQQs. All QSO2s with a *WISE* counterpart and MIR luminosity $L_{12\mu m} > 3 \times 10^{44}$ erg s^{-1} are included (as described in Section 5.5), mimicking our selection strategy, and resulting in a sample of 1,990 QSO2s. The OQQ sample is reasonably well-matched to the sample of QSO2s: at 5100 Å the average luminosity of the QSOs is slightly dimmer, and the same (to a lesser extent) at 12 µm.

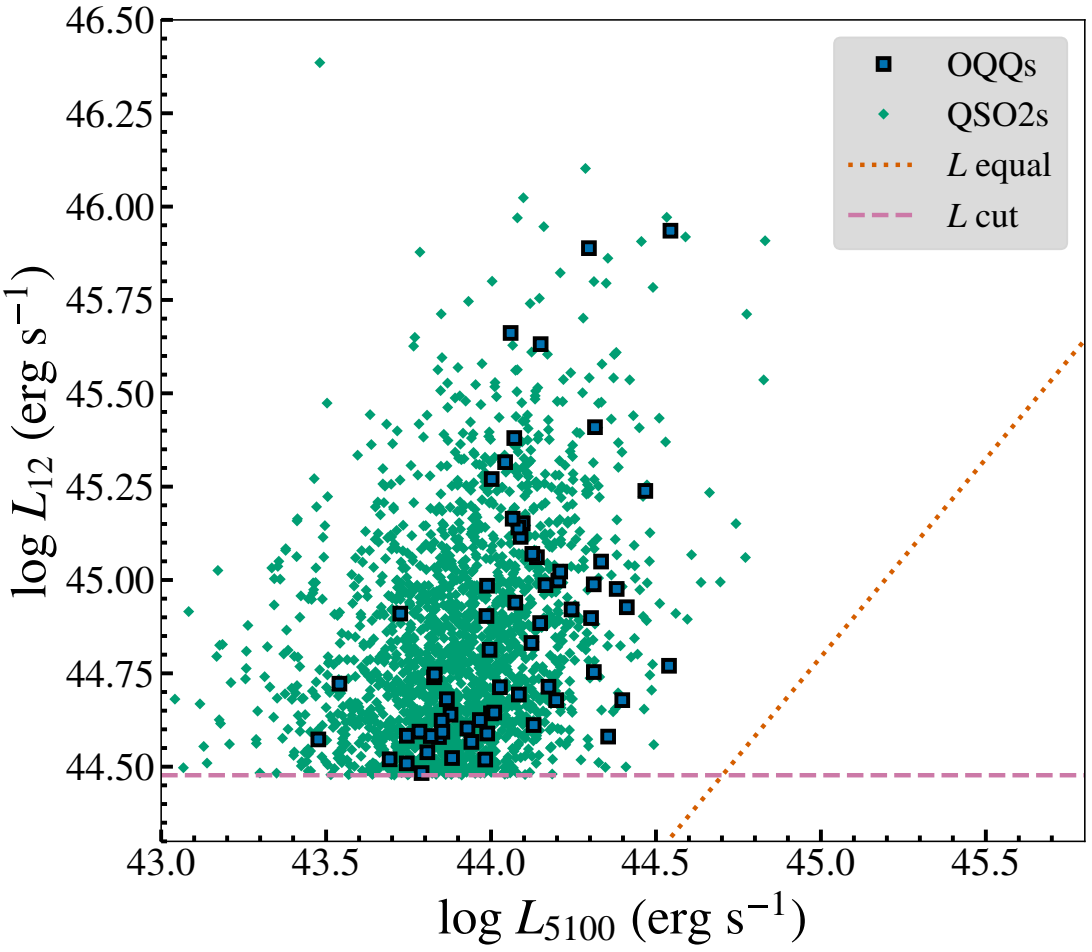

FIGURE 5.7: Comparison of *WISE*, SDSS and bolometric luminosities. OQQs are represented by outlined blue squares, and QSO2s by small green diamonds. Our luminosity threshold is shown by a horizontal dashed line. The dotted line represents where we would expect the points to lie if the IR and optical luminosities were equal.

5.7.2 4000 Å break

The 4000 Å break (D4000 from this point on), an indicator of a significant population of old stars, was calculated as described in Balogh et al. (1999), as the ratio between red (4000 Å - 4100 Å) and blue (3850 Å - 3950 Å) continuum fluxes. A large 4000 Å break could be indicative of significant host galaxy light dilution. The ranges used here are slightly more restrictive than in previous works, as this was found to improve on the repeatability of D4000 between separate measurements, and shows less sensitivity to reddening. The values are found in Tables 5.3 and 5.4: 61 out of 64 (95%) objects have a significant D4000. The median value is 1.42 (including only the significant breaks, defined as >3 standard deviations above unity). The QSO2 sample found only 114/377 (30%) had a significant D4000. The difference can be seen in Figure 5.8.

In considering the implications of the scale of D4000 in the OQQs, it is also informative to place them into context with more general galaxies and QSOs. Figure 5.9 shows the

OQQ with SDSS sources separated according to their classification in `galSpecIndex`[7]. We compare with three categories: (a) QSOs, (b) galaxies, (c) starforming. The starforming group is a subset of both other categories, and contains sources with `SUBCLASS` equal to '`STARBURST`', '`STARFORMING`' or '`BROADLINE`' versions of either. OQQ D4000 values cover a range, but are generally higher than the average QSO or starforming galaxy, and lower than the bulk of general galaxies. The distributions are broad for each category, and although the OQQ values are generally consistent with a dead, inactive galaxy population, they are not a significant departure from the starforming population.

D4000 is generally assumed to be reasonably insensitive to effects from dust attenuation, but this is not perfectly true. The definition of D4000 adopted in this work (from Balogh et al., 1999) uses a shorter range of wavelengths than previous works, which partially improves the effects of dust. MacArthur (2005) examine susceptibility for several absorption based galaxy indices including D4000, and find that large attenuation effects can be seen, particularly for older populations. There is no simple correction for this, and thus we do not make an attempt with the OQQs. Therefore, the exact D4000 values should be considered an indicator of the stellar population and not a specific measure.

5.7.3 Emission Line Properties

Fig. 5.10 compares the 3σ limits on the [O III] line luminosity with the observed MIR power. The dashed line denotes the relation $L_{[\mathrm{O\,III}]} = 4 \times 10^{-5}\, L_{12\mu\mathrm{m}}$, which is the median ratio of the [O III] limits to the 12 µm detections for the OQQs. The plot shows that our sources have a similar MIR luminosity distribution as QSO2s above the selection threshold of $L_{12} > 3 \times 10^{44}\,\mathrm{erg\,s^{-1}}$. On the other hand, the $L_{[\mathrm{O\,III}]}$ limits of OQQs clearly lie much below the corresponding typical line detections for QSO2s.

In the following steps, we fit lines to the OQQ and QSO2 populations, in order to estimate the reddening effect of the obscuring material, on average rather than individual source level. This line should not be taken as an indication of a relationship between the two properties - as we are only fitting upper limits it will be heavily effected by e.g., level of obscuration, intrinsic luminosity of the source. For this reason we have not made any special considerations in the fitting method for the fact that these are upper limits.

A simple linear fit to the relation between $L_{[\mathrm{O\,III}]}$ and $L_{12\mu\mathrm{m}}$ (in log space) for QSO2s gives us the equation:

[7] This SDSS processed table contains derived parameters from MPA-JHU spectroscopic reanalysis. Contains 1,477,411 rows, but is limited to earlier SDSS, not BOSS.

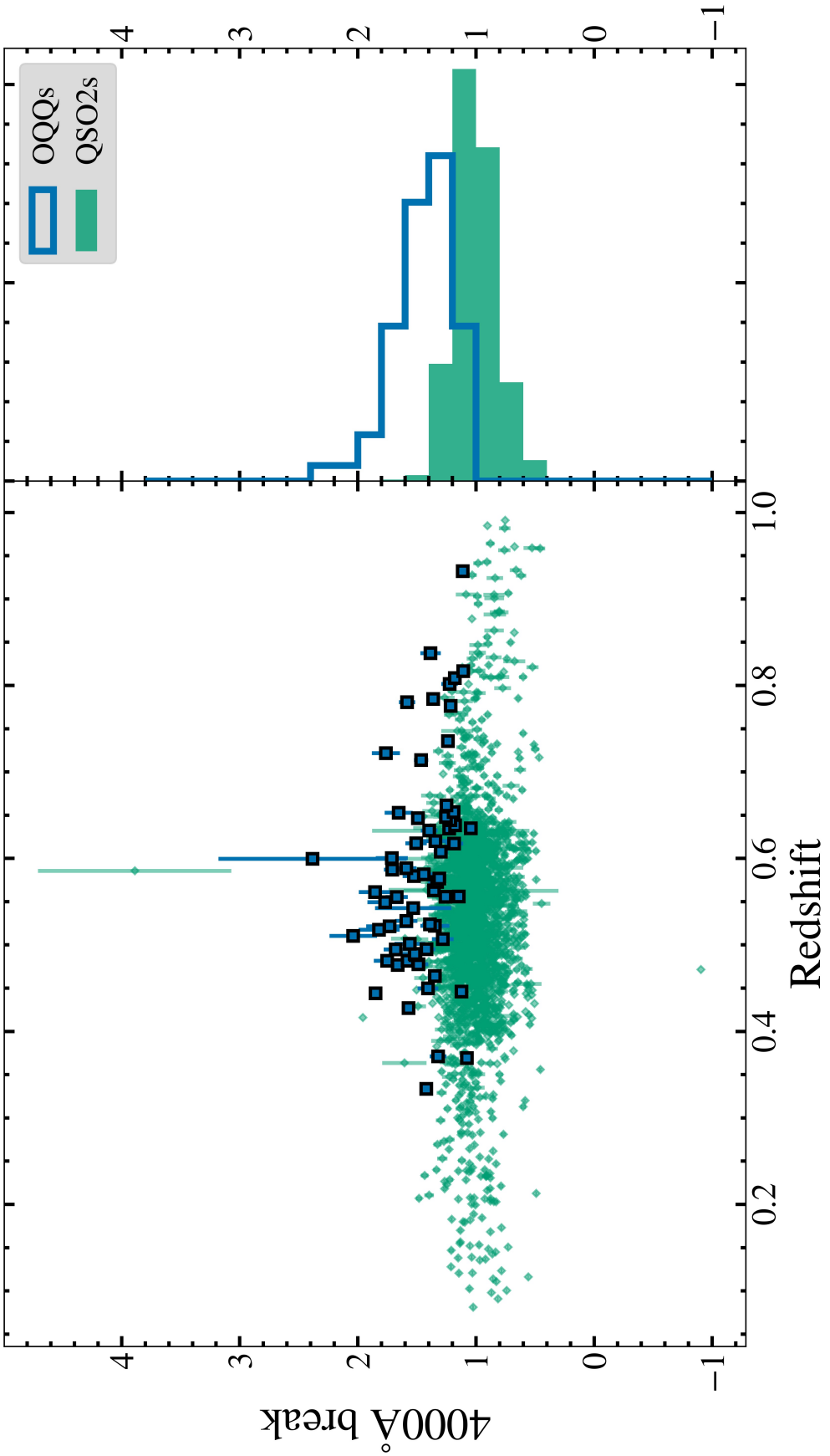

FIGURE 5.8: 4000Å break data. Blue points are the OQQs, with cross markers showing those with D4000 significantly greater than 1. Orange markers are the QSO2 comparison sample. Right panel shows a histogram of the two separate distributions, with systematically higher D4000 values for the OQQs.

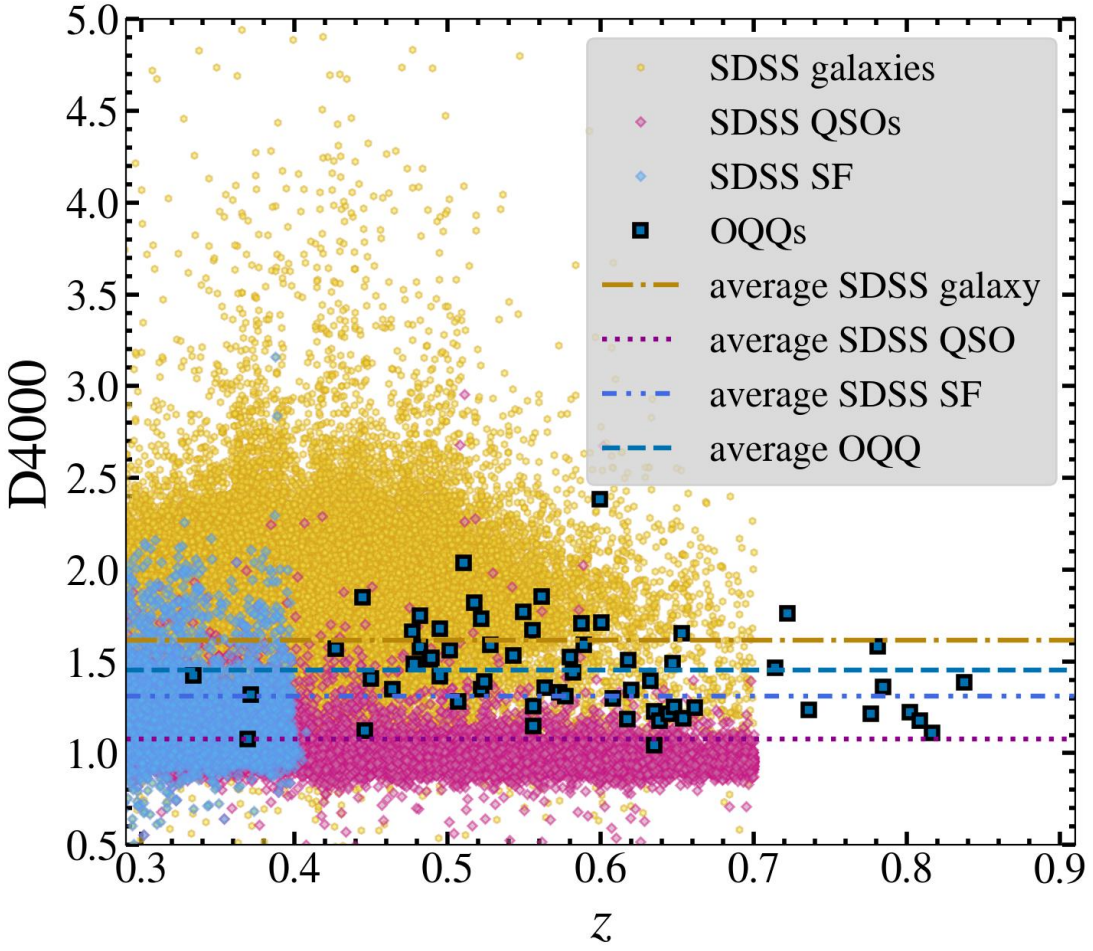

FIGURE 5.9: 4000Å break data. Blue squares are the OQQs, orange markers are SDSS galaxies, and pink diamonds are SDSS QSOs. Horizontal lines show the mean values for each population.

$$\log(\frac{L_{[\mathrm{O\,III}]}}{L_{\odot}}) = (-37.75 \pm 0.13) + (1.04 \pm 0.02)\log(\frac{L_{12}}{\mathrm{erg\,s^{-1}}}) \tag{5.1}$$

This fit is based upon the ordinary least squares bisector method of Isobe et al. (1990). There is significant scatter of 0.11 dex and a Spearman rank correlation coefficient of 0.40 indicates that the relation is not very strong. Nevertheless, this serves as a guide for comparison to OQQs.

The dotted line denotes an [O III] deficit of $\sim$1197 $\times$ from the above fit. This is the mean deficit of our OQQs relative to the expected intrinsic [O III] luminosity if they are typical quasars similar to QSO2s. Since these are upper limits, this should not be considered a true fit to the data, but merely allows us to estimate the scale of obscuration present. The actual deficits could be much larger, and potentially show a different relationship to 12 µm luminosity.

One can perform a similar comparison using the Hα emission line, as it is less affected by reddening. The result is shown in Fig. 5.11.

The corresponding relation for QSO2s is

$$\log(\frac{L_{H\alpha}}{\mathrm{erg\,s^{-1}}}) = (-10.44 \pm 2.30) + (1.18 \pm 0.29)\log(\frac{L_{12}}{\mathrm{erg\,s^{-1}}}) \tag{5.2}$$

QSO2 [O III]λ5007 fluxes from the source papers (Reyes et al., 2008, Yuan et al., 2016) were used, but H$\alpha\lambda$6562 were drawn from the `emissionLinesPort` table. Since we are only using the QSO2 sample for comparison, we did not perform our own Hα line flux measurements. Above $z \approx 0.35$, when redshifted Hα is shifted to $\gtrsim 9000$ Å, the sky background noise can often render lines difficult for the pipeline to measure correctly. Therefore, we restricted the QSO2 sample to below this redshift for extracting robust automated Hα fluxes. This results in few QSO2s for the above fit, all of which have a significant Hα detection without having been specifically selected on this line, as one would expect for a standard quasar spectrum. The scatter in this case is 0.10 dex with a Spearman rank correlation coefficient of 0.48.

The OQQs have a median distribution (either a detection or a limit) consistent with an Hα deficit of ≈ 27. This is less than the deficit found from [O III] partly because of the lower reddening affecting Hα, and partly because redshifted Hα typically lies in the reddest portions of the spectra with strong noise from sky emission lines resulting in less sensitive non-detection flux limits. However, Hα is a significantly less clean tracer of AGN activity than [O III] as it can be produced by star formation. A reasonable conclusion could be that detected Hα in OQQs is predominantly from SF - with extensive photometry that would allow us to obtain reliable SED-based star formation rates for a large fraction of the OQQs detangling the relative contributions of Hα could provide information on the reddening of the OQQs.

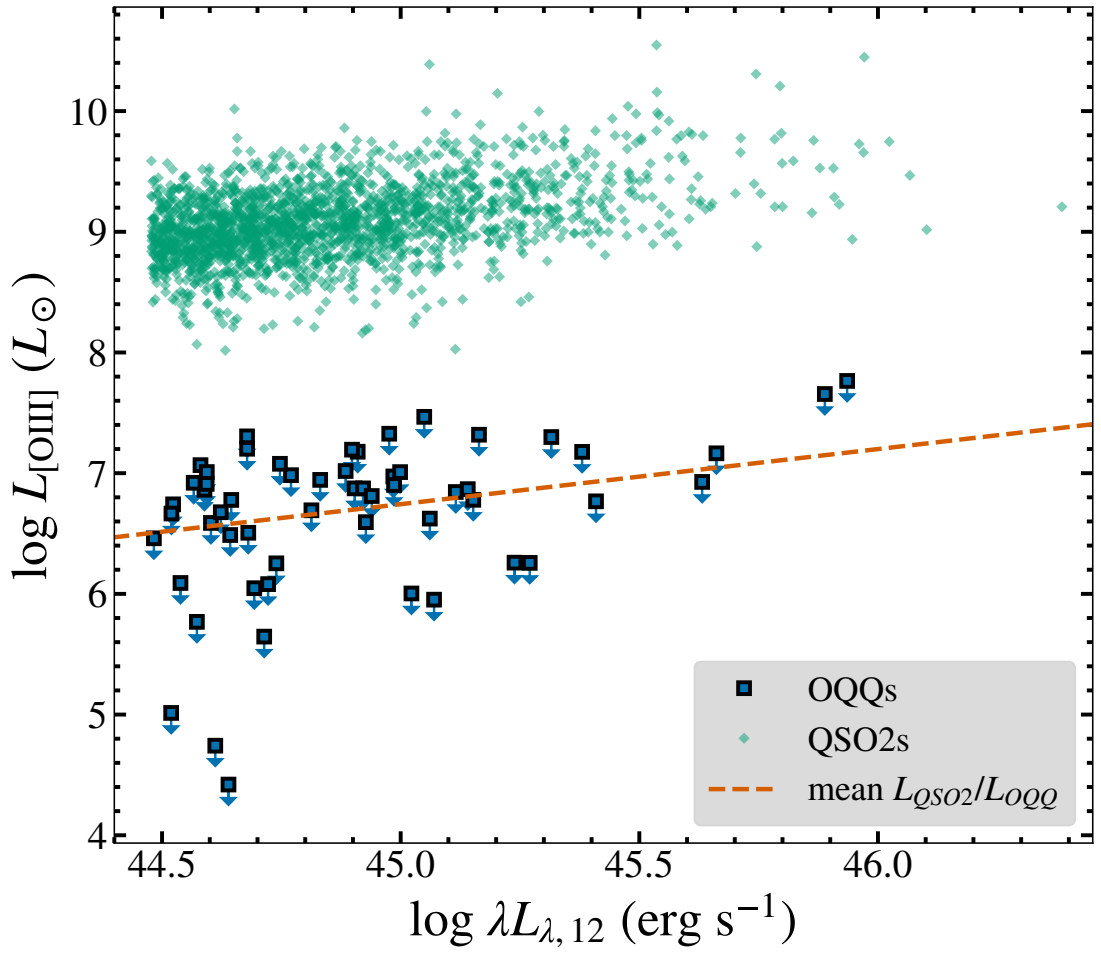

FIGURE 5.10: A comparison of the 3σ upper limits on the [O III]λ5007 luminosity of the OQQs (large outlined blue square markers) and of the QSO2 sample (small green diamond markers), and their respective 12 µm luminosities. The dashed line assumes that the slope of the relationship is the same for the OQQs as for the QSO2s, but applies the average [O III] deficit.

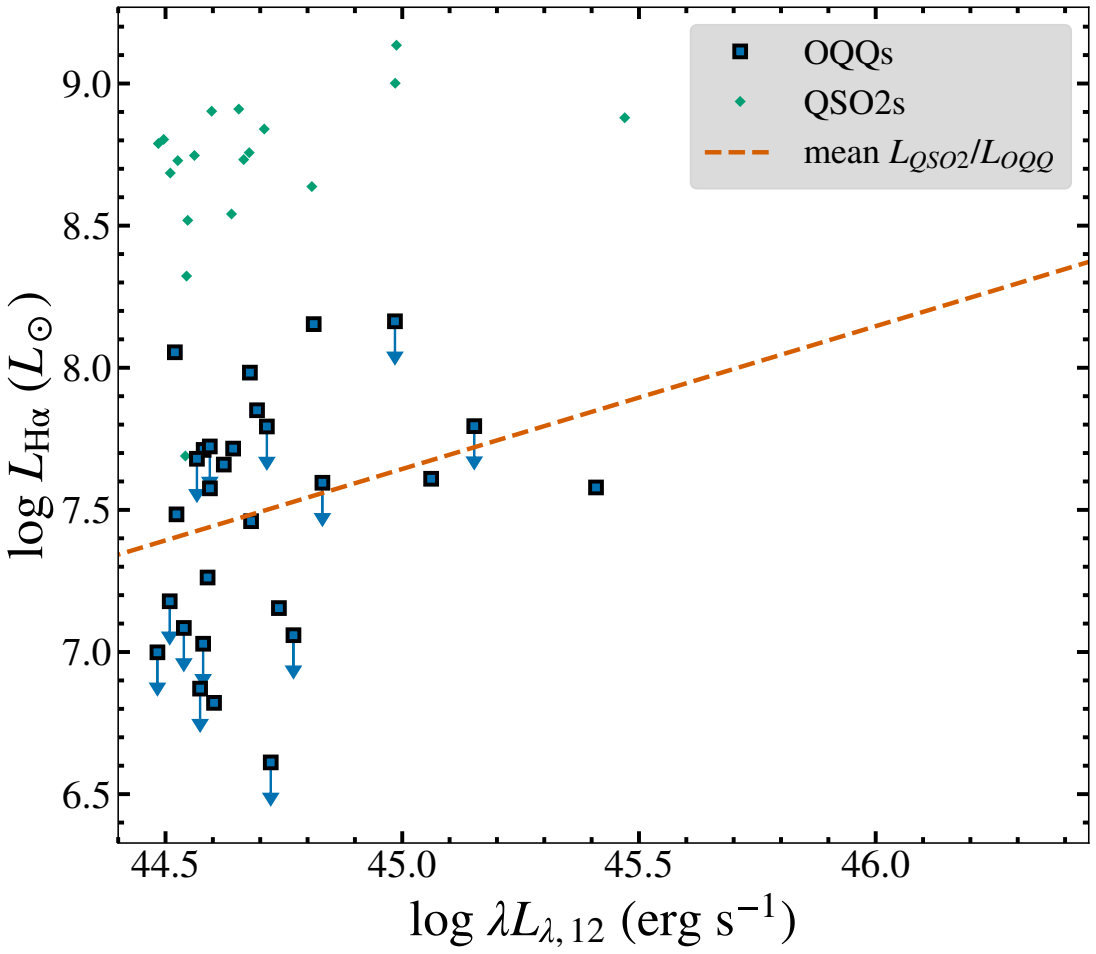

FIGURE 5.11: A comparison of the H$\alpha\lambda$6562 luminosity (or its upper limit - out of the sample of 64 OQQs, 15 have detected Hα emission lines, and 13 more have upper limits), with OQQs (large blue markers) and QSO2s (small orange markers), and their respective 12 µm luminosities (for those objects where H$\alpha\lambda$6562 is not redshifted out of the SDSS range). The dashed line assumes that the slope of the relationship is the same for the OQQs as for the QSO2s, but applies the average Hα deficit.

5.7.4 Optical Reddening

(Non)detection of emission lines can be used to place constraints on the optical depth of the theoretical cocoons, if present (see Section 5.12). We assume that the QSO2s have low extinction to their NLRs (an approximation), and that therefore the relationship between 12 μm and [O III] luminosity (H α luminosity; equations 5.1 and 5.2 above) can be used to predict the approximate intrinsic flux of a cocooned source at the same 12 μm luminosity (assuming that all OQQs had [O III] signals at the upper limit of detection. The extinction A_V can be calculated using this predicted flux, the actual measured flux, and the standard Milky Way extinction law of Cardelli et al. (1989) with an $R_V = 3.1$[8]. The resultant values of the extinction A_V as derived from the two lines are listed in Tables 5.3 and 5.4. Since QSO2s are also likely to suffer mild NLR extinction (Reyes et al. 2008), these should be regarded as lower limits on the true A_V. The A_V limits measured from the [O III] non-detections range over 3.4–10.5 mag, with a median value of 4.69.

What would be the corresponding column density of gas for this extinction? A factor of 100 deficit in [O III] does not need extreme columns. Our median extinction $A_V = 4.69$ mag is equivalent to a neutral gas column of $N_H^{\perp} \sim 7 \times 10^{22}$ assuming the gas–to–dust ratios found in AGN environments by Maiolino et al. (2001) - a relationship corresponding to $N_H \approx 10^{22.2} A_V$ The parameter $N_H^{\perp}$ is used to denote the fact that these gas columns are relevant for the NLR, which is likely to probe angles out of the direct l.o.s., thus making the distinction from the N_H^{los} measured from X-rays in Section 5.9 and Chapter 4. Further speculations on the gas columns or spatial distributions with only one detected object would be premature. The $N_H^{\perp}$ values are lower limits inferred from the limits on the optical extinction, so it is unexpected that the N_H^{los} would be lower.

Figure 5.12 shows the $N_H^{\perp}$ values inferred from [O III] and H α extinction. Where a H α-inferred value is available, the predicted N_H is consistently lower, and as some of these emission lines are measured rather than upper limits, are likely to be closer to the true value. Note that the conversion between N_H and A_V relies on an assumption of gas-to-dust ratio that is highly uncertain, and also that changes in this ratio will vary the effect of the obscuring potential of the material on optical and X-ray emission in different ways.

5.7.5 General Examination of Spectra

In Appendix D the SDSS spectra of the OQQs are presented. By design, these show no [O III], and as shown in Figure 5.11 H α is also generally low, where measurable.

[8] This choice of extinction law, while not usual for AGN, was made for simplicity and will not significantly affect results in the rest-frame optical.

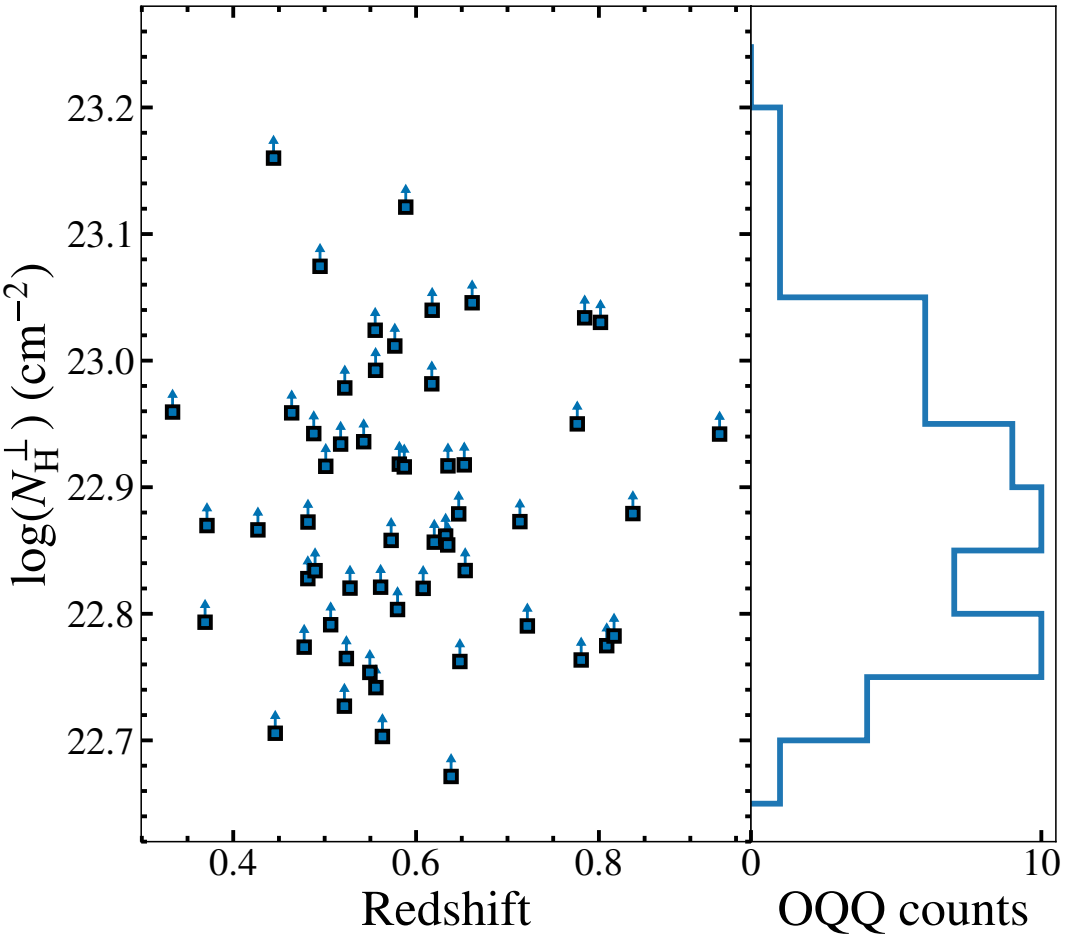

FIGURE 5.12: Inferred $N_H^{\perp}$ values from [O III] (i.e., obscuring the NLR, distinct from the N_H^{los} related to X-ray obscuration).

However, some optical spectra show other indicators of AGN presence and/or other interesting features.

- **Blue continuum shapes**: although any sources with extremely blue spectra were removed in Section 5.2, some remain with a blue upturn beyond the 4000Å break (for example, sources shown in Figure 5.13, top), which may indicate some contribution to the continuum from the accretion disc. This is a small number of sources and are unlikely to represent a major part of the OQQ population, but the combination of continuum shape and lack of emission lines may make these interesting sources.

- **Broad emission lines**: generally emission lines are low level or narrow for the majority of the sample, but there are some exceptions. J0948+0958 in Figure 5.13 (middle) shows broad Hα emission, possibly implying a source with greater velocity dispersion than expected from the galaxy, and likely AGN-related. Hα is present in several more sources but generally less broad. It is outside of the clean

spectroscopic range for a large proportion of the OQQs, making judgement of population properties in this case harder.

- **SF vs. dead galaxy indications**: some SED fitting shows a contribution to MIR luminosities from SF (see Section 4.2.2), but only a small fraction of OQQs have sufficient data to draw reliable conclusions about their properties from these fits. Nevertheless, it implies that not all of the OQQs are dead galaxies with very little star formation, and observed properties of some spectra also lead to this conclusion. Narrow emission lines such as [O II] may indicate a younger stellar population and thus recent or ongoing star formation, and some sources (e.g. sources in Figure 5.13, (bottom)) may show this. A strong 4000 Å break and Ca H and K absorption lines could instead imply an older population (e.g. J1443 in Figure D.6). However, as discussed in Section 5.7.2, this may not be conclusive.

We can conclude from inspection of the spectra (along with other properties) that it is unlikely that OQQs represent a *single intrinsic type*. Rather, it is more likely that they represent multiple classes that, due to obscuration or accretion properties, appear similar in terms of OQQ selection (see Section 5.12). Future work is needed to effectively and conclusively distinguish between intrinsic properties.

5.8 Photometric Properties

5.8.1 Optical (SDSS, PanSTARRS)

From an examination of the morphologies of X-ray–selected optically-dull AGN, Rigby et al. (2006) found that such sources exhibited a wide range of axis ratios as compared to optically-active AGN which showed only very round axis ratios. They conclude that extranuclear dust within the host galaxy is responsible for an optically-dull nature. The OQQ sample has few axis ratios (the ratio of the semi-major and semi-minor axes, as modelled by SDSS in r band) consistent with non-circular (above the uncertainty generated by SDSS). Figure 5.14a shows the SDSS *r*-band axis ratios for the OQQs and the QSO2s. No objects show particularly large axis ratios, nor is there a wide range of values as might be expected for similar X-ray selected objects. On this basis it seems unlikely that large scale mergers would be involved in the production of these objects, but high angular resolution optical/ultraviolet imaging of our sample would be required in order to test whether the lack of optical signatures is due to extranuclear dust (as in Rigby et al. 2006), or a smaller cocoon. Examination of SDSS Petrosian radii (see Figure 5.14b) shows no extremely large objects, in line with OQQs being small, compact galaxies without obvious structure.

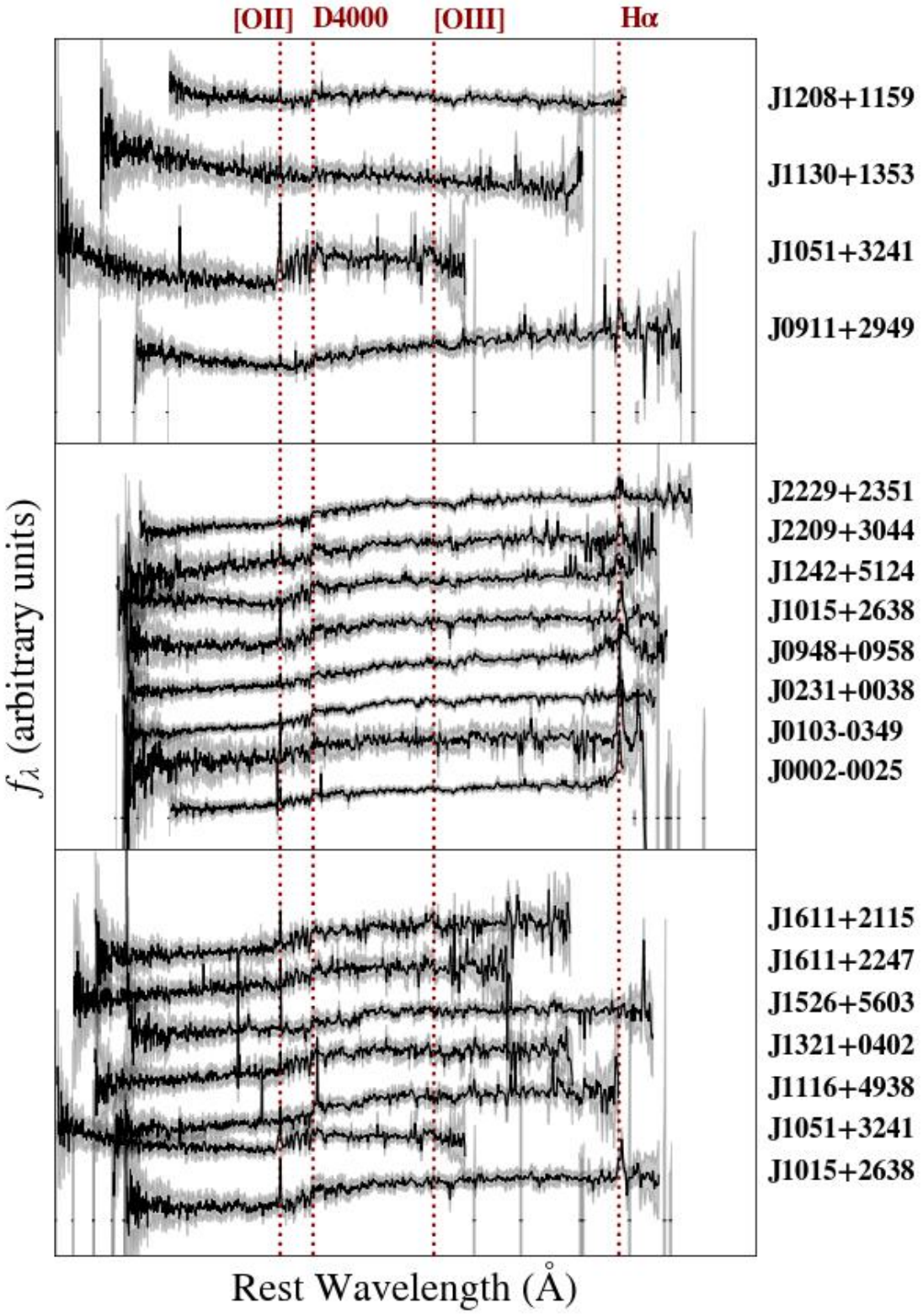

FIGURE 5.13: OQQ spectra showing selected spectra with the following properties: (top) spectra showing blue rises, (middle) spectra showing strong and/or broad Hα emission, (bottom) spectra showing narrow [O II] emission.

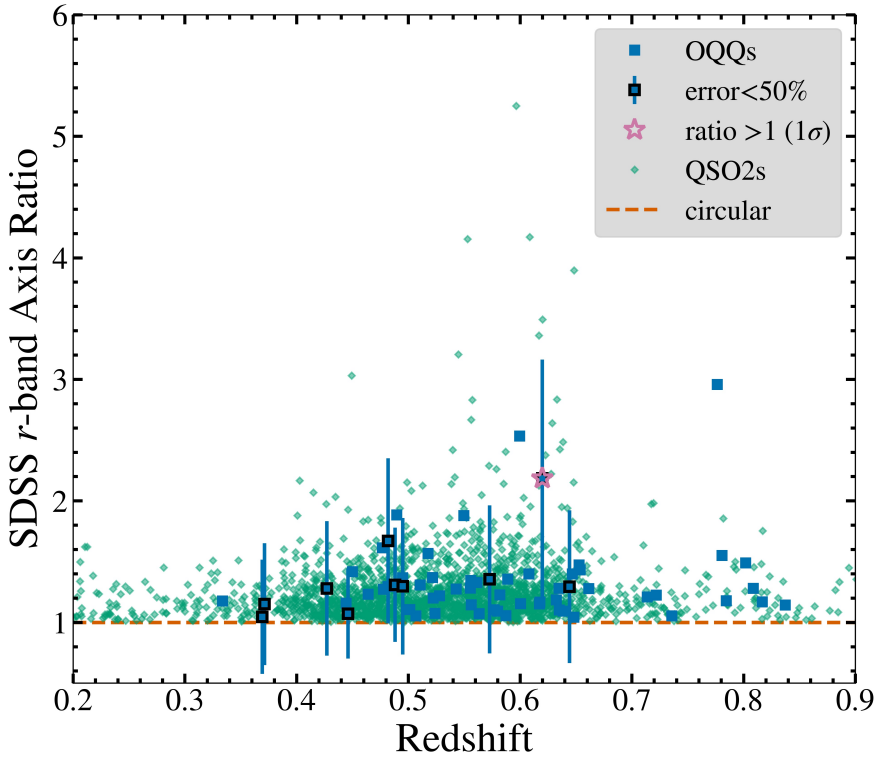

(A) SDSS *r*-band axis ratios (blue circles). Many of the objects have a large error on these values, leaving only 10 with <50 % error (filled in circles). Out of those, one shows an axis ratio greater than 1 (to 1 σ) (pink stars).

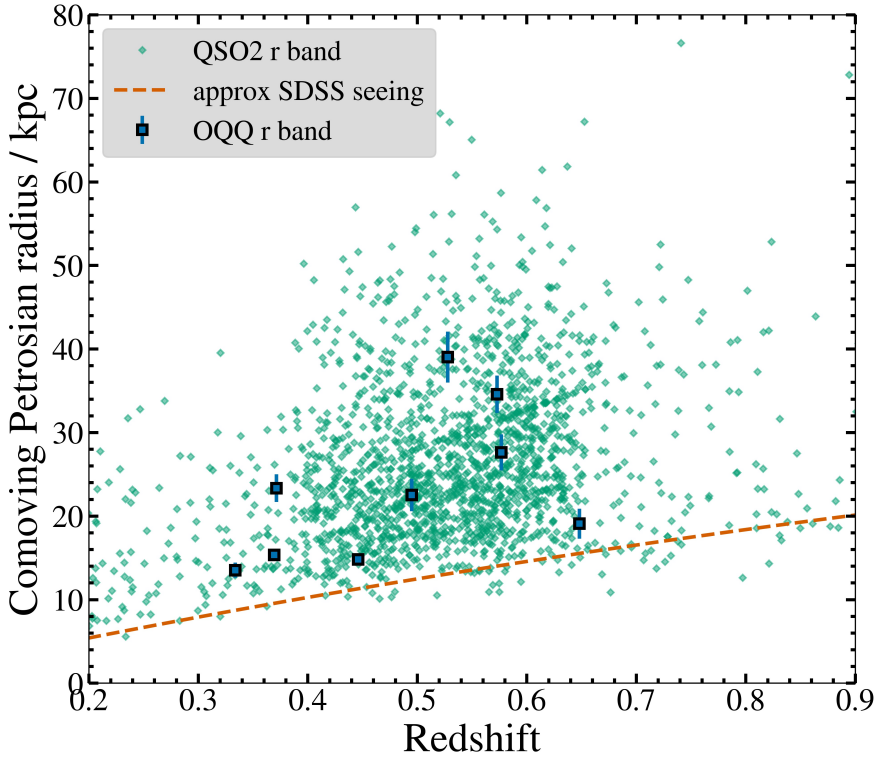

(B) SDSS Petrosian radii converted to comoving size in kpc. SDSS seeing limit is estimated from the median r band seeing limit (1.32″). A limited number of OQQs have radii processed by SDSS.

FIGURE 5.14: SDSS derived properties of OQQ host galaxies: radius and axis ratio.

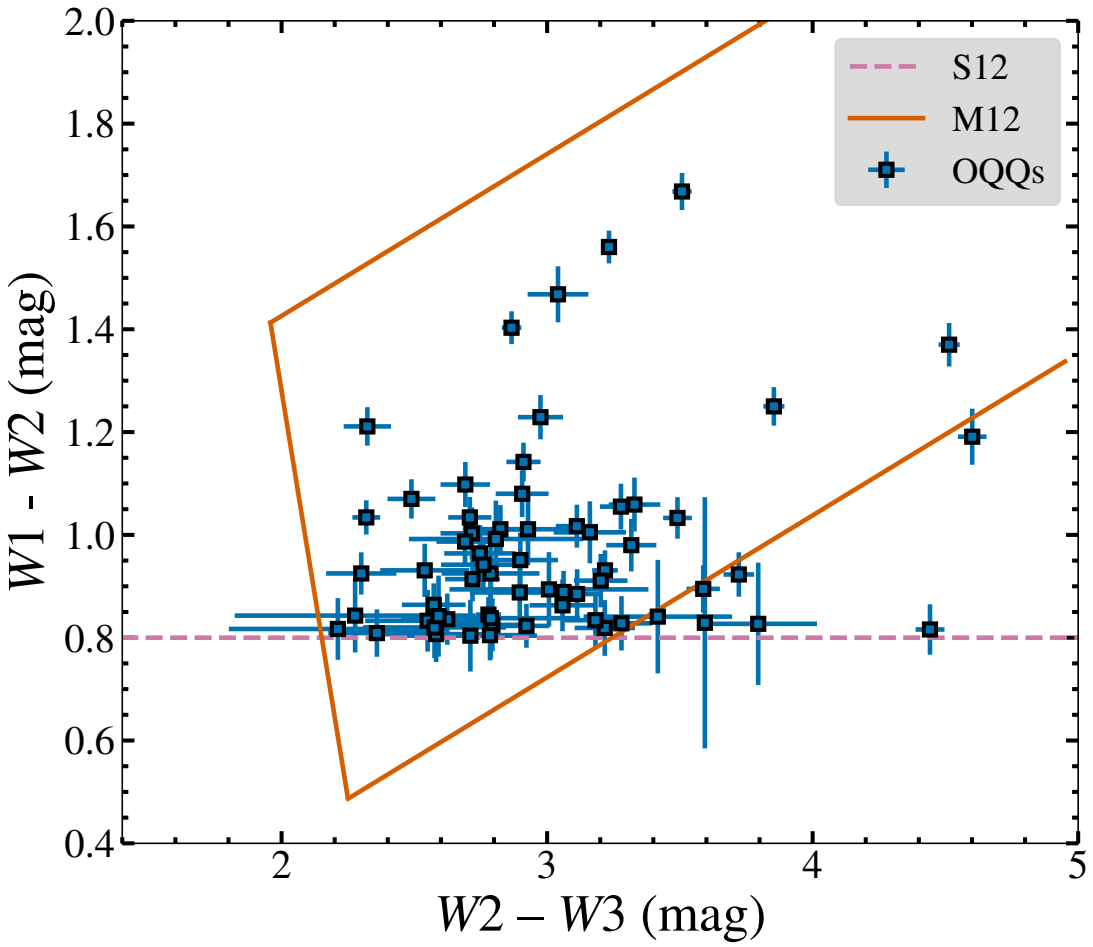

FIGURE 5.15: The *WISE* colours of the OQQ as plotted on the standard colour-colour plane. The dashed line shows the Stern cut (Stern et al., 2012), which all candidates pass by selection. The solid lines are the AGN wedge as proposed by Mateos et al. (2012); most OQQ also pass according to this test.

5.8.2 IR (*WISE*)

With regard to the infrared properties of the sources, the *WISE* colours are plotted in Fig. 5.15 on the canonical *WISE* colour–colour plane. The colours of all sources are consistent with being AGN-dominated in the MIR according to the Stern et al. (2012) colour cut, by selection. In addition, most of the sources also lie within the *WISE* AGN wedge proposed by Mateos et al. (2012).

5.9 X-ray Properties

5.9.1 Serendipitous Observations

In the absence of AGN spectroscopic signatures in the optical and infrared, X-ray observations arguably provide the best evidence for the presence of an AGN. We checked the HEASARC archive[9] for pointed or serendipitous observations by X-ray satellites, and discovered OQQs several observed during targeted observations of other nearby objects. We have also obtained joint *XMM-Newton* and *NuSTAR* (Harrison et al., 2013) data for our prototypical OQQ, and these results are discussed in Section 4.3.

Figure 5.16 shows the results of analysis of data from *XMM-Newton* and *Chandra*, and *Swift*-XRT[10] for OQQ candidates with serendipitous observations - in total 11 separate OQQ.

The *XMM-Newton* mission has one of the best combination of effective area and angular resolution of current X-ray missions, and is therefore an ideal tool to help us analyse the X-ray properties of OQQ. *Chandra*, which has very low background noise, can also be valuable in detecting dim sources. We also examine *Swift-XRT* data - this is generally less sensitive, but in cases where no *XMM-Newton* or *Chandra* data is available can be useful to place limits on the X-ray emission. Figure 5.16 shows the comparison between X-ray and 12 µm luminosity, including the predicted relationship between intrinsic X-ray and nuclear 12 µm luminosity from Asmus et al. (2015) and between X-ray and 6 µm luminosity, (Stern, 2015): for the latter, 6 µm luminosities were converted to 12 µm luminosities using a relationship derived from the QSO template of Hao et al. 2007). The OQQ X-ray luminosities are slightly lower than the relations would predict, but this may be due to the difference between observed and intrinsic IR luminosities - if the OQQs are heavily obscured, their intrinsic luminosities may be higher. The dotted line in Figure 5.16 shows the effect of CT levels of obscuration on the MIR-predicted X-ray luminosities (Asmus et al., 2015, Stern, 2015). This would imply that most OQQs lie somewhere between Compton thick and unobscured. However, if they are intrinsically similar to OQQ J0751+4028 (Chapter 4; Greenwell et al., 2022) the obscuration depth is light ($N_{\rm H}\sim$22), and thus the intrinsic values for the OQQs may be only slightly higher.

For these sources, we extracted source and background spectra using standard FTOOLS tasks and recommended reduction steps, and analysed the data using the `xspec` package (Arnaud, 1996). We then assessed the false detection probability based on counts in the source region relative to counts in a background region, and this derived either estimated fluxes or upper limits for each target.

[9] `heasarc.gsfc.nasa.gov/docs/archive.html`
[10] See Table 5.5a.

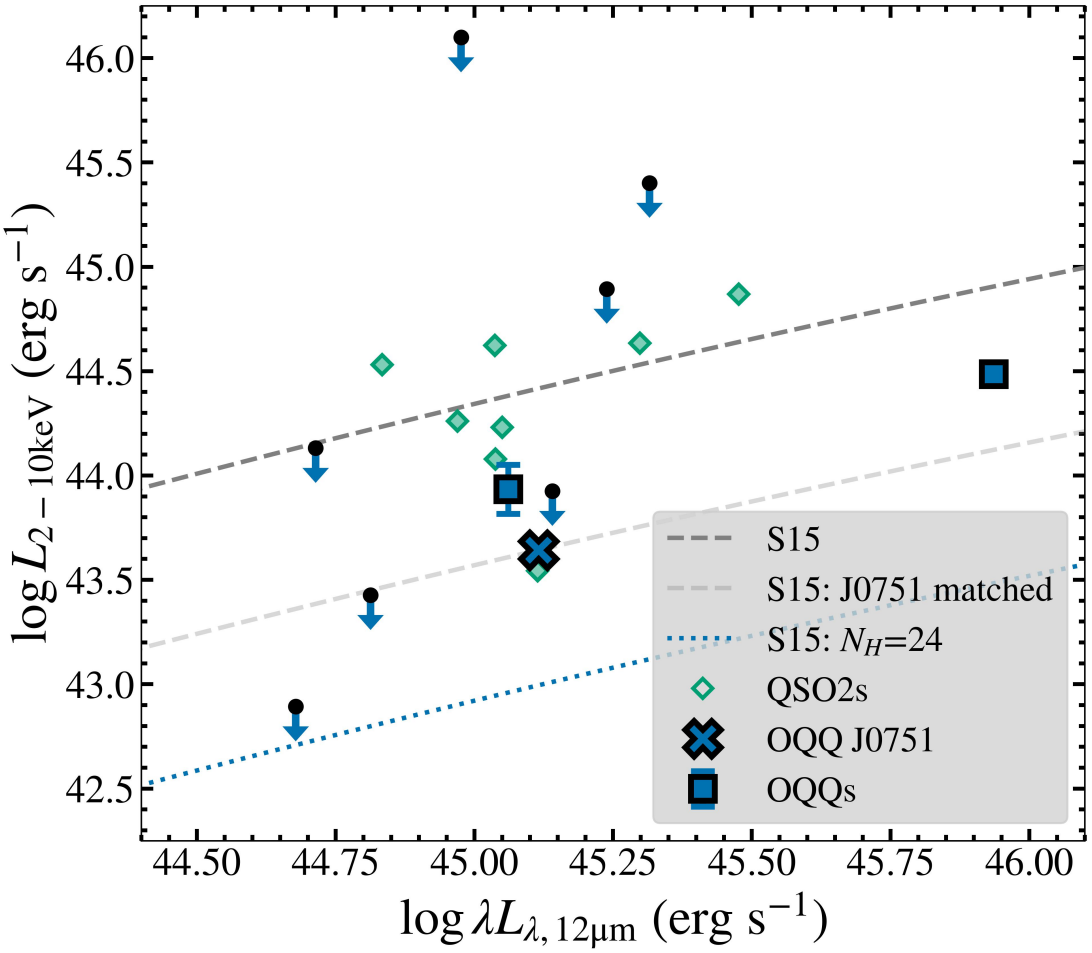

FIGURE 5.16: 2–10 keV luminosities of the OQQs (blue squares for detected sources, and arrows for upper limits) plotted against their 12 µm luminosities. OQQ J0751+4028 is shown as a large cross. For comparison, available QSO2 luminosities are shown as diamonds (see Table 5.5b). We also show MIR predicted values for intrinsic luminosities (dark grey dashed line, S15; Stern, 2015). If this relationship is scaled to the luminosity of J0751 (pale grey dashed line; Greenwell et al., 2022), the other detected OQQs are more consistent with this expectation. Upper limits may be better explained by a Compton thick scenario: dotted blue line shows the obscuration of the S15 relation by Compton thick material.

One serendipitous OQQ had sufficient *XMM-Newton* counts to be analysed further with `xspec`, and for all sources (with the exception of our targeted observation; Chapter 4), we have assumed the same photon index as for this source, and used WebPIMMS[11] to estimate the luminosity of each source, given the net counts (or upper limit) observed.

We find that the detected OQQs are underluminous compared with expectations. If the non-detected OQQs are equally underluminous, they may still be detectable with sufficiently long observations.

[11] `https://heasarc.gsfc.nasa.gov/cgi-bin/Tools/w3pimms/w3pimms.pl`

(A) X-ray observation IDs for OQQs other than J0751 used in Section 5.9.

Name (1)	Instrument (2)	Observation ID(s) (3)
OQQ J0002-0025	*Swift*-XRT	38112001,38112003,38112009,38112002,38112007,38112008,38112005,38112006,38112004
OQQ J0109+0103	*Swift*-XRT	47886001
OQQ J0231+0038	*XMM-Newton*	652400801
OQQ J0805+3724	*Swift*-XRT	282066002,282066001,282066003
OQQ J0835+4428	*Swift*-XRT	87091005
OQQ J1051+3241	*XMM-Newton*	781410101,781410201
OQQ J1435+5844	*XMM-Newton*	601781401,872390901
OQQ J1611+2247	*Chandra*	15679
OQQ J1617+0854	*Swift*-XRT	46227001,46227006,46227004,46227005,46227003

(B) X-ray and [O III] data for QSO2s used in Section 5.9. (a) Vignali et al. (2006), (b) Vignali et al. (2010), (c) Lamastra et al. (2009).

Name (1)	RA (2)	Dec (3)	$\log L_{12\,\mu m}$ erg s^{-1} (4)	$\log L_{2-10\,keV}$ erg s^{-1} (5)	$\log L_{[O\,III]}$ $L_\odot$ erg s^{-1} (6)	$\log N_H$ cm^{-2} (7)	Reference (8)
WISEA J012341.47+004435.8	20.923	0.743	44.83	44.53	9.13	23.16	(b)
WISEA J080154.26+441234.0	120.476	44.209	45.04	44.62	9.58	23.63	(a)
WISEA J081253.10+401859.9	123.221	40.317	45.05	44.23	9.39	22.33	(b)
WISEA J083945.98+384318.9	129.942	38.722	44.97	44.26	9.71	22.52	(c)
WISEA J115314.38+032658.6	178.310	3.450	45.04	44.08	9.61	22.19	(a)
WISEA J122656.47+013124.3	186.735	1.523	45.30	44.63	9.66	22.42	(a)
WISEA J122845.73+005018.8	187.191	0.839	45.11	43.54	9.28	23.18	(b)
WISEA J164131.72+385840.7	250.382	38.978	45.48	44.87	9.92	22.74	(a)

TABLE 5.5: Details of the X-ray observations and references used in Section 5.9.

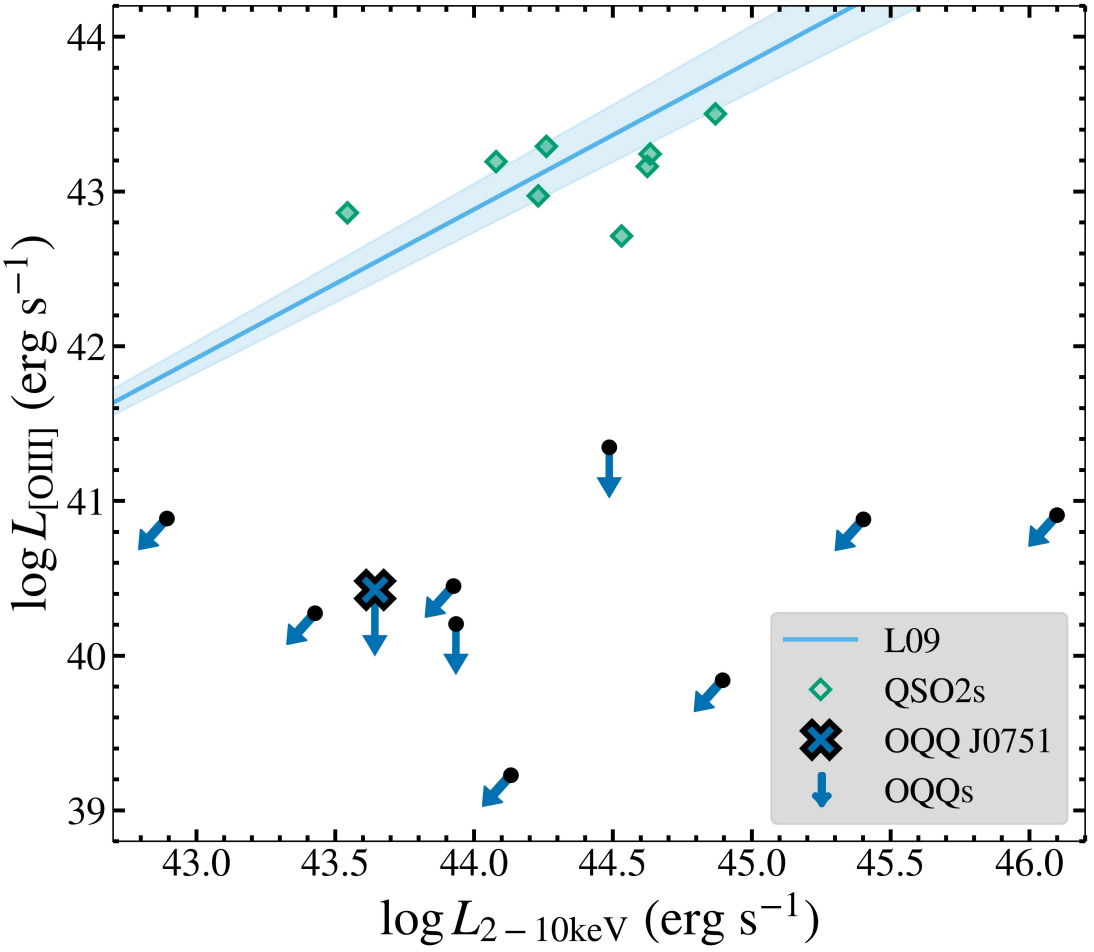

FIGURE 5.17: 2–10 keV luminosities of the OQQs (arrows: X-ray detected sources are upper limits in one dimension, other sources are upper limits in both), plotted against their [O III] upper limit luminosities. OQQ J0751+4028 is shown as a large cross. For comparison, available QSO2 luminosities are shown as diamonds (see Table 5.5b). We also show [O III] predicted values for intrinsic luminosities (dashed line; Lamastra et al., 2009).

5.9.2 Targeted Observations

We obtained targeted observations of our prototypical candidate with the aim of confirming its AGN nature and constraining its properties. Following standard procedure with `xspec` we modelled the source, finding that it is under-luminous at 2–10 keV (compared to IR-predicted intrinsic luminosity), and appears to be lightly obscured ($\sim 10^{22}$ cm^{-2}). Further detail can be found in Chapter 4 and Greenwell et al. (2021).

This analysis uses the following coordinated observations:

- *NuSTAR* OBSID 60701009002: 50.6 ks, 2021 September 25 (start time: 12:06:09)

- *XMM-Newton* OBSID 0884080101: 36.9 ks[12] of exposure, 2021 September 25 (start time: 13:28:37)

We fit several models, starting with an absorbed power law (CABS*ZWABS*POW), moving on to more physically realistic models (MYTORUS, Murphy and Yaqoob, 2009; BNSPHERE, Brightman and Nandra, 2011) and finally a more complex model involving a lightly obscured leak in an otherwise Compton thick sphere of obscuration. Using Bayesian X-ray Analysis (BXA; Buchner et al., 2014) we can compare the results and determine the model most likely to have produced the data. We find that BNSPHERE is favoured - a spherical obscuration model that implies a 'cocooned' obscuring structure may be a plausible explanation for the X-ray appearance of OQQ J0751+4028.

Figure 5.16 shows OQQ J0751+4028 in context with the serendipitous observations and the empirical relationship between 12 µm and intrinsic 2-10 keV luminosity. The unobscured rest frame 2-10 keV luminosity is 4.39 $\times$ 10^{43} erg/s, approximately a factor of 6 lower than expected given the 12 µm luminosity, but sufficient to categorically demonstrate the presence of an AGN. Photon index is harder than usual for an AGN (Γ=$1.32^{+0.21}_{-0.19}$), and obscuration is thin (log ($N_{\rm H}$ / cm^{-2}) = 21.95). If Γ is fixed to a more usual AGN-like value of 1.9, obscuration increased only slightly to log ($N_{\rm H}$ / cm^{-2}) = 22.3 (for details see 4 and Greenwell et al., 2022).

5.10 SED Fitting

5.10.1 `agnfitter` background

We use `agnfitter` (Calistro Rivera et al., 2016) to fit the SED of a selection of OQQs and determine contributions to the observed emission from different components of the AGN/galaxy system. This method uses the multiwavelength data available to find the most likely weighted contributions to the overall SED. The most important parameter for this analysis is the contribution to the SED from the AGN obscuring material. We select the candidates with the best long wavelength data (2MASS, *Herschel*), as this is key to constraining some components. After experimenting with different Markov Chain Monte Carlo (MCMC) lengths, we selected one sufficient to achieve an autocorrelation time indicating convergence for the OQQ AGN-heated dust component (see Foreman-Mackey et al. (2013) & Calistro Rivera et al. (2016) for details)[13].

[12] After cleaning 16.4/28.3/29.3 ks on pn/MOS1/MOS2.
[13] Settings used: 100 walkers; two burn in sets (10,000 steps each); set length 200,000.

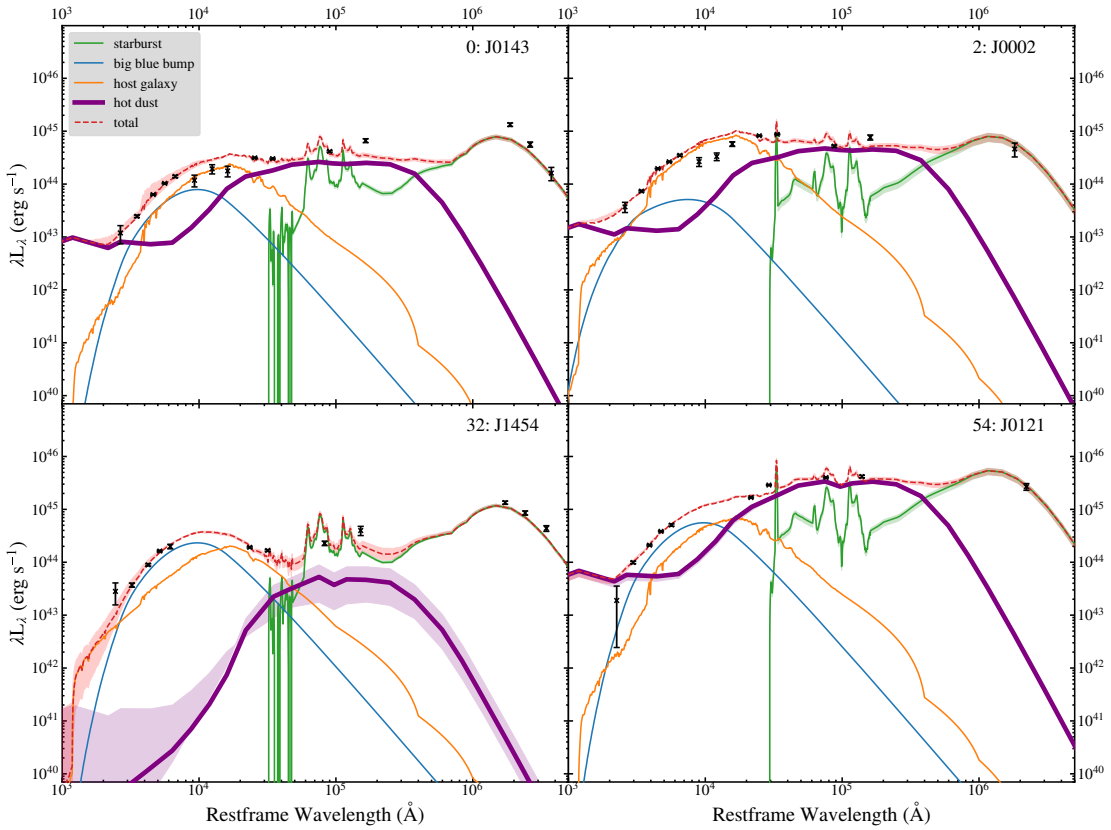

FIGURE 5.18: `agnfitter` results for four candidate OQQs with long wavelength IR data. The hot dust component - that most indicative of an AGN - is highlighted (thick purple line). Errors are shown for this component and the total.

5.10.2 Dust fraction

In some cases the hot dust component (e.g. the top two plots in Figure 5.18) rises towards the blue end. This would not occur in a purely physical model component, but it is an empirical template based on combinations of AGN SEDs from Silva et al. (2004), and the range of values these can take can be seen in Figure 1 of Calistro Rivera et al. (2016) and Figure 1 of Silva et al. (2004); they are based on $N_{\rm H}$ and assumed AGN type. As can be seen in these figures, the peak remains unchanged, varying only with normalisation. With further data into the blue and near-UV, we may be able to take this as some indication that the OQQ in question is lightly obscured, or at least has some accretion disc emission visible, but currently degeneracy with 'host galaxy' emission (solid orange line) makes this conclusion premature. Nevertheless, a high normalisation of the 'hot dust' component (see Figure 5.18, thick purple line) is required to reproduce the central part of the OQQ SEDs regardless of the tail shape. We conclude it is very likely each of these objects contains an AGN bright enough to heat its obscuring dust to produce this component.

We can quantify the contribution and compare the SED based 12 µm luminosity with the *WISE* luminosity used for selection. Figure 5.19 shows the ratio between `agnfitter`

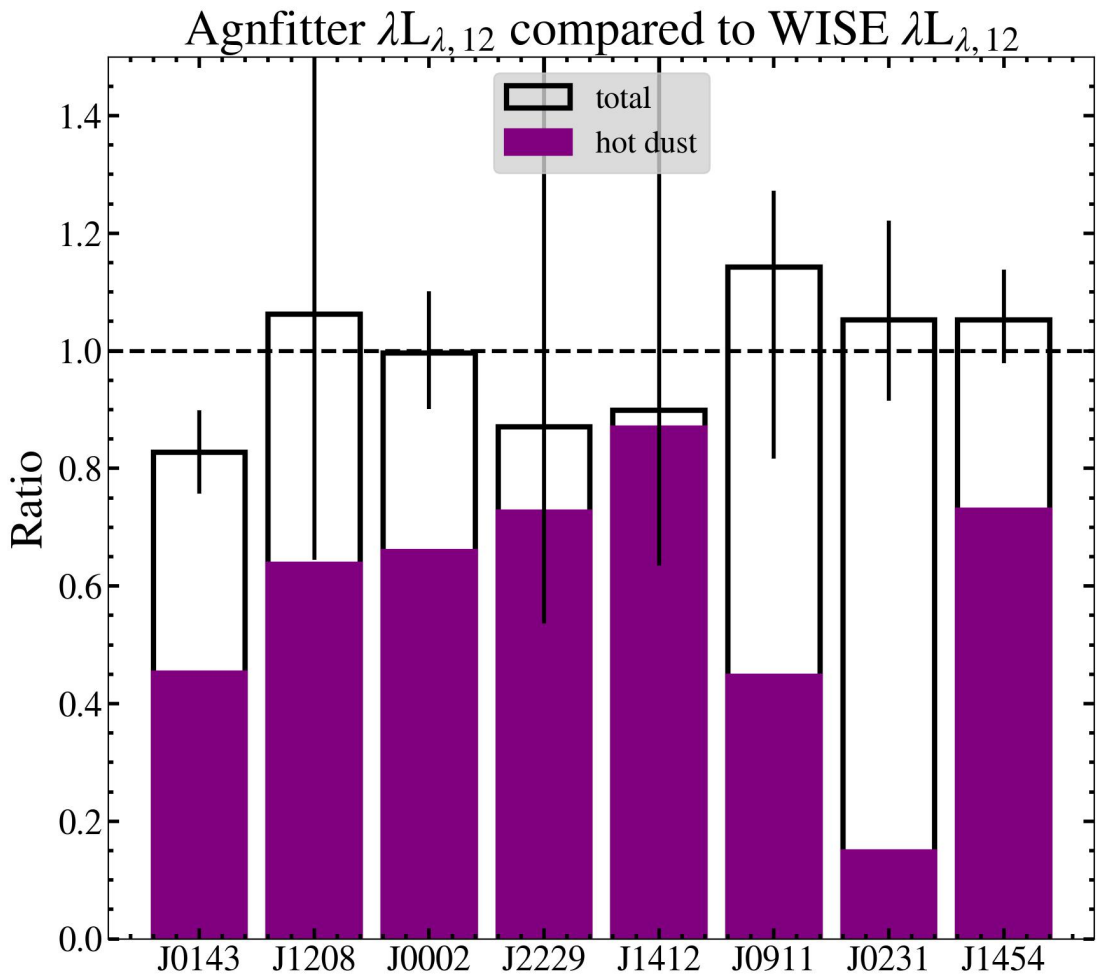

FIGURE 5.19: Fraction of total luminosity from hot dust, compared to observed *WISE* luminosity. Black bar outlines are total 12 µm luminosity, with purple bars showing the fraction from the `agnfitter` hot dust component.

and observed *WISE* luminosity, with purple bar sections representing the fraction of MIR luminosity from hot dust, according to `agnfitter`. Although this appears to show that some sources have very low hot dust fractions, we must consider that the SED fitting is not well constrained in many cases, due to lack of extended photometry. Figure 5.20 demonstrates that the vast majority of OQQs would still be selected based on `agnfitter` total 12 µm luminosity (vertical dotted line shows the selection threshold, and all sources to the right remain selected), and a large proportion would be selected with extracted hot dust emission (horizontal dotted line). Of those that would be deselected, most show very poor fit statistics (paler coloured points) and thus should not be discarded based on this alone.

5.10.3 SFR from `agnfitter`

`agnfitter` makes two separate estimates of SFR - one in the optical, and one in the

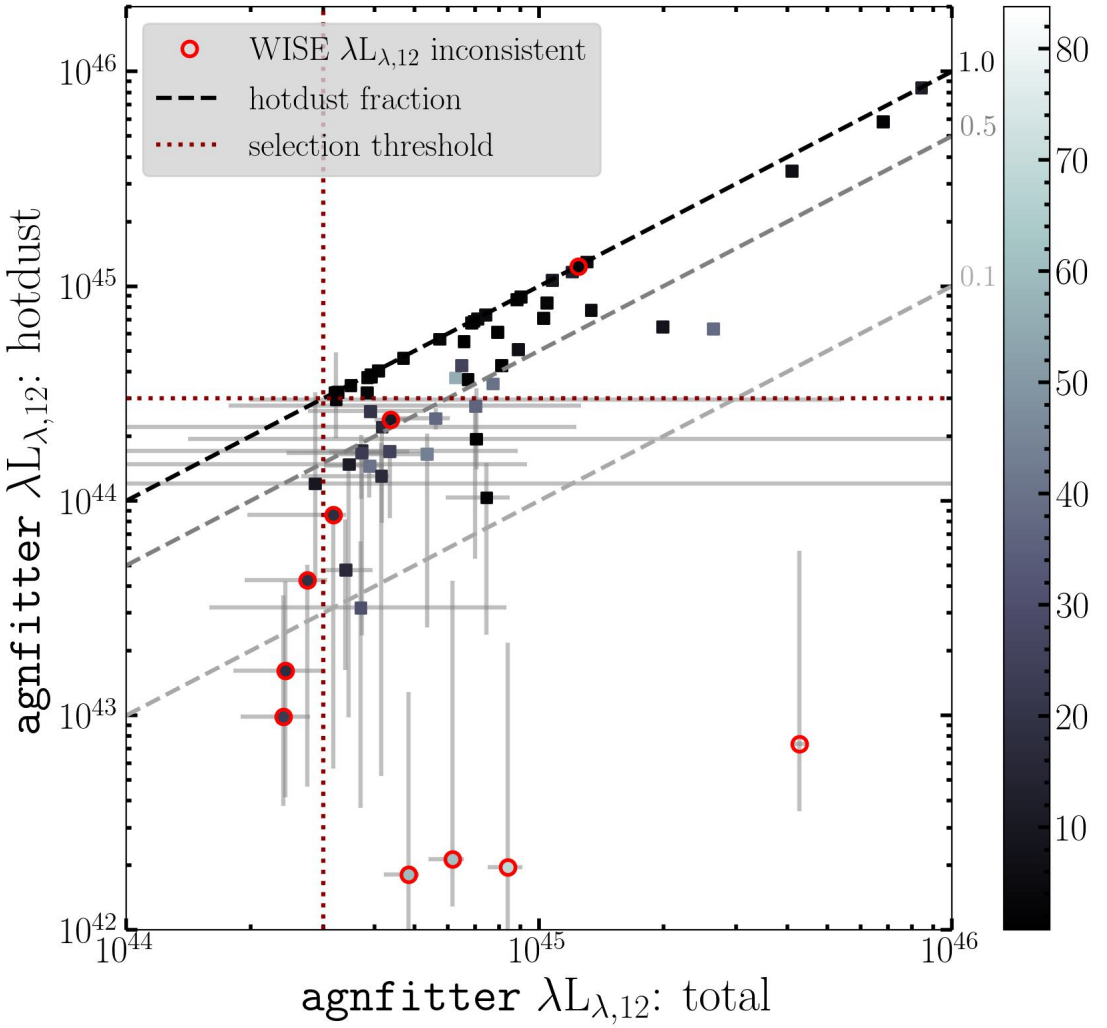

FIGURE 5.20: `agnfitter` hot dust fractions of the OQQ population. Points are coloured to represent the reduced χ^2 of each fit (i.e. darker implies more reliable fit), and dotted lines show the selection threshold used for this work. Dashed lines show hot dust emission as fractions of the total (1.0, 0.5, and 0.1). Points highlighted in red are those with `agnfitter` 12 µm luminosity inconsistent with observed *WISE* luminosity. Error bars for points above the hot dust only selection threshold have been removed for clarity.

FIR. The FIR SFR provides an estimate of potential obscured star formation, but we note that not every candidate has reliable data in that region, so we cannot make any conclusions about the whole OQQ population. This estimate (and that of stellar mass) is obtained from host galaxy template parameters (for more detail, see Calistro Rivera et al. 2016). Figure 5.21 shows the measured values for OQQs: the majority of values are either not unusual ($<100\ M_\odot\ yr^{-1}$) or have high uncertainties.

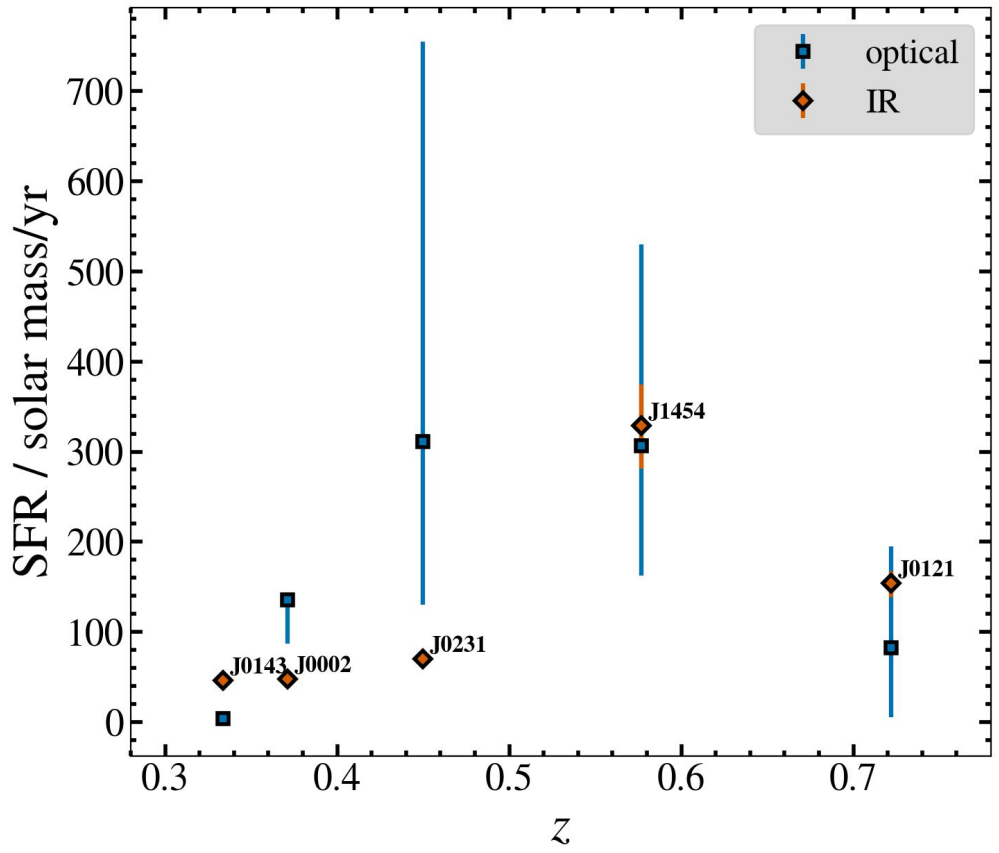

FIGURE 5.21: Star formation rates from `agnfitter`, as measured in both IR (orange diamonds) and optical (blue squares) for sources with data in IR beyond *WISE*.

5.11 Host Galaxies

Referring back to Section 5.8 very few of the OQQs show large radii or significant deviation from circular in appearance. Figure 5.22 presents PanSTARRS colour images of a sub-sample of OQQs - consistent with the SDSS properties, all appear small and red with no clear signs of recent interaction.

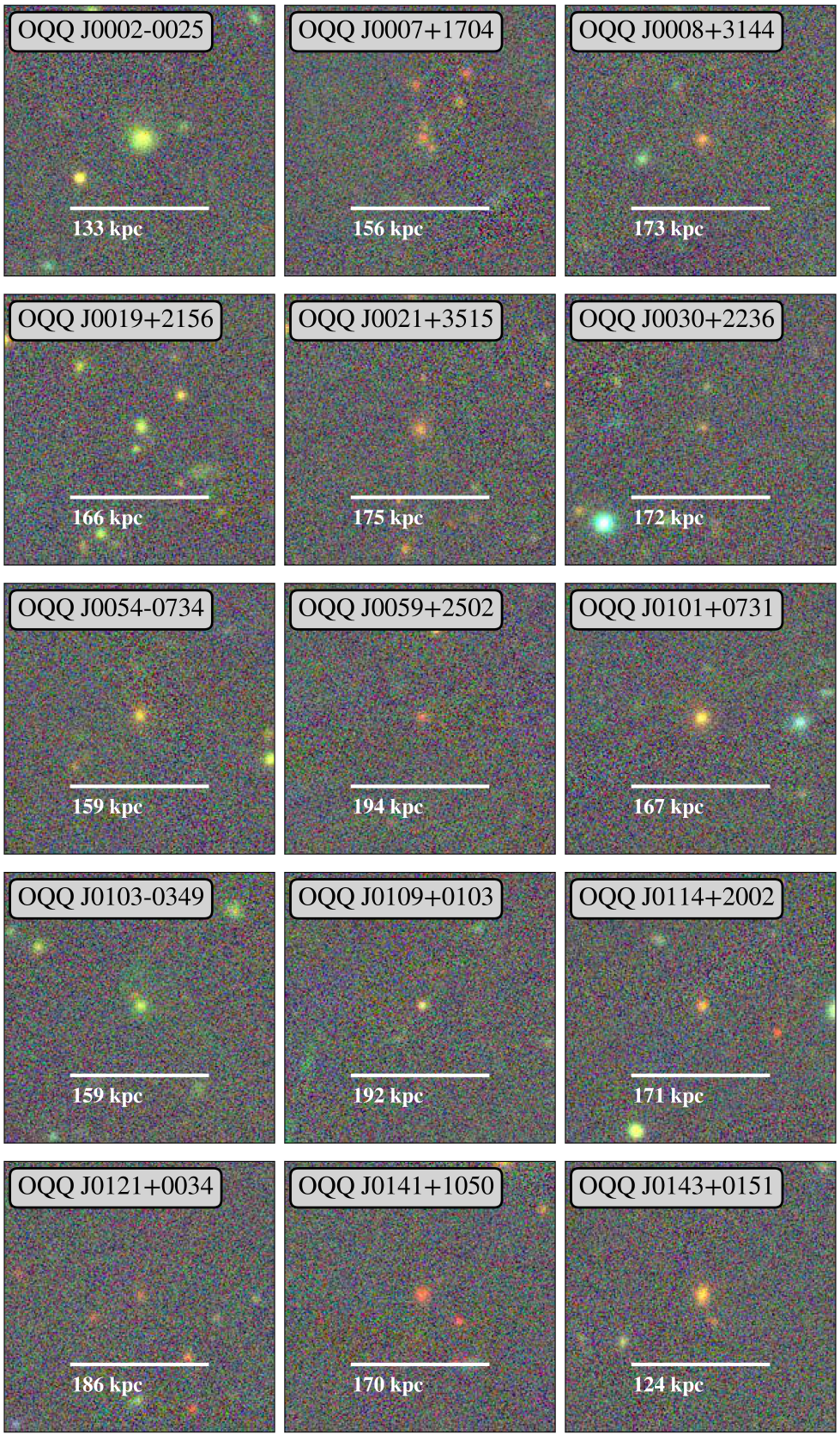

FIGURE 5.22: PanSTARRS colour images of the first 15 OQQs by RA.

5.12 Possible Theories on the True Nature of OQQs

This part of the chapter will discuss the possible intrinsic explanations for the observed properties of OQQs, and compare with known subclasses of AGN.

The combination of *WISE* all-sky MIR photometry and SDSS optical spectroscopy have enabled us to identify an interesting class of sources showing all the characteristics of luminous AGN in the MIR (based upon their colours and luminosities) but no obvious signatures of the corresponding AGN activity in the optical.

Multiple physical scenarios can explain these observations, principally based on whether the optical AGN signatures are obscured, or intrinsically absent. In the former, we can consider the OQQ in terms of the spatial scale of its obscuration. As opposed to the putative doughnut shape envisaged by the AGN unified torus scheme, full or near full sky covering by dusty 'cocoons' could easily explain the optical absence of emission signatures by not allowing an extended NLR to form or be ionised in the first place. Such cocoons would still reprocess the intrinsic AGN emission to the MIR, and the high *WISE* luminosities (along with bright hot dust component, where SED fitting is available) of these sources strongly suggest that the underlying power sources are luminous quasars, as does the MIR comparison with SDSS-selected QSO2s. For the latter scenario, AGN emission lines are not currently produced by the OQQ. We can envisage this as a 'Young' AGN - recently switched on, with the AGN radiation not yet ionising the Narrow Line Region, and consequently no narrow emission lines. It is still likely that this is an obscured AGN, i.e., that it is being viewed through a dusty torus, which would hide any broad emission lines (produced closer to the SMBH, and therefore earlier in the switching on process). As in the 'cocooned' picture, reprocessed intrinsic emission can still produce the observed IR properties.

It is difficult at this stage to make definitive statements about the true intrinsic nature of OQQs, but we can speculate on some likely possibilities. A schematic comparison between QSO2s and theories on OQQs can be found in Figure 5.23. In Section 5.13 we discuss how these theories might relate OQQs to various other object classes.

5.12.1 Intrinsically optically quiescent

An anti-correlation between [O III] and the relative intensity of Fe II has been shown in analyses of emission-line and accretion properties of AGN (Eigenvector 1; e.g., Boroson and Green, 1992, Shen and Ho, 2014). This relationship can be explained by differences in Eddington ratio - an intrinsically high accretion rate could be associated with a *low* [O III] luminosity. To assess the plausibility of the scenario for statistically significant numbers of the OQQ population, accurate measurements of the BH masses would be needed; while this is out of the scope of this paper, analysis of NIR broad lines that

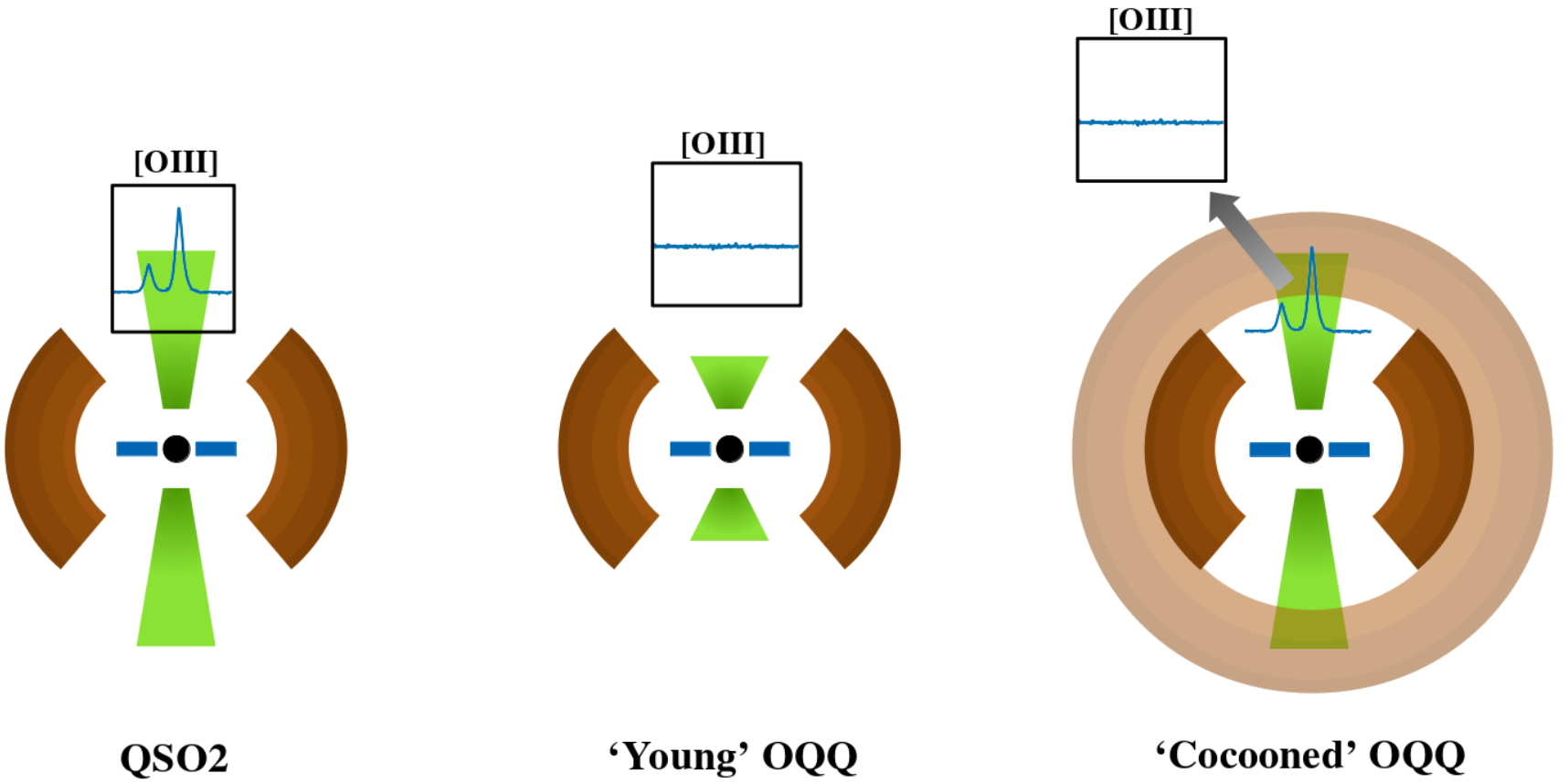

FIGURE 5.23: Schematic showing (left) a typical QSO2, producing a spectrum with strong [O III], (middle) an OQQ that is intrinsically 'young', with no [O III] produced, and (right) a 'cocooned' OQQ, producing typical [O III] emission that is obscured by a larger region of material. Inset boxes show a zoom in on the [O III] region of the spectrum - a strong line in the QSO2, but not detected in the two OQQs. Components are as follows: black central SMBH, blue accretion disk, dark brown standard torus, green ionised gas, lighter brown 'cocoon'.

may be less obscured (e.g., NIR measurements; Onori et al., 2017a) could provide the necessary information. Results from OQQ J0751+4028 do not support this (Chapter 4; Greenwell et al., 2021, 2022), as it is not luminous enough to imply a sufficiently high Eddington ratio.

5.12.2 'Young' AGN

A form of 'changing look' AGN (see Section 1.1.6 and e.g., Yang et al., 2018), objects belonging to this class have been recently activated, such that they heat the torus to produce strong IR signals, but radiation has not extended far enough to ionise the outer NLR, where the [O III] we normally see in QSO2s is produced (middle diagram in Figure 5.23). For example, Gezari et al. (2017) present an example of a 'switching-on' AGN that goes from the appearance of a LINER to a Type-I quasar over less than 1 year. No [O III] is found in the 'before' or 'after' spectra, due to [O III] following longer term AGN activity than other narrow emission lines, such as Hα, which increase strongly. If OQQs are an obscured analogue to this object, it follows that we are unable to detect other emission lines. They must be observed through the torus, as otherwise we would still observe the broad emission lines produced closer in. If this is the case, and we expect broad emission lines to be present, then detection of these in spectral ranges less subject to obscuration could provide evidence for this explanation (e.g., NIR measurements; Onori et al., 2017b).

5.12.3 'Cocooned' AGN

This type of OQQ would be more mature than a 'Young' AGN, and has similar intrinsic features to a QSO2, but with a larger 'cocoon' of obscuring material preventing observation of the NLR (bottom diagram in Figure 5.23). This 'cocoon' is likely to be unstable, and as such these objects may only have a short lifetime, supported by the small number counts found when compared to QSO2s. High resolution imaging might be expected to show very late stage mergers or other disturbances in the centres of these galaxies, as the source of the 'cocoon' (see Section 3.4.2 for more discussion on merger-AGN connections).

At $z \approx 0.5$ for most of our sample, a physical size of 1 kpc would correspond to an angular size of 0.16″, so any circumnuclear dust on sub-kpc scales would certainly be unresolved in most ground-based imaging. We searched public archives such as MAST[14] and the Virtual Observatory[15] for any high angular resolution imaging of our targets, but these fields have not been observed with *HST*, nor with any other large ground-based observatory. In SDSS imaging (as well as *WISE*), the targets do not show

[14] https://archive.stsci.edu/
[15] http://www.usvao.org/

any special characteristics, preferred morphologies or orientations, nor obvious disturbances.

This appears to support small physical scales for any putative dust cocoons in our sample. However, it must be cautioned that SDSS imaging is seeing-limited and not very deep, so for fainter sources, signatures of interaction may be missed.

5.13 OQQ in the AGN Zoo

Although the idea of cocooned AGN is not new, there are no close counterparts of our selected sample, at least in the local universe. In this section, we briefly compare and contrast other related samples with the OQQs.

5.13.1 Ultra-Luminous Infra-Red Galaxies (ULIRGs)

Our selected targets have total MIR powers within or close to the ULIRG regime. ULIRGs tend to be hosted in chaotic appearing systems, with little clear structure and sometimes lack important optical emission lines, but are not usually completely devoid of strong emission signatures. For example, Mrk 231 has much stronger H α than [O III]λ5007 emission (Malkan et al., 2017, Lacy et al., 1982). Several local ULIRGs are also considered as being 'buried' AGN obscured along all lines of sight (e.g., Imanishi et al., 2001, Oyabu et al., 2011). These are typically associated with sources that have LINER-like optical spectra with clear emission lines (Imanishi et al., 2007).

As discussed in Section 5.7.3, 15 of the 28 sources for which redshifted H α lies within the SDSS spectral range show significant H α in emission. These sources may be similar to ULIRGs such as Mrk 231, though the comparison with SDSS-selected QSO2s implies that H α also suffers some extinction, as already discussed. The remaining objects clearly differ from local ULIRGs in their lack of H α. This may be explained by correspondingly higher NLR dust covering factors in the 'cocooned AGN' scenario. It could also be a sign that the dust distribution in the galaxy is less centrally located, additionally obscuring H α from sources other than AGN ionisation.

Compact Obscured Nuclei (CONs) are found in LIRGs and ULIRGs (e.g., Falstad et al., 2021). They are dense, IR bright cores found at the centre of an optically normal galaxy. The strength of the IR emission indicates a heavily obscured nucleus, with either a compact starburst or AGN powering the luminosity. One intensively studied example is NGC 4418 (Costagliola et al., 2013, Asmus et al., 2014, Ohyama et al., 2019), which appears optically as an early type spiral, and is part of an interacting pair. Extreme visual obscuration is demonstrated by a very deep silicate absorption feature, and high resolution imagery shows a small, optically thick core. Ohyama et al. (2019) find that a dusty wind and compact starburst activity are present in the core, but that an additional energy source in the core is still required to explain the observations; it is still currently unknown whether this is an AGN or an extremely compact starburst.

CONs are not very well understood, and there are not many examples. Falstad et al. (2021) search LIRGs and ULIRGs for compact sources of HCN vibrational emission, which are only found in extreme environments. They find that 40% of ULIRGs and 20% of LIRGs contain a CON, noting that their sample size is not large, and that the

selection in the FIR does introduce some biases. This indicates that CONs are relatively common in (U)LIRGs; however, (U)LIRGs themselves are not extremely common.

OQQs are also bright in the IR, but are at larger distances than these prototypical CONs tend to be. Without good high resolution, it is impossible to definitively say whether the OQQs are equally compact. Unlike NGC 4418, OQQs appear to be small red galaxies, and have no obvious signs of interaction.

5.13.2 Weak Line and Lineless Quasars

At higher redshifts, several studies have been made of 'Weak Line Quasars' (WLQs; e.g., Meusinger and Balafkan, 2014). Similarly to OQQs, these appear as normal quasars in terms of continuum emission, but show weak or absent emission lines. Examination of WLQs ($z \lessapprox 2.5$; OQQs: $z \lessapprox 1.0$) with *Chandra* snapshots and multi-wavelength analysis from Wu et al. (2012a) and Luo et al. (2015) find spectra that rise in the optical blue end, in contrast to the majority of the OQQs, and mostly weak but detectable X-ray emission. At higher redshift, Shemmer et al. (2010) examine the region around the Hβ and [O III] lines of two WLQs at $z \approx 3.5$, finding extremely weak Hβ and no detectable [O III]. Wu et al. (2012a) show results consistent with a weak, or 'anaemic' BLR producing weaker emission lines, and Luo et al. (2015) suggest that a 'puffed up' inner accretion disc could be preventing ionisation of the BLR. WLQs are not selected or restricted in terms of MIR colour or luminosity, which is a key factor in our OQQ selection. Where possible, spectroscopic measurements of more emission lines, along with targeted X-ray observations, could shed light on the link between low redshift OQQs and higher redshift WLQs.

Laor and Davis (2011) suggest a cold accretion disc could produce 'Lineless Quasars' - if the accretion rate of the AGN is low, then no ionisation can occur, and no emission lines will be observed. They argue that in the case of a cold disc, the ionising component is the X-ray power law alone. These may cross over with Weak Line Quasars if the X-ray luminosity is high enough, but will appear lineless if $L_X \ll L_{bol}$. Considering the underluminous X-ray results of OQQ J0751+4028 (see Section 4.3) this may be one reasonable explanation for an intrinsic lack of lines, if that is the case. The optical-NUV-FUV continuum would be expected to be blue in shape, and at this time the wavelength coverage of OQQs does not extend far enough to further investigate this possibility.

5.13.3 Low X-ray Scattering Fraction AGN

An interesting population of AGN selected from hard X-ray surveys has been identified by Ueda et al. (2007). These sources show apparently low X-ray scattering fractions (as inferred from the comparison of the soft and the hard X-ray spectra), with scattering

fractions being at least an order of magnitude weaker than observed in typical Seyferts, and weak [O III] as expected from a geometrically thick torus (Ueda et al., 2015). Interstellar dust reddening is also likely to play a role in depressing the scattered flux, as evidenced from the fact that a significant fraction appear to be hosted in edge-on host galaxies (Hönig et al., 2014).

Gupta et al. (2021) present a detailed study on 386 *BAT* AGN, looking at the relationship between scattering fraction and various AGN properties. They find a significant correlation between scattering fraction and ratio of [O III] and X-ray luminosity - i.e., low soft X-ray scattering fraction also show low [O III]. In the context of OQQs, it follows that if the [O III] emission is intrinsically not present (as in the 'Young' AGN theory), there may also be less scattered soft X-rays. However, if the obscuring material in the 'cocoon' is sufficiently thick to absorb soft X-rays, we may not be able to distinguish between the theories in this way. In the same paper they find that low scattering fraction AGN are also likely to have higher intrinsic column densities, compounding the problem of selecting obscured AGN via optical methods.

Since our sample is MIR–selected, it may be better suited to search for any Compton-thick counterparts to low X-ray scattering AGN. Detailed comparison of the OQQs to this sample will require more X-ray observations than is available so far. However, as noted in Section 5.8, our sample does not have preferred host galaxy orientation angles unlike the preferred edge-on orientations for many low X-ray scattering AGN.

5.13.4 X-ray Bright Optically Normal Galaxies (XBONGs)

The class of objects known as XBONGs are X-ray selected AGN that are hosted in optically-normal galaxies lacking (optical) AGN signatures. This lack has been attributed to extinction along all lines of sight, or due to dilution by host galaxy light in a substantial fraction. However, as opposed to our targets, XBONGs tend to generally possess lower Seyfert-like luminosities (Moran et al., 2002, Comastri et al., 2002, Civano et al., 2007, Caccianiga et al., 2007, Smith et al., 2014). In such cases, it can be easier for the host galaxy to dominate over the AGN and dilute AGN optical signatures. This becomes much harder for the quasar-like luminosities for our targets, and we do not believe dilution to be important for the sample presented herein.

In order to demonstrate this, in Fig. 5.24 we compare their broadband SEDs with the low resolution broadband AGN template compiled by Assef et al. (2010). The SEDs have been normalised at 12 µm for comparison. All wavelengths referred to here are in rest-frame. The median optical–to–MIR flux ratio for our sample is 0.31 when measured at 5500 Å and 12 µm. The template AGN SED clearly lies *above* most of our sample in terms of median optical normalised fluxes, with an optical–to–MIR ratio of 0.40. This

implies that host galaxy dilution alone is unlikely to be a major effect, if our sample harbours typical central AGN.

Not all XBONG classifications are considered to be a result of dilution, and XBONGs that are good candidates to be fully covered (Maiolino et al. 2003) may constitute the lower luminosity end of our selected sample. In fact, one of the sources from the sample of Caccianiga et al. (2007), XBS J134656.7+580315, overlaps with our sample, and our X-ray analysis results for this source are consistent with theirs (Section 5.9).

5.13.5 Other IR-selected Quasars

Using the *WISE*-*WISE* colour plane, as done here for OQQs, Hviding et al. (2018) focus on a different region of the plane, choosing targets more likely to be heavily obscured. They also make no selection based on emission lines, and the majority of their sources appear more optically typical than the OQQs. However, while there is no direct overlap between these samples, they are likely to be close cousins with unusually heavy obscuration instead of unusually distributed. Further investigation of the targets with insufficient spectral lines or features to assign a spectroscopic redshift leads Hviding et al. (2018) to hypothesise that a subset of these may be powerful AGN with emission lines attenuated by thick line of sight obscuration.

Extremely red quasars (ERQs) are quasars that show an unusually high IR to optical ratio (e.g., Banerji et al., 2015, Glikman et al., 2022). Ross et al. (2015) select these objects based on a comparison between SDSS and *WISE* magnitudes, producing a sample of objects up to z$\sim$4. An interesting subset of these, at z $\sim$2-3, show extremely broad emission lines which are not easily explained by current models. The ERQs could be intrinsically similar to the OQQ, but due to the selection processes (which included SDSS quasars only) do show typical AGN emission lines.

Glikman et al. (2012) select candidate red quasars based on 2MASS (IR) and FIRST (radio) data. A detailed examination of the radio properties of OQQs is outside the scope of this paper, but we searched the FIRST catalogue (Becker et al., 1995) and found 7 FIRST counterparts to OQQ candidates, of which 4 are $>$10mJy. The OQQs are therefore not consistently radio bright or dim, and unlikely to be similar, population-wise to radio-selected objects.

5.13.6 Blazars

One potential source of contamination in this sample is likely to be blazars - the chance viewing of AGN head on to a relativistic jet (Landt et al., 2004), producing a bright, variable source, strong in radio emission. These are known to be very bright objects, with some exhibiting very flat spectra. As such, there may be a number that pass the

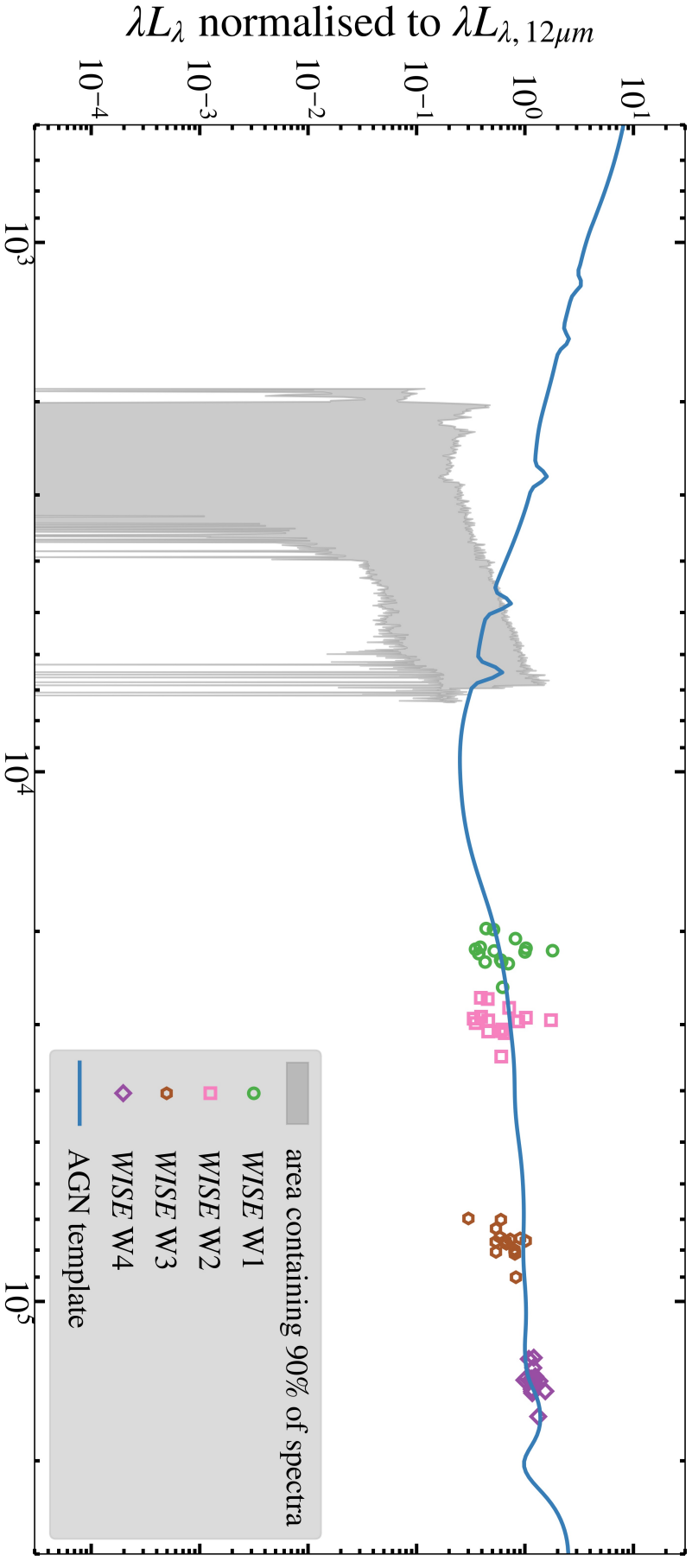

FIGURE 5.24: Comparison between SDSS spectra (thin grey lines), *WISE* derived luminosities (coloured points) and the AGN spectral template (solid blue line) from Assef et al. (2010).

criteria specified in Section 5.2, but that are not relevant objects for this paper. It would be useful therefore to be able to estimate the level of such contaminants in our sample, and if possible to remove some in order to improve the reliability of the sample.

D'Abrusco et al. (2014) created a catalogue of γ-ray emitting blazars, assembled from *WISE* sources. Comparison of overlapping sources from this catalogue (*WIBRaLS*) with our OQQ sample, and with respect to various parameters, could help identify the unwanted objects. Massaro et al. (2012) identified the *WISE* Gamma-ray Strip (WGS), which uses colour-colour diagrams to distinguish possible blazars. They divide these into two sub-categories - BZBs (BL Lac objects, with featureless optical spectra - galactic absorption lines or weak emission lines only), and BZQs (flat spectrum radio quasars, where the optical spectrum should show broad emission lines). According to these definitions, the most likely category for any contaminant objects will be BZB. Massaro et al. (2012) quantify the likelihood of a source being within the WGS, based on its location on three *WISE* colour-colour diagrams, and the uncertainties on those colours. Figure 5.25 shows the application of this method to our objects. This is not considered a sufficiently reliable classification to remove any sources from the OQQ list, merely to assess the level of contamination from BZB sources.

Furthermore, given the flat spectrum characteristic of blazars they tend to have weak values of D4000. Recalling Figure 5.8 the OOQs tend to show significant breaks, and this can be seen in the individual optical spectra (Figure 5.5). Hence, a visual check of the spectra substantially reduces the likelihood of blazar contamination (Section 5.3.3).

One property common to all blazar types is that they exhibit high, irregular variability across the whole spectrum. As such, this may be a useful way to distinguish likely blazars from OQQs.

After the completion of the main *WISE* mission, the NEOWISE project (Mainzer et al., 2011) scanned the sky approximately ten times in five years, depending on sky location, with the *W1* and *W2* bands (*W3* and *W4* cannot operate without cryogenic cooling, and this was exhausted during the main phase). The primary science aim of this phase is the study of near Earth objects. However, as the single exposure images and source magnitudes are available from the NEOWISE database[16], it provides a measure of the $\sim$5 year timescale infra-red variability.

To approximately quantify the level of variability in each source, the data from each *WISE* measurement epoch was averaged, then these combined points fit to a time-invariant line. χ^2 was used to assess whether this invariant state could reasonably explain the observed variation in *WISE* detections[17]. If it could not, then intrinsic uncertainty was added to the points. The size of this intrinsic uncertainty was used as

[16] http://wise2.ipac.caltech.edu/docs/release/neowise/

[17] The *W3* (12 µm) band magnitudes were chosen as most representative of the region of interest. A more detailed investigation would examine the effects with luminosities rather than magnitudes.

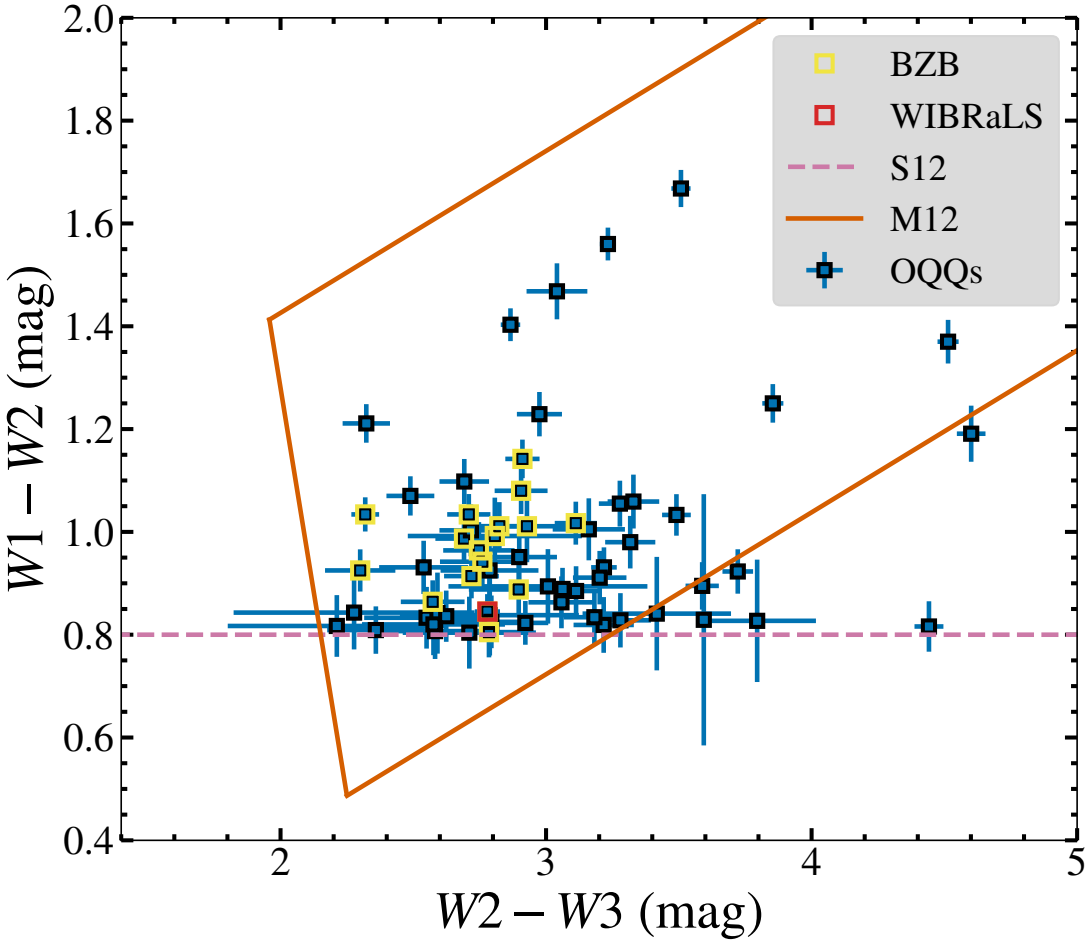

FIGURE 5.25: *WISE* colour-colour diagram (as in selection; see Figure 5.15) showing the categorisation of the OQQs, with AGN selection thresholds from Stern et al. (2012, S12) and Mateos et al. (2012, M12). OQQs that pass in all three planes of Massaro et al. (2012, BZB) are outlined with yellow squares. The orange squares shows the single object that is present in the WIBRaLS catalogue, also classified as a BZB according to the WGS.

an estimate of the variability of the source. Figure 5.27 shows the fitting with the two showing highest variability.

The number of objects found that are above the threshold for being within the WGS BZB is 17 out of 64 OQQ. The number of objects with matches in the WIBRaLS table is 8 out of 64 OQQs - these are all also above the BZB threshold. The number of objects with high variability is currently difficult to quantify without a comparison threshold. The QSO2 variability is slightly lower on average (mean 0.031/median 0.020 for OQQ, mean 0.026, median 0.017, for QSO2s) and includes no very high variability objects.

If we take the lower limit of high variability as 0.1, then there are 2 OQQs above this threshold, both of which are likely BZBs. Of the 62 OQQs below the threshold, 24% are likely BZBs. In comparison, 57 QSO2s (out of 1,990; 2.9%) pass the BZB threshold

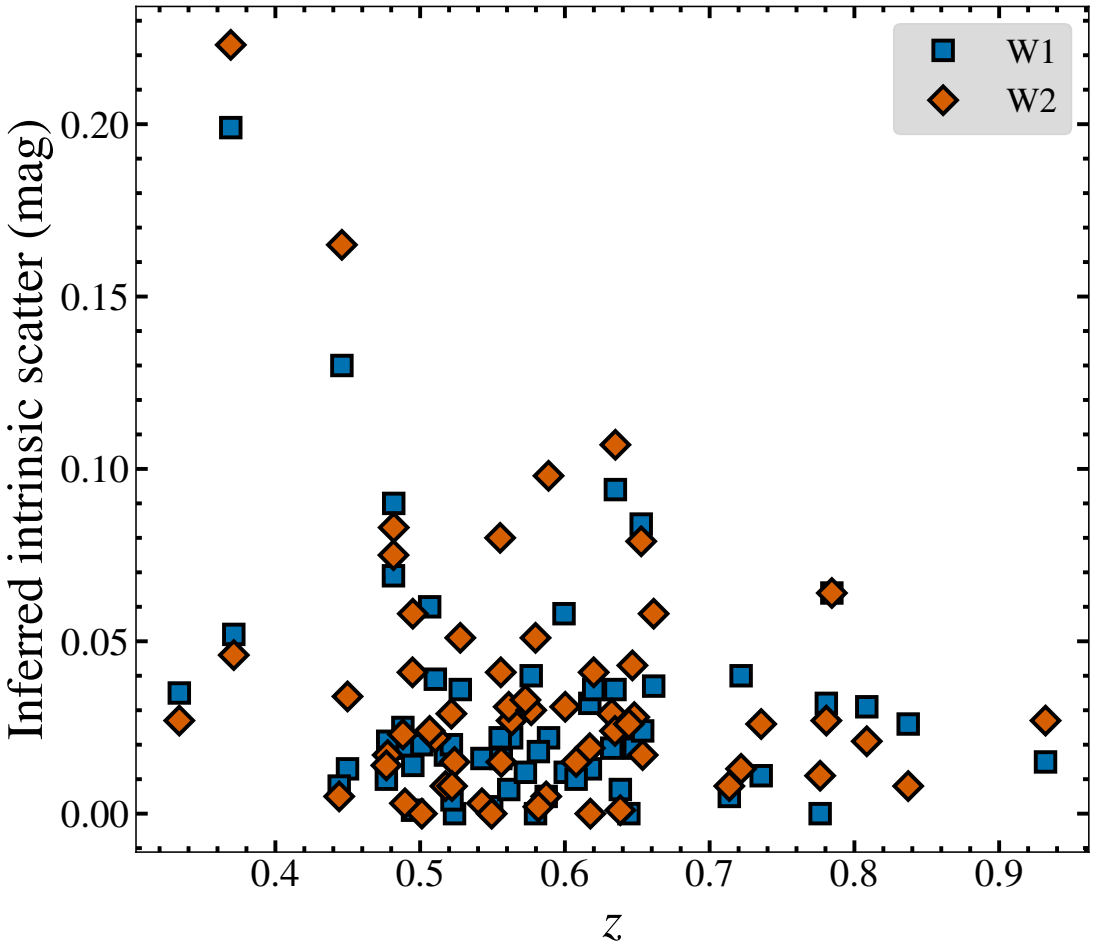

FIGURE 5.26: Inferred intrinsic scatter added to force the *WISE* data to be consistent with an unvarying source - higher values indicate that the source is more variable, and less likely to be stable.

overall. An examination of the variability of a large sample of non-AGN and various types of AGN would be illuminating, but outside the scope of this work.

Due to the high uncertainties on these methods, it is difficult to fully quantify the number of BL Lac objects that could be interfering in the results here: anything from 3% to 25% may be possible.

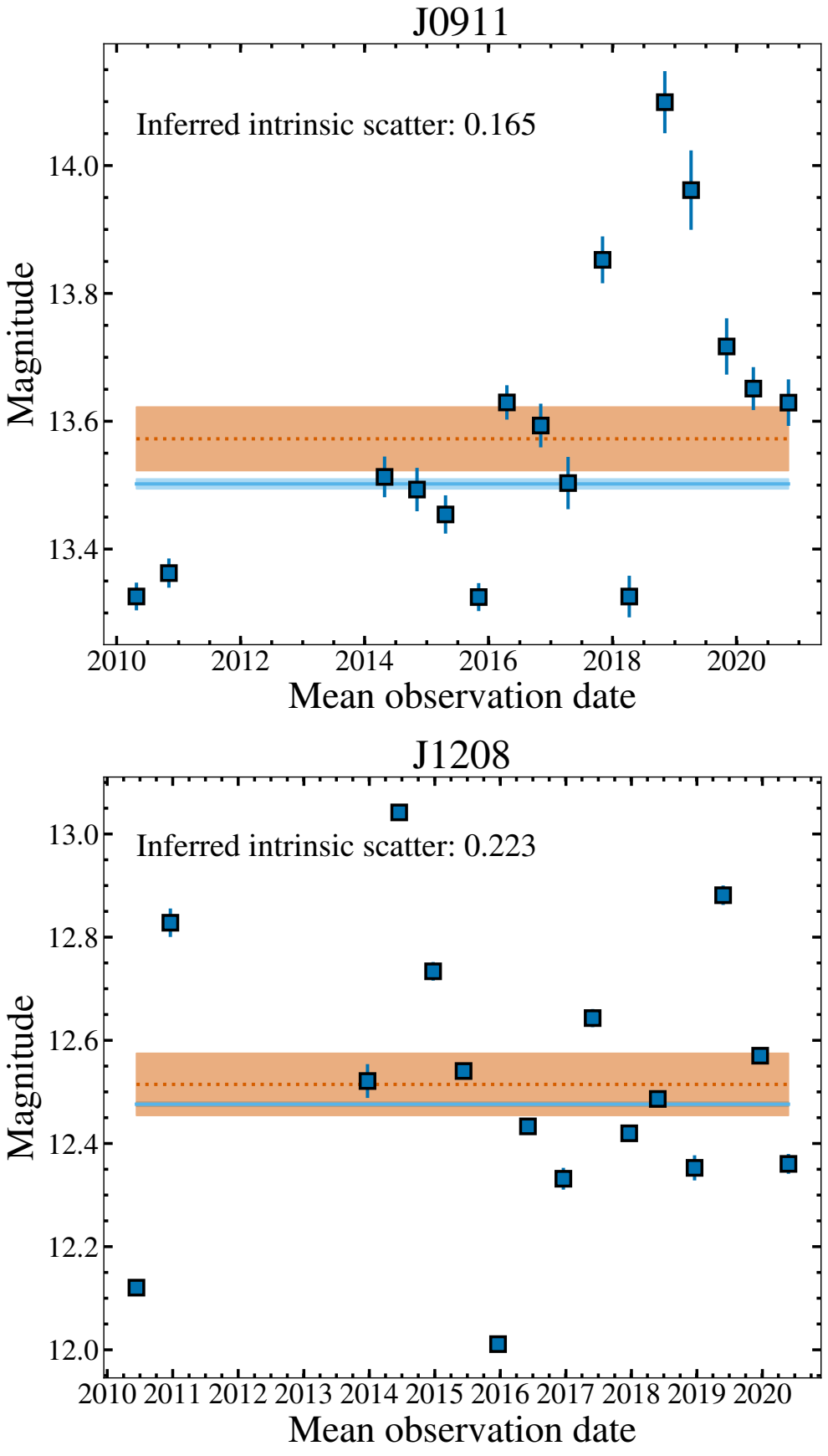

FIGURE 5.27: *W2* variability of significantly variable sources.

5.14 Evolutionary Context

It is important to consider the cosmological situations where we might find OQQs. Many works have examined the life cycle of galaxies and the AGN within as the host galaxies go through mergers (e.g., Hopkins et al., 2006, Springel et al., 2005, Di Matteo et al., 2005). As the two galaxies interact, the ISM from both comes together, and the resultant enhanced density of matter leads to increased star formation, and (as the bulk of the merging galaxy reaches the nucleus of its pair) we may see increased AGN activity. This brightening starts as the AGN is still enshrouded in dust and gas from the merger, but as the emission increases in intensity, energy and matter feedback starts to clear out the obscuring matter. Our OQQ sample objects, for the most part, do not show signs of high star formation rate (SFR) as may be expected if they lie in this part of the sequence. Thus, OQQs do not obviously fit the standard paradigm for AGN and host galaxy evolution.

Springel et al. (2005) show that in a modelled merger of two disc galaxies, including AGN feedback and BH growth, the peak of SFR precedes the black hole accretion rate (BHAR) peak by a small amount of time. SFR begins to drop before the BHAR, so there may be a short period of time where the SFR is well below peak, but BHAR is high. As BHAR is proportional to AGN luminosity, the OQQ objects might be objects in this short transitional phase. Some SF would still be expected, and would contribute somewhat to MIR luminosities. Disentangling the relative contribution of SF and AGN to observed emission would be important in placing OQQs into context, but without independent measurements of either (e.g. well constrained SED fitting or NIR emission lines) assumptions and estimates must be made. We find fewer OQQs compared to QSO2s, suggesting that the OQQ duty cycle is shorter than the duty cycle of Type 2 quasars. Interestingly, the difference in median redshift between these two samples (e.g., Fig. 5.6) implies that there may be genuine evolutionary differences between their populations, with OQQs peaking earlier than QSO2s. However, incompleteness issues could impact both source samples at the upper redshift end, and the number of nearby OQQs may be artificially low simply due to easier detectability of faint [O III].

The two galaxies are coalescing at this point so would not necessarily be clearly identifiable as advanced mergers, especially with the images currently available. Additional high resolution imagery could be valuable in identifying any late stage mergers among the sample. For the OQQs to be objects existing in this brief period of time, we may expect strong outflows to be visible, if the SFR is being quenched by AGN activity. These will manifest as blueshifted absorption lines, or broadened and asymmetric emission lines at the systemic velocity of the source. With the current spectra this is impossible to either confirm or rule out, but measurements of select likely candidates with more sensitive instruments could provide more insight into these scenarios.

The absence of obvious merger signatures may instead point towards high mass ratio mergers, with the smaller galaxy not massive enough to significantly disrupt the morphology of the larger primary, nor massive enough to trigger substantial star formation throughout the body of the primary. However, an efficient mechanism to channel the gas from the donor galaxy to the central SMBH would be required in this case. Whether *secular* processes such as efficient gas flows can trigger AGN activity without simultaneous star formation remains unclear.

Alternatively, the 'Young AGN' scenario presents a different evolutionary perspective. If the triggering event is recent enough, the AGN could be switching on, mimicking the phase described by Schawinski et al. (2015) as 'Optically Elusive AGN'. They show that there could be a period of $\sim 10^4$ years in which the AGN is visible in X-rays but has not yet photoionised the extended area that will later become the Narrow Line Region. As the dusty torus (the source of reprocessed IR emission, and the IR colour that we select for in this work) is closer to the central engine than the NLR, we expect that sign of AGN life to appear prior to any narrow optical emission lines.

5.15 Estimated Population Counts

Schawinski et al. (2015) calculated the full duty cycle of an AGN as $\sim 10^5$ years, and the *optically elusive* phase as $\sim 10^4$ years. If we expect the IR bright OQQ phase to be some fraction of the optically elusive phase, this puts the OQQ lifetime at less than $\sim$10% of the 'normal AGN' duty cycle. The viewing angle of OQQs and QSO2s is likely to be similar - both viewed through the torus, obscuring any broad emission lines - so assuming they have similar covering factors, we would expect to see them in the same proportions as the full range of AGN types: approximately 10:1. We find $\sim$1000 QSO2s and 64 OQQs: approximately 16:1; encouragingly close, but somewhat fewer OQQs than expected, especially if we consider that some OQQs may be 'cocooned' rather than 'young'. As stated above, however, the 10:1 ratio is a *lower limit*, based on the full 'optically elusive' timescale. If every OQQ is a 'young AGN' our results are consistent with the IR bright stage being approximately two thirds of the 'optically elusive' phase. These are merely crude estimates that do not fully account for selection and modelling biases, much of which remain unknown.

5.16 Summary

By selecting MIR–luminous sources with red *WISE* colours and a marked absence of optical emission lines, we have presented a newly formalised category of AGN: Optically Quiescent Quasars. They were selected as candidates for being enshrouded within dust cocoons, but alternative explanations based on *inherent* lack of [O III] are also considered. These OQQs may not be *intrinsically* uniform, and may indeed represent diverse objects, but they are observationally similar and thus are overlooked from standard AGN selection in the same ways. The overall sample shows broadband continuum properties very similar to those of SDSS-selected QSO2s, but with an [O III]λ5007 emission line suppression factor of $\gtrsim$120. We show that host galaxy dilution is unlikely to be a major effect in most cases.

The idea of fully enshrouded AGN is far from new. Various models suggest that the bulk of AGN growth occurs in highly obscured phases (e.g., Fabian and Iwasawa, 1999, Hopkins et al., 2006). The shape of the cosmic X-ray background spectrum also requires similar numbers of Compton-thick ($N_{\rm H} > 10^{24}$ cm^{-2} obscured AGN compared to unobscured). Ananna et al. (2019) calculate the required proportion at z = 1.0 as 56% $\pm$ 7%. A number of dedicated legacy surveys with *NuSTAR* that are selected in the infrared are finding CT fractions $\gtrsim$30% within $\lesssim$200 Mpc (e.g., the *NuSTAR* Local AGN NH Distribution Survey – NuLANDS, Boorman et al., in prep., and the [Ne V] survey; Annuar et al. (2020)). In any evolutionary paradigm, this would naturally include fully obscured sources in the stochastic competition between gas feeding from large scales and AGN feedback, especially if there is a delay between the two competing processes (noting that NuLANDS currently includes optical classification as part of the sample definition; the preliminary infrared selection should still include such fully-covered objects). It may also imply the existence of obscured objects that do not occur as part of the merger-driven growth phase, but instead represent a separate path.

The receding torus model also suggests that the covering factor of AGN decreases with luminosity (e.g., Lawrence, 1991) so fully covered AGN may be more likely to occur at low AGN luminosities. This issue is far from settled, however, with conflicting results from a variety of studies in different bands (e.g., Lawrence and Elvis, 2010, Toba et al., 2014). An element of bias can be introduced by requiring that optical emission lines be present for secure source redshift and type identification - any sample based on this selection criteria may be missing objects with some emission lines blocked, either completely or to a level below measurable. The strength of our selection criteria is to instead rely upon the reprocessed thermal spectrum (i.e., MIR colours) and luminosities, allowing us to search for objects in which potential 4π or near 4π covering completely extinguishes the optical lines.

Without more high quality X-ray data, it is difficult to place the OQQs onto the summary plot, as with the *NuSTAR* sources and J0751. Instead, we use an estimate of the

larger scale line of sight N_H from Section 5.7.4 - the amount of obscuration necessary to reduce an intrinsic [O III] emission line of the same luminosity as a typical QSO2 to below the upper limits observed for OQQs. Figure 5.28 adds the OQQs to the plot. As with J0751, this simple representation of z and N_H does not fully convey the unusual nature of OQQs. Rather than being exceptional in terms of their column depths, 'cocooned' AGN instead belong to a population unusual in covering factor, and 'young' AGN a brief and thus elusive phase of AGN growth.

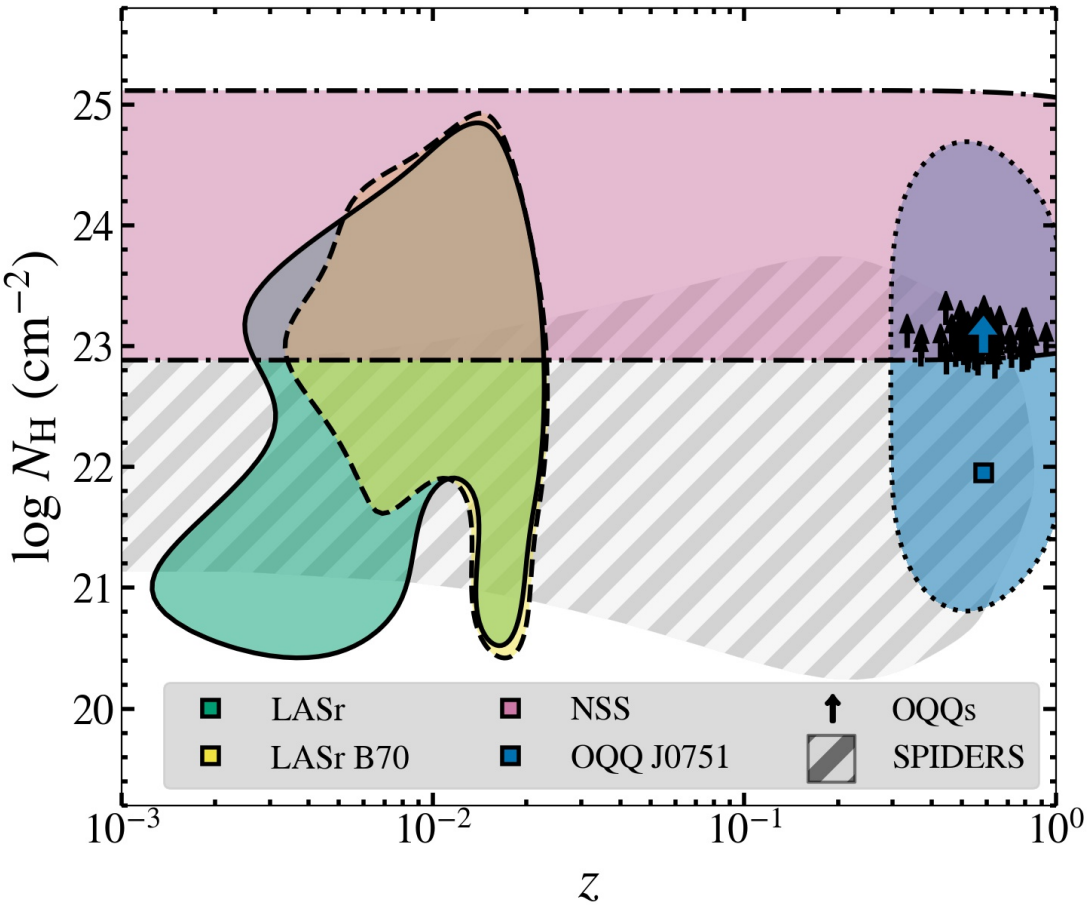

FIGURE 5.28: Parameter space covered by the known AGN in the LASr-GPS (green shaded region, solid edge), by the B70 AGN (yellow shaded region, dashed edge), the region targeted by *NuSTAR* serendipitous selection (pink shaded area, dot-dash edge), the region targeted by this chapter (blue shaded area, dotted edge), the result from OQQ J0751+4028 (blue diamond), and the results from the remaining OQQs (blue squares). Note that the N_H values for the OQQs are estimated from [O III] deficits, and are therefore not necessarily the same as X-ray N_H values.

Chapter 6

Conclusions: Implications from these rare AGN and comparisons with similar objects

This chapter will summarise the work done across the range of AGN properties. How do the new AGN relate to known AGN e.g., QSO2s? There are many groundbreaking large surveys just beginning, or in the late stages of preparation, e.g., *LSST*, 4MOST, eROSITA. This chapter will describe the potential of these datasets to uncover more unusual AGN, including but not limited to OQQs. This final section will pull together the work from the previous chapters, present answers to the main research questions of this thesis, and discuss the potential for these future surveys in making robust searches for rare AGN.

6.1 Summary of work

6.1.1 Local AGN Survey

Knowledge of AGN demographics - the distribution of accretion rate, obscuration depths, intrinsic luminosities, and more - is vital to understanding the life cycles of AGN and their influence on their environments. Without an accurate census of AGN, uncertainties propagate through the chain: for example, if we are unclear on the number of obscured AGN, we cannot understand how SMBH grow through their active phases. With this in mind, the Local AGN Survey (LASr) project aims to complete this census in the local universe, where biases can be minimised and detailed studies of sources can be made - even for low luminosity AGN. The first part of Chapter 2 described the underlying basis of this search, which is an assembly of a Galaxy Parent Sample. We

constructed a list of local galaxies based on combining large databases: NED, SIMBAD, 2MRS, SDSS. With careful selection of clean redshifts, removal of duplicate and false objects, and inclusion of redshift-independent distances where possible, a reliable catalogue of ∼49,000 galaxies within 100 Mpc was created: the LASr-GPS. The second part of Chapter 2 presented the main focus of this Chapter: constructing a relatively unbiased sample of AGN, and selecting thus far unknown candidate AGN. We found ∼4,300 known AGN, from a combination of X-ray specific (*Swift*-BAT 70-month Baumgartner et al., 2013) and more general (Véron-Cetty & Véron, Véron-Cetty and Véron, 2010; Zaw, Chen & Farrar, Zaw et al., 2019) catalogues. Of great interest are the *unknown* AGN - how many of the remaining ∼44,700 galaxies contain AGN that are so far undetected? What types of AGN primarily contribute to these numbers?

We applied a MIR selection criterion (designated R90, from Assef et al., 2018) to the galaxies, aiming for high reliability (i.e., a high chance that a selected galaxy contains an AGN, at the expense of not selecting a large number of AGN). Applying correction factors for various selection biases gave an expected number of AGN of 362^{+145}_{-116} with $L^{\rm nuc}_{12\,\mu{\rm m}} > 10^{42.3}$ erg s^{-1}; compared with 172 known AGN we saw that a significant number remain missing.

In the final part of Chapter 2 I addressed the AGN candidates: are they truly AGN? If so, what is the reason for their non-detection? Are they obscured, as population demographics might imply? X-SHOOTER (Vernet et al., 2011) is an instrument on ESO's VLT, and takes spectra from 3000–24,800Å. As such, it is an ideal tool for studying both optical and NIR emission lines. We apply optical and NIR diagnostics (Kewley et al., 2006, Riffel et al., 2013) to each of three AGN candidates observed in our programme so far and additionally a known AGN that is potentially a rare Compact Obscured Nucleus (see Sections 2.5.2.3 and 5.13.1). One candidate was found to be an optical AGN, and another a NIR AGN, with other diagnostics showing either ratios typical of star-forming galaxies or borderline positions. The difference in results for optical vs. NIR diagnostics highlighted the importance of broad band spectroscopy for AGN selection, rather than relying solely on optical emission lines, particularly for obscured AGN where NIR emission lines may be more prominent.

6.1.2 *NuSTAR* Serendipitous Sources

With the results from the LASr search for unknown AGN, we next addressed what is likely to be one of the major sources of undetected AGN: heavily obscured and Compton thick (CT) AGN. Based on the expected intrinsic fraction of CT AGN (see Section 2.4.4) we expected 38±25 (out of 137 R90 non-B70 AGN candidates) more *Swift*-BAT detections than we find. Thus we may expect a significant number of CT AGN, or otherwise extremely obscured AGN. With the aim of investigating more effective selection of missing CT AGN in mind, Chapter 3 searched for new CT AGN candidates with

NuSTAR, a hard X-ray (3-78 keV) telescope better capable of detecting AGN emission through high column density obscuration, with significantly improved spatial resolution compared to *Swift*-BAT. Unlike the X-ray selected known AGN in the LASr-GPS which come from *Swift*-BAT, *NuSTAR* has to date only covered a small fraction of the sky. Thus I did not restrict this search to any particular redshift, although it does naturally restrict itself given the changing shape of the spectrum (see Figure 3.20) and decreasing flux from distant sources.

Using serendipitous sources (i.e., not targeted for *NuSTAR* observations but detected in the FOV) from the 80-month catalogue (NSS80; Klindt et al., 2022, submitted) I selected sources based on the band ratio (BR; ratio of flux in the 8-24 keV and 3-8 keV bands). This provides an approximation for the shape of the spectrum - higher values indicate a harder spectrum, and a harder spectrum indicates a more obscured source (see Figure 3.3). Building on the work of Lansbury et al. (2017a) from the 40-month catalogue, I examined sources with new *NuSTAR* observations (including one selected by L2017 with new, simultaneous *XMM-Newton* and *NuSTAR* data). From these, I checked the detection significances and source counts, and performed spectral modelling for those with high net counts. I found four of these to be Compton thick based on modelling with BORUS02 (Baloković et al., 2018). I considered what the addition of these sources to the ranks of hard X-ray selected CT AGN means, and studied the fraction of these sources that appear to be interacting – the effect of galaxy mergers on AGN is contested, and thus any contribution to the numbers of CT AGN in isolated or interacting galaxies is useful. Three new *NuSTAR*-selected AGN, plus one confirmation of a source with previously only lower quality data, is a significant improvement on the number already known. When combined with *NuSTAR* CT AGN from Lansbury et al. (2017a), I found a CT fraction (15^{+10}_{-6}% for $z<0.07$, Section 3.4.1) and merger fraction (29^{+21}_{-12}%, higher than 'normal' *NuSTAR* AGN at 8^{+12}_{-5}%; Section 3.4.2) larger than other observed values.

6.1.3 Optically Quiescent Quasars

Chapters 4 and 5 discussed the selection and properties of AGN chosen to represent another group missing from the known AGN in LASr: objects that are bright, AGN-coloured IR sources from *WISE* (Wright et al., 2010) with no clear optical signatures of AGN presence. This optical–IR disparity sets any such AGN apart from standard selection techniques. I designated such sources as 'Optically Quiescent Quasars' (OQQs).

Chapter 4 began with an in-depth study of a single, prototypical OQQ: OQQ J0751+4028, published in Greenwell et al. (2021). The source properties are analysed based on archival multi-wavelength data and SED fitting with `agnfitter` finds that significant contribution from hot dust is required to produce the observed properties. The chapter continued with the first targeted X-ray observations of an OQQ, published in Greenwell et al. (2022). I demonstrated how X-ray observations provide an important tool for

analysing the intrinsic emission of AGN – particularly in the case of AGN with atypical properties. Simultaneous measurements with *XMM-Newton* and *NuSTAR* showed detection of X-ray emission up to 24 keV. OQQ J0751+4028 is underluminous in X-rays compared to MIR emission, but bright enough that it confirmed the presence of an AGN. X-ray modelling found that the most likely model of obscuration is spherical (based on BNSPHERE; Brightman and Nandra, 2011), consistent with a 'cocooned' scenario.

These targeted observations can be used to estimate where J0751 would lie compared to *NuSTAR* obscured source selection. Figure 6.1 shows the band ratio data for all NSS80 sources, with the hard sources highlighted. The band ratio from J0751 is shown as a cross; noting that as this source is only detected up to 16 keV, the flux up to 24 keV is extrapolated from the model in the detected range. In Chapter 4 I found that this source is lightly obscured, and its band ratio of ∼1.3 agrees with that: it is below the threshold of 1.7 used to select heavily obscured sources, but higher than a large proportion of the remaining NSS80 sources.

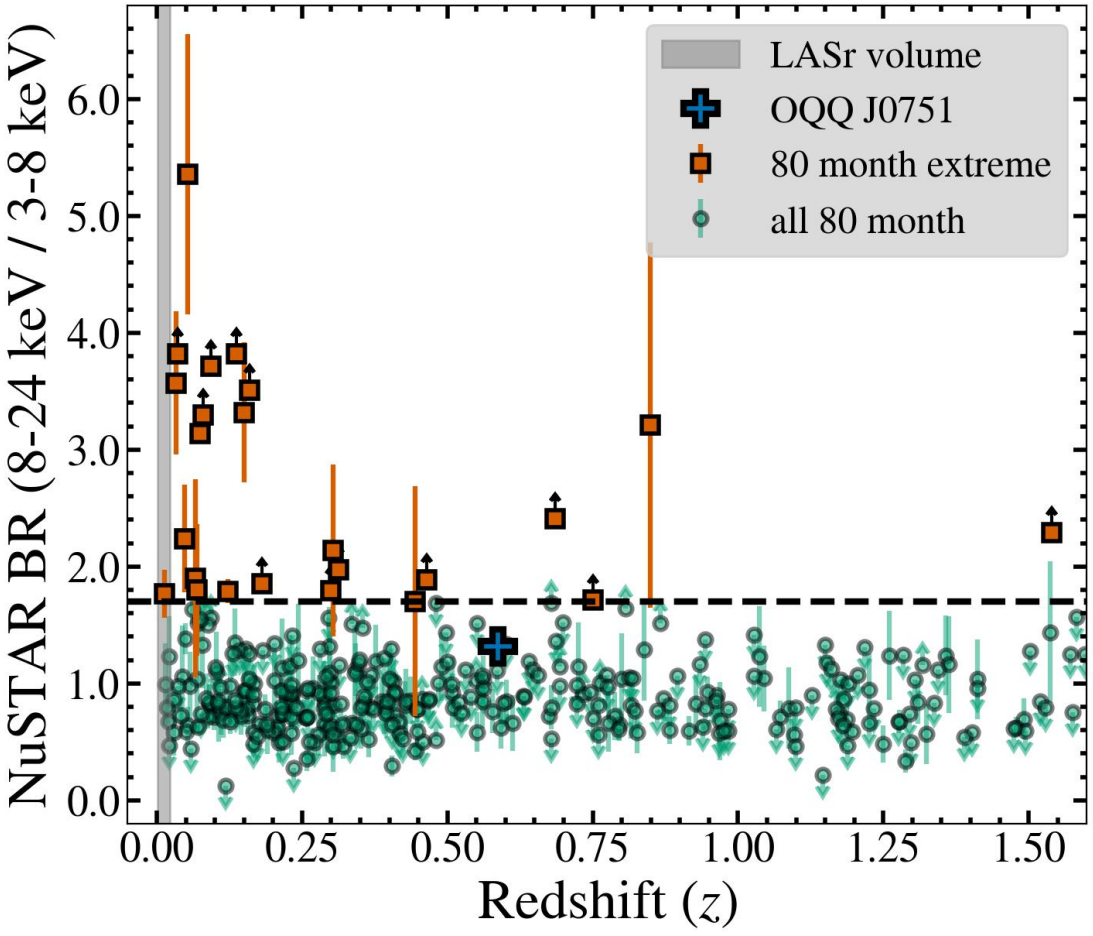

FIGURE 6.1: Sources by band ratio and redshift (as in Figure 3.6). Green circles are all NSS80 sources. Orange squares are NSS80 sources with high band ratios. Blue cross is the position of OQQ J0751+4028 (Chapter 4). Grey vertical bar shows the redshift range covered by LASr (Chapter 2).

In Chapter 5 I continued this investigation, expanding on the selection to construct a sample of objects based on (a) *WISE* colour $W1 - W2 > 0.8$, a threshold chosen for high reliability in selecting AGN (Stern et al., 2012); (b) no optical signatures of AGN, specifically the [O III] λ5007 Å forbidden line, among the strongest lines found in the narrow-line regions (NLR) of AGN; and (c) MIR powers in the quasar regime, in order to mitigate host galaxy dilution (Moran et al., 2002) as a possible cause of the lack of optical emission lines. I found that these candidate OQQs are primarily small, red galaxies, with galaxy-like spectral continua. Comparing the [O III] upper limits of the OQQs to measured [O III] luminosities from comparable QSO2s (Reyes et al., 2008, Yuan et al., 2016) found a large deficit, implying that if OQQs are intrinsically similar to QSO2s a large amount of obscuration must be present. However, optical extinction of emission lines further from the BH than the NLR may not be the only reason that optical emission lines are not detected. I also considered a scenario where emission lines are simply not produced in the NLR, for example if the AGN has only recently become active and thus has not yet ionised the NLR.

These two likely physical scenarios that may explain the observed properties of OQQs are:

- 'Cocooned' AGN – the optical emission lines are not seen because the AGN is completely enshrouded in a (presumably transient) 'cocoon' of gas and dust.
- 'Young' AGN – the AGN has recently switched on, and has not yet ionised the narrow line region (NLR): no [O III] line has yet been excited.

Both scenarios are interesting from an evolutionary perspective. AGN growth within fully enshrouding cocoons is suggested by some models (Fabian, 1999), and OQQs would represent a systematic search for this class of source, though such candidates appear in various prior sub-samples (e.g., Gandhi et al., 2002, Hviding et al., 2018). Similarly, in the young AGN scenario, it may be possible to constrain the duty cycle of NLR excitation (Schawinski et al., 2015, Gezari et al., 2017).

6.2 How do these small numbers of unusual AGN fit in with other studies?

In Figure 6.2 I compare the results from this work with comparable AGN subtypes and catalogues, focusing in particular on similarly selected objects.

(1) LASr: Shown here are the *known* AGN from the LASr Galaxy Parent Sample (LASr-GPS; Section 2.2). Yellow squares represent AGN from the 70-month *Swift*-BAT catalogue (Ricci et al., 2017a) - hard X-ray selected AGN distributed across the whole sky,

but limited by flux depth. Large squares are B70 AGN in LASr; smaller yellow squares show the full extent of this catalogue which extends beyond the redshift limit of LASr. It does not stretch further in bulk than z$\sim$0.1 with the number of sources decreasing sharply up to that point, particularly at high column densities. Four green arrows show the redshift positions of the follow-up sources (Section 2.5.2). Yellow and green regions show where the majority (68%) of LASr sources lie. The gap in the middle is likely to be due to the difference in the main contributions to the known AGN in the catalogue (Section 2.1.1) - optically selected AGN are more likely to be found at lower $N_{\rm H}$ and drop off in number at higher redshifts. *Swift*-BAT selection can find higher-$N_{\rm H}$ sources and extends to higher redshifts than the optical catalogues used here.

(2) *NuSTAR* Serendipitous Sources: Pink squares show the sources found in Chapter 3 and Lansbury et al. (2017a) (large and small markers, respectively). The region shows the target zone of this parameter space: high $N_{\rm H}$ (heavily obscured up to and beyond Compton thick), but without redshift restrictions other than those implicitly imposed by the band ratio selection. Figure 3.20 shows the shape of the X-ray spectrum - as redshift increases, the shape within the energy bands changes until it is no longer informative. Figure 3.20 overplots the region where CT AGN are expected to lie - at $z \gtrsim$1.5 these will not appear with high band ratio values.

(3) COSMOS Legacy Survey: A small area of sky (2.2 deg^2 in the COSMOS field) was observed by *Chandra* to obtain deep soft X-ray data on sources within this region. The \-hatched area in Figure 6.2 shows where the demographics of the AGN within this survey lie (Marchesi et al., 2016, Civano et al., 2016). Redshifts are known, and $N_{\rm H}$ values are estimated from hardness ratios. It appears at higher redshift, despite no specific restrictions on redshift – as a deep, small area survey, the numbers of sources are relatively small thus less likely to be very local. Soft X-ray selection lends itself better to low $N_{\rm H}$ sources, even with very deep measurements and excellent flux limits. This selection is a soft X-ray analogue to *NuSTAR* selection - a single contiguous area in this case rather than many smaller areas, as with the *NuSTAR* serendipitous catalogue. Generally lower $N_{\rm H}$ values lead to higher apparent fluxes, thus the higher redshift coverage compared to *NuSTAR* selection.

(4) Optically Quiescent Quasars: The blue region shows our estimated target area (Chapters 4 and 5) for OQQs. The high-quality X-ray result from Chapter 4, J0751, is shown as a blue square. Additionally, the *lower limits* placed on $A_{\rm V}$ from [O III] upper limit measurements are shown (converted approximately to $N_{\rm H}$ using gas-to-dust ratios from Maiolino et al., 2001, : $N_{\rm H} \sim 10^{22.2} A_V$) – this makes the (significant) assumptions that the OQQs are *intrinsically* as powerful in [O III] as the QSO2s, and that the $N_{\rm H}^{\rm los}$ is comparable to $N_{\rm H}^{\perp}$. As can be seen from the J0751 result (large blue arrow), this is not the case for this source but at this stage it remains to be seen how this will appear for other OQQs.

(5) Optically Elusive AGN: Selected from *XMM-Newton* and SDSS (Pons and Watson, 2014), these objects are X-ray AGN that are optically misclassified. Some are thought to be underluminous Seyfert 2s (possibly true Seyfert 2s) diluted by host galaxy star-formation emission. For OQQ selection, we removed any galaxies with significant star-formation contributions to their emission line fluxes. Thus these optically elusive 'diluted' AGN may be cousins of the OQQs, in galaxies with more star-formation. In the parameter space, these appear at lower redshift, and generally with low $N_{\rm H}$ (small blue squares; upper limits shown with small blue arrows).

(6) Extremely Red Quasars: This class of object (see Section 5.13.5) is bright in IR compared to optical. In the parameter space figure, orange diamonds show heavily reddened quasars (Banerji et al., 2012) that are found to have large dust extinction values (converted here to approximate $N_{\rm H}$ as with the OQQs). X-ray observations of similar objects (Lansbury et al., 2020) with known $N_{\rm H}$ values are shown as orange squares. These are selected at higher redshifts than the OQQs, but appear to cover a similar $N_{\rm H}$ range - close cousins to 'cocooned ' AGN.

(7) Spectroscopic IDentification of ERosita Sources: SPIDERS (Dwelly et al., 2017) is an observing programme of SDSS which aims to provide optical spectroscopy for eROSITA-detected X-ray sources. Prior to this, it began with sources from the *ROSAT* all-sky survey (RASS; Boller et al., 2016) and *XMM-Newton* slew survey (Saxton et al., 2008, XMM-SSC, 2018). The resulting catalogue (Comparat et al., 2020) is thus a soft X-ray selected catalogue covering a range of redshifts ($0.006 \lesssim z \lesssim 2.5$), with the bulk of these at $z < 1$ as shown in Figure 6.2 - the /-hatched area shows where 68% of sources lie. For illustration purposes, values for $N_{\rm H}$ have been randomly selected for each source from a distribution centred around log $N_{\rm H}$=22 cm^2.

We have compared the AGN found in this work to deep small area surveys (e.g. COSMOS), large area follow-up surveys (e.g. SPIDERS), works targeting specific types (e.g. ERQs, Optically Elusive AGN; OEA), and catalogues of confirmed AGN (e.g. BASS, contributions to LASr). Each of these methods covers different parameter spaces, adding to the big picture of the AGN population. The chapters of this thesis show how assessment of the weaknesses and gaps in AGN selection can lead us to methods that will deal specifically with those flaws. *NuSTAR* serendipitous sources have expanded the number of hard X-ray selected CT AGN; particularly noting that the higher spatial resolution of *NuSTAR* compared to *Swift*-BAT enables better distinction of optical and IR counterparts, thus making detailed multi-wavelength possible. The OQQs appear as intermediate redshift AGN, closer than many ERQs and further than other optically unusual sources such as OEA. They fall into a rarely explored parameter space that is not easily shown on this plot - 'cocooned' AGN are high covering factor, and 'young' AGN are changing state - and hence may represent a path to make population studies of AGN in these observationally unusual forms.

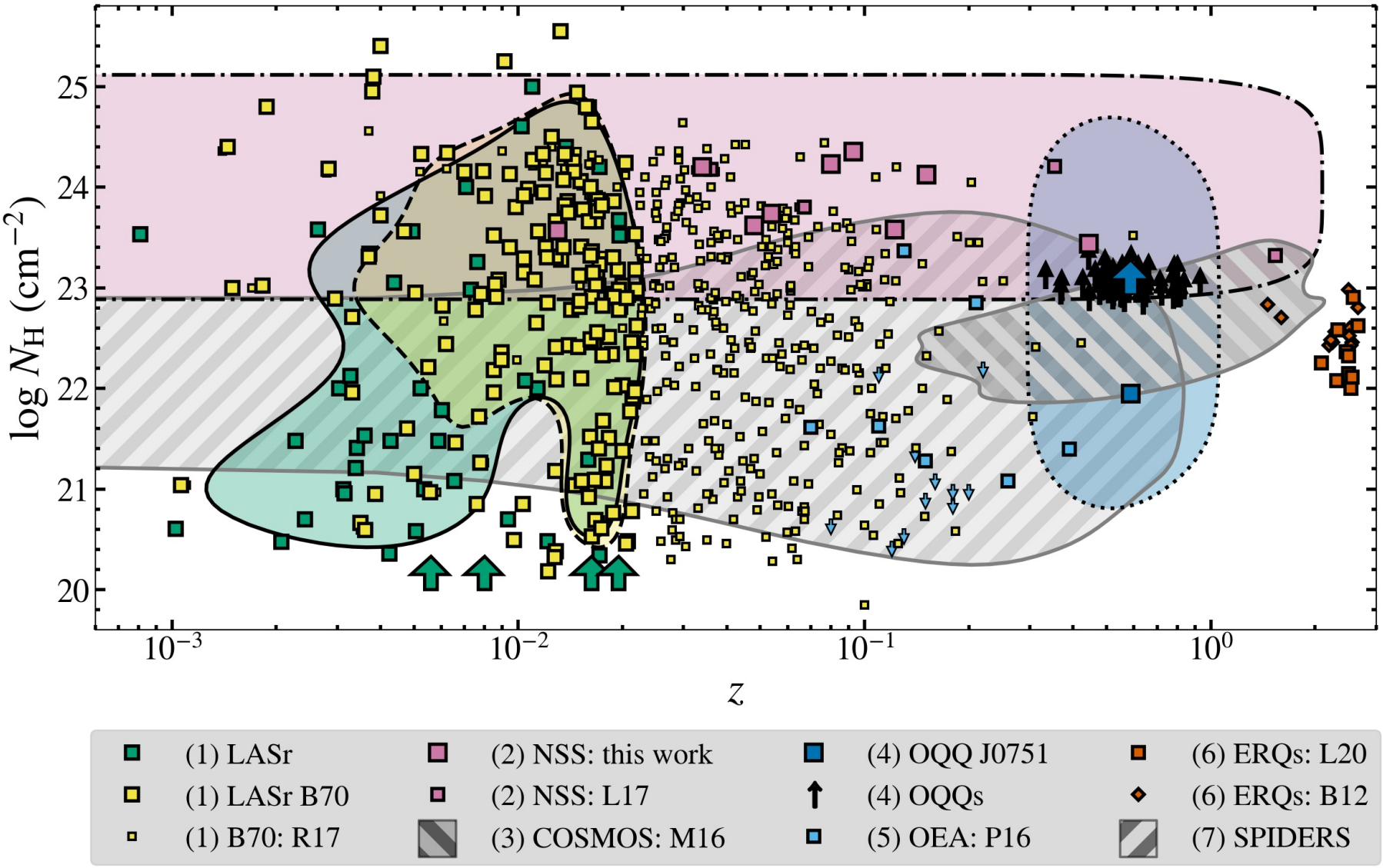

FIGURE 6.2: Parameter space covered by the known AGN in LASr (green shaded region, solid edge), by the LASr B70 AGN only (yellow shaded region, dashed edge), the region targeted by *NuSTAR* selection (pink shaded area, dot-dash edge), and the region targeted by OQQ selection (blue shaded area, dotted edge). Also shown are the results from these chapters, and several comparison populations (see Section 6.2).

6.3 How can the results for this work inform future work?

Each section of this work is not without open questions. The quest to find all AGN will never be complete, and even in the local universe we can only push closer to a full census via better understanding of our biases, alongside improved measurement and selection techniques.

6.3.1 LASr

Analysis of current AGN candidates remains incomplete - with 61 in total selected as promising bright sources, we must continue to inspect these. As discussed in Section 2.3.3, based on current estimates of the Compton thick AGN fraction we might expect a significant fraction of these candidate AGN to be CT. An accurate count of AGN - particularly CT AGN - among these candidates would be an important contribution towards understanding this part of the AGN population. In addition to optical and NIR spectroscopy, further multi-wavelength information would also be invaluable - for example, X-rays from eROSITA for AGN detection, FIR for SED fitting (see e.g., Section 4.2.2 for OQQ work on this subject).

Known AGN that pass both the R90 and luminosity criteria used for selection of candidates only make up a small fraction of the total known AGN. Other selection criteria may be less reliable, but worth investigating to increase the completeness of our candidate AGN sample. Especially of interest are low-luminosity AGN, where selection is commonly very incomplete.

There are a significant number of galaxies that *may* be located in the LASr volume - the very local universe - but that do not have reliable redshifts. Upcoming spectroscopic surveys (e.g., 4MOST) may begin to reduce this number, adding new potential candidates to the LASr-GPS. At the expense of completeness it will be possible, as spectroscopic completeness and quality improves, to extend the volume limit on LASr and thus increase the number counts of AGN and AGN candidates.

I have shown in Chapter 4 that targeted X-ray observations can be a powerful tool for AGN confirmation and study. Sources from LASr that are candidates for obscured AGN based on high ratios of MIR luminosity to upper limits on X-ray non-detections with *Swift*-BAT could be considered similar to the high band ratio NSS80 sources, and thus would be strong targets for deeper hard X-ray observations.

6.3.2 NSS

Thus far we have only examined the X-ray observations of the CT AGN candidates, but this is not the only data that would give useful information on the properties of

these sources. Techniques used in Chapter 2 (emission line diagnostics) and Chapter 5 (SED fitting) would look at these sources from a different perspective, and as demonstrated in this thesis multiple analysis methods are vital for examining elusive AGN. Additionally, detailed model comparison techniques such as Bayesian X-ray Analysis (BXA; Buchner et al., 2014, see also Chapter 4) would allow for better statistical comparison and more physically informed parameter priors. Currently the intrinsic spectral shape had to be fixed for some sources in order to achieve an acceptable fit, but a physical prior (a statistical preference towards more likely intrinsic AGN values) would improve comparison between possible models.

In this work and L2017 selection with band ratio was done in a simple way - a single value across all redshifts. Two alternatives present themselves: either vary the bands used (i.e., the observed energies of intrinsic 3-8 keV decrease in energy as redshift increases), or vary the band ratio threshold with redshift (see e.g., the lower bound of the shaded grey area in Figure 3.20). For a more extensive and complete selection, spectral curvature (Koss et al., 2016) could be used. This technique works using emission from the 'Compton hump' at ∼10-30 keV - specifically with *NuSTAR* a function of 8-14 keV, 14-20 keV, and 20-30 keV on-axis count rates. For serendipitous sources, which are by definition off-axis, the function would need to be adjusted to take this into account. Spectral curvature selection retains a bias against extremely Compton thick AGN simply due to lack of counts, but would select a larger number of promising and robust candidate CT AGN.

6.3.3 OQQs

The key next steps for the OQQs is to look closer: can we unravel the clues we have and work out the intrinsic nature of these sources? What extra data might give us the information we need?

In Chapter 4 we saw how targeted X-ray observations could provide far better information on a single source than serendipitous soft X-ray data can on sources not selected in that regime. Further X-ray data – enough to be a representative sample of the population – could start to answer questions about the OQQs as a whole group, including whether they should be considered to be a single class according to their *intrinsic* nature rather than observed properties. We found OQQ J0751+4028 to be lightly obscured and under-luminous, with obscuration in a spherical form consistent with a 'cocooned' model. The sparse X-ray data for the main population (see Section 5.9) indicates that they are *observationally* under-luminous, but without sufficient spectral quality the intrinsic luminosity is harder to assess. Thus, further targeted and deeper X-ray observations would help answer questions about the true power of OQQs: are they generally intrinsically under-luminous in X-rays? Are any heavily obscured, or does the enshrouding material tend to have lower column densities?

With X-rays we can probe the AGN activity close to the BH, i.e., the 'current' accretion state of each OQQ. However, if we want to distinguish between our theories of OQQ nature (primarily 'cocooned' or 'young' AGN; are optical emission lines produced in the narrow line region or not - see Section 5.12) then we must search for evidence of AGN activity producing signals at greater distances from the BH (i.e., indicating that accretion has been ongoing for a longer period of time, and the AGN is not a 'young' source).

In Chapter 2 we showed the power of high quality optical and NIR spectra for following-up MIR selected AGN. This could easily be applied to improve the optical spectra for the OQQs, tightening the [O III] upper limits or even detecting weak [O III] lines. Joint optical and NIR spectra could provide important emission line information, to contribute to multi-wavelength diagnostics.

If the OQQs are 'cocooned', we expect them to have intrinsic emission lines, with these being optically extincted by the enshrouding material. Currently, we have SDSS spectra for each OQQ (by selection) which show no [O III], but this means that we do not yet have detailed spectral evidence that OQQs host AGN. With X-SHOOTER (Vernet et al., 2011) we could search for signatures of the BLR in the NIR, for example Fe II (1.26 µm), Paβ, H_2 (2.12 µm), Brγ, and coronal lines, e.g., [Si VI] (1.96 µm) and [Si X] (1.43 µm). If broad lines with typical widths of several thousand km s^{-1} are detected, this would be unambiguous additional evidence of the presence of an AGN. There is some evidence that Narrow Line Seyfert 1s can show broader lines in the IR than the optical, despite the BLR being directly visible (e.g., Nagar et al., 2002), or the appearance of Seyfert 1.8/1.9 AGN can be due to reddened broad lines. X-SHOOTER would also provide optical spectra of much improved quality compared to SDSS. Thus it would enable tighter upper limits on [O III] flux or detection of weak [O III] emission, which if found would place OQQs as extreme examples of Weak Line Quasars (e.g., Meusinger and Balafkan, 2014).

To observe hidden emission line regions, rather than observing them directly (as with narrow lines in QSO2s, or broad lines in Seyfert 1s) we can instead observe the *scattered* emission from obscured emission lines. Spectropolarimetry has been used to detect hidden broad line regions in Seyfert 2s (Ramos Almeida et al., 2016). A very high signal-to-noise is required to detect the polarised scattered emission, which is only a few percent of the total. Thus if we aim to search for a hidden *narrow line region*, this same method may prove fruitful.

6.3.4 How will upcoming large surveys provide more answers?

Selection of OQQs has so far been limited to SDSS spectra, which (while numerous) are restricted to only part of the sky and with targeting strategies that do not completely

align with our aims. A hugely expanded selection of spectra will in turn expand the sample of OQQs, allowing us to get a better statistical handle on their properties, and make better considerations of their place in the wider population of AGN. For example, 4MOST (see Section 1.3.9) aims to obtain spectra for up to 1 million IR-selected AGN - if the same proportion of these pass some of the OQQ selection steps, we could more than triple the numbers of OQQs, as well as expanding into the Southern hemisphere. If we can find more OQQs (and similarly rare and interesting objects) we will be able to get a better statistical handle on their properties, and make better considerations of their place in the wider population of AGN and influence on host galaxy activity. Deliberate selection of *WISE* AGN as targets will also enable us to make much more robust calculations of OQQ number density compared to the general QSO2 population, without some of the biases due to SDSS target selection, and with knowledge of their duty cycle, the place of OQQ in galaxy formation and evolution will be possible to consider quantitatively. The vast new dataset from 4MOST also opens up possibilities for new AGN subtypes even further from standard paths, and even rarer than OQQs.

The 4MOST survey of X-ray selected AGN also offers the intriguing possibility of an optical/X-ray selected sample, analogous to OQQs - if we discard the requirement for bright IR and AGN colour, replacing it with eROSITA detection, can we find Optically Quiescent Quasars in the spectra for these targets? How will they be different to IR selected OQQs?

One limitation on finding new CT AGN candidates based on NSS80 is lack of redshift. Of NSS80 objects $\sim$60% have no redshift. Of the high band ratio sources, $\sim$75% have no redshift. Currently we exclude sources without redshift, and a follow-up programme at Palomar is filling up the gaps. However, if 4MOST can provide redshifts for more of the serendipitous sources, especially Southern hemisphere sources, we might expect to double again the sample of candidate CT AGN.

6.4 Final Lessons

In this thesis, I started with a local AGN census, and used the results from this to influence the direction of the following rare AGN searches. We calculated that the number of Compton thick AGN among the 'missing' AGN from LASr was likely to be high, based on the lack of *Swift*-BAT detections. We also understand that AGN may be misclassified if they show an absence of 'typical' AGN optical signatures, whether this is an intrinsic effect (i.e., no ionisation lines produced) or extinction (i.e., ionisation lines are reduced by line-of-sight absorption).

Whether the cause of AGN being overlooked is heavy obscuration, fully covering obscuration, or intrinsic behaviour, one of the most reliable and relatively unbiased ways to select candidates is in the MIR; as used in both LASr (Chapter 2) and with the OQQs

(Chapters 4 and 5). In Figure 6.3 I place these selection criteria onto a single plot, along with the positions of the *NuSTAR* sources analysed in Chapter 3 and Appendix C (see Appendix B.3). The OQQs are, by selection, red enough and luminous enough to have also been chosen as AGN candidates if they were in the LASr volume; however, they are all at much larger distances. This is likely to be a combination of sheer increase in numbers over the greater volume (and thus increased chance of finding rare AGN), and weak [O III] lines that become increasingly dominated by noise in the spectrum at higher distances. The *NuSTAR* serendipitous sources studied in Chapter 3 are all at least as red in *W*1-*W*2 as the bulk of LASr known AGN, but do not all pass the selection criteria (out of 9 in total, 5 sources pass the LASr colour selection threshold, Assef et al., 2018; 3 pass the more restrictive OQQ selection threshold, Stern et al., 2012). Some of these, and most of the remaining serendipitous sources (those not analysed due to low counts) show noisy *WISE* data (see Appendix B.3), and thus may also have been excluded from selection due to insufficient SNR or not significant detections. This highlights the weakness of MIR selection in that it is restricted to bright MIR sources, and some of its incompleteness will be due to thresholds set against low brightness sources to improve reliability. Many known AGN do not pass the MIR selection criteria; the majority of these are lower luminosity and/or selected with optical spectroscopy. When setting a higher luminosity threshold (see e.g. Sections 2.4.3, 2.4.5) we still find that a high proportion are not selected, reinforcing the need for a multi-wavelength approach.

Figure 6.4 summarises the structure of the AGN studied in this work. It is a simplified schematic, showing only orientation based explanations for each source, and is intended as a guide to the main sources found and studied in this thesis. Each quadrant shows AGN from a different chapter, showing their various appearances and contrast from more 'typical' AGN. The top left corner shows the known AGN from LASr which tend to be typical in the optical, or bright/less obscured in X-rays. These appear as 'normal' AGN in the unification scheme (Section 1.1.3), with a mix of Type 1 and Type 2 AGN; as represented by the broad arrow showing the wide range of viewing angles. In the bottom left, the central system remains the same, but Compton thick column densities obscure the AGN activity, representing *NuSTAR*-selected hard X-ray AGN. These may or not may not show a typical optical spectrum, but are more likely to be Type 2 if they do. The right hand side of the diagram shows OQQs. In the top, a 'cocooned' OQQ, producing intrinsically typical [O III] emission that is obscured by a larger region of material; the column depth of this could take any value, but must be optically thick enough to extinct any emission. In the bottom, an OQQ that is intrinsically 'young', with no [O III] produced. Ionising radiation has not reached the region where narrow emission lines would be produced. By selection, these objects are still optically obscured with no broad emission lines.

As a final summary, Figure 6.5 shows the areas of obscuration depth and geometry that the searches in this thesis cover: LASr known AGN are primarily optically confirmed,

and thus lower in covering factor; NSS hard AGN are heavily obscured, but covering factor neutral; and OQQs (*if* 'cocooned'; see Section 5.12) are high covering factor, but with potentially any obscuration depth. Disparate in properties, they all share in their ability to escape selection. I have shown here that although our knowledge of the AGN population is constantly improving, there are areas and specific AGN classes where lack of completeness and a dearth of confirmed sources place high uncertainties onto any conclusions. As suggested here, we must both widen the selection of AGN to more atypical objects and study their properties in detail.

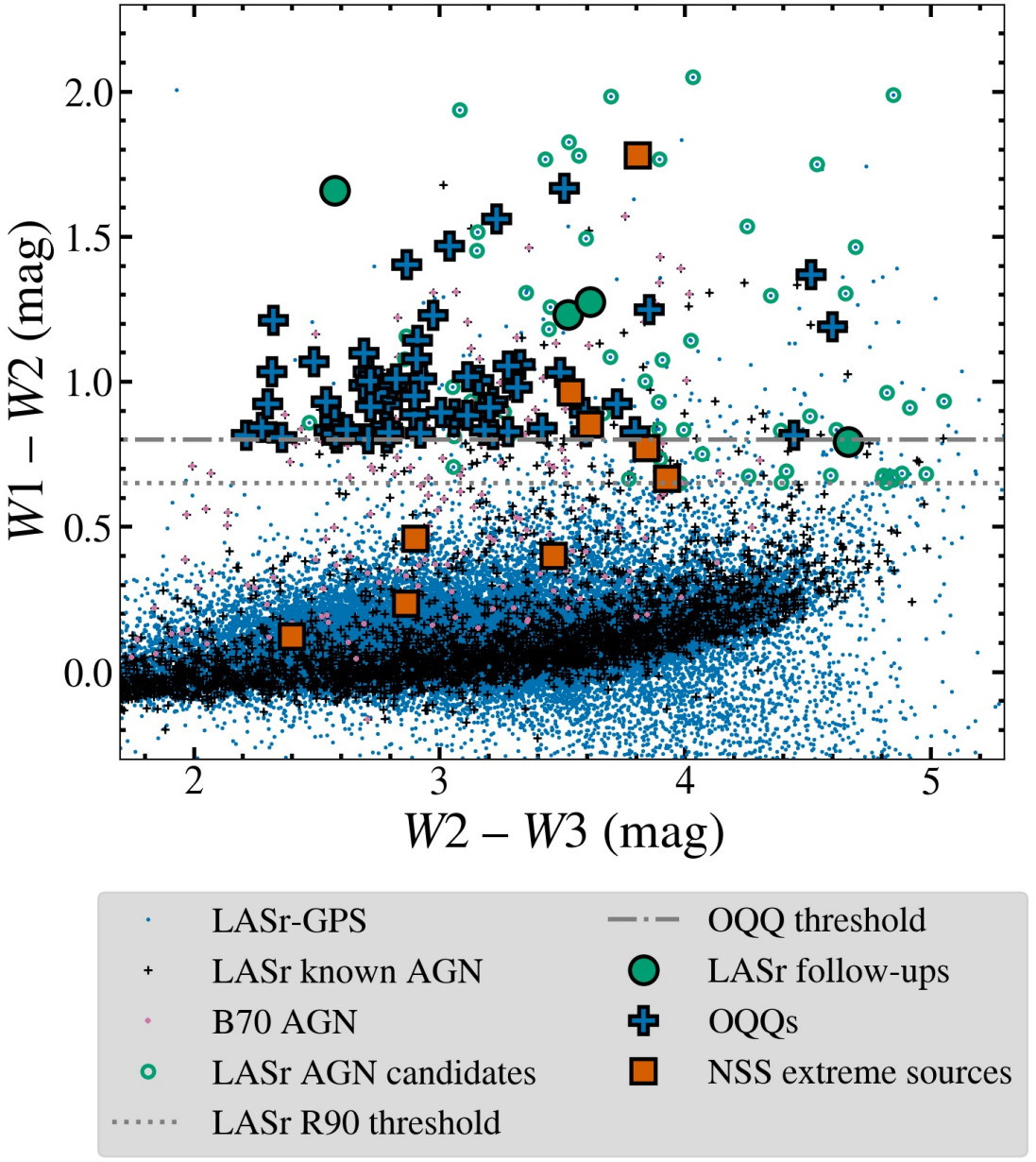

FIGURE 6.3: $W1 - W2$ versus $W2 - W3$ colour-colour diagram (as in Figure 2.3a), with all detected galaxies in the combined GPS (blue). Also shown: known AGN in LASr (black crosses), LASr candidate AGN (small green circles), LASr follow-up targets (large green circles), OQQs (blue crosses), and NSS sources (orange squares). R90 selection threshold is shown as a dashed grey line.

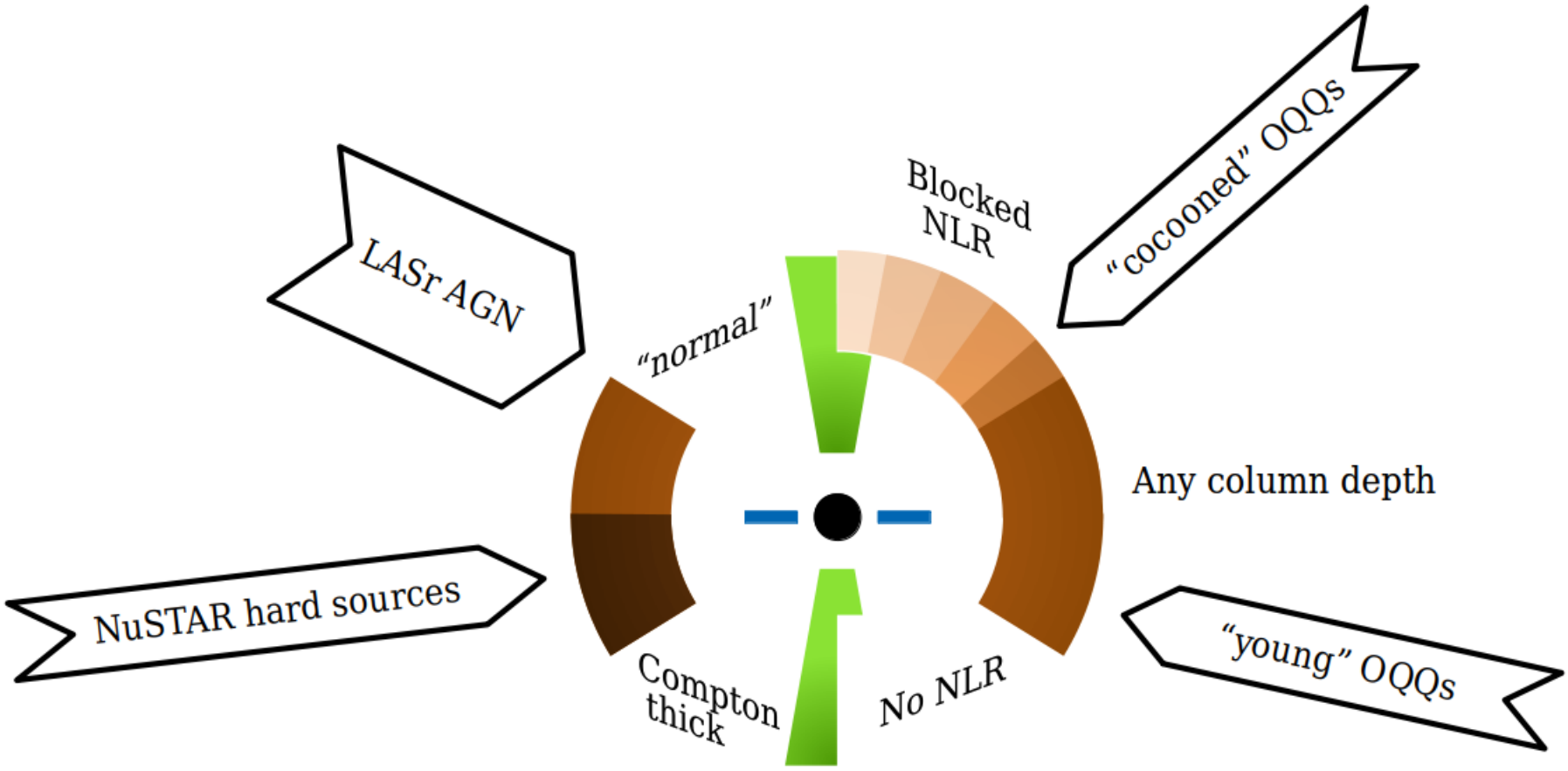

FIGURE 6.4: Schematic showing the variant AGN structures selected for in this thesis. As in Figure 5.23, components are as follows: black central SMBH, blue accretion disk, green ionised gas (NLR), brown obscuration (darker indicating higher column densities). Top left corner: known AGN from LASr, tending to be typical in the optical, or bright/less obscured in X-rays. Bottom left corner: *NuSTAR*-selected hard X-ray AGN, which show spectra likely to be the result of Compton thick obscuration; may or not may not show a typical optical spectrum, but more likely to be Type 2 if it does. Top right corner: a 'cocooned' OQQ, producing typical [O III] emission that is obscured by a larger region of material; the column depth of this could take any value. Bottom right corner: an OQQ that is intrinsically 'young', with no [O III] produced; still optically obscured with no broad emission lines.

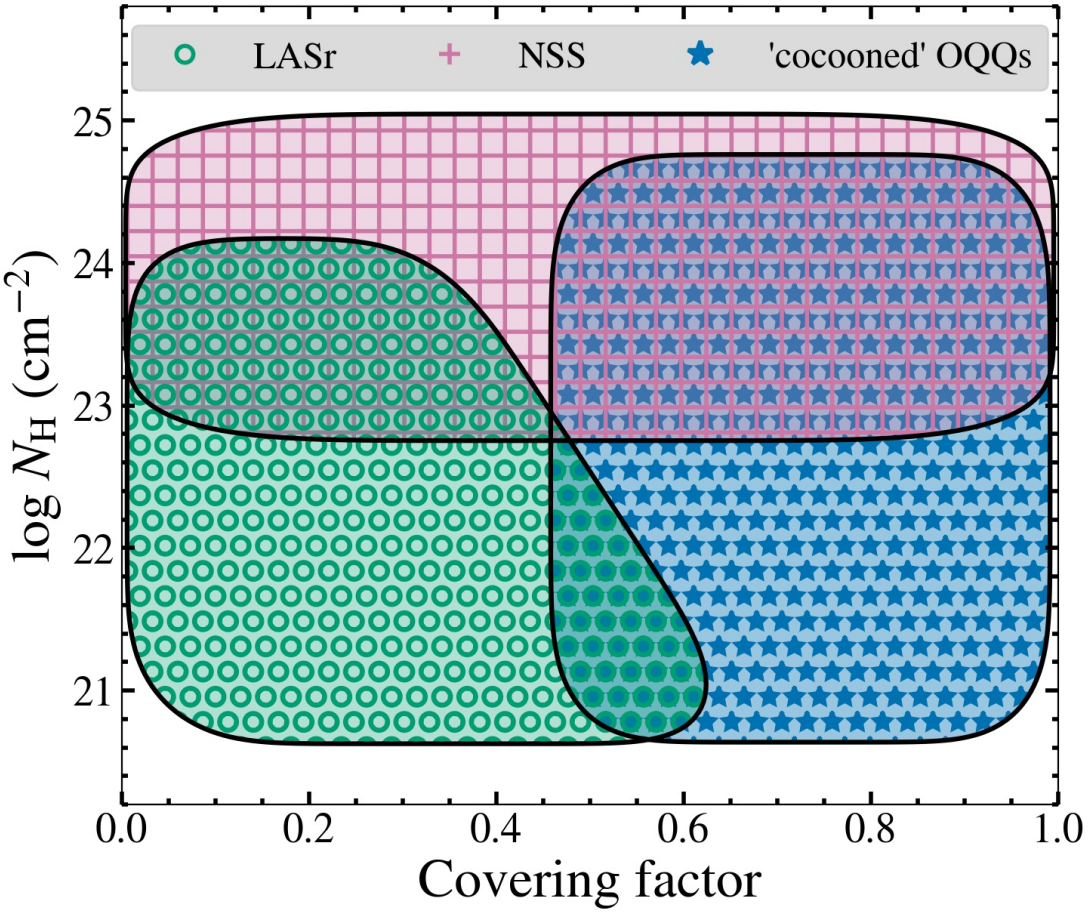

FIGURE 6.5: Schematic showing how the different search methods in this thesis discover different AGN obscuration.

Appendix A

LASr AGN candidates with X-SHOOTER: further information

A.1 *Swift*-XRT observations of ESO495

Serendipitous observations of ESO495 are available with *Swift*-XRT. While this source does not appear in the 2SXPS catalogue (Evans et al., 2020b), the online tool (Evans et al., 2009) for combining and reducing all available data at a given location does result in a detection, and a spectrum can be produced (see Figure A.1). I fitted this with an absorbed powerlaw (the same as the basic model in Chapters 3 and 4). This results in a very low, unabsorbed $N_{\rm H}$ level. A free fit results in an extremely high photon index ($>$3), so instead is fixed to a high but more typical value of 2.2 (see e.g., Ricci et al., 2017a). Fit statistic is 160 with d.o.f. 131. Observation IDs: 00047667001, 00047667002, 00082892002, 00082892003, 00089159001.

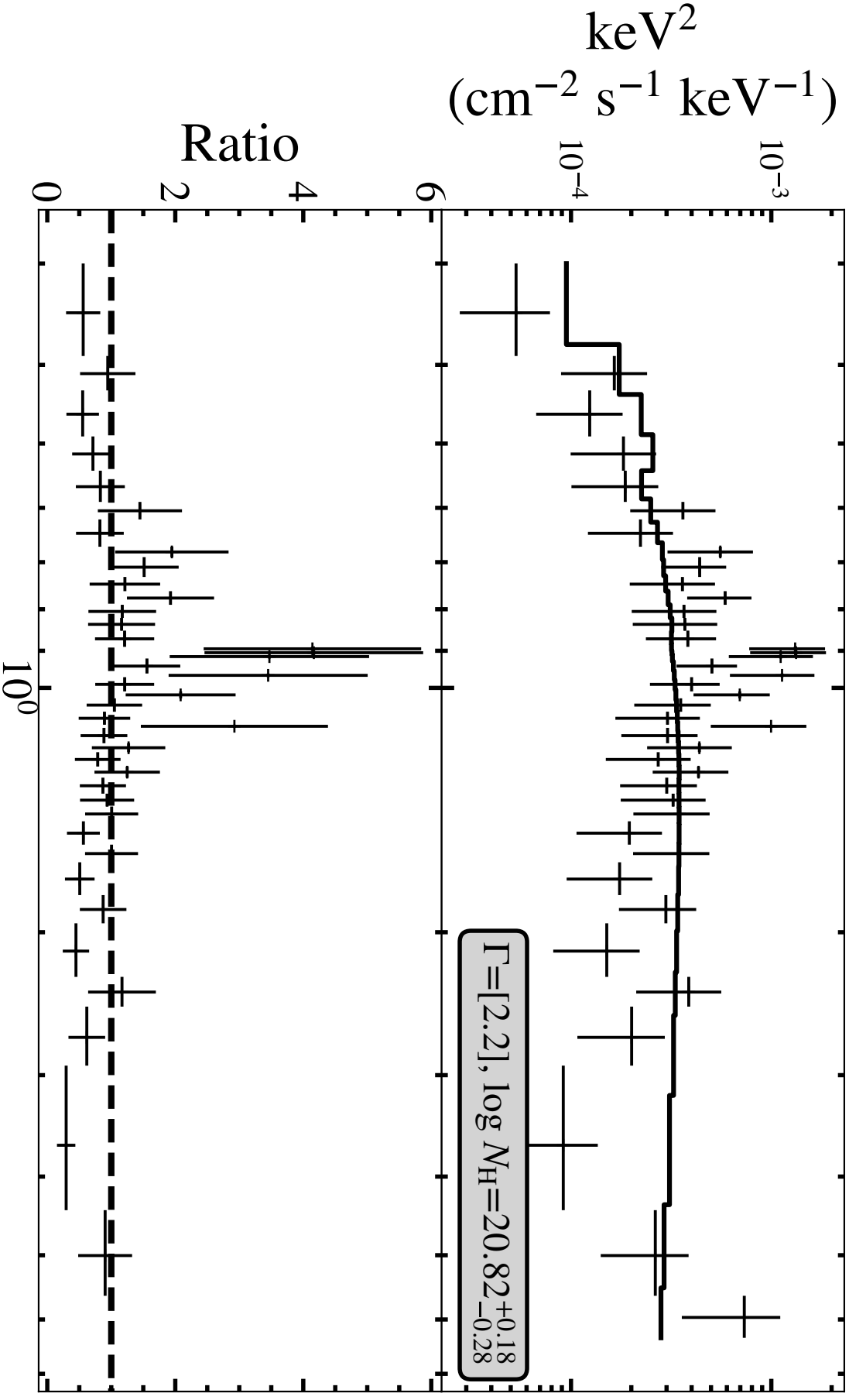

FIGURE A.1: *Swift*-XRT spectrum of ESO495 with photon index Γ fixed to 2.2.

A.2 *WISE* four band images

In this section we present the *WISE* images for each band: $W1$ (3.4 µm), $W2$ (4.6 µm), $W3$ (12 µm), and $W4$ (22 µm). The AGN candidates from LASr are all selected in the MIR using $W1$-$W2$ (Section 2.3.2) and $W3$ luminosities (where the emission is most dominated by AGN heated dust). Thus here we show each band separately for illustration, and to compare the appearance of nearby objects in the IR. Also shown are the PanSTARRS *irg* images with $W1$ contours overlaid. CGCG058 shows tidal tails, possibly a sign of recent interaction. ESO343 is a close pair, both bright IR sources; the partner is a known AGN. ESO495 may show a second bright region, but without a separate redshift this is not confirmed to be part of the same system. The relationship between galaxy mergers and AGN activity is discussed further in 3.4.2.

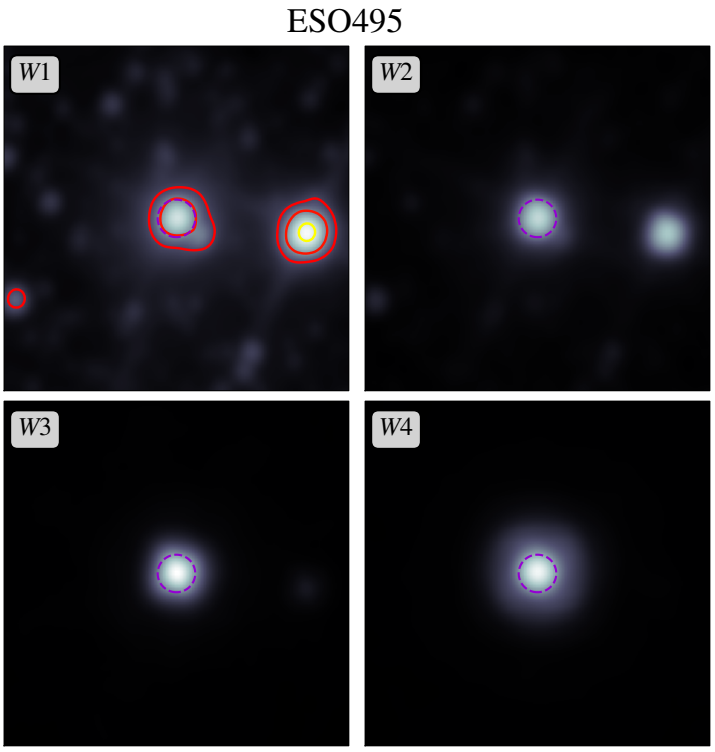

(A) Four band *WISE* images of ESO495, log scale, with dashed circles of radius 9 arcseconds centred on the catalogue coordinates.

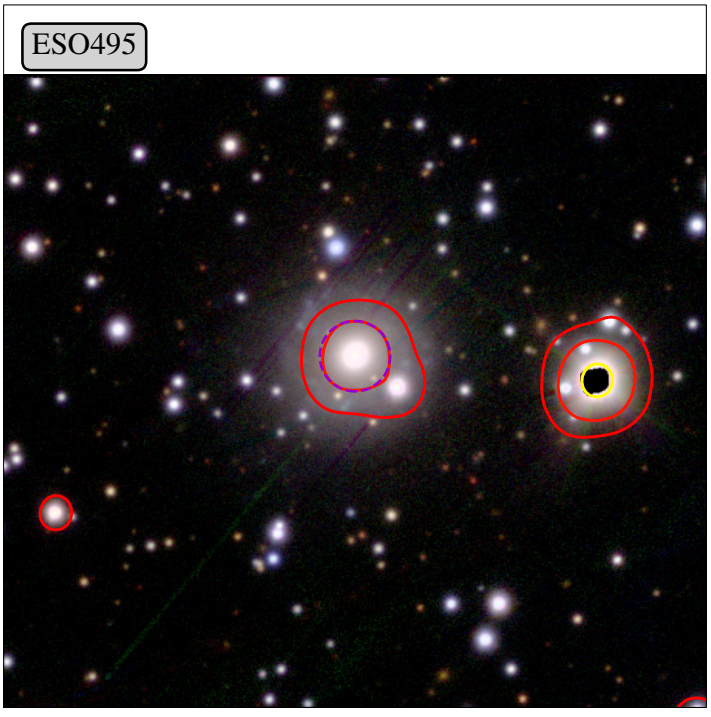

(B) PanSTARRS *irg* bands converted to RGB image of ESO495. Dashed circle has 9 arcsec radius and is centred on the catalogue source coordinates. Contours show *WISE* *W*1 data, with levels at 1, 5, and 50% of maximum.

FIGURE A.2: *WISE* and PanSTARRS images of ESO495.

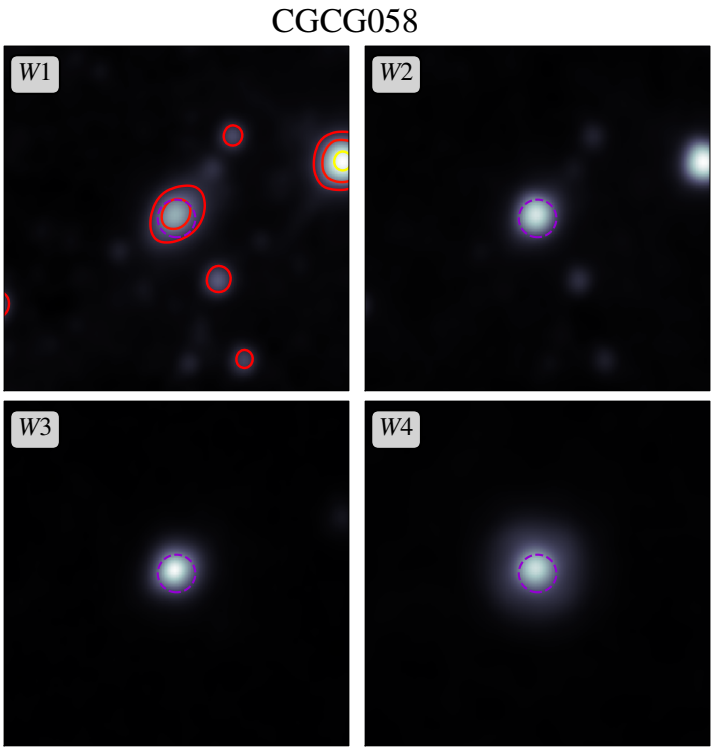

(A) Four band *WISE* images of CGCG058, log scale, with dashed circles of radius 9 arcseconds centred on the catalogue coordinates.

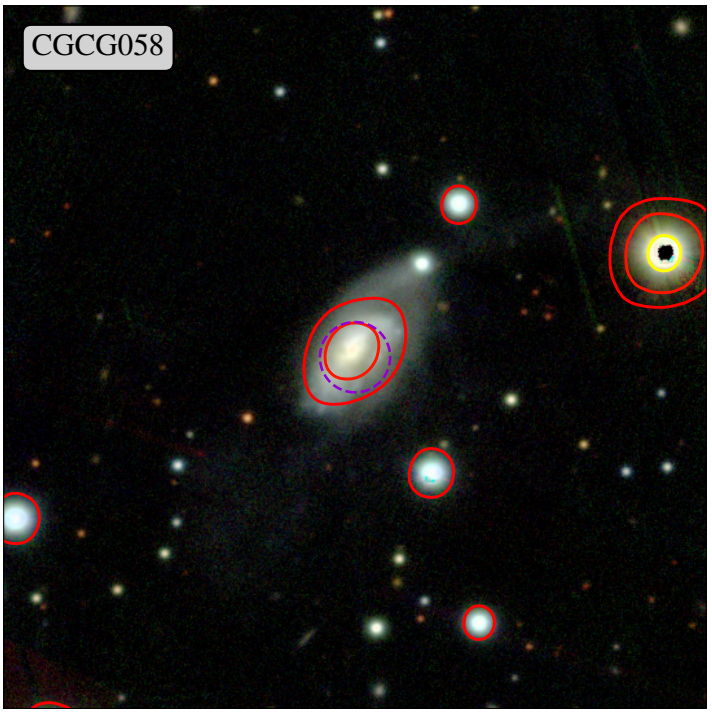

(B) PanSTARRS *irg* bands converted to RGB image of CGCG058. Dashed circle has 9 arcsec radius and is centred on the catalogue source coordinates. Contours show *WISE* *W*1 data, with levels at 1, 5, and 50% of maximum.

FIGURE A.3: *WISE* and PanSTARRS images of CGCG058.

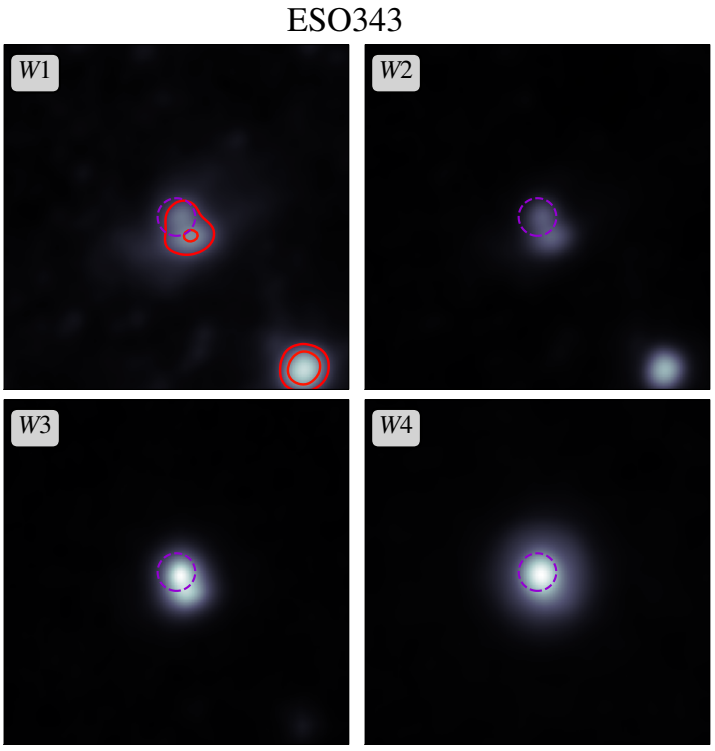

(A) Four band *WISE* images of ESO343, log scale, with dashed circles of radius 9 arcseconds centred on the catalogue coordinates.

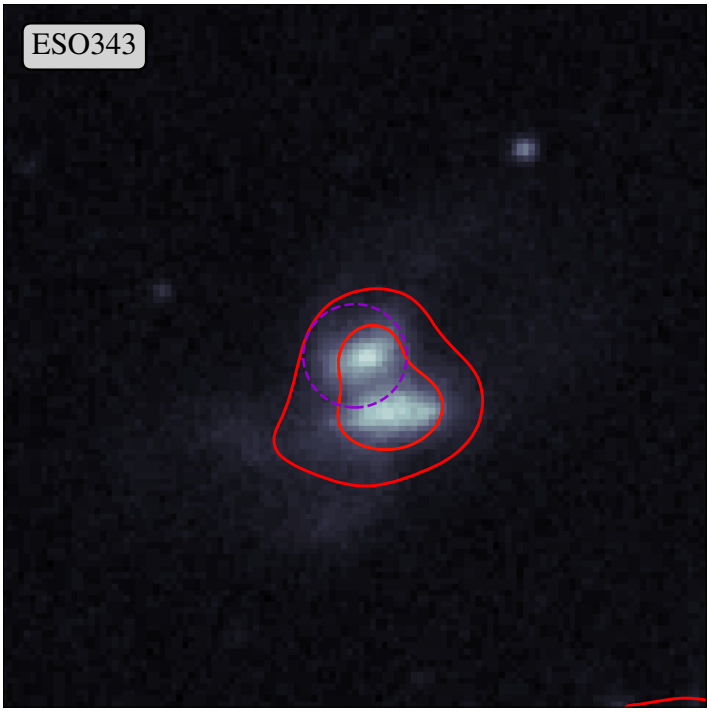

(B) DSS2 red image of ESO343. Dashed circle has 9 arcsec radius and is centred on the catalogue source coordinates. Contours show *WISE* W1 data, with levels at 1, 5, and 50% of maximum.

FIGURE A.4: *WISE* and PanSTARRS images of ESO343.

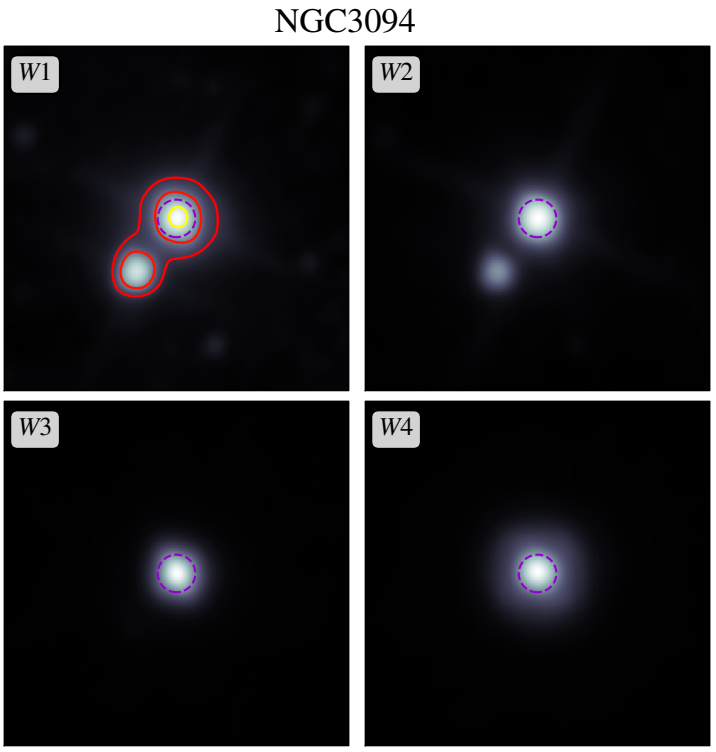

(A) Four band *WISE* images of NGC3094, log scale, with dashed circles of radius 9 arcseconds centred on the catalogue coordinates.

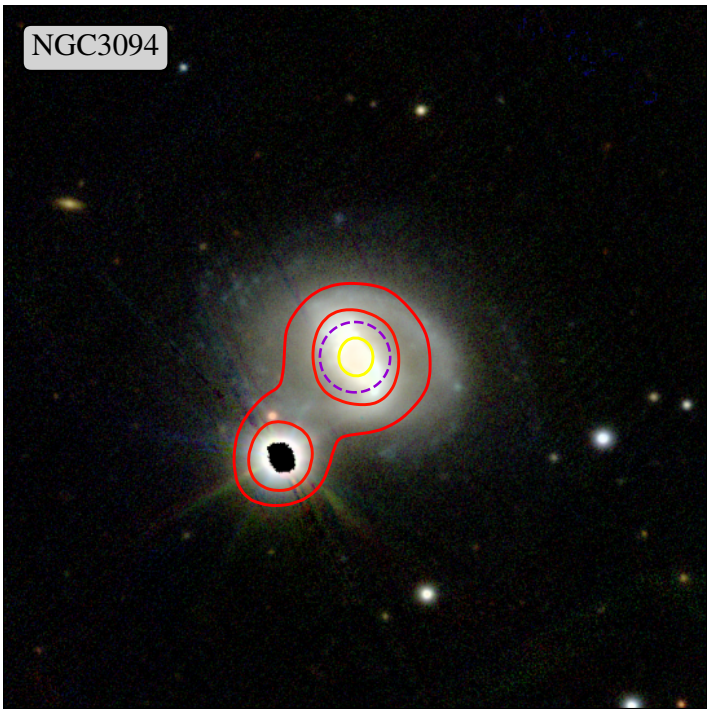

(B) PanSTARRS *irg* bands converted to RGB image of NGC3094. Dashed Circle has 9 arcsec radius and is centred on the catalogue source coordinates. Contours show *WISE* *W*1 data, with levels at 1, 5, and 50% of maximum.

FIGURE A.5: *WISE* and PanSTARRS images of NGC3094.

A.3 Additional optical and NIR emission lines

This Appendix presents additional emission lines not presented in Section 2.5.2. We focus on high ionisation lines typically seen in AGN: the hydrogen Paα and Brγ lines, the forbidden [Si VI] line and Neon lines from NUV and NIR ([Ne II], [Ne III], and [Ne V]). In ESO 495 the region around [Si VI] shows a wave-like pattern that could be the result of CCD fringing.

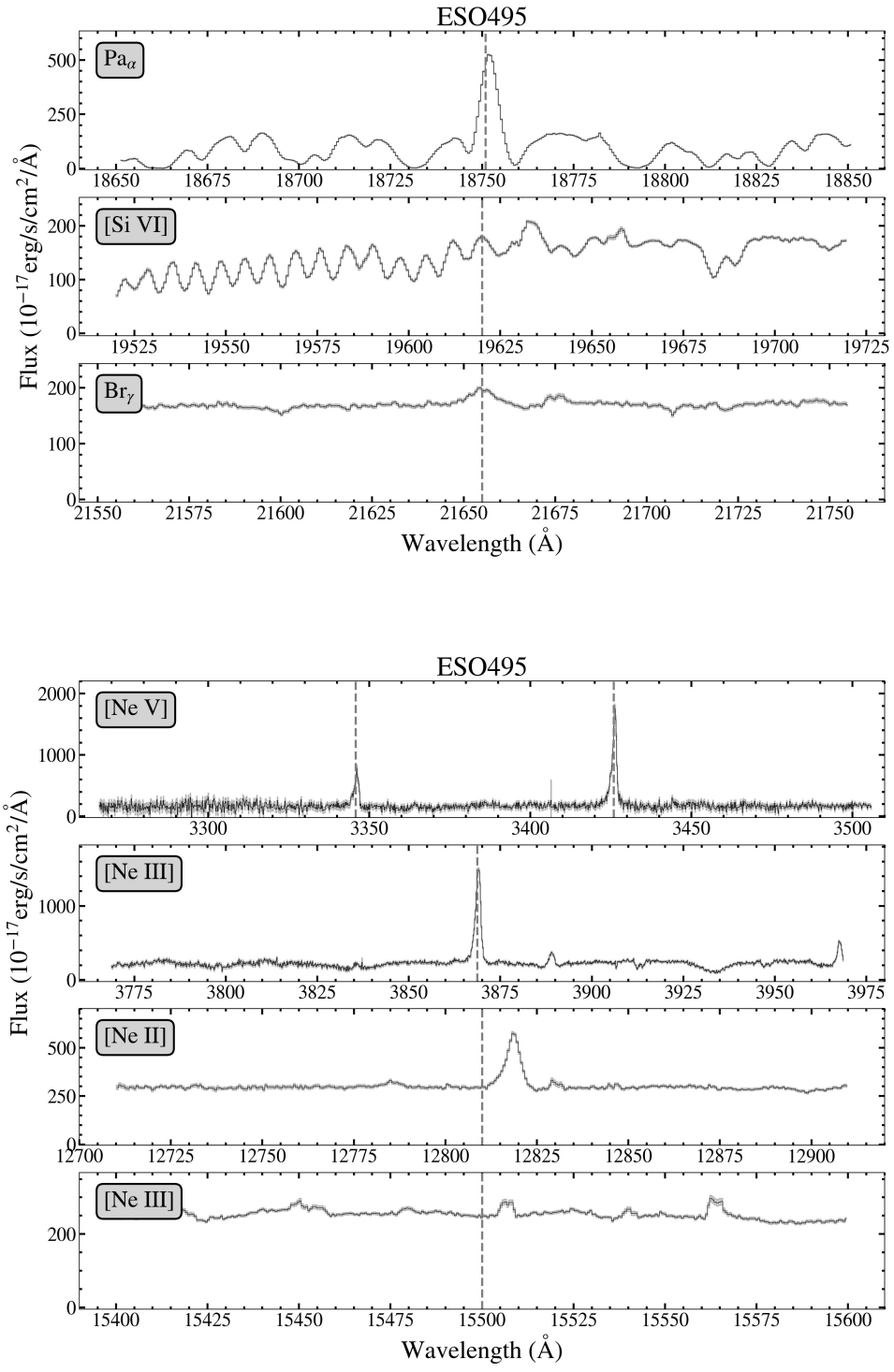

FIGURE A.6: Additional emission lines typical of AGN from ESO495.

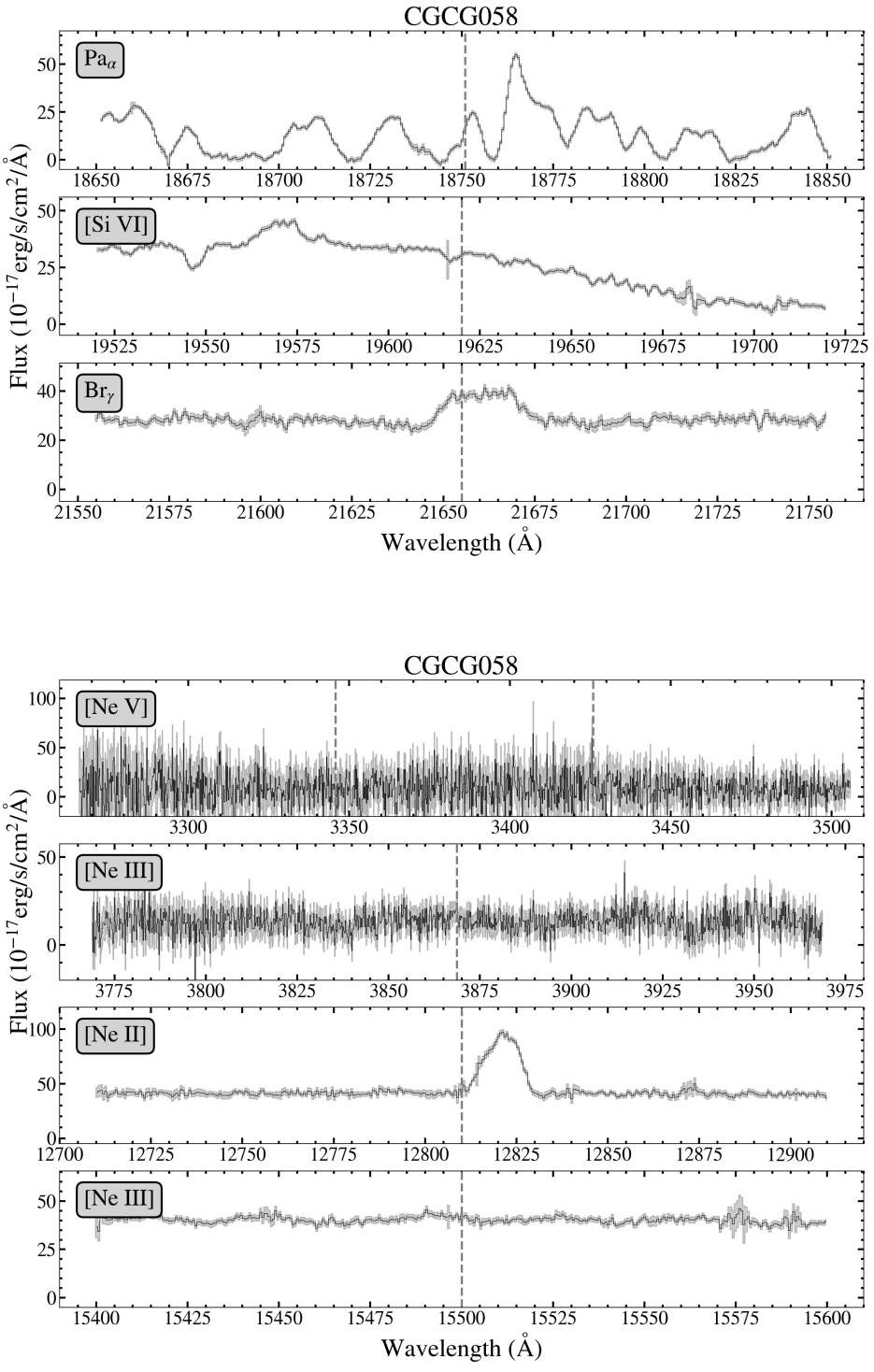

FIGURE A.7: Additional emission lines typical of AGN from CGCG058.

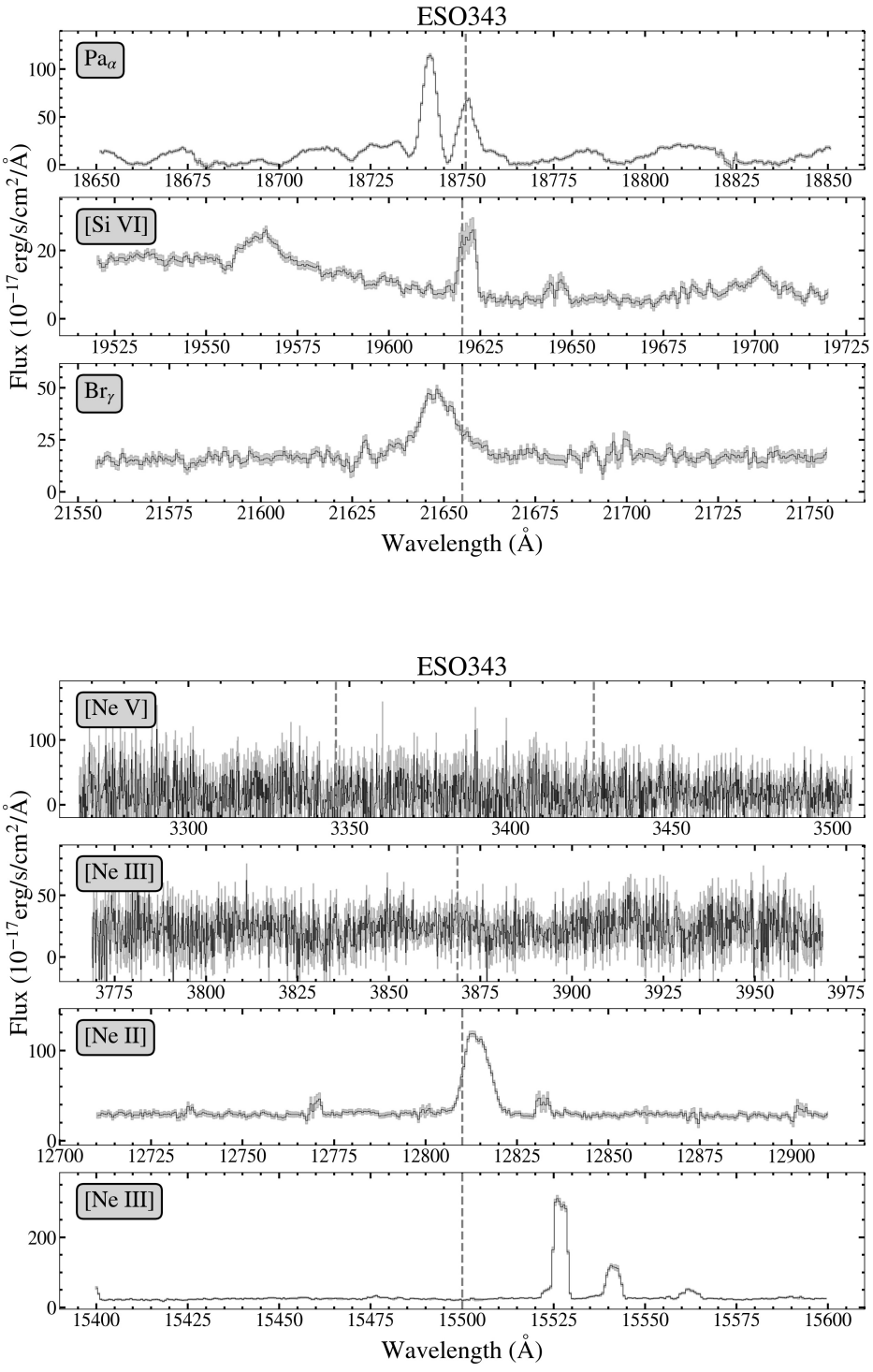

FIGURE A.8: Additional emission lines typical of AGN from ESO343.

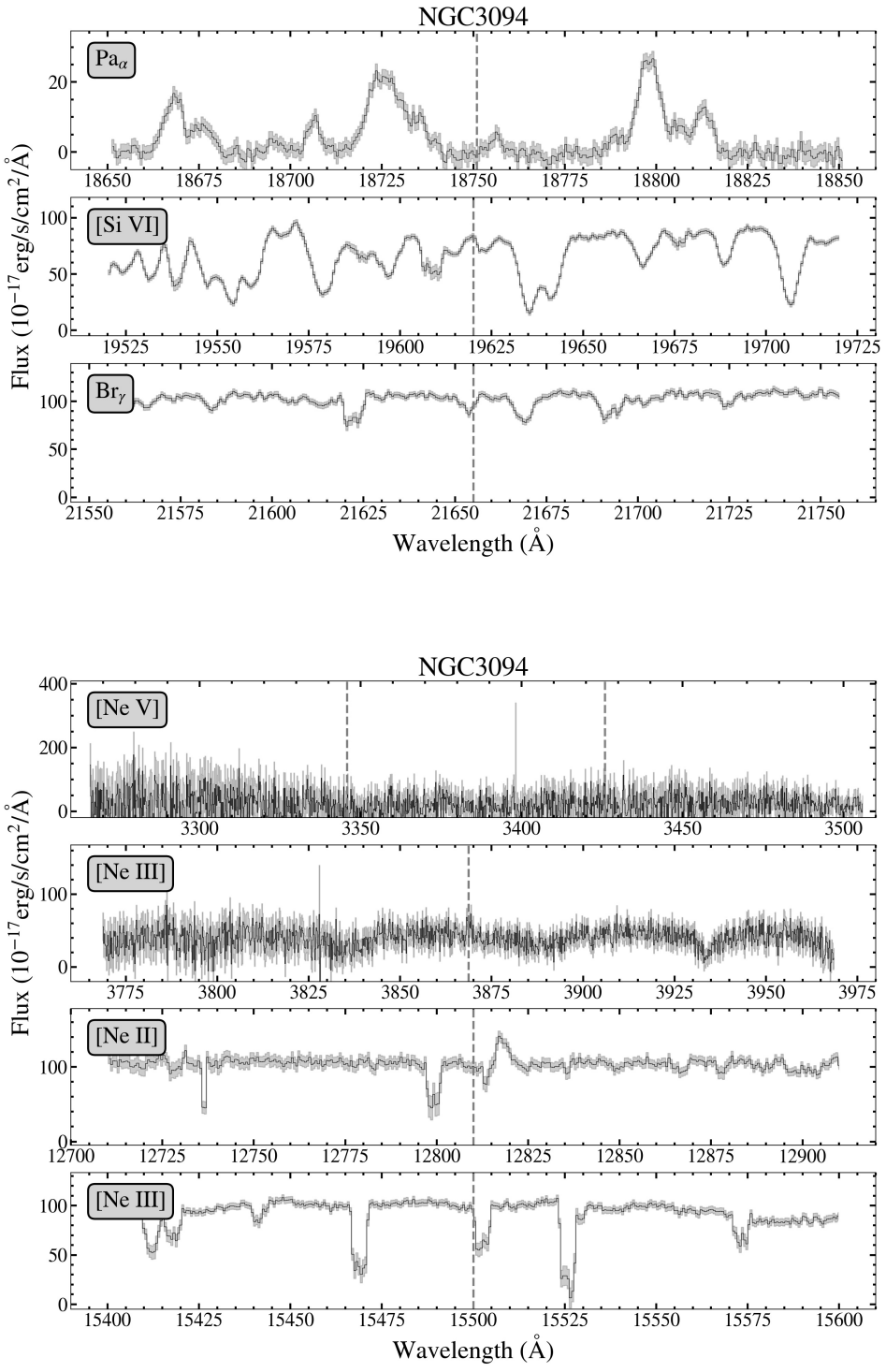

FIGURE A.9: Additional emission lines typical of AGN from NGC3094.

Appendix B

NSS80 extreme sources: further information

This Appendix contains extra information on classification of sources in the NSS80 catalogue and infra-red *WISE* data for the sources analysed in Chapter 3 and Appendix C.

B.1 Known AGN in the NSS80 catalogue

As in Chapter 2, we cross-matched the NSS80 sources with AGN catalogues to find any objects which are previously known to be AGN, with visual checking to confirm that these catalogue entries matched the likely origin of emission according to NSS80. We matched with sources in the Véron-Cetty & Véron catalogue (13th edition; Véron-Cetty and Véron, 2010, hereafter VCV), the analysed 2MRS spectra from Zaw et al. (2019) (hereafter ZCF), and additionally any SDSS automatic classifications (see Section 2.1.1). Figure B.1 shows the proportion of the total sources that are classified as such, and the number of those that were selected as high band ratio sources in Chapter 3. Figure B.2 shows where these sources lie in terms of their redshifts and band ratios. The sources above the threshold classed as AGN are: NuSTARJ050559-2349.9 (ZCF AGN, a source from L2017), NuSTARJ115658+5508.2 (an SDSS QSO found to be a CT AGN in this work), and NuSTARJ103456+3939.6 (a VCV AGN and SDSS QSO, also found to be a CT AGN in this work). There are also four objects in the catalogue that may be matches to sources in the *Swift*-BAT 105 month catalogue (Oh et al., 2018), but all have either no redshift or an undefined band ratio and thus are not candidates to appear in this work. One source, NuSTARJ023536-2938.6, is defined as a BL Lac object in VCV, but has no redshift in either that catalogue or NSS80.

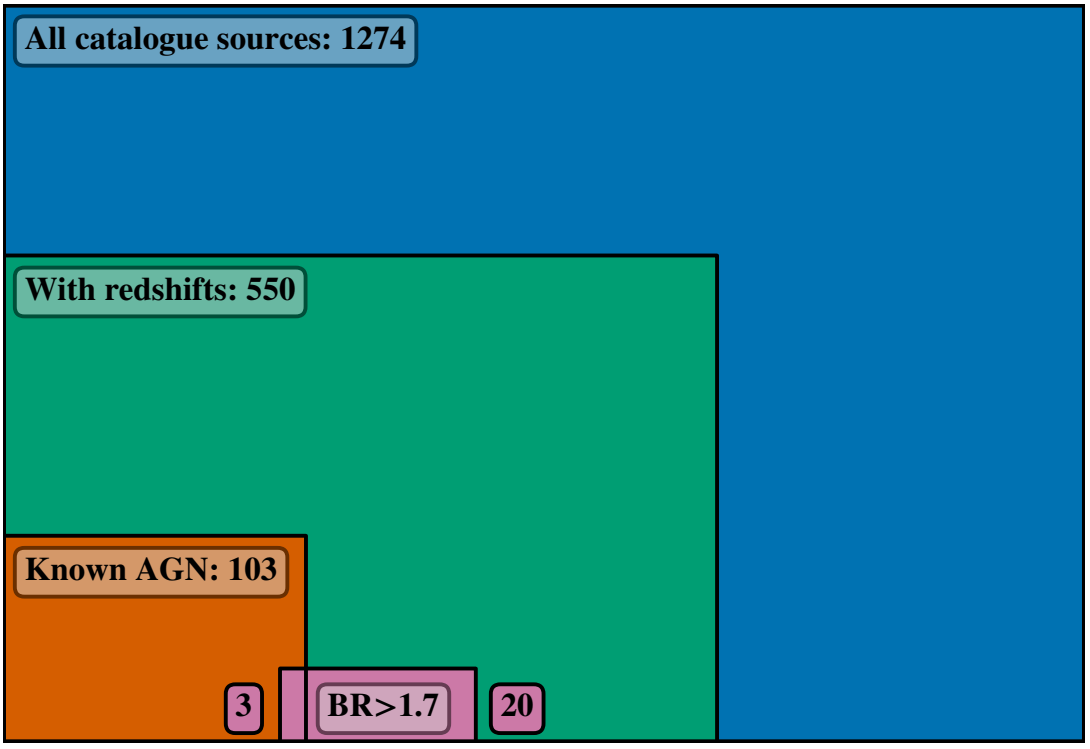

FIGURE B.1: Classification of sources from NSS80. The largest section shows the full catalogue, with (in descending order) sources with redshifts, known AGN (including QSOs), and sources with band ratio >1.7. The last category is divided into two: those that are already categorised as AGN, and those which are not.

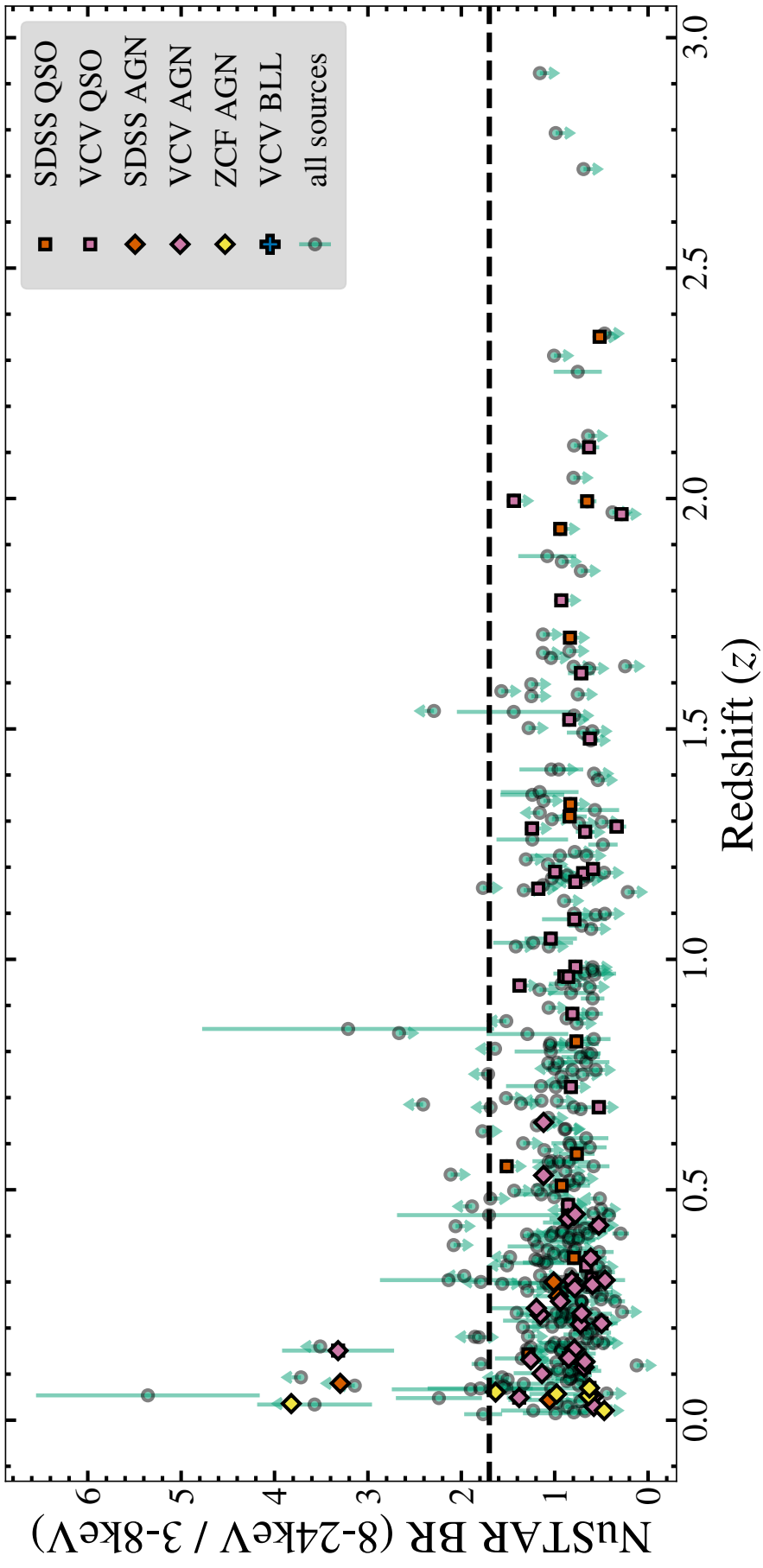

FIGURE B.2: Known AGN among sources with extreme BR from NSS80. Green circles show all sources with a redshift. Square markers are those classified as 'QSO', and diamonds those classified as 'AGN'..

B.2 Science targets of observations

Table B.1 shows information about the science targets of each observation used in this work. Several targets are *Swift*-BAT AGN - this is an associated also noted in L2017, where AGN tend to be located in large loose clusters. Two selected sources are known to be close in redshift to the science targets. None of the serendipitous sources are closely interacting with the science targets, or part of the analysis by the proposers[1], so we can treat them independently for modelling purposes.

B.3 *WISE*

MIR selection is a reliable method of selecting AGN (see Sections 2.3.2, 5.2). Here we show the *NuSTAR* serendipitous sources on the *WISE* colour-colour plane, with thresholds used for selection in other parts of this work, and images from each *WISE* band ($W1$ (3.4 µm), $W2$ (4.6 µm), $W3$ (12 µm), and $W4$ (22 µm). They are mostly clear sources in the MIR, but only a small fraction pass the selection threshold used in Chapters 4 and 5 (S12; Stern et al., 2012). The fraction of sources passing the R90 colour threshold used in Chapter 2 (A18; Assef et al., 2018) is 5/9 - consistent with the completeness found for the B70 AGN in Section 2.4.3. However, as shown in Figures B.4 to B.17 the *WISE* data for these sources can be noisy, with low detection significances. Thus, they may not pass strict MIR selection due to low SNR.

[1]J1502 is briefly mentioned in analysis of the supernova remnant; see Section C.2. However, it is not their aim and is not considered in detail.

TABLE B.1: Notes about the *NuSTAR* science targets of each observation with a selected hard serendipitous source.

Name (1)	Counterpart z (2)	Obs ID (3)	Obs Target (NED) (4)	Obs Target z (5)	Close in z? (6)	Proposed work (7)
J0107	0.048	60260004002	WISEA J010739.64-113911.2	0.047	✓	Extragalactic Legacy Survey
J0229	0.300	60401005002	MRK 1044	0.016		NLS1 MRK1044 (joint XMM)
J0229	0.300	60160109002	MRK 1044	0.016		EGS targeting Swift-BAT AGN
J0359	0.685	60160175002	SARS 059.33488-30.34397	0.097		EGS targeting Swift-BAT AGN
J0949	0.093	60201052002	WISE J094857.31+002225.6	0.584		NLS1 PMN J0948+0022
J1034	0.151	60401004002	KUG 1031+398	0.043		AGN RE J1034+396 (looking for QPOs, joint XMM)
J1156	0.080	60375001002	NGC 3982	0.004		CT candidate NGC3982
J1502	0.054	40110002002		–		SNR SN1006
J1506	0.034	60301023002				Serendip is target
J1506	0.034	60061261002	2MASX J15064412+0351444	0.037	✓	EGS targeting Swift-BAT AGN
J1606	0.122	60161629002	WISEA J160523.25-725356.3	0.052		EGS targeting Swift-BAT AGN
J1631	0.751	60260011002	WISEA J163115.53+235257.7	0.059		Extragalactic Legacy Survey
J1942	0.849	60201028002	NGC 6814	0.005		bright AGN NGC6814
J2143	0.013	80202036002		–		variable star SS Cyg (joint XMM, proposed) (local)
J2143	0.013	90701304002		–		variable star SS Cyg (joint XMM, ToO) (local)
J2143	0.013	90702309004		–		—"—
J2143	0.013	90702309002		–		—"—
J2249	0.445	60101027002	MCG -03-58-007	0.031		Seyfert 2 MCG-03-58-007 (joint XMM, deep obs)
J2249	0.445	60502004004	MCG -03-58-007	0.031		Seyfert 2 MCG-03-58-007 (joint XMM, monitoring)
J2318	0.464	60201003002	NGC 7582	0.005		CTk AGN NGC7582 (joint XMM)
J2318	0.464	60061318002	NGC 7582	0.005		EGS targeting Swift-BAT AGN
J2318	0.464	60061318004	NGC 7582	0.005		—"—

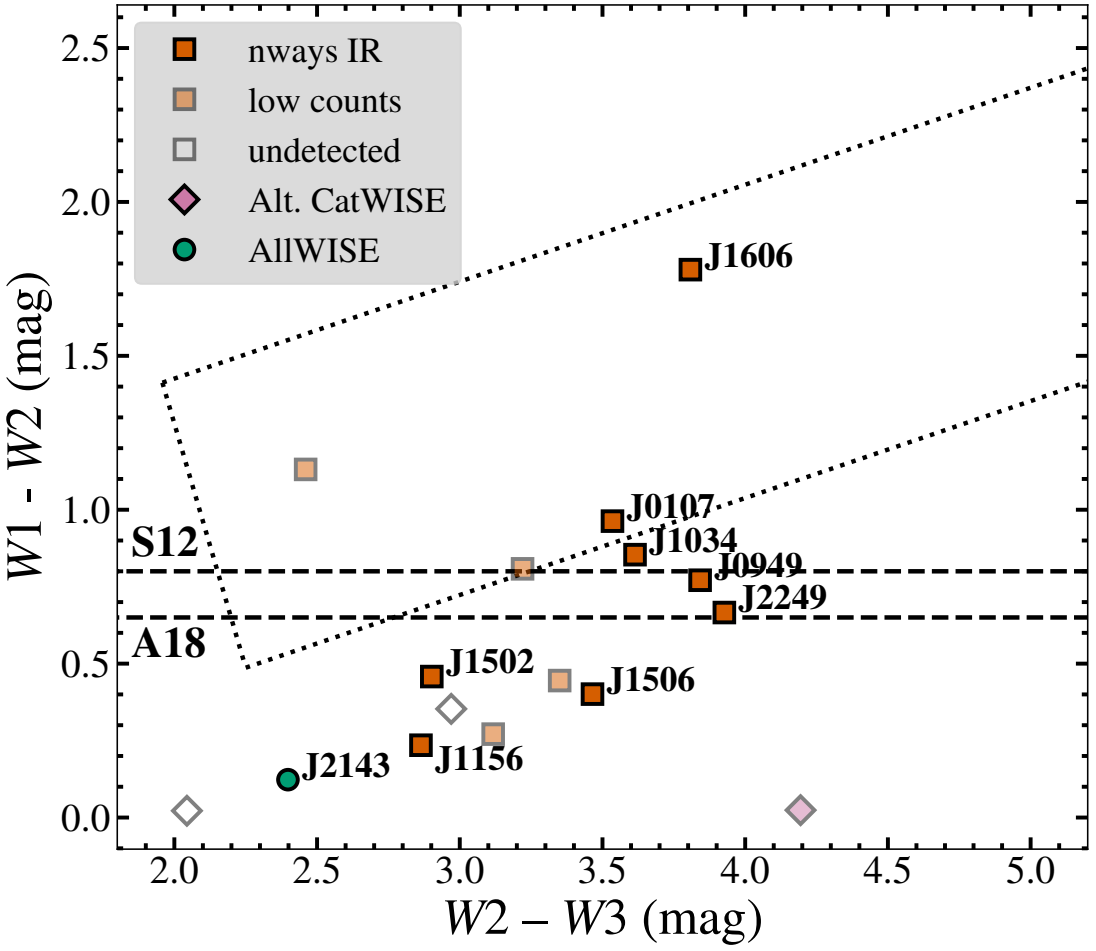

FIGURE B.3: *WISE* colour-colour diagram of the high band ratio serendipitous sources. Solid boxes represent the nine sources analysed in detail (Section 3.3.1 and Appendix C). Faded boxes represent the low count detected sources, and empty boxes the non-detected sources. For two sources the IR source selected in the NSS80 catalogue was incorrect, and these are noted as 'Alt. CatWISE'(i.e., a different source from CatWISE was chosen) and 'AllWISE' (a source from the older AllWISE catalogue was preferred; see Section C.4).

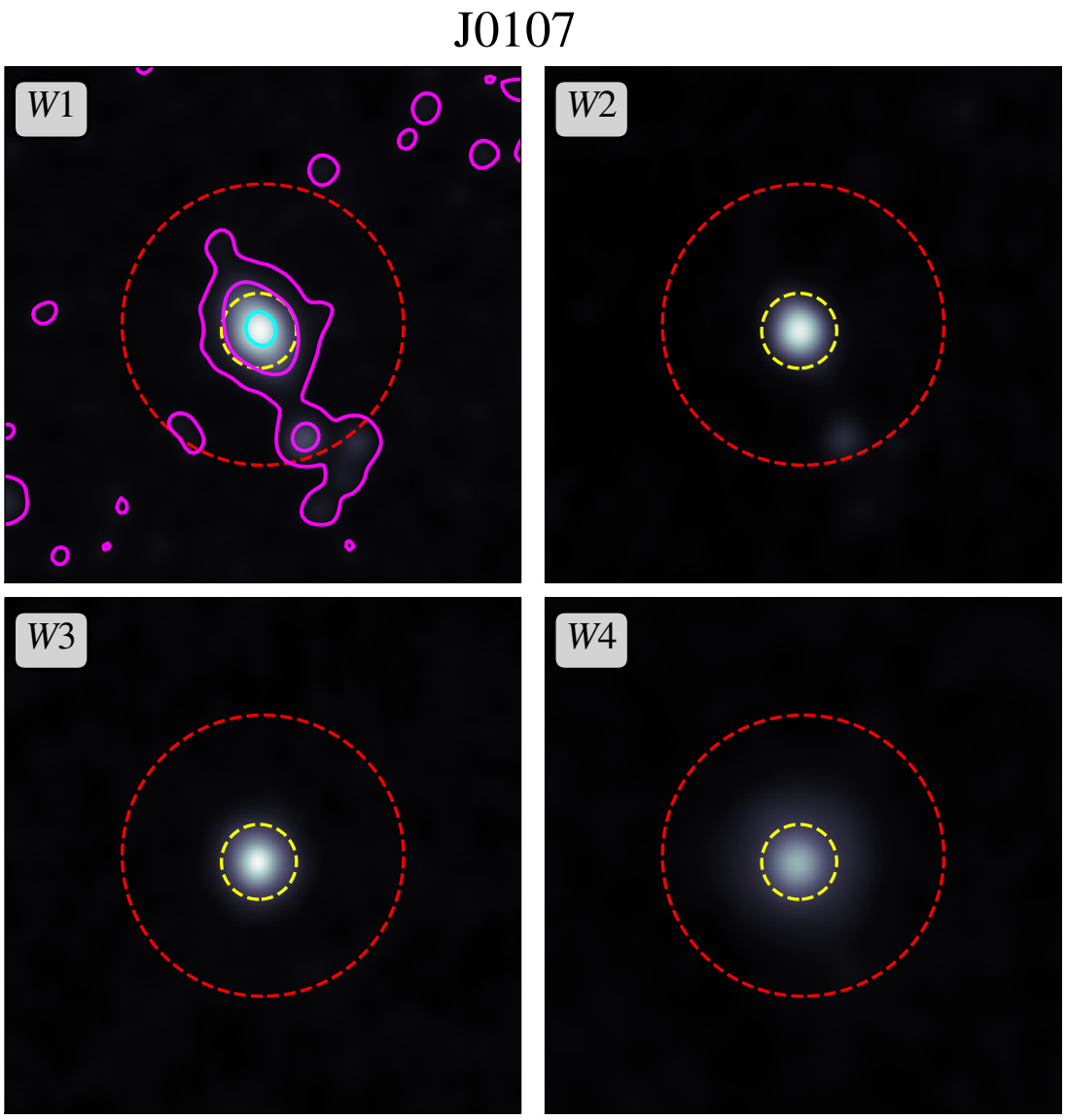

FIGURE B.4: J0107: *WISE* W1-W4. Small yellow circle shows the coordinates of the optical counterpart, and the larger red circles the coordinates of the *WISE* source. Pink contours show emission in the *WISE* W1 band.

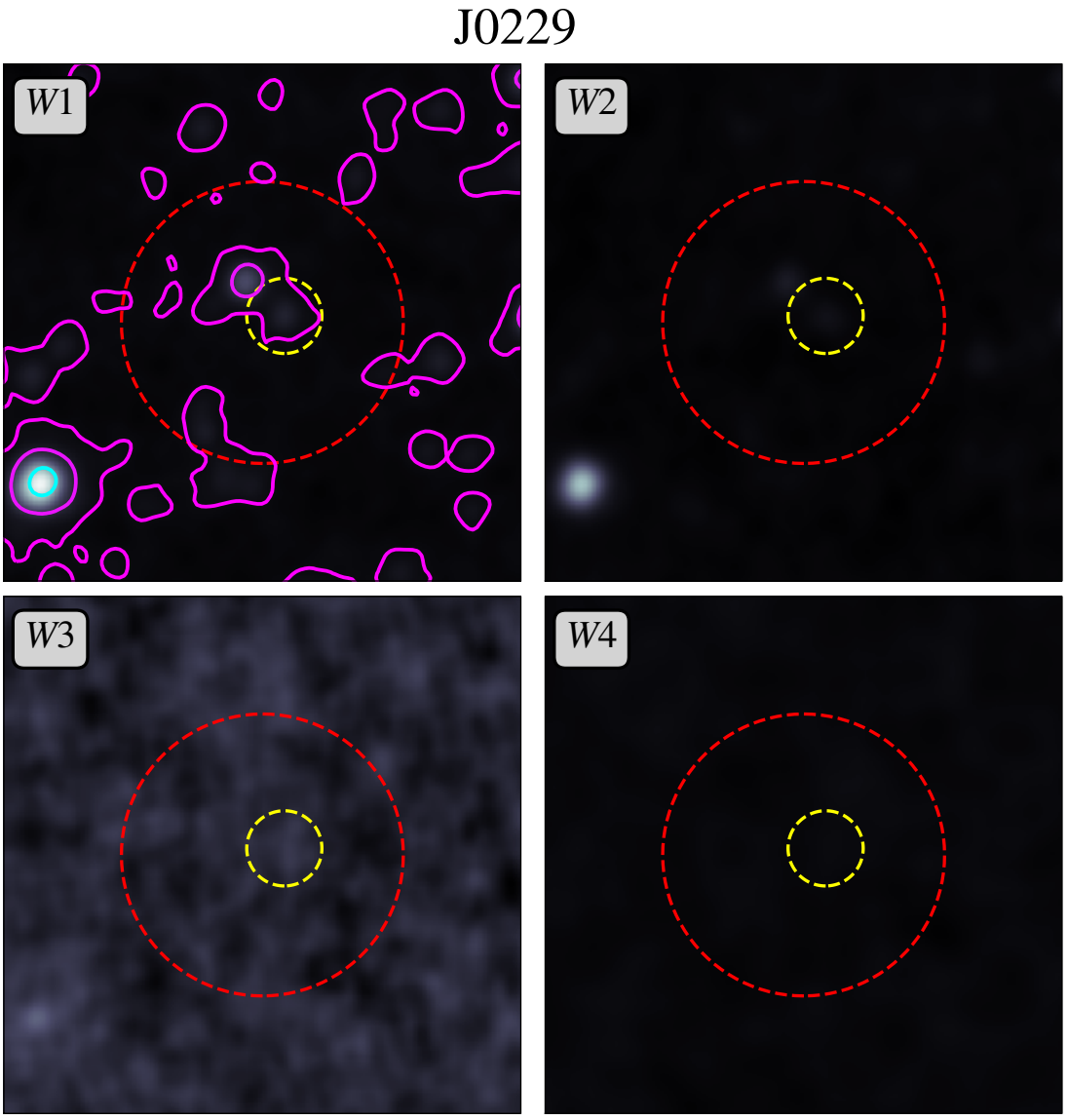

FIGURE B.5: J0229: *WISE* W1-W4. Small yellow circle shows the coordinates of the optical counterpart, and the larger red circles the coordinates of the *WISE* source. Pink contours show emission in the *WISE* W1 band.

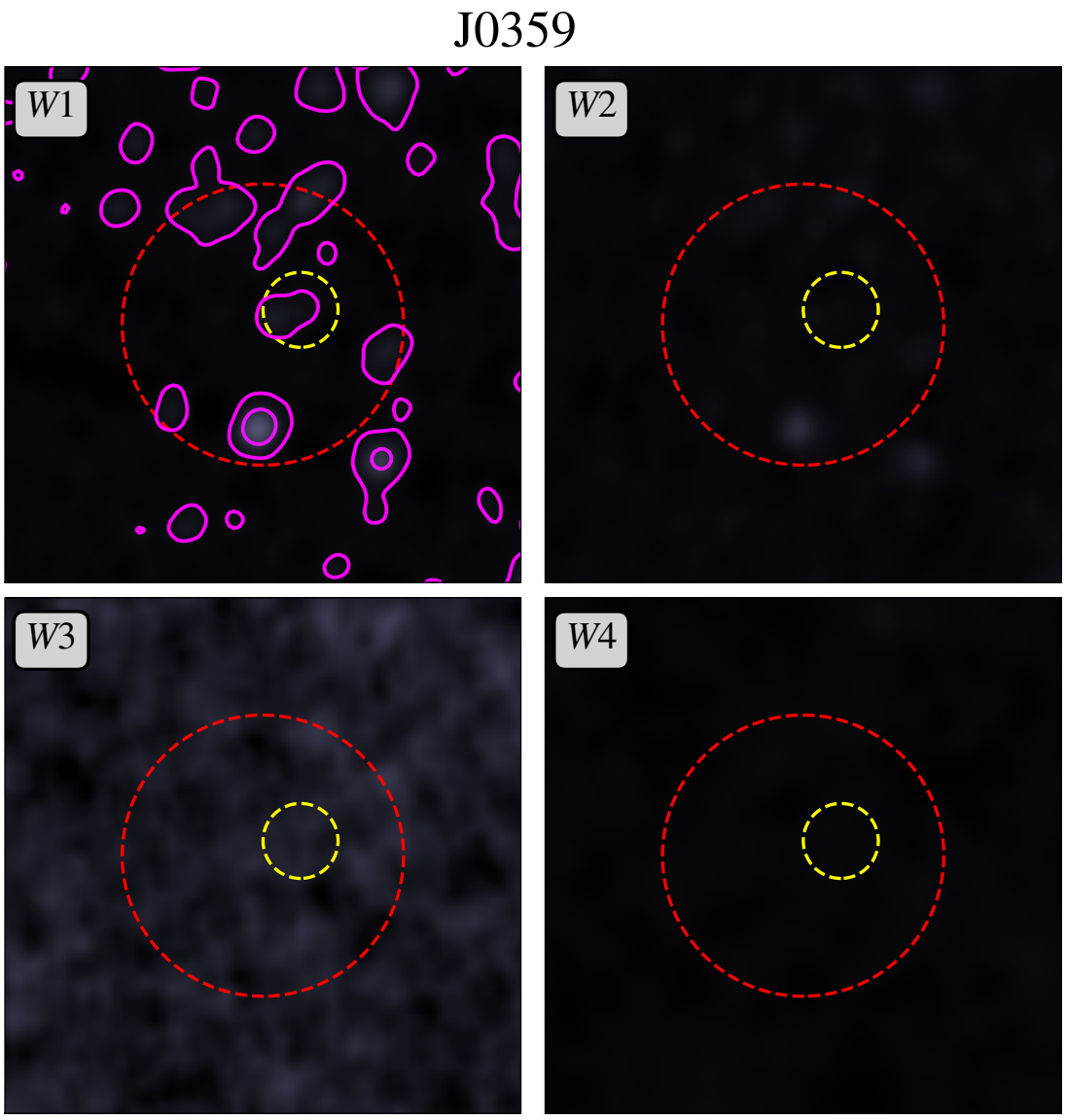

FIGURE B.6: J0359: *WISE* W1-W4. Small yellow circle shows the coordinates of the optical counterpart, and the larger red circles the coordinates of the *WISE* source. Pink contours show emission in the *WISE* W1 band.

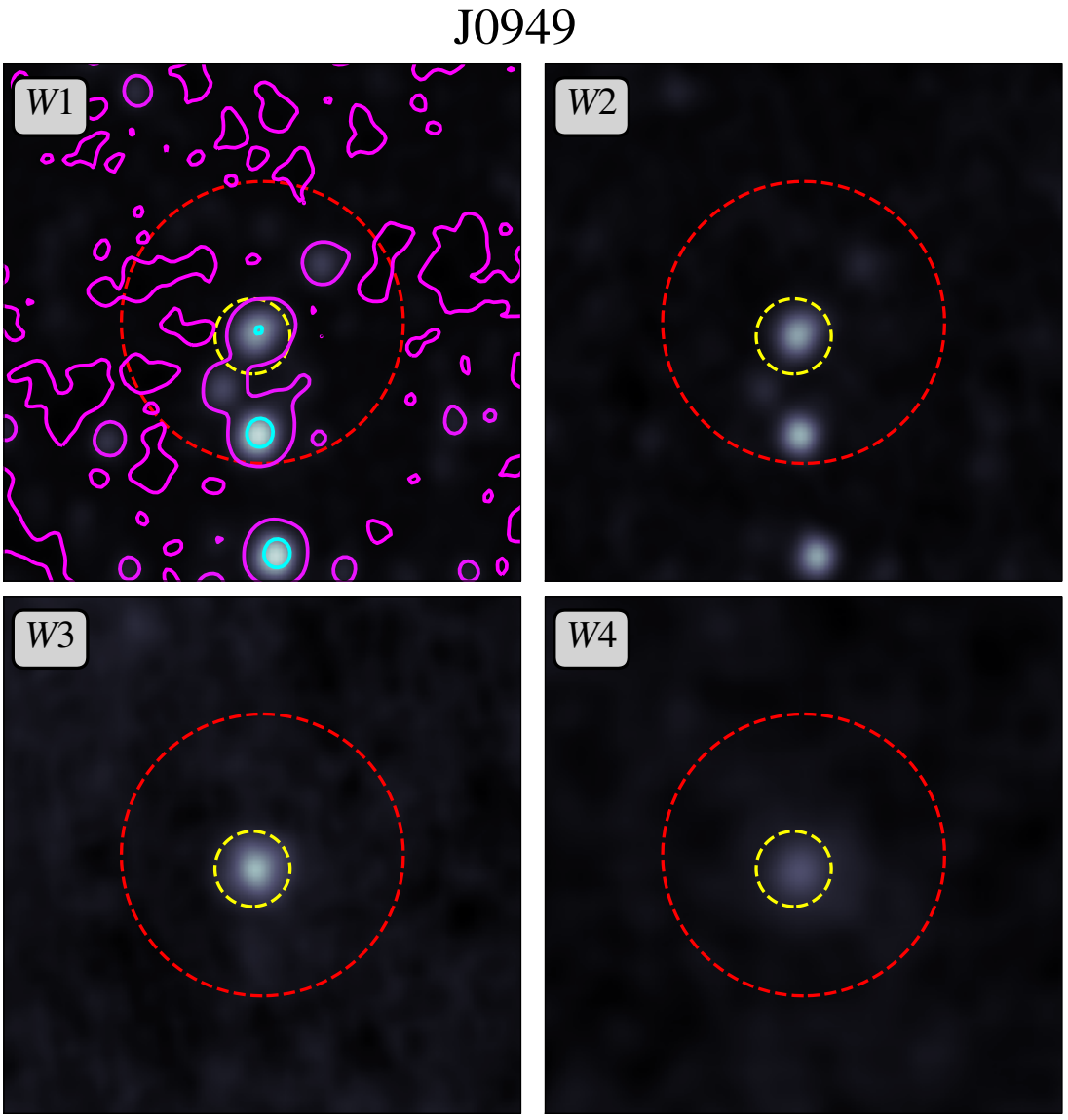

FIGURE B.7: J0949: *WISE* W1-W4. Small yellow circle shows the coordinates of the optical counterpart, and the larger red circles the coordinates of the *WISE* source. Pink contours show emission in the *WISE* W1 band.

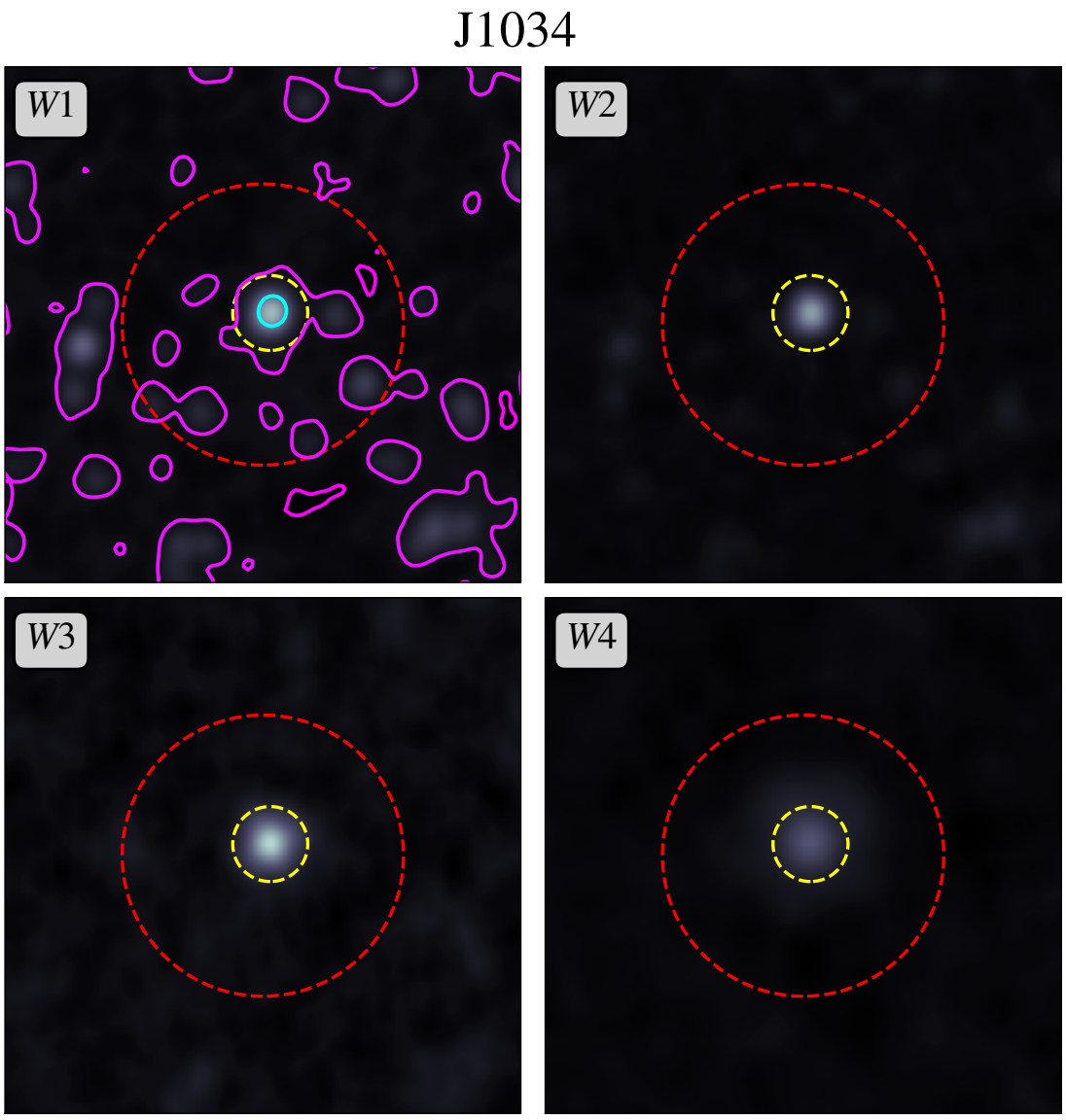

FIGURE B.8: J1034: *WISE* W1-W4. Small yellow circle shows the coordinates of the optical counterpart, and the larger red circles the coordinates of the *WISE* source. Pink contours show emission in the *WISE* W1 band.

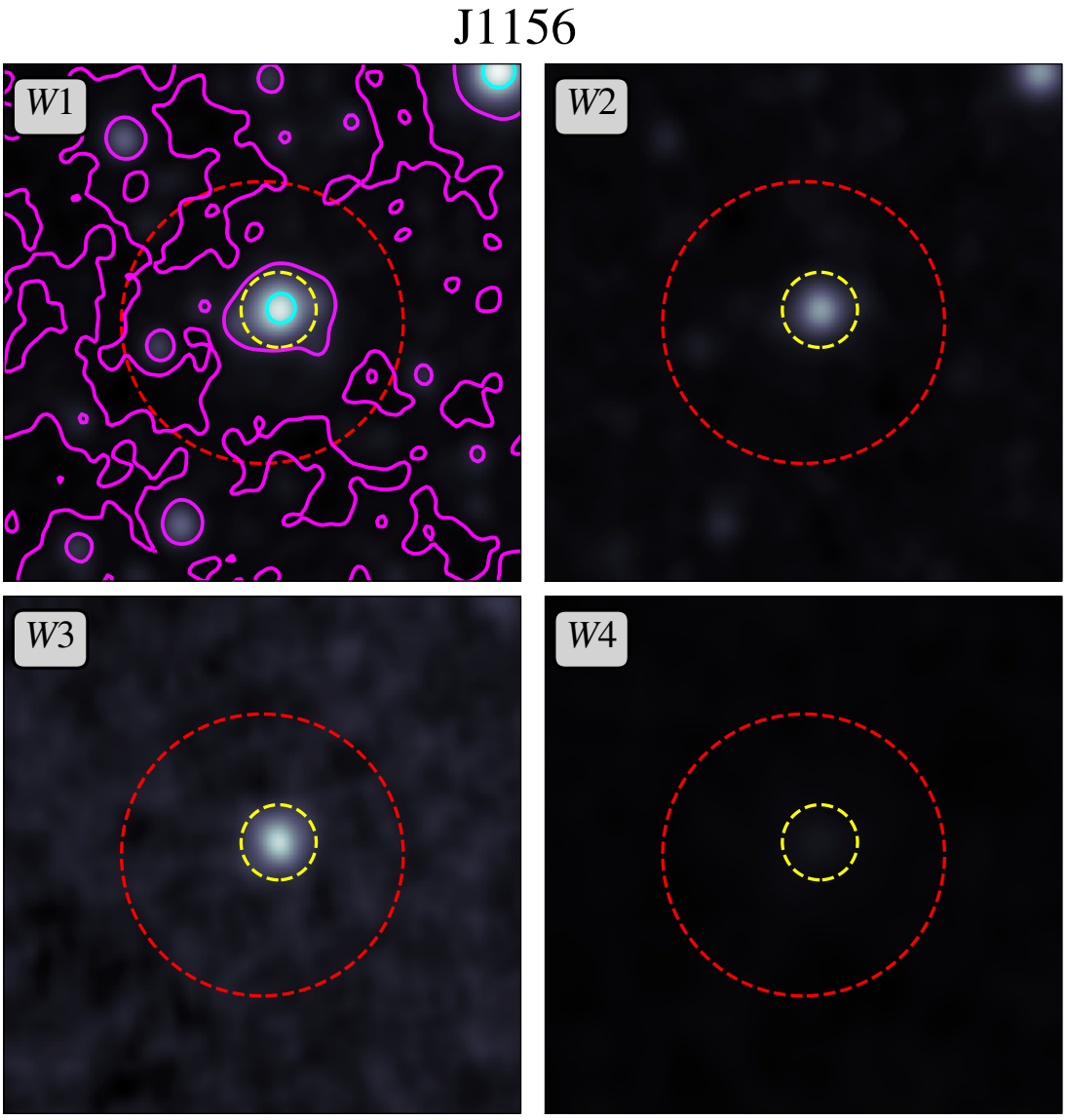

FIGURE B.9: J1156: *WISE* W1-W4. Small yellow circle shows the coordinates of the optical counterpart, and the larger red circles the coordinates of the *WISE* source. Pink contours show emission in the *WISE* W1 band.

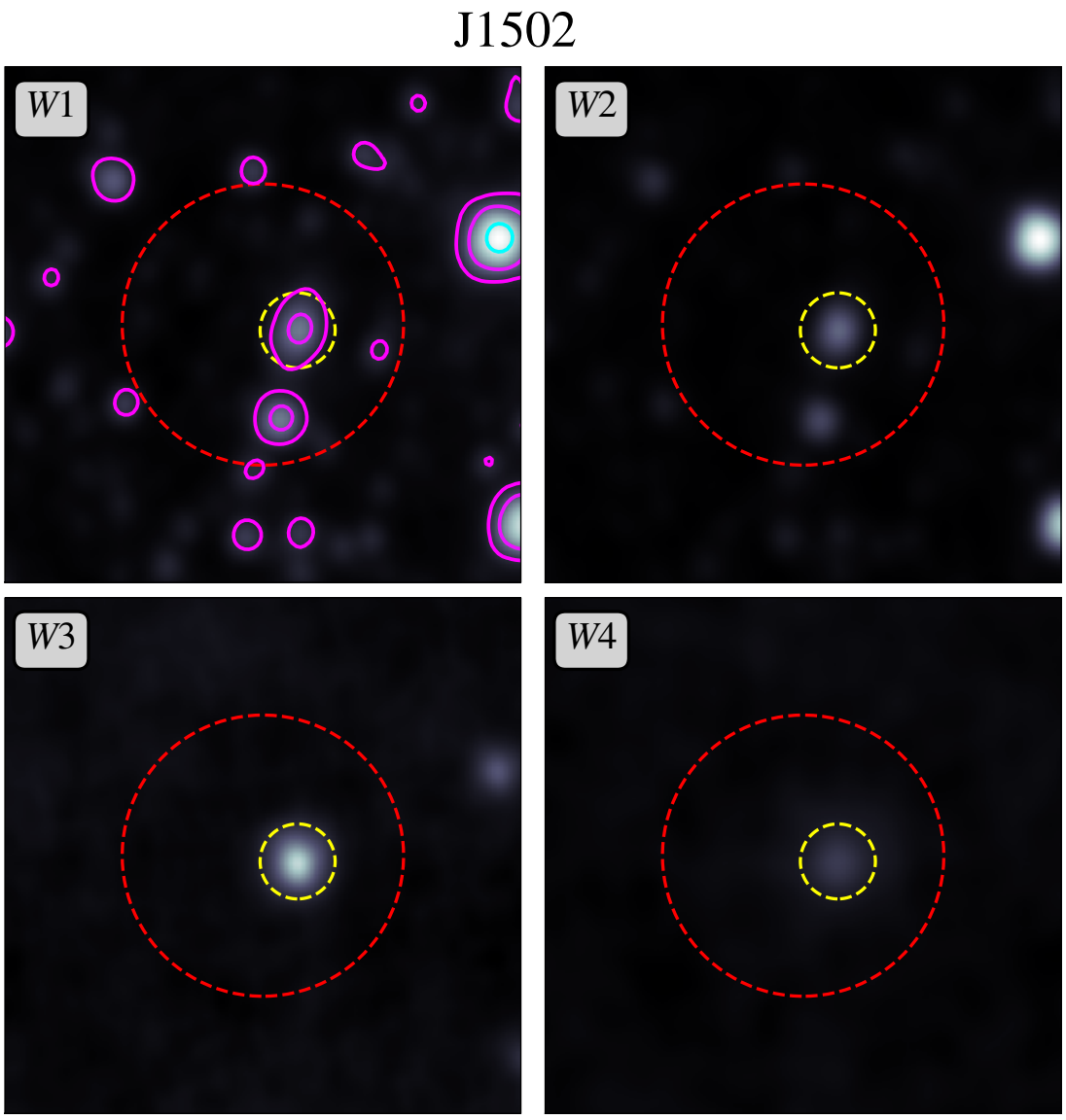

FIGURE B.10: J1502: *WISE* W1-W4. Small yellow circle shows the coordinates of the optical counterpart, and the larger red circles the coordinates of the *WISE* source. Pink contours show emission in the *WISE* W1 band.

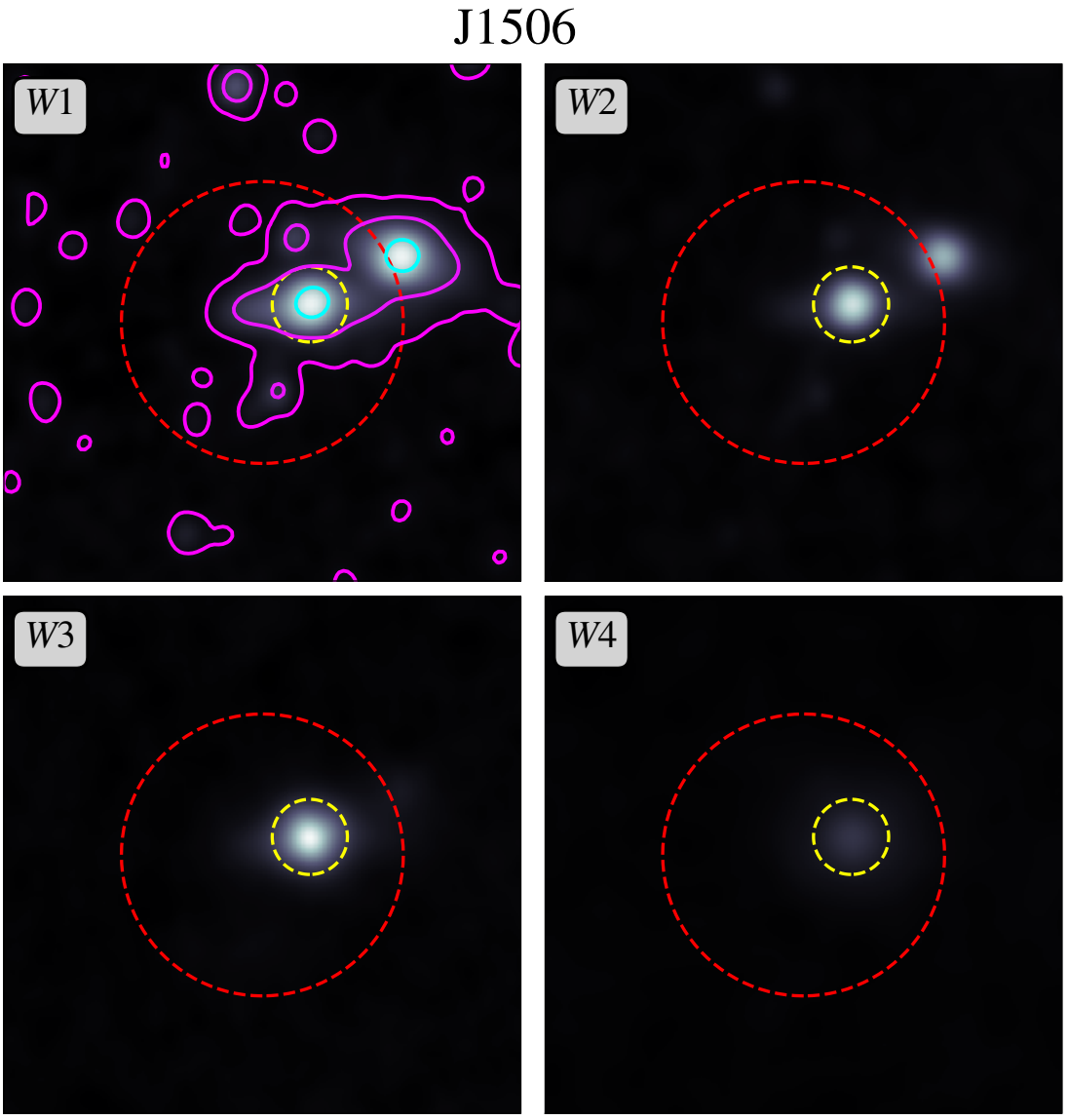

FIGURE B.11: J1506: *WISE* W1-W4. Small yellow circle shows the coordinates of the optical counterpart, and the larger red circles the coordinates of the *WISE* source. Pink contours show emission in the *WISE* W1 band.

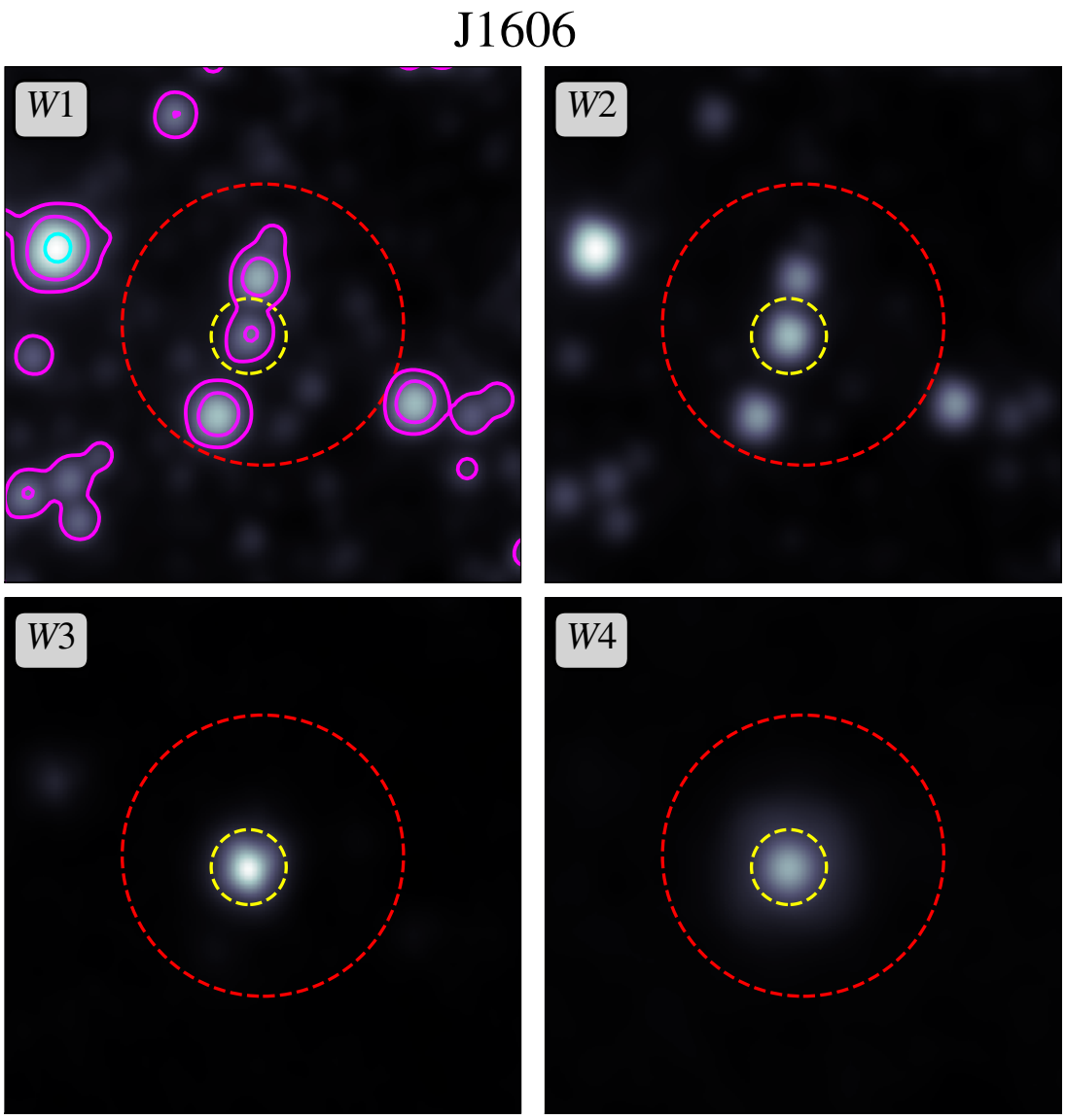

FIGURE B.12: J1606: *WISE* W1-W4. Small yellow circle shows the coordinates of the optical counterpart, and the larger red circles the coordinates of the *WISE* source. Pink contours show emission in the *WISE* W1 band.

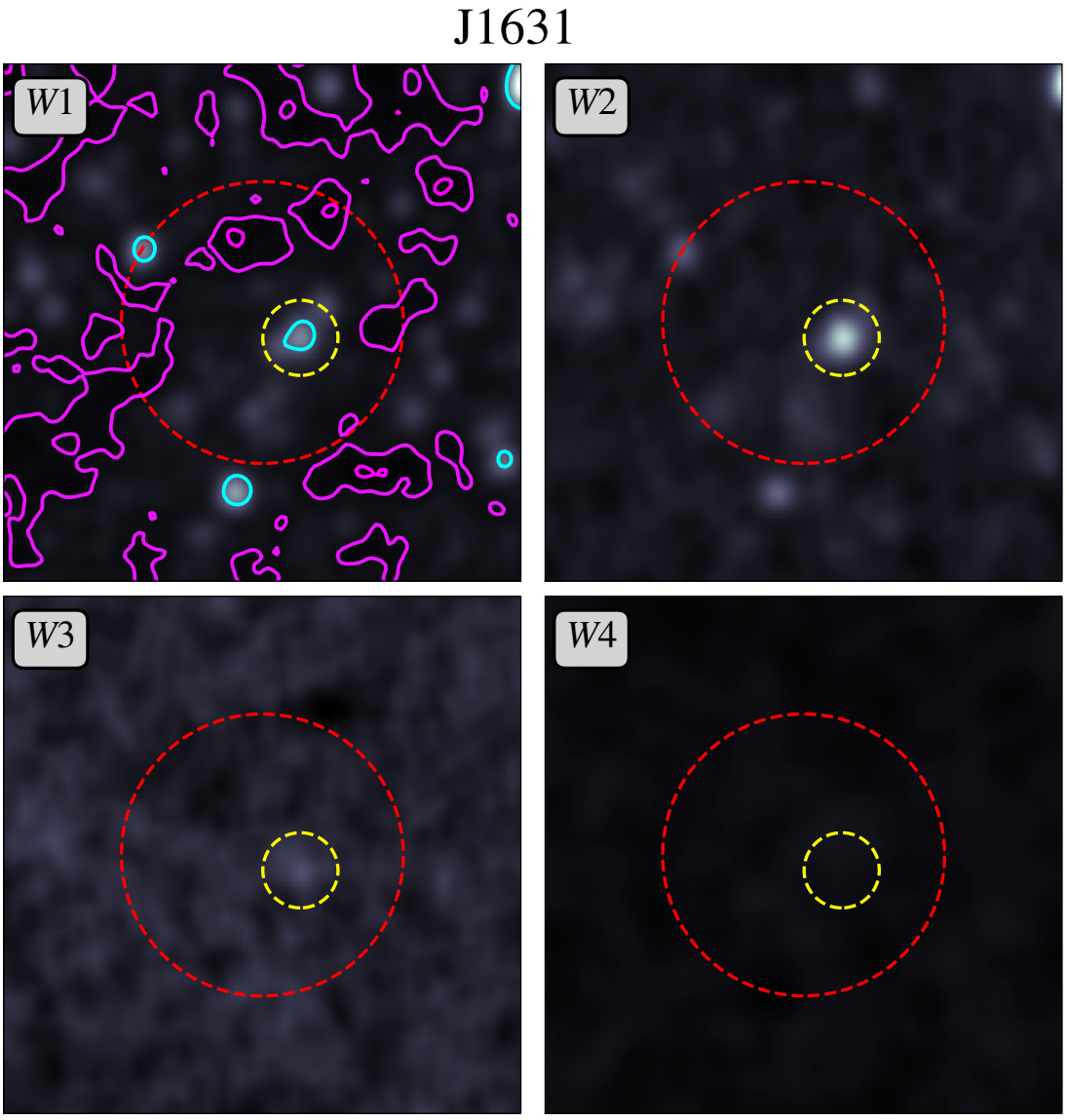

FIGURE B.13: J1631: *WISE* W1-W4. Small yellow circle shows the coordinates of the optical counterpart, and the larger red circles the coordinates of the *WISE* source. Pink contours show emission in the *WISE* W1 band.

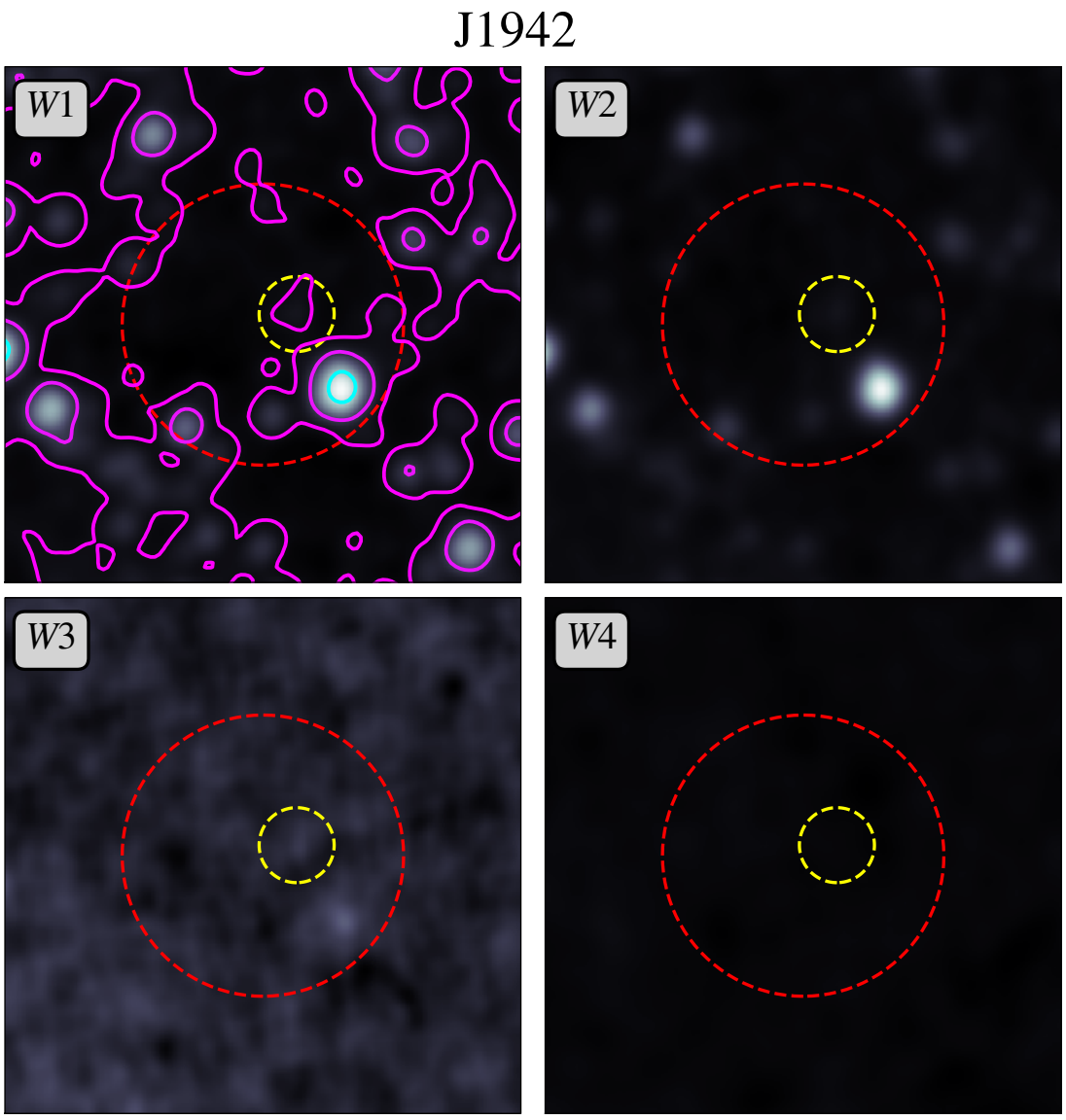

FIGURE B.14: J1942: *WISE* W1-W4. Small yellow circle shows the coordinates of the optical counterpart, and the larger red circles the coordinates of the *WISE* source. Pink contours show emission in the *WISE* W1 band.

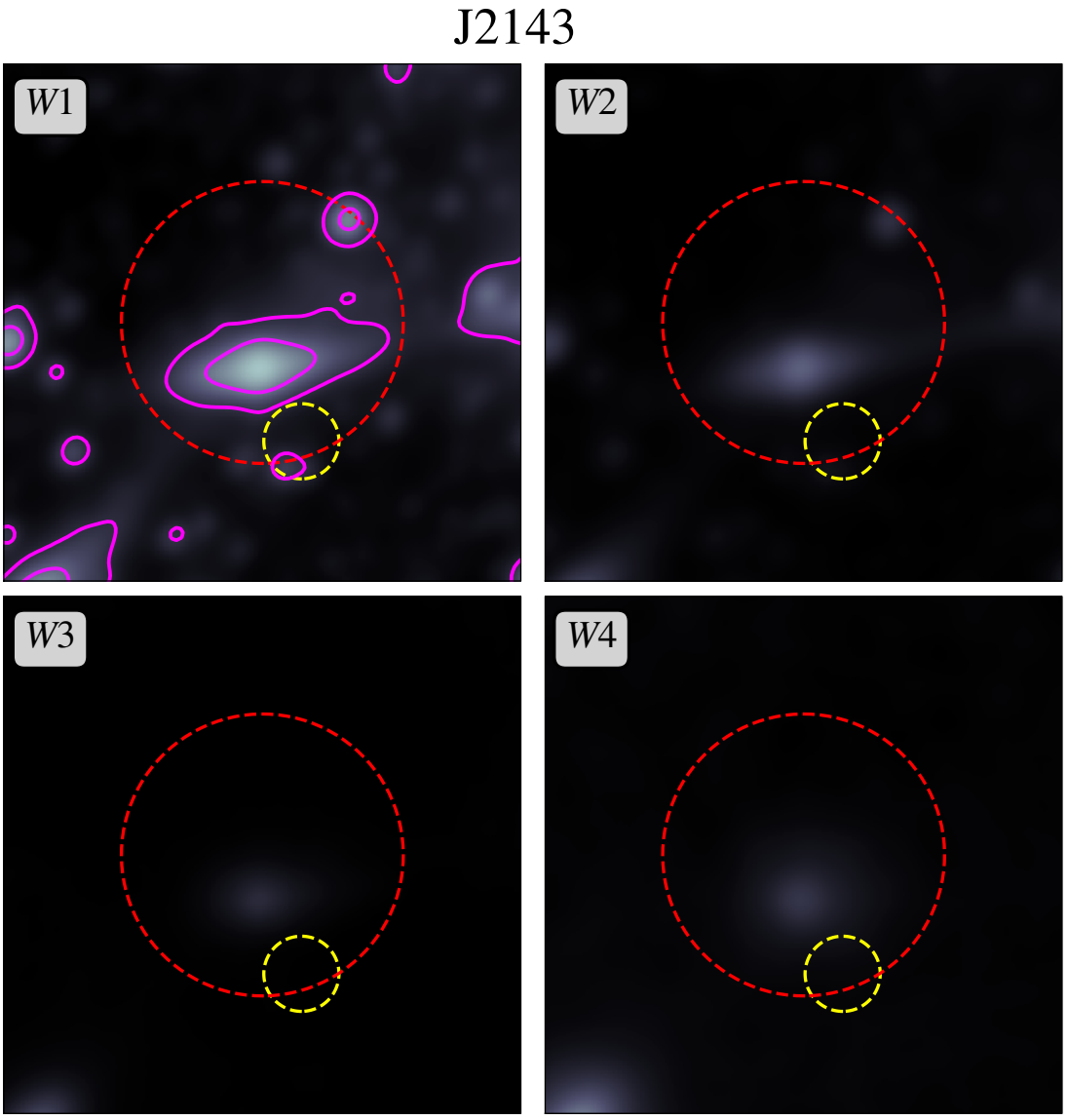

FIGURE B.15: J2143: *WISE* W1-W4. Small yellow circle shows the coordinates of the optical counterpart, and the larger red circles the coordinates of the *WISE* source. Pink contours show emission in the *WISE* W1 band.

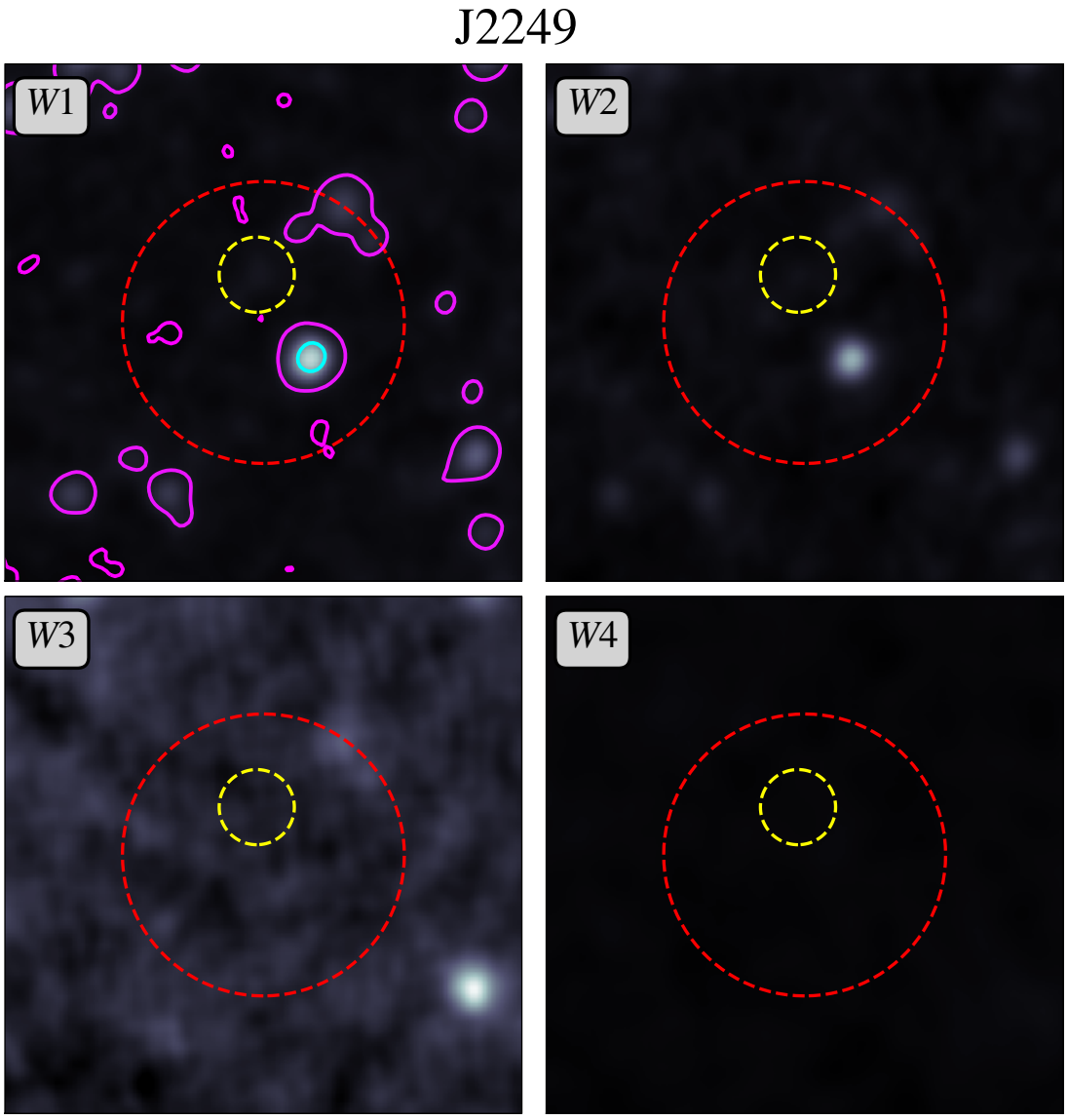

FIGURE B.16: J2249: *WISE* W1-W4. Small yellow circle shows the coordinates of the optical counterpart, and the larger red circles the coordinates of the *WISE* source. Pink contours show emission in the *WISE* W1 band.

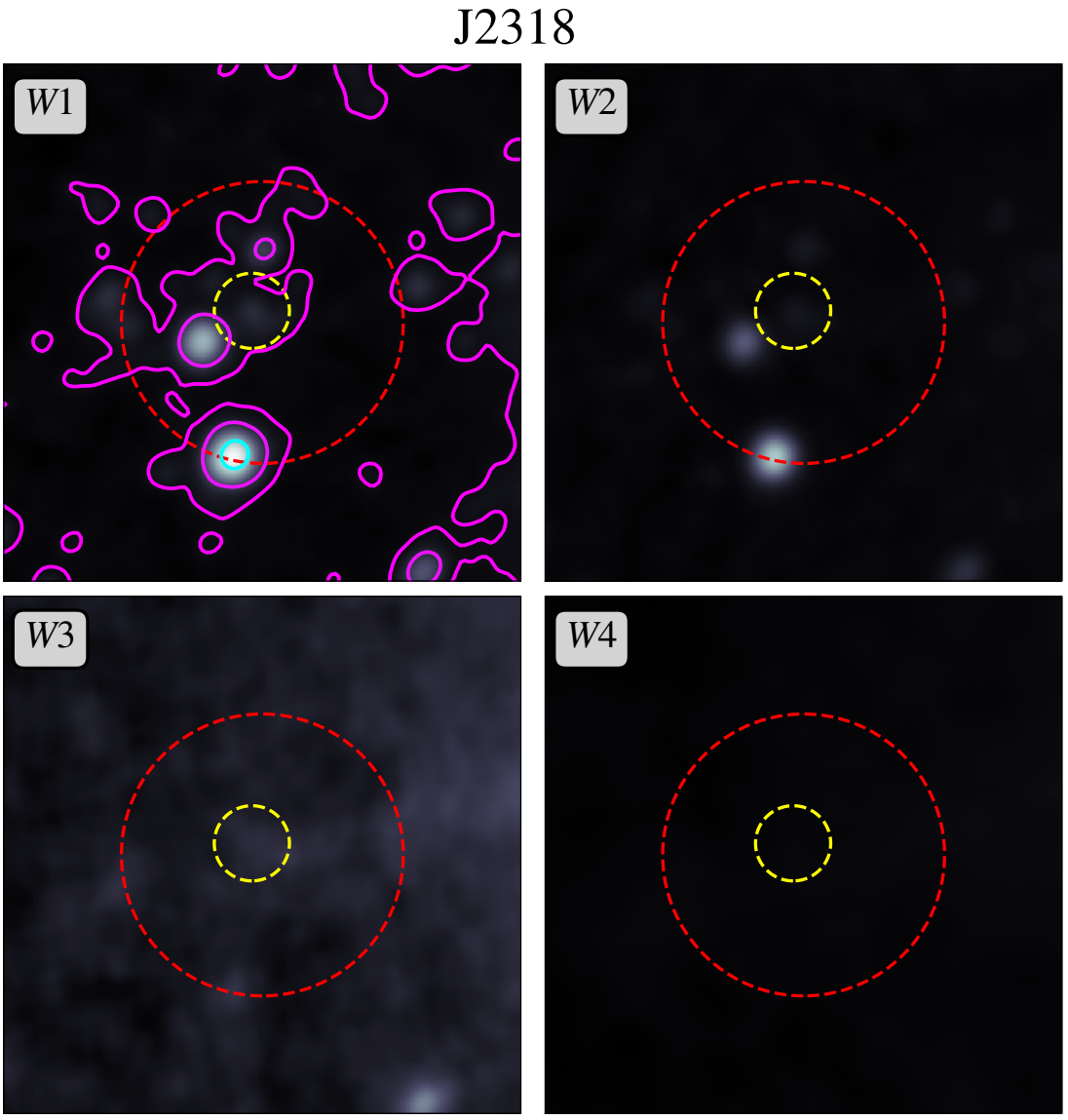

FIGURE B.17: J2318: *WISE* W1-W4. Small yellow circle shows the coordinates of the optical counterpart, and the larger red circles the coordinates of the *WISE* source. Pink contours show emission in the *WISE* W1 band.

Appendix C

NSS80 extreme sources: Compton thin sources

In this Appendix we present the discussion and results of each source not found to be Compton thick. Each are heavily obscured (log $N_{\rm H} > 23$ cm^{-2}). In particular, J2143 (Section C.4) presents with a clear increase in luminosity between *NuSTAR* measurements and appears to be an intrinsic change rather than an obscuration change. It is interacting, in a group of three galaxies, the other two of which are soft X-ray sources.

C.1 NuSTARJ010739-1139.1

In optical imaging (PanSTARRS) NuSTARJ010739-1139.1 (hereafter J0107) appears to be an edge-on galaxy (see Figure C.1a, left). A smaller galaxy, similar in appearance, can be seen to the bottom right of the PanSTARRS image (outside of the *NuSTAR* circle) at a close redshift to J0107. The *NuSTAR*, soft X-ray, IR and optical coordinates according to NWAY matching from the 80-month catalogue are closely aligned (in Figure C.1, the red, blue, orange and cyan circles respectively), so we can conclude that there is no ambiguity about the source of the emission. In its optical spectrum (taken at Palomar; see Klindt et al., 2022, submitted) it shows only narrow lines; thus for spectral fitting we assume that the system is being viewed at a low angle.

It is bright in *WISE* (see Figure C.1a (right), and Figure B.4). Its *W*1-*W*2 colour is 0.963, placing it above the threshold used in LASr (see Section 2.3.2) for selecting AGN candidates.

In X-rays, it is detected from 3–50 keV with *NuSTAR*, and additionally in a single *Chandra* observation (see Figure C.1). Towards the bottom right of the *Chandra* image, there is a second source visible which appears to be associated with an unrelated galaxy, visible in the PanSTARRS image. This galaxy is also visible in the *WISE* *W*1 image, but

less brightly, especially for bands $W2-4$. It is not close enough in the *Chandra* image to interfere with the soft spectrum, however it is possible that it contributes to the *NuSTAR* spectrum. It is not clear in the *NuSTAR* imaging that a separate source is present, and at this stage we have assumed that its effect will be small.

The results of fitting the *NuSTAR* and *Chandra* spectra of J0107 with the simple absorbed powerlaw can be seen in Figure C.2. The intrinsic photon index of the powerlaw was found to be $1.18^{+0.41}_{-0.35}$. This is unusually low for an AGN, but due to the low quality of the *Chandra* data, high uncertainty on Γ, and possible interference of the second source, this result was accepted as the final result for J0107. The obscuration depth was found to be $\log N_{\rm H}$=$23.62^{+0.15}_{-0.18}$ cm^{-2} – not at Compton thick levels, but heavily obscured. The observed luminosities were $L_{2-10\ \rm keV}$=1.90×10^{42} erg^{-1} s^{-1} and $L_{10-40\ \rm keV}$=1.69×10^{43} erg^{-1} s^{-1}.

J0107 is a previously known X-ray AGN - it is present in the BAT catalogues (Baumgartner et al., 2013, Oh et al., 2018) and is part of a study by Zhao et al. (2021), who fit the *NuSTAR* and *Chandra* data with an uncoupled BORUS02 model (with line-of-sight and torus $N_{\rm H}$ not identical). They found a torus $N_{\rm H}$ of 23.47 and an unconstrained lower limit on the l.o.s. $N_{\rm H}$ of 24.48 with a low covering factor of 0.1, indicating that it may be Compton thick, depending on the complexity of the model used.

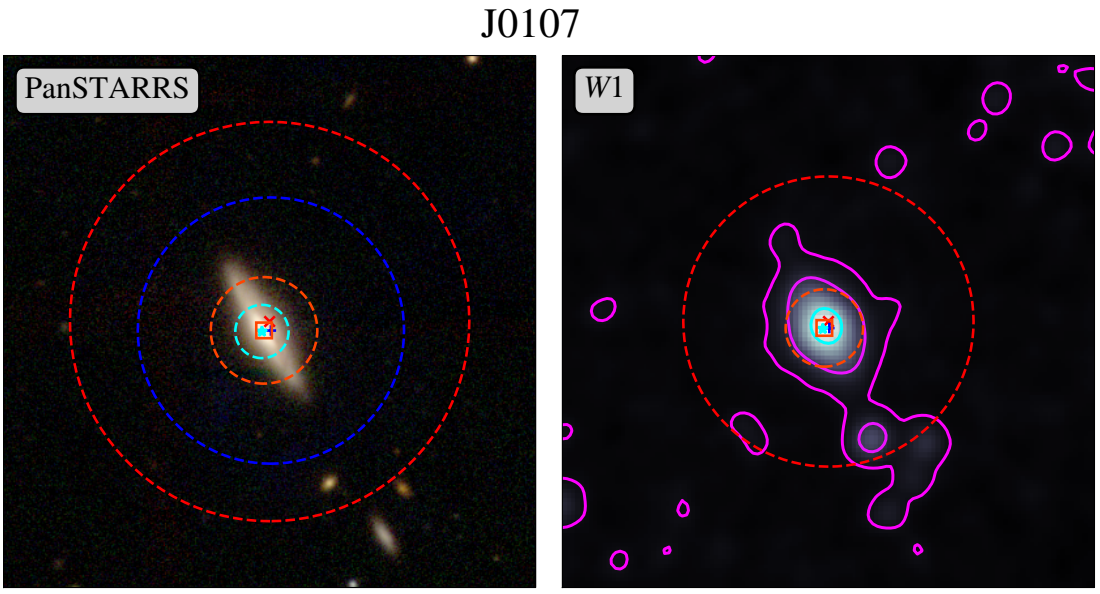

(A) J0107: (left) PanSTARRS *irg* image, (right) *WISE W*1 image.

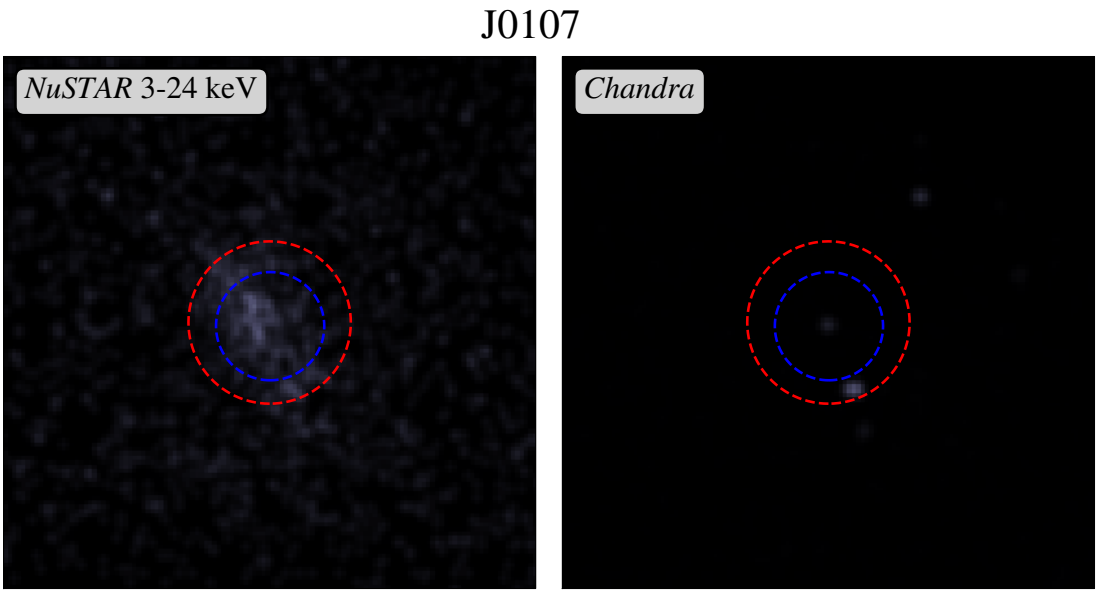

(B) (left) *NuSTAR* 3–24 keV image, (right) *XMM-Newton* 0.5–10 keV image.

FIGURE C.1: Images of J0107, with multi-wavelength coordinates shown as follows: *NuSTAR* (red, 45 arcseconds), *XMM-Newton* (blue, 30 arcseconds), *WISE* (yellow, 12 arcseconds), PanSTARRS (cyan, 6 arcseconds).

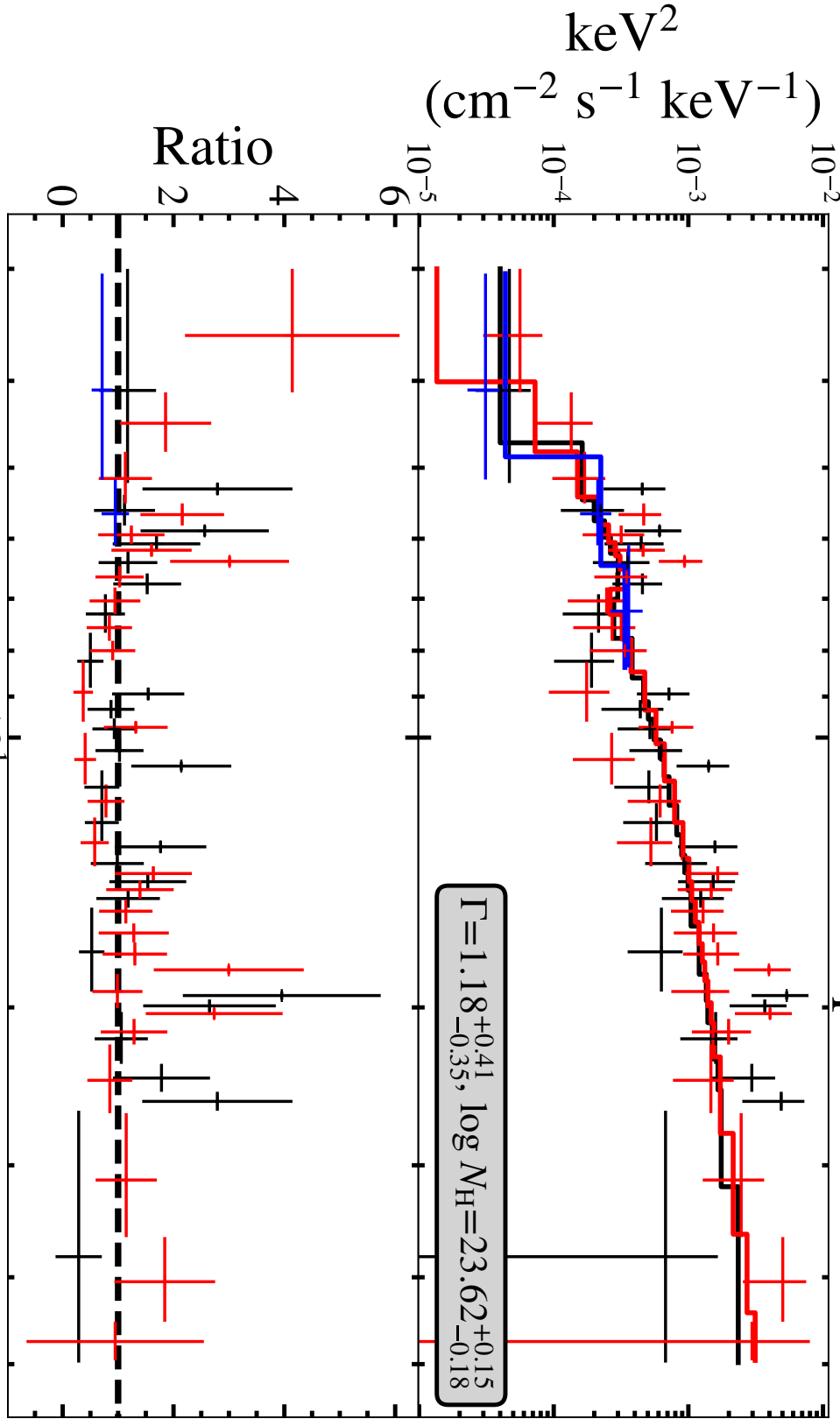

FIGURE C.2: J0107: (top) Spectrum of best fit CABS×ZWABS×POW model; (bottom) ratio between data and model. Shown is each observation separately, as listed in Table 3.1, binned to a minimum of 2 counts per bin.

C.2 NuSTARJ150225-4208.3

NuSTARJ150225-4208.3 (hereafter J1502) is located within a supernova remnant (SN1006), which is strongly visible in the soft X-ray images (see Figure C.3). The source itself is clearly distinct from this structure - it is mentioned as a >50 keV detected point source in a study of the SNR ('SW point source 1'; Li et al., 2018) and identified as a background AGN. The high background levels make it a difficult source to analyse. In Figure C.3 the *XMM-Newton* image is shown in different bands: full band (0.5-10 keV), 1-10 keV, 2-10 keV, and 5-10 keV. The remnant is most clearly visible in the images including the shorter bands, and is almost gone in the final image. Thus for this analysis we restrict all data (*XMM-Newton* and *NuSTAR*) to >5 keV. For a more in depth analysis, separate modelling of background and source spectra could produce good results, but for the purposes of this investigation the simplest solution was chosen.

In optical imaging (DSS2, blue) J1502 appears to be an edge-on galaxy, but this is not very clear due to the low resolution (see Figure C.4a, left). The *NuSTAR*, soft X-ray, IR coordinates are closely aligned. In its optical spectrum (from UKST/6dF) it shows no emission lines, only absorption; thus for spectral fitting we assume that the system is being viewed at a low angle, and may be more obscured. The spectrum is not particularly high quality; further analysis may benefit from a new observation.

It is clearly visible in *WISE* (see Figure C.4a, right). Its *W*1-*W*2 colour is 0.458. As with J1156, this does not indicate that J1502 is not an AGN. A second *WISE* source is present within the *NuSTAR* region, but it does not appear to be blended with J1502 and does not have an associated X-ray source in *XMM-Newton* or *Chandra*.

In X-rays, it is detected from 3–50 keV with *NuSTAR*, with *XMM-Newton*, and with *Chandra* (see Figure C.4). Background regions were chosen to represent the SN emission at the source coordinates as closely as possible. *XMM-Newton* and *NuSTAR* only were used for spectral fitting.

J1502 was not fit well with the absorbed powerlaw, and was fit instead with BORUS02, the results of which are shown in Figure C.5. The cross-calibration constants of the *XMM-Newton* data were allowed to vary (with the ratio between detectors kept constant for individual observations). The intrinsic photon index of the powerlaw was found to be $\Gamma=1.45^{+0.17}_{-0.17}$ cm^{-2}. The obscuration depth was found to be $\log N_{\rm H}=23.73^{+0.20}_{-0.20}$ cm^{-2} – heavy but not Compton thick obscuration. The observed luminosities were $L_{2-10\ \rm keV}=1.53\times10^{42}$ erg^{-1} s^{-1} and $L_{10-40\ \rm keV}=1.10\times10^{43}$ erg^{-1} s^{-1}.

J1502

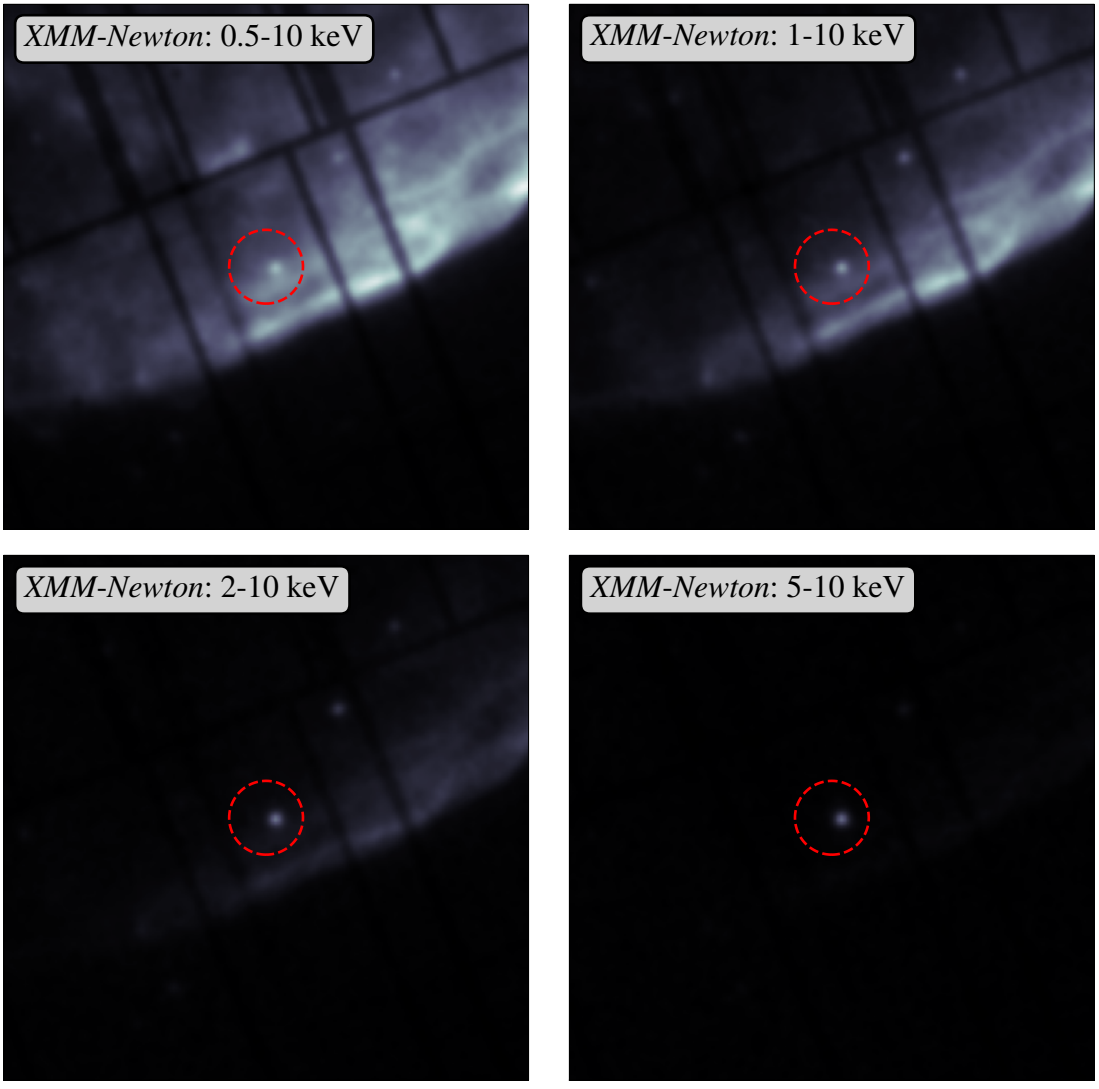

FIGURE C.3: J1502: (top left) *XMM-Newton* 0.5–10 keV image, (top right) *XMM-Newton* 1–10 keV image, (bottom left) *XMM-Newton* 2–10 keV image, (bottom right) *XMM-Newton* 5–10 keV image. High background from SN remnant decreases a higher energies.

J1502

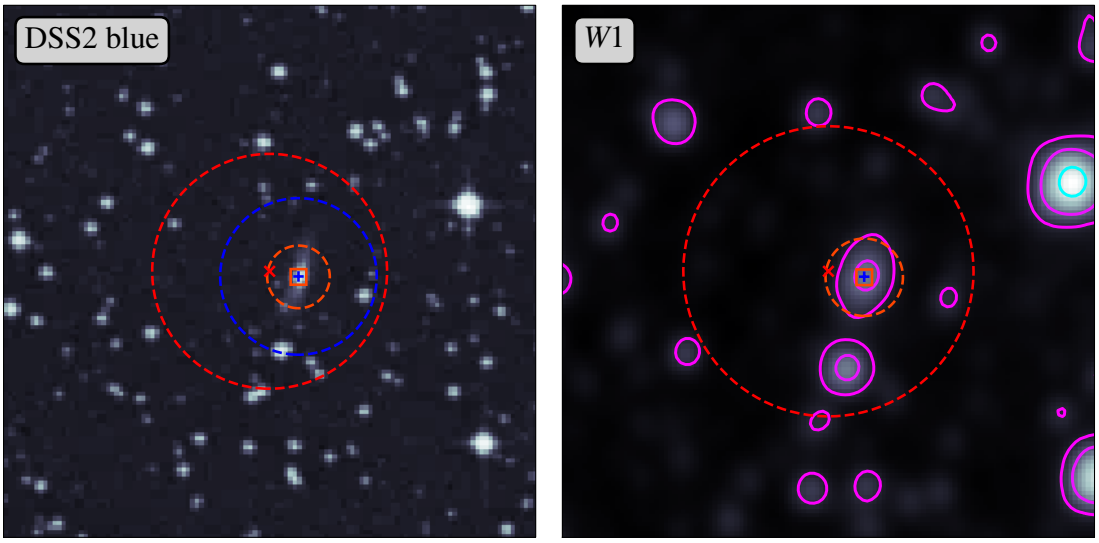

(A) J1502: (left) PanSTARRS *irg* image, (right) *WISE* W1 image.

J1502

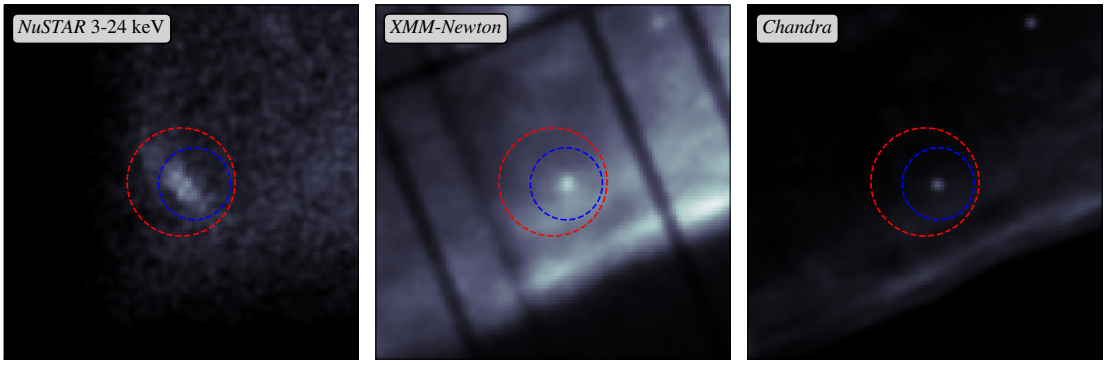

(B) (left) *NuSTAR* 3–24 keV image, (middle) *XMM-Newton* 0.5–10 keV image, (right) *Chandra* full band image.

FIGURE C.4: Images of J1502, with multi-wavelength coordinates shown as follows: *NuSTAR* (red, 45 arcseconds), *XMM-Newton* (blue, 30 arcseconds), *WISE* (yellow, 12 arcseconds), PanSTARRS (cyan, 6 arcseconds).

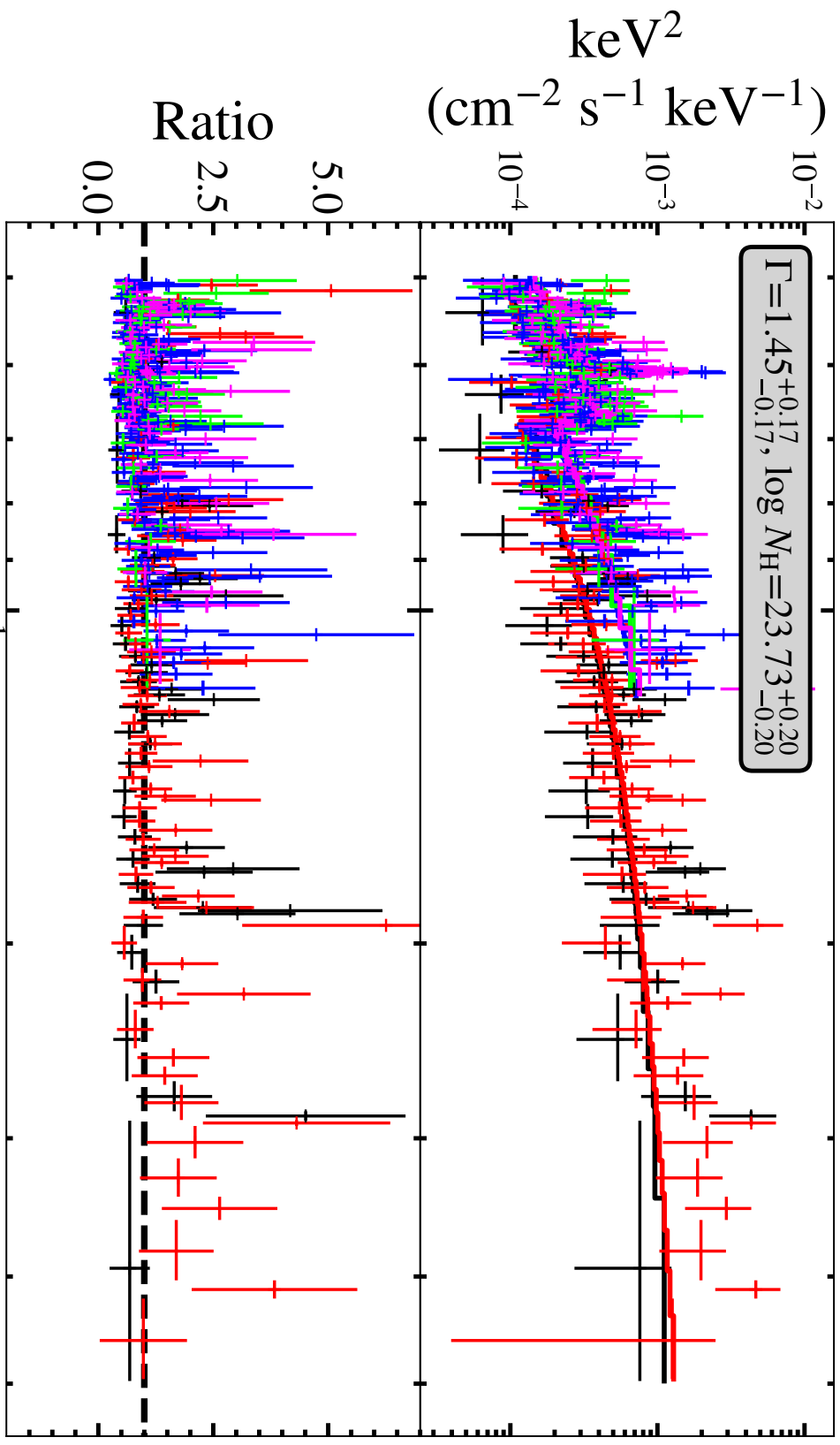

FIGURE C.5: J1502: (top) Spectrum of best fit BORUS02 model; (bottom) ratio between data and model. Shown is each observation separately, as listed in Table 3.1, binned to a minimum of 2 counts per bin.

C.3 NuSTARJ160605-7252.6

NuSTARJ160605-7252.6 (hereafter J1606) is a known INTEGRAL and *Swift* source. Molina et al. (2021) find that this INTEGRAL source is a blend of two separate AGN, and analyse the *Swift*-XRT and *NuSTAR* data from these sources separately. In this paper, J1606 is referred to as LEDA 259580 and is fitted with an absorbed powerlaw similar to our initial model, finding $\log N_{\rm H}$=25.30$^{+4.87}_{-4.31}$ cm^{-2}. This value would indicate extreme absorption, easily Compton thick - however noting the high uncertainties it cannot be decisively defined. They conclude that it is likely that J1606 is the major source of the INTEGRAL and *Swift*-BAT emission in the region. The redshift from NSS80 does not match that in Molina et al. (2021); for this analysis we use the NSS80 value.

In optical imaging (DSS2, blue) J1606 is too small to make out any structure (see Figure C.6a, left). The *NuSTAR*, soft X-ray, and IR coordinates are closely aligned. No optical spectrum is currently available.

It is clearly visible in *WISE* (see Figure C.6a, right). Its *W*1-*W*2 colour is 1.78 - extremely red, and well above MIR AGN selection thresholds. A second *WISE* source is present within the *NuSTAR* region - it is brighter than J1606 in *W*1, but less bright at longer wavelengths (Figure B.12). Given the less AGN-like colour of this second source and the position of the *Swift*-XRT source, we can assume that J1606 is the source of the *NuSTAR* emission.

In X-rays, it is detected from 3–50 keV with *NuSTAR* and with *Swift*-XRT (see Figure C.6). Along with *NuSTAR*, stacked *Swift*-XRT spectra from the online tool (Evans et al., 2009) were used for fitting.

The absorbed powerlaw made a reasonable fit to J1606, the results of which are shown in Figure C.7. The intrinsic photon index of the powerlaw was found to be Γ=1.51$^{+0.12}_{-0.11}$ cm^{-2}. The obscuration depth was found to be $\log N_{\rm H}$=23.58$^{+0.06}_{-0.06}$ cm^{-2} – heavy but not Compton thick obscuration. The observed luminosities were $L_{2-10\ \rm keV}$=5.92$\times$10^{43} erg^{-1} s^{-1} and $L_{10-40\ \rm keV}$=3.35$\times$10^{44} erg^{-1} s^{-1}.

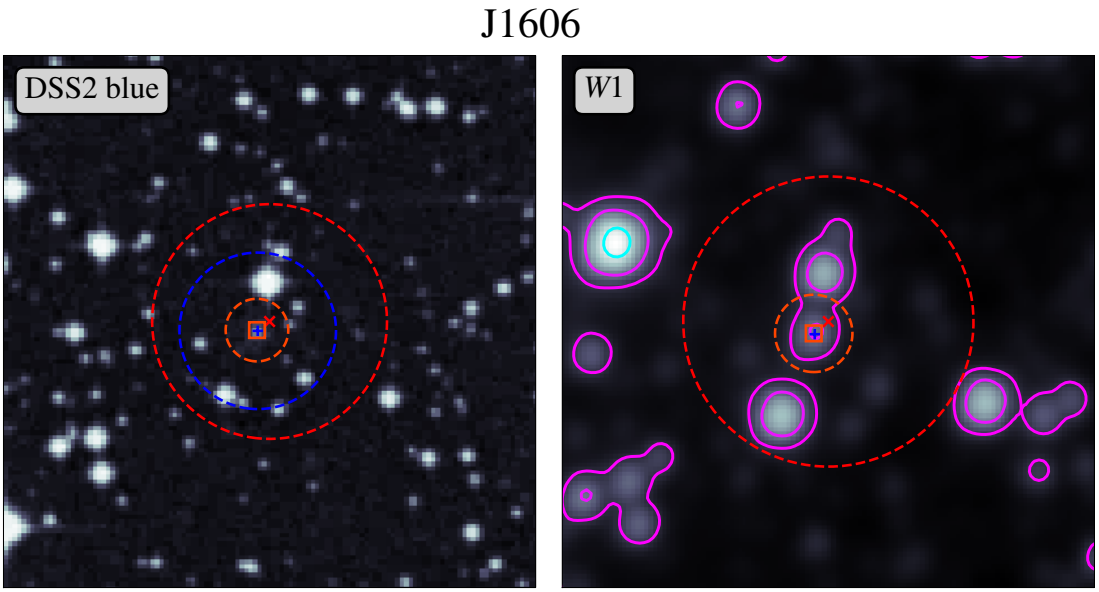

(A) J1606: (left) PanSTARRS *irg* image, (right) *WISE* W1 image.

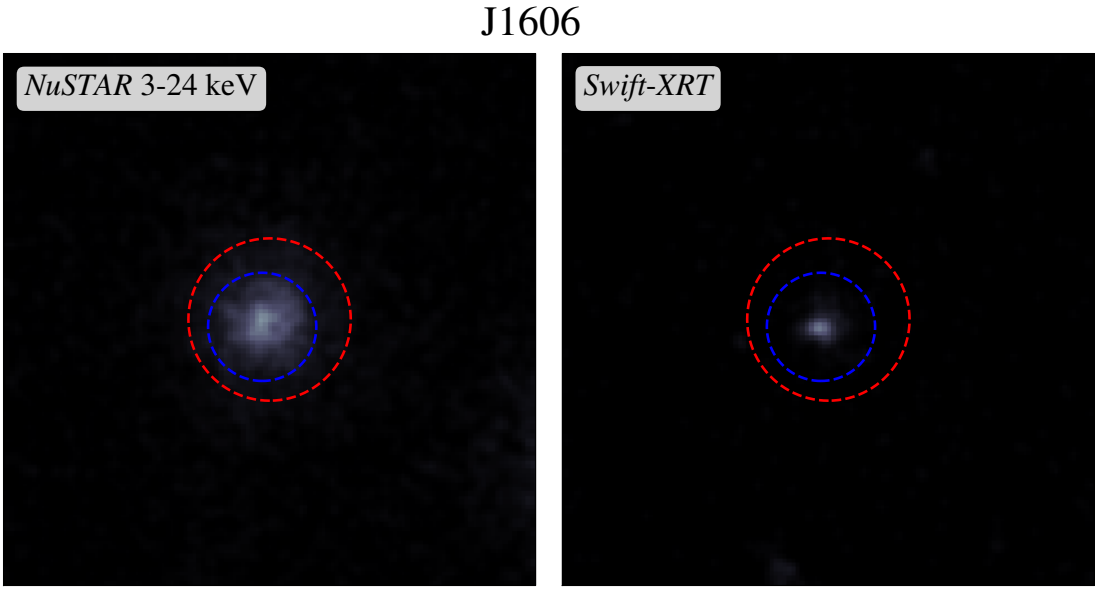

(B) (left) *NuSTAR* 3–24 keV image, (right) *Swift*-XRT full band image.

FIGURE C.6: Images of J1606, with multi-wavelength coordinates shown as follows: *NuSTAR* (red, 45 arcseconds), *XMM-Newton* (blue, 30 arcseconds), *WISE* (yellow, 12 arcseconds), PanSTARRS (cyan, 6 arcseconds).

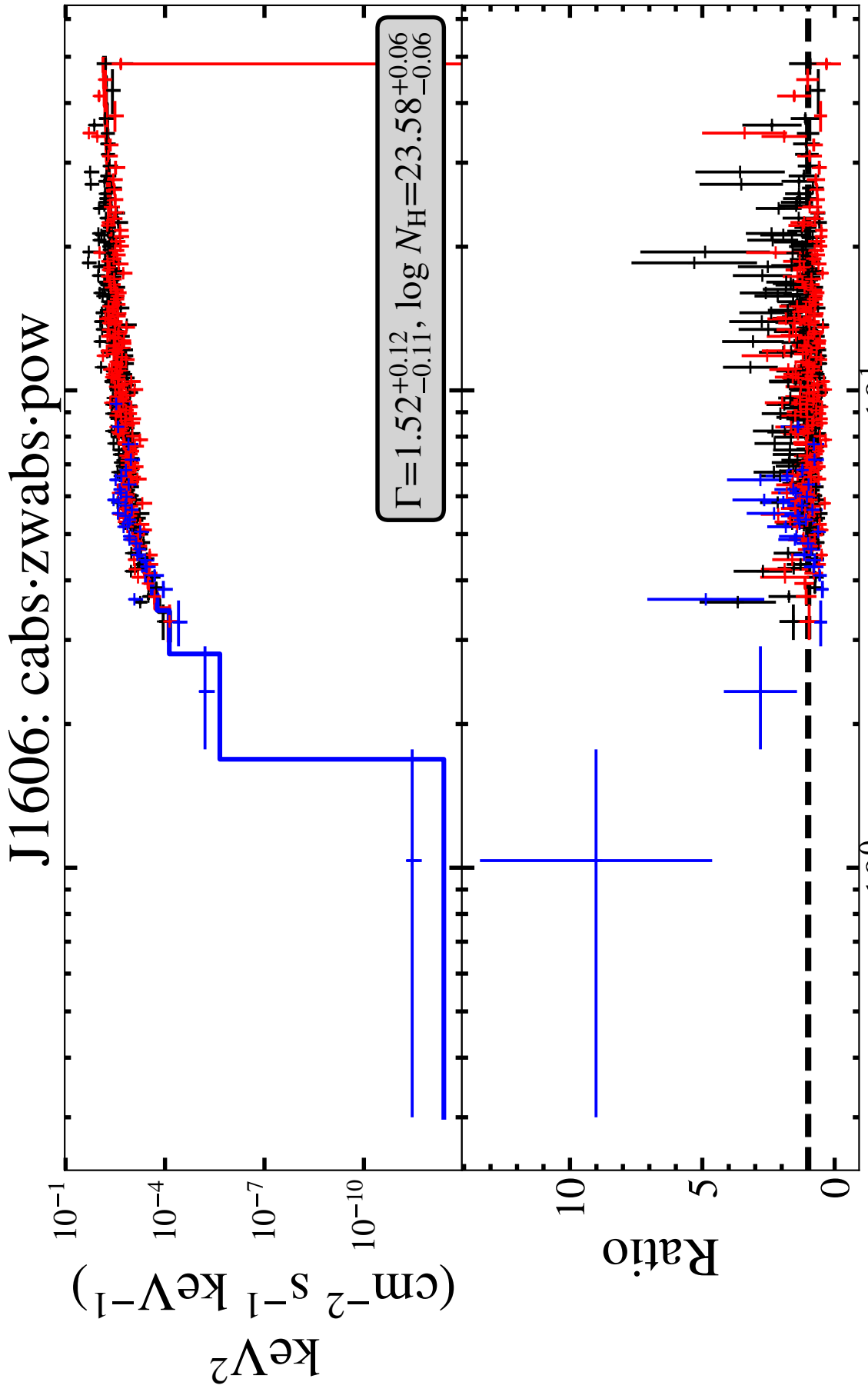

FIGURE C.7: J1606: (top) Spectrum of best fit CABS×ZWABS×POW model; (bottom) ratio between data and model. Shown is each observation separately, as listed in Table 3.1, binned to a minimum of 2 counts per bin.

C.4 NuSTARJ214320+4334.8

NuSTARJ214320+4334.8 (hereafter J2143, also known as UGC 11797) is part of a group of galaxies (UGC 11798 and UGC 11801) (see Figure C.8a). Both companions are detected by *XMM-Newton* (see Figure C.8b), and thus may also be AGN hosts. The optical spectrum from Palomar shows broad emission lines. J2143 was host to a Ia supernova in 2015 (Holoien et al., 2017), but this is unlikely to significantly contaminate AGN emission[1]. J2143 is located at a low angle in the galactic plane (Seeberger and Saurer, 1998) and therefore has a significantly higher galactic absorption than the other sources. In L2017, sources in this region were rejected, partly because it may be difficult to distinguish them from galactic sources. However, in the case of J2143, it is clear that this is a true extragalactic source.

The *WISE* source assigned in NSS80 using NWAY is show with a yellow square in Figure C.9a. In most cases we choose to trust the catalogue information; however, here there is an obvious better match (shown in Figure C.9a with a yellow diamond). This is a bright *WISE* source, closely aligned with the optical and soft X-ray coordinates, but it does not appear in the CatWISE catalogue. We replace the *WISE* information for this source with values from the older AllWISE catalogue instead, and the $W1 - W2$ colour from this catalogue is 0.123 – low for an AGN.

This source was measured over multiple epochs, and we fit the data in the following groups (see Table 3.1 for observation IDs):

- 2016: *NuSTAR* only; for the absorbed powerlaw, a fit including soft data was not possible.
- 2016: *XMM-Newton* (2016-05-16) and *NuSTAR*(2016-05-16); BORUS02.
- Jan 2021: *XMM-Newton* from 2018-11-24, *NuSTAR* from 2021-01-29; BORUS02, with cross-calibration constant for *XMM-Newton* allowed to vary.
- Feb 2021: *XMM-Newton* from 2018-11-24, *NuSTAR* from 2021-02-28; BORUS02, with cross-calibration constant for *XMM-Newton* allowed to vary.
- Mar 2021: *XMM-Newton* from 2018-11-24, *NuSTAR* from 2021-03-06; BORUS02, with cross-calibration constant for *XMM-Newton* allowed to vary.

Table 3.1 shows the results of each model fit - each BORUS02 model provides a good fit to the data, and the intrinsic spectral shape and $N_{\rm H}$ remain consistent within uncertainties across each epoch. The mean Γ=1.51, and mean log$N_{\rm H}$=23.59 cm^{-2} (individual values are in Table 3.1), making it a heavily obscured but not Compton thick source.

[1]The literature shows another supernova in 2001 – this is a mis-identification of the host galaxy.

Spectra from each epoch are shown in Figure C.10 and the change in luminosity is shown in Figure C.11.

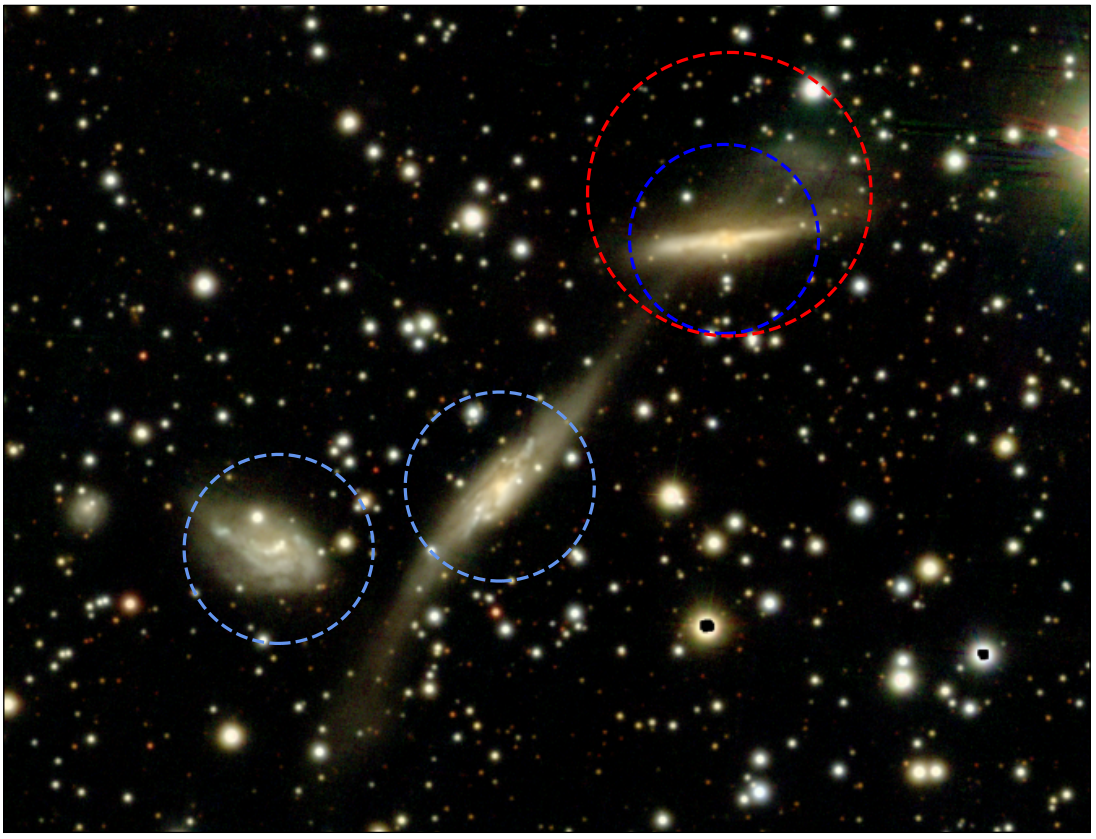

(A) PanSTARRS *irg* image of J2143 and surrounding region.

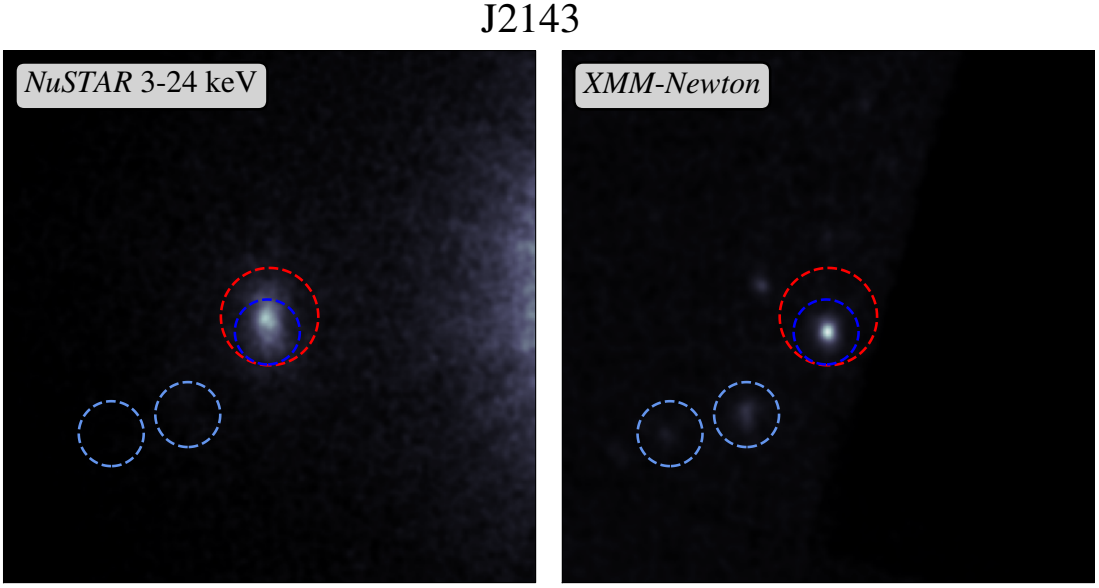

(B) (left) *NuSTAR* 3–24 keV image, (right) *XMM-Newton* 0.5–10 keV image.

FIGURE C.8: Images of J2143, with coordinates shown as follows: *NuSTAR* (red, 45 arcseconds), *XMM-Newton* (blue, 30 arcseconds), companion *XMM-Newton* (light blue, 30 arcseconds).

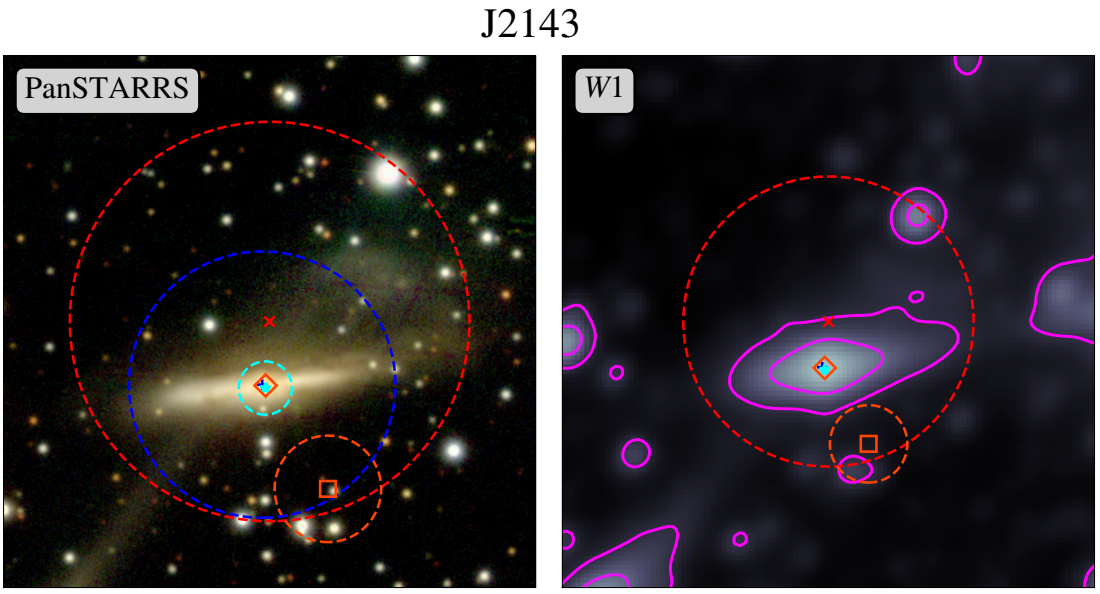

(A) J2143: (left) PanSTARRS *irg* image, (right) *WISE W*1 image.

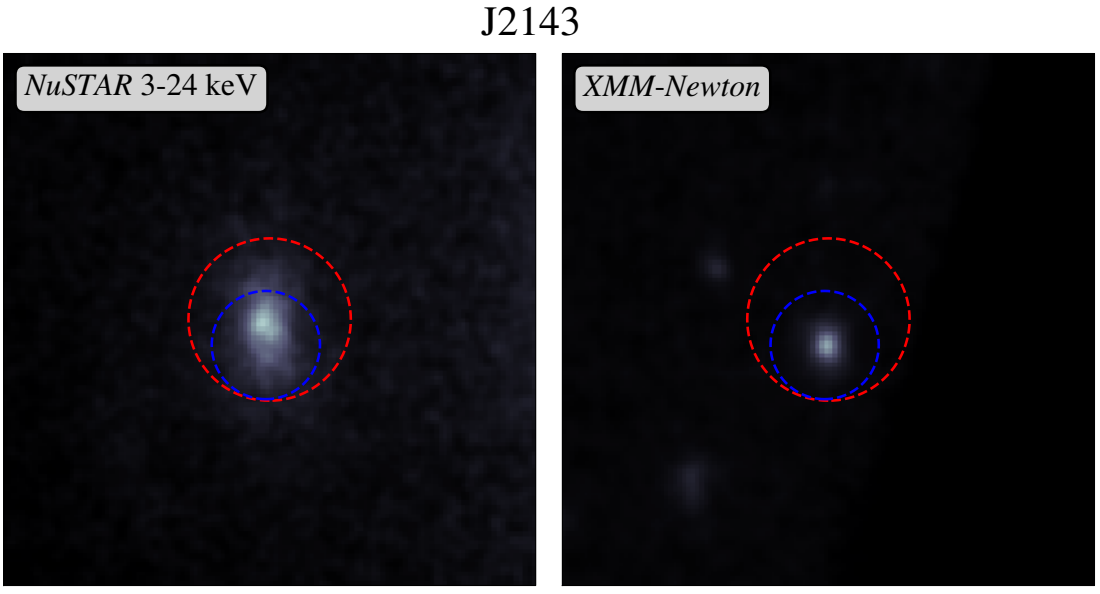

(B) (left) *NuSTAR* 3–24 keV image, (right) *XMM-Newton* 0.5–10 keV image.

FIGURE C.9: Images of J2143, with multi-wavelength coordinates shown as follows: *NuSTAR* (red, 45 arcseconds), *XMM-Newton* (blue, 30 arcseconds), *WISE* (yellow, 12 arcseconds), PanSTARRS (cyan, 6 arcseconds).

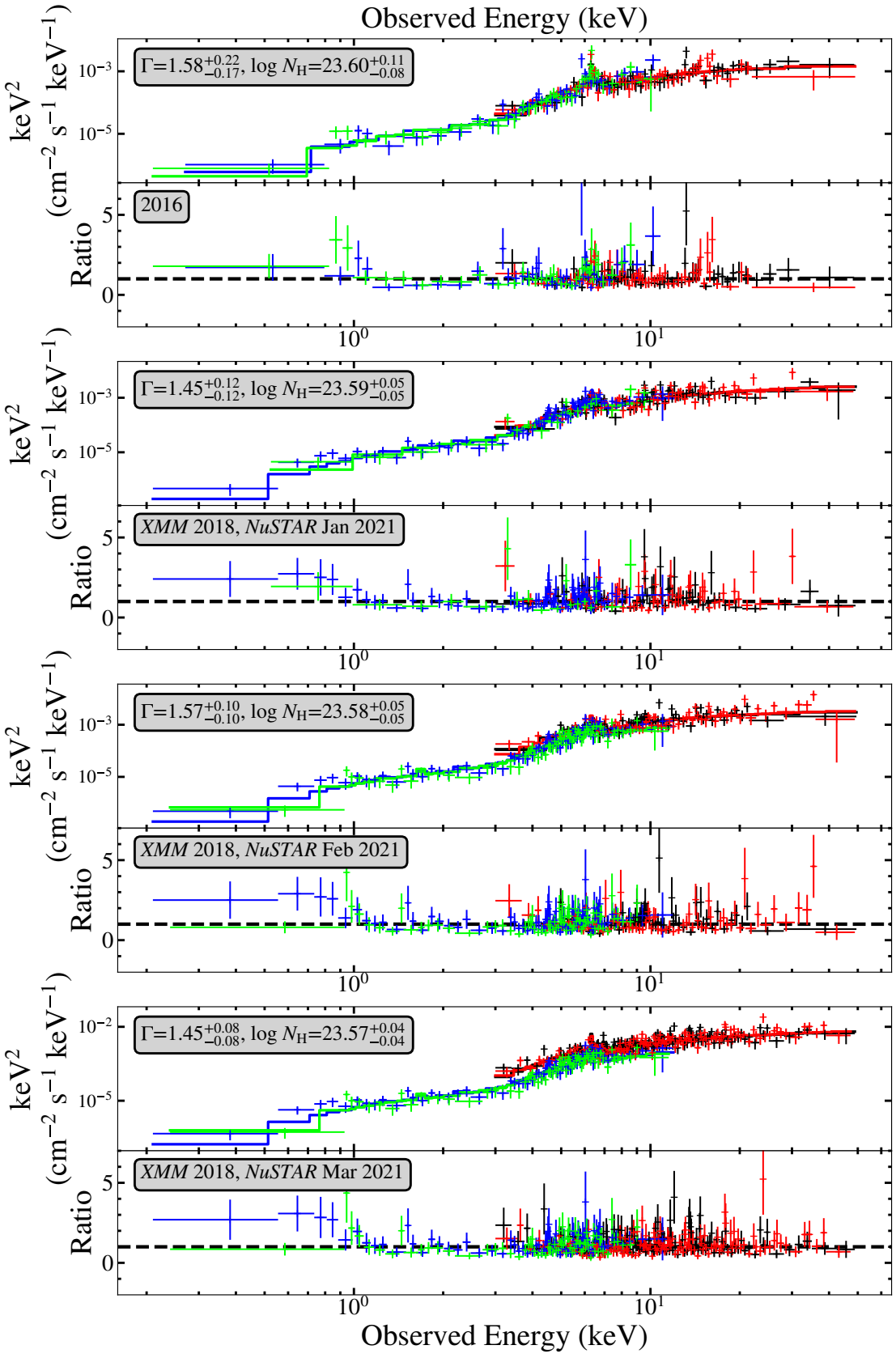

FIGURE C.10: J2143: spectra across measurement epochs.

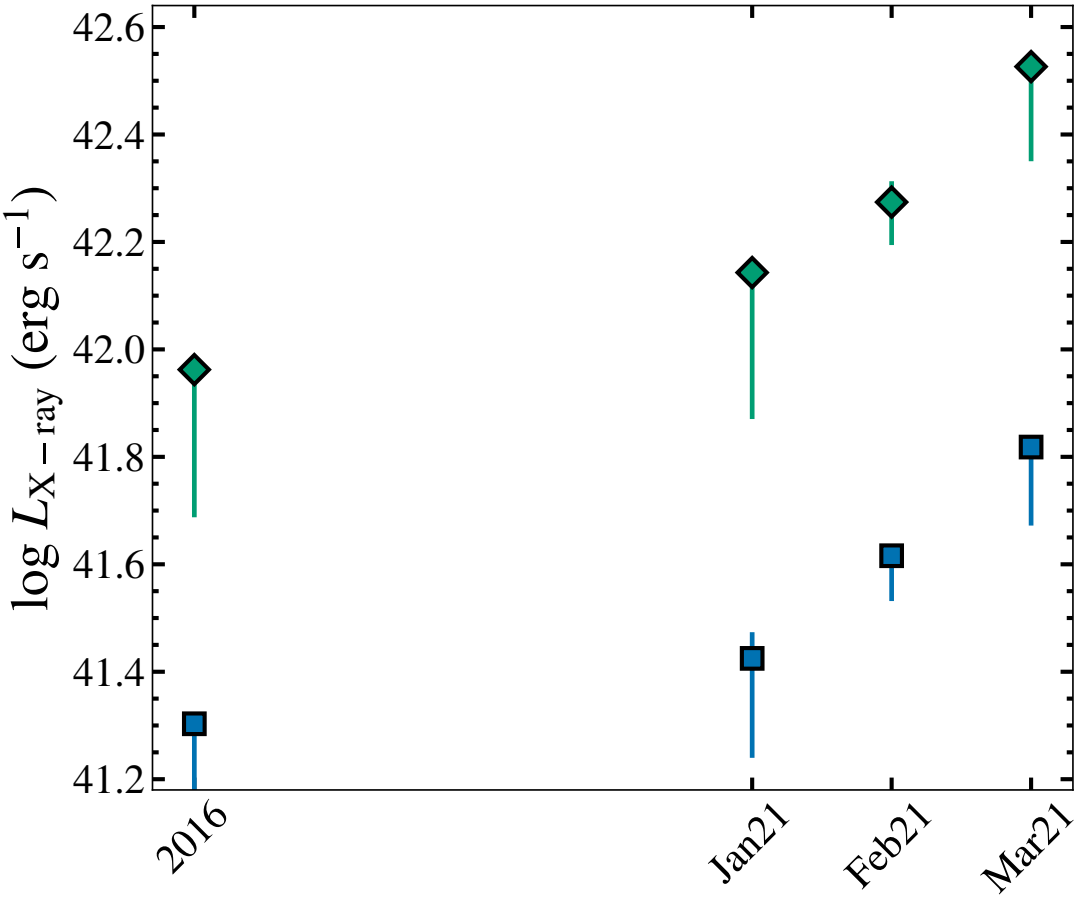

FIGURE C.11: J2143: change in observed luminosity across measurement epochs.

C.5 NuSTARJ224925-1917.5

NuSTARJ224925-1917.5 (hereafter J2249) is detected in PanSTARRS (coordinates indicated by a cyan circle in Figure C.12a, left), but is not clearly visible in the image. The optical spectrum from Palomar is faint but shows narrow line emission. It is not an otherwise previously known source. The optical, soft X-ray, and IR coordinates are closely aligned.

It is detected in *WISE* but not clearly visible as a bright source (see Figure C.6a, right). Its *W*1-*W*2 colour is 0.666 - for a source this dim in *W*2, the colour threshold for selection is increased, and it does not pass as a MIR selected AGN. A second *WISE* source is present within the *NuSTAR* region - brighter in *W*1 and *W*2, but dropping out in *W*3 and *W*4 (Figure B.16). There is no soft X-ray emission at these coordinates, so we assume that the *NuSTAR* emission is from J2249. This source is present in the optical image, but no redshift is available.

In X-rays, it is detected from 3–24 keV with *NuSTAR*and *XMM-Newton* (see Figure C.12). Including the soft data could not produce a good fit with the absorbed powerlaw so it was excluded, and due to the low counts of the data a BORUS02 fit was not attempted. The results of the absorbed powerlaw are shown in Figure C.13. The intrinsic photon index was fixed at Γ=1.9 cm^{-2}. The obscuration depth was found to be $\log N_{\rm H}$=$23.44^{+0.36}_{-2.07}$ cm^{-2} – note the large lower uncertainty on this value, indicating that the obscuration on this object is likely to be lighter than other sources included here. The observed luminosities were $L_{2-10\ \rm keV}$=1.56×10^{43} erg^{-1} s^{-1} and $L_{10-40\ \rm keV}$=4.57×10^{43} erg^{-1} s^{-1}.

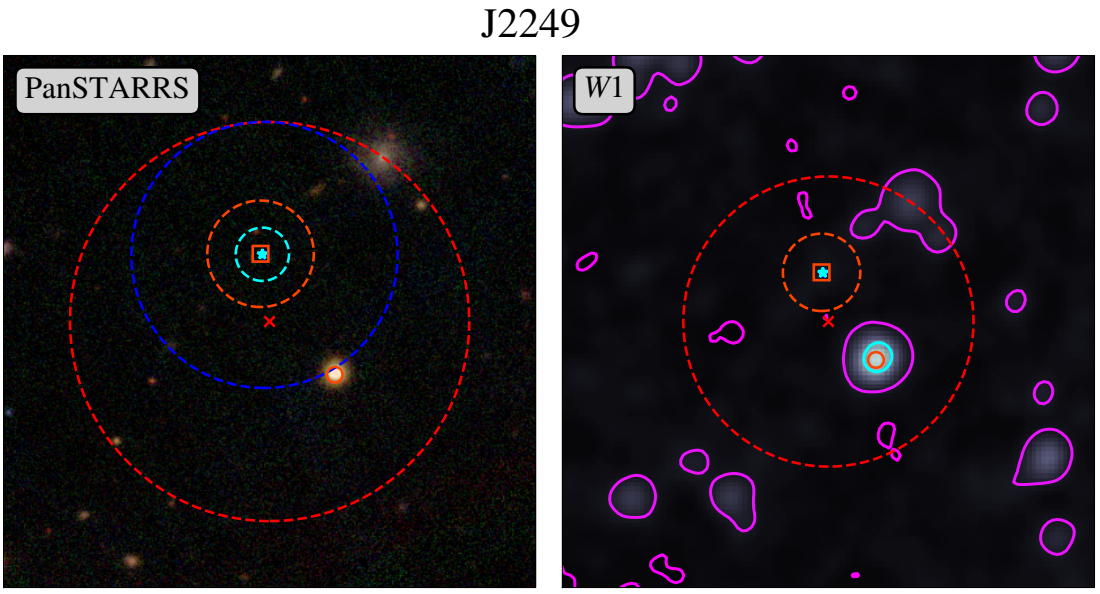

(A) J2249: (left) PanSTARRS *irg* image, (right) *WISE W*1 image.

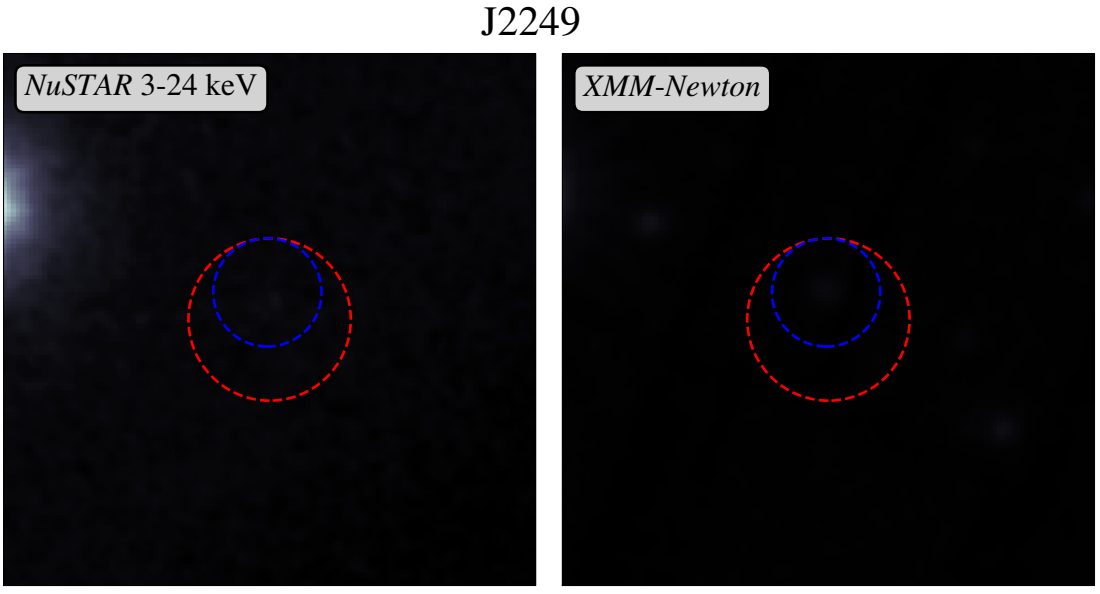

(B) (left) *NuSTAR* 3–24 keV image, (right) *XMM-Newton* 0.5–10 keV image.

FIGURE C.12: Images of J2249, with multi-wavelength coordinates shown as follows: *NuSTAR* (red, 45 arcseconds), *XMM-Newton* (blue, 30 arcseconds), *WISE* (yellow, 12 arcseconds), PanSTARRS (cyan, 6 arcseconds).

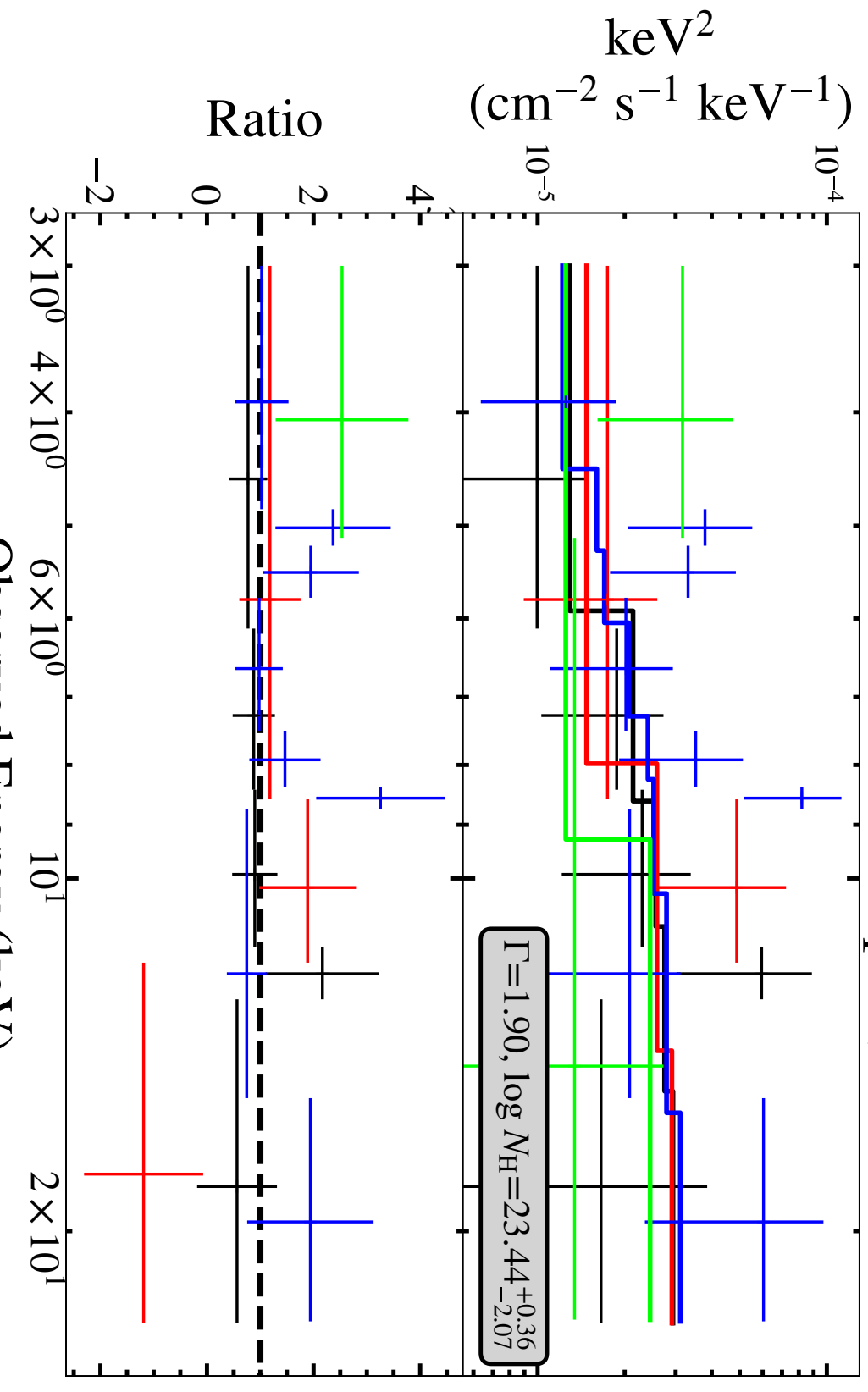

FIGURE C.13: J2249: (top) Spectrum of best fit CABS×ZWABS×POW model; (bottom) ratio between data and model. Shown is each observation separately, as listed in Table 3.1, binned to a minimum of 2 counts per bin.

Appendix D

SDSS Spectra of OQQs

In this section I present the SDSS spectra of each OQQ. The first eight are shown in Chapter 5, Figure 5.5. Wavelength shown in observed, and in the top left of each group I show the location of three important features: [O III], H α, and the 4000 Å break.

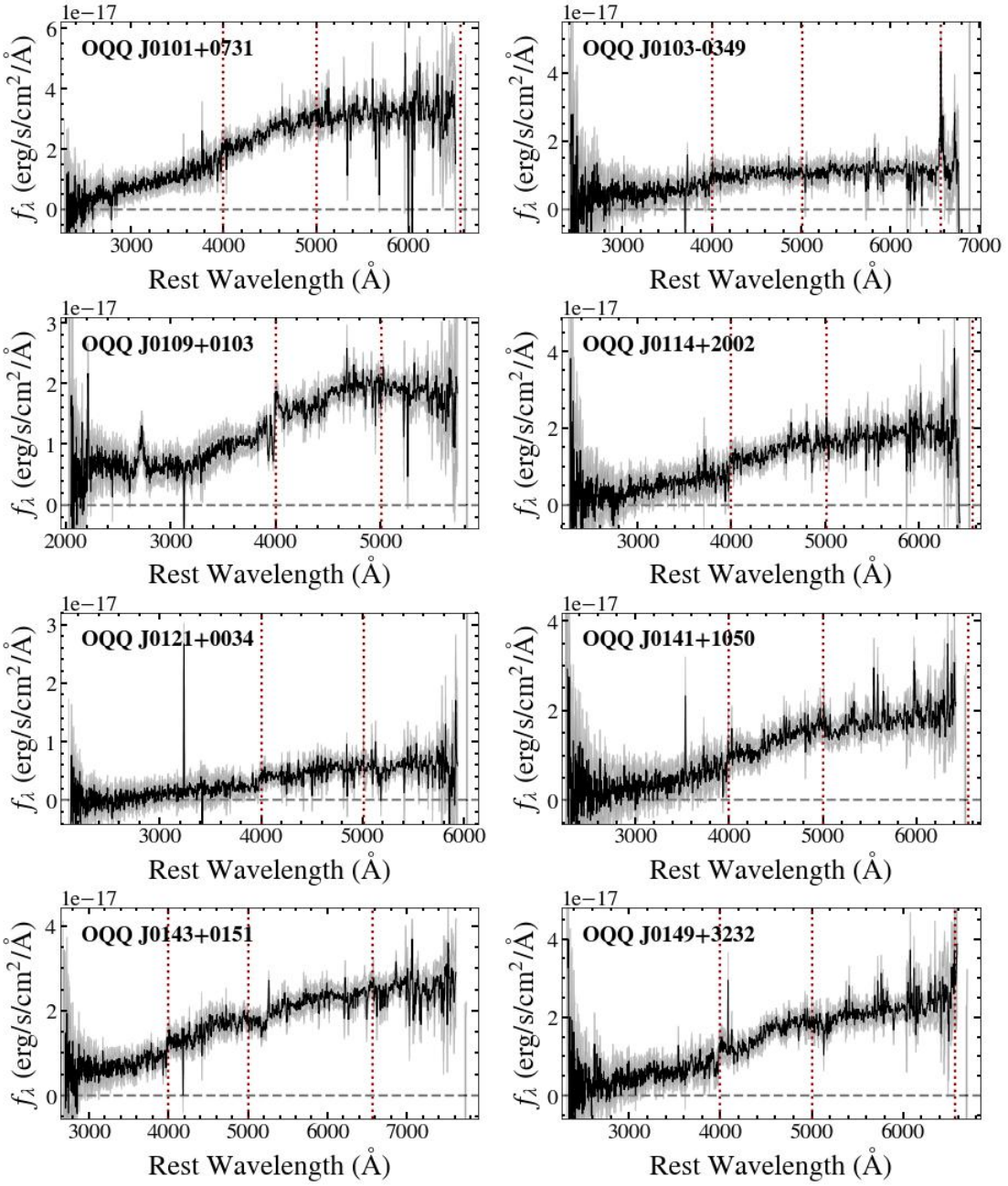

FIGURE D.1: SDSS spectra of the OQQs by RA, part two.

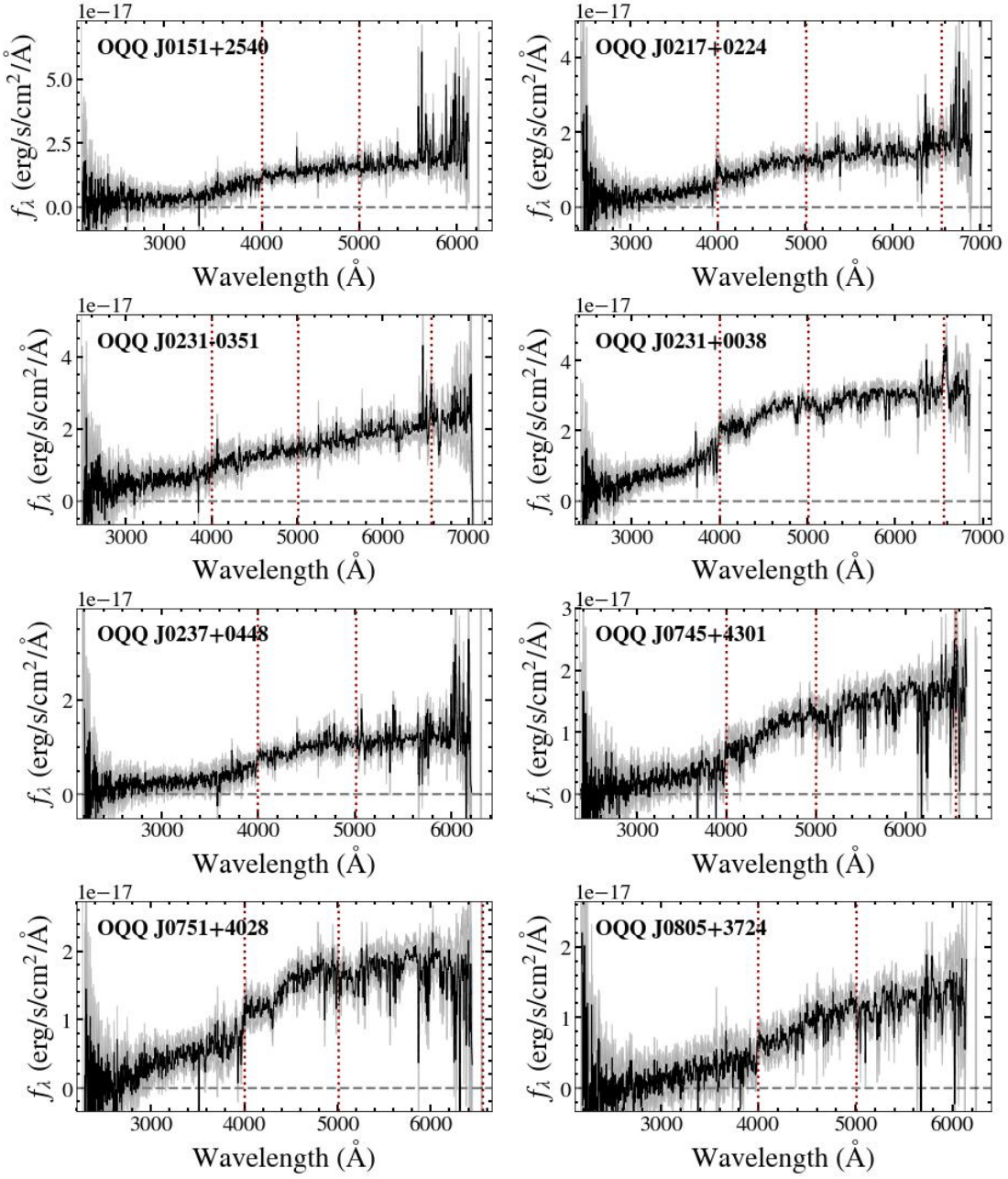

FIGURE D.2: SDSS spectra of the OQQs by RA, part three.

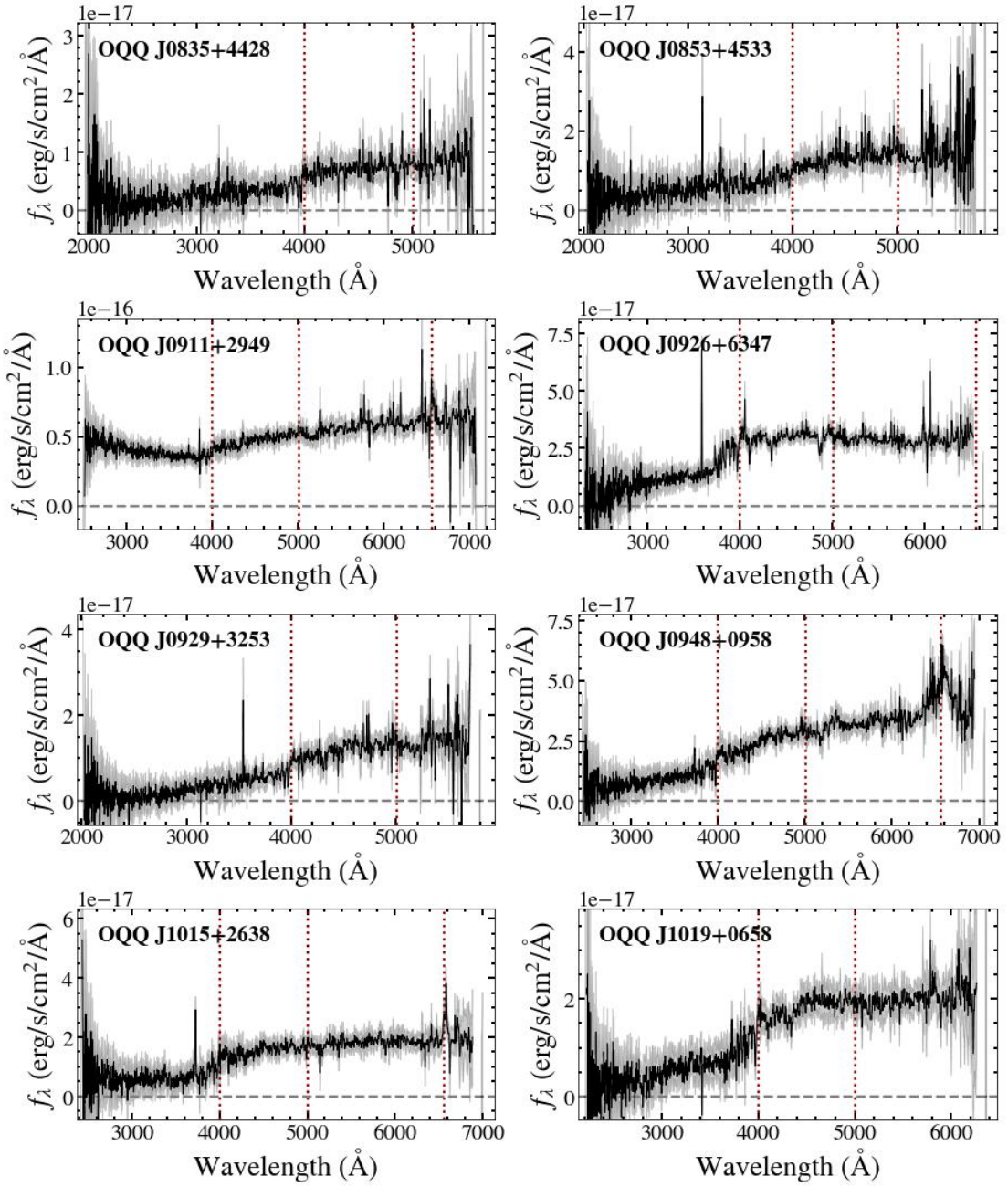

FIGURE D.3: SDSS spectra of the OQQs by RA, part four.

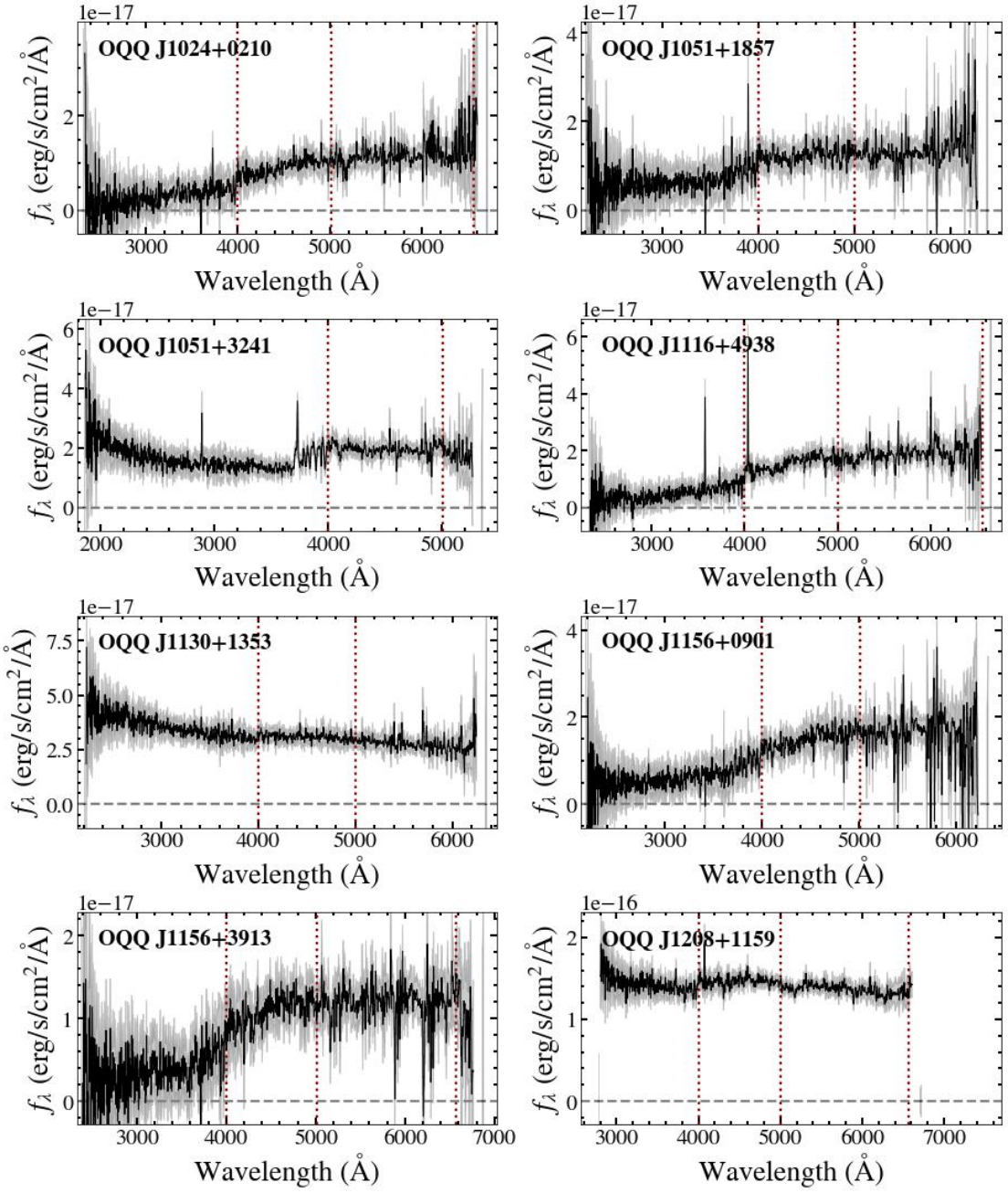

FIGURE D.4: SDSS spectra of the OQQs by RA, part five.

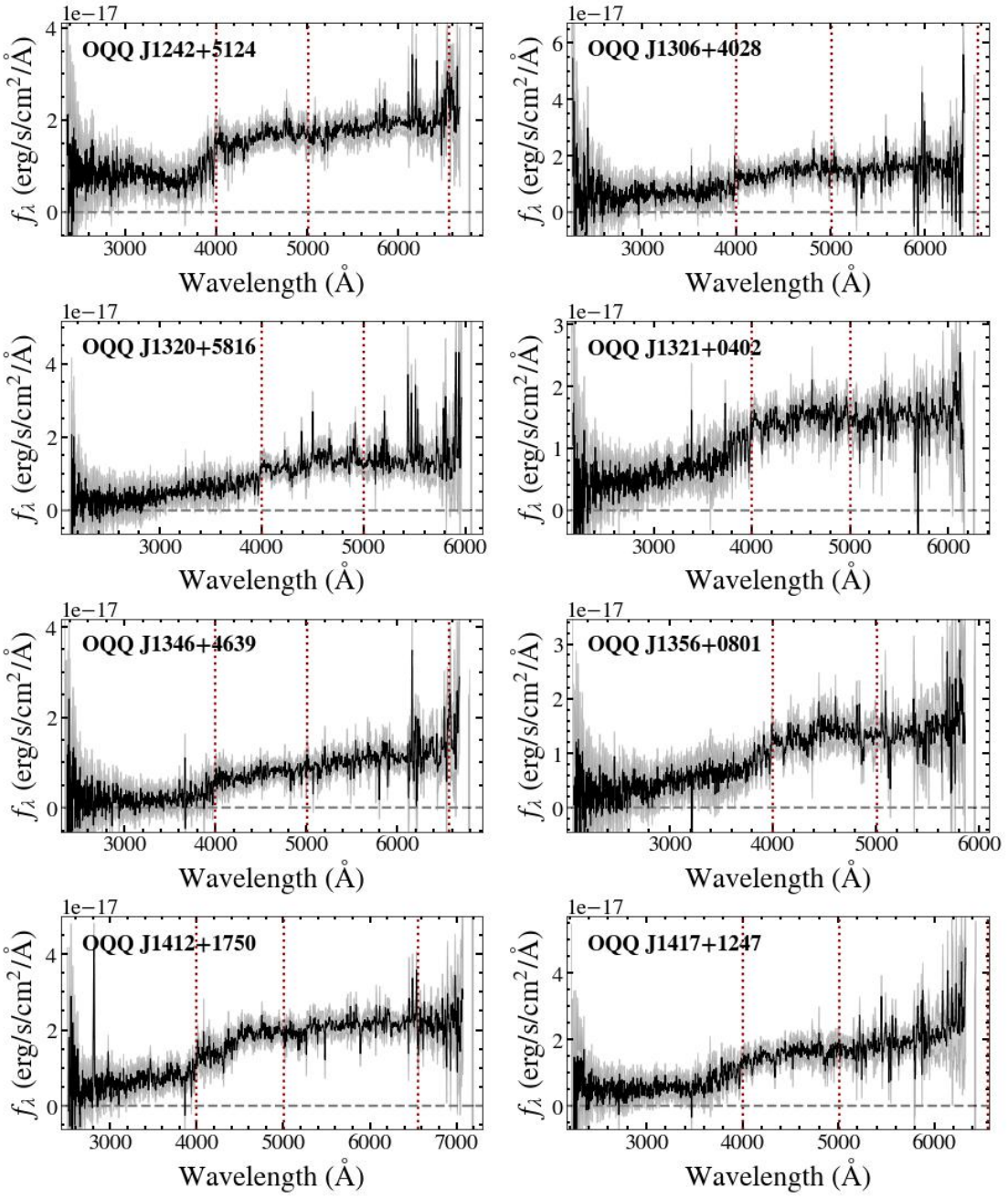

FIGURE D.5: SDSS spectra of the OQQs by RA, part six.

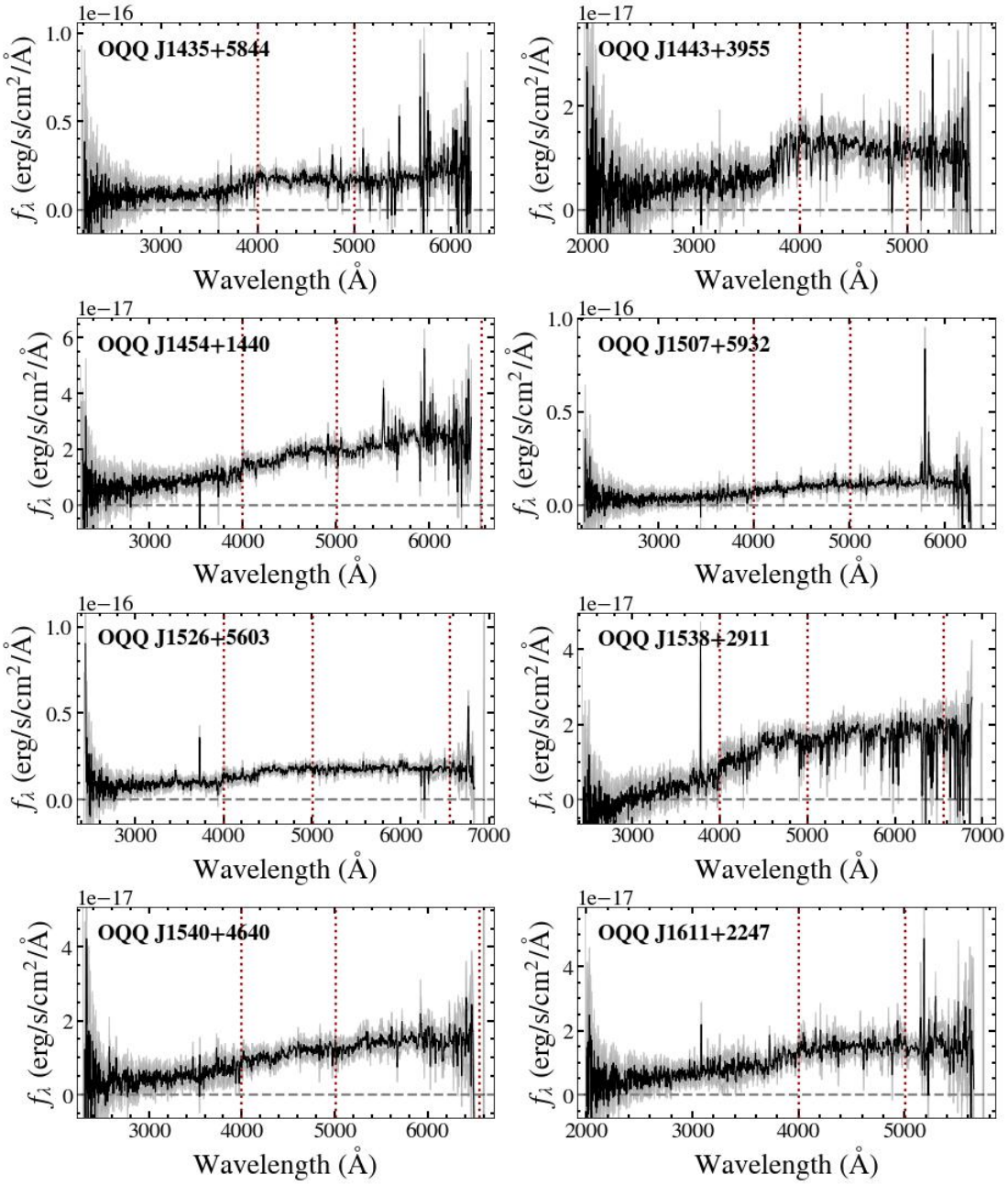

FIGURE D.6: SDSS spectra of the OQQs by RA, part seven.

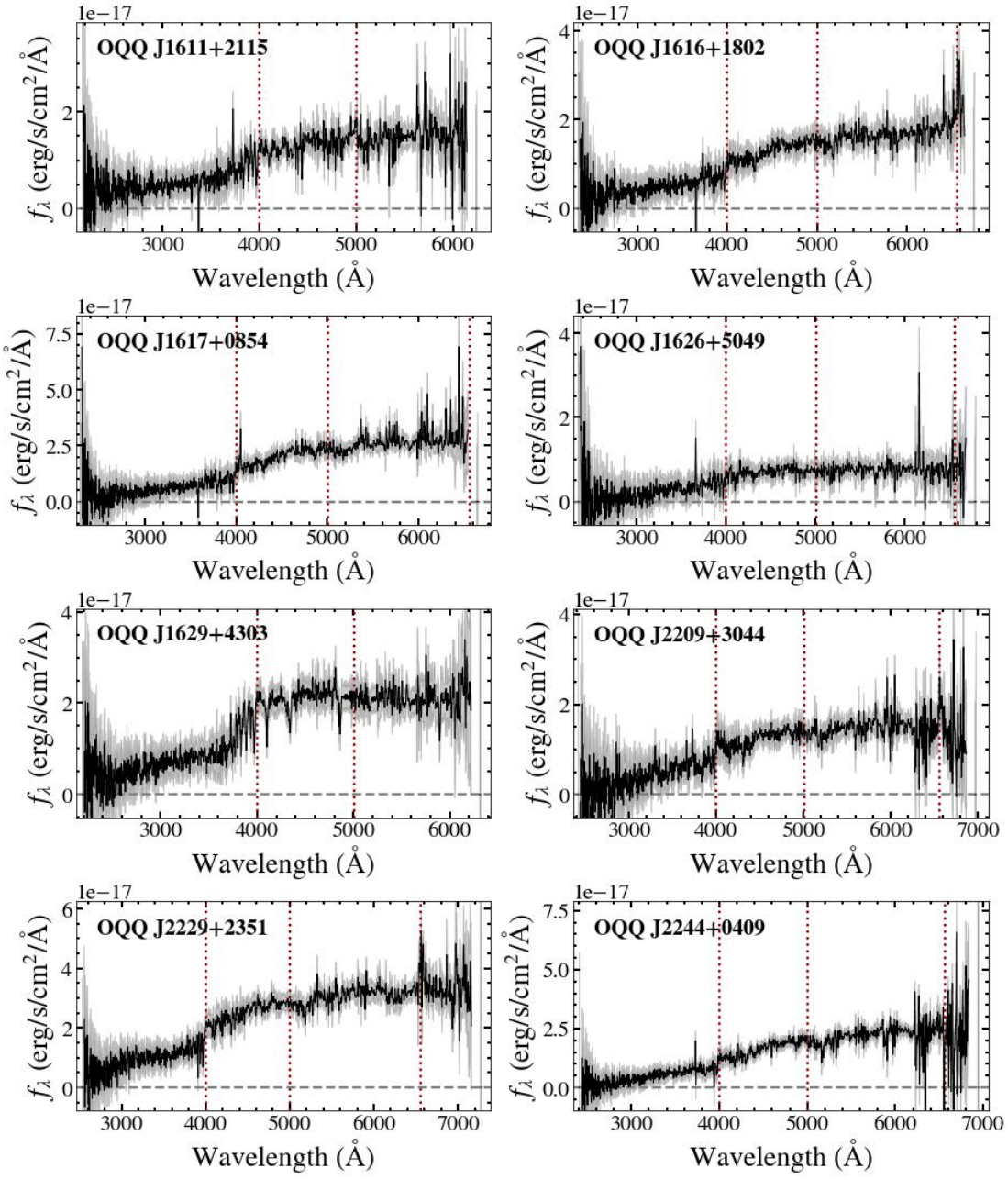

FIGURE D.7: SDSS spectra of the OQQs by RA, part eight.

References

Abdurro'uf, Accetta, K., Aerts, C. et al. The Seventeenth Data Release of the Sloan Digital Sky Surveys: Complete Release of MaNGA, MaStar, and APOGEE-2 Data. *ApJS*, 259:35, Apr. 2022. ISSN 0067-0049. . URL https://ui.adsabs.harvard.edu/abs/2022ApJS..259...35A. ADS Bibcode: 2022ApJS..259...35A.

Agostino, C.J. and Salim, S. Crossing the Line: Active Galactic Nuclei in the Star-forming Region of the BPT Diagram. *ApJ*, 876(1):12, May 2019. .

Aguado, D.S., Ahumada, R., Almeida, A. et al. The Fifteenth Data Release of the Sloan Digital Sky Surveys: First Release of MaNGA-derived Quantities, Data Visualization Tools, and Stellar Library. *ApJS*, 240(2):23, Feb. 2019. .

Aird, J., Nandra, K., Laird, E.S. et al. The evolution of the hard X-ray luminosity function of AGN. *MNRAS*, 401(4):2531–2551, Feb. 2010. ISSN 00358711, 13652966. . URL https://academic.oup.com/mnras/article-lookup/doi/10.1111/j.1365-2966.2009.15829.x.

Aird, J., Coil, A.L., Georgakakis, A. et al. The evolution of the X-ray luminosity functions of unabsorbed and absorbed AGNs out to z∼5. *MNRAS*, 451(2):1892–1927, Aug. 2015. ISSN 1365-2966, 0035-8711. . URL http://academic.oup.com/mnras/article/451/2/1892/1747784/The-evolution-of-the-Xray-luminosity-functions-of.

Akylas, A. and Georgantopoulos, I. Distribution of the coronal temperature in Seyfert 1 galaxies. *A&A*, 655:A60, Nov. 2021. .

Akylas, A., Georgantopoulos, I., Ranalli, P. et al. Compton-thick AGN in the 70-month *Swift* -BAT All-Sky Hard X-ray Survey: A Bayesian approach. *A&A*, 594: A73, Oct. 2016. ISSN 0004-6361, 1432-0746. . URL http://www.aanda.org/10.1051/0004-6361/201628711.

Alexander, D.M. and Hickox, R.C. What drives the growth of black holes? *ar*, 56(4):93–121, June 2012. ISSN 1387-6473. . URL http://www.sciencedirect.com/science/article/pii/S1387647311000583.

Alexander, D.M., Stern, D., Del Moro, A. et al. The NuSTAR Extragalactic Survey: A First Sensitive Look at the High-energy Cosmic X-Ray Background Population. *ApJ*, 773:125, Aug. 2013. .

Alonso-Herrero, A., Ramos Almeida, C., Mason, R. et al. TORUS AND ACTIVE GALACTIC NUCLEUS PROPERTIES OF NEARBY SEYFERT GALAXIES: RESULTS FROM FITTING INFRARED SPECTRAL ENERGY DISTRIBUTIONS AND SPECTROSCOPY. *ApJ*, 736(2):82, Aug. 2011. ISSN 0004-637X, 1538-4357. . URL http://stacks.iop.org/0004-637X/736/i=2/a=82?key=crossref.f0fccf9cf3eef2df322d03a433ae40bc.

Ananna, T.T., Treister, E., Urry, C.M. et al. The Accretion History of AGNs. I. Supermassive Black Hole Population Synthesis Model. *ApJ*, 871(2):240, Feb. 2019. .

Ananna, T.T., Treister, E., Urry, C.M. et al. Accretion History of AGNs. II. Constraints on AGN Spectral Parameters Using the Cosmic X-Ray Background. *ApJ*, 889(1):17, Jan. 2020. .

Andonie, C., Alexander, D.M., Rosario, D. et al. A panchromatic view of infrared quasars: excess star formation and radio emission in the most heavily obscured systems. *arXiv e-prints*, art. arXiv:2209.13321, Sept. 2022.

Annuar, A., Alexander, D.M., Gandhi, P. et al. NuSTAR observations of four nearby X-ray faint AGNs: low luminosity or heavy obscuration? *MNRAS*, 497(1):229–245, Sept. 2020. .

Antonucci, R. Unified models for active galactic nuclei and quasars. *ARA&A*, 31:473–521, 1993. .

Aranzana, E., Kording, E., Uttley, P. et al. Short time-scale optical variability properties of the largest AGN sample observed with Kepler/K2. *MNRAS*, 476(2):2501–2515, May 2018. ISSN 0035-8711, 1365-2966. . URL http://arxiv.org/abs/1802.08058. arXiv: 1802.08058.

Armus, L., Heckman, T.M. and Miley, G.K. Long-Slit Optical Spectroscopy of Powerful Far-Infrared Galaxies: The Nature of the Nuclear Energy Source. *ApJ*, 347:727, Dec. 1989. .

Arnaud, K.A. XSPEC: The First Ten Years. In Jacoby, G.H. and Barnes, J., editors, *Astronomical Data Analysis Software and Systems V*, volume 101 of *Astronomical Society of the Pacific Conference Series*, page 17, Jan. 1996.

Asmus, D., Hönig, S.F., Gandhi, P. et al. The subarcsecond mid-infrared view of local active galactic nuclei - I. The N- and Q-band imaging atlas. *MNRAS*, 439:1648–1679, Feb. 2014. .

Asmus, D., Gandhi, P., Hönig, S.F. et al. The subarcsecond mid-infrared view of local active galactic nuclei – II. The mid-infrared–X-ray correlation. *MNRAS*, 454(1):766–803, Nov. 2015. ISSN 0035-8711, 1365-2966. . URL https://academic.oup.com/mnras/article-lookup/doi/10.1093/mnras/stv1950.

Asmus, D., Greenwell, C.L., Gandhi, P. et al. Local AGN survey (LASr): I. Galaxy sample, infrared colour selection, and predictions for AGN within 100 Mpc. *MNRAS*, 494(2):1784–1816, May 2020. .

Assef, R.J., Kochanek, C.S., Brodwin, M. et al. LOW-RESOLUTION SPECTRAL TEMPLATES FOR ACTIVE GALACTIC NUCLEI AND GALAXIES FROM 0.03 TO 30 μm. *ApJ*, 713(2):970–985, Apr. 2010. ISSN 0004-637X, 1538-4357. . URL http://stacks.iop.org/0004-637X/713/i=2/a=970?key=crossref.7eb319b700e5fe4524c3c41bdc6c2376.

Assef, R.J., Stern, D., Kochanek, C.S. et al. MID-INFRARED SELECTION OF ACTIVE GALACTIC NUCLEI WITH THE *WIDE-FIELD INFRARED SURVEY EXPLORER* . II. PROPERTIES OF *WISE* -SELECTED ACTIVE GALACTIC NUCLEI IN THE NDWFS BOÖTES FIELD. *ApJ*, 772(1):26, July 2013. ISSN 0004-637X, 1538-4357. . URL http://stacks.iop.org/0004-637X/772/i=1/a=26?key=crossref.11479e3b5e38279dd93053b29798ee80.

Assef, R.J., Eisenhardt, P.R.M., Stern, D. et al. HALF OF THE MOST LUMINOUS QUASARS MAY BE OBSCURED: INVESTIGATING THE NATURE OF *WISE* -SELECTED HOT DUST-OBSCURED GALAXIES. *ApJ*, 804(1):27, Apr. 2015. ISSN 1538-4357. . URL http://stacks.iop.org/0004-637X/804/i=1/a=27?key=crossref.79287b5fbb9d2b35a415391ee084f73f.

Assef, R.J., Stern, D., Noirot, G. et al. The *WISE* AGN Catalog. *Astrophys. J. Suppl. Ser.*, 234(2):23, Jan. 2018. ISSN 1538-4365. . URL http://stacks.iop.org/0067-0049/234/i=2/a=23?key=crossref.c53d7941eb653dbfe205d779ad4b4a66.

Atwood, W.B., Abdo, A.A., Ackermann, M. et al. The Large Area Telescope on the Fermi Gamma-Ray Space Telescope Mission. *ApJ*, 697(2):1071–1102, June 2009. .

Balbus, S.A. Enhanced Angular Momentum Transport in Accretion Disks. *ARA&A*, 41:555–597, Jan. 2003. .

Balbus, S.A. and Hawley, J.F. A Powerful Local Shear Instability in Weakly Magnetized Disks. I. Linear Analysis. *ApJ*, 376:214, July 1991. .

Baldry, I.K., Liske, J., Brown, M.J.I. et al. Galaxy And Mass Assembly: the G02 field, Herschel-ATLAS target selection and data release 3. *MNRAS*, 474(3):3875–3888, Mar. 2018. .

Baldwin, J.A., Phillips, M.M. and Terlevich, R. Classification parameters for the emission-line spectra of extragalactic objects. *PASP*, 93:5, Feb. 1981. ISSN 0004-6280, 1538-3873. . URL http://iopscience.iop.org/article/10.1086/130766.

Balogh, M.L., Morris, S.L., Yee, H.K.C. et al. Differential Galaxy Evolution in Cluster and Field Galaxies at z~0.3. *ApJ*, 527(1):54–79, Dec 1999. .

Baloković, M., Smolčić, V., Ivezić, Ž. et al. Disclosing the Radio Loudness Distribution Dichotomy in Quasars: An Unbiased Monte Carlo Approach Applied to the SDSS-FIRST Quasar Sample. *ApJ*, 759(1):30, Nov. 2012. .

Baloković, M., Brightman, M., Harrison, F.A. et al. New Spectral Model for Constraining Torus Covering Factors from Broadband X-Ray Spectra of Active Galactic Nuclei. *ApJ*, 854(1):42, Feb. 2018. .

Banerji, M., McMahon, R.G., Hewett, P.C. et al. Heavily reddened quasars at z ~ 2 in the UKIDSS Large Area Survey: a transitional phase in AGN evolution: Heavily reddened quasars at z ~ 2 in UKIDSS LAS. *MNRAS*, 427(3):2275–2291, Dec. 2012. ISSN 00358711, 13652966. . URL https://academic.oup.com/mnras/article-lookup/doi/10.1111/j.1365-2966.2012.22099.x.

Banerji, M., Alaghband-Zadeh, S., Hewett, P.C. et al. Heavily reddened type 1 quasars at z ¿ 2 - I. Evidence for significant obscured black hole growth at the highest quasar luminosities. *MNRAS*, 447(4):3368–3389, Mar. 2015. .

Baronchelli, L., Nandra, K. and Buchner, J. Relativistic accretion disc reflection in AGN X-ray spectra at z = 0.5-4: a study of four Chandra Deep Fields. *MNRAS*, 498(4): 5284–5298, Nov. 2020. .

Barthelmy, S.D., Barbier, L.M., Cummings, J.R. et al. The Burst Alert Telescope (BAT) on the SWIFT Midex Mission. *Space Sci. Rev.*, 120:143–164, Oct. 2005. .

Baumgartner, W.H., Tueller, J., Markwardt, C.B. et al. THE 70 MONTH *SWIFT* -BAT ALL-SKY HARD X-RAY SURVEY. *ApJS*, 207(2):19, July 2013. ISSN 0067-0049, 1538-4365. . URL http://stacks.iop.org/0067-0049/207/i=2/a=19?key=crossref.e66b4f87884ee861060141a06c6a9961.

Becker, R.H., White, R.L. and Helfand, D.J. The FIRST Survey: Faint Images of the Radio Sky at Twenty Centimeters. *ApJ*, 450:559, Sept. 1995. .

Blecha, L., Snyder, G.F., Satyapal, S. et al. The power of infrared AGN selection in mergers: a theoretical study. *MNRAS*, 478(3):3056–3071, Aug. 2018. .

Boller, T., Freyberg, M.J., Trümper, J. et al. Second ROSAT all-sky survey (2RXS) source catalogue. *A&A*, 588:A103, Apr. 2016. .

Boroson, T.A. and Green, R.F. The emission-line properties of low-redshift quasi-stellar objects. *ApJS*, 80:109–135, May 1992. .

Brandt, W.N. and Alexander, D.M. Cosmic X-ray surveys of distant active galaxies. The demographics, physics, and ecology of growing supermassive black holes. *A&ARv*, 23:1, Jan. 2015. .

Brightman, M. and Nandra, K. An XMM-Newton spectral survey of 12 μm selected galaxies - I. X-ray data. *MNRAS*, 413(2):1206–1235, May 2011. .

Brusa, M., Comastri, A., Gilli, R. et al. HIGH-REDSHIFT QUASARS IN THE COSMOS SURVEY: THE SPACE DENSITY OF $z > 3$ X-RAY SELECTED QSOs. *ApJ*, 693(1):8–22, Mar. 2009. ISSN 0004-637X, 1538-4357. . URL http://stacks.iop.org/0004-637X/693/i=1/a=8?key=crossref.44fd247f55bac3d8e0c1aacd2477066d.

Buchner, J. and Bauer, F.E. Galaxy gas as obscurer - II. Separating the galaxy-scale and nuclear obscurers of active galactic nuclei. *MNRAS*, 465(4):4348–4362, Mar. 2017. .

Buchner, J., Georgakakis, A., Nandra, K. et al. X-ray spectral modelling of the AGN obscuring region in the CDFS: Bayesian model selection and catalogue. *A&A*, 564: A125, Apr. 2014. .

Buchner, J., Schulze, S. and Bauer, F.E. Galaxy gas as obscurer - I. GRBs x-ray galaxies and find an $N_H{}^3 \propto$ M_{star} relation. *MNRAS*, 464(4):4545–4566, Feb. 2017. .

Burrows, D.N., Hill, J.E., Nousek, J.A. et al. The Swift X-Ray Telescope. *Space Sci. Rev.*, 120:165–195, Oct. 2005. .

Caccianiga, A., Severgnini, P., Della Ceca, R. et al. Elusive AGN in the *XMM-Newton* bright serendipitous survey. *Astronomy & Astrophysics*, 470(2):557–570, Aug. 2007. ISSN 0004-6361, 1432-0746. . URL http://www.aanda.org/10.1051/0004-6361:20077732.

Calistro Rivera, G., Lusso, E., Hennawi, J.F. et al. AGNfitter: A Bayesian MCMC Approach to Fitting Spectral Energy Distributions of AGNs. *ApJ*, 833(1):98, Dec. 2016. .

Cappelluti, N., Li, Y., Ricarte, A. et al. The Chandra COSMOS Legacy Survey: Energy Spectrum of the Cosmic X-Ray Background and Constraints on Undetected Populations. *ApJ*, 837(1):19, Mar. 2017. .

Cardelli, J.A., Clayton, G.C. and Mathis, J.S. The Relationship between Infrared, Optical, and Ultraviolet Extinction. *ApJ*, 345:245, Oct 1989. .

Cash, W. Parameter estimation in astronomy through application of the likelihood ratio. *ApJ*, 228:939–947, Mar. 1979. URL http://ukads.nottingham.ac.uk/cgi-bin/nph-bib_query?bibcode=1979ApJ...228..939C&db_key=AST.

Chan, C.H. and Krolik, J.H. Geometrically Thick Obscuration by Radiation-driven Outflow from Magnetized Tori of Active Galactic Nuclei. *ApJ*, 843(1):58, July 2017. .

Civano, F., Mignoli, M., Comastri, A. et al. The HELLAS2XMM survey: XI. Unveiling the nature of X-ray bright optically normal galaxies. *Astronomy & Astrophysics*, 476 (3):1223–1233, Dec. 2007. ISSN 0004-6361, 1432-0746. . URL http://www.aanda.org/10.1051/0004-6361:20077945.

Civano, F., Hickox, R.C., Puccetti, S. et al. The Nustar Extragalactic Surveys: Overview and Catalog from the COSMOS Field. *ApJ*, 808(2):185, Aug. 2015. .

Civano, F., Marchesi, S., Comastri, A. et al. The Chandra Cosmos Legacy Survey: Overview and Point Source Catalog. *ApJ*, 819(1):62, Mar. 2016. .

Clerc, N., Merloni, A., Zhang, Y.Y. et al. SPIDERS: the spectroscopic follow-up of X-ray selected clusters of galaxies in SDSS-IV. *MNRAS*, 463(4):4490–4515, Dec. 2016. .

Cocchia, F., Fiore, F., Vignali, C. et al. The HELLAS2XMM survey: VIII. Optical identifications of the extended sample. *Astronomy & Astrophysics*, 466(1):31–40, Apr. 2007. ISSN 0004-6361, 1432-0746. . URL http://www.aanda.org/10.1051/0004-6361:20065170.

Comastri, A. Compton-Thick AGN: The Dark Side of the X-Ray Background. In Barger, A.J., editor, *Supermassive Black Holes in the Distant Universe*, volume 308 of *Astrophysics and Space Science Library*, page 245, Aug. 2004. .

Comastri, A., Brusa, M., Ciliegi, P. et al. On the nature of X-ray Bright Optically Normal galaxies. *astro-ph/0203019, "New Visions of the X-ray Universe in the XMM-Newton and Chandra Era", 26-30 November 2001, ESTEC, The Netherlands*, Mar. 2002. URL http://ukads.nottingham.ac.uk/cgi-bin/nph-bib_query?bibcode=2002astro.ph..3019C&db_key=PRE.

Comparat, J., Richard, J., Kneib, J.P. et al. The 0.1 ¡z ¡ 1.65 evolution of the bright end of the [O ii] luminosity function. *A&A*, 575:A40, Mar. 2015. .

Comparat, J., Merloni, A., Dwelly, T. et al. The final SDSS-IV/SPIDERS X-ray point source spectroscopic catalogue. *A&A*, 636:A97, Apr. 2020. .

Costagliola, F., Aalto, S., Sakamoto, K. et al. High-resolution mm and cm study of the obscured LIRG NGC 4418 . A compact obscured nucleus fed by in-falling gas? *A&A*, 556:A66, Aug. 2013. .

Cusumano, G., La Parola, V., Segreto, A. et al. The Palermo Swift-BAT hard X-ray catalogue. III. Results after 54 months of sky survey. *A&A*, 524:A64, Dec. 2010. .

Cutri, R.M. and et al. VizieR Online Data Catalog: WISE All-Sky Data Release (Cutri+ 2012). *VizieR Online Data Catalog*, page II/311, Apr. 2012. URL https://ui.adsabs.harvard.edu/abs/2012yCat.2311....0C. ADS Bibcode: 2012yCat.2311....0C.

Cutri, R.M., Skrutskie, M.F., van Dyk, S. et al. VizieR Online Data Catalog: 2MASS All-Sky Catalog of Point Sources (Cutri+ 2003). *VizieR Online Data Catalog*, art. II/246, June 2003.

Cutri, R.M., Wright, E.L., Conrow, T. et al. Explanatory Supplement to the AllWISE Data Release Products. Technical report, Nov. 2013.

Cutri, R.M., Wright, E.L., Conrow, T. et al. VizieR Online Data Catalog: AllWISE Data Release (Cutri+ 2013). *VizieR Online Data Catalog*, art. II/328, Feb. 2021.

D'Abrusco, R., Massaro, F., Paggi, A. et al. THE *WISE* BLAZAR-LIKE RADIO-LOUD SOURCES: AN ALL-SKY CATALOG OF CANDIDATE γ-RAY BLAZARS. *Astrophys. J. Suppl. Ser.*, 215(1):14, Oct. 2014. ISSN 1538-4365. . URL http://stacks.iop.org/0067-0049/215/i=1/a=14?key=crossref.6e19e7fa45e62fc6c9f63ffe8ffedeb0.

Dawson, K.S., Schlegel, D.J., Ahn, C.P. et al. The Baryon Oscillation Spectroscopic Survey of SDSS-III. *AJ*, 145(1):10, Jan. 2013. .

Dawson, K.S., Kneib, J.P., Percival, W.J. et al. The SDSS-IV Extended Baryon Oscillation Spectroscopic Survey: Overview and Early Data. *AJ*, 151(2):44, Feb. 2016. .

de Grijp, M.H.K., Miley, G.K., Lub, J. et al. Infrared Seyferts: a new population of active galaxies? *Nature*, 314:240–242, Mar. 1985. ISSN 0028-0836. . URL https://ui.adsabs.harvard.edu/abs/1985Natur.314..240D. ADS Bibcode: 1985Natur.314..240D.

de Grijp, M.H.K., Lub, J. and Miley, G.K. Warm IRAS sources. I. A catalogue of AGN candidates from the point source catalog. *A&AS*, 70:95–114, July 1987.

de Jong, R.S., Barden, S.C., Bellido-Tirado, O. et al. 4MOST: the 4-metre Multi-Object Spectroscopic Telescope project at preliminary design review. In Evans, C.J., Simard, L. and Takami, H., editors, *Ground-based and Airborne Instrumentation for Astronomy VI*, volume 9908 of *Society of Photo-Optical Instrumentation Engineers (SPIE) Conference Series*, page 99081O, Aug. 2016. .

Delvecchio, I., Daddi, E., Aird, J. et al. The Evolving AGN Duty Cycle in Galaxies Since z $\sim$ 3 as Encoded in the X-Ray Luminosity Function. *ApJ*, 892(1):17, Mar. 2020. .

Di Matteo, T., Springel, V. and Hernquist, L. Energy input from quasars regulates the growth and activity of black holes and their host galaxies. *Nature*, 433(7026):604–607, Feb 2005. .

Dickinson, M., Giavalisco, M. and GOODS Team. The Great Observatories Origins Deep Survey. In Bender, R. and Renzini, A., editors, *The Mass of Galaxies at Low and High Redshift*, page 324, Jan. 2003. .

Dietrich, J., Weiner, A.S., Ashby, M.L.N. et al. The AGN luminosity fraction in merging galaxies. *MNRAS*, 480(3):3562–3583, Nov. 2018. .

Doi, M., Tanaka, M., Fukugita, M. et al. Photometric Response Functions of the Sloan Digital Sky Survey Imager. *AJ*, 139(4):1628–1648, Apr. 2010. .

Donley, J.L., Koekemoer, A.M., Brusa, M. et al. Identifying Luminous Active Galactic Nuclei in Deep Surveys: Revised IRAC Selection Criteria. *ApJ*, 748:142, Apr. 2012. .

Donoso, E., Yan, L., Tsai, C. et al. ORIGIN OF 12 μm EMISSION ACROSS GALAXY POPULATIONS FROM *WISE* AND SDSS SURVEYS. *ApJ*, 748(2):80, Apr. 2012. ISSN 0004-637X, 1538-4357. . URL http://stacks.iop.org/0004-637X/748/i=2/a=80?key=crossref.d38107493d0351a92d388c962234f730.

Dwelly, T., Salvato, M., Merloni, A. et al. SPIDERS: selection of spectroscopic targets using AGN candidates detected in all-sky X-ray surveys. *MNRAS*, 469:1065–1095, July 2017. ISSN 0035-8711. . URL https://ui.adsabs.harvard.edu/abs/2017MNRAS.469.1065D. ADS Bibcode: 2017MNRAS.469.1065D.

Eisenhardt, P.R.M., Marocco, F., Fowler, J.W. et al. The CatWISE Preliminary Catalog: Motions from WISE and NEOWISE Data. *ApJS*, 247(2):69, Apr. 2020. .

Eisenstein, D.J., Annis, J., Gunn, J.E. et al. Spectroscopic Target Selection for the Sloan Digital Sky Survey: The Luminous Red Galaxy Sample. *AJ*, 122(5):2267–2280, Nov. 2001. .

Elitzur, M. On the Unification of Active Galactic Nuclei. *ApJ*, 747(2):L33, Mar. 2012. .

Ellison, S.L., Viswanathan, A., Patton, D.R. et al. A definitive merger-AGN connection at z $\sim$ 0 with CFIS: mergers have an excess of AGN and AGN hosts are more frequently disturbed. *MNRAS*, 487(2):2491–2504, Aug. 2019. .

Evans, I.N., Primini, F.A., Glotfelty, K.J. et al. The Chandra Source Catalog. *ApJS*, 189 (1):37–82, July 2010. .

Evans, I.N., Primini, F.A., Miller, J.B. et al. The Chandra Source Catalog — A Billion X-ray Photons. In *American Astronomical Society Meeting Abstracts #235*, volume 235 of *American Astronomical Society Meeting Abstracts*, page 154.05, Jan. 2020a.

Evans, P.A., Beardmore, A.P., Page, K.L. et al. Methods and results of an automatic analysis of a complete sample of Swift-XRT observations of GRBs. *MNRAS*, 397: 1177–1201, Aug. 2009. .

Evans, P.A., Page, K.L., Osborne, J.P. et al. 2SXPS: An Improved and Expanded Swift X-Ray Telescope Point-source Catalog. *ApJS*, 247(2):54, Apr. 2020b. .

Evans, P.A., Page, K.L., Bearmore, A.P. et al. The Living Swift-XRT Point Source catalogue and real-time transient detector. *arXiv e-prints*, art. arXiv:2208.14478, Aug. 2022.

Fabian, A.C. The obscured growth of massive black holes. *MNRAS*, 308(4):L39–L43, Oct. 1999. ISSN 0035-8711, 1365-2966. . URL https://academic.oup.com/mnras/article-lookup/doi/10.1046/j.1365-8711.1999.03017.x.

Fabian, A.C. and Iwasawa, K. The mass density in black holes inferred from the X-ray background. *MNRAS*, 303:L34–L36, Feb. 1999. URL http://ukads.nottingham.ac.uk/cgi-bin/nph-bib_query?bibcode=1999MNRAS.303L..34F&db_key=AST.

Falstad, N., Aalto, S., König, S. et al. CON-quest. Searching for the most obscured galaxy nuclei. *A&A*, 649:A105, May 2021. .

Fanaroff, B.L. and Riley, J.M. The morphology of extragalactic radio sources of high and low luminosity. *MNRAS*, 167:31P–36PP, May 1974. URL http://ukads.nottingham.ac.uk/cgi-bin/nph-bib_query?bibcode=1974MNRAS.167P..31F&db_key=AST.

Fazio, G.G., Hora, J.L., Allen, L.E. et al. The Infrared Array Camera (IRAC) for the Spitzer Space Telescope. *ApJS*, 154:10–17, Sept. 2004. .

Feltre, A., Charlot, S., Mignoli, M. et al. Ultraviolet/optical emission of the ionised gas in AGN: diagnostics of the ionizing source and gas properties. *Frontiers in Astronomy and Space Sciences*, 4:32, Nov. 2017. .

Foreman-Mackey, D., Hogg, D.W., Lang, D. et al. emcee : The MCMC Hammer. *PASP*, 125(925):306–312, Mar. 2013. ISSN 00046280, 15383873. . URL http://iopscience.iop.org/article/10.1086/670067.

Gandhi, P. X-ray studies of active galactic nuclei. *Asian Journal of Physics*, 13:90–107, Jan. 2005.

Gandhi, P. and Fabian, A.C. X-ray background synthesis: the infrared connection. *MNRAS*, 339(4):1095–1102, Mar. 2003. ISSN 0035-8711, 1365-2966. . URL https://academic.oup.com/mnras/article-lookup/doi/10.1046/j.1365-8711.2003.06259.x.

Gandhi, P., Crawford, C.S. and Fabian, A.C. Very Large Telescope near-infrared spectra of hard serendipitous Chandra sources. *MNRAS*, 337(3):781–794, Dec. 2002. ISSN 0035-8711, 1365-2966. . URL https://academic.oup.com/mnras/article-lookup/doi/10.1046/j.1365-8711.2002.05805.x.

Gandhi, P., Crawford, C.S., Fabian, A.C. et al. Powerful, obscured active galactic nuclei among X-ray hard, optically dim serendipitous Chandra sources. *MNRAS*, 348:529–550, Feb. 2004.

Gandhi, P., Horst, H., Smette, A. et al. Resolving the mid-infrared cores of local Seyferts. *Astronomy & Astrophysics*, 502(2):457–472, Aug. 2009. ISSN 0004-6361, 1432-0746. . URL http://www.aanda.org/10.1051/0004-6361/200811368.

Gao, F., Wang, L., Pearson, W.J. et al. Mergers trigger active galactic nuclei out to z $\sim$ 0.6. *A&A*, 637:A94, May 2020. .

Gehrels, N., Chincarini, G., Giommi, P. et al. The Swift Gamma-Ray Burst Mission. *ApJ*, 611:1005–1020, Aug. 2004. .

Gezari, S., Hung, T., Cenko, S.B. et al. iPTF Discovery of the Rapid "Turn-on" of a Luminous Quasar. *ApJ*, 835(2):144, Feb. 2017. .

Giacconi, R., Gursky, H., Paolini, F.R. et al. Evidence for x Rays From Sources Outside the Solar System. *Phys Rev Lett*, 9(11):439–443, Dec. 1962. ISSN 0031-9007. . URL https://link.aps.org/doi/10.1103/PhysRevLett.9.439.

Gilli, R., Zamorani, G., Miyaji, T. et al. The spatial clustering of X-ray selected AGN in the XMM-COSMOS field. *A&A*, 494(1):33–48, Jan. 2009. .

Glikman, E., Urrutia, T., Lacy, M. et al. FIRST-2MASS Red Quasars: Transitional Objects Emerging from the Dust. *ApJ*, 757(1):51, Sept. 2012. .

Glikman, E., Simmons, B., Mailly, M. et al. Major Mergers Host the Most-luminous Red Quasars at z ~2: A Hubble Space Telescope WFC3/IR Study. *ApJ*, 806(2):218, June 2015. .

Glikman, E., Lacy, M., LaMassa, S. et al. The WISE-2MASS Survey: Red Quasars Into the Radio Quiet Regime. *ApJ*, 934(2):119, Aug. 2022. .

Gonzalez, A.G., Wilkins, D.R. and Gallo, L.C. Probing the geometry and motion of AGN coronae through accretion disc emissivity profiles. *MNRAS*, 472(2):1932–1945, Dec. 2017. .

Goulding, A.D. and Alexander, D.M. Towards a complete census of AGN in nearby Galaxies: a large population of optically unidentified AGN. *MNRAS*, 398:1165–1193, Sept. 2009. .

Goulding, A.D., Alexander, D.M., Mullaney, J.R. et al. Searching for Compton-thick active galactic nuclei at z$\sim$ 0.1. *MNRAS*, 411(2):1231–1244, Feb. 2011. .

Greenwell, C., Gandhi, P., Stern, D. et al. A candidate optically quiescent quasar lacking narrow emission lines. *MNRAS*, 503(1):L80–L84, May 2021. .

Greenwell, C., Gandhi, P., Lansbury, G. et al. XMM and NuSTAR Observations of an Optically Quiescent Quasar. *ApJ*, 934(2):L34, Aug. 2022. .

Grogin, N.A., Kocevski, D.D., Faber, S.M. et al. CANDELS: The Cosmic Assembly Near-infrared Deep Extragalactic Legacy Survey. *ApJS*, 197(2):35, Dec. 2011. .

Gunn, J.E., Carr, M., Rockosi, C. et al. The Sloan Digital Sky Survey Photometric Camera. *AJ*, 116(6):3040–3081, Dec. 1998. .

Gupta, K.K., Ricci, C., Tortosa, A. et al. BAT AGN Spectroscopic Survey XXVII: scattered X-Ray radiation in obscured active galactic nuclei. *MNRAS*, 504(1):428–443, June 2021. .

Haardt, F. and Maraschi, L. A Two-Phase Model for the X-Ray Emission from Seyfert Galaxies. *ApJ*, 380:L51, Oct. 1991. .

Haas, M., Siebenmorgen, R., Schulz, B. et al. Spitzer IRS spectroscopy of 3CR radio galaxies and quasars:testing the unified schemes. *Astronomy & Astrophysics*, 442(3): L39–L43, Nov. 2005. ISSN 0004-6361, 1432-0746. . URL http://www.aanda.org/10.1051/0004-6361:200500185.

Hainline, K.N., Shapley, A.E., Greene, J.E. et al. The Rest-frame Ultraviolet Spectra of UV-selected Active Galactic Nuclei at z ~2-3. *ApJ*, 733(1):31, May 2011. .

Hainline, K.N., Reines, A.E., Greene, J.E. et al. Mid-infrared Colors of Dwarf Galaxies: Young Starbursts Mimicking Active Galactic Nuclei. *ApJ*, 832(2):119, Dec. 2016. .

Hao, L., Weedman, D.W., Spoon, H.W.W. et al. The Distribution of Silicate Strength in *Spitzer* Spectra of AGNs and ULIRGs. *ApJ*, 655(2):L77–L80, Feb. 2007. ISSN 0004-637X, 1538-4357. . URL http://stacks.iop.org/1538-4357/655/i=2/a=L77.

Harrison, C. *Observational constraints on the influence of active galactic nuclei on the evolution of galaxies*. PhD thesis, Durham University, UK, Sept. 2014.

Harrison, F.A., Craig, W.W., Christensen, F.E. et al. The Nuclear Spectroscopic Telescope Array (NuSTAR) High-energy X-Ray Mission. *ApJ*, 770(2):103, June 2013. .

HI4PI Collaboration, Ben Bekhti, N., Flöer, L. et al. HI4PI: A full-sky H I survey based on EBHIS and GASS. *A&A*, 594:A116, Oct. 2016. .

Hickox, R.C. and Alexander, D.M. Obscured Active Galactic Nuclei. *ARA&A*, 56:625–671, Sept. 2018. .

Holoien, T.W.S., Brown, J.S., Stanek, K.Z. et al. The ASAS-SN bright supernova catalogue - II. 2015. *MNRAS*, 467(1):1098–1111, May 2017. .

Hönig, S.F. Redefining the Torus: A Unifying View of AGNs in the Infrared and Submillimeter. *ApJ*, 884(2):171, Oct. 2019. .

Hopkins, P.F., Hernquist, L., Cox, T.J. et al. A Unified, Merger-driven Model of the Origin of Starbursts, Quasars, the Cosmic X-Ray Background, Supermassive Black Holes, and Galaxy Spheroids. *Astrophys. J. Suppl. Ser.*, 163(1):1–49, Mar. 2006. ISSN 0067-0049, 1538-4365. . URL http://stacks.iop.org/0067-0049/163/i=1/a=1.

Hopkins, P.F., Hernquist, L., Cox, T.J. et al. A Cosmological Framework for the Co-evolution of Quasars, Supermassive Black Holes, and Elliptical Galaxies. I. Galaxy Mergers and Quasar Activity. *Astrophys. J. Suppl. Ser.*, 175(2):356–389, Apr. 2008. ISSN 0067-0049, 1538-4365. . URL http://stacks.iop.org/0067-0049/175/i=2/a=356.

Houck, J.R., Roellig, T.L., Van Cleve, J. et al. The infrared spectrograph on the Spitzer Space Telescope. In Mather, J.C., editor, *Optical, Infrared, and Millimeter Space Telescopes*, volume 5487 of *Society of Photo-Optical Instrumentation Engineers (SPIE) Conference Series*, pages 62–76, Oct. 2004. .

Huchra, J.P., Macri, L.M., Masters, K.L. et al. The 2MASS Redshift Survey – Description and Data Release. *ApJS*, 199:26, Apr. 2012. .

Hviding, R.E., Hickox, R.C., Hainline, K.N. et al. Characterizing the WISE-selected heavily obscured quasar population with optical spectroscopy from the Southern African Large Telescope. *MNRAS*, 474(2):1955–1969, Feb. 2018. .

Hönig, S.F., Watson, D., Kishimoto, M. et al. A dust-parallax distance of 19 megaparsecs to the supermassive black hole in NGC 4151. *at*, 515(7528):528–530, Nov. 2014. ISSN 0028-0836, 1476-4687. . URL http://www.nature.com/articles/nature13914.

Imanishi, M. The 3.4-μm absorption feature towards three obscured active galactic nuclei. *MNRAS*, 319(1):331–336, Nov. 2000. .

Imanishi, M., Dudley, C.C. and Maloney, P.R. Strong Evidence for a Buried Active Galactic Nucleus in UGC 5101: Implications for LINER-type Ultraluminous Infrared Galaxies. *ApJ*, 558(2):L93–L96, Sept. 2001. ISSN 0004637X. . URL http://stacks.iop.org/1538-4357/558/i=2/a=L93.

Imanishi, M., Dudley, C.C., Maiolino, R. et al. A Spitzer IRS Low-Resolution Spectroscopic Search for Buried AGNs in Nearby Ultraluminous Infrared Galaxies: A Constraint on Geometry between Energy Sources and Dust. *ApJS*, 171:72–100, July 2007. .

Imanishi, M., Maiolino, R. and Nakagawa, T. Spitzer Infrared Low-Resolution Spectroscopic Study of Buried Active Galactic Nuclei in a Complete Sample of Nearby Ultraluminous Infrared Galaxies. *ApJ*, 709(2):801–815, Feb. 2010. .

Isobe, T., Feigelson, E.D., Akritas, M.G. et al. Linear Regression in Astronomy. I. *ApJ*, 364:104, Nov 1990. .

Jansen, F., Lumb, D., Altieri, B. et al. XMM-Newton observatory: I. The spacecraft and operations. *A&A*, 365(1):L1–L6, Jan. 2001. ISSN 0004-6361, 1432-0746. . URL http://www.aanda.org/10.1051/0004-6361:20000036.

Jarrett, T.H., Chester, T., Cutri, R. et al. 2MASS Extended Source Catalog: Overview and Algorithms. *AJ*, 119(5):2498–2531, May 2000. .

Jarrett, T.H., Cohen, M., Masci, F. et al. THE *SPITZER* - *WISE* SURVEY OF THE ECLIPTIC POLES. *ApJ*, 735(2):112, July 2011. ISSN 0004-637X, 1538-4357. . URL http://stacks.iop.org/0004-637X/735/i=2/a=112?key=crossref.7d76f0b24bb67a1842b4eeac9d163dc8.

Jarrett, T.H., Cluver, M.E., Brown, M.J.I. et al. The WISE Extended Source Catalog (WXSC). I. The 100 Largest Galaxies. *ApJS*, 245(2):25, Dec. 2019. .

Joye, W.A. and Mandel, E. New Features of SAOImage DS9. In Payne, H.E., Jedrzejewski, R.I. and Hook, R.N., editors, *Astronomical Data Analysis Software and Systems XII*, volume 295 of *Astronomical Society of the Pacific Conference Series*, page 489, Jan. 2003.

Kennicutt, Jr., R.C. Star Formation in Galaxies Along the Hubble Sequence. *ARA&A*, 36:189–232, 1998. .

Kewley, L.J., Groves, B., Kauffmann, G. et al. The host galaxies and classification of active galactic nuclei. *MNRAS*, 372(3):961–976, Nov. 2006. ISSN 0035-8711, 1365-2966. . URL https://academic.oup.com/mnras/article-lookup/doi/10.1111/j.1365-2966.2006.10859.x.

Klindt, L., Alexander, D.M., Rosario, D.J. et al. Fundamental differences in the radio properties of red and blue quasars: evolution strongly favoured over orientation. *arXiv:1905.12108 [astro-ph]*, May 2019. URL http://arxiv.org/abs/1905.12108. arXiv: 1905.12108.

Kocevski, D.D., Brightman, M., Nandra, K. et al. Are Compton-thick AGNs the Missing Link between Mergers and Black Hole Growth? *ApJ*, 814(2):104, Dec. 2015. .

Kochanek, C.S., Eisenstein, D.J., Cool, R.J. et al. AGES: The AGN and Galaxy Evolution Survey. *ApJS*, 200(1):8, May 2012. .

Kollatschny, W., Grupe, D., Parker, M.L. et al. Optical and X-ray discovery of the changing-look AGN IRAS 23226-3843 showing extremely broad and double-peaked Balmer profiles. *A&A*, 638:A91, June 2020. .

Kollmeier, J.A., Zasowski, G., Rix, H.W. et al. SDSS-V: Pioneering Panoptic Spectroscopy. *arXiv e-prints*, art. arXiv:1711.03234, Nov. 2017.

Kong, M. and Ho, L.C. The Black Hole Masses and Eddington Ratios of Type 2 Quasars. *ApJ*, 859(2):116, June 2018. .

Kormendy, J. and Ho, L.C. Coevolution (Or Not) of Supermassive Black Holes and Host Galaxies. *ARA&A*, 51(1):511–653, Aug. 2013. ISSN 0066-4146, 1545-4282. . URL http://arxiv.org/abs/1304.7762. arXiv: 1304.7762.

Koss, M., Trakhtenbrot, B., Ricci, C. et al. BAT AGN Spectroscopic Survey. I. Spectral Measurements, Derived Quantities, and AGN Demographics. *ApJ*, 850(1):74, Nov. 2017. .

Koss, M.J., Assef, R., Baloković, M. et al. A New Population of Compton-thick AGNs Identified Using the Spectral Curvature above 10 keV. *Astrophys J*, 825:85, July 2016. ISSN 0004-637X. . URL https://ui.adsabs.harvard.edu/abs/2016ApJ...825...85K. ADS Bibcode: 2016ApJ...825...85K.

Koulouridis, E., Georgantopoulos, I., Loukaidou, G. et al. The XMM spectral catalog of SDSS optically selected Seyfert 2 galaxies. *A&A*, 586:A3, Feb. 2016. .

Kulkarni, S.R., Perley, D.A. and Miller, A.A. The Redshift Completeness of Local Galaxy Catalogs. *ApJ*, 860(1):22, June 2018. .

Lackner, C.N., Silverman, J.D., Salvato, M. et al. Late-Stage Galaxy Mergers in Cosmos to z $\sim$ 1. *AJ*, 148(6):137, Dec. 2014. .

Lacy, J.H., Soifer, B.T., Neugebauer, G. et al. Infrared optical, and ultraviolet observations of hydrogen line emission from Seyfert galaxies. *ApJ*, 256:75–82, May 1982. .

Lacy, M., Storrie-Lombardi, L.J., Sajina, A. et al. Obscured and Unobscured Active Galactic Nuclei in the Spitzer Space Telescope First Look Survey. *ApJS*, 154:166–169, Sept. 2004.

Lacy, M., Petric, A.O., Sajina, A. et al. Optical Spectroscopy and X-Ray Detections of a Sample of Quasars and Active Galactic Nuclei Selected in the Mid-Infrared from Two Spitzer Space Telescope Wide-Area Surveys. *AJ*, 133(1):186–205, Jan. 2007. .

Lacy, M., Ridgway, S.E., Gates, E.L. et al. The Spitzer Mid-infrared Active Galactic Nucleus Survey. I. Optical and Near-infrared Spectroscopy of Obscured Candidates and Normal Active Galactic Nuclei Selected in the Mid-infrared. *ApJS*, 208(2):24, Oct. 2013. .

Lacy, M., Ridgway, S.E., Sajina, A. et al. The Spitzer Mid-infrared AGN Survey. II. The Demographics and Cosmic Evolution of the AGN Population. *ApJ*, 802(2):102, Apr. 2015. .

LaMassa, S.M., Yaqoob, T., Ptak, A.F. et al. Delving Into X-ray Obscuration of Type 2 AGN, Near and Far. *ApJ*, 787:61, May 2014. .

LaMassa, S.M., Cales, S., Moran, E.C. et al. THE DISCOVERY OF THE FIRST "CHANGING LOOK" QUASAR: NEW INSIGHTS INTO THE PHYSICS AND PHENOMENOLOGY OF ACTIVE GALACTIC NUCLEI. *ApJ*, 800(2):144, Feb. 2015. ISSN 1538-4357. . URL http://stacks.iop.org/0004-637X/800/i=2/a=144?key=crossref.10a57273ddc10b68aa236b72d9cf297d.

Lamastra, A., Bianchi, S., Matt, G. et al. The bolometric luminosity of type 2 AGN from extinction-corrected [OIII]: No evidence of Eddington-limited sources. *Astronomy & Astrophysics*, 504(1):73–79, Sept. 2009. ISSN 0004-6361, 1432-0746. . URL http://www.aanda.org/10.1051/0004-6361/200912023.

Landt, H., Padovani, P., Perlman, E.S. et al. A physical classification scheme for blazars. *MNRAS*, 351(1):83–100, June 2004. ISSN 00358711,

13652966. . URL https://academic.oup.com/mnras/article-lookup/doi/10.1111/j.1365-2966.2004.07750.x.

Lansbury, G.B., Alexander, D.M., Aird, J. et al. The NuSTAR Serendipitous Survey: Hunting for the Most Extreme Obscured AGN at ¿10 keV. *ApJ*, 846(1):20, Sept. 2017a. .

Lansbury, G.B., Stern, D., Aird, J. et al. The NuSTAR Serendipitous Survey: The 40-month Catalog and the Properties of the Distant High-energy X-Ray Source Population. *ApJ*, 836(1):99, Feb. 2017b. .

Lansbury, G.B., Jarvis, M.E., Harrison, C.M. et al. Storm in a Teacup: X-Ray View of an Obscured Quasar and Superbubble. *ApJ*, 856(1):L1, Mar. 2018. .

Lansbury, G.B., Banerji, M., Fabian, A.C. et al. X-ray observations of luminous dusty quasars at z ¿ 2. *MNRAS*, 495(3):2652–2663, Jan. 2020. .

Laor, A. and Davis, S.W. Cold accretion discs and lineless quasars. *MNRAS*, 417(1): 681–688, Oct. 2011. .

Lawrence, A. The relative frequency of broad-lined and narrow-lined active galactic nuclei: implications for unified schemes. *MNRAS*, 252(4):586–592, Oct. 1991. ISSN 0035-8711, 1365-2966. . URL https://academic.oup.com/mnras/article-lookup/doi/10.1093/mnras/252.4.586.

Lawrence, A. and Elvis, M. MISALIGNED DISKS AS OBSCURERS IN ACTIVE GALAXIES. *ApJ*, 714(1):561–570, May 2010. ISSN 0004-637X, 1538-4357. . URL http://stacks.iop.org/0004-637X/714/i=1/a=561?key=crossref.0391d3732a87caa08fa222d193262415.

Levenson, N.A., Radomski, J.T., Packham, C. et al. ISOTROPIC MID-INFRARED EMISSION FROM THE CENTRAL 100 pc OF ACTIVE GALAXIES. *ApJ*, 703(1):390–398, Sept. 2009. ISSN 0004-637X, 1538-4357. . URL http://stacks.iop.org/0004-637X/703/i=1/a=390?key=crossref.31c27291e9c33a912b5541901f6f6bb0.

Li, J.T., Ballet, J., Miceli, M. et al. Spatially Resolved Broadband Synchrotron Emission from the Nonthermal Limbs of SN1006. *ApJ*, 864(1):85, Sept. 2018. .

Liske, J., Baldry, I.K., Driver, S.P. et al. Galaxy And Mass Assembly (GAMA): end of survey report and data release 2. *MNRAS*, 452(2):2087–2126, Sept. 2015. .

LSST Science Collaboration, Abell, P.A., Allison, J. et al. LSST Science Book, Version 2.0. *arXiv e-prints*, art. arXiv:0912.0201, Dec 2009.

Luo, B., Brandt, W.N., Hall, P.B. et al. X-ray Insights into the Nature of PHL 1811 Analogs and Weak Emission-line Quasars: Unification with a Geometrically Thick Accretion Disk? *ApJ*, 805(2):122, June 2015. .

Lusso, E., Comastri, A., Vignali, C. et al. The X-ray to optical-UV luminosity ratio of X-ray selected type 1 AGN in XMM-COSMOS. *A&A*, 512:A34, Mar. 2010. .

Lusso, E., Comastri, A., Simmons, B.D. et al. Bolometric luminosities and Eddington ratios of X-ray selected active galactic nuclei in the XMM-COSMOS survey. *MNRAS*, 425(1):623–640, Sept. 2012. .

MacArthur, L.A. Dust Sensitivity of Absorption-Line Indices. *ApJ*, 623(2):795–814, Apr. 2005. .

MacLeod, C.L., Green, P.J., Anderson, S.F. et al. Changing-look Quasar Candidates: First Results from Follow-up Spectroscopy of Highly Optically Variable Quasars. *ApJ*, 874(1):8, Mar. 2019. .

Madsen, K.K., Harrison, F.A., Markwardt, C.B. et al. Calibration of the NuSTAR High-energy Focusing X-ray Telescope. *ApJS*, 220(1):8, Sept. 2015. .

Magnier, E.A., Schlafly, E.F., Finkbeiner, D.P. et al. Pan-STARRS Photometric and Astrometric Calibration. *ApJS*, 251(1):6, Nov. 2020. .

Magorrian, J., Tremaine, S., Richstone, D. et al. The Demography of Massive Dark Objects in Galaxy Centers. *AJ*, 115(6):2285–2305, June 1998. ISSN 00046256. . URL http://stacks.iop.org/1538-3881/115/i=6/a=2285.

Mainieri, V., Bongiorno, A., Merloni, A. et al. Black hole accretion and host galaxies of obscured quasars in XMM-COSMOS. *Astronomy & Astrophysics*, 535:A80, Nov. 2011. ISSN 0004-6361, 1432-0746. . URL http://www.aanda.org/10.1051/0004-6361/201117259.

Mainzer, A., Bauer, J., Grav, T. et al. Preliminary Results from NEOWISE: An Enhancement to the Wide-field Infrared Survey Explorer for Solar System Science. *ApJ*, 731 (1):53, Apr. 2011. .

Maiolino, R., Marconi, A., Salvati, M. et al. Dust in active nuclei: I. Evidence for "anomalous"properties. *Astronomy & Astrophysics*, 365(2):28–36, Jan. 2001. ISSN 0004-6361, 1432-0746. . URL http://www.aanda.org/10.1051/0004-6361:20000177.

Maiolino, R., Comastri, A., Gilli, R. et al. Elusive active galactic nuclei. *MNRAS*, 344(4): L59–L64, Oct. 2003. ISSN 0035-8711, 1365-2966. . URL https://academic.oup.com/mnras/article-lookup/doi/10.1046/j.1365-8711.2003.07036.x.

Maiolino, R., Shemmer, O., Imanishi, M. et al. Dust covering factor, silicate emission, and star formation in luminous QSOs. *A&A*, 468(3):979–992, June 2007. ISSN 0004-6361, 1432-0746. . URL http://www.aanda.org/10.1051/0004-6361:20077252.

Majewski, S.R., Schiavon, R.P., Frinchaboy, P.M. et al. The Apache Point Observatory Galactic Evolution Experiment (APOGEE). *AJ*, 154(3):94, Sept. 2017. .

Malkan, M.A., Jensen, L.D., Rodriguez, D.R. et al. Emission Line Properties of Seyfert Galaxies in the 12 μm Sample. *ApJ*, 846(2):102, Sept. 2017. .

Marchesi, S., Civano, F., Elvis, M. et al. The Chandra COSMOS Legacy survey: optical/IR identifications. *ApJ*, 817(1):34, Jan. 2016. .

Marconi, A., Risaliti, G., Gilli, R. et al. Local supermassive black holes, relics of active galactic nuclei and the X-ray background. *MNRAS*, 351(1):169–185, June 2004. ISSN 00358711, 13652966. . URL https://academic.oup.com/mnras/article-lookup/doi/10.1111/j.1365-2966.2004.07765.x.

Marin, F. Are there reliable methods to estimate the nuclear orientation of Seyfert galaxies? *MNRAS*, 460(4):3679–3705, Aug. 2016. .

Marocco, F., Eisenhardt, P.R.M., Fowler, J.W. et al. The CatWISE2020 Catalog. *ApJS*, 253 (1):8, Mar. 2021. .

Márquez, I., Masegosa, J., González-Martin, O. et al. The AGN nature of LINER nuclear sources. *Frontiers in Astronomy and Space Sciences*, 4:34, Nov. 2017. .

Martini, P. and Weinberg, D.H. Quasar Clustering and the Lifetime of Quasars. *ApJ*, 547(1):12–26, Jan. 2001. .

Massaro, F., D'Abrusco, R., Tosti, G. et al. THE *WISE* GAMMA-RAY STRIP PARAMETERIZATION: THE NATURE OF THE GAMMA-RAY ACTIVE GALACTIC NUCLEI OF UNCERTAIN TYPE. *ApJ*, 750(2):138, May 2012. ISSN 0004-637X, 1538-4357. . URL http://stacks.iop.org/0004-637X/750/i=2/a=138?key=crossref.f4efdc1e60fd369fba41a39e4d2af590.

Mateos, S., Alonso-Herrero, A., Carrera, F.J. et al. Using the Bright Ultrahard *XMM-Newton* survey to define an IR selection of luminous AGN based on *WISE* colours: AGN selection with WISE. *MNRAS*, 426(4):3271–3281, Nov. 2012. ISSN 00358711. . URL https://academic.oup.com/mnras/article-lookup/doi/10.1111/j.1365-2966.2012.21843.x.

Mechtley, M., Jahnke, K., Windhorst, R.A. et al. Do the Most Massive Black Holes at z = 2 Grow via Major Mergers? *ApJ*, 830(2):156, Oct. 2016. .

Merloni, A., Predehl, P., Becker, W. et al. eROSITA Science Book: Mapping the Structure of the Energetic Universe. *eROSITA Science Book: Mapping the Structure of the Energetic Universe, arXiv:1209.3114*, Sept. 2012.

Merloni, A., Alexander, D.A., Banerji, M. et al. 4MOST Consortium Survey 6: Active Galactic Nuclei. *The Messenger*, 175:42–45, Mar. 2019. .

Messias, H., Afonso, J., Salvato, M. et al. A New Infrared Color Criterion for the Selection of 0 ¡ z ¡ 7 AGNs: Application to Deep Fields and Implications for JWST Surveys. *ApJ*, 754(2):120, Aug. 2012. .

Meusinger, H. and Balafkan, N. A large sample of Kohonen-selected SDSS quasars with weak emission lines: selection effects and statistical properties. *Astronomy & Astrophysics*, 568:A114, Aug. 2014. ISSN 0004-6361, 1432-0746. . URL http://www.aanda.org/10.1051/0004-6361/201423810.

Molina, M., Malizia, A., Masetti, N. et al. Investigating the true nature of three hard X-ray sources. *MNRAS*, 507(3):3423–3433, Nov. 2021. .

Moran, E.C., Filippenko, A.V. and Chornock, R. "Hidden" Seyfert 2 Galaxies and the X-Ray Background. *ApJ*, 579(2):L71–L74, Nov. 2002. ISSN 0004637X, 15384357. . URL http://stacks.iop.org/1538-4357/579/i=2/a=L71.

Mullaney, J.R., Daddi, E., Béthermin, M. et al. The hidden "AGN main sequence": Evidence for a universal black hole accretion to star formation rate ratio since z˜2 producing a M_bh-M* relation. *ApJ*, 753(2):L30, July 2012. ISSN 2041-8205, 2041-8213. . URL http://arxiv.org/abs/1204.2824. arXiv: 1204.2824.

Mullaney, J.R., Del-Moro, A., Aird, J. et al. The NuSTAR Extragalactic Surveys: Initial Results and Catalog from the Extended Chandra Deep Field South. *ApJ*, 808:184, Aug. 2015. .

Murphy, K.D. and Yaqoob, T. An X-ray spectral model for Compton-thick toroidal reprocessors. *MNRAS*, 397(3):1549–1562, Aug. 2009. .

Myers, A.D., Palanque-Delabrouille, N., Prakash, A. et al. The SDSS-IV Extended Baryon Oscillation Spectroscopic Survey: Quasar Target Selection. *ApJS*, 221(2):27, Dec. 2015. .

Nagar, N.M., Oliva, E., Marconi, A. et al. NGC 5506 unmasked as a Narrow Line Seyfert 1:. A direct view of the broad line region using near-IR spectroscopy. *A&A*, 391:L21–L24, Aug. 2002. .

Nandra, K. On the origin of the iron Kα line cores in active galactic nuclei. *MNRAS*, 368(1):L62–L66, May 2006. .

Nenkova, M., Sirocky, M.M., Ivezić, Ž. et al. AGN Dusty Tori. I. Handling of Clumpy Media. *ApJ*, 685:147–159, Sept. 2008a. .

Nenkova, M., Sirocky, M.M., Nikutta, R. et al. AGN Dusty Tori. II. Observational Implications of Clumpiness. *ApJ*, 685:160–180, Sept. 2008b. .

Netzer, H. Revisiting the Unified Model of Active Galactic Nuclei. *ARA&A*, 53(1):365–408, Aug. 2015. ISSN 0066-4146, 1545-4282. . URL http://arxiv.org/abs/1505.00811. arXiv: 1505.00811.

Netzer, H. and Laor, A. Dust in the Narrow-Line Region of Active Galactic Nuclei. *ApJ*, 404:L51, Feb 1993. .

Netzer, H., Mainieri, V., Rosati, P. et al. The correlation of narrow line emission and X-ray luminosity in active galactic nuclei. *Astronomy & Astrophysics*, 453(2):525–533, July 2006. ISSN 0004-6361, 1432-0746. . URL http://www.aanda.org/10.1051/0004-6361:20054203.

Neugebauer, G., Habing, H.J., van Duinen, R. et al. The Infrared Astronomical Satellite (IRAS) mission. *ApJ*, 278:L1–L6, Mar. 1984. .

Oh, K., Koss, M., Markwardt, C.B. et al. The 105-Month Swift-BAT All-sky Hard X-Ray Survey. *ApJS*, 235(1):4, Mar. 2018. .

Ohyama, Y., Sakamoto, K., Aalto, S. et al. Dusty Superwind from a Galaxy with a Compact Obscured Nucleus: Optical Spectroscopic Study of NGC 4418. *ApJ*, 871(2):191, Feb. 2019. .

Onori, F., La Franca, F., Ricci, F. et al. Detection of faint broad emission lines in type 2 AGN - I. Near-infrared observations and spectral fitting. *MNRAS*, 464(2):1783–1832, Jan. 2017a. .

Onori, F., Ricci, F., La Franca, F. et al. Detection of faint broad emission lines in type 2 AGN - II. On the measurement of the black hole mass of type 2 AGN and the unified model. *MNRAS*, 468(1):L97–L102, June 2017b. .

Oyabu, S., Ishihara, D., Malkan, M. et al. AKARI detections of hot dust in luminous infrared galaxies: Search for dusty active galactic nuclei. *Astronomy & Astrophysics*, 529:A122, May 2011. ISSN 0004-6361, 1432-0746. . URL http://www.aanda.org/10.1051/0004-6361/201014221.

Padovani, P. The faint radio sky: radio astronomy becomes mainstream. *A&ARv*, 24 (1):13, Sept. 2016. .

Padovani, P., Alexander, D.M., Assef, R.J. et al. Active galactic nuclei: what's in a name? *The Astronomy and Astrophysics Review*, 25(1):2, Aug. 2017. ISSN 1432-0754. . URL https://doi.org/10.1007/s00159-017-0102-9.

Pavlinsky, M., Akimov, V., Levin, V. et al. The ART-XC Instrument on board the SRG Mission. In O'Dell, S.L. and Pareschi, G., editors, *Society of Photo-Optical Instrumentation Engineers (SPIE) Conference Series*, volume 8147 of *Society of Photo-Optical Instrumentation Engineers (SPIE) Conference Series*, page 814706, Sept. 2011. .

Pavlinsky, M., Levin, V., Akimov, V. et al. ART-XC / SRG overview. In den Herder, J.W.A., Nikzad, S. and Nakazawa, K., editors, *Space Telescopes and Instrumentation 2018: Ultraviolet to Gamma Ray*, volume 10699 of *Society of Photo-Optical Instrumentation Engineers (SPIE) Conference Series*, page 106991Y, July 2018. .

Pons, E. and Watson, M.G. A new sample of X-ray selected narrow emission-line galaxies. I. The nature of optically elusive AGN. *A&A*, 568:A108, Aug. 2014. .

Powell, M.C., Cappelluti, N., Urry, C.M. et al. The Swift/BAT AGN Spectroscopic Survey. IX. The Clustering Environments of an Unbiased Sample of Local AGNs. *ApJ*, 858(2):110, May 2018. .

Prakash, A., Licquia, T.C., Newman, J.A. et al. The SDSS-IV Extended Baryon Oscillation Spectroscopic Survey: Luminous Red Galaxy Target Selection. *ApJS*, 224(2):34, June 2016. .

Predehl, P., Andritschke, R., Böhringer, H. et al. eROSITA on SRG. In Arnaud, M., Murray, S.S. and Takahashi, T., editors, *Space Telescopes and Instrumentation 2010: Ultraviolet to Gamma Ray*, volume 7732 of *Society of Photo-Optical Instrumentation Engineers (SPIE) Conference Series*, page 77320U, July 2010. .

Raimundo, S.I. and Fabian, A.C. Eddington ratio and accretion efficiency in active galactic nuclei evolution. *MNRAS*, 396(3):1217–1221, July 2009. .

Ramos Almeida, C. and Ricci, C. Nuclear obscuration in active galactic nuclei. *Nature Astronomy*, 1:679–689, Oct. 2017. .

Ramos Almeida, C., Levenson, N.A., Rodríguez Espinosa, J.M. et al. THE INFRARED NUCLEAR EMISSION OF SEYFERT GALAXIES ON PARSEC SCALES: TESTING THE CLUMPY TORUS MODELS. *ApJ*, 702(2):1127–1149, Sept. 2009. ISSN 0004-637X, 1538-4357. . URL http://stacks.iop.org/0004-637X/702/i=2/a=1127?key=crossref.7d9a23fd539dd6b0b2bdd94dba1f5420.

Ramos Almeida, C., Martínez González, M.J., Asensio Ramos, A. et al. Upholding the unified model for active galactic nuclei: VLT/FORS2 spectropolarimetry of Seyfert 2 galaxies. *MNRAS*, 461(2):1387–1403, Sept. 2016. .

Reyes, R., Zakamska, N.L., Strauss, M.A. et al. SPACE DENSITY OF OPTICALLY SELECTED TYPE 2 QUASARS. *AJ*, 136(6):2373–2390, Dec. 2008. ISSN 0004-6256, 1538-3881. . URL http://stacks.iop.org/1538-3881/136/i=6/a=2373?key=crossref.6aca35679c996f9325c588a62b5462e2.

Ricci, C. *Active galactic nuclei at hard X-ray energies: absorption, reflection and the unified model*. PhD thesis, University of Geneva, Switzerland, Jan. 2011.

Ricci, C., Ueda, Y., Koss, M.J. et al. Compton-thick Accretion in the Local Universe. *ApJ*, 815(1):L13, Dec. 2015. .

Ricci, C., Bauer, F.E., Arevalo, P. et al. IC 751: A New Changing Look AGN Discovered by NuSTAR. *ApJ*, 820:5, Mar. 2016. .

Ricci, C., Trakhtenbrot, B., Koss, M.J. et al. BAT AGN Spectroscopic Survey. V. X-Ray Properties of the Swift/BAT 70-month AGN Catalog. *ApJS*, 233(2):17, Dec. 2017a. .

Ricci, C., Trakhtenbrot, B., Koss, M.J. et al. The close environments of accreting massive black holes are shaped by radiative feedback. *Nature*, 549(7673):488–491, Sept. 2017b. .

Richards, G.T., Fan, X., Schneider, D.P. et al. Colors of 2625 Quasars at 0¡Z¡5 Measured in the Sloan Digital Sky Survey Photometric System. *AJ*, 121(5):2308–2330, May 2001. .

Richards, G.T., Fan, X., Newberg, H.J. et al. Spectroscopic Target Selection in the Sloan Digital Sky Survey: The Quasar Sample. *AJ*, 123:2945–2975, June 2002. ISSN 0004-6256. . URL https://ui.adsabs.harvard.edu/abs/2002AJ....123.2945R. ADS Bibcode: 2002AJ....123.2945R.

Riffel, R., Rodríguez-Ardila, A., Aleman, I. et al. Molecular hydrogen and [Fe II] in active galactic nuclei - III. Low-ionization nuclear emission-line region and star-forming galaxies. *MNRAS*, 430(3):2002–2017, Apr. 2013. .

Rigby, J.R., Rieke, G.H., Donley, J.L. et al. Why X-Ray-selected Active Galactic Nuclei Appear Optically Dull. *ApJ*, 645(1):115–133, July 2006. ISSN 0004-637X, 1538-4357. . URL http://stacks.iop.org/0004-637X/645/i=1/a=115.

Risaliti, G., Maiolino, R. and Salvati, M. The Distribution of Absorbing Column Densities among Seyfert 2 Galaxies. *ApJ*, 522:157–164, Sept. 1999. URL http://adsabs.harvard.edu/cgi-bin/nph-bib_query?bibcode=1999ApJ...522..157R&db_key=AST.

Risaliti, G., Marconi, A., Maiolino, R. et al. A new population of soft X-ray weak quasars. *A&A*, 371:37–44, May 2001. .

Risaliti, G., Elvis, M., Fabbiano, G. et al. Rapid Compton-thick/Compton-thin Transitions in the Seyfert 2 Galaxy NGC 1365. *ApJ*, 623:L93–L96, Apr. 2005. .

Roming, P.W.A., Kennedy, T.E., Mason, K.O. et al. The Swift Ultra-Violet/Optical Telescope. *Space Sci. Rev.*, 120(3-4):95–142, Oct. 2005. .

Roseboom, I.G., Lawrence, A., Elvis, M. et al. IR-derived covering factors for a large sample of quasars from WISE–UKIDSS–SDSS. *MNRAS*, 429(2):1494–1501, Feb. 2013. ISSN 0035-8711, 1365-2966. . URL http://academic.oup.com/mnras/article/429/2/1494/1042738/IRderived-covering-factors-for-a-large-sample-of.

Ross, N.P., Myers, A.D., Sheldon, E.S. et al. The SDSS-III Baryon Oscillation Spectroscopic Survey: Quasar Target Selection for Data Release Nine. *ApJS*, 199(1):3, Mar. 2012. .

Ross, N.P., Hamann, F., Zakamska, N.L. et al. Extremely Red Quasars from SDSS, BOSS and WISE: Classification of Optical Spectra. *MNRAS*, 453(4):3933–3953, Nov.

2015. ISSN 0035-8711, 1365-2966. . URL http://arxiv.org/abs/1405.1047. arXiv: 1405.1047.

Rovilos, E. and Georgantopoulos, I. Optical colours of AGN in the extended Chandra deep field South: obscured black holes in early type galaxies. *A&A*, 475(1):115–120, Nov. 2007. .

Ruiz, A., Georgakakis, A., Gerakakis, S. et al. The RapidXMM upper limit server: X-ray aperture photometry of the XMM-Newton archival observations. *MNRAS*, 511 (3):4265–4284, Apr. 2022. .

Salvato, M., Buchner, J., Budavári, T. et al. Finding counterparts for all-sky X-ray surveys with NWAY: a Bayesian algorithm for cross-matching multiple catalogues. *MNRAS*, 473(4):4937–4955, Feb. 2018. .

Sartori, L.F., Schawinski, K., Koss, M.J. et al. Joint NuSTAR and Chandra analysis of the obscured quasar in IC 2497 - Hanny's Voorwerp system. *MNRAS*, 474(2):2444–2451, Feb. 2018. .

Satyapal, S., Secrest, N.J., Ricci, C. et al. Buried AGNs in Advanced Mergers: Mid-infrared Color Selection as a Dual AGN Candidate Finder. *ApJ*, 848(2):126, Oct. 2017. ISSN 1538-4357. . URL http://stacks.iop.org/0004-637X/848/i=2/a=126?key=crossref.4a2e5746beb545b9042e9218022c7d1c.

Saxton, R.D., Read, A.M., Esquej, P. et al. The first XMM-Newton slew survey catalogue: XMMSL1. *A&A*, 480(2):611–622, Mar. 2008. .

Schawinski, K., Thomas, D., Sarzi, M. et al. Observational evidence for AGN feedback in early-type galaxies. *MNRAS*, 382(4):1415–1431, Dec. 2007. .

Schawinski, K., Koss, M., Berney, S. et al. Active galactic nuclei flicker: an observational estimate of the duration of black hole growth phases of $\sim 10^5$ yr. *MNRAS*, 451(3): 2517–2523, Aug. 2015. .

Schmidt, M. 3C 273 : A Star-Like Object with Large Red-Shift. *Nature*, 197:1040, Mar. 1963. .

Seeberger, R. and Saurer, W. Penetrating the "zone of avoidance". V. an optical survey for hidden galaxies in the region 90degr ¡= L ¡= 110degr , -10degr ¡= B ¡= +10degr. *A&AS*, 127:101–105, Jan. 1998. .

Shakura, N.I. and Sunyaev, R.A. Black holes in binary systems. Observational appearance. *A&A*, 24:337–355, 1973. URL http://ukads.nottingham.ac.uk/cgi-bin/nph-bib_query?bibcode=1973A%26A....24..337S&db_key=AST.

Shemmer, O., Trakhtenbrot, B., Anderson, S.F. et al. WEAK LINE QUASARS AT HIGH REDSHIFT: EXTREMELY HIGH ACCRETION RATES OR ANEMIC

BROAD-LINE REGIONS? *ApJ*, 722(2):L152–L156, Oct. 2010. ISSN 2041-8205, 2041-8213. . URL http://stacks.iop.org/2041-8205/722/i=2/a=L152?key=crossref.432f9e09fb987a17578cf7307de429af.

Shen, Y. and Ho, L.C. The diversity of quasars unified by accretion and orientation. *Nature*, 513(7517):210–213, Sept. 2014. .

Sheng, Z., Wang, T., Jiang, N. et al. Mid-infrared Variability of Changing-look AGNs. *ApJ*, 846(1):L7, Sept. 2017. .

Shu, X.W., Yaqoob, T. and Wang, J.X. The Cores of the Fe Kα Lines in Active Galactic Nuclei: An Extended Chandra High Energy Grating Sample. *ApJS*, 187(2):581–606, Apr. 2010. .

Silva, L., Maiolino, R. and Granato, G.L. Connecting the cosmic infrared background to the X-ray background. *MNRAS*, 355(3):973–985, Dec. 2004. .

Skrutskie, M.F., Cutri, R.M., Stiening, R. et al. The Two Micron All Sky Survey (2MASS). *AJ*, 131:1163–1183, Feb. 2006. .

Smith, K.L., Koss, M. and Mushotzky, R.F. AN INFRARED AND OPTICAL ANALYSIS OF A SAMPLE OF XBONGs AND OPTICALLY ELUSIVE AGNs. *ApJ*, 794(2):112, Sept. 2014. ISSN 1538-4357. . URL http://stacks.iop.org/0004-637X/794/i=2/a=112?key=crossref.2131121b51893d70056ea11ed5ea3801.

Springel, V., Di Matteo, T. and Hernquist, L. Modelling feedback from stars and black holes in galaxy mergers. *MNRAS*, 361(3):776–794, Aug. 2005. ISSN 00358711, 13652966. . URL https://academic.oup.com/mnras/article-lookup/doi/10.1111/j.1365-2966.2005.09238.x.

Stalevski, M., Ricci, C., Ueda, Y. et al. The dust covering factor in active galactic nuclei. *MNRAS*, 458(3):2288–2302, May 2016. .

Stern, D. THE X-RAY TO MID-INFRARED RELATION OF AGNs AT HIGH LUMINOSITY. *ApJ*, 807(2):129, July 2015. ISSN 1538-4357. . URL http://stacks.iop.org/0004-637X/807/i=2/a=129?key=crossref.2effb0c12f3a786d3a1fb426d2b511bb.

Stern, D., Eisenhardt, P., Gorjian, V. et al. Mid-Infrared Selection of Active Galaxies. *ApJ*, 631(1):163–168, Sept. 2005. ISSN 0004-637X, 1538-4357. . URL http://stacks.iop.org/0004-637X/631/i=1/a=163.

Stern, D., Assef, R.J., Benford, D.J. et al. MID-INFRARED SELECTION OF ACTIVE GALACTIC NUCLEI WITH THE *WIDE-FIELD INFRARED SURVEY EXPLORER* . I. CHARACTERIZING *WISE* -SELECTED ACTIVE GALACTIC NUCLEI IN COSMOS. *ApJ*, 753(1):30, July 2012. ISSN 0004-637X, 1538-4357. . URL http://stacks.iop.org/0004-637X/753/i=1/a=30?key=crossref.3454bf97ff9babbde824d1f5c1ca7a6e.

Stern, D., McKernan, B., Graham, M.J. et al. A Mid-IR Selected Changing-look Quasar and Physical Scenarios for Abrupt AGN Fading. *ApJ*, 864(1):27, Sept. 2018. .

Strauss, M.A., Weinberg, D.H., Lupton, R.H. et al. Spectroscopic Target Selection in the Sloan Digital Sky Survey: The Main Galaxy Sample. *AJ*, 124(3):1810–1824, Sept. 2002. .

Strüder, L., Briel, U., Dennerl, K. et al. The European Photon Imaging Camera on XMM-Newton: The pn-CCD camera. *A&A*, 365:L18–L26, Jan. 2001. .

Tanimoto, A., Ueda, Y., Odaka, H. et al. XCLUMPY: X-Ray Spectral Model from Clumpy Torus and Its Application to the Circinus Galaxy. *ApJ*, 877(2):95, June 2019. .

Toba, Y., Oyabu, S., Matsuhara, H. et al. The 9 and 18 Micrometer Luminosity Functions of Various Types of Galaxies with AKARI: Implication for the Dust Torus Structure of AGN. *Publ. Astron. Soc. Jpn.*, 65(5):113, Oct. 2013. ISSN 0004-6264, 2053-051X. . URL https://academic.oup.com/pasj/article-lookup/doi/10.1093/pasj/65.5.113.

Toba, Y., Oyabu, S., Matsuhara, H. et al. LUMINOSITY AND REDSHIFT DEPENDENCE OF THE COVERING FACTOR OF ACTIVE GALACTIC NUCLEI VIEWED WITH *WISE* AND SLOAN DIGITAL SKY SURVEY. *ApJ*, 788(1):45, May 2014. ISSN 0004-637X, 1538-4357. . URL http://stacks.iop.org/0004-637X/788/i=1/a=45?key=crossref.152cc26089b7c02d2dfa0b3a648e62ca.

Torres-Albà, N., Marchesi, S., Zhao, X. et al. Compton-thick AGN in the NuSTAR Era VI: The Observed Compton-thick Fraction in the Local Universe. *ApJ*, 922(2):252, Dec. 2021. .

Trindade Falcão, A., Kraemer, S.B., Fischer, T.C. et al. Hubble Space Telescope observations of [O III] emission in nearby QSO2s: physical properties of the ionized outflows. *MNRAS*, 500(1):1491–1504, Jan. 2021. .

Tsuchikawa, T., Kaneda, H., Oyabu, S. et al. A systematic study of silicate absorption features in heavily obscured AGNs observed by Spitzer/IRS. *A&A*, 651:A117, July 2021. .

Turner, M.J.L., Abbey, A., Arnaud, M. et al. The European Photon Imaging Camera on XMM-Newton: The MOS cameras. *A&A*, 365:L27–L35, Jan. 2001. .

Ueda, Y., Eguchi, S., Terashima, Y. et al. *Suzaku* Observations of Active Galactic Nuclei Detected in the *Swift* BAT Survey: Discovery of a "New Type" of Buried Supermassive Black Holes. *ApJ*, 664(2):L79–L82, Aug. 2007. ISSN 0004-637X, 1538-4357. . URL http://stacks.iop.org/1538-4357/664/i=2/a=L79.

Ueda, Y., Akiyama, M., Hasinger, G. et al. Toward the Standard Population Synthesis Model of the X-Ray Background: Evolution of X-Ray Luminosity and Absorption Functions of Active Galactic Nuclei Including Compton-Thick Populations. *ApJ*, 786

(2):104, Apr. 2014. ISSN 0004-637X, 1538-4357. . URL http://arxiv.org/abs/1402.1836. arXiv: 1402.1836.

Ueda, Y., Hashimoto, Y., Ichikawa, K. et al. [O iii] λ5007 and X-Ray Properties of a Complete Sample of Hard X-Ray Selected AGNs in the Local Universe. *ApJ*, 815(1): 1, Dec. 2015. .

Uttley, P., Cackett, E.M., Fabian, A.C. et al. X-ray reverberation around accreting black holes. *A&ARv*, 22:72, Aug. 2014. .

Vasudevan, R.V., Fabian, A.C., Gandhi, P. et al. The power output of local obscured and unobscured AGN: crossing the absorption barrier with Swift/BAT and IRAS. *MNRAS*, 402:1081–1098, Feb. 2010. .

Vernet, J., Dekker, H., D'Odorico, S. et al. X-shooter, the new wide band intermediate resolution spectrograph at the ESO Very Large Telescope. *A&A*, 536:A105, Dec. 2011. .

Véron-Cetty, M.P. and Véron, P. A catalogue of quasars and active nuclei: 13th edition. *A&A*, 518:A10, July 2010. .

Vestergaard, M. and Peterson, B.M. Determining Central Black Hole Masses in Distant Active Galaxies and Quasars. II. Improved Optical and UV Scaling Relationships. *ApJ*, 641(2):689–709, Apr. 2006. ISSN 0004-637X, 1538-4357. . URL http://stacks.iop.org/0004-637X/641/i=2/a=689.

Vignali, C., Alexander, D.M. and Comastri, A. The quest for Type 2 quasars: Chandra observations of luminous obscured quasars in the Sloan Digital Sky Survey. *MNRAS*, 373(1):321–329, Nov. 2006. .

Vignali, C., Alexander, D.M., Gilli, R. et al. Discovery of Compton-thick quasars in the Sloan Digital Sky Survey. *MNRAS*, 404(1):48–59, May 2010. .

Villforth, C., Koekemoer, A.M. and Grogin, N.A. A New Extensive Catalog of Optically Variable Active Galactic Nuclei in the GOODS Fields and a New Statistical Approach to Variability Selection. *ApJ*, 723(1):737–754, Nov. 2010. .

Villforth, C., Hamann, F., Rosario, D.J. et al. Morphologies of z $\sim$ 0.7 AGN host galaxies in CANDELS: no trend of merger incidence with AGN luminosity. *MNRAS*, 439(4): 3342–3356, Apr. 2014. .

Villforth, C., Hamilton, T., Pawlik, M.M. et al. Host galaxies of luminous z $\sim$ 0.6 quasars: major mergers are not prevalent at the highest AGN luminosities. *MNRAS*, 466(1):812–830, Apr. 2017. .

Voges, W., Aschenbach, B., Boller, T. et al. The ROSAT all-sky survey bright source catalogue. *A&A*, 349:389–405, Sept. 1999.

Wachter, K., Leach, R. and Kellogg, E. Parameter estimation in X-ray astronomy using maximum likelihood. *ApJ*, 230:274–287, May 1979. .

Wang, S., Liu, J., Qiu, Y. et al. CHANDRA ACIS Survey of X-Ray Point Sources: The Source Catalog. *ApJS*, 224(2):40, June 2016. .

Weaver, J.R., Kauffmann, O.B., Ilbert, O. et al. COSMOS2020: A Panchromatic View of the Universe to z 10 from Two Complementary Catalogs. *ApJS*, 258(1):11, Jan. 2022. .

Webb, N.A., Coriat, M., Traulsen, I. et al. The XMM-Newton serendipitous survey. IX. The fourth XMM-Newton serendipitous source catalogue. *A&A*, 641:A136, Sept. 2020. .

Weisskopf, M.C., Tananbaum, H.D., Van Speybroeck, L.P. et al. Chandra X-ray Observatory (CXO): overview. In Truemper, J.E. and Aschenbach, B., editors, *X-Ray Optics, Instruments, and Missions III*, volume 4012 of *Society of Photo-Optical Instrumentation Engineers (SPIE) Conference Series*, pages 2–16, July 2000. .

Wen, X.Q., Wu, H., Zhu, Y.N. et al. The stellar masses of galaxies from the 3.4 μm band of the WISE All-Sky Survey. *MNRAS*, 433(4):2946–2957, Aug. 2013. .

Wenger, M., Ochsenbein, F., Egret, D. et al. The SIMBAD astronomical database. The CDS reference database for astronomical objects. *A&AS*, 143:9–22, Apr. 2000. .

Werner, M.W., Roellig, T.L., Low, F.J. et al. The Spitzer Space Telescope Mission. *ApJS*, 154(1):1–9, Sept. 2004. .

Weston, M.E., McIntosh, D.H., Brodwin, M. et al. Incidence of WISE-Selected Obscured AGNs in Major Mergers and Interactions from the SDSS. *MNRAS*, 464(4):3882–3906, Feb. 2017. ISSN 0035-8711, 1365-2966. . URL http://arxiv.org/abs/1609.04832. arXiv: 1609.04832.

Wilkes, B.J., D'Abrusco, R. and Martínez-Galarza, R. Chandra X-ray Observatory Overview. In Wilkes, B. and Tucker, W., editors, *The Chandra X-ray Observatory*, pages 2–1. 2019. .

Wright, E.L., Eisenhardt, P.R.M., Mainzer, A.K. et al. The Wide-field Infrared Survey Explorer (WISE): Mission Description and Initial On-orbit Performance. *AJ*, 140:1868–1881, Dec. 2010. .

Wu, J., Brandt, W.N., Anderson, S.F. et al. X-Ray and Multiwavelength Insights into the Nature of Weak Emission-line Quasars at Low Redshift. *ApJ*, 747(1):10, Mar. 2012a. .

Wu, X.B., Hao, G., Jia, Z. et al. SDSS Quasars in the WISE Preliminary Data Release and Quasar Candidate Selection with Optical/Infrared Colors. *AJ*, 144(2):49, Aug. 2012b. .

XMM-SSC. VizieR Online Data Catalog: XMM-Newton slew survey Source Catalogue, version 2.0 (XMM-SSC, 2017). *VizieR Online Data Catalog*, art. IX/53, Jan. 2018.

Yan, L., Donoso, E., Tsai, C.W. et al. CHARACTERIZING THE MID-INFRARED EXTRAGALACTIC SKY WITH *WISE* AND SDSS. *AJ*, 145(3):55, Jan. 2013. ISSN 0004-6256, 1538-3881. . URL http://stacks.iop.org/1538-3881/145/i=3/a=55?key=crossref.244a395849871b0ff85f729585a37870.

Yang, G., Brandt, W.N., Alexander, D.M. et al. Evident black hole-bulge coevolution in the distant universe. *MNRAS*, 485(3):3721–3737, May 2019. ISSN 0035-8711, 1365-2966. . URL http://arxiv.org/abs/1903.00003. arXiv: 1903.00003.

Yang, G., Boquien, M., Buat, V. et al. X-CIGALE: Fitting AGN/galaxy SEDs from X-ray to infrared. *MNRAS*, 491(1):740–757, Jan. 2020. .

Yang, Q., Wu, X.B., Fan, X. et al. Discovery of 21 New Changing-look AGNs in the Northern Sky. *ApJ*, 862(2):109, July 2018. ISSN 1538-4357. . URL http://stacks.iop.org/0004-637X/862/i=2/a=109?key=crossref.783b7d79f5da4f340af1776afcecd9ef.

York, D.G., Adelman, J., Anderson, John E., J. et al. The Sloan Digital Sky Survey: Technical Summary. *AJ*, 120(3):1579–1587, Sep 2000. .

Yu, Q. and Tremaine, S. Observational constraints on growth of massive black holes. *MNRAS*, 335:965–976, Oct. 2002. URL http://ukads.nottingham.ac.uk/cgi-bin/nph-bib_query?bibcode=2002MNRAS.335..965Y&db_key=AST.

Yuan, S., Strauss, M.A. and Zakamska, N.L. Spectroscopic identification of type 2 quasars at z ¡ 1 in SDSS-III/BOSS. *MNRAS*, 462(2):1603–1615, Oct. 2016. .

Zakamska, N.L., Strauss, M.A., Krolik, J.H. et al. Candidate Type II Quasars from the Sloan Digital Sky Survey. I. Selection and Optical Properties of a Sample at 0.3<Z<0.83. *AJ*, 126:2125–2144, Nov. 2003. .

Zaw, I., Chen, Y.P. and Farrar, G.R. A Uniformly Selected, All-sky, Optical AGN Catalog. *ApJ*, 872(2):134, Feb. 2019. .

Zhao, X., Marchesi, S., Ajello, M. et al. The properties of the AGN torus as revealed from a set of unbiased NuSTAR observations. *A&A*, 650:A57, June 2021. .